INFORMATION TO USERS

This manuscript has been reproduced from the microfilm master. UMI films the text directly from the original or copy submitted. Thus, some thesis and dissertation copies are in typewriter face, while others may be from any type of computer printer.

The quality of this reproduction is dependent upon the quality of the copy submitted. Broken or indistinct print, colored or poor quality illustrations and photographs, print bleedthrough, substandard margins, and improper alignment can adversely affect reproduction.

In the unlikely event that the author did not send UMI a complete manuscript and there are missing pages, these will be noted. Also, if unauthorized copyright material had to be removed, a note will indicate the deletion.

Oversize materials (e.g., maps, drawings, charts) are reproduced by sectioning the original, beginning at the upper left-hand corner and continuing from left to right in equal sections with small overlaps. Each original is also photographed in one exposure and is included in reduced form at the back of the book.

Photographs included in the original manuscript have been reproduced xerographically in this copy. Higher quality 6" x 9" black and white photographic prints are available for any photographs or illustrations appearing in this copy for an additional charge. Contact UMI directly to order.

UMI

A Bell & Howell Information Company
300 North Zeeb Road, Ann Arbor MI 48106-1346 USA
313/761-4700 800/521-0600

THE EFFECTS OF TANK SIZE AND IMPELLER TYPE ON TURBULENT FLOCCULATION

BY

JOEL JEAN DUCOSTE

B.S., Rensselaer Polytechnic Institute, 1988
M.Eng., Rensselaer Polytechnic Institute, 1989

THESIS

Submitted in partial fulfillment of the requirements for the degree of
Doctor of Philosophy in Environmental Engineering in Civil Engineering
in the Graduate College of the
University of Illinois at Urbana-Champaign, 1996

Urbana, Illinois

UNIVERSITY OF ILLINOIS AT URBANA-CHAMPAIGN

THE GRADUATE COLLEGE

OCTOBER 1996

WE HEREBY RECOMMEND THAT THE THESIS BY

JOEL JEAN DUCOSTE

ENTITLED THE EFFECTS OF TANK SIZE AND IMPELLER TYPE ON TURBULENT FLOCCULATION

BE ACCEPTED IN PARTIAL FULFILLMENT OF THE REQUIREMENTS FOR THE DEGREE OF DOCTOR OF PHILOSOPHY

Director of Thesis Research

Head of Department

Committee on Final Examination†

Chairperson

† Required for doctor's degree but not for master's.

O-517

ABSTRACT

A basic conceptual and experimental study of the flocculation process is described. Current understanding of flocculation is based on the use of the average input power per unit volume, G_m, in both the design and operation of the flocculator. However, recent studies have shown that when G_m is held constant, the flocculation performance varies with tank size and impeller type. Therefore, this research was directed toward a more fundamental understanding of the relationship between the turbulence generated in the flocculation basin and the resulting steady state floc size distribution.

The turbulence in three square flocculation reactors of size $(6.7in)^3$ (≈5L), $1ft^3$ (≈28L), and $(2.7\ ft)^3$ (≈560L) with two impeller types (Rushton turbine and A310 fluid foil impeller) were evaluated experimentally using a laser Doppler velocimeter (LDV) and numerically using a computational fluid dynamic software called FIDAP. The results of both the experimental and numerical characterization of the fluid mechanics in the flocculation basin indicate that when G_m = constant, the rms turbulent fluctuating velocity was proportional to the impeller tip speed and increased with increasing tank size regardless of impeller type. The fluid mechanics results also indicate that the turbulence intensity (defined as the rms fluctuating velocity divided by the tip speed) was higher for the Rushton turbine than for the A310 foil impeller especially in the impeller discharge zone. Furthermore, the rms value in the impeller discharge zone was found to be proportional to $N_p^{0.5}ND$ regardless of tank size and impeller type. N_p represents the dimensionless impeller power number, N is the impeller angular velocity, and D is the impeller diameter. $N_p^{0.5}ND$ represents the magnitude of the rms fluctuating velocity in a region where the turbulent flow is anisotropic. These turbulence results suggest that G_m does not adequately describe the turbulence produced by the Rushton turbine or the A310 foil impeller in the 5L, 28L, and 560L square tanks.

The steady state floc size distribution was measured in situ using a photographic technique. The results of the photographic measurements show a shift in the cumulative particle size distribution from larger particles to smaller particles with increasing tank size regardless of impeller type. These photographic results also indicate a shift in the distribution from larger particles to smaller particles moving from the A310 foil impeller to the Rushton turbine. As a

measure of the steady state floc size distribution, the volume mean particle size, standard deviation, and maximum particle size were evaluated for each tank size and impeller type setup. These three particle distribution statistics were found to be a function of $N_p^{0.5}ND$. The experimental results showed that by increasing the quantity $N_p^{0.5}ND$, the volume mean particle size, standard deviation, and maximum particle size all decreased.

A population balance model was developed that included the turbulence intensity in the impeller discharge zone in the breakup part of the population balance rate equation. Reinforcing the photographic results of the floc size distribution, the population balance model predicts the shift in the particle size distribution from larger particles to smaller particles with increasing tank size. The model is also effective at predicting the shift in the particle size distribution from larger particles to smaller particles moving from the A310 foil impeller to the Rushton turbine.

The results from the flocculation experiments and model simulations suggest that the steady state floc size distribution is limited by the turbulence intensity in the impeller discharge zone. These results clearly show that steady state floc size distribution is not a function of the average intensity of the turbulent motion throughout the reactor volume as suggested in the models based on G_m.

DEDICATION

To my mother, Elsie Ducoste, for demonstrating hard work, commitment, and excellence to the medical field.

To my father, Ludner Ducoste, for sharing his love of mathematics and for always demonstrating his faith in my capabilities.

"There is in this world no such force as the force of a man determined rise"

W.E.B. Du Bois, March 5, 1910

ACKNOWLEDGMENT

I would like to express my sincere gratitude to my advisor, Dr. Mark M. Clark and committee members, Dr. Vernon L. Snoeyink and Dr. Ronald J. Adrian for their guidance and for sharing their extensive knowledge in water treatment and fluid mechanics.

I would also like to express my sincere gratitude to the following people at LIGHTNIN: Mr. James L. Stanton, Mr. Paul M. Kubera, Dr. Ronald J. Weetman, and Mr. Craig B. Bahr. Thank you for sharing your laser lab facility, mixing equipment, and your extensive knowledge in the field of mixing.

I would further like to thank all my friends whom I have met over the last five years. These friendships have made my experience in Champaign-Urbana a pleasant one.

I would also like to extend my gratitude to Mr. Tim Kramer (soon to be Dr. Kramer in 1997) for his friendship and for being a great officemate these last four years. I have enjoyed all our conversations about mixing, life, and southern talk (C. M. B. D. ii). I particularly enjoyed your sense of humor which made the week day go by quickly.

Most importantly, I would like to thank my soulmate Mrs. Dawn D. Ducoste for sharing your love, support, and for typing this very small thesis. I could not have made it this far without your friendship.

This research was funded by the National Science Foundation (BCS-90-57387 PYI) and by in-kind support from LIGHTNIN.

TABLE OF CONTENTS

LIST OF TABLES

LIST OF FIGURES

LIST OF SYMBOLS

The following were used in this manuscript:

C	= coefficient related to the characteristics of the floc particles
D	= impeller diameter
d	= particle diameter (m)
d_{max}	= maximum stable floc size (μm)
g	= gravitational acceleration (μm)
G	= local velocity gradient (m/s^2)
G_m	= characteristic average velocity gradient in the flocculation basin (1/s)
H	= location of impeller from bottom (m)
k	= turbulent kinetic energy (m^2/s^2)
L	= integral length scale (m)
n	= number concentration of particles
N	= rotational speed (rpm)
N_Q	= impeller flow number
N_p	= power number
P	= power drawn by mixer (Watt)
P_{dau}	= particle size distribution of daughter fragments from breakup
Q	= orthogonal tensor or transformation tensor
Q_p	= volumetric flow rate (m^3/s)
$t(I)$	= burst time (s)
T	= tank diameter (m)
$u(I)$	= fluctuating velocity component (m/s)
V	= tank volume (m^3)
w	= width of impeller blade tip (m)
$\overline{U_r}$	= radial mean velocity (m/s)
$\overline{U_\theta}$	= tangential mean velocity (m/s)
α	= collision efficiency factor
β	= collision frequency function (1/s)
ε	= local energy dissipation rate (m^2/s^3)
$\overline{\varepsilon}$	= tank average energy dissipation rate (m^2/s^3)
μ	= dynamic viscosity (kg/m s)
ρ	= density of fluid (kg/m^3)
ν	= kinematic viscosity (m^2/s^2)
σ	= rms fluctuating velocity (m/s)
τ	= time lag (s)
τ_c	= circulation time (s)
Φ	= work per unit volume per unit time or power per unit volume
e_r, e_θ, e_z	= unit vectors in old coordinate system
e_r^a, e_t^a, e_z^a	= unit vectors in new coordinate system

$\overline{TS}$	= impeller tip speed (m/s)
$\overline{v_r v_t}$	= radial-tangential Reynolds shear stress (m^2/s^2)
$\overline{v_r v_z}$	= radial-axial Reynolds shear stress (m^2/s^2)
$\overline{v_z v_t}$	= axial-tangential Reynolds shear stress (m^2/s^2)
$\overline{V}$	= resultant mean velocity (m/s)
V	= instantaneous velocity (m/s)
Vol	= tank volume (m^3)
$R_{v_r^a v_r^a}$	= autocorrelation coefficient of the velocity fluctuation in the radial direction in new coordinate system
δ_{ij}	= Kronecker delta

1.0 INTRODUCTION

In drinking water treatment, flocculation pilot plant tests are done frequently to gather information for use in designing or retrofitting full scale flocculation processes. In order to accurately translate the results found during a pilot plant study to full scale operation, a good understanding of the flocculation process is required. The purpose of flocculation is to physically transform smaller particles into larger aggregates that will eventually settle. The rate at which these aggregates grow is determined in large part by the speed at which interparticle collisions occur. As these aggregates or flocs increase in size, they are more susceptible to breakup caused by the hydrodynamic forces in the flocculation basin. This process of agglomeration and breakup leads to a steady state maximum floc size.

It has been shown by many investigators (Thomas, 1964; Parker et al., 1972; Francois, 1987; Sonntag & Russel, 1987; Tambo & Francois, 1991; Kusters, 1991) that this steady state maximum floc size is related to the average intensity of the turbulent fluid motion. While the complexity of this relationship varies with investigator, all of the formulations can be represented by the following equation:

$$d_{max} = \frac{C}{G_m{}^n} \tag{1.1}$$

where d_{max} is the maximum stable floc size, C is a coefficient related to the characteristics of the floc particles, G_m is the characteristic average velocity gradient in the flocculation basin, and n is a coefficient related to the particle breakup mode and the size of eddies that cause the disruption in either the inertial or the viscous subrange of turbulence, and the fractal dimension of the floc aggregate. Setting G_m = constant, Equation 1.1 would predict a fixed maximum stable floc size regardless of tank size. However, recent researchers have shown that a different floc size distribution was produced when the size of the flocculation process was changed with G_m=constant (Oldshue & Mady, 1978; Clark & Fiessinger, 1991; Clark et al., 1994). Equation

1.1 also fails to predict the changes in flocculation performance observed by other investigators using different kinds of mixing impellers with G_m=constant (Drobny, 1963; Patwardhan & Mirajgaonkar, 1970; Hanson & Cleasby, 1990; Clark et al., 1994; Sajjad & Cleasby, 1995).

In the past, investigators have tried to simulate the dynamics of the flocculation process using sophisticated population balance models. The models were developed to understand the mechanisms which influenced the dynamics of particle agglomeration and breakup during flocculation. These models included terms for both agglomeration and breakup of particles. The kinetics of particle agglomeration have been typically described by Smoluchowski's (1918) bimolecular-collision rate equation using a frequency function described by Saffman & Turner (1956) for the collision of two particles in turbulent fluid motion. The kinetics of particle breakup have been described by rate equations which are first order in particle concentration. Because of the random nature of floc breakage, some investigators (Lu & Spielman, 1985) have also included stochastic techniques to describe the distribution of the daughter size particles produced from the breakup of a parent particle. Many of the methods for breakup modeling include a maximum particle size cutoff definition similar to Equation 1.1 in order to model the maximum stable floc size found experimentally (Tambo & Watanabe, 1979; Lu & Spielman, 1985; Koh et al., 1987; Kusters, 1991).

Although these models were able to fit the particular investigators' experimental data, these models contain many empirical parameters and are not capable of predicting changes in particle size distributions due to changes in tank size and impeller type. This is not surprising since the use of Equation 1.1 assumes that breakup is only a function of the spatially averaged local turbulent intensity which is related to the dissipation rate at or below the Kolmogoroff microscale. There is, however, past photographic evidence that breakup typically occurs in the impeller discharge zone where the turbulence intensity is much higher than the spatial average (Hsu & Glasgow, 1983). Furthermore, the turbulence intensity in the impeller discharge region cannot be related to the local energy dissipation rate since the turbulent flow in this region is anisotropic (Ito et al., 1974, 1975).

There is growing evidence that a more complex relationship exists between particle agglomeration/breakup and the fluid mechanics generated in a flocculation basin that cannot be

fully described by existing population balance models nor by Equation 1.1. The inability of these models to properly predict the flocculation performance may lie with the oversimplified description of the three dimensional turbulent nature of the fluid mechanics with G_m. Consequently, there is a need to better understand how changes in tank size and impeller type affect the relationship between the complex fluid mechanics in a flocculation basin and the agglomeration/breakup process. This research project, then, focuses on studying the impact that turbulence, tank size, and impeller type have on flocculation performance.

The objectives of this project are the following:

1) To analyze the influence of tank size and impeller type on flocculation fluid mechanics when the average volumetric power input (G_m) is held constant using an experimental fluid mechanics technique called Laser Doppler Velocimetry (LDV).
2) To numerically model the flow field in a square stirred tank using a finite element software package called FIDAP in order to provide more detailed information about the fluid mechanics that would be very difficult to obtain experimentally.
3) To examine how the influence of tank size and impeller type on the fluid mechanics affect the growth of floc particles in the flocculation process.
4) To develop an agglomeration/breakup model that shows sensitivity to tank size and impeller type.

To accomplish the objectives stated above, three tank sizes (5 liters, 28 liters, 560 liters) and two impeller types (Rushton turbine and A310 fluid foil impeller) were investigated in this study. The fluid mechanics in these tanks were measured using an LDV system. The LDV experimental results were compared with the numerical results from FIDAP to check the accuracy of the FIDAP model. FIDAP results were then used to investigate the fluid flow in other regions of the tank not measured experimentally. After the flocculation experiments were performed, the resulting particle size distributions were measured. Next, the agglomeration/breakup model was developed using turbulence information from the LDV experiments and the FIDAP models.

Finally, the experimental particle size distributions were compared with the modeled particle size distributions to check the accuracy and predictability of the model.

The underlying theme throughout this study has been that given the same water chemistry, a successful prediction of the flocculation performance or the steady state floc size distribution in a turbulent mixing vessel requires information about the type of mixing impeller being used, the level of the turbulence intensity in the impeller discharge zone, and the size and shape of the mixing vessel. It is the hope of the author that the information found in this thesis will help researchers better understand the complex relationship that exists between the turbulence produced in the flocculation basin and the agglomeration/breakup dynamics of floc particles. The author hopes that this thesis will also better prepare water treatment professionals in the design and operation of pilot and full scale flocculators.

2.0 BACKGROUND & LITERATURE REVIEW

2.1 Fluid Mechanics Literature on Stirred Tank Reactors

Mechanical agitation of fluids using mixing impellers is one of the most important operations in process industries. Because of its importance, there have been many studies of measuring the fluid mechanics generated by different types of impellers in a stirred tank reactor. This section is devoted to reviewing those works which best describe some of the important flow phenomenon produced by a Rushton turbine and an A310 foil impeller in a stirred tank reactor.

2.1.1 Rushton Turbine in a Fully Baffled Cylindrical Tank

The most studied impeller-tank configuration is a Rushton turbine in a fully baffled cylindrical tank. This setup is shown in Figure 2.1.1. A Rushton turbine is considered to be a radial flow impeller. Upon impeller rotation, the Rushton turbine produces a flow that moves radially outward through the vertical section of the impeller swept volume. This fast moving jet flow entrains the surrounding fluid and reduces speed as the flow nears the tank wall. Close to the tank wall, the flow is divided into two parts which circulate in the bulk region of the tank and return to the impeller region (Figure 2.1.2). This qualitative description of the flow phenomena is well documented by many investigators. Some of the more particular flow structures documented by these investigators are tabulated in Appendix A.

As Appendix A suggests, the flow in the impeller discharge stream is characterized by the existence of strong radial and tangential components of the mean velocity and intense turbulence. The maximum radial velocity measured near the impeller tip ranges from 60 to 80 percent of the impeller tip speed. The maximum tangential velocity measured behind the impeller blade has been found to exceed the impeller tip speed by as much as 20 percent. However, the tangential velocity was found to decay more rapidly than the radial velocity in the radial direction (Figure 2.1.3). The variations found in the magnitude of the radial and tangential velocities reported are due to the different methods used to measure the fluid velocities (i.e. flow visualization, pitot tubes, hot wire anemometry, LDV), due to different fluid media used (i.e. air or water), and due

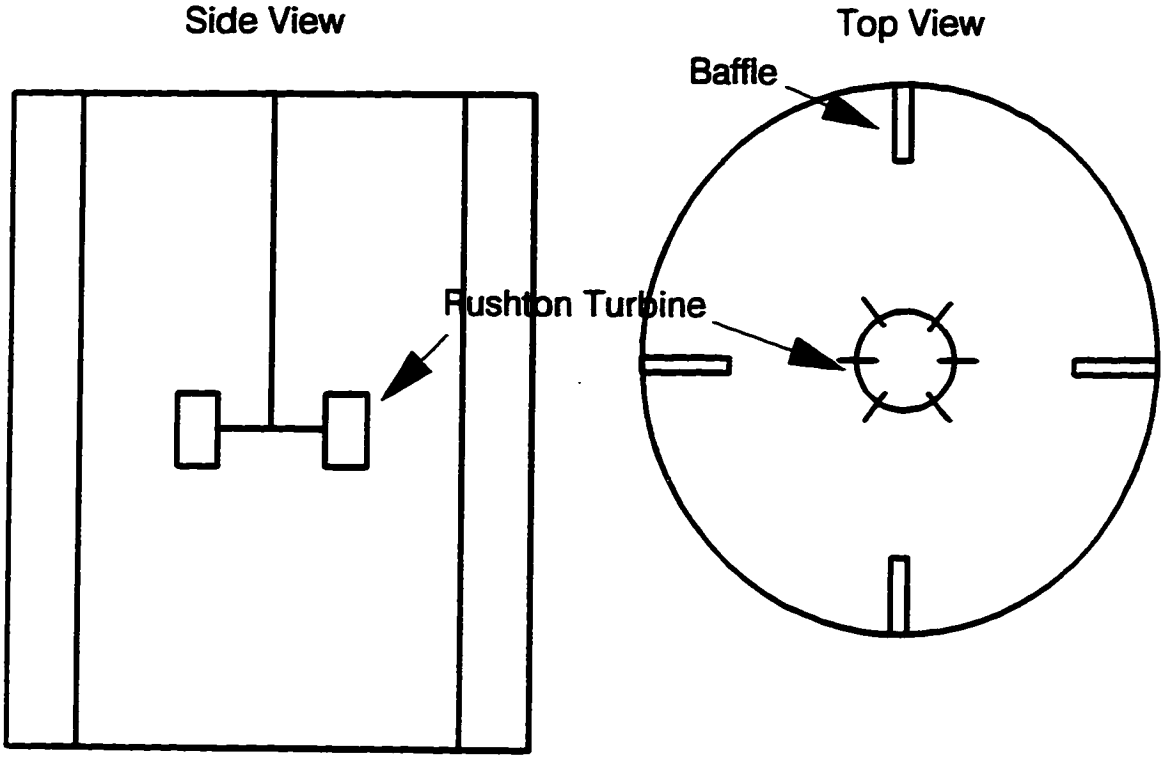

Figure 2.1.1: Rushton Turbine in a Fully Baffled Cylindrical Tank

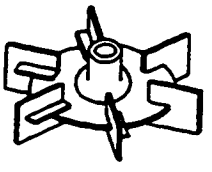

R100

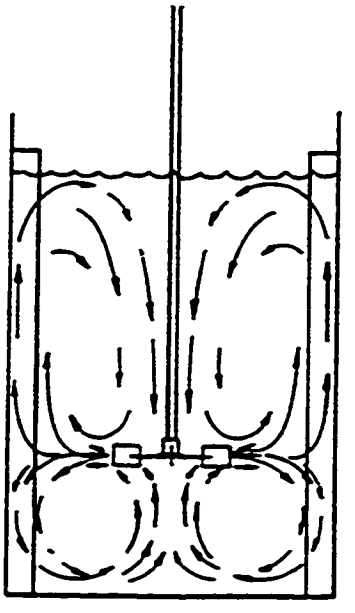

Figure 2.1.2: Flow Pattern of the Rushton Turbine (Oldshue & Herbst, 1992)

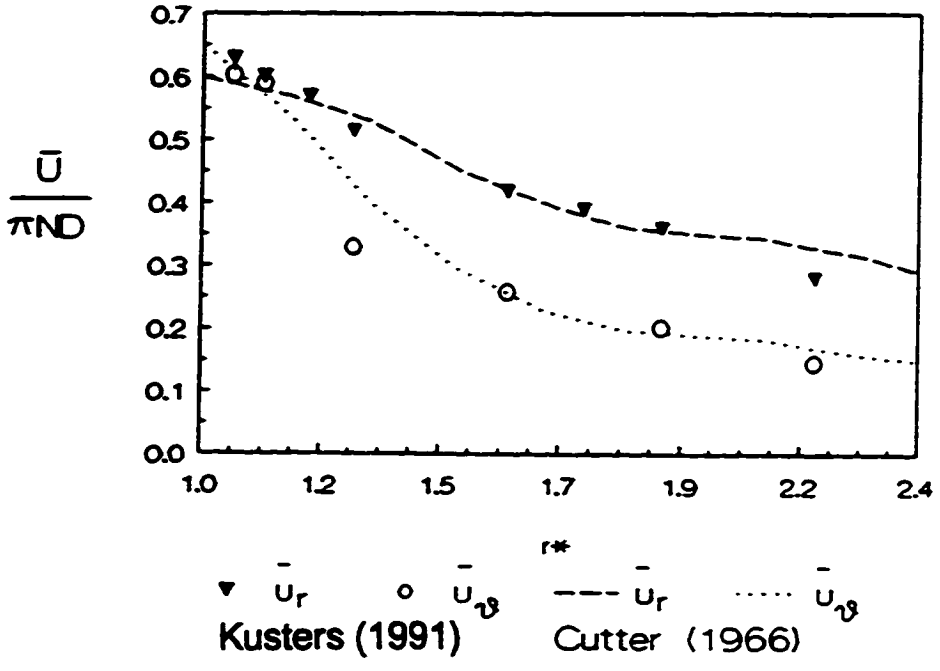

Figure 2.1.3: Comparison of the Radial and Tangential Velocity in the Rushton Turbine Impeller Discharge Stream (Kusters, 1991), $\overline{U_r}$ = radial mean velocity, $\overline{U_\theta}$ = tangential mean velocity, N = 7.5 s^{-1}, D = 33.2 mm

to the frame of reference chosen for the velocity measurements (i.e. fixed frame or impeller rotating frame).

The flow emanating from the blade is dominated by vortex eddy pairs coming from behind the impeller blade extending into the impeller region (Figure 2.1.4). The vortex pairs, above and below the Rushton disk, have been found to rotate in opposite directions with a zero mean velocity at the center of the vortex relative to a frame of reference moving with the impeller. These trailing vortex pairs have been found to extend out as far as 0.5 times the impeller radius beyond the impeller tip. Complete destruction of the trailing vortex into smaller eddies has been reported to occur beyond this point. Researchers found that the angular velocity distribution did not vary along the core of the vortex. However, the angular velocity was reported to be a function of the vortex radius and impeller Reynolds number. These vortices were continually generated behind the blade but upon leaving the blade, had a short duration time and broke up erratically. The axis of the vortex was not stationary blade passage to blade passage and moved about in an erratic behavior. The intense recirculation zone caused by the vortices behind the impeller blade was reported to cause the tangential velocities to exceed the impeller tip speed. On average, however, the location of the vortex axis was found to be a function of the impeller diameter.

Besides the measurement of the mean velocity, a periodic velocity component has also been detected near the impeller tip. This periodic velocity was found to be caused by the passage of the impeller blade. The power spectra of the fluctuating velocity component in the discharge flow revealed strong peaks at frequencies of the blade passage and its harmonics. The periodic velocities were found to decay to zero very rapidly in the radial direction. The location where the periodic velocities were zero also coincides with the location where complete destruction of the trailing vortices occur.

The turbulence characteristics of the Rushton turbine in the impeller region have been studied by many investigators (Appendix A). Very few have reported the turbulence generated in the bulk region. In the impeller region, the profiles of the root mean square (rms) values of the fluctuating velocity components were found to follow similar trends to the mean velocities. The rms value of the resultant fluctuating component ranged between 30 and 50 percent of the

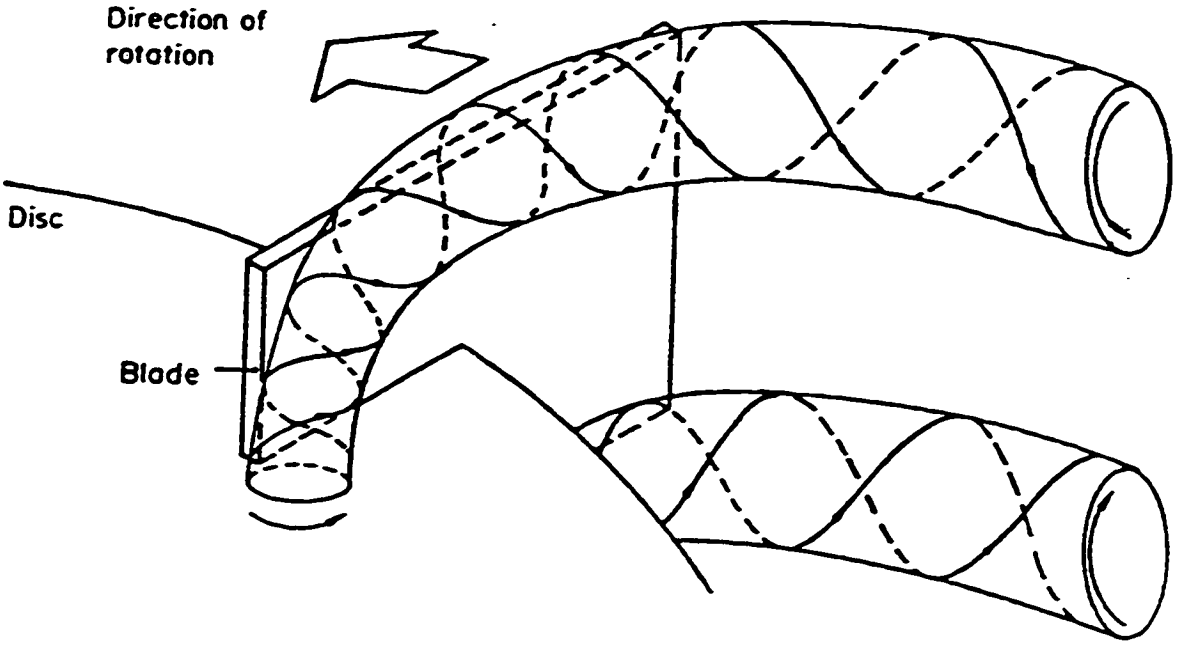

Figure 2.1.4: Vortex Eddy Pairs Generated by the Rushton Turbine (Van Riet & Smith, 1978)

impeller tip speed near the impeller tip. The maximum rms value occurred around 1.4 times the impeller radius in the radial direction above the outer edge of the blade tip. This is the same location where investigators have found the maximum extension of the trailing vortices. Beyond this point, the rms value of the resultant fluctuating component decayed radially to 10-20 percent of the impeller tip speed. The wide range of values found for the maximum rms value of the fluctuating velocity in the impeller region is due to some investigators not removing the periodic velocity component. Nonetheless, all investigators have found that the turbulence in the impeller discharge region near the blade tip is strongly anisotropic. In the bulk region, the rms value of the resultant fluctuating velocity was found to be less than 10 percent of the impeller tip speed. Contrary to the impeller region, the turbulence in the bulk region has been found to be isotropic.

The most widely scattered information reported by different investigators concerns the turbulent energy dissipation rate. Since direct measurement of the energy dissipation rate involves determining the product of the gradients of the fluctuating velocities, only indirect measurements are possible (Frost and Moulden, 1977). However, the indirect methods used to compute the local energy dissipation rate are further complicated by the existence of non-isotropic regions in the impeller region and by the multitude of different indirect methods to compute the energy dissipation rate.

Figure 2.1.5 displays several measurements of the radial profile of the local energy dissipation rate at the impeller. As can be seen in Figure 2.1.5, the studies show major differences in the profile of the energy dissipation rate, particularly near the impeller tip. Several reasons can account for these differences. First, some investigators neglected to remove the periodic velocity component from the rms fluctuating velocity component. The periodic velocity tends to elevate the energy dissipation rate. Second, different kinds of measuring techniques, fluid media and frames of reference were used by different researchers. Techniques like LDV and hot wire anemometry have been better suited to compute turbulent parameters than flow visualization or pitot tubes. Third, different indirect methods were used to compute the local energy dissipation rate. Figure 2.1.6 displays the axial profile of the local energy dissipation rate. It is clear from Figure 2.1.6 that the rate of energy dissipation in the impeller region is much higher than the rate of energy dissipation in the bulk region.

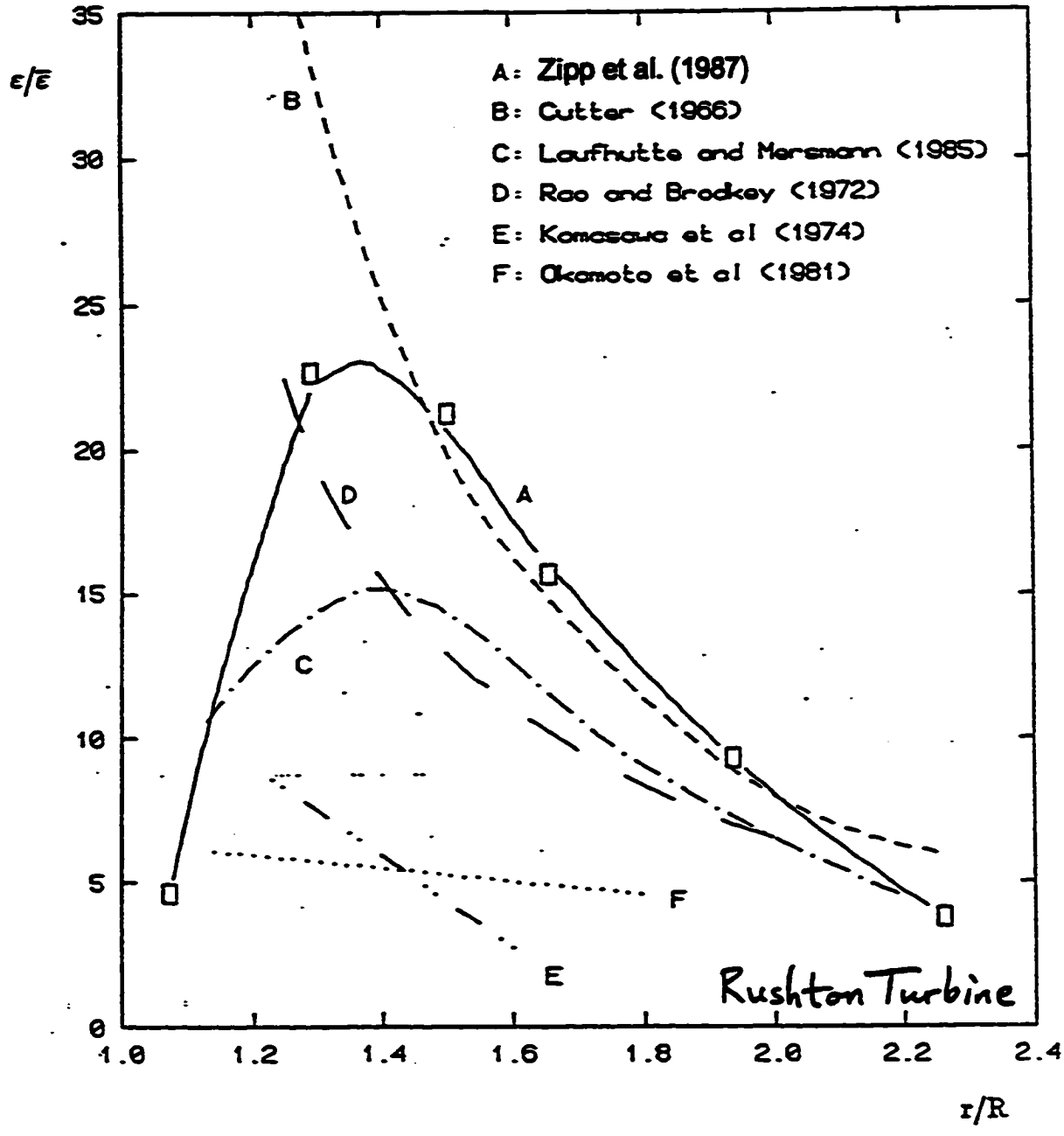

Figure 2.1.5: Radial Profile of the Local Energy Dissipation Rate at the Centerline of the Rushton Turbine Discharge Region (Zipp et al., 1987), ε= local energy dissipation rate, $\bar{\varepsilon}$= tank average energy dissipation rate, R = impeller radius, r = location of measurement in radial direction

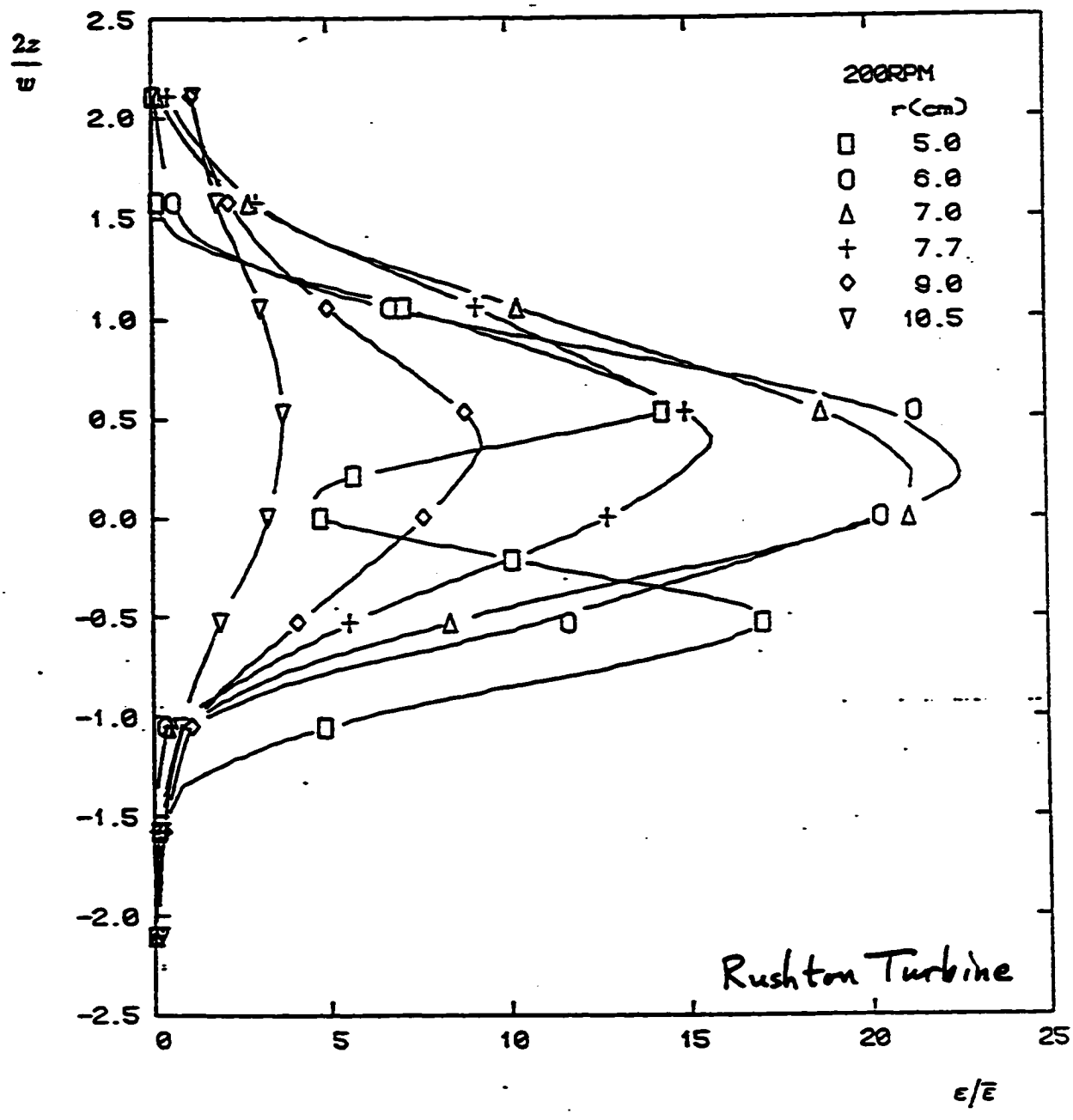

Figure 2.1.6: Axial Profile of the Local Energy Dissipation Rate for the Rushton Turbine (Zipp et al., 1987), w = width of the impeller blade tip, z = location of measurement in axial direction

While some differences in fluid flow measurements of a Rushton turbine in a fully baffled cylindrical tank have been found in the literature, it is clear that the flow field produced by this impeller is very complex. This is particularly true in the impeller discharge zone where vortical structures exist.

2.1.2 A310 Foil Impeller in a Fully Baffled Cylindrical Tank

An A310 fluid foil impeller is considered to be an axial flow impeller. Figure 2.1.7 displays a schematic of the A310 impeller. Upon impeller rotation, the foil impeller has been shown to produce a flow that moves axially downward toward the bottom of the tank. As the flow nears the tank bottom it entrains the surrounding fluid and slows down. Close to the tank bottom, the flow is divided into two flows which circulate in the bulk region and return to the impeller from above (Figure 2.1.8). Contrary to the four circulation patterns generated by the Rushton turbine (Figure 2.1.2), the foil impeller generates only two large circulation patterns.

In contrast to the many reported studies on the Rushton turbine, there has not been a lot of published work on quantifying the fluid mechanics generated by an A310 foil impeller in a fully baffled tank. Weetman and Oldshue (1988) described the power, flow, and shear characteristics of many different kinds of impellers including the A310 foil impeller.

The power drawn by an agitator in a liquid mixing system is expected to be a function of the impeller diameter, rotational speed, density of the fluid, viscosity of the fluid, gravitational acceleration, tank diameter, location of the impeller in the tank, and shape of the tank. This can be simply described by the following equation:

$$P = f(D, N, \rho, \mu, g, T, H) \qquad (2.1)$$

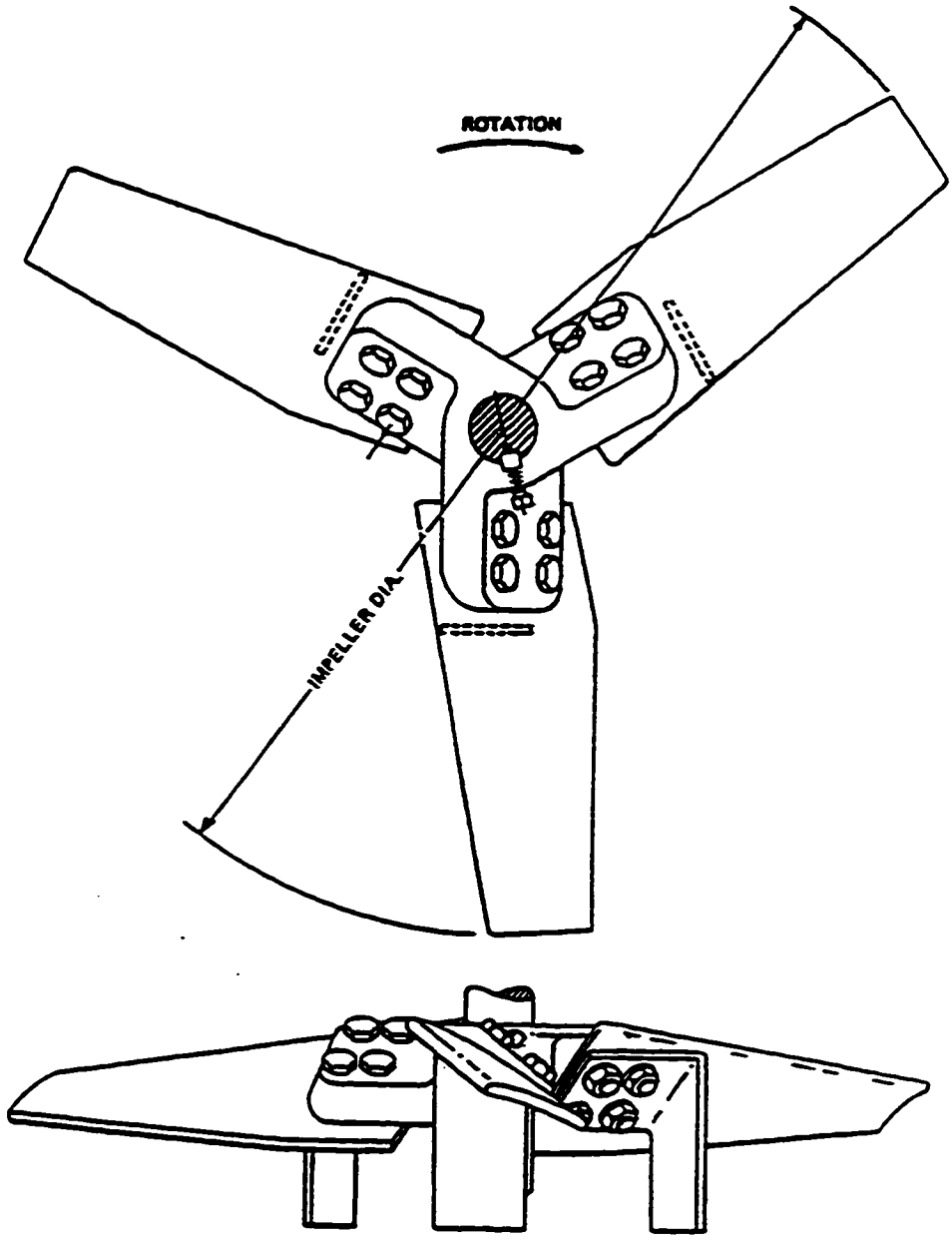

Figure 2.1.7: LIGHTNIN A310 Fluid Foil Impeller (Clark et al., 1994)

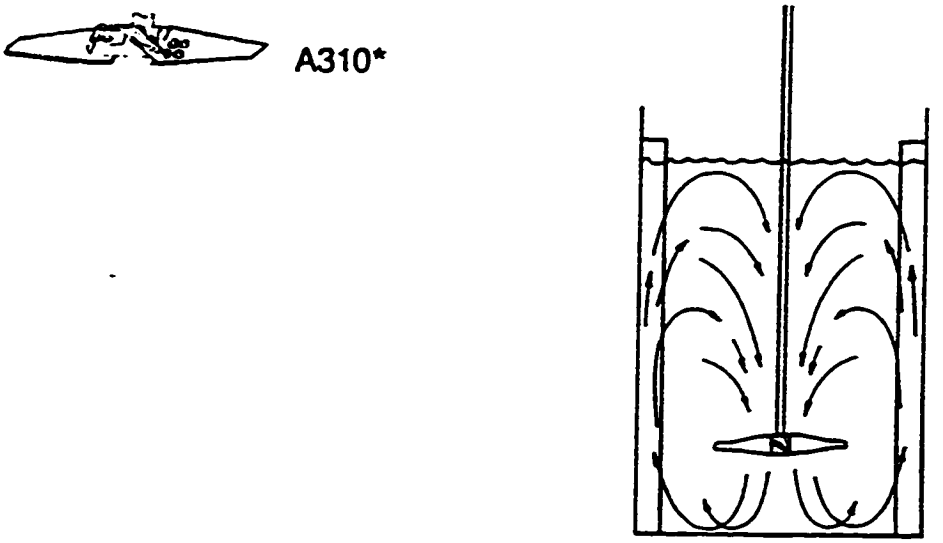

Figure 2.1.8: Flow Pattern of the A310 Fluid Foil Impeller (Oldshue & Herbst, 1992)

where

P = power drawn by mixer ($M L^2/T^3$)

D = impeller diameter (L)

μ = viscosity of fluid (M L/T)

N = rotational speed (T^{-1})

g = gravitational acceleration (L/T^2)

T = tank diameter (L)

H = location of impeller from bottom (L)

ρ = density of fluid (M/L^3)

Using Buckingham π theorem to non-dimensionalize Equation 2.1, we can obtain the following relationship:

$$\frac{P}{\rho N^3 D^5} = f\left(\frac{N^2 d}{g}, \frac{\rho N D^2}{\mu}, \frac{D}{T}, \frac{H}{T}\right) \qquad (2.2)$$

The term on the left hand side of the equal sign is called the power number (N_p). Therefore, N_p is a function of the impeller Froude number, the impeller Reynolds number, and some geometric terms. If we have a mixing condition where there is no vortex formation at the free surface and if we also maintain geometric similarity between different mixing setups, then N_p is only a function of the Reynolds number. Studies have shown that at high Reynolds number, i.e. turbulent conditions, N_p is constant (Holland & Chapman, 1966).

Weetman and Oldshue (1988) reported a much lower N_p for the A310 foil impeller than the Rushton turbine. The A310 foil impeller N_p was 0.30 while the Rushton N_p was 5.2. The Rushton turbine N_p is well within the range of values reported by many other investigators (Oldshue, 1983). This clearly indicates that for the same operating speeds and impeller diameter,

the power drawn by the A310 foil impeller is much less than the power drawn by the Rushton turbine.

Weetman and Oldshue (1988) also reported the maximum and average shear gradients at the outlet of the A310 foil impeller and Rushton turbine. These velocity gradients are computed from the difference between adjacent mean radial velocities divided by the distance between these velocities. Figure 2.1.9 displays their results. In Figure 2.1.9, Weetman and Oldshue (1988) found that the average shear gradient is much lower at the outlet of the A310 foil impeller than for the Rushton turbine. They also found different functional dependence for the maximum shear gradients between the A310 foil impeller and the Rushton turbine. The maximum shear gradients for the A310 foil impeller was a function of the impeller angular velocity whereas the maximum shear gradients for the Rushton turbine was a function of the impeller tip speed. Different functional dependence for the maximum shear gradients between the two impellers may suggest that different scaleup rules would apply for processes which are controlled by the maximum shear gradients (Weetman & Oldshue, 1988). However, the authors noted that more work needs to be done to evaluate the maximum shear gradients in other regions of the mixing vessel.

Although there has not been a lot of work published about the fluid mechanics generated by an A310 foil impeller, there have been studies done on low power number axial flow impellers which fall into the same class as the A310. Laufhutte & Mersmann (1985), Mersmann & Geisler (1991), and Geisler et al. (1994) have measured the turbulence generated by a radial flow impeller (Rushton turbine) and two axial flow impellers (3 blade propeller, 2 stage Intermig). They found that the low power number axial flow impellers produced turbulent fluctuating velocities which are lower than those of the high power number radial flow impellers (Table 2.1.1). They also showed that spatial distributions of the local energy dissipation rate near the axial flow impellers were much lower than those produced by the radial flow impeller. Mersmann and Geisler (1991) found that a relationship exists between the maximum values of the dimensionless local energy dissipation rates $(\varepsilon_{loc}/\varepsilon_{avg})_{max}$, impeller power number, and the diameter ratio (D/T) (Figure 2.1.10). Based on Figure 2.1.10, Mersmann and Geisler (1991) determined the following equation:

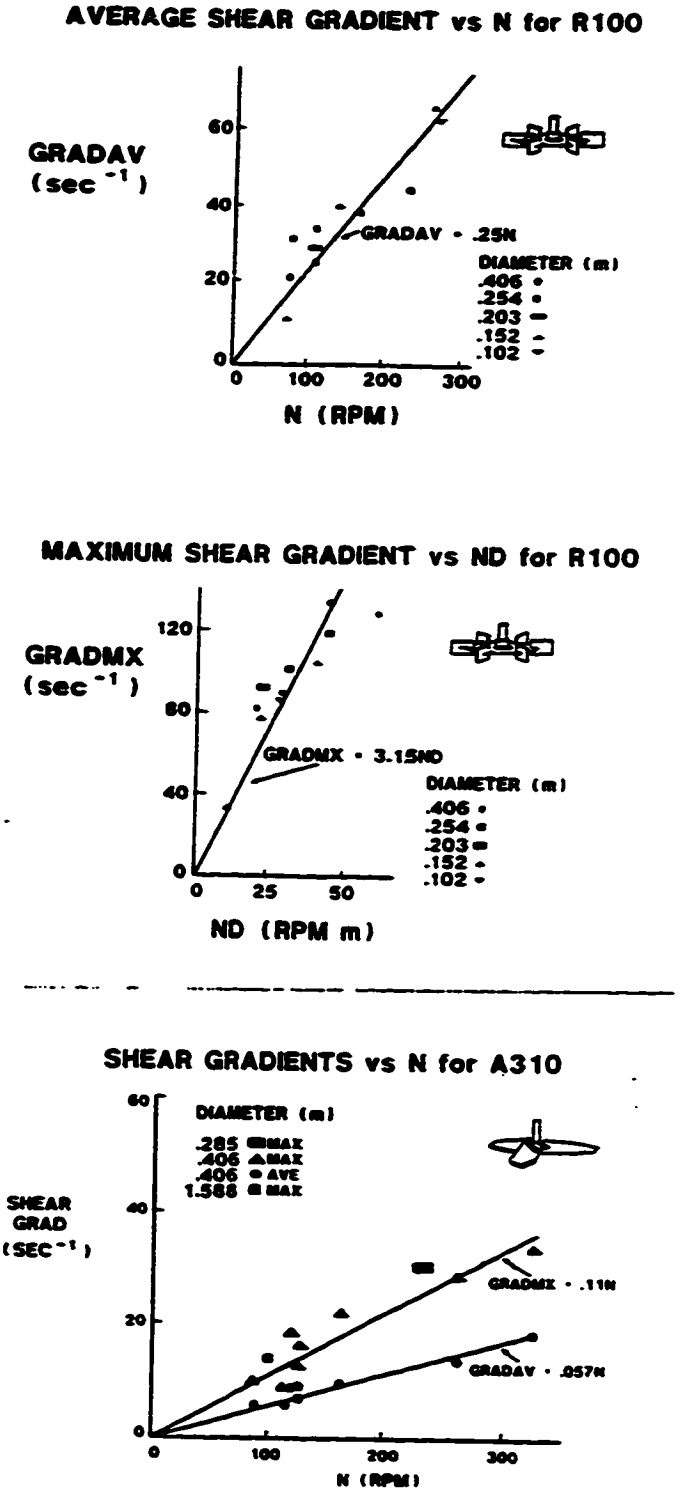

Figure 2.1.9: Average Shear Gradient of the Rushton Turbine and A310 Foil Impeller at the Impeller Outlet (Weetman et al., 1988)

Table 2.1.1: Comparison between the Turbulent Fluctuating Velocities Produced by Low Power Number Axial Flow Impeller and High Power Number Radial Flow Impellers

type of stirrer	d/D	$\frac{u'_{max}}{\pi nd}$	Coordinates z/D	Coordinates $\frac{2r}{D}$
6-blade Rushton turbine	1/3	0.35	≈0	0.4
3-blade propeller	1/3	0.2	−0.05	0.13
	1/2	0.11	−0.05	0.18
2-stage Intermig impeller	0.6	0.2	0.1	0.74
	0.7	0.2	0.4	0.74

Laufhutte & Mersmann (1985)

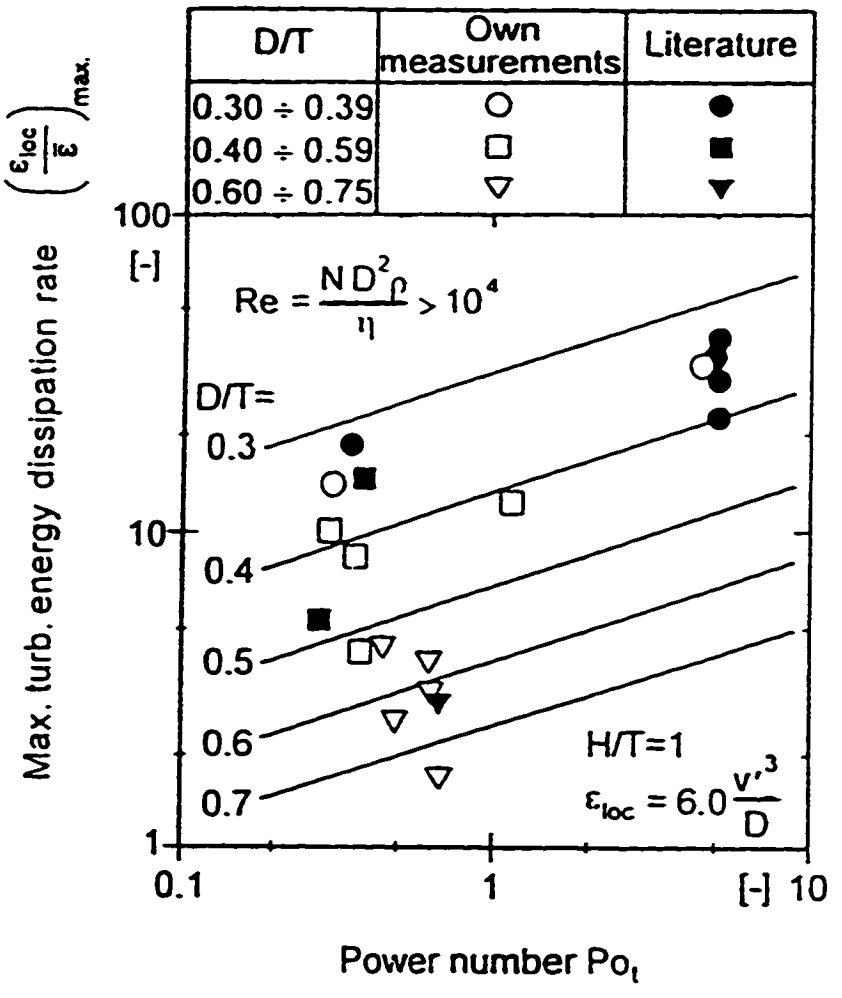

Figure 2.1.10: Relationship between the Maximum local Energy Dissipation rate, Impeller power number, and D/T ratio Rushton turbine, marine propeller, and an Intermig impeller were used to produce the above graph. (Geisler et al., 1994)

$$\left(\frac{\varepsilon_{loc}}{\varepsilon_{avg}}\right)_{max} = 0.14 C N_p^{1/3} \left(\frac{D}{T}\right)^{-3} \qquad (2.3)$$

Ranade et al. (1992) studied the influence of various axial flow impeller shapes on the turbulence produced in an agitated vessel. The list of impellers include three six bladed pitch downflow turbines (blade angle: 30°, 45°, 60°), a multiple bladed pitch downflow turbine, a convex pitch blade turbine, a curved pitch blade turbine, a marine propeller, and a modified 2 blade pitch down flow turbine. In general, the results of Ranade et al. (1992) indicate that the turbulence produced in the impeller discharge zone of all the impellers studied are lower than what has been reported for the Rushton turbine. Within these sets of impellers studied, Ranade et al. (1992) found that the highest turbulence levels were produced by the 60° pitch blade turbine and the lowest with the modified 2 blade pitch downflow turbine. The marine propeller, which is most closely related to the A310, also produced one of the lowest turbulence levels. The results of Ranade et al. (1992) suggest that by varying the angle and shape of the impeller tip, the turbulence produced in the impeller discharge region can be reduced. Based on Equation 2.3 and the experimental results of Laufhutte & Mersmann (1985), Mersmann & Geisler (1991), Ranade et al. (1992) and Geisler et al. (1994), we can expect the turbulent kinetic energy, turbulent energy dissipation rate, and the rms turbulent fluctuating velocity generated by the A310 fluid foil impeller to be lower than that produced by the Rushton turbine.

2.1.3 Scaleup Investigation in Stirred Tank Reactors

Scaleup investigations of the turbulent flow generated in stirred vessels have not been carried out by many investigators. Although turbulence measurements have been done in mixing tanks of different sizes, their geometries were different. Currently, only Van der Molen & Van Maanen (1978), Kusters (1991) and Rutherford et al. (1996) have carried out detailed measurements of the fluid mechanics generated in three stirred vessels of exactly the same

geometry.

Van der Molen & Van Maanen (1978) conducted turbulence measurements in the impeller discharge zone of a Rushton turbine in three vessels with diameters 0.12, 0.29, and 0.90 meters. The measurements were done using a one dimensional LDV system. All their experiments were carried with the same power per unit mass, $\varepsilon_{avg} = 5.7 \times 10^{-2} m^2 s^{-3}$.

Van der Molen & Van Maanen (1978) found that the mean radial velocity was proportional to the impeller tip speed and decayed radially to the tank wall. Van der Molen & Van Maanen (1978) also reported the existence of a periodic velocity component which coincided with the blade passage frequency. Like other investigators (Appendix A), they found that the periodic velocity would decay rapidly to zero in the radial direction. However, they were able to determine that the peak to peak amplitude of the periodic velocity tends to increase with tank size.

Van der Molen & Van Maanen (1978) also computed the turbulence power spectra at the same relative position in the three vessels. They expected that since the power input per unit mass was equal for all three vessels, the high wave number section of the spectra would overlap. However, Van der Molen & Van Maanen (1978) found that the high wave number portion of the power spectra tends to decrease with increasing tank size near the impeller tip. This indicates that the local energy dissipation rate near the impeller tip decreases with increasing tank size. They also noted that the slope of the power spectra in the high wave number region was steeper than -5/3, which denotes a departure from Kolmogorov's universal equilibrium range. However, near the tank wall, Van der Molen & Van Maanen (1978) found that difference between the power spectra for the three tank sizes were much smaller and the slope was equal to -5/3. They suggested that the reason for the difference between the power spectra at the impeller tip was due to the influence of the trailing vortices near the impeller tip.

Van der Molen & Van Maanen (1978) also computed the turbulence intensities. The turbulence intensities were computed by integrating the power spectrum and taking the square root of the result to obtain the rms value and dividing the rms by the mean velocity. They found that the turbulence intensity tends to increase with increasing tank size. Based on their experiments, Van Der Molen & Van Maanen (1978) concluded that:

a) The time average velocity is proportional to the tip speed.
b) The amplitude of the periodic velocity increases with tank size in proportion to $D^{1/6}$.
c) The turbulence intensity in the impeller region will also increase with tank size in proportion to $D^{1/6}$.
d) The energy in the smaller eddies decreases with tank size in proportion to $D^{-1/2}$.

Kusters (1991) performed turbulence measurements in both the impeller region and the bulk region of cylindrical baffled tanks with Rushton turbines. The three tanks had diameters of 0.102, 0.200, and 0.388 meters, respectively. Kusters (1991) measured the mean velocities, turbulent fluctuating velocities, integral length scales, and energy dissipation rates in the impeller discharge region and bulk region. The measurements were done using a one dimensional LDV system. LDV measurements were made in the baffle plane and a plane halfway between two baffles. All of Kusters (1991) experiments were carried out with ε_{ave} = constant.

Kusters (1991) found that the profile of the mean velocity near the impeller blade tip in the axial direction was parabolic and proportional to the tip speed. The mean velocity was also found to decay radially towards the tank wall. Consistent with the results of Van der Molen & Van Maanen (1978), Kusters (1991) found that the profile of the mean velocity normalized by the impeller tip speed does not change with tank size.

Kusters (1991) also detected the presence of a periodic velocity component which had a frequency equal to that of the blade passage. The periodic velocity was found to decay rapidly to zero in the radial direction. Kusters (1991) determined that the peak to peak amplitude of the periodic velocity also increased with tank size at a rate similar to Van der Molen & Van Maanen (1978). However, Kusters (1991) did notice that the periodic velocity would decay to zero at a slower rate in the radial direction as the tank size increased. Kusters speculated that this slower decay rate in the radial direction with scale was due to deeper penetration of the trailing vortices in the radial direction with increasing tank size.

Kusters (1991) found that the turbulent fluctuating velocity was proportional to the tip speed. In the impeller discharge region the fluctuating velocity was between 15 and 33 percent of the impeller tip speed. In the bulk region, however, the fluctuating velocity would be around

6 percent of the tip speed. Kusters (1991) determined that with increasing tank size, the turbulent fluctuating velocity decreases in value in the impeller discharge region and increases in value in the bulk region.

Kusters (1991) determined the spatial distribution of the energy dissipation rate in the baffle plane and in a plane halfway between two baffles. He found that the maximum energy dissipation rate occurred near the impeller blade tip and decreased with increasing tank size. The maximum values of ($\varepsilon/\varepsilon_{avg}$) near the blade tip were 45, 37, and 28 for tank sizes of 0.10, 0.20, and 0.39 m, respectively. However, the energy dissipation rates in the bulk region were found to increase with vessel size. The corresponding average normalized energy dissipation rates in bulk region amount to around 0.07, 0.11, and 0.15.

Rutherford et al. (1996) measured the turbulence produced by a dual Rushton turbine setup in two stirred vessels of diameter 100 and 294 mm for ε_{ave} = constant. Rutherford et al. (1996) used flow visualization, power consumption, mixing time, and 360° ensembled-averaged and 1° angle resolved laser Doppler velocimetry measurement techniques to accomplish their study. Part of their results showed that the turbulence distributions in the two vessels display similar characteristics.

Rutherford et al. (1996) reported that the root mean square velocity levels were generally the same in both 100mm and 294mm diameter vessels. The rms velocity and turbulent kinetic energy were found to be everywhere proportional to the impeller tip speed and impeller tip speed squared respectively. This result was found regardless of tank size. From dimensional analysis, Rutherford et al. (1996) indicate that for the same power per unit volume, the rms value would increase with increasing tank size. In both vessels, the locations of the maximum rms velocity and maximum kinetic energy were between 1.2 and 1.5 times the impeller radius in the radial direction. This is the same approximate location where the maximum extension of the trailing vortices was found to occur (Appendix A). No local energy dissipation rates were reported in their study.

It is clear from the results of Van der Molen & Van Maanen (1978) and Kusters (1991) that maintaining constant average energy dissipation rate between different tank sizes does not translate to the same spatial distribution of the local energy dissipation rate. Van der Molen &

Van Maanen (1978), Kusters (1991), and Rutherford et al. (1996) all found that for the same power per unit volume, the turbulent rms fluctuating velocity and kinetic energy do not remain constant with tank size. It is likely that the local variations of these quantities with tank size can affect the operation of the flocculation process.

2.1.4 Summary

There have been many experimental studies of the fluid mechanics generated by different types of impellers in a fully baffled cylindrical tank. By far the most studied impeller is the Rushton turbine. However, not much work has been published about the fluid mechanics generated by a Rushton turbine in a square vessel. Moreover, even less is known about the A310 fluid foil impeller. It is important to quantify the behavior of these two impellers in square tank geometry since it is this setup which is found more commonly in flocculation processes.

In a general sense, the data reviewed in Sections 2.1.1-2.1.3 have revealed some interesting flow characteristics in stirred tanks. Characteristics which may be important to this research include the following:

a) The turbulence generated by a high power number radial flow impeller is much different from the turbulence generated by a low power number axial flow impeller.

b) The local turbulent rms fluctuating velocity, kinetic energy and energy dissipation rate do not remain the same with tank size when the impeller power per unit volume is constant.

c) The local energy dissipation rate in the impeller region is many times higher than the local energy dissipation rate in the bulk region.

These results seem to indicate that in order to model the flocculation process properly, it will be important for the model to be sensitive to the type of impeller being used (e.g. high power number radial flow or low power number axial flow) and the process scale.

2.2 Scaleup Studies in the Flocculation Process

In flocculation, the idea of scale has not been studied extensively. Oldshue and Mady (1978), Clark and Fiessinger (1991), and Clark et al. (1994) are the only experimental studies of how the scale of the flocculation process affects its performance. These studies required that all the different size flocculation tanks received the same source of water plus coagulant. In doing this, any scale related effects due to the rapid mixer were eliminated. Kusters (1991) also conducted studies related to scaleup in flocculation. However, Kusters (1991) performed his flocculation experiments with non-traditional flocculation operating speeds, coagulants, and source water turbidity. Nevertheless, his findings on the influence of turbulence in the agglomeration of small particles in stirred vessels are important.

Oldshue and Mady (1978) studied the performance of four different impeller types at two different batch reactor scales. The four impeller types were the Rushton (R100), rake, A200 pitch blade, and A212 fluid foil. The sizes of the two tanks were 460 and 760 mm in diameter. They set the flocculation time for 10 minutes and the turbidity values were measured many times during a 60 minute settling period following flocculation. Based on the criterion of minimum residual turbidity after 60 minutes of sedimentation, their results imply that the optimum batch flocculation G value decreases with increasing scale (Table 2.2.1). However, they did not recommend extrapolating their results to full scale because the dimension difference between the two tanks was not large enough. In other words, if one were to extrapolate their results to full scale, the average operating G values would be very small and unrealistic.

Clark and Fiessinger (1991) examined batch scaleup in two fully baffled Rushton mixers of 1 liter and 20 liters. Solutions of 10 mg/l humic acid were flocculated with aluminum sulfate. The humic acid and turbidity removal were monitored over the course of a 60 minute settling period. Clark and Fiessinger (1991) conducted the scaleup experiments with two different configurations.

In the first configuration, a common rapid mix and coagulant addition was used for each vessel. As mentioned previously, this configuration assured isolating the effects of scale in the flocculation process only. In this configuration, the experiment proceeded by beginning the rapid

Table 2.2.1: G Factor at Minimum Turbidity (1/sec) (Oldshue and Mady, 1978)

Average G Value at Minimum Turbidity

Impeller Type	4.6-cm Diameter Impeller	7.6-cm Diameter Impeller
Rake (D/T = 0.8)	148	112
LIGHTNIN A212 (D/T = 0.3)	110	34
LIGHTNIN A212 (D/T = 0.2)	58	27
LIGHTNIN A200 (D/T = 0.2)	77	60
Rushton (D/T = 0.2)	116	69

mix and coagulant addition in the larger vessel, which contained 21 liters of humic acid solution. Following the addition of aluminum sulfate and 60 seconds of rapid mixing, 1 liter was dipped out into the smaller vessel and both vessels were agitated for 30 minutes using separate mixers operating at the same average G value. In the second configuration, each vessel was operated independently, having its own 60 second rapid mix stage. This second configuration couples the effects of scale in both the rapid mix process and in the flocculation process.

Table 2.2.2 displays the results from the Clark and Fiessinger (1991) experiments. From, Table 2.2.2, both experiments had a higher residual turbidity and lower humic acid removal for the larger tank than for the smaller tank when both were operated at the same average G value. These results suggest that the flocculation process is sensitive to scale.

Part of the work done by Clark et al. (1994) looked into scale related effects in flocculation. In their work, three square, geometrically identical, continuous flow flocculation tanks were fed from a common initial mixer prototype. The square flocculation tanks had side dimensions of 1 ft, 2.5 ft, and 4 ft. The water depths were held at 0.75 ft, 1.88 ft, and 3 ft respectively. This meant that the fluid volumes in the tanks were 0.75 ft^3, 11.7 ft^3, and 48 ft^3.

Flow rates to each tank were adjusted in order to maintain a 20 minute mean residence time. Clark et al. (1994) clearly found that the flocculation-sedimentation performance degrades

Table 2.2.2: Data for Turbidity and Humic Acid Removal after 60 minutes of Settling (Clark and Fiessinger, 1991)

Average G Value		Same Rapid Mix		Separate Rapid Mix	
		1 L	20 L	1 L	20 L
40	Turbidity	0.4	0.5	0.58	0.63
100	Turbidity	--	--	0.55	0.66
40	% Organic Removal	78	72	86	82
100	% Organic Removal	--	--	88	80

with increasing tank size. As can be seen from Figure 2.2.1, the total particle count and turbidity for tank 4 were higher than the total particle count for tank 2.5 and tank 1. Almost without exception, this trend was shown to be true no matter what initial mixer was used.

Trussell et al. (1992) argued that this deterioration in flocculation performance is due to the fact that with equivalent geometry and equal volumetric power input (G_m = constant), the volume of the fluid in a small tank would be more easily induced to rotate as a whole than the volume of fluid in a larger tank. Thus the relative velocities between the impeller tip and the fluid in the small tank would be less than those in the larger scale tank. This means that the smaller tank had lower shear rates near the impeller. High impeller shear rates can cause the floc particle to breakup. The results of Trussell et al. (1992) would suggest scaleup of the flocculation process with constant Froude number. According to Trussell et al., scaleup with constant Froude number would cause the relative velocities between the impeller tip and the fluid to remain the same with increasing tank size. However, scaleup with constant Froude number conflicts with the results of Oldshue and Mady (1978). Oldshue and Mady's (1978) results suggest that

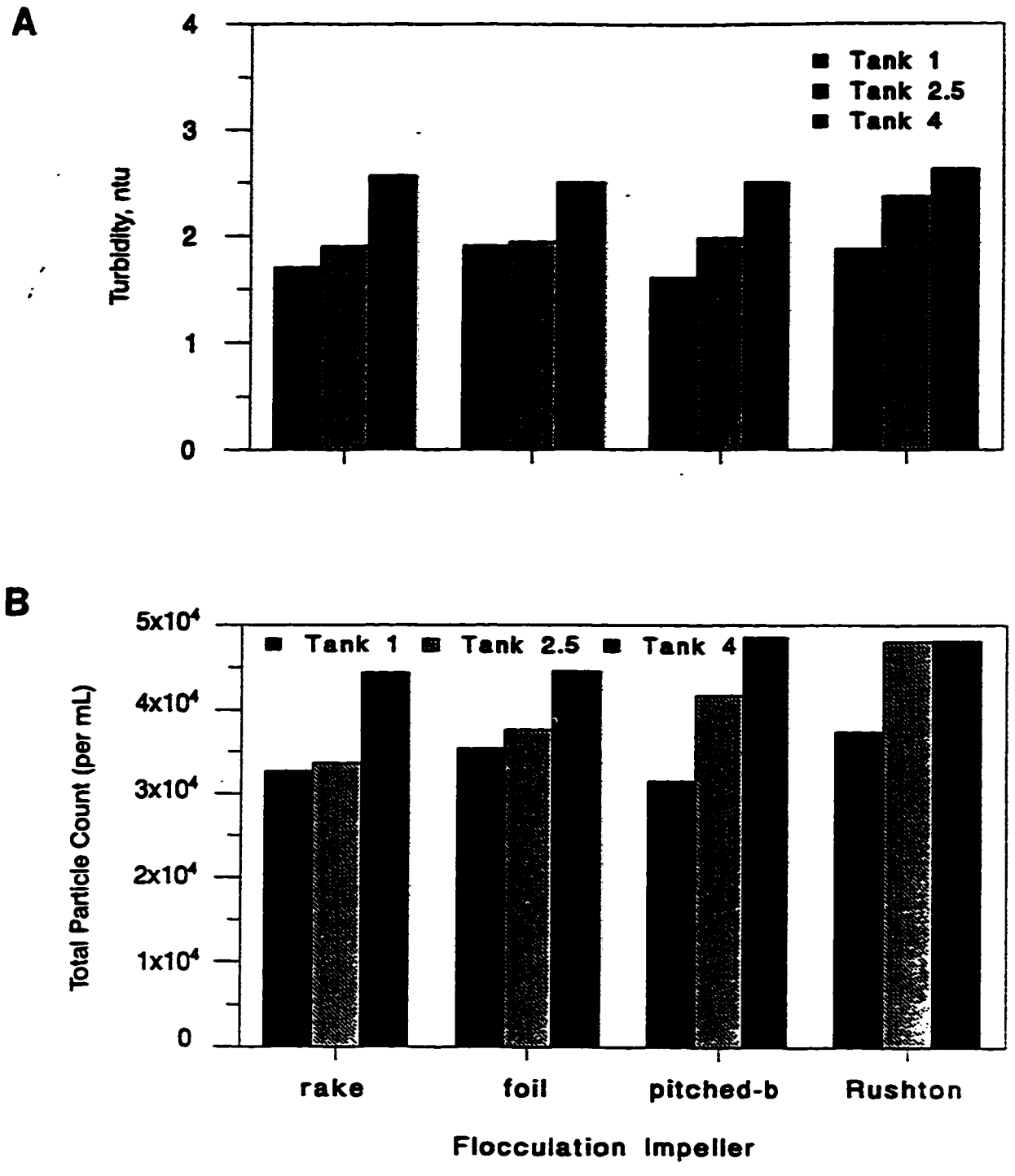

Figure 2.2.1: A) Turbidity and B) Total Particle Count after 20 minutes of Flocculation and 20 minutes of Sedimentation: Results for Hydraulic Jet Initial Mixer (Clark et al., 1994)

constant tip speed would be a better scaleup parameter.

The flocculation experiments carried out by Kusters (1991) were done in stirred tanks of diameters 0.10, 0.20, and 0.39 m. Kusters (1991) used aqueous mono-dispersions of spherical polystyrene particles with a mean diameter of 1 μm. Sodium chloride was used as the coagulant. The concentration of the sodium chloride was chosen to ensure complete destabilization of the polystyrene particles. However, Kusters (1991) did not describe the technique used to measure the energy at the Stern surface (hypothetical boundary of the diffuse double layer).

Kusters (1991) found that increasing the impeller speed caused the volume mean diameter to shift towards smaller values. This was not surprising since increasing the impeller speed causes the shear stresses acting on the agglomerates to increase in strength. He also found that increasing the polystyrene particle concentration increases the mean diameter. This also was not surprising since increasing the solids concentration increases the rate at which flocculation would occur with respect to the breakup rate.

However, the surprise came with the results of how the volume mean diameter changed with tank size. Kusters' (1991) results showed that by maintaining constant average energy dissipation rate in all the tanks, the volume mean diameter first decreased then increased as the tank size increased. Part of Kusters' (1991) results are shown in Table 2.2.3. He found this mean diameter response with two coagulant concentrations shown in Table 2.2.3. Kusters' (1991) results seem to largely contradict the flocculation scaleup results of Oldshue & Mady (1978), Clark & Fiessinger (1991), and Clark et al. (1994). Kusters (1991) argues that eventual growth of the mean particle diameter makes sense since he found that the maximum energy dissipation rate decreased with scale in the impeller discharge region where breakup of aggregates tends to occur. The decrease in the mean particle diameter at the intermediate tank size (20 cm) was not explained.

However, Kusters (1991) does admit that his flocculation scaleup results may change by increasing the primary particle concentration. For higher solids concentrations, Kusters (1991) mentioned that the coagulation rate becomes faster with respect to circulation times in stirred tanks. Consequently, breakup of aggregates would occur in the bulk region where he found the energy dissipation rate to increase with increasing tank size. The net result would be a decrease

Table 2.2.3: Variation of Steady State Volume Mean Diameter with Scale (Kusters, 1991). Cp = volume of dispersed phase / volume of continuous phase

D43 in μm.

C_P m^3/m^3	T (cm) 10	20	39
$3 \cdot 10^{-4}$	7.6 ± 1.0	7.4 ± 1.0	9.4 ± 1.0
$6 \cdot 10^{-4}$	10.0 ± 1.0	9.4 ± 1.0	18.0 ± 2.0

in particle mean diameter with increasing tank size. Kusters' (1991) results may also change if different coagulants were used or if the mode of destabilization was sweep floc rather than double layer compression. However, Kusters did not explore the effects of different coagulants and mode of destabilization on the steady-state volume mean diameter.

From the results of Oldshue & Mady (1978), Clark & Fiessinger (1991), and Clark et al. (1994), it is not completely clear what is causing the flocculation performance to degrade with increasing tank size. However, it is likely that the degradation is related to the fluid mechanics in the flocculation tank. In order to find the cause of degradation in flocculation performance with tank size, a detailed study of the fluid mechanics of the flocculation tank must be done while varying physical parameters such as tank size.

2.3 Investigations of Flocculation Impeller Type

Many investigators have studied the effects of impeller type on flocculation performance. In most of these reports, the influence of impeller shape, the location of the impeller in the stirred reactor, and the extent of the impeller boundary in the reactor volume have been found to play a significant role in the formation of particle aggregates.

Drobny (1963) studied the effects of five different paddle characteristics on flocculation performance. The paddle characteristics studied include surface roughness, paddle perforations, paddle curvature, paddle area, and paddle height to width ratio. The material flocculated was a mixture of aluminum sulfate, sodium carbonate, and a small quantity of Fuller's earth. All measurements were made with constant power per unit volume. Although the results were mainly qualitative, Drobny (1963) found some interesting relationships between these paddle characteristics and floc formation.

Drobny (1963) found that increasing the surface roughness improved floc formation by enhancing the velocity gradients due to increased drag imparted on the impeller surface. However, Drobny noted that there was a limit on the surface roughness beyond which no improvement in floc formation was indicated. Drobny (1963) also found that number and size of the paddle perforations increased the floc formation in the reactor. Eight perforated holes with

a 0.0625 in. diameter produced the best result.

Drobny (1963) showed that both a slight paddle curvature and an optimal paddle cross sectional area that was 33 percent of the tank vertical cross-sectional area enhanced floc formation. He also noted that a low or high paddle height to width ratio increased floc formation in the reactor. Based on these results, Drobny (1963) concluded that the flocculation process can be made more efficient with respect to the power input by simply varying the impeller design.

Patwardhan and Mirajgaonkar (1970) investigated the effects of paddle cross-sectional area, paddle edge length, and width of paddle blades and perforations on the flocculation performance. Six specially designed small paddles were used in this study. All of the paddles studied extended well into the reactor volume. The raw water used in this study was obtained by adding clay to tap water. The average turbidity of the supernatant after one hour of settling time was used as a measure of the flocculation performance.

Patwardhan and Mirajgaonkar (1970) found that an optimal paddle cross-sectional area that was 35% of the tank vertical cross-sectional area gave the lowest residual turbidity and highest settling velocity. This result is consistent Drobny (1963). Patwardhan and Mirajgaonkar (1970) also noted that increasing the edge length produced the lowest residual turbidity.

As part of their conclusions, Patwardhan and Mirajgaonkar (1970) recommended that in selecting a paddle design, no regions in the vessel should have higher local velocity gradients than the desired setup. They pointed out that very high velocity gradients at certain points in the vessel will break flocs that have grown to large sizes. Thus to achieve good results, it is essential to narrow down the range of variation of velocity gradients.

Part of the work presented by Argaman and Kaufman (1970) looked at the influence of the turbulence produced by a two-blade radial flow impeller and a stake & stator impeller on the flocculation performance in continuous stirred tank reactors. The turbulence in the reactor was measured using a hot film anemometer probe. Although the power spectra for the two impellers showed no sign of periodicity, it was not clear whether the authors filtered out the periodic velocity component from the velocity data. The flocculation performance was determined by measuring the net number of primary particles removed through growth to larger floc particles. Along with these primary particle concentration measurements, Argaman and Kaufman (1970)

also took some photographs of floc particles under a microscope to observe the effects of stirrer type on floc size.

Argaman and Kaufman's (1970) flocculation results indicate that the concentration of primary particles was lower for the stake & stator impeller. This suggests that the stake & stator impeller outperformed the two blade turbine. However, Argaman and Kaufman's (1970) turbulence measurement results show that the volumetric average of the mean square velocity fluctuations was higher for the stake & stator than for the two blade turbine. These turbulence results would suggest that the flocculation performance would be poorer for the stake & stator impeller than for the two blade turbine.

Argaman and Kaufman (1970) interpret these results by suggesting that the collision rate is enhanced by the higher volumetric average mean square fluctuating velocity. Consequently, fewer primary particles would be found with the stake & stator impeller. However, a more likely reason for this result could be that the distribution of the local mean square fluctuating velocity is wider for the two blade turbine than for the stake & stator impeller. For example, Figure 2.3.1 displays a possible spatial distribution of the mean square fluctuating velocity for the stake & stator impeller and two blade turbine. Figure 2.3.1 suggests that the mean is higher for the stake & stator impeller than for the two-blade turbine. But Figure 2.3.1 also implies that the variance is greater for the two blade turbine. Figure 2.3.1 suggests that there are regions in the reactor where the maximum mean square fluctuating velocity of the two blade turbine is much higher than the maximum mean square fluctuating velocity of the stake & stator impeller. Circulation of the floc particles into this highly turbulent region will cause more breakup and consequently poorer flocculation performance. Since no statistics such as in Figure 2.3.1 were presented by Argaman & Kaufman (1970), this scenario cannot be verified.

Argaman and Kaufman's (1970) photographic floc size measurements indicated no effect of stirrer type on floc size. However, floc breakup may have occurred when the floc samples were taken from the reactor. Particle breakup during the sample removal procedure will cause errors in the floc size measurements. Forcing particles through a constriction such as a syringe or particle counter may cause floc breakup (Clark et al., 1994). No particle size distributions were reported by Argaman and Kaufman (1970).

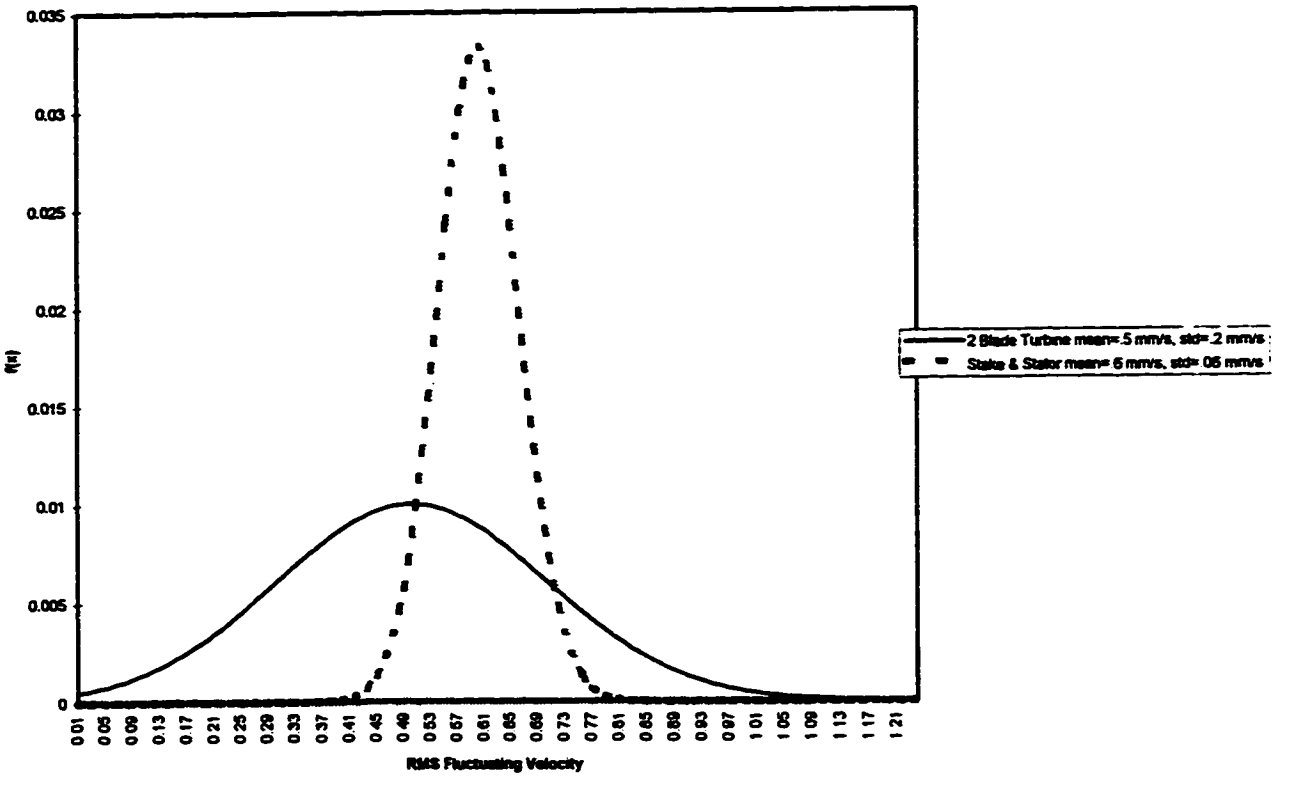

Figure 2.3.1: A Hypothetical Spatial Distribution of the Mean Square Fluctuating Velocity for the Two Blade Turbine and for the Stake & Stator Impeller

Along with scaleup results, (Section 2.2) Oldshue and Mady (1978) also reported the performance of four different impeller types. These impellers include two axial flow impellers (A200: constant pitch impeller, A212: variable pitch impeller), a radial flow impeller (Rushton turbine) and a rake impeller. The turbidity was measured after 10 minutes of flocculation and 60 minutes of settling. Oldshue and Mady's (1978) results show that the rake outperformed all the other impellers. Similar turbidity results were found for the A200 and the A212 impellers. The Rushton turbine produced the worst flocculation results.

Hanson and Cleasby (1990) investigated the effects of temperature, impeller type, and solution chemistry on turbulent flocculation. Only the impeller type results will be presented in this section of the literature review. A majority of the work by Hanson and Cleasby (1990) was carried out in the adsorption-destabilization flocculation region. The raw water used in their study was made with 25 mg/l of 1.88 micron diameter kaolin particles in tap water buffered with 100 mg $NaHCO_3$/L. A stake & stator impeller and a two-blade turbine similar to those used by Argaman and Kaufman (1970) were used in their study. The flocculation performance was determined by measuring the particle size distribution and the total particle count of the flocculated suspension.

Hanson and Cleasby (1990) found that the removal of primary particles at 20°C was not sensitive to the impeller geometry. However, at 5°C, the impeller geometry was more significant in the removal of primary particles. At this temperature, the stake & stator impeller produced better flocculation results than the two-blade turbine. Hanson and Cleasby (1990) also investigated the breakup rate of each impeller. The flocs used in these breakup experiments were prepared by flocculating a suspension for 45 minutes. The flocs were then broken up by subjecting them to the same turbulence intensity used during the rapid mix.

Hanson and Cleasby (1990) found that the two-blade turbine generated many more primary particles than the stake & stator impeller. Hanson and Cleasby (1990) concluded that the local turbulence intensity in the impeller discharge region of the two-blade turbine is much higher then the local turbulence intensity produced by the stake & stator impeller for the same energy input. Hence, the two-blade turbine causes more breakup and greater number of primary particles.

McConnachie (1991) studied the effects the turbulence produced by three impellers on flocculation performance. A picket gate, two blade paddle, and a branched impeller were used in a 100 mm square tank. Measurement of the fluid velocities and the local turbulence intensities was accomplished using a laser Doppler velocimeter. An artificial raw water was made by mixing kaolin with distilled water. The coagulant used was aluminum sulfate. The pH was equal to 7.0 after alum addition. The flocculation performance was evaluated by measuring the residual turbidity after twenty minutes of sedimentation.

McConnachie (1991) found that the minimum residual turbidity was not influenced by the impeller type used in their study. All the stirrers produced the same minimum residual turbidity for the same power input. However, McConnachie (1991) noted that the branched type impeller produced relatively low turbidities over a wider range of power input. He concluded that impellers which extend throughout the reactor volume and had sharp blade edges are more versatile than other types.

Along with the scale-up work (Section 2.2), Clark et al. (1994) also evaluated four different flocculation impellers (Rushton, pitched blade, foil, rake) at four different D/T ratios (0.2, 0.3, 0.5, 0.66). Clark et al. (1994) noted that none of the flocculation impellers clearly out performed the others when the impellers were tested for residual turbidity and total particle count after 20 minutes of sedimentation. However, more often than not, they did detect a mild degradation in flocculation-sedimentation performance moving from the rake to the foil to the pitch blade and to the Rushton impellers. They also mentioned that more exhaustive tests with more replication would be required to make any final judgments on flocculation impeller efficiency.

Sajjad and Cleasby (1995) investigated the effects of different mixing impellers on the kinetics of flocculating kaolin clay suspensions using ferric nitrate as the coagulant. This study was conducted at both cold and warm water temperatures (5°C,23°C), at two pH levels (6.0, 7.8) and several clay concentrations. The flocculation kinetics were measured using a Photometric Dispersion Analyzer (PDA) and a conventional Hach ratio turbidimeter. The PDA measured the flocculation kinetics continuously while turbidity measurements were taken at discrete times during the flocculation process. Five different mixing impellers were investigated (A310 foil

impeller, two blade turbine, modified stake impeller, wire mesh impeller, two blade vertical stack impeller). The A310 foil impeller and two blade turbine were located at the center of the reactor while the modified stake, wire mesh, and two blade vertical stack extended well into the reactor volume.

Sajjad and Cleasby (1995) found that the impeller geometry had a significant impact on the flocculation kinetics. In their study, Sajjad and Cleasby (1995) found the wire mesh impeller produced the best flocculation results while the A310 foil impeller produced the worst. Their study showed that the agglomeration rate was higher with the wire mesh impeller than for the two blade turbine and the A310 foil impeller. Sajjad and Cleasby (1995) theorized that the mesh impeller generates more homogeneous turbulence than the foil and turbine impellers. The mesh impeller also reduced the characteristic mixing time through direct contact with the entire reactor volume. As a result of direct contact with the entire volume, the necessity of bulk flow is reduced and all the impeller power input is directed towards increasing the velocity fluctuations throughout the reactor volume. According to Sajjad and Cleasby (1995), the rate of particle collisions would increase per unit volume of suspension due to the increased velocity fluctuations.

The results of Sajjad and Cleasby (1995) also suggest that larger particles were formed by the wire mesh impeller than for the two blade turbine and the A310 foil impeller. This was demonstrated by the lower turbidity results and declining flocculation index curve from the PDA for the wire mesh impeller. However, these results are in question since the authors noted that settling occurred with the two blade and wire mesh impellers during the flocculation process. It is not clear whether Sajjad & Cleasby (1995) took into account the increased settling time for the two blade and wire mesh impellers in comparing the turbidity measurements for all the impellers investigated. Also, no particle size distributions were presented to verify the size of the maximum floc.

The results of Drobny (1963), Patwardhan & Mirajgaonkar (1970), Argaman & Kaufman (1970), Oldshue & Mady (1978), Hanson & Cleasby (1990), McConnachie (1991), Clark et al. (1994) and Sajjad & Cleasby (1995) clearly show that impeller type has an influence on flocculation performance. However, most of the authors did not characterize the steady state particle size distribution in order to determine how each impeller affected different size class

particles. Moreover, only two of these investigators measured the turbulence produced by the impellers throughout the reactor volume. In order to fully understand the effect of impeller type on the flocculation process, both the local turbulence characteristics throughout the reactor volume and the steady state particle size distribution need to be evaluated.

2.4 Particle Agglomeration and Breakup Models in Flocculation

The rate of agglomeration is a function of the rate at which collisions occur between particles and the effectiveness of these collisions in permitting attachment. Over the years, many mathematical models have been developed to describe the rate at which collisions occur between particles in order to predict the resulting flocculation performance. Early modeling work took the form of studying the driving mechanisms which brought particles together.

The basic mathematical description of particle agglomeration was developed by Smoluchowski (1918). Smoluchowski's rate equation describes the change in the number concentration of particles at any size assuming binary collisions between particles. Smoluchowski's equation can be expressed as (Clark, 1996):

$$\frac{dn_k}{dt} = \frac{1}{2}\alpha \sum_{i+j=k} \beta(i,j) n_i n_j \; - \; \alpha n_k \sum_{i=1}^{\max} \beta(i,k) n_i \qquad (2.4)$$

$$I \qquad\qquad II$$

where

n = number concentration of particles

α = collision efficiency factor = fraction of successful collisions

$\beta(i,j)$ = collision frequency function = mechanism of interparticle contact

I, j, k = subscripts describing a particular particle size

Equation 2.4 simply states that the rate of change of a particle concentration of size k is increased by the collision of two smaller particles whose combined volume is that of a size k particle (part I of Eqn. 2.4) and decreased by the collision of a size k particle with any other size

particle (part II of Eqn. 2.4).

Researchers have defined three driving mechanisms which bring particles together in liquids: 1) Brownian motion (perikinetic flocculation): interparticle contacts resulting from thermal motion, 2) Fluid shear (orthokinetic flocculation): interparticle contact resulting from bulk fluid motion, and 3) Differential sedimentation: interparticle contact resulting from the collision of two particles settling at different velocities. Those mechanisms are shown in Table 2.3.1. Although all three mechanisms can be incorporated into the collision frequency function $\beta(I, j)$ to model the flocculation process (Lawler et al ., 1983; Lawler and Wilkes, 1984), it has been shown that fluid shear is the dominate collision mechanism during the flocculation process (Appendix B). This will depend on the primary particle size (Clark, 1996). Consequently, the other two mechanisms can be neglected.

In order to better approximate the fluid shear collision mechanism in a mixing tank, Camp & Stein (1943) developed the concept of the root mean square velocity gradient, G. G was developed by considering the angular distortion of an elemental volume of water due to tangential surface forces or shear stresses. The authors assumed that the following equation would be valid for both viscous and turbulent flow:

$$\Phi=\mu G^2=\mu\left[\left(\frac{\delta u}{\delta y}+\frac{\delta v}{\delta x}\right)^2+\left(\frac{\delta u}{\delta z}+\frac{\delta w}{\delta x}\right)^2+\left(\frac{\delta v}{\delta z}+\frac{\delta w}{\delta y}\right)^2\right] \qquad (2.5)$$

where

Φ = work per unit volume per unit time or power per unit volume

μ = dynamic viscosity

As it pertains to mixing, the authors noted that the velocity gradients throughout the tank will vary considerably in magnitude. However, under steady conditions of power input, there is a mean velocity gradient which corresponds with the mean value of Φ throughout the tank. Hence G_m can be defined as

Table 2.3.1: Collision Mechanisms for Particle Agglomeration (Stumm & Morgan, 1983)

Transport Mechanism	Rate Constant for Heterodisperse Suspensions		Rate Constant If $d_1 = d_2$	
Brownian diffusion	$k_b = \frac{2}{3}\frac{\mathbf{k}T}{\eta}\frac{(d_1 + d_2)^2}{d_1 d_2}$	(1)	$k_p = \frac{4\mathbf{k}T}{3\eta}$	(4)
Laminar shear	$k_{sh} = \frac{(d_1 + d_2)^3}{6} G$	(2)	$k_{ii} = \frac{2}{3} d_p^3 G$	(5)
Differential settling	$k_s = \frac{\pi g(\rho - 1)}{72\nu}(d_1 + d_2)^3 (d_1 - d_2)$	(3)	$k_s = 0$	(6)

[a] The rate at which particles of sizes d_1 and d_2 come into contact by the jth transport mechanism is given by $F_j = k_j N_{d_1} N_{d_2}$. F_j = collision rate in collisions per unit volume ($cm^{-3}\ sec^{-1}$); k_j = bimolecular rate constant ($cm^3\ sec^{-1}$) for the jth mechanism; N_{d_1} and N_{d_2} = number concentrations of particles of size d_1 and d_2, respectively (cm^{-3}); $\mathbf{k}$ = Boltzmann constant ($1.38 = 10^{-23}\ J\ K^{-1}$; η = absolute viscosity ($g\ cm^{-1}\ sec^{-1}$, or $N\ cm^{-2}\ sec$); ν = kinematic viscosity ($cm^2\ sec^{-1}$); ρ = specific gravity of the solids ($g\ cm^{-3}$); g = gravity acceleration ($cm\ sec^{-1}$); G = mean velocity gradient (sec^{-1}); T = absolute temperature (K).

$$G_m = \sqrt{\frac{P}{Vol\,\mu}} \qquad (2.6)$$

where

G_m = average root mean square velocity gradient

P = power input by impeller

Vol = tank volume

However, G_m has been shown by other researchers to be inadequate to describe the fluid mechanics in a flocculation basin. Cleasby (1984) concluded that G_m is only a valid parameter for the flocculation of particles smaller than the Kolmogoroff microscale. Particles of this size are not common in water or wastewater flocculation practice. Cleasby (1984) also found that the power per unit mass to the two thirds power is a more appropriate parameter than G_m. Clark (1985) concluded that Camp & Stein average root mean square velocity gradient is fundamentally incorrect since they require that a three dimensional flow be represented by a two dimensional flow.

More recently, Kramer and Clark (1996a) found that the approach of Camp & Stein (1943) was deficient in three areas:

1) The general existence of a pure maximum shear form of the velocity gradient tensor does not occur in a three dimensional flow field.

2) The use of velocity gradients as an alternative for strain rates is conceptually invalid when applied to the flocculation process and in the calculation of the dissipation function.

3) The assumption that the square root of global average dissipation function is equal to the average velocity gradient is invalid.

Furthermore, Kramer and Clark (1996a) showed that under certain flow conditions, the error in using G_m increases as the variance of the spatial distribution of the local energy dissipation rate increases. Although Cleasby (1984), Clark (1985), and Kramer & Clark (1996a) have shown that Camp & Stein's (1943) G_m is inappropriate to describe the flocculation fluid mechanics, it is still widely used by water treatment researchers to compute the level of fluid motion in the complex mixing environment of a stirred tank.

In a later study, Saffman & Turner (1956) approached the problem of flocculation by fluid motion in a purely turbulent flow field. In developing their relationship, Saffman & Turner (1956) assumed that the turbulent flow field was homogeneous and isotropic and that the floc particles were smaller than the Kolmogorov microscale. The collision frequency function was derived as

$$\beta(i,j) = \frac{1}{6.18}(d_i + d_j)^3\left(\frac{\varepsilon}{\nu}\right)^{\frac{1}{2}} \tag{2.7}$$

where

ε = energy dissipation rate per unit mass of fluid

ν = kinematic viscosity

d = particle diameter

Substituting Equation 2.7 into Smoluchowski's rate Equation 2.4, we obtain the following flocculation rate equation in turbulent flow:

$$\frac{dn_k}{dt} = \frac{1}{12.36}\alpha\sum_{i+j=k}(d_i+d_j)^3\left(\frac{\varepsilon}{\nu}\right)^{1/2} n_i n_j - \frac{\alpha}{6.18} n_k \sum_{i=1}^{max}(d_i+d_k)^3\left(\frac{\varepsilon}{\nu}\right)^{1/2} n_i \tag{2.8}$$

One problem with the above model is that it predicts an indefinite growth of small particles to larger aggregates. Clearly, flocculation experiments have demonstrated that this indefinite growth of agglomerates does not occur and that aggregates grow until a maximum stable floc size is reached. In order to model the development of a maximum stable floc size, investigators have incorporated particle breakup routines in their simulations.

There have been many publications on the hydrodynamics of floc breakage. Thomas (1964) proposed that the rupture of flocs was due to the pressure fluctuations on opposite sides of aggregates. Borts and Gapalo (1971) suggested that the breakdown of a floc began when the stresses acting on a floc reached the limiting failure strength. Argaman and Kaufman (1970) suggested that erosion of primary particles from the surface due to fluid shear is a more important breakup mechanism than floc rupture. Parker et al. (1972) also proposed that primary particle erosion was the main breakup mechanism. They argued that the maximum stress would be imparted by eddies of size similar to the floc particle. Other researchers such as Adler and Mills (1979), Kao and Mason (1975), and Sonntag & Russel (1986, 1987) developed similar breakup routines which use either the concept of floc rupture or floc erosion. However, the mathematical models developed by all these investigators were designed to only simulate the change in the number of primary particles. In order to truly describe a process where individual particle sizes are modified by agglomeration and breakup, a population balance equation is the most appropriate method.

Many investigators have developed population balance models to describe the flocculation process. Appendix B displays some of the comprehensive population balance equations developed over the last seventeen years that include both agglomeration and breakup. Tambo and Watanabe (1979) proposed a floc growth equation that took into account the reduction in floc density with increasing floc size. The floc growth equation was designed to allow the agglomeration process to continue until a certain size was reached. After that particle size was attained, any larger particles were returned to the original components before the collision occurred. Tambo and Watanabe (1979) found that a constant collision efficiency, α_o, did not allow the floc growth equation to match the experimental results. The authors designed a collision efficiency, α_R, to be a function of the initial collision efficiency, α_o, a function of the

number of primary particles in the floc, R, and a function of the number of primary particles in the maximum size floc, S.

Lu and Spielman (1985) developed a population balance model which took into account the stochastic nature of the agglomeration breakup process. They believed that floc breakage in turbulent flow can only be described by means of a statistical treatment when dealing with a large number of particles. Lu and Spielman (1985) included terms for both floc rupture and erosion of primary particles. In their design of the population balance model, Lu and Spielman (1985) assumed a constant floc density for all particle sizes. In reality, however, floc density has been found to decrease with increasing floc size. Although their model fit their experimental data fairly well, the rate equation required the determination of thirteen empirical constants.

Koh et al. (1987) used a population balance model developed by Batterham et al. (1981) for pelletization. The model uses descretized rate equations designed for sizes in geometric progression. In other words, the volume doubles after each size interval. Floc breakup is not included as a separate mechanism in the population balance but instead, breakup is accounted for in the collision efficiency function. The collision efficiency function is designed such that when two particles collide to produce an agglomerate larger than the maximum stable floc size, the value of the collision efficiency is zero. In conjunction with the population balance equation, Koh et al (1987) divided the stirred tank volume into two compartments of uniform shear rate and found better correspondence between predictions and experimental results.

Chen et al. (1990) developed a simple population balance model where the particles collided to form spherical, nonporous aggregates. The breakup of an aggregate was assumed to be a splitting process resulting in two fragments of equal size. Chen et al. (1990) designed the breakup rate to have a power-law dependence on aggregate size. Unfortunately, their model was not compared to any experimental data.

Kusters (1991) proposed the most comprehensive population balance model to date. Kusters' (1991) model is similar to Koh et al.'s (1987) model in that it also uses discretized rate equations designed for sizes in geometric progression. Unlike Koh et al. (1987), Kusters (1991) does include floc breakup terms in the rate equation. He assumed that the breakup rate was first order in particle number concentration. Kusters (1991) also assumed a fractal description of the

floc structure and a power law dependence of the floc strength on the solids' volume concentration.

Kusters (1991) developed a two dimensional numerical particle tracking simulation in a turbine agitated vessel to predict the movement of the dispersed phase particles throughout the vessel. Using this simulation, he was able to determine the amount of time particles spend in zones of low and high shear stress. Kusters (1991) argued that since the values of the local energy dissipation rate in a turbine agitated vessel are distributed over a wide range of values, aggregates will only agglomerate during the time spent in regions of low energy dissipation rate. Breakup, on the other hand, occurs during the time spent in regions of high energy dissipation rate. Based on the particle tracking simulation, Kusters (1991) was able to incorporate the time spent in different shear zones into his population balance model. The resulting model was able to predict the effects of tank size on flocculation performance.

Other population balance models have also been developed to characterize the agglomeration and breakup process (Ray & Hogg, 1986; Sastry & Gaschlgnard, 1981; Hounslow et al. 1988; Hounslow, 1990; Hill and Ng, 1995, 1996; Litser et al., 1995). Although all of these population balance models were developed to mathematically describe the agglomeration and breakup process, physics of the fluid flow is absent. These models do not contain any parameters that represent the intensity of the fluid mechanics. In other words, the models presented by these researchers would not predict a shift in the particle distribution due to change in the fluid intensity without significant changes to empirical constants.

The population balance models shown in Appendix B have all demonstrated the ability to match the experimental results of the model developers. These investigators achieved this by using a least squares fit algorithm to determine the appropriate empirical constants in the model. However, the models produced by Tambo and Watanabe (1979), Lu and Spielman (1985), and Chen et al. (1990) were not able to predict changes in flocculation performance due to changes in impeller type and tank size that were noted experimentally by other investigators (See Section 2.2). Clearly these models do not take into account the spatial variation of the turbulence measured in a stirred tank reactor (See Section 2.1).

The population balance model of Koh et al. (1986) might be more sensitive to the spatial

variations of the turbulence because they incorporated a two compartment model which divides the stirred tank into a region of high shear rate and low shear rate. However, the two compartment model requires a lot of empirical information in order to model the change in fluid mechanics due to changes in impeller type or tank size. Kusters (1991) population balance model has been able to demonstrate the effects of changing tank size on particle aggregation. This was achieved by incorporating a coagulation rate constant and a breakup frequency determined from a numerical particle tracking simulation. The coagulation rate constant and the breakup frequency were determined for each aggregate size. However, like Koh et al. (1986), Kusters' (1991) population balance model is very complex and requires several empirical parameters. In order to simply model the flocculation performance in a stirred tank, a population balance model must be developed that incorporates all the dynamics of the fluid flow in the stirred tank with a minimum amount of empirical fitting parameters. A simple population balance model that accurately describes the intensity of the turbulence in a stirred tank will not need many empirical parameters and still show sensitivity to both impeller type and tank size.

2.5 Lessons Learned From Drop Breakup Research

There have been many studies in the breakup of immiscible liquid drops in another liquid medium in turbulent flow. Most of the work done tried to understand the mechanisms responsible for drop breakup. In the course of trying to define the mechanisms for breakup, past researchers developed models to correlate the drop deformation and breakup rate with variables such as continuous or dispersed phase viscosities, surface tension, shear rate, and turbulent energy dissipation rate. Unfortunately, like particle breakup, a majority of the drop breakup models assumed local isotropic conditions and that drop breakup can be correlated to average turbulent properties. However, some researchers have found that drop breakup has occurred in regions where the turbulent flow is anisotropic (Chang et al., 1981; Konno et al., 1983). Other researchers have obtained photographic evidence that drop breakup occurred through the interaction of the large scale flow field with the oil droplet (Chang et al., 1981; Konno et al., 1983; Clark, 1988).

Chang et al. (1981), using viscous oil, found that the oil droplets in the impeller discharge region of a Rushton turbine would stretch and break up in the direction of the mean flow. This was the only location where drop breakup occurred in the stirred tank. Clark (1988) provided photographic evidence that drop breakup occurred only in the region behind a special grid type impeller. Clark (1988) indicated that drop breakup was probably due to large pressure fluctuations experienced by the drop in the vicinity of the impeller.

Konno et al. (1983) did extensive work in both photographing and modeling the breakup of oil droplets in a stirred tank reactor with a Rushton turbine. In their study, Konno et al. (1983) showed photographic evidence that a large portion of the oil droplets were broken behind the Rushton turbine blade. Similar to the results of Chang et al. (1981), Konno et al. (1983) found that the breaking drops took an outward flow path behind and below the impeller blade. This preferred direction in the breaking of drops suggests that the turbulent flow in the impeller discharge region of the Rushton turbine is anisotropic.

Konno et al. (1983) also showed that the dynamics of drop breakup modeling could not be achieved by assuming isotropic turbulence. They found that by including terms for breakup in the anisotropic region in the impeller discharge zone, the model accurately described the droplet size distribution in the stirred tank.

Part of the work by Konno et al. (1983) also looked at the effects of tank size on drop breakup. Their results indicate that for the same ε_{avg}, the drop breakup frequency increased as the tank size increased. Their droplet size distribution model was also able to predict a shift in the distribution function to the smaller droplet sizes with increasing tank size. The Konno et al. (1983) model showed sensitivity to tank size because they realized that drop breakup occurred through the interaction of the large scale flow field with the oil droplets.

The results of Chang et al. (1981), Konno et al. (1983), and Clark (1988) seem to indicate that drop breakup does not occur in regions where the turbulent flow is isotropic. Their results also indicate that breakup does not occur at small scales of motion where average turbulence parameters are sufficient to describe the fluid mechanics. It is possible that the same actions leading to the breakup of oil droplets in turbulent flow may help to explain the increase in floc breakup with increasing tank size. Floc breakup may be occurring in regions of the flow where

the turbulence is anisotropic. If this is true, then the population balance model to describe the flocculation process must include terms which describe the large scales of motion in the anisotropic region (i.e. the impeller discharge zone).

2.6 Design Standards for Vertical Shaft Mechanical Mixers in a Single Flocculation Tank

The ultimate objective in flocculator design is the optimal removal of floc particles during subsequent sedimentation and filtration. The goal in designing the flocculator system (i.e. basin configuration, inlet & outlet conditions, mechanical mixer configuration, mixing intensity, and number of baffles) is to generate a turbulence pattern that will produce large and dense floc particles. These floc particles will then settle out easily during the sedimentation process.

In general, there are two mechanical mixer configurations used in water treatment. They are the horizontal shaft with a paddle wheel impeller and the vertical shaft with a marine propeller or turbine type impeller. Although the horizontal/paddle wheel configuration is the most common setup in water treatment plants, the vertical/impeller configuration is being used in the design of new flocculator systems. This trend in flocculator design is due to the ease of maintenance and fewer breakdown occurances that have been recorded with the vertical shaft flocculator system.

The design criteria used for mechanical mixers are G_m and the mean residence time,τ. Typical detention times range from 15 to 45 minutes. Although these times should only be influenced by the influent water conditions, type of coagulant, and requirements of downstream processes, they also vary with the source of the design standards manual [$\tau \geq 30$ mins: Health Education Services (1976); $15 \leq \tau \leq 45$ mins: Environmental Protection Agency (1985)]. For a single basin design, the value of G_m ranges from 20-100 1/sec. Along with these values of G_m, the design standards specify a maximum allowable tip speed between 2-6 ft/s (0.61- 2 m/s). The tip speed specification was included to reduce the amount of floc breakage in the basin (Bean, 1953). The variation in the maximum tip speed was a function of the design manual that was being referenced [$v_{tip} \leq 0.61$ m/s: Health Education Services (1976); $v_{tip} \leq 2$ m/s: James Montgomery Engineers (1985)].

Other important design criteria used in flocculation systems include the inlet and outlet

conditions and the number of baffles in the basin. Inlet and outlet turbulence is a major source of destructive energy in the flocculation basin. Typically designers try to maintain a flow through velocity between 0.5 and 3 ft/s in order to minimize floc breakage in the basin as a result of the inlet and outlet design. By adding inlet diffusers to improve the uniformity of the velocity distribution and by enlarging connecting conduits between the floc basin and the sedimentation basin, designers can achieve a reasonable turbulence level at the inlet and outlet. Baffles are sometimes used to reduce vortex formation in the flocculation basin. The formation of a vortex in the flocculation basin will significantly reduce the efficiency of the mixing process. Baffles are also used at the inlet and outlet to improve basin circulation and achieve a more uniform flow field.

In this study, only the design standards for G_m, τ, and the maximum tip speed are relevant. The inlet and outlet design criteria are not important since this study was done in batch flocculator tanks. Also, no baffles were included in the three square tanks used in this study. From these three design criteria, one can reasonably conclude that as long as the product of power per unit volume and the mean detention time are the same regardless of tank size or impeller type and that the maximum tip speed is less than 2 m/s, the flocculation performance should not be a function of tank size or impeller type. However, the flocculation experiments done by Clark et al. (1994) show that maintaining $G_m\tau$ = constant with $v_{tip} < 2$ m/s does not produce the same flocculation performance with different tank sizes or impeller types. These results would indicate that the current design standards are not adequate to use in the design and operation of a flocculator system.

2.7 Summary & Research Direction

The spatial distribution of the local turbulence parameters in a stirred tank has been shown to vary significantly from position to position. Several investigators have measured the turbulence generated by a Rushton turbine and shown that the local energy dissipation rate in the impeller discharge region can be as much as 50 times the average energy dissipation in the tank. These researchers have also shown that the local energy dissipation rate in the bulk regions of the

tank is only a fraction of the average energy dissipation rate. Some researchers have demonstrated that the spatial distribution of the local turbulence energy dissipation rate is a function of the impeller power number and the size of the tank.

Past researchers suggest that the performance of the flocculation process is sensitive to the size of the process and to the type of agitation device used. Clearly, Oldshue and Mady (1978), Clark and Fiessenger (1991), and Clark et al. (1994) have shown that for the same average energy dissipation rate in the tank, the performance of the flocculation process decreased with increasing tank size. Other investigators have also shown that for the same average energy dissipation rate, the performance of the flocculation process was better when a low power axial flow impeller (A310 fluid foil) was used and worse when a high power radial flow impeller (Rushton turbine) was used.

These results seem to indicate that the performance of the flocculation process cannot be simply related to the average turbulence energy dissipation rate. In fact, Kramer & Clark (1996a) showed the error in trying to describe the flocculation fluid mechanics with the average energy dissipation rate increases as the spatial variance of the local energy dissipation rate increases. Furthermore, Chang et al. (1981), Konno et al. (1983), and Clark (1988) have come to the conclusion that during emulsification, the breakup process has less to do with the average energy dissipation rate and more to do with the local high regions of the large scale fluid motion such as the turbulent fluctuating velocity and the frequency of passage through these high regions. Van der Molen and Van Maanen (1978) found that the high regions of the rms turbulent fluctuating velocity increased with increasing tank size. All these results seem to reaffirm the idea that breakup of particles might actually be due to the local high regions of the rms turbulent fluctuating velocity and the passage through these high regions.

Clearly, the evidence presented thus far suggests that in order to design and simulate the flocculation process, information about the impeller being used, the intensity of turbulence in the impeller discharge zone, and the frequency of particle circulation into this region of high turbulence must be incorporated into the model. To develop this model, the following research involves a number of steps. These steps are briefly outlined below and are discussed in more detail in Chapters 3 and 4.

1) Perform fluid mechanics measurements in a square tank reactor using laser Doppler velocimetry.
2) Perform finite element simulation of the fluid mechanics generated in a square tank reactor.
3) Develop a population balance model that includes information about the local turbulence intensity in a square tank reactor.
4) Conduct flocculation experiments maintaining constant G_m, flocculation time, and $v_{tip} <$ 2 m/s between different tank sizes and impeller types.
5) Compare population balance model with the experimental particle size distribution from the flocculation experiments.

3.0 EXPERIMENTAL METHODS & MATERIALS

3.1 Determination of Operating pH and Coagulant Dose for the Flocculation Experiments

Jar tests were conducted on the makeup water in order to determine the operating pH and coagulant dosage. The type of coagulant used was aluminum sulfate (Alum; $Al_2(SO_4)_3 \cdot 14H_2O$). Two types of jar test experiments were conducted: (1) the pH was held constant and the concentration of alum added was varied, and (2) the alum dose was held constant and the pH was varied. The turbidity and the final pH after 20 minutes of sedimentation was recorded for each pH/alum dose combination. The pH range and alum dose range studied in the jar test was based on Amirtharajah and Mills (1982) coagulation diagram for optimal turbidity removal.

The synthetic raw water was made by adding 50 mg/l Kaolin clay to ground water from a well below Newmark Civil Engineering Laboratory at the University of Illinois Urbana-Champaign. This ground water was chosen because it is an abundant natural water source with a fairly stable chemical composition. Table 3.1.1 displays the chemical characteristics of the groundwater. The initial pH of the ground water was around 8.0. Hydrochloric acid and sodium

Table 3.1.1: Characteristics of Illinois Groundwater (Adham, 1993)

Calcium	60 mg Ca^{2+}/L
Magnesium	25 mg Mg^{2+}/L
Hardness	310 mg/L as $CaCO_3$
Alkalinity	290 mg/L as $CaCO_3$
TOC	2.8 - 3.2 mg/l
UV Absorbance (254nm)	0.8 - 1.4
pH	7.4 - 8.0
Turbidity	0.1 - 1.1 ntu

hydroxide were added to the raw water when pH adjustment was necessary to achieve the target final pH after alum addition. The concentration of Kaolinite clay chosen was in the range of

synthetic water used by previous investigators (Tekippe and Ham, 1971; Vrale and Jordan, 1971; Andreau-Villegas and Letterman, 1976; Hong-Xiao and Stumm, 1987). Typically, the turbidity level for ground water is less than 5 NTU whereas for surface waters, the turbidity level can be as high as 100 NTU. The addition of the 50 mg/l of Kaolinite clay was found in the lab to produce a turbidity level of 78 NTU for the synthetic raw water.

The jar test experiments were done using a six paddle gang stirrer (Laboratory Stirrer, Phipps and Bird, Inc., Richmond, VA) in six 2 liter square beakers. The turbidity measurements were done using a Hach Ratio/ XR Turbidimeter (Model 43900, Hach Co., Loveland, CO). As can be seen from the results presented in Figure 3.1.1, the lowest turbidity was achieved with an alum concentration of 30 mg/l at a pH = 8.0. In order to achieve a final pH of 8.0 with 30 mg/l of alum, 10 ml of 0.1 N NaOH was added to the 2L jar. As a result of this jar test study, all the flocculation experiments to analyze the effects of tank size and impeller type on floc size distribution were conducted with an alum dose of 30 mg/l at a pH = 8.0.

3.2 Flocculation Scaleup Pilot Plant

The schematic of the batch flocculation scaleup pilot plant is displayed in Figure 3.2.1. As can be seen in Figure 3.2.1, the pilot plant was designed with three flocculation tanks. The largest flocculation tank was also used as the rapid mix tank. The size of this rapid mix/flocculation tank was large enough to feed all three flocculation tanks with the same artificial water and coagulant. The rapid mix tank has a side mounted Rushton turbine. This Rushton turbine was used to blend the coagulant, pH adjustment chemicals, and Kaolinite slurry into the groundwater. Figure 3.2.2 displays the rapid mix/flocculation tank design. A ½ HP LIGHTNIN VEKTOR DC adjustable speed motor (LIGHTNIN, Rochester, NY) was used to drive the Rushton turbine.

The size of the three square flocculation tanks are 557 L, 28 L, and 5 L volume. The size of the flocculation tanks were chosen to satisfy laboratory space constraints and impeller size constraints. The LDV measurements cannot be conducted in square tanks larger than 2.7 X 2.7 X 2.7 ft^3 due to limited floor space in the laser lab. The smallest impeller manufactured by

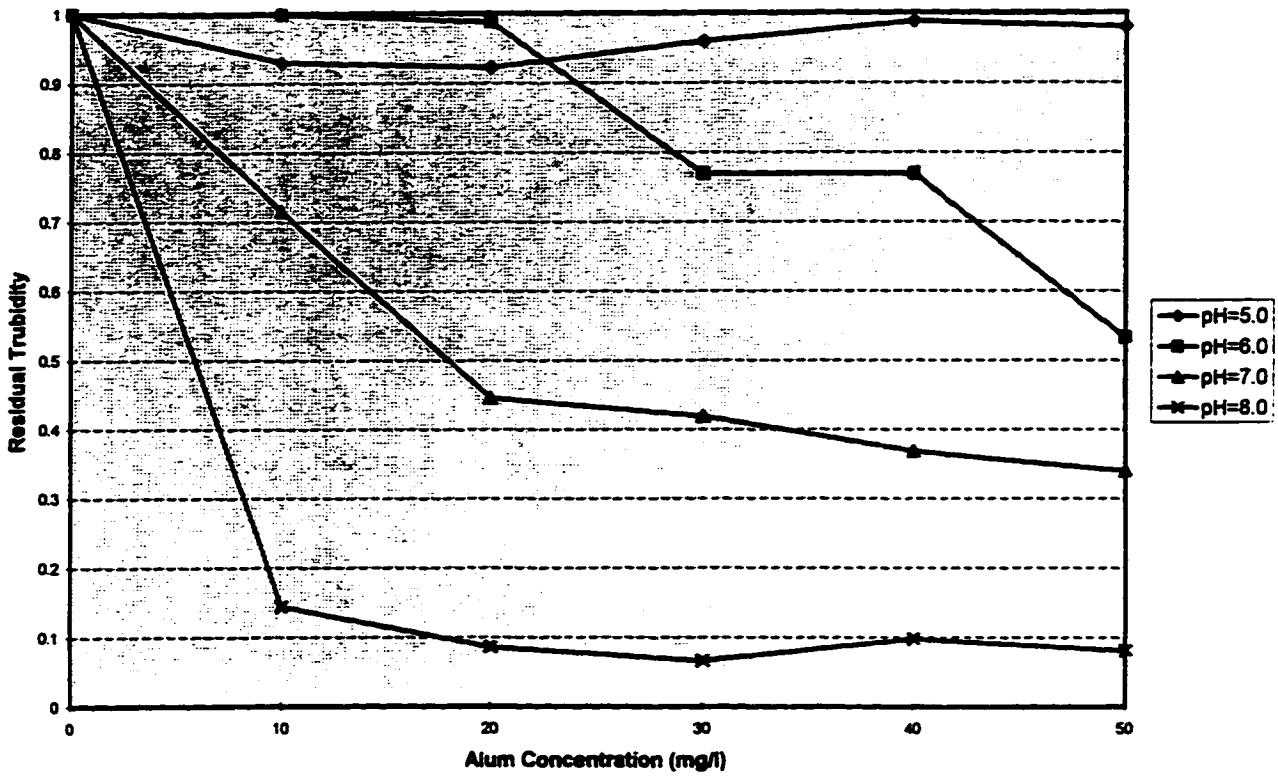

Figure 3.1.1: Jar Test Result

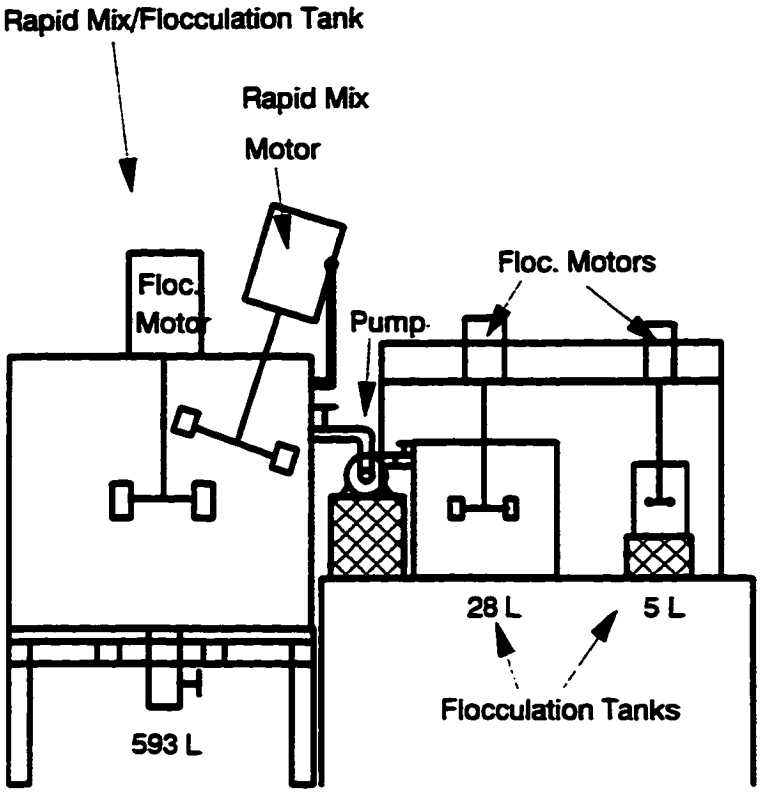

Figure 3.2.1: Flocculation Pilot Plant Setup

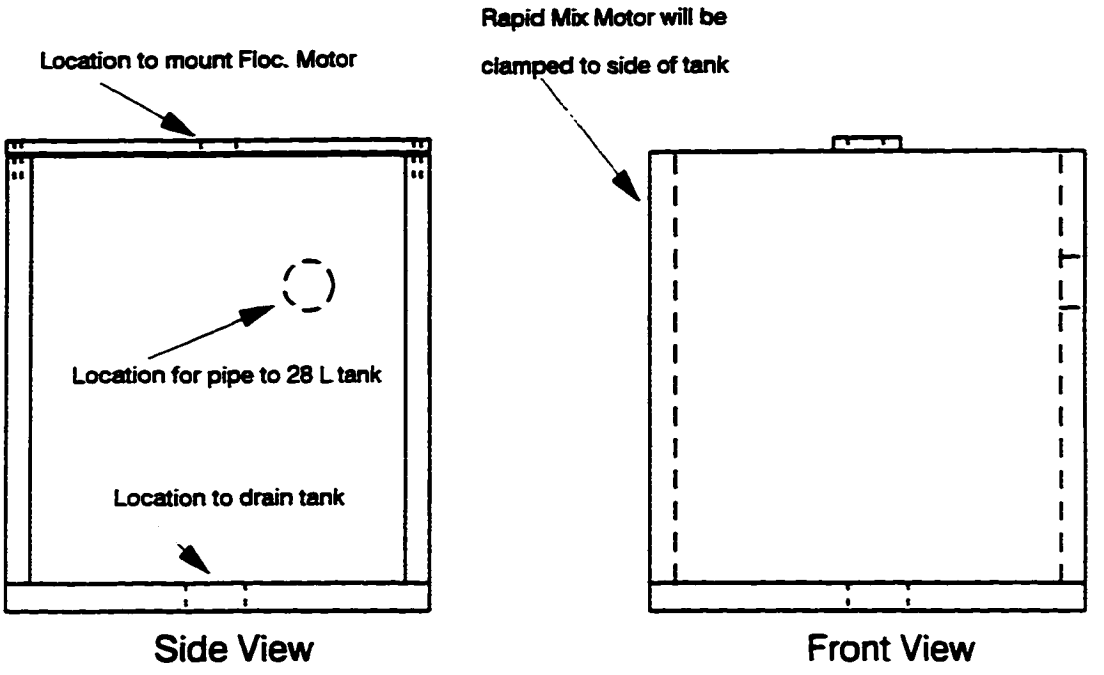

Figure 3.2.2: Rapid Mix/Flocculation Tank Design

LIGHTNIN has a 2.5 in. diameter. Therefore, the smallest square tank that can be tested and satisfy an equivalent D/T ratio equal to 1/3 is 6.7 X 6.7 X 6.7 in^3 (D=impeller diameter, T=tank diameter). The flocculation tanks were made out of clear plexiglass in order to facilitate the use of the laser during the LDV measurements and the floc photographic measurements (Figure 3.2.3). The types and sizes of each impeller used in this project are shown in Table 3.2.1 and Table 3.2.2. In Table 3.2.2 the A310 foil dimensions are based on airfoil technology (Abbot and Von Doenhoff, 1959).

Table 3.2.1: Summary of Flocculation Impeller Diameters

	Tank 1 (5 Liters)		Tank 2 (28 Liters)		Tank 3 (557 Liters)	
Impeller Type	D (in.)	D/T	D(in.)	D/T	D(in.)	D/T
A310 Foil	2.5	0.33	4.5	0.33	12.8	0.35
Rushton	2.5	0.33	4.5	0.33	12.8	0.35

Table 3.2.2: Characteristic Dimensions of the Rushton Turbine and A310 Foil Impeller

Rushton Turbine	A310 Foil Impeller
Blade Width: 0.2 D	Tip Chord Angle: 22°
Blade Thickness: 0.016 D	Width between Leading & Trailing
Blade Length: 0.25 D	Edge:
Disc Diameter: 0.68 D	0.10 D at impeller tip
Disc Thickness: 0.016 D	0.15 D at hub.
Hub Diameter: 0.24 D	Camber: 0.05 D at impeller tip
Hub Height: 0.14 D	0.0 D at impeller hub
	NACA Specification: 5510

Figure 3.2.3: Flocculation Tank Design

The flocculation impellers for the 28 L and 5 L tank were powered by 1/8 HP variable speed heavy duty stirrer (GK Heller Series H Motor Controller and Heavy-Duty Laboratory Stirrer, GK Heller Corp., Floral Park, NY). The flocculation impeller for the 557 L tank was powered by a ½ HP Minarik Electric DC adjustable speed motor (Minarik Electric Company, Los Angeles, CA).

3.3 Laser Doppler Velocimetry Experimental Setup

3.3.1 LDV Setup

LDV involves the measurement of fluid velocities by detecting the Doppler frequency shift of laser light that has been scattered by small particles moving with the fluid at one particular point (Figure 3.3.1) (Goldstein, 1983). The laser gives a beam of monochromatic light which is divided into two. The beams are then focussed at the measuring point by special optics. The two beams cross to produce interference fringes. If a small solid particle, assumed to follow the fluid flow perfectly, enters the measuring volume, it will move through these interference fringes, scattering light with a modulated intensity corresponding to its velocity through the successive fringes. This light is then collected by a photo multiplier and analyzed in the frequency domain, so as to give information on the velocity of the particle, perpendicular to the planes of interference.

The LDV measurements were conducted at points shown in Figure 3.3.2. The LDV measurements were conducted for the Rushton and fluid foil impellers at a D/T ratio of 0.33. This D/T ratio is common in the chemical process industry and is within the range of values used in the water treatment industry. The operating conditions listed on Table 3.3.1 were tested at each point.

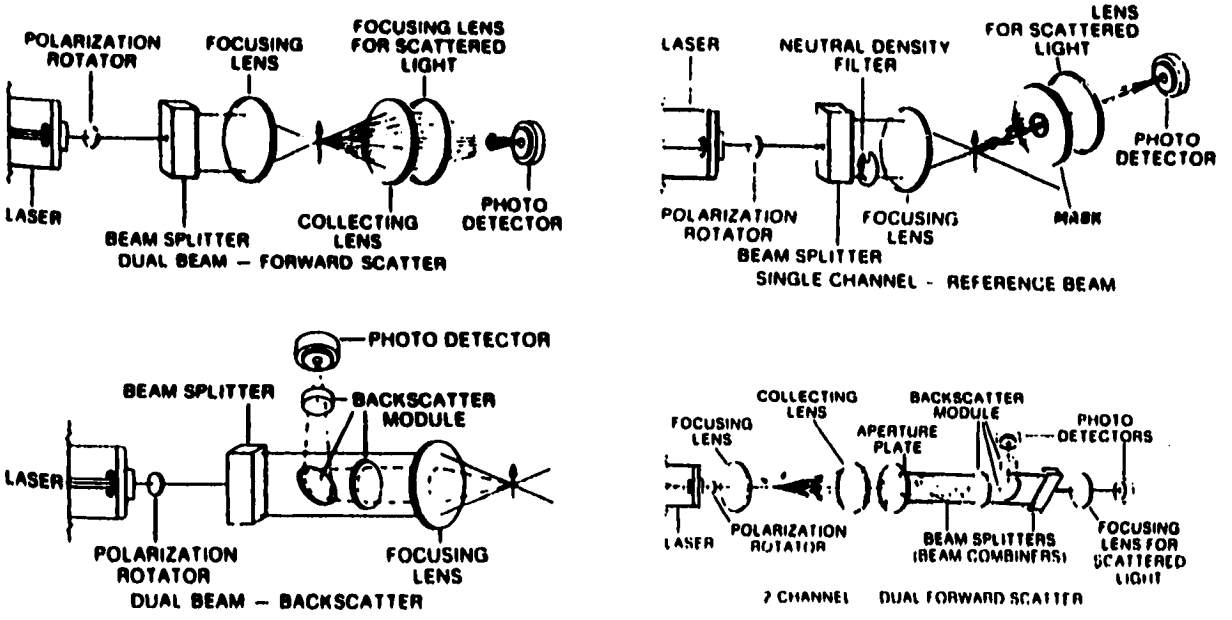

Figure 3.3.1: Different Examples of LDV Setups (Goldstein, 1983)

Figure 3.3.2: Location of LDV Measurements for an Axial and Radial Impeller

Table 3.3.1: Operating Conditions for Each Impeller/Tank Configuration

Water Temp.= 20 °C

Impeller Type	T=5L N (rev/min)	T=28L N (rev/min)	T=557L N (rev/min)
Rushton Turbine	84.32	56.22	26.68
A310 Fluid Foil	173.9	115.94	55.02

Measurement of the fluid velocities in the flocculation tanks were performed at LIGHTNIN using a dual channel laser Doppler velocimeter. The Dantec type 60X two-color laser Doppler velocimeter allows measurement of two velocity components simultaneously. The laser head was mounted on a computer controlled traversing mechanism which allows the user to conduct a complete scan of the flocculation tank. The measurements were collected via back scattering, with both receiving and transmitting optics in the same module. This setup eliminates the need to realign the receiving optics at each measuring point, ultimately reducing the time it takes for the laser system to scan the entire flocculation vessel.

The sizes of the LDV measuring volume diameter and length were 143 μm and 2.28 mm, respectively. The LDV measuring volume is defined as the volume within which the interference fringe pattern is formed by the two laser beams. The ellipsoid shape is a consequence of the Gaussian intensity profile of the laser beam. The number of interference fringes formed within the measuring volume is 36.

The calibration factors used to convert frequency data to velocity data were 4.1405(m/s)/MHZ and 3.9193 (m/s)/MHZ for the vertical and horizontal velocity components, respectively. The calibration factors alone are not enough to determine the direction of the velocity within the horizontal and vertical planes. In other words, the frequency is not dependent on the sign of the velocity. A positive or negative velocity with the same magnitude will result in the same Doppler shift. To overcome this problem, the frequency of one of the crossing beams in the vertical and horizontal planes is shifted slightly. Consequently, the fringe pattern is no longer stationary and moves at a constant velocity.

In the DANTEC LDV equipment, a frequency shift of 40 MHZ was used. Those particles

crossing against the moving fringes produced a higher Doppler frequency whereas those moving with the fringes produced a lower Doppler frequency. Therefore, directional ambiguity was removed once the shift frequency of 40 MHZ was subtracted from the signal.

The fluid in the stirred tank was seeded with alumina particles with a mean particle size of 8 μm. The alumina particles were chosen because of their high refractive index. With a maximum allowable error of ten percent, an 8 μm alumina particle in water will follow fluctuations (Lagrangian) in the flow up to 16 KHZ (Goldstein, 1983). Data acquisition and preprocessing of the particle velocity information was done using a DANTEC Burst Spectrum Analyzer (BSA). Computation of the mean, rms, power spectrum, and correlations were all done using a Fortran program implemented on a Hewlet Packard 715/75 workstation.

The BSA operates on signals generated by particles passing through the measuring volume. In this process, the arrival rate of the particles is a function of the flow velocity which brings them to the measuring volume. A simple arithmetic mean cannot be used to compute the mean velocity because it would be biased towards higher velocities (Figure 3.3.3). Previous researchers have found that an unbiased mean velocity measurement can be computed by weighting each velocity measurement with the time the particle spends in the measuring volume. This time is known as the transit time or burst time. The following equation was used to determine the unbiased mean velocity, U, using the aforementioned methodology:

$$U = \frac{\sum_{i=1}^{4096} u(i)\Delta t(i)}{\sum_{i=1}^{4096} \Delta t(i)} \qquad (3.1)$$

where

Δt(I)=burst time

u(I)=fluctuating velocity component

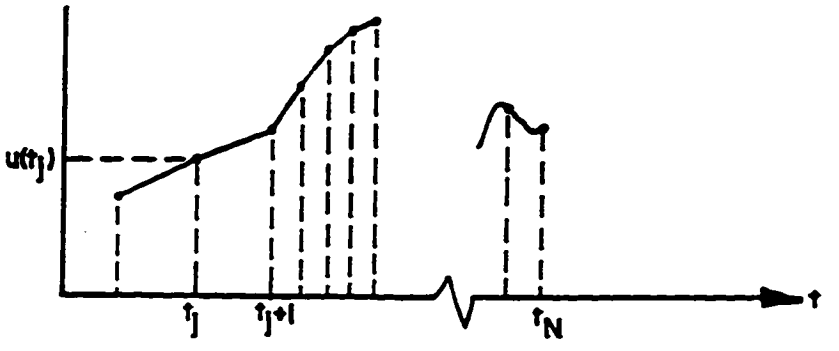

Note that the data points are close together when the velocity is high because there are more fast particles passing through the measurement volume than slow ones.

Figure 3.3.3: Sampling Characteristic for the Velocity with an LDV System (Adrian, 1993)

The number of samples used to compute the mean in each direction is 4096. In order to compute the unbiased mean square of the fluctuating component, the following equation was used:

$$\langle u^2_{random} \rangle = \frac{\sum_{i=1}^{4096} [u(i)-U]^2 \Delta t(i)}{\sum_{i=1}^{4096} \Delta t(i)} \qquad (3.2)$$

In order to compute the power spectrum and autocorrelation, the time trace of the 4096 velocity measurements was reconstructed. This was due to the requirement of the algorithm used to compute these correlations and power spectra (Press et al., 1992). The algorithm required that the data input be equi-spaced in time. This was not true of the particle velocity data. The particle arrival times or the time a particle enters the measuring volume, was random. Reconstructing the time trace of the velocity measurements and then resampling this new time trace at equidistant time intervals satisfied the algorithm used in the Fortran program developed in this project.

Typically, researchers have reconstructed the velocity time trace using a simple sample and hold technique (Figure 3.3.4). With the sample and hold technique, the data are sampled and held at the current value until the next data point is sampled. This process is continued until the last point is sampled. The problem with this technique is that the holding procedure results in masking high frequency information (Adrian and Yao, 1987). In the sample and hold technique shown in Figure 3.3.4, there are essentially discontinuities in the velocity time trace. When a power spectrum of the reconstructed velocity data is generated using the Fourier transform method, high frequency noise appears in the spectrum as a result of the discontinuities. This is known as the Gibbs phenomenon.

The high frequencies caused by the Gibbs phenomenon are larger than the high frequencies from the fluctuating velocity data. In order to remove the contribution of the Gibbs-related high frequencies and effectively increase the range of frequency from the fluctuating velocity data, Adrian and Yao (1987) recommend that better interpolation schemes such as linear

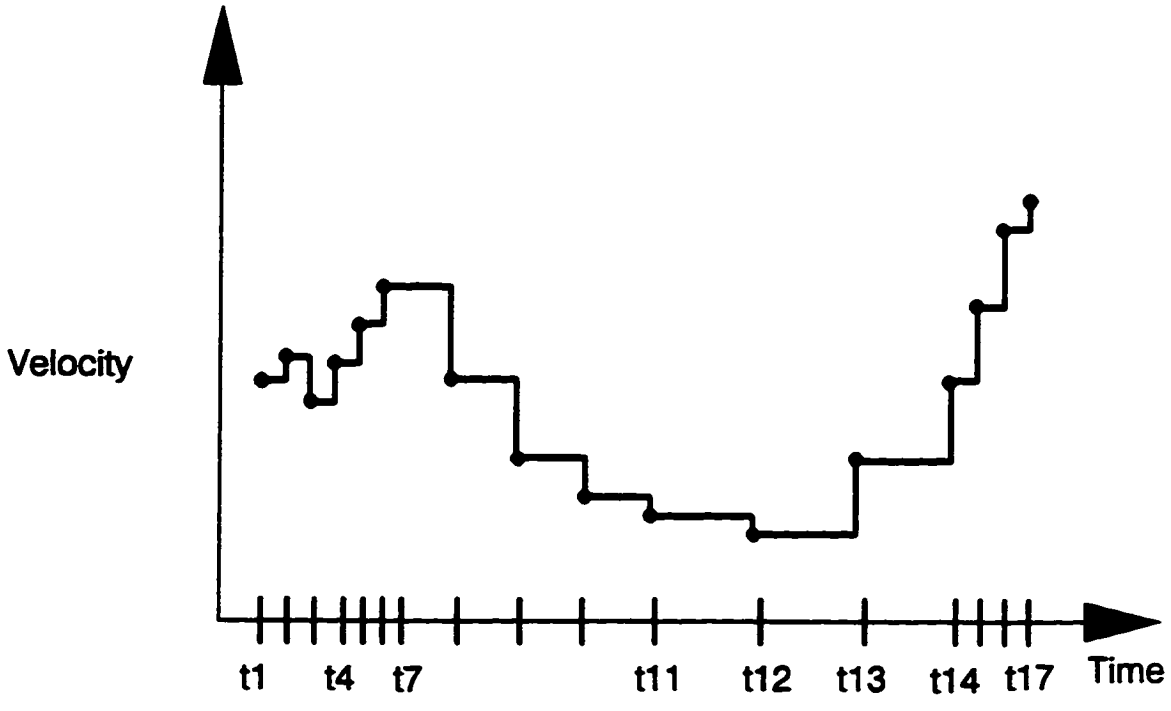

Figure 3.3.4: Reconstruction of the Velocity Time Trace Using a Sample and Hold Method

or quadratic splines be used to reconstruct the velocity time trace. In this Fortran program, a linear interpolation scheme was used between particle arrival times (Figure 3.3.5). The power spectrum was computed by performing a Fast Fourier Transform (FFT) on the reconstructed data (Press et al., 1992). The autocorrelations were also computed using the FFT method.

3.3.2 Computation of Length Scales, Energy Dissipation Rate, and Turbulent Kinetic Energy

Taylor (1938) first determined how to measure a characteristic size of the energy containing eddies using the autocorrelation curve with the assumption that the eddy passed the point of measurement with the speed of the mean velocity (i.e. Taylor's frozen field hypothesis). His experiments were conducted in a channel where the mean flow was primarily in one direction (Figure 3.3.6). In the flocculation tank, the mean flow direction will not be strictly in one direction as shown in Figure 3.3.7. It will generally retain all three components of velocity.

The current method researchers use to determine a characteristic size of the energy containing eddy when the mean flow retains all three components is to assume that part of the eddy will pass a point in each direction. As a result of this method, three lengths (L_{e_r}, L_{e_t}, L_{e_z}) each representing a projected length of the eddy size has to be determined. Using the Pythagorean theorem, researchers have computed the size of the energy containing eddy as

$$L_{eddy}=(L_{e_r}^2+L_{e_t}^2+L_{e_z}^2)^{1/2}$$

However, this method, is not consistent with Taylor's (1938) experiments where the energy containing eddy is convected past a point in the direction of the resultant mean velocity.

In order to properly compute the integral length scale in the direction of the mean flow assuming Taylor's frozen field hypothesis, a coordinate transformation can be done (Figure 3.3.8). As a result of a coordinate transformation, the mean flow will be in one direction in the new coordinate system. Once the mean flow is in one direction, the integral length scale (a characteristic size of the energy containing eddy) can be easily computed along this direction.

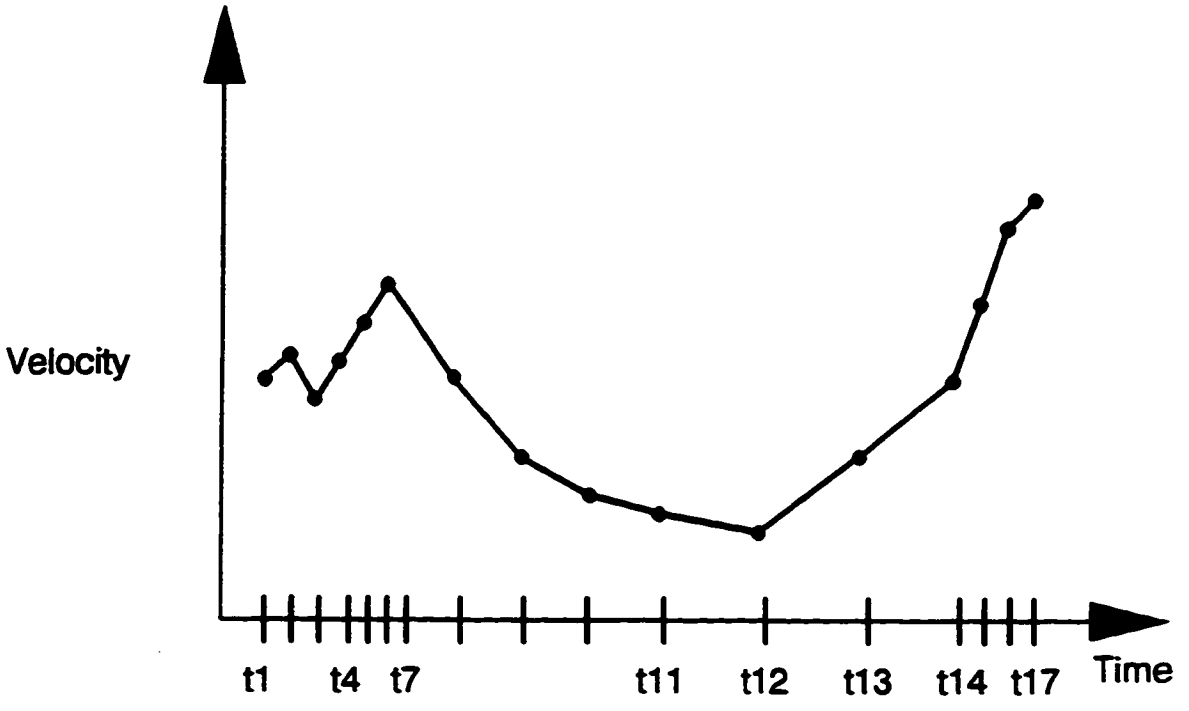

Figure 3.3.5: Reconstruction of the Velocity Time Trace Using a Linear Interpolation Method

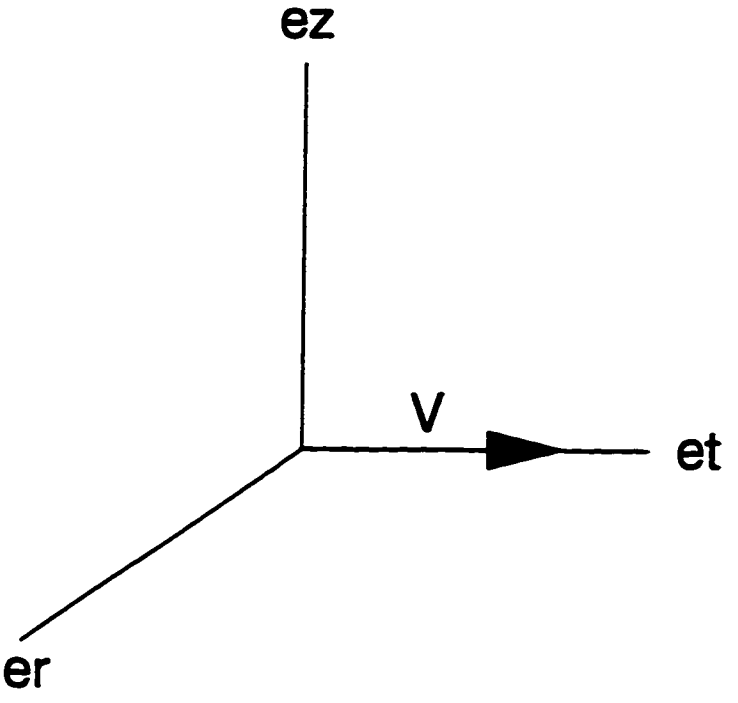

Figure 3.3.6: Direction of the Mean Flow with Only One Component

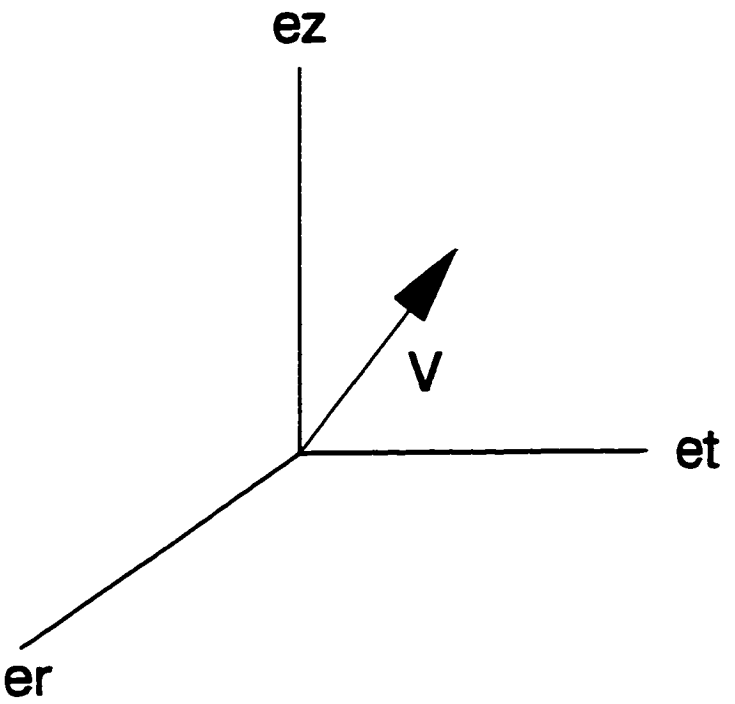

Figure 3.3.7: Direction of the Mean Flow with Three Components

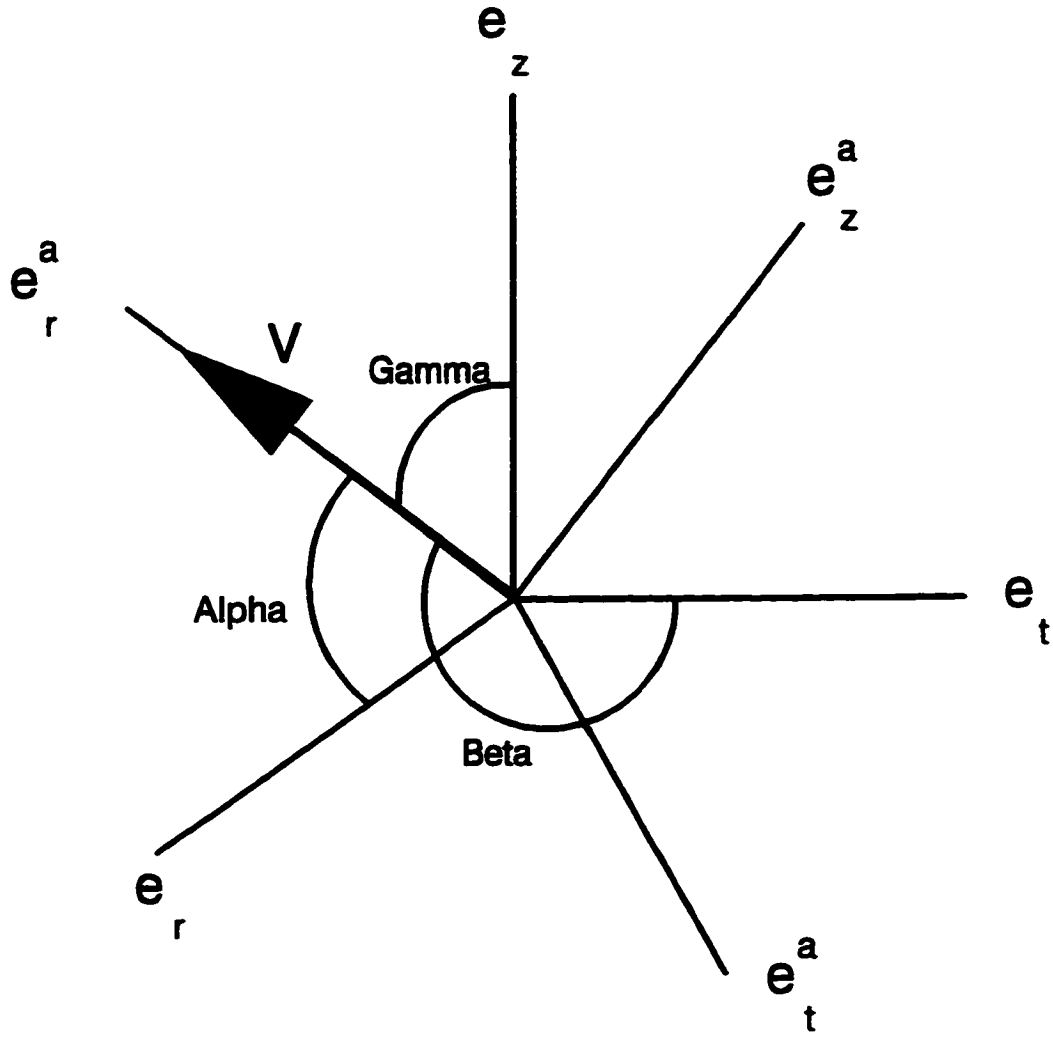

Figure 3.3.8: Coordinate Transformation of the Mean Flow

Using Figure 3.3.8 as a guide, the new unit vectors e_r^a, e_t^a, e_z^a, are computed in terms of the original unit vectors:

$$
\begin{aligned}
e_r^a &= Q_{rr}e_r + Q_{tr}e_t + Q_{zr}e_z \\
e_t^a &= Q_{rt}e_r + Q_{tt}e_t + Q_{zt}e_z \\
e_z^a &= Q_{rz}e_r + Q_{tz}e_t + Q_{zz}e_z \\
e_i^a &= Q\ e_i = Q_{mi}e_m
\end{aligned}
$$

where

$$Q_{mi}Q_{mj} = Q_{im}Q_{jm} = \delta_{ij}$$

We can see from Figure 3.3.8 that the above equations are true assuming that both coordinate systems correspond to two rectangular Cartesian coordinate systems with the same origin. Note that

$$Q_{mi} = e_m \cdot Qe_i = e_m \cdot e_i^a = \cos\ (e_m,\ e_i^a)$$

where

$$\cos\ (e_m,\ e_i^a) = \textit{cosine of the angle between } e_m\ ,\ e_i^a$$

In essence, the two coordinate systems are related by an orthogonal tensor or transformation tensor, Q, shown as:

$$\underline{Q} = \begin{bmatrix} Q_{rr} & Q_{tr} & Q_{zr} \\ Q_{rt} & Q_{tt} & Q_{zt} \\ Q_{rz} & Q_{tz} & Q_{zz} \end{bmatrix}$$

To convert a velocity vector in the old coordinate system of the form

$$\overline{V} = V_r e_r + V_t e_t + V_z e_z$$

to the new coordinate system of the form

$$\overline{V^a} = V_r^a e_r^a + V_t^a e_t^a + V_z^a e_z^a \quad ,$$

we simply multiply the old velocity vector by the transformation tensor Q:

$$\begin{bmatrix} V_r^a \\ V_t^a \\ V_z^a \end{bmatrix}_{e^a} = \begin{bmatrix} Q_{rr} & Q_{tr} & Q_{zr} \\ Q_{rt} & Q_{tt} & Q_{zt} \\ Q_{rz} & Q_{tz} & Q_{zz} \end{bmatrix} \begin{bmatrix} V_r \\ V_t \\ V_z \end{bmatrix}_e$$

Now, in the new coordinate system, the resultant velocity vector exists only in one direction. In this case, the resultant velocity vector is non-zero in the e_t^a direction only. Therefore, the resultant velocity vector in the new coordinate system is as follows:

$$V_r^a = Q_{rr}V_r + Q_{tr}V_t + Q_{zr}V_z \qquad (3.3)$$

where

$$Q_{rr} = \frac{V_r}{\sqrt{V_r^2 + V_t^2 + V_z^2}} = \cos\alpha$$

$$Q_{tr} = \frac{V_t}{\sqrt{V_r^2 + V_t^2 + V_z^2}} = \cos\beta$$

$$Q_{zr} = \frac{V_z}{\sqrt{V_r^2 + V_t^2 + V_z^2}} = \cos\gamma$$

Q_{rr}, Q_{tr}, and Q_{zr} are also known as direction cosines. The next step is to compute the autocorrelation function of the turbulent velocity fluctuation in the radial direction in this new coordinate system. If we assume that:

$$V_r^a = \overline{V_r^a} + v_r^a$$

where

$\overline{V_r^a}$ = *mean velocity component new coordinate system*

v_r^a = *turbulent fluctuating velocity component new coordinate system*

then the correlation function, $\overline{v^a(t)\ v^a(t+\tau)}$, is defined by the following equation:

$$\begin{aligned}\overline{v_r^a(t)\, v_r^a(t+\tau)} &= \overline{v_r(t)\, v_r(t+\tau)}Q_{rr}^2 + \overline{v_t(t)\, v_t(t+\tau)}Q_{tr}^2 + \overline{v_z(t)\, v_z(t+\tau)}Q_{zr}^2 \\ &+ \left(\overline{v_r(t)\, v_t(t+\tau)} + \overline{v_t(t)\, v_r(t+\tau)}\right)Q_{rr}Q_{tr} \\ &+ \left(\overline{v_r(t)\, v_z(t+\tau)} + \overline{v_z(t)\, v_r(t+\tau)}\right)Q_{rr}Q_{zr} \\ &+ \left(\overline{v_z(t)\, v_t(t+\tau)} + \overline{v_t(t)\, v_z(t+\tau)}\right)Q_{tr}Q_{zr}\end{aligned} \tag{3.4}$$

The mean square of the velocity fluctuation in the radial direction in the new coordinate system is defined by the following equation:

$$\begin{aligned}(\sigma_r^a)^2 &= \sigma_r^2 Q_{rr}^2 + \sigma_t^2 Q_{tr}^2 + \sigma_z^2 Q_{zr}^2 + 2\,\overline{v_r v_t}\, Q_{rr} Q_{tr} \\ &+ 2\,\overline{v_r v_z}\, Q_{rr} Q_{zr} + 2\,\overline{v_z v_t}\, Q_{zr} Q_{tr}\end{aligned} \tag{3.5}$$

where

σ_r^2 = mean square velocity fluctuation in the old coordinate system in the radial direction

σ_t^2 = mean square velocity fluctuation in the old coordinate system in the tangential direction

σ_z^2 = mean square velocity fluctuation in the old coordinate system in the axial direction

$(\sigma_r^a)^2$ = mean square velocity fluctuation in the new coordinate system in the radial direction

The autocorrelation coefficient of the velocity fluctuation in the radial direction in the new coordinate system is now defined by the following equation:

$$R_{v_r^a v_r^a}(\tau) = \frac{\overline{v_r^a(t)\, v_r^a(t+\tau)}}{(\sigma_r^a)^2} \tag{3.6}$$

Finally, the integral length scale is then determined by integrating the above autocorrelation coefficient in the new coordinate system with respect to τ, the time lag, and multiplying the result by the magnitude of the mean velocity. This is shown by the following equation:

$$L = |V_r^a| \int_0^{\infty} R_{v_r^a v_r^a}(\tau)\, d\tau \tag{3.7}$$

Since the flocculation process operates at a high Reynolds number, the rate of energy dissipated by the small scale eddies can be defined as the product of the energy flux across the large scale eddies and the characteristic time of these large scale eddies (Batchelor, 1953). From dimensional analysis, the energy flux across the large scale eddies is on the order of $(\sigma_r^a)^2$ and the characteristic time of these eddies is on the order $\frac{\sigma_r^a}{L}$. Therefore, the energy dissipation rate, ε, is then computed by the following equation:

$$\varepsilon = A \frac{(\sigma_r^a)^3}{L} \tag{3.8}$$

where A is constant equal to 1 (Batchelor, 1953). The turbulent kinetic energy is computed as

$$KE = \frac{1}{2}\left(\sigma_r^2 + \sigma_t^2 + \sigma_z^2\right) \tag{3.9}$$

3.4 Measurement of Impeller Power and Flow Numbers

Power numbers were computed by using Equation 3.10

$$N_p = \frac{Power}{\rho N^3 D^5} \tag{3.10}$$

The power is defined as:

$$Power = (Torque)\ (\omega)$$

where

$$\omega = 2\pi \frac{N}{60}$$

The torque was measured by using an in-line torque meter from Bex-ometer, mounted vertically below any structure used to support the weight of the impellers (Clark et al., 1994). The torque readings were made visually. However, this requires that the rotation of the torque meter be slow enough to record the torque value.

When the rotation of the torque meter is faster than can be read directly, a video graphic technique was employed (Figure 3.4.1). In this technique, a video recording of the rotating torque meter was taken at each rotational speed. Using a VCR that allows the user to view the recording one frame at a time, the torque was read from the video frame. In order for the video recording to capture the right point in the meter's rotation, a reed switch was attached to the impeller drive support near the rotating shaft. A small magnet was attached to the rotating shaft in such a way as to trip the reed switch. As the magnet swings near the switch, a strobe light was triggered. The entire operation was conducted in a darkened room to provide the best contrast.

The impeller flow number was computed by using the following equation:

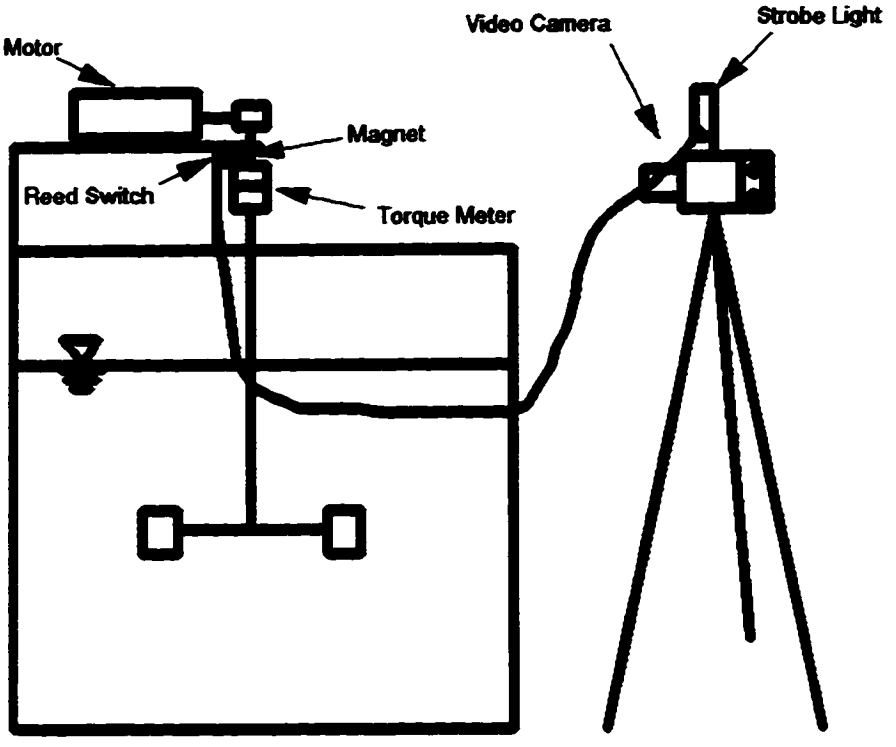

Figure 3.4.1: Setup for Measuring Applied Torque

$$N_Q = \frac{Q_P}{ND^3} \tag{3.11}$$

where

Q_P = volumetric flow rate

D = diameter of impeller

Q_P was calculated by computing the flow of fluid out of the impeller region, which for a radial flow impeller is given as

$$Q_P = \pi(D+2d)\int_{-W/2}^{W/2} U(Z)dZ$$

and for an axial impeller as

$$Q_P = 2\pi\int_{0}^{D/2} U(r)r\,dr$$

where

d = distance from impeller tip

U(Z), U(r) = mean velocity in Z and r directions

W = blade width

Figure 3.4.2 displays the integration boundary for the calculation of N_Q. Knowing the impeller flow number, the circulation time can be computed since it is equal to the total tank volume divided by the impeller pumping capacity. The circulation time affects the frequency of passage of floc through the impeller region where particle break up has been reported to occur (Hsu and Glasgow, 1983). The circulation time was computed as

$$\tau_c = \frac{Vol}{Q_p}$$

where

τ_c= circulation time

Vol = tank volume

Q_p = primary flow through impeller discharge boundary

3.5 Coagulant/Flocculation Experimental Setup

The flocculation experiments were carried out at D/T = 0.33 and H/T = 0.5. Each of the steps outlined below were repeated for the Rushton turbine and A310 fluid foil impeller, at the optimum coagulant concentration (Section 3.1). The flocculation experiments were conducted at the operating conditions outlined in Table 3.3.1.

Before each flocculation experiment, 588 liters of groundwater from a local groundwater tap was put into the rapid mixer/large flocculation tank. The groundwater was allowed to sit in the tank for more than 30 hours. This step allowed the temperature of the groundwater to reach room temperature (19°C ± 1°C). The Kaolinite clay, a product of SIGMA Chemical Co. was added to the groundwater as a one liter 29.3 g/l slurry solution. The one liter 29.3 g/l Kaolinite slurry was allowed to mix for several hours to assure that a homogeneous suspension was produced. The Kaolinite slurry was then added to the groundwater and mixed for one hour prior to the addition of alum. One minute prior to the addition of alum, 300 ml of 1.0 N NaOH.

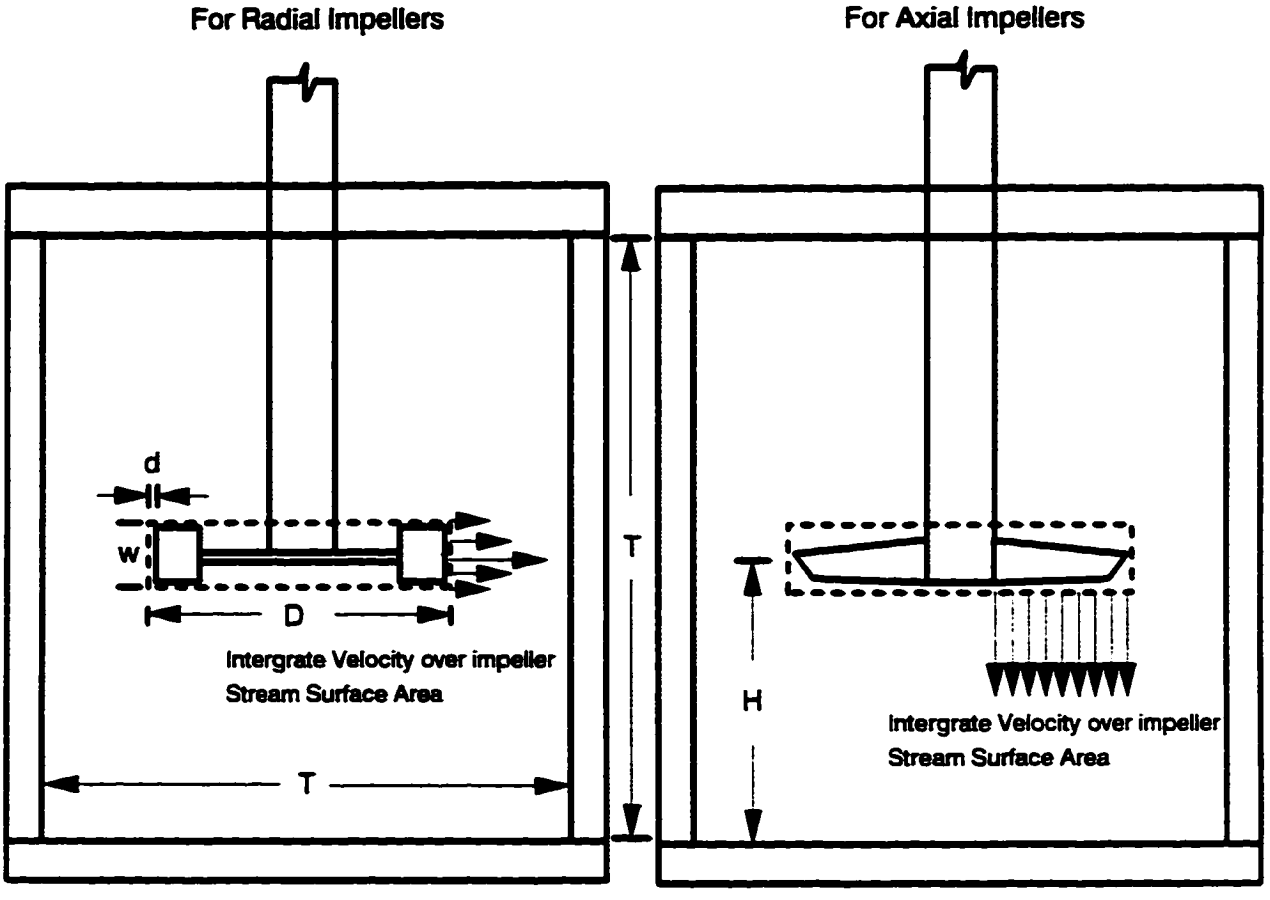

Figure 3.4.2: Setup for Computing Impeller Pumping Numbers (N_Q)

solution was added to the synthetic raw water. This amount of base was needed to achieve a pH = 8.0 ± 0.3 after coagulant addition for each flocculation experiment.

The artificial surface water was blended with a one liter 17.7 g/l aluminum sulfate solution in the rapid mixer/large flocculation tank. Enough raw water was put in this tank to feed all three flocculation tanks. The combined raw water/alum mixture was mixed in the rapid mixer/large flocculation tank for one minute. After this rapid mix stage, some of the raw water/alum mixture exited the tank through flexible tubing and filled the 28 liter flocculation tank. Some of the raw water/alum mixture was also dipped out of the rapid mixer/large flocculation tank to fill the 5 liter vessel. It did not take more than one minute to fill the 28 and 5 liter tanks. Once the flocculation tanks were full, the motors for the flocculation impeller were started at the proper rpm to achieve a constant average energy dissipation rate between the three tanks. The flocculation process continued for 30 minutes.

Immediately after rapid mix stage, samples were collected for analysis of the initial particle size distribution. Initial particle size distribution samples were withdrawn from a location halfway between the tank wall and the impeller swept volume and just below the water surface from the rapid mixer/large flocculation tank. These samples were withdrawn gently using a counting cell designed by Hanson (1989). Figure 3.5.1 displays a schematic of the sample counting cell. Slip covers were used to protect the samples once they were placed in the counting cell. Once the sample cell was loaded, it sat for two hours in order to allow time for the particles to settle to the bottom of the cell. The bottom of the sample cell was set as the focal plane of the microscope. An Aus JENA LABOVAL 4 microscope with a 400x magnification setting was used to view the initial particle size distribution.

The final particle size distribution was determined using a photographic technique developed by Kramer & Clark (1996b). The photography was conducted using a Nikon FA 35 mm camera mounted to a PB-6 bellows with a PB-6a extension, a Nikkor AF-20 mm lens mounted in reverse, and a Vivitan model 5000 ring flash. The camera shutter speed and f-stop was set to 1/250 and 5.6 respectively. Kramer & Clark (1996b) found that an f-stop of 5.6 to 8.0 in conjunction with a ring flash can effectively generate still photographs of the particles that are moving within a stirred vessel.

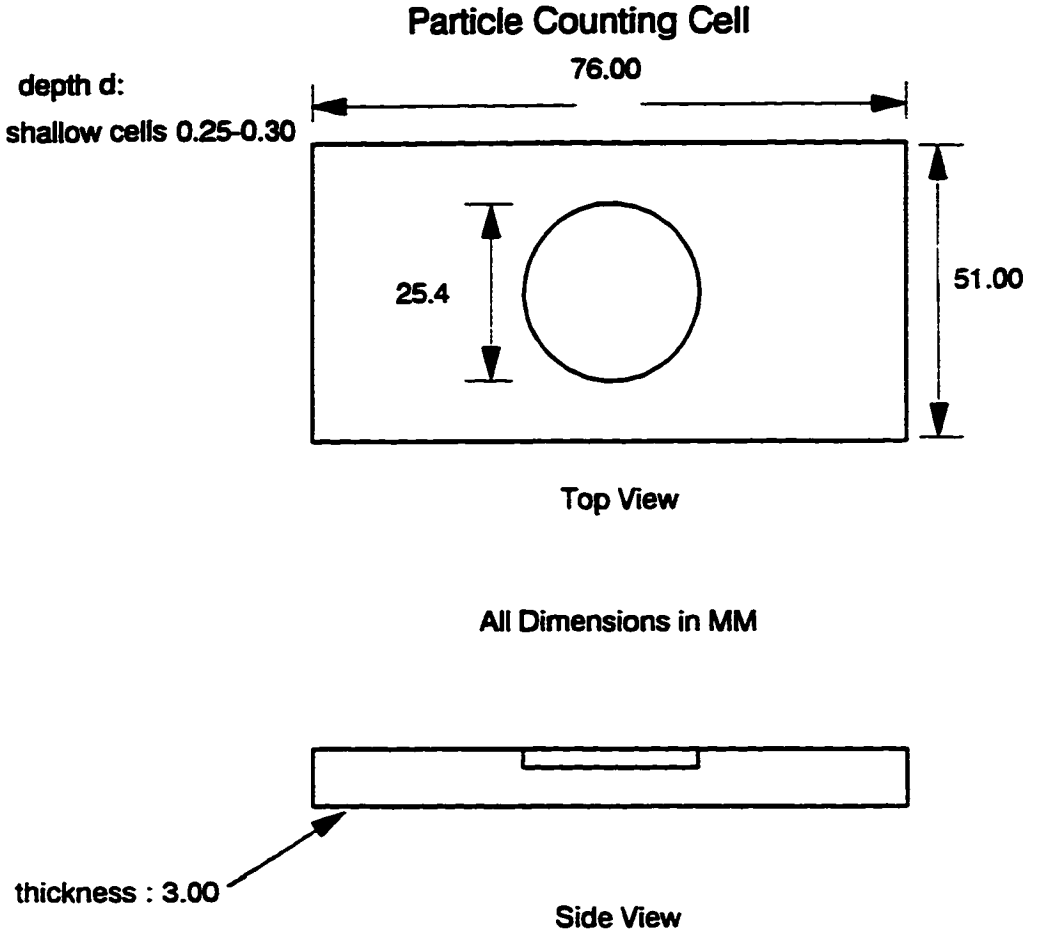

Figure 3.5.1: Schematic of Particle Counting Cell (Hanson, 1989)

Lighting was an important element in obtaining quality pictures of particles. Additional lighting was provided by two 4000 lumen, quality halogen lamps. The light from each lamp was fed into dual fiber optic goose neck extensions and aimed at the focal point directly ahead of the camera lens. This achieved a fore-lighting configuration which Kramer & Clark (1996b) found to work the best. Figure 3.5.2 displays a schematic of the photographic assembly. The bellows were extended to produce a 40X magnification. This magnification was found to be optimal over a particle concentration range of 0.0001% to 0.05% solids on a mass basis (Kramer & Clark 1996b). The smallest particle size that can be measured using this magnification is 3 μm. Below 3 μm, Kramer & Clark (1996b) found the percent error in diameter measurement to be 100%. Figure 3.5.3 displays photographs of the flocculated synthetic raw water.

The film used was ester AH base technical pan with the negatives developed for high contrast using D-19 developer solution at 70°F for 6 ½ minutes. The photographic assembly was placed next to the flocculation tank wall to capture the image of the floc particles. The position of the photographic assembly was such that the focal plane was located 0.125 in. beyond the tank wall into the fluid. The depth of field is dependent on the magnification, the f-stop number, and other parameters that depend on the lens' optics. Jacobson (1978) defines the following relationship for the depth of field:

$$h = 2d_c N_{fs}\left(\frac{1+m}{m^2}\right)$$

where

h = depth of field

d_c = diameter of the circle of confusion (objects beyond which are out of focus)

N_{fs} = f-stop number

m = magnification

Typically for a 35 mm negative, d_c is equal to 30 μm (Morton, 1984). Based on the photographic setup (d_c = 30 μm, m = 40, N_{fs} = 5.6), the depth of field was approximately 9 μm.

The initial and final distribution samples were analyzed using an image analysis system

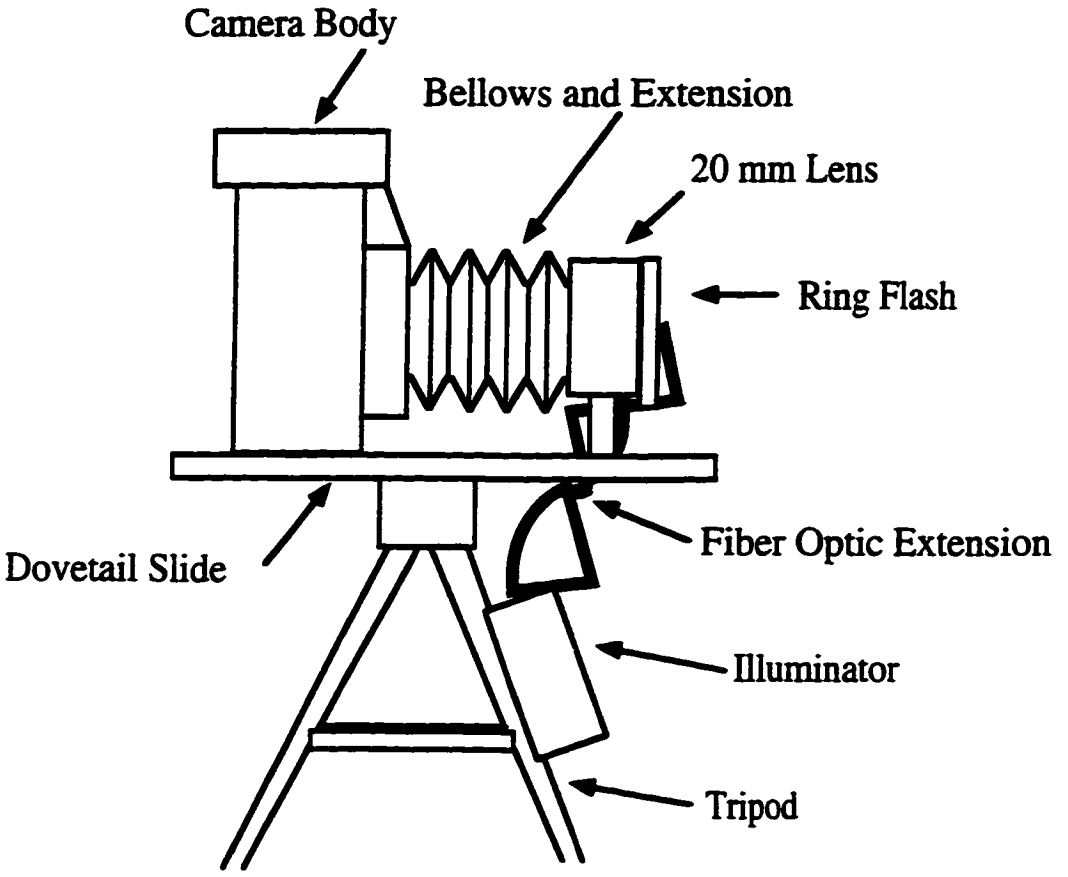

Figure 3.5.2: Schematic of Photographic Assembly (Kramer & Clark, 1996b)

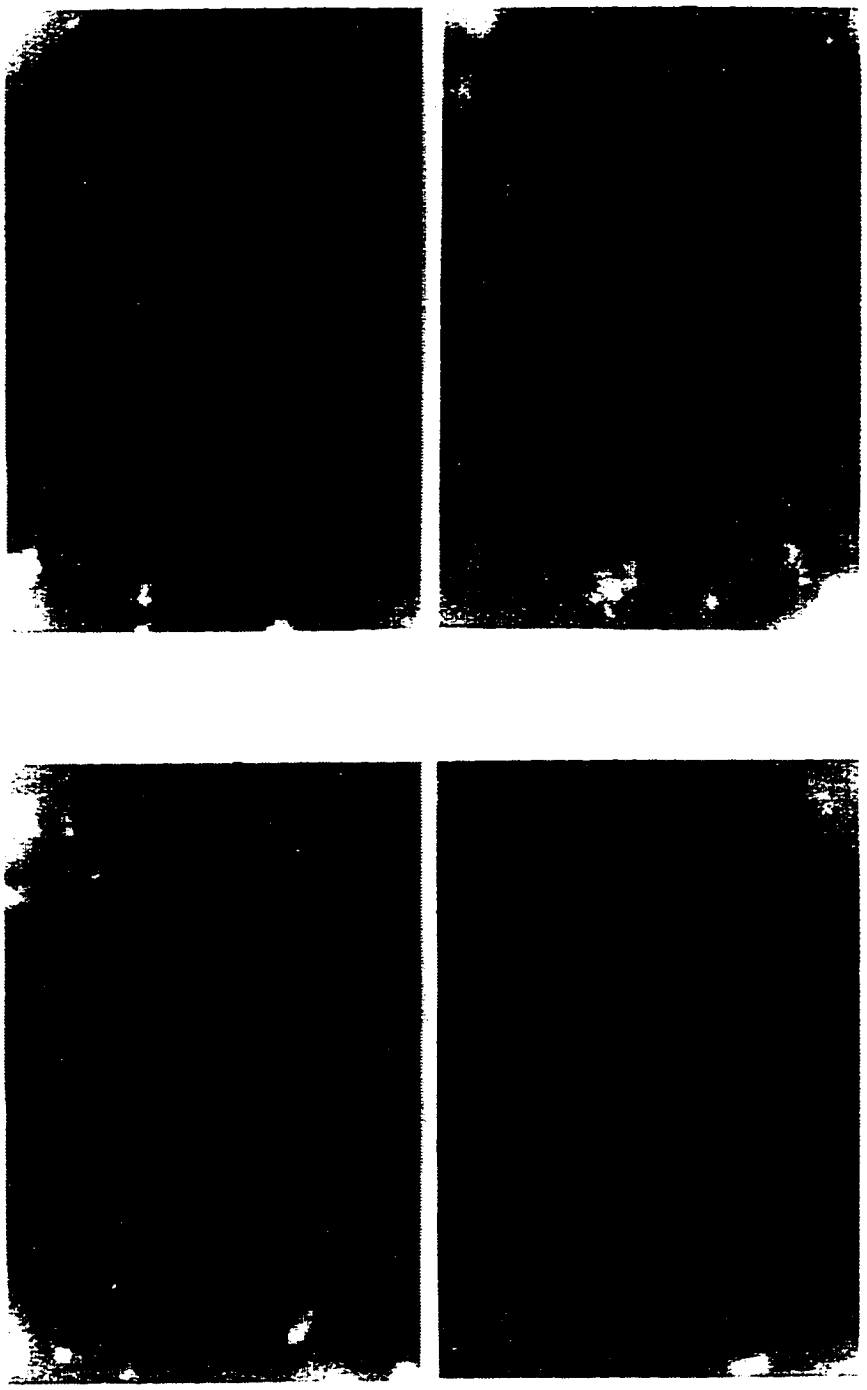

Figure 3.5.3 Photographs of Flocculated Particles after 30 Minutes of Flocculation

(Figure 3.5.4). The image analysis system is based on the Optimus software (Optimus Corp., Edmonds, Washington). The digitized image was provided by a high resolution video camera that was interfaced to a 24 bit full color frame grabber card. The frame was installed in a personal computer with a 75 MHZ pentium processor and 8 mb ram. The image analysis system was used to digitize the floc particles and compute the area of each particle by tracing its perimeter. These areas were then transferred to a data worksheet and the average floc diameter and relative frequency histogram were computed.

The computation of these average floc diameters assumes that a floc particles can be represented by an equivalent area circle diameter. 119 floc particles were analyzed to provide a confident estimate of the average floc size. In a study of oil droplet breakup Clark (1985) found that in order to produce a 95 percent or better confidence interval for the average particle size, the total number of particles measured must be greater than 90. The analysis of 119 floc particles was achieved by digitizing on average more than 15 pictures.

Prior to photographing the particles, a photograph was made of a 1 mm division scale at the 40x magnification. The photograph of the scale was used to calibrate the image analysis system. A similar technique was used to evaluate the initial particle size distribution except that a 2 μm division scale was used at the 400x magnification instead of the 1 mm division scale. The photographic technique outline above was done for each tank size and impeller type used in this study. This process was repeated for each tank size and impeller type to evaluate the reproducability of the particle size distribution results.

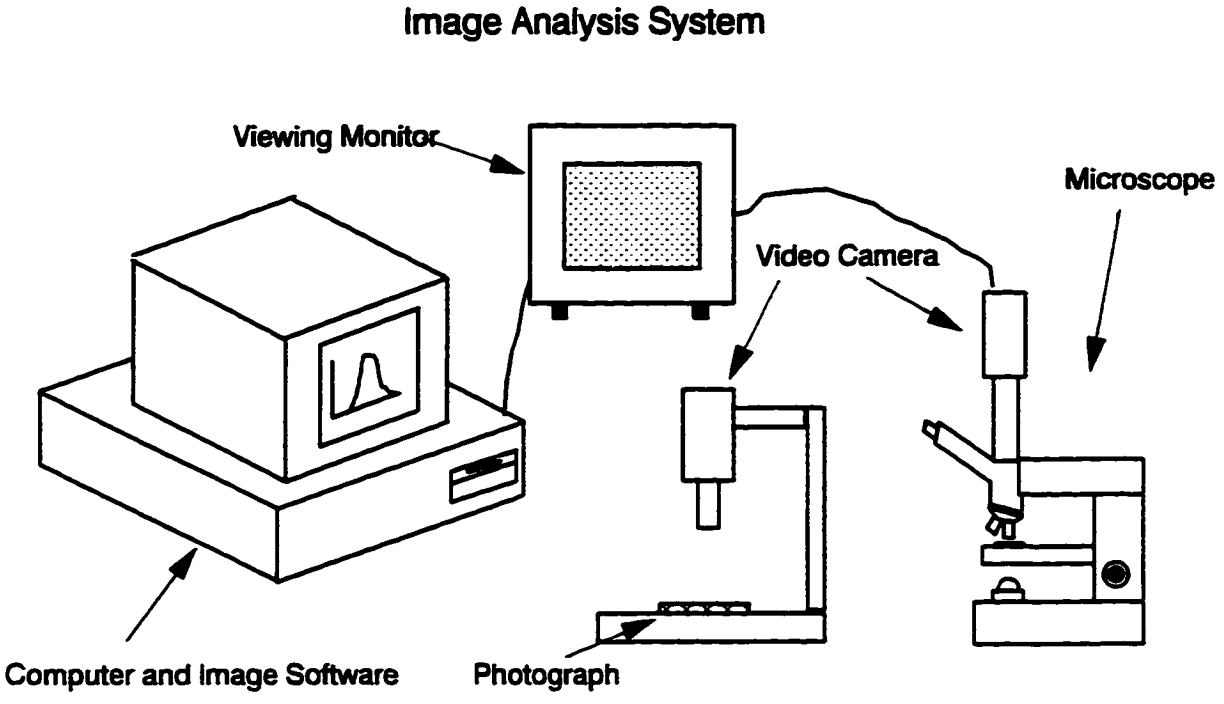

Figure 3.5.4: Schematic of Image Analysis System

4.0 MATHEMATICAL MODELING METHODS

4.1 Fluid Mechanics Model Selection

There is growing evidence which suggests that in order to model the agglomeration/breakup mechanism accurately during the flocculation process, it is important to understand how the local turbulence properties vary throughout the flocculation basin. However, it is very difficult to provide detailed information about the flow field at every location using an LDV system. Fortunately, computational fluid dynamics (CFD) software packages have now made it possible to obtain information about the flow field at every point in the flow regime. By inputting the appropriate boundary conditions, previous investigators have found good correspondence between their CFD models and experimental data collected from a stirred tank (Hutchings et al, 1989; Ranade et al, 1989; Ranade and Joshi, 1990; Kresta & Wood, 1991; Ranade et al., 1992; Bakker and Van Der Akken, 1994, Sahu and Joshi, 1995). In this project, a commercially available CFD code called FIDAP was used to simulate the turbulent flow field in the flocculation tank given the velocity boundary conditions measured from the LDV experiments. The following subsections describe the software package and the model setup.

4.1.1 Numerical Simulation of Fluid Mechanics in a Flocculation Tank

A Rushton turbine and an A310 fluid foil impeller generate a complex, three dimensional turbulent flow field in a square tank. The exact calculations which describe turbulent motion cannot be performed with today's computers. This is primarily due to the presence of the large range of length scales in the flow. These length scales need to be determined in order to describe the flow regime accurately. To simulate the turbulent flow, turbulence models have been developed. In general, turbulence models relate the turbulent Reynolds stresses to the mean velocity gradient in order to provide closure of the Navier Stokes equations. In modeling the turbulent flow produced by an impeller in a square stirred-tank reactor, two-equation turbulence models have been used. The two-equation turbulence models were developed to describe both the transport of the kinetic energy and the length scale of the large energy-containing eddies

throughout the flow domain. Other transport models (i.e. zero equation model or one equation mixing length model) are not capable of modeling the wide range of length scales found in stirred tank reactors. The k-ε model is one form of the two equation turbulence models that has been shown to work well at high Reynolds numbers flows where local isotropy prevails (Rodi, 1984). k in k-ε represents the turbulent kinetic energy and ε represents the turbulent energy dissipation rate. The governing equations used to describe the flow include

Continuity Equation

$$\frac{\partial U_i}{\partial x_i} = 0 \tag{4.1}$$

Momentum Equations

$$U_j \frac{\partial U_i}{\partial x_j} = \frac{-1}{\rho} \frac{\partial P}{\partial x_i} + \frac{\partial}{\partial x_j}\left(\nu \frac{\partial U_i}{\partial x_j} - \overline{u_i u_j} \right) \tag{4.2}$$

Kinetic Energy Equation

$$U_i \frac{\partial k}{\partial x_i} = \frac{\partial}{\partial x_i}\left(\frac{\nu_t}{\sigma_k} \frac{\partial K}{\partial x_i} \right) + \nu_t \left(\frac{\partial U_i}{\partial x_j} + \frac{\partial U_j}{\partial x_i} \right) \frac{\partial U_i}{\partial x_j} - \varepsilon \tag{4.3}$$

Energy Dissipation Rate Equation

$$U_i \frac{\partial \varepsilon}{\partial x_i} = \frac{\partial}{\partial x_i}\left(\frac{\nu_t}{\sigma_\varepsilon} \frac{\partial \varepsilon}{\partial x_i} \right) + C_1 \frac{\varepsilon}{k}\left(\nu_t \left(\frac{\partial U_i}{\partial x_j} + \frac{\partial U_j}{\partial x_i} \right) \frac{\partial U_i}{\partial x_j} \right) - C_2 \frac{\varepsilon^2}{k} \qquad (4.4)$$

Reynolds Stress Equation

$$-\overline{u_i u_j} = \nu_t \left(\frac{\partial U_i}{\partial x_j} + \frac{\partial U_j}{\partial x_i} \right) - \frac{2}{3} k \delta_{ij} \qquad (4.5)$$

Eddy Viscosity Equation

$$\nu_t = C_\mu \frac{k^2}{\varepsilon} \qquad (4.6)$$

The k-ε model includes five empirical constants derived from comparing the model to turbulent measurements behind a grid (Rodi, 1984). Table 4.1.1 displays the value of these constants. Equations 4.1 - 4.4 assume that the turbulent flow is incompressible and at steady state. The ε equation (Eqn. 4.4) provides the effect of dissipation and vortex stretching on the length scale. Dissipation destroys the small scale eddies and thus effectively increases the eddy size while vortex stretching connected with the energy cascade, reduces the eddy size. The k-ε

turbulence model was used in FIDAP to simulate the turbulent flow regime in the flocculation basin.

Table 4.1.1: Empirical Constants for k-ε Turbulence Model (Rodi, 1984)

C_μ	σ_k	σ_ε	C_1	C_2
0.09	1.00	1.30	1.44	1.92

4.1.2 Finite Element Formulation using FIDAP

FIDAP is a finite element code based on the Galerkin formulation. The objective of the finite element method is to reduce the continuous problem (infinite number of degrees of freedom) of fluid equations to a discrete problem (finite number of degrees of freedom) described by a system of algebraic equations. The first step is to divide the continuum region of interest into a number of simple shaped regions called elements. Within each element, the unknowns, such as velocities, temperature, or pressure are interpolated in terms of values to be determined at a set of nodal points.

The following equations display the approximations of the velocity field and pressure field (assuming steady state and isothermal conditions):

$$u_i(x) = \phi^T U_i$$
$$p(x) = \psi^T P$$

where

U_i, P - column vectors of the element model points (unknowns)

ϕ, Ψ - column vectors of the interpolation functions

x - position vector for the element

Substitution of these approximations into the equations of momentum and continuity and boundary conditions yield the following relationship:

$$f_1(\phi, \psi, U_i, P) = R_1$$

$$f_2(\phi, U_i) = R_2$$

where

R_1, R_2 - residuals (errors) resulting from the approximations

The Galerkin method seeks to reduce these errors to zero. This is done by making the residuals orthogonal to the interpolation functions of each element. These conditions are expressed by the following relationship:

$$(f_1, \phi) = (R_1, \phi) = 0$$

$$(f_2, \psi) = (R_2, \psi) = 0$$

where (,) denotes the inner product:

$$(a, b) = \int_v a * b \, dv$$

and v is the volume of the element.

Using the above technique, FIDAP transforms Equations 4.1 - 4.6 and solves for the boundary

conditions and geometric shape given for a Rushton turbine or A310 fluid foil impeller in a square tank.

4.1.3 FIDAP Simulation Setup

The model is based on a simple geometric representation of a submerged mixing impeller in a square stirred tank reactor. The impeller was modeled as a cylinder whose diameter and height matched that of the Rushton turbine or A310 foil impeller (Figure 4.1.1). Due to its complexity, a free surface was not included in any of the FIDAP simulations. A wall boundary was simulated instead of the free surface. As a result of the large computational requirements of the FIDAP simulation, only the 5L and 28L tank sizes were modeled with both the Rushton turbine and A310 foil impeller (Section 4.1.3.2).

4.1.3.1 Boundary and Initial Conditions

The velocity boundary conditions for the Rushton turbine and the A310 foil impeller were defined using the LDV experimental measurements. The mean radial and tangential velocity profiles were used for the Rushton turbine. The mean axial velocity was ignored because its magnitude was very small relative to the radial and tangential components. In the case of the impeller boundary condition for the A310 foil impeller, the flow was assumed to be purely axial. From the experimental measurements, the radial and tangential velocities were very small compared to the axial velocity. In all the simulations, the fluid properties (i.e. viscosity, density) were defined at a temperature of 20°C. All solid surfaces were assumed to have no-slip velocity boundary conditions.

The turbulent boundary conditions for the Rushton turbine and the A310 foil impeller were evaluated at T = 5L using 3 methods: 1) prescribed initial conditions, 2) turbulence intensity and length scale from LDV experimental results, and 3) kinetic energy and energy dissipation rate profiles from LDV experimental results. The method that best fit the experimental results in the

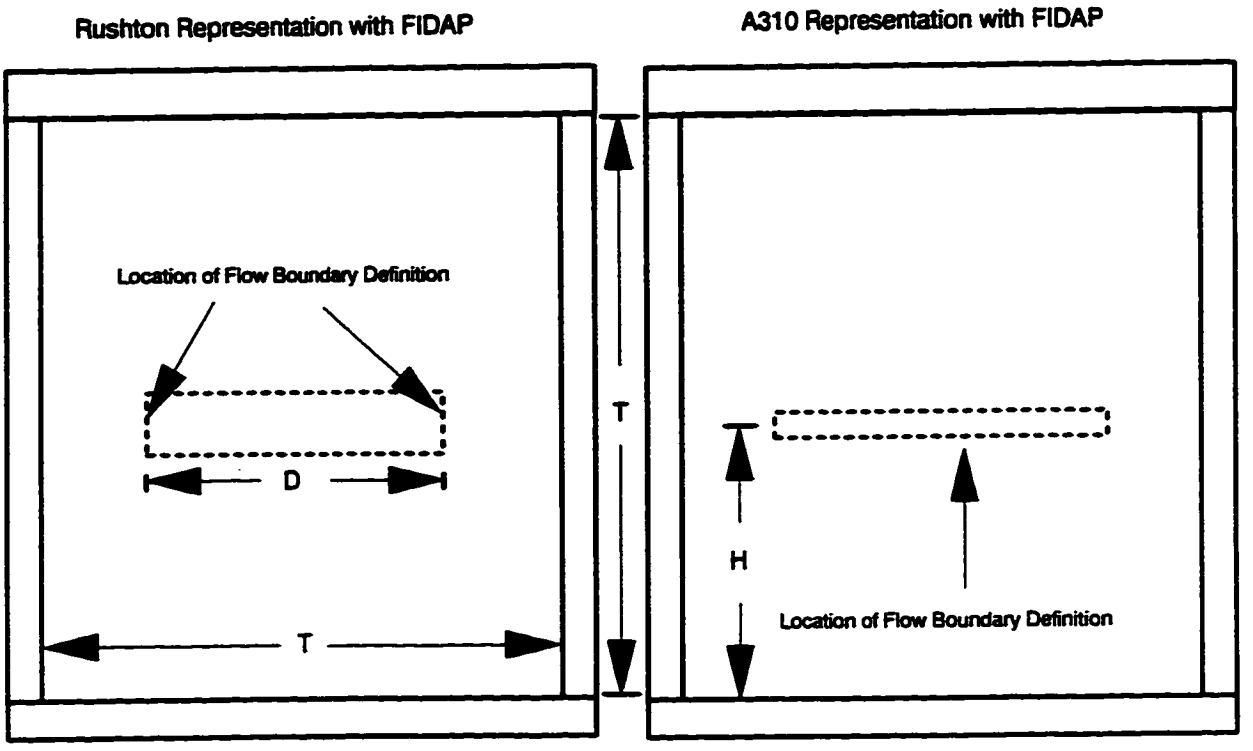

Figure 4.1.1: Cylindrical Approximation for the Mixing Impeller A) Rushton Turbine B) A310 Foil Impeller

flow domain was used to simulate the turbulence in the T = 28L tank size.

Since the k-ε model presented in Equations 4.1 - 4.6 is considered a high Reynolds number turbulence model, high gradients present near the solid wall regions present some numerical difficulties. In simulating the fluid flow near the wall, FIDAP incorporates a set of wall-laws or wall functions to bridge the gap between the fully turbulent region beyond a buffer layer and the conditions at the wall.

4.1.3.2 Mesh Generation

The mesh was generated using FIMESH, the FIDAP mesh generating subprogram. 18,880 elements were used to discretize the flow domain in the 5L square tank with an A310 foil impeller and 108,072 elements were used to discretize the 28L tank with an A310 foil impeller. To discretize the flow domain in the 5L and 28L square tank with the Rushton turbine, 22,640 and 139,032 elements respectively were used. More elements were required for the larger tank size to maintain an equivalent average mesh density between the 5L tank and the 28L tank. The average mesh density at 5L tank size was found to be fine enough to produce a grid independent solution of the mean and turbulent flow field. To produce a grid independent solution for the 560L tank size with an average mesh density similar to the 5L and 28L tank sizes, more than 2 million elements would be required. This number of elements would exceed the memory capacity of the workstation used in this study. Consequently, the 560L tank was not modeled using FIDAP.

Within the flow domain, a higher local mesh density was used in the impeller discharge zone. Results from the LDV measurements showed that the turbulence underwent a much sharper variation in the impeller discharge region than in the bulk region of the square tank. A higher local mesh density in the impeller discharge zone was required to resolve the details of the turbulence field.

4.1.3.3 Solution Technique

The discretized governing equations were solved using a segregated algorithm approach. With this approach, the global system of linear equations are decomposed into a set of decoupled sub-equation systems for each of the primary flow equations (i.e. three components of the momentum equation, continuity equation, and the equations for k & ε) instead of being solved in a fully coupled environment. These smaller systems of equations are solved in a sequential manner using a conjugate gradient type scheme. An advantage of using the segregated method include a significantly reduced memory requirement.

FIDAP has three segregated algorithms that can be selected: A) the pressure projection (PPROJECTION), B) the pressure update (PUPDATE), and C) the pressure correction (PCORRECTION). A detailed description of how these algorithms work can be found in the FIDAP manuals (Fluid Dynamics International, 1993). Of the three segregated solvers, PPROJECTION is the most robust solution solver. The convergence for PUPDATE and PCORRECTION segregated solvers is very slow for large finite element problems and for most turbulent problems. In this study, the PPROJECTION segregated solver was used as the solution algorithm. This segregated algorithm was specified as default by FIDAP.

Streamline upwinding was also incorporated in the solution technique. Streamline upwinding is a numerical technique which introduced a false numerical diffusion along the streamwise direction (Fluid Dynamics International, 1993). This technique helps reduce streamwise oscillation in the various flow variables that occur in convection dominated flow regions. In essence, streamline upwinding improves the numerical stability of the finite element model. The amount of upwinding used for each flow variable is displayed in Table 4.1.2

Table 4.1.2: Upwinding Values for Flow Variables

U	V	W	P	T	k	ε
1	1	1	0	0	5	5

The recommended range of upwinding values that can be used in FIDAP is 1-2 for the

velocity terms and 5-10 for the turbulence terms (Fluid Dynamics International, 1993). The FIDAP model would continue to execute until the following convergence criterion was met:

$$\left\| \frac{v_i - v_{i-1}}{v_i} \right\| = 0.001$$

where v_i represents the solution vector at the i^{th} iteration. The double bar represents the root mean square norm summed over all equations for the model. The model was executed on a Hewlet Packard 715/75 workstation with 128 mb of RAM.

4.2 Particle Agglomeration & Breakup Model Selection

The population balance models shown in Appendix B are inadequate to display changes in flocculation performance due to changes in impeller type, tank size, or both at constant average energy dissipation rate. Clearly, a model having that kind of sensitivity must include information about the local turbulence intensity in the impeller discharge zone of the flocculation tank where floc breakup has been shown to occur (Hsu and Glasgow, 1983). This section describes the population balance model developed in this study.

4.2.1 Agglomeration Modeling

The agglomeration part of the population balance rate equation, used in this project, was similar to that derived by Chen et al. (1990):

$$\left(\frac{dn(d)}{dt}\right)_{agglm} = \frac{1}{2}\int_0^d \alpha\beta[l,(d^3-l^3)^{1/3}]n(l)n\left((d^3-l^3)^{1/3}\right)\,dl - n(d)\int_0^{max} \alpha\beta(l,d)n(l)\,dl \qquad (4.7)$$

where

n(d) = particle number concentration of size class d

α = collision efficiency factor

$\beta(l, d)$ = collision frequency function

l, d = size class of particles

The collision frequency function in a turbulent flow was assumed to be described by the Saffman and Turner (1956) relationship:

$$\beta(l,d) = 0.1616\ (l+d)^3 \left(\frac{\varepsilon}{\nu}\right)^{1/2} \tag{4.8}$$

4.2.2 Breakup Modeling

The breakup part of the population balance rate equation used in this project is expressed by the following relationship:

$$\left(\frac{dn(d)}{dt}\right)_{break} = 2\int_{d}^{max} k_b(l)P_{dau}(l,d)n(l)dl - k_b(d)n(d) \tag{4.9}$$

where

k_b (l) = particle breakup frequency

$P_{dau}(l,d)$ = probability distribution of daughter particles with size d formed by breakup of a parent particle with size l.

Equation 4.9 is similar to that used by Konno et al. (1983). Particle breakup as described by Equation 4.9 occurs because the inertial stresses exceed the limiting failure strength of the floc. The first term on the right hand side describes the gain of floc particles to size class d due to the breakup of larger particles. The second term describes the loss of size d floc particles from breakup to smaller size class floc particles.

One of the assumptions in Equation 4.9 was that particle breakup takes place under conditions where the relative fluctuating velocity across the floc diameter exceeds a critical value. Borrowing drop breakup terminology to describe particle breakup, Borts and Gupalo (1972) describe this critical fluctuating velocity as:

$$u_{crit}(d) = \left(\frac{\sigma_e}{d\rho} \right)^{1/2} \quad (4.10)$$

where

σ_e = effective surface tension at the boundary between the floccule and the fluid

ρ = density of fluid

d = floc particle diameter

Although, surface tension is typically used when describing the interface between two liquids, σ_e can be considered here as a measure of the binding energy per unit surface area of the floc aggregate. σ_e can only be determined experimentally. As it pertains to floc particles, Equation 4.10 does display the reduction in floc strength with increasing size floc. Larger floc particles will require smaller critical fluctuating velocities to cause breakup. This reduction in floc strength with increasing floc size has been shown experimentally by other researchers. (Tambo & Watanabe, 1979; Lu & Spielman, 1985; Kusters, 1991).

The particle breakup frequency function, $k_b(d)$, is defined using the relationship of Konno et al. (1983):

$$k_b(d) = C_1 N_Q N \int_{u_{crit}(d)}^{\infty} P(u(d))d(u(d)) \qquad (4.11)$$

where

C_1 = constant for geometrically similar mixing vessels

P(u(d)) = probability density function of the relative velocity across particle diameter

N = angular velocity of the spinning impeller

u(d) = relative fluctuating velocity across particle diameter

N_Q = impeller flow number

In deriving Equation 4.11, Konno et al. (1983) assumed that breakup occurred in regions where the energy containing eddies are no longer isotropic and have their largest velocity component in the direction of the mean flow. In Equation 4.11, the breakup frequency is proportional to the product of the frequency of particle circulation in a stirred vessel and the fraction of particles which are in a transient state of breaking up in the anisotropic turbulent regions. The frequency of particle circulation is described as

$$f_c = \frac{1}{\tau_c} = \frac{Q_p}{V} = \frac{N_Q N D^3}{C D^3} \propto N_Q N \qquad (4.12)$$

where

C = constant of proportionality

Konno et al. (1983) originally described the frequency of particle circulation as being proportional to the impeller speed only. As they noted, this proportionality holds for geometrically similar tanks and impeller configurations. Hence, for geometrically similar tanks

and impeller configurations, N_Q can be assumed constant in Equation 4.12. However, different impeller types will produce different frequency of particle circulations. In order to correct the frequency of particle circulation for different impeller types, N_Q must remain in Equation 4.12. The fraction of breaking particles equals the probability that the relative fluctuating velocity across the particle diameter, u(d), has a higher value than $u_{crit}(d)$ at any instance in time.

Konno et al. (1983) assumed that P(u(d)) can be described by a Gaussian distribution function. This is shown by the following equation:

$$P(u(d)) = \frac{1}{\sqrt{2\pi\overline{u^2(d)}}} \exp\left(-\frac{u^2(d)}{2\overline{u^2(d)}}\right) \tag{4.13}$$

where

$$\overline{u^2(d)} = \textit{mean square value of } u(d)$$

In their model, Konno et al. (1983) assumed that the root mean square value of u(d) is proportional to the average velocity of the main flow:

$$\overline{u^2(d)} \propto (ND)^2$$

where

D = impeller diameter

This assumption, however, is also valid only for geometrically similar tanks and impellers. Researchers have shown that for geometrically similar tanks, different impeller types will produce different spatial distributions of turbulent fluctuating velocities (Mersmann and Geisler, 1991; Geisler et al,1994). Geisler et al. (1994) demonstrated that a relationship exists between the impeller power number, N_p, and the small scale turbulence produced by the impeller (Equation

2.3). Hence, a relationship should exist between N_p and the large scale turbulence since the energy of large scale turbulent motion provides energy to the small scale turbulent motion. Therefore, it is more appropriate to assume that the root mean square value of u(d) is proportional to the product of N_p^x and the average velocity of the main flow:

$$\overline{u^2(d)} \propto (N_P^x ND)^2 \tag{4.14}$$

where

x = empirically determined exponent from the LDV data

The value of x will be identified in Section 5.1.3. From Equations 4.10, 4.11, 4.13, and 4.14, the breakup frequency in the anisotropic turbulent regions is derived as:

$$k_b(d) = C_1 N_Q N \, erfc[\, C_2 \sigma_e^{1/2} / (N_P^x ND \rho^{1/2} d^{1/2}) \,] \tag{4.15}$$

where

C_1, C_2 = constants which depend on vessel geometry

erfc[ ] = complementary error function

The product of C_2 and $\sigma_e^{1/2}$ is lumped into a constant C_3 since it is difficult to experimentally measure C_2 and $\sigma_e^{1/2}$ individually. C_1 and C_3 will be determined empirically from the flocculation experimental results.

Konno et al. (1983) also derived a breakup frequency for the isotropic turbulent region and included it in the breakup rate equation. However, based on their experimental results, Konno et al. (1983) found that the contribution of the breakup frequency in the isotropic regions is several orders of magnitude smaller than the breakup frequency in the anisotropic regions. If we assume that the mechanism governing drop breakup is similar to that for floc breakup, then

the breakup frequency in the isotropic regions can be neglected in this model.

In Equation 4.9, it is assumed that two daughter particles are produced from the breakup of a parent floc particle. The daughter particle distribution is described by the following equation derived by Konno et al. (1983):

$$P_{dau}(l,d) = \frac{\Gamma(12)}{\Gamma(3)\Gamma(9)}\left(\frac{d}{l}\right)^8\left(1-\frac{d}{l}\right)^2 \qquad (4.16)$$

where

$$\Gamma(x) = \int_0^\infty e^{-t}t^{x-1}dt = \textit{gamma function}$$

Konno et al. (1983) found Equation 4.16 to match their extensive model simulations of the resulting distribution of daughter droplets. The resulting distribution produced by Equation 4.16 is shown in Figure 4.2.1.

Although Konno et al. (1983) found this type of distribution accurately describes the distribution of the daughter droplets, research done by Kusters (1991) indicate that it can also describe the resulting daughter particle distribution in flocculation. Kusters (1991) showed that the parent floc will breakup into uneven fragments with at least one daughter particle radius equal to 78 percent of the parent floc radius (i.e. d/l = 0.78). Therefore, the distribution function described by Equation 4.16 should accurately reflect the resulting daughter particle distribution since this distribution is skewed to higher fractions of d/l.

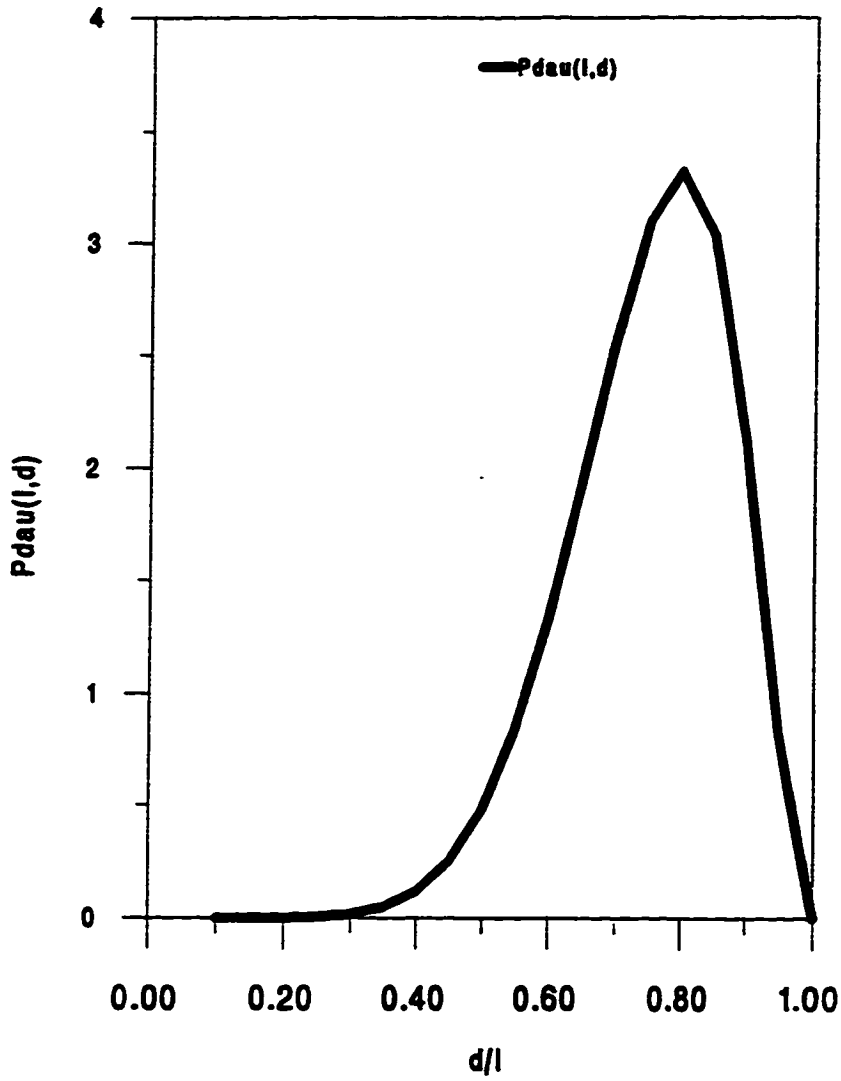

Figure 4.2.1: Plot of Daughter Particle Distribution $P_{dau}(l,d)$

4.2.3 Numerical Methods for Population Balance Model

The overall population balance model used in this project is as follows:

$$\frac{dn(d)}{dt} = \int_{d_{min}}^{d_{max}} [M_1(d)\alpha\beta[l,(d^3-l^3)^{1/3}]n(l)n((d^3-l^3)^{1/3}) - \alpha\beta(l,d)n(l)n(d) + 2M_2(d)k_b(l)P_{dau}(l,d)n(l)]\,dl - k_b(d)n(d) \quad (4.17)$$

where

$$M_1(d) = \begin{cases} 1 & l \le d \\ 0 & l > d \end{cases}$$

$$M_2(d) = \begin{cases} 0 & l \le d \\ 1 & l > d \end{cases}$$

A finite difference predictor - corrector method was used to solve the above population balance model. A first order Adams-Bashforth formula was used as the predictor equation. A second order Adams-Moulton formula was used as the corrector equation. Table 4.2.1 and Table 4.2.2 display a general representation of both the Adams-Bashforth and Adams-Moulton formulas, respectively.

The predictor-corrector method has been used successfully by previous researchers in solving systems of stiff ordinary differential equations similar to Equation 4.17 (Appendix B). The integrating term in Equation 4.17 was approximated using Trapezoidal Rule as the numerical integration technique. The integral was discretized at 87 different particle sizes between 2 μm and 820 μm. A constant bin size was not used between 2 μm and 820 μm because of numerical instability. The range of bin sizes used between 2 μm and 820 μm is displayed in Figure 4.2.2.

Table 4.2.1: General Adams-Bashforth Formula (Celia and Gray, 1992)

Differential Equation.

$$\frac{du}{dt} = f(u,t)$$

Adams-Bashforth Formula.

$$U^{n+1} = U^n + \frac{\Delta t}{A_p}\sum_{k=0}^{p-1}\alpha_{n-k}F^{n-k}$$

Leading Error Term.

$$U^{n+1} = u^{n+1} + (n+1)\Delta t\,\hat{C}_p\left.\frac{d^{p+1}u}{dt^{p+1}}\right|_{t=\frac{n+1}{\Delta t}}(\Delta t)^p$$

p	A_p	α_n	α_{n-1}	α_{n-2}	α_{n-3}	α_{n-4}	α_{n-5}	$\hat{C}_p$
1	1	1						−1/2
2	2	3	−1					−5/12
3	12	23	−16	5				−9/24
4	24	55	−59	37	−9			−251/720
5	720	1901	−2744	2616	−1274	251		−475/1440
6	1440	4277	−7923	9982	−7298	2877	−475	−19,087/60,480

Table 4.2.2: General Adams-Moulton Formula (Celia and Gray, 1992)

Differential Equation.

$$\frac{du}{dt} = f(u,t)$$

Adams-Moulton Formula.

$$U^{n+1} = U^n + \frac{\Delta t}{A_p}\sum_{k=0}^{p-1}\alpha_{n+1-k}F^{n+1-k}$$

Leading Error Term.

$$U^{n+1} = u^{n+1} + (n+1)\Delta t\, C_p \left.\frac{d^{p+1}u}{dt^{p+1}}\right|_{t=\frac{n+1}{\Delta t}} (\Delta t)^p$$

p	A_p	α_{n+1}	α_n	α_{n-1}	α_{n-2}	α_{n-3}	α_{n-4}	C_p
1	1	1						1/2
2	2	1	1					1/12
3	12	5	8	−1				1/24
4	24	9	19	−5	1			19/720
5	720	251	646	−264	106	−19		27/1440
6	1440	475	1427	−798	482	−173	27	863/60,480

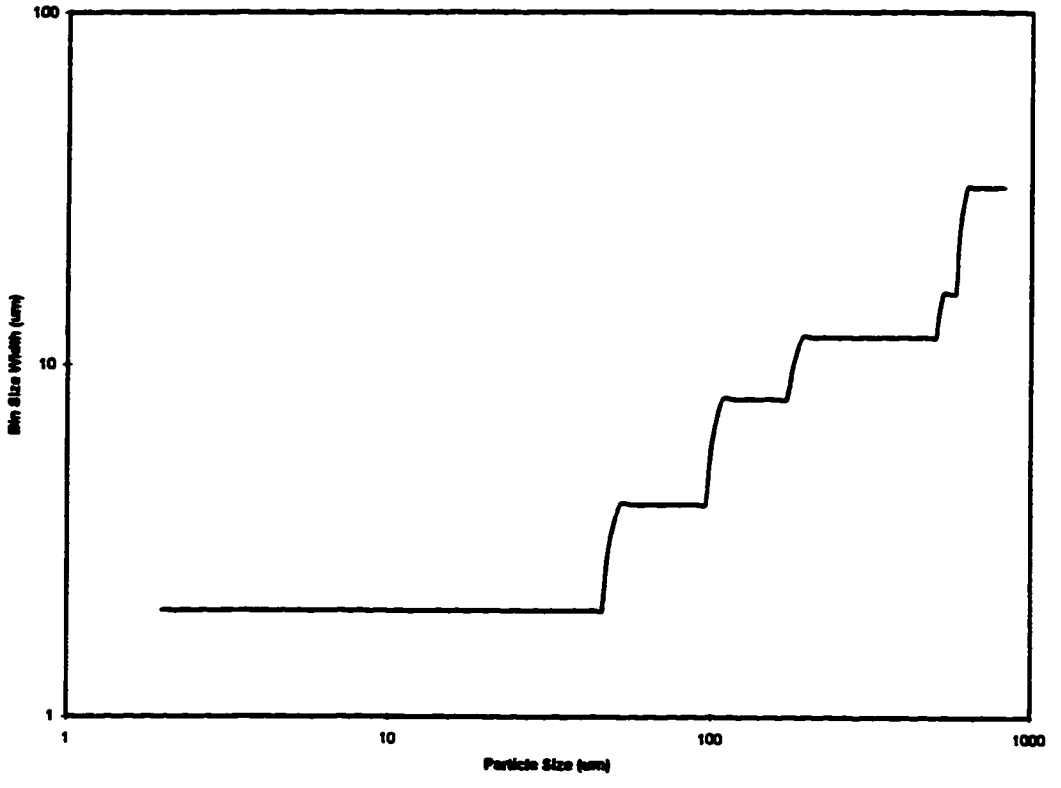

Figure 4.2.2: Range of Bin Sizes in the Population Balance Model

As can be seen in Figure 4.2.2, the bin size varies from 2 μm in the low particle size range and grows to 32 μm in the large particle size range. This range of bin sizes was found to be numerically stable with the predictor-corrector solution scheme used in this study.

The integrand was evaluated at each of these discrete particle sizes and an array of these values was sent to a numerical integration subroutine. The population balance model was set to run for a simulated 30 minutes with a time step of 0.2 seconds. A time step of 0.2 was the largest step size used in the model without sacrificing numerical stability (Figure 4.2.3). As can be seen from Figure 4.2.3, the cumulative particle size distribution does not change with the time step until $\Delta t = 0.5$.

The initial condition for the population balance model was determined by computing the total theoretical number of 2 μm particles in the rapid mix tank. The calculation of the total number of 2 μm particles is based on the total volume of clay particles contained in the system. The following equation was used to compute the total number of 2 μm particles:

$$N_{part}(d) = \frac{10^{-6}[c]/SG}{Vol_p(d)} \tag{4.18}$$

where

$N_{part}(d)$ = number of particles of size class d
[c] = clay concentration (mg/l)
SG = clay specific gravity (gm/cm^3)
$Vol_p(d)$ = particle volume of size class d = $\frac{\pi d^3}{6}$ (cm^3)
d = diameter of particle (cm)

In this study, [c] = 50 mg/l, SG = 2.64 gm/cm^3 and d = 2 x 10^{-4} cm. Substituting the above values into Equation 4.18, $N_{part}(d)$ = 4.52145 x 10^6. Once the initial conditions and all the auxiliary functions and parameters were specified, Equation 4.17 was solved numerically using the time marching predictor - corrector method.

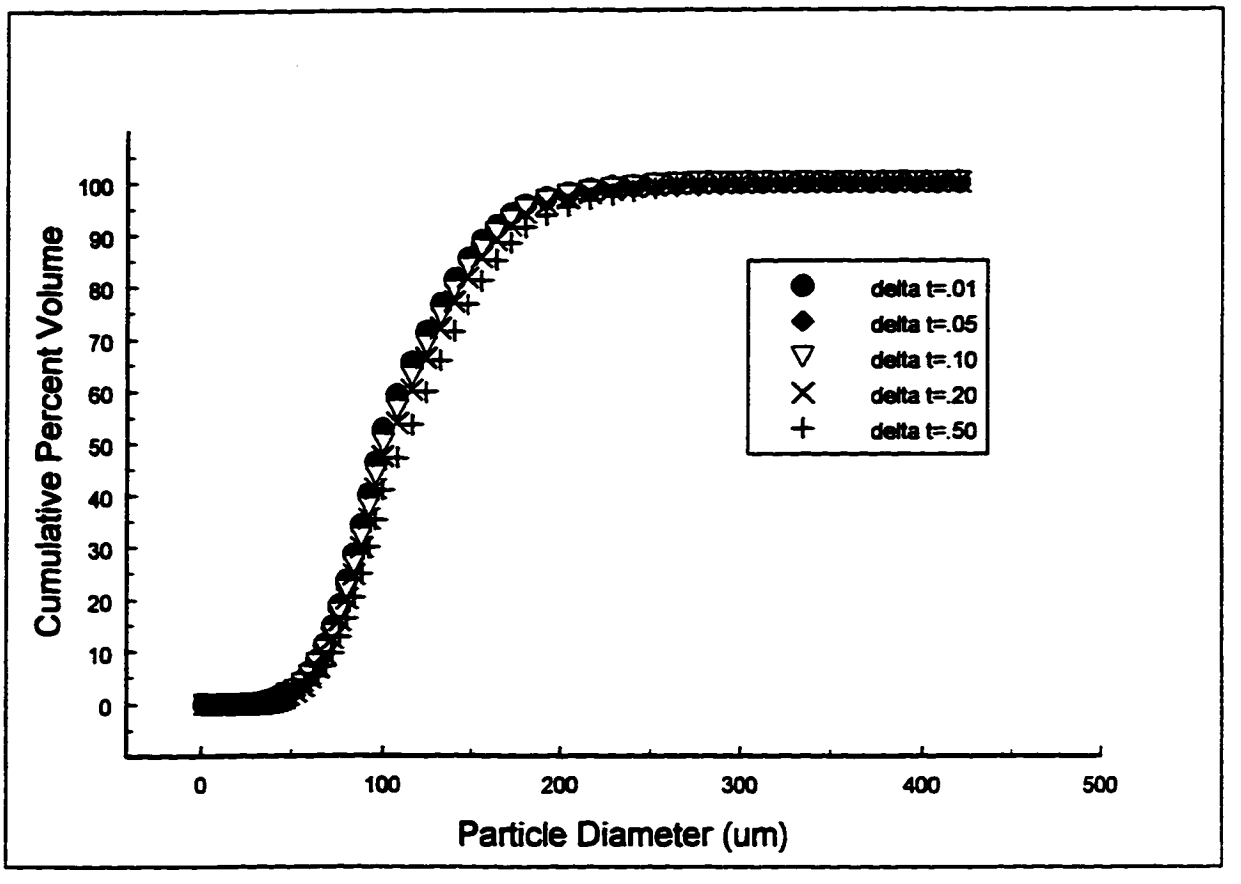

Figure 4.2.3: Effect of Time Step Size on the Population Balance Model at 30 Minutes of Simulated Flocculation

In order to optimize the empirical constants in the population balance model, a response surface methodology was used (Cornell, 1990). The strategy of the response surface method is to determine the shape of the following response variable as a function of parameter values α, C_1, and C_3:

$$SSR(\alpha, C_1, C_3) = (d_{10E} - d_{10s})^2 + (d_{30E} - d_{30s})^2 + (d_{50E} - d_{50s})^2 + (d_{60E} - d_{60s})^2 + (d_{90E} - d_{90s})^2 \quad (4.19)$$

where

$SSR(\alpha, C_1, C_3)$ = Response Variable

d_{10} = 10 percent of the sample particle size are smaller on a volume basis.

d_{30} = 30 percent of the sample particle size are smaller on a volume basis.

d_{50} = 50 percent of the sample particle size are smaller on a volume basis.

d_{60} = 60 percent of the sample particle size are smaller on a volume basis.

d_{90} = 90 percent of the sample particle size are smaller on a volume basis.

Subscript S = simulation prediction

Subscript E = experimental outcome

d_{10}, d_{30}, and d_{60} in Equation 4.19 were chosen due to their wide use in characterizing the shape of the distribution of soil samples. d_{50} and d_{90} were added to increase the model fit to the entire particle size distribution. In essence, $SSR(\alpha, C_1, C_3)$ is simply the sum of the squares of residuals of five particle sizes from the cumulative particle size distribution. The goal of computing the shape of the response surface variable is to determine the minimum of $SSR(\alpha, C_1, C_3)$. The best values for α, C_1, and C_3 were determined by finding the minimum point of the response variable, $SSR(\alpha, C_1, C_3)$.

The response surface methodology was applied only to the 5L tank size results for the Rushton turbine. Typically, researchers and engineers are interested in translating the flocculation results from a bench top flocculator to a full scale flocculator. Hence, the model should be calibrated using the smallest tank size in order to evaluate its effectiveness at predicting the larger

tank sizes. Once these optimal empirical constants have been computed, the model was used to predict the particle size distribution at T = 28L and T = 560L tank sizes. These same optimal values for α, C_1, C_3 were used to also predict the particle size distribution with the A310 foil impeller at T = 5L, T = 28L, and T = 560L. This strategy will also assess the effectiveness at predicting other impeller types. Ultimately, this simple population balance model will be judged on its ability to predict the particle size distribution in three different flocculation vessels and with two different impeller types given the intensity of the turbulence within those vessels.

5.0 FLUID MECHANICS IN STIRRED SQUARE VESSELS

5.1 LDV Experimental Results

5.1.1 Impeller Power Number and Flow Number

The impeller power number, N_p, and impeller flow number N_Q, were calculated using the technique described in Section 3.4. Figures 5.1.1 and 5.1.2 display the results of the N_p measurements for the Rushton turbine and the A310 foil impeller, respectively. As can be seen from Figures 5.1.1 and 5.1.2, N_p is effectively constant in the turbulent flow region ($Re > 10^4$) as described by Holland and Chapman (1966). Figures 5.1.1 and 5.1.2 also indicate that N_p does not depend on tank size. This was also seen by Clark et al. (1994) for the same impellers. These figures also indicate a significant difference between the value of N_p for the Rushton turbine and A310 foil impeller.

From Figures 5.1.1 and 5.1.2, $N_p = 2.8$ for the Rushton turbine and $N_p = 0.32$ for the A310 foil impeller. These results are consistent with the order of magnitude difference found between a flat bladed radial flow impeller and an axial flow impeller used by other researchers (Weetman et al., 1988; Mersmann and Geisler, 1991; Geisler et al., 1994, Clark et al., 1994). In fact, Clark et al. (1994) reported very similar N_p values for both the Rushton turbine and A310 foil impeller ($N_p = 2.4$ for Rushton; $N_p = .319$ for A310). Their work was also done in a square tank. The value of N_p for the Rushton turbine in a square tank is about half of what is typically found for a Rushton turbine in a fully baffled cylindrical tank. In a square tank, the resistance to rotation of water with a Rushton turbine is provided by the drag on the tank walls. In a fully baffled cylindrical tank, the baffles enhance the resistance to fluid rotation. Consequently, more power would be required to maintain the same tip speed in a fully baffled cylindrical tank than in a square tank. No significant difference was found between the values of N_p for a fluid foil impeller in a square tank versus a fully baffled cylindrical tank. This is not surprising since the A310 foil impeller is an axial flow impeller and does not cause the fluid to rotate in either tank style. Hence, the power required to mix the fluid is not a function of the drag imposed by the walls or baffles.

Table 5.1.1 displays the N_Q results for the Rushton turbine and the A310 fluid foil

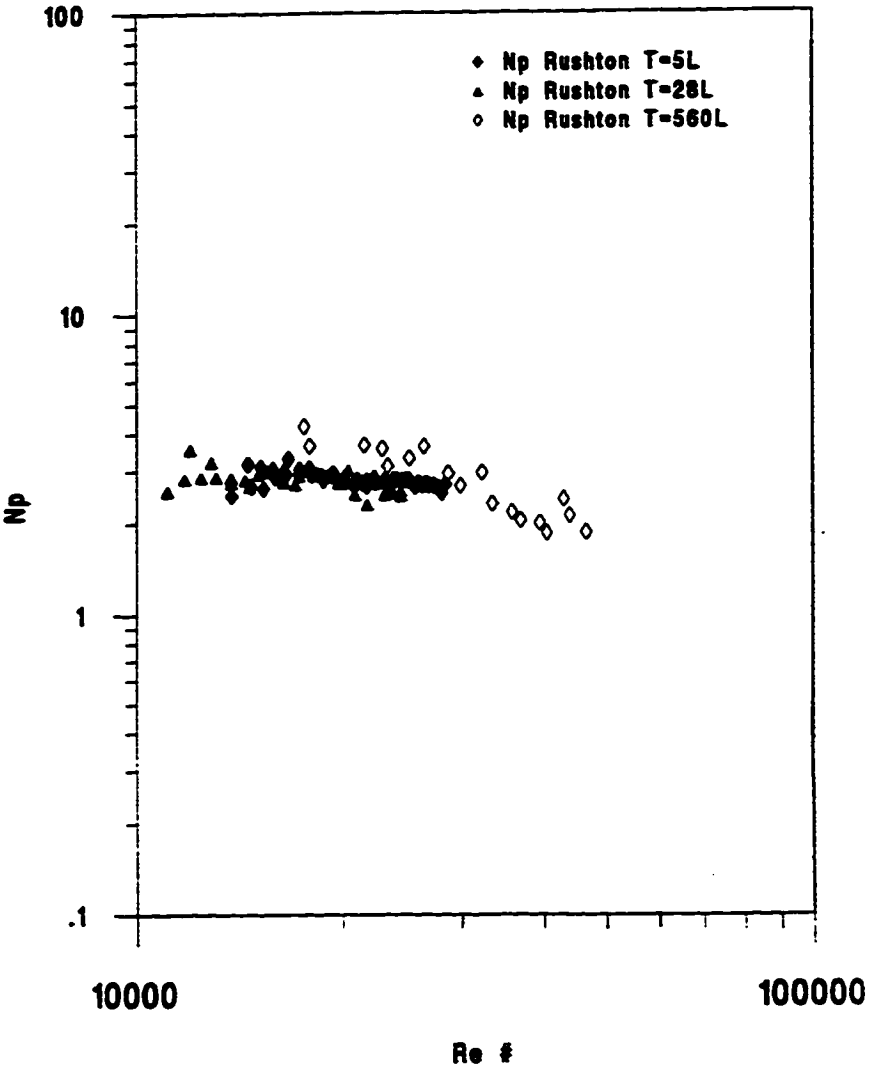

Figure 5.1.1: Power Number Measurements for the Rushton Turbine

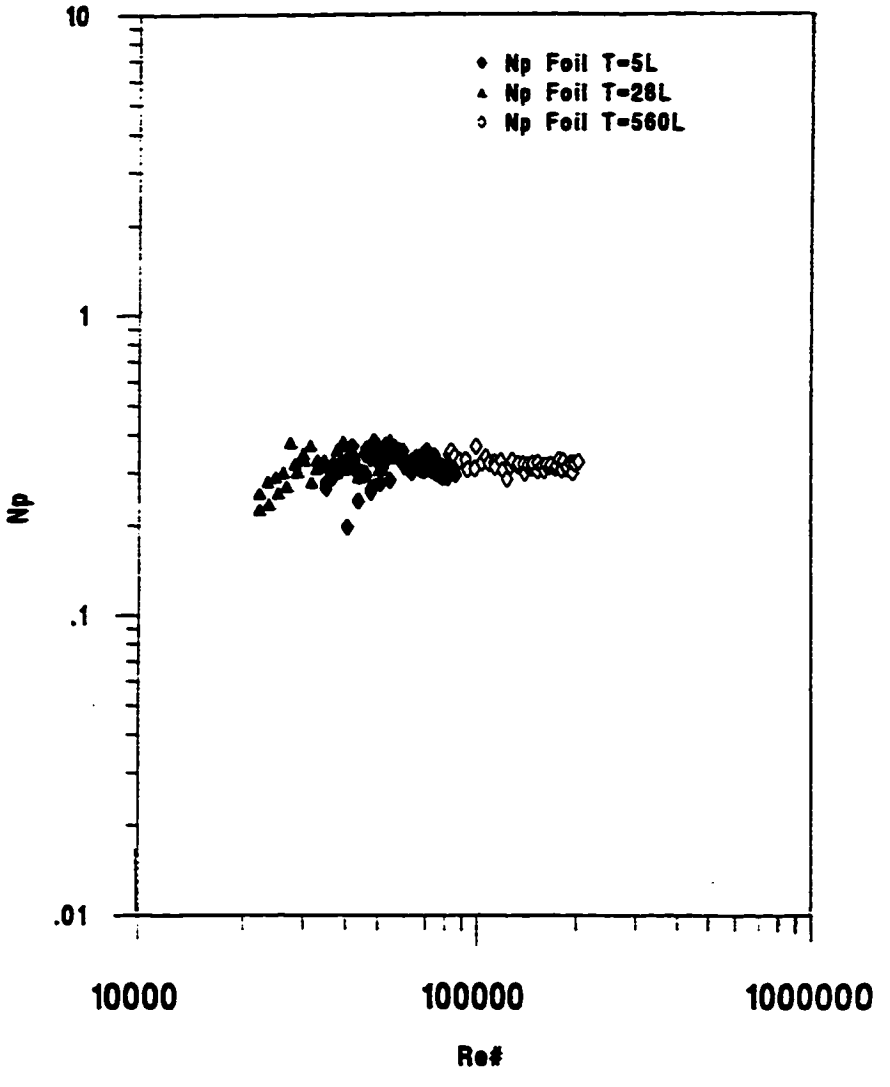

Figure 5.1.2: Power Number Measurements for the A310 Fluid Foil Impeller

Table 5.1.1: Impeller Flow Number, N_Q

Impeller	T = 5L	T = 28L	T = 560L	Avg
Rushton	0.77	0.73	0.76	0.75
A310 Foil	0.57	0.58	0.58	0.58

impeller. The mean velocity profile in the impeller discharge region shown in Section 5.1.2 was used to generate N_Q. The results in Table 5.1.1 indicate that like N_p, N_Q does not depend on the tank size. However, there is a difference between N_Q of the Rushton turbine and the A310 fluid foil impeller. These results are consistent with those N_Q values reported by other investigators (Oldshue, 1983; Weetman et al., 1988). Oldshue (1983) reports $N_Q = 0.75 \pm 0.15$ for the Rushton turbine and Weetman et al. (1988) reports $N_Q = 0.56$ for the A310 foil impeller. The results in Table 5.1.1 suggest that for the same impeller diameter and angular velocity, the primary flow from the Rushton turbine boundary is slightly higher than that produced at the A310 foil impeller boundary.

5.1.2 Mean Velocity Profile

The mean velocity profile at the impeller discharge boundary for the Rushton turbine and the A310 fluid foil impeller are displayed in Figures 5.1.3 and 5.1.4 respectively. In Figure 5.1.3, the mean velocity profile for the Rushton turbine displays the familiar radial jet profile described by many investigators. Figure 5.1.3 also shows that when normalized by the impeller tip speed, the Rushton mean velocity profile does not depend on the size of the tank.

In Figure 5.1.4, the mean velocity profile for the A310 foil impeller displays a sharp reduction in mean velocity near the center of the impeller ($r/R < 0.2$) and near the impeller tip ($r/R > 0.9$). These reductions in mean velocity are due to the proximity of the impeller hub at $r/R = 0 - 0.1$ and due to the production of impeller tip vortices at $r/R = 0.9 - 1.0$. The velocity profile for the foil impeller is almost constant between $r/R = 0.4$ and $r/R = 0.8$.

The profiles of the resultant radial and axial mean velocity vectors in the plane perpendicular to the tank wall are displayed in Figures 5.1.5 and 5.1.6 for the Rushton turbine

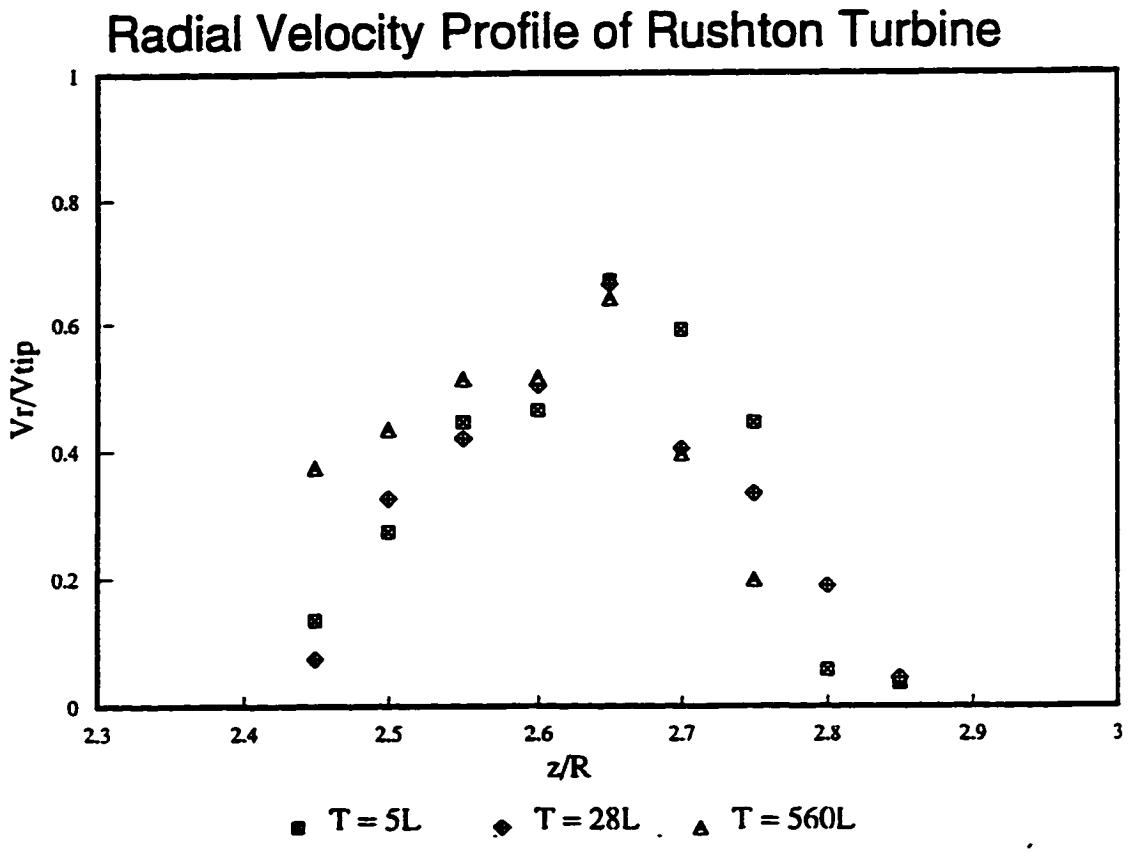

Figure 5.1.3: Mean Velocity Profile at the Impeller Discharge Boundary of the Rushton Turbine

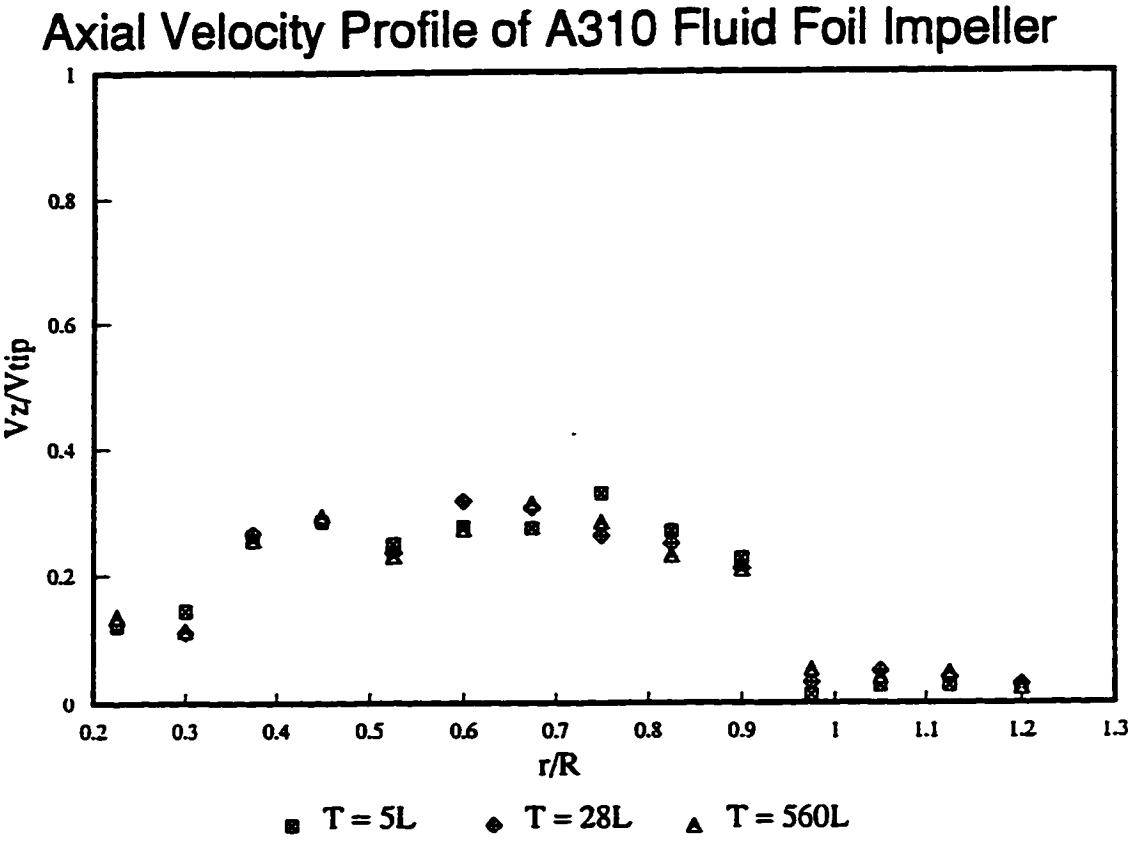

Figure 5.1.4: Mean Velocity Profile at the Impeller Discharge Boundary of the A310 Foil Impeller

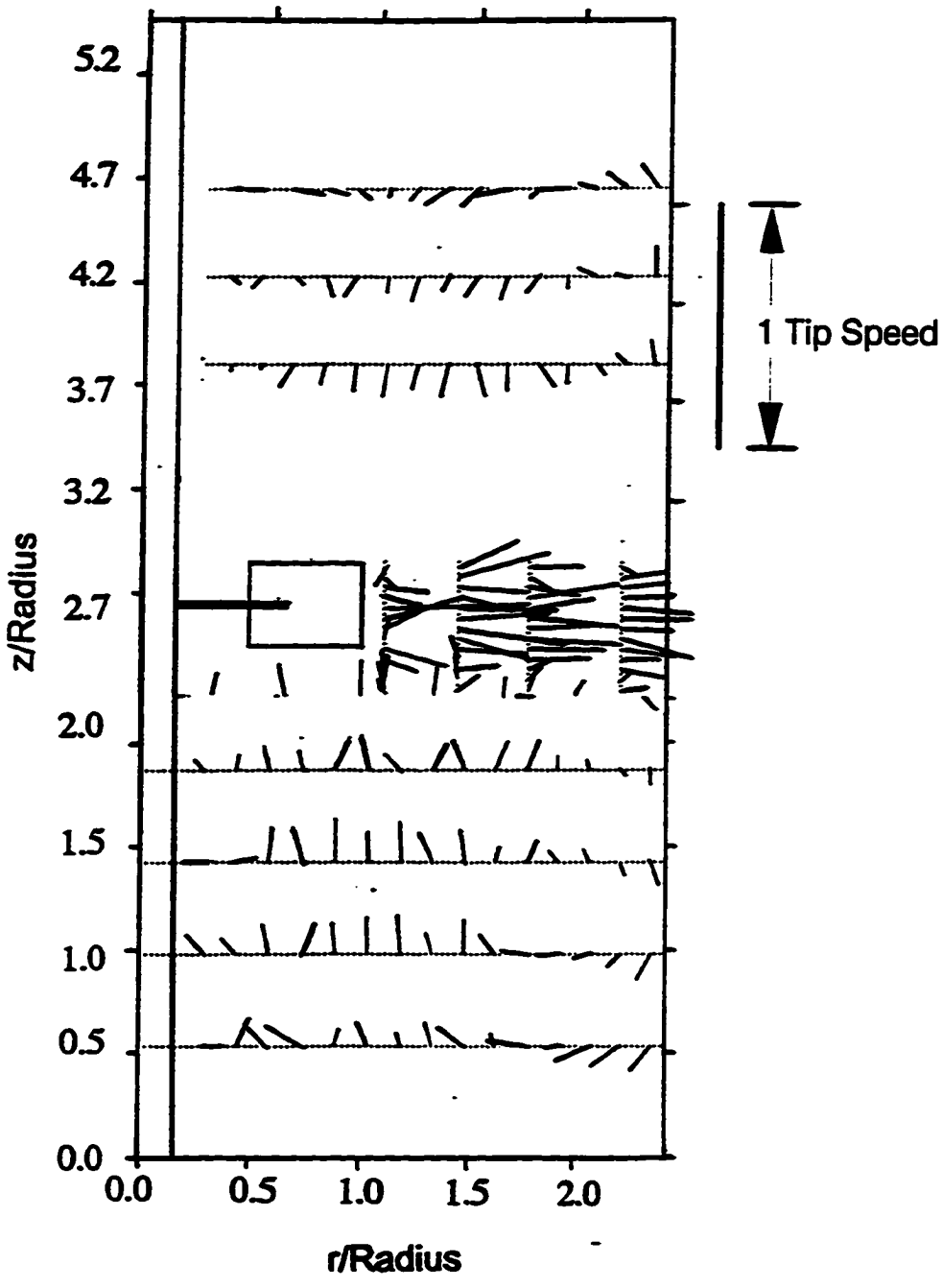

Figure 5.1.5: Mean Velocity Flow Pattern for the Rushton Turbine (T = 5L) (velocity normalized by tip speed)

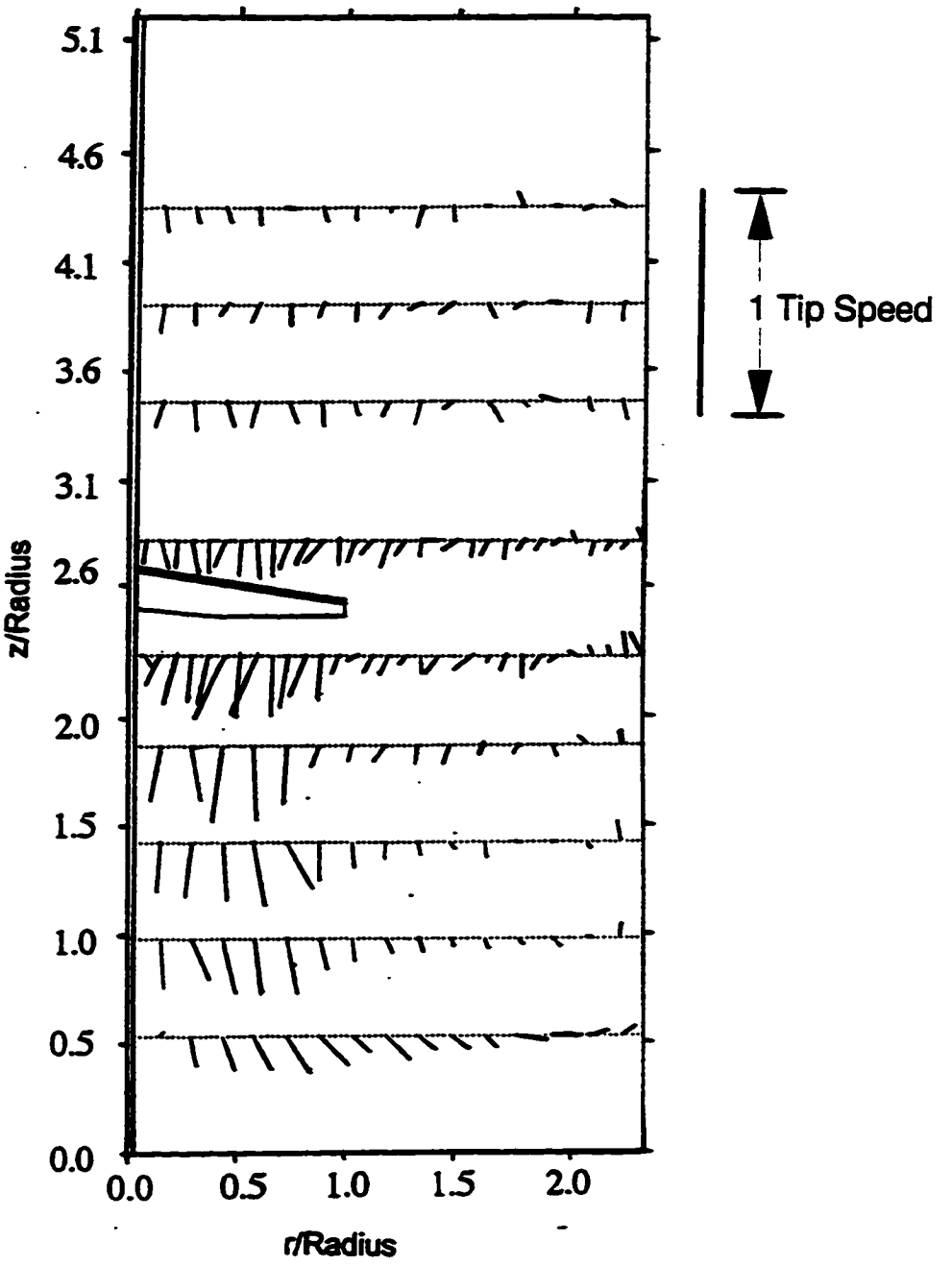

Figure 5.1.6: Mean Velocity Flow Pattern for the A310 Foil Impeller (T = 5L) (velocity normalized by tip speed)

and A310 foil impeller, respectively. The profile of the Rushton turbine shown in Figure 5.1.5 is typical of that measured by other investigators (Desouza & Pike, 1972; Weetman & Oldshue, 1988; Kusters, 1991). The center of the flow pattern circulation loop is located at r/R = 1.8 - 2.0. It is not clear where the center of the circulation loop exists in the z/R direction. More measurements would be needed in the z/R direction to ascertain the exact location.

In Figure 5.1.6, the velocity profile, below the impeller centerline, of the A310 foil impeller is similar to that produced by other axial flow impellers. However, above the impeller centerline, the velocity profile near the tank wall seems to deviate from the flow pattern produced by a typical axial flow impeller. Figure 5.1.6 seems to indicate that in the plane perpendicular to the tank wall, a circulation loop only exists below the impeller centerline. However, in order for the flow pattern to satisfy the continuity equation, fluid flow must circulate from the bottom to the top of the tank. Although no LDV measurements were taken close to the tank wall due to interference of the laser beams with the tank wall, it would seem that from visual observations of the free surface, most of the flow is circulating from the bottom to the top of the tank near the tank corners. However, more LDV measurements would be needed to confirm this observation. The flow patterns shown in Figures 5.1.5 and 5.1.6 were found to be the same at the three different tank sizes investigated in this study. The FIDAP simulation will be used to further investigate the circulation pattern throughout the tank (Section 5.2.1).

5.1.3 Turbulent Fluctuating Velocity and Kinetic Energy

5.1.3.1 Resultant RMS Turbulent Fluctuating Velocity Equation without Reynolds Shear Stress

The resultant rms turbulent fluctuating velocity in the direction of the mean flow was determined at each point using Equation 3.5. The LDV system at LIGHTNIN was not setup to compute the Reynolds shear stresses (i.e. $\overline{u_i u_j}$ for I ≠ j) used in Equation 3.5. In order to properly compute the Reynolds shear stresses, each data point in the velocity time trace for each direction must be sampled at the same time. This was not possible at LIGHTNIN. Hence, the cross correlations in Equation 3.4 and the Reynolds shear stress in Equation 3.5 were neglected

in the computation of the resultant rms value.

In general, the error in approximating the resultant rms value using Equation 3.5 without the Reynolds shear stresses is highest where the turbulent flow is anisotropic and lowest where the flow is isotropic. Studies done in shear layers where the turbulence is anisotropic have shown the following relationship (Hudson, 1993)

$$\overline{u_i u_j} \approx .45 \sigma_i \sigma_j$$

where

σ_i = rms fluctuating velocity in the I direction

σ_j = rms fluctuating velocity in the j direction

In isotropic turbulence that constant (i.e. 0.45) goes down to 0.1. Ito et al. (1974, 1975) did some three dimensional measurements of the velocity in a stirred tank with a Rushton turbine using a spherical electrode probe. Along with measuring the mean velocity and the rms fluctuating velocity, Ito et al. (1974, 1975) also measured the Reynolds shear stresses. They found that in the impeller discharge region, the magnitude of the Reynolds shear stress was about 25 to 50 percent of the mean square fluctuating velocity (i.e. $\overline{u_i u_j} \approx 0.5\overline{u_i^2}$). This value occurred closest to the impeller tip. However, away from the impeller tip and in the bulk region, the magnitude of the Reynolds shear stress was about 0 to 5 percent of the mean square fluctuating velocity.

Another important problem with leaving out the Reynolds shear stresses from Equations 3.5 - 3.7 is in the usage of Equation 3.8 to calculate the local energy dissipation rate. Recall that in order to use Equation 3.8, the local turbulent Reynolds number must be sufficiently large. Table 5.1.2 displays the average local turbulent Reynolds number in the impeller discharge region of the Rushton turbine for the three different tank sizes. The local Reynolds number is based on the product of the local turbulence intensity and the length scale of the energy containing eddies divided by the kinematic viscosity (Hinze, 1975). As Table 5.1.2 suggests, the local turbulent Reynolds number is on the order of 10^3 which is high enough to use Equation 3.8 (Tennekes &

Lumley, 1972, Hinze, 1975). The same order of magnitude was found for the local turbulent Reynolds number in the impeller region of the foil impeller.

Table 5.1.2: Average Local Turbulent Reynolds for the Rushton Turbine in the Impeller Discharge Region

r/R	T = 5L	T = 28L	T = 560L
1.1	4610	5915	8079
1.444	4469	8366	11817
1.778	3546	4805	7271
2.222	2557	4628	8344

Clearly, the results from Ito et al. (1974, 1975) and Hudson (1993) suggest that leaving out the Reynolds shear stress can impact the accuracy of Equation 3.5 only near the impeller blade tip. But the high values of the local Reynolds number in the Table 5.1.2 indicates that leaving out the Reynolds shear stress does not impact the use of Equation 3.8 for calculating the local turbulent energy dissipation rate. In the bulk region, the contribution of the Reynolds shear stress is negligible. The beauty of Equation 3.5 is that for the first time, it provides a simple way to compute the resultant rms fluctuating velocity in the direction of the mean flow in stirred tanks. This method is more consistent with Taylor's frozen field hypothesis than previous methods used for calculating the turbulence in stirred tanks.

5.1.3.2 Turbulent Fluctuating Velocity and Kinetic Energy Results

The resultant root mean square of the turbulent fluctuating velocity, in the direction of the mean flow, was determined at each point using Equation 3.5 without the Reynolds shear stress. In the course of measuring the rms fluctuating velocity near the impeller tip, a periodic velocity component was determined to exist. This was not surprising since other investigators have also found the existence of a periodic velocity component (Appendix A). This periodic velocity has

a mean velocity of zero. It has the ability to inflate the value of the rms fluctuating velocity and cause what other investigators have called "pseudo-turbulence." Clearly, the periodic velocity is not a turbulent quantity and must be removed in order to compute the true rms fluctuating velocity.

In this study, a digital Butterworth band-pass filter (Beauchamp and Yuen, 1979) was used to remove the specific frequencies of the periodic velocities. These frequencies were found to coincide with the blade passage frequency and its harmonics. Figures 5.1.7 and 5.1.8 display the autocorrelation and power spectrum, respectively, of the fluctuating velocity with the periodic velocity component for the Rushton turbine operating at 106 rpm. As can be seen from Figure 5.1.7, the periodic velocity causes the autocorrelation to cycle around zero. The frequency of the periodic velocity is easily shown in Figure 5.1.8 where large peaks in the power spectrum are seen at 10.6 and 21 Hz. By using the Butterworth band-pass filter, these frequencies are largely removed (Figure 5.1.9, 5.1.10).

Figures 5.1.11, 5.1.12, and 5.1.13 display the results of the resultant rms turbulent fluctuating velocity for the Rushton turbine in three square tanks. As frequently observed, these results seem to indicate that when the rms fluctuating velocity is normalized by the impeller tip speed, the rms fluctuating velocity does not depend on the tank size. However, it is clear that the rms fluctuating velocity is a function of the location of measurement in the square tank. Figures 5.1.11 and 5.1.12 show that the rms fluctuating velocity is about 8-10 percent of the impeller tip speed in the bulk region above and below the impeller. Figure 5.1.13, however, shows that the rms fluctuating velocity is about 10-20 percent of the impeller tip speed in the impeller discharge region.

Figures 5.1.14 and 5.1.15 display the resultant rms turbulent fluctuating velocities for the A310 foil impeller in three square tanks. These results also indicate that when the rms fluctuating velocity is normalized by the impeller tip speed, the rms value does not depend on the tank size. It only depends on the location of the measurement in the square tank. In Figure 5.1.14, the rms fluctuating velocity is about 6-8 percent of the impeller tip speed below the foil impeller discharge region. In Figure 5.1.15, the rms fluctuating velocity is about 3-5 percent of the impeller tip speed above the foil impeller discharge region.

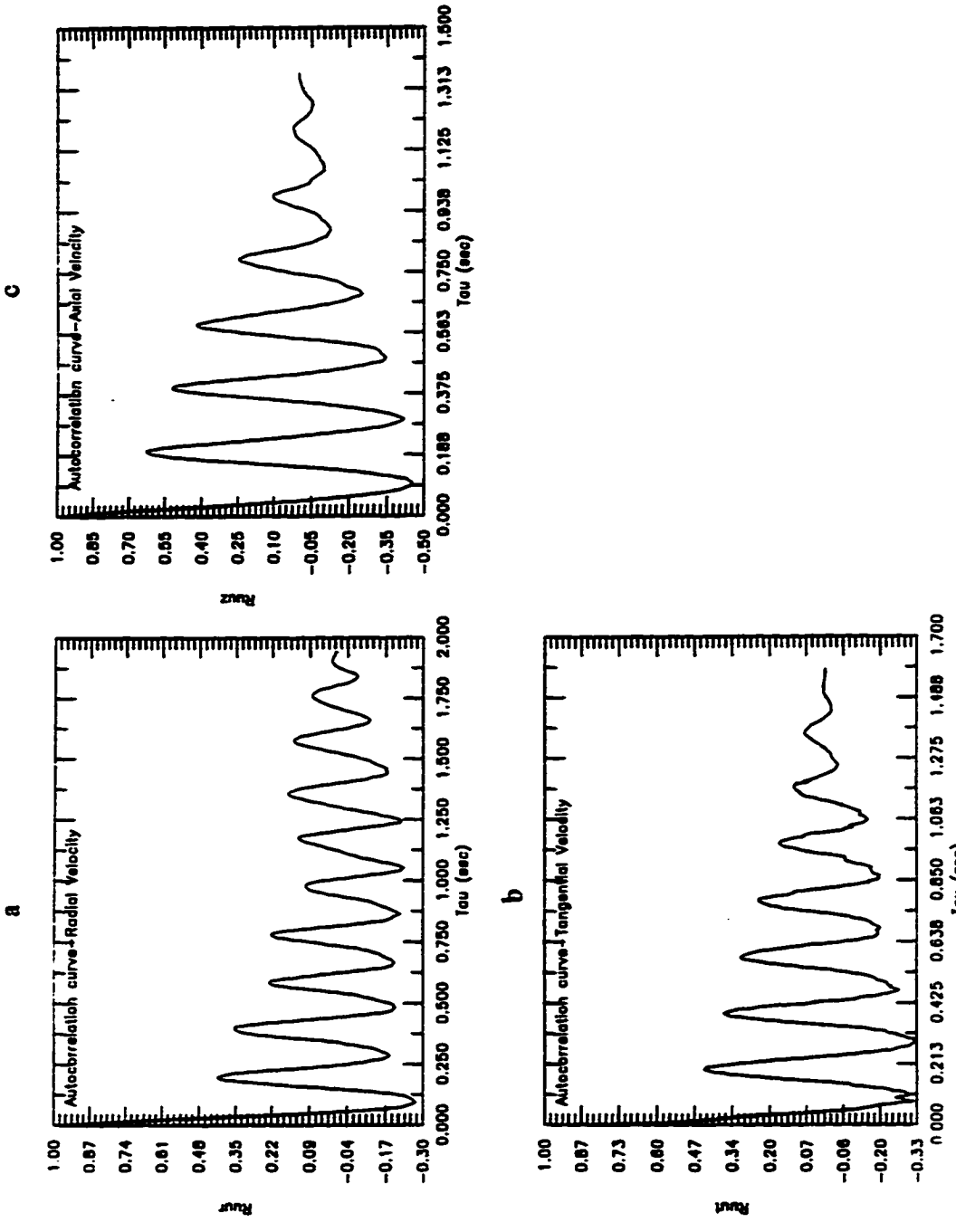

Figure 5.1.7: Autocorrelation of the turbulent Velocity Fluctuations with Periodic Component a) Radial Velocity Fluctuation, b) Tangential Velocity Fluctuation, c) Axial Velocity Fluctuation

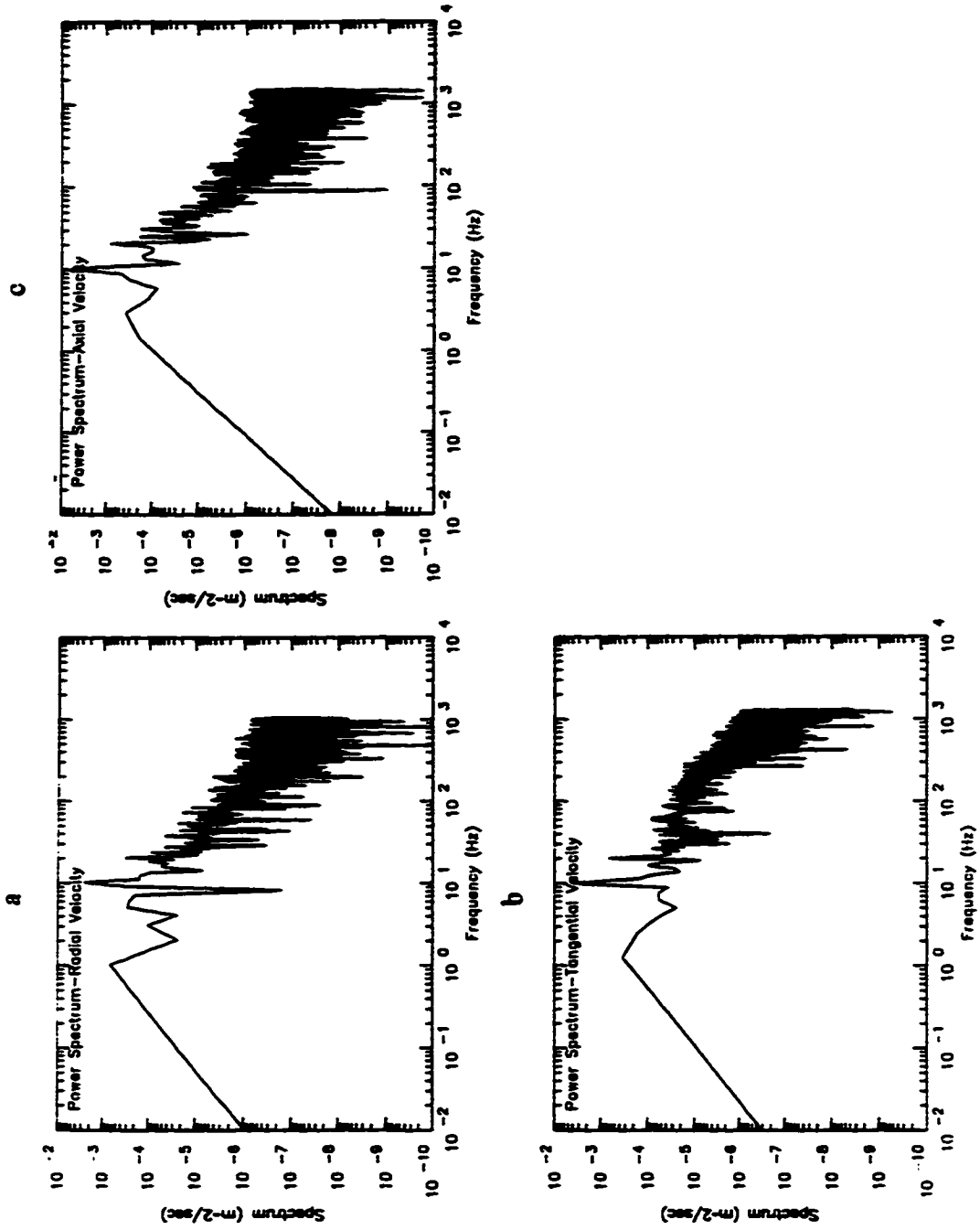

Figure 5.1.8: Power Spectra of the Turbulent Velocity Fluctuations with Periodic Component a) Radial Velocity Fluctuation, b) Tangential Velocity Fluctuation, c) Axial Velocity Fluctuation

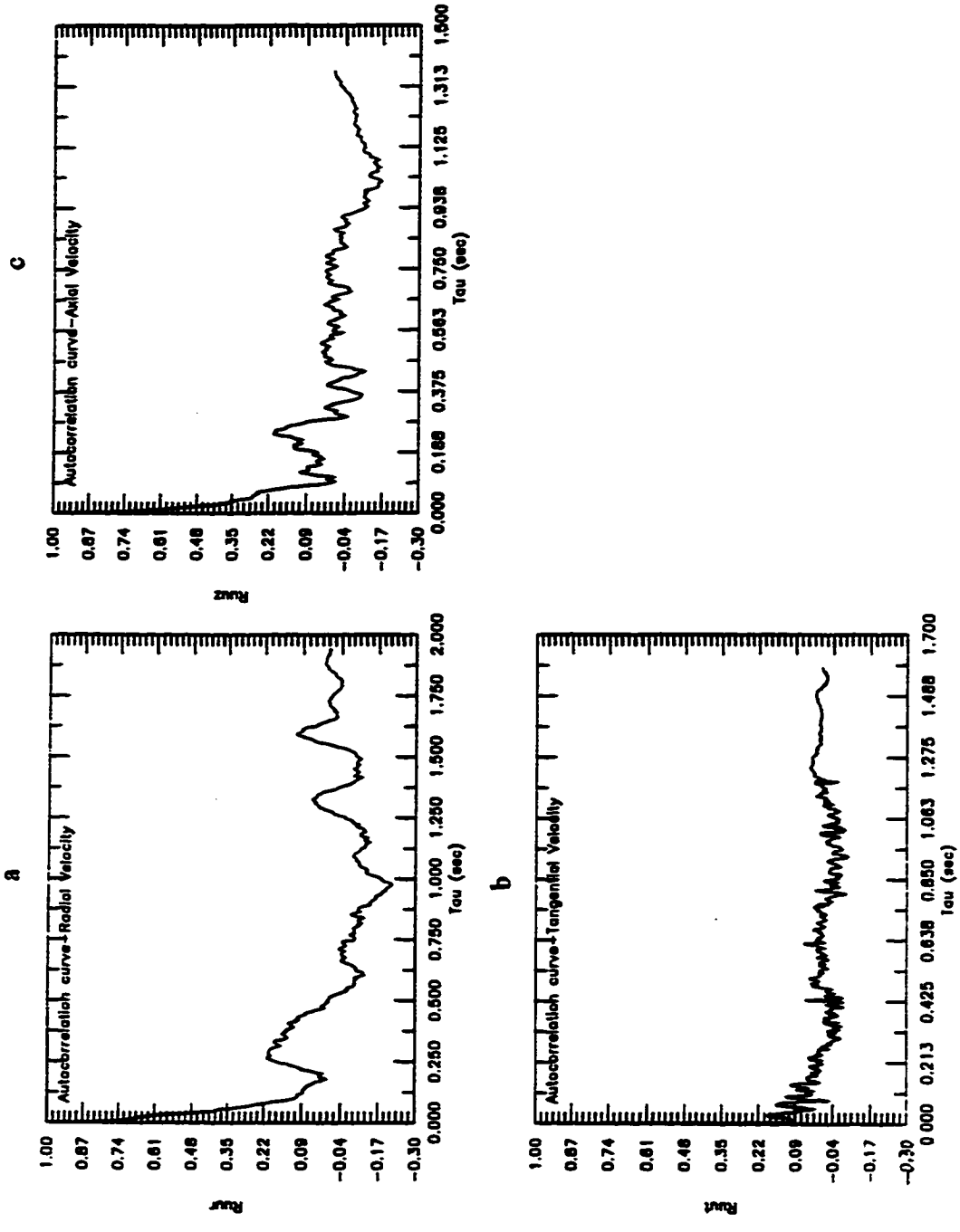

Figure 5.1.9: Autocorrelation of the Turbulent Velocity Fluctuation without Periodic Component a) Radial Velocity Fluctuation, b) Tangential Velocity Fluctuation, c) Axial Velocity Fluctuation

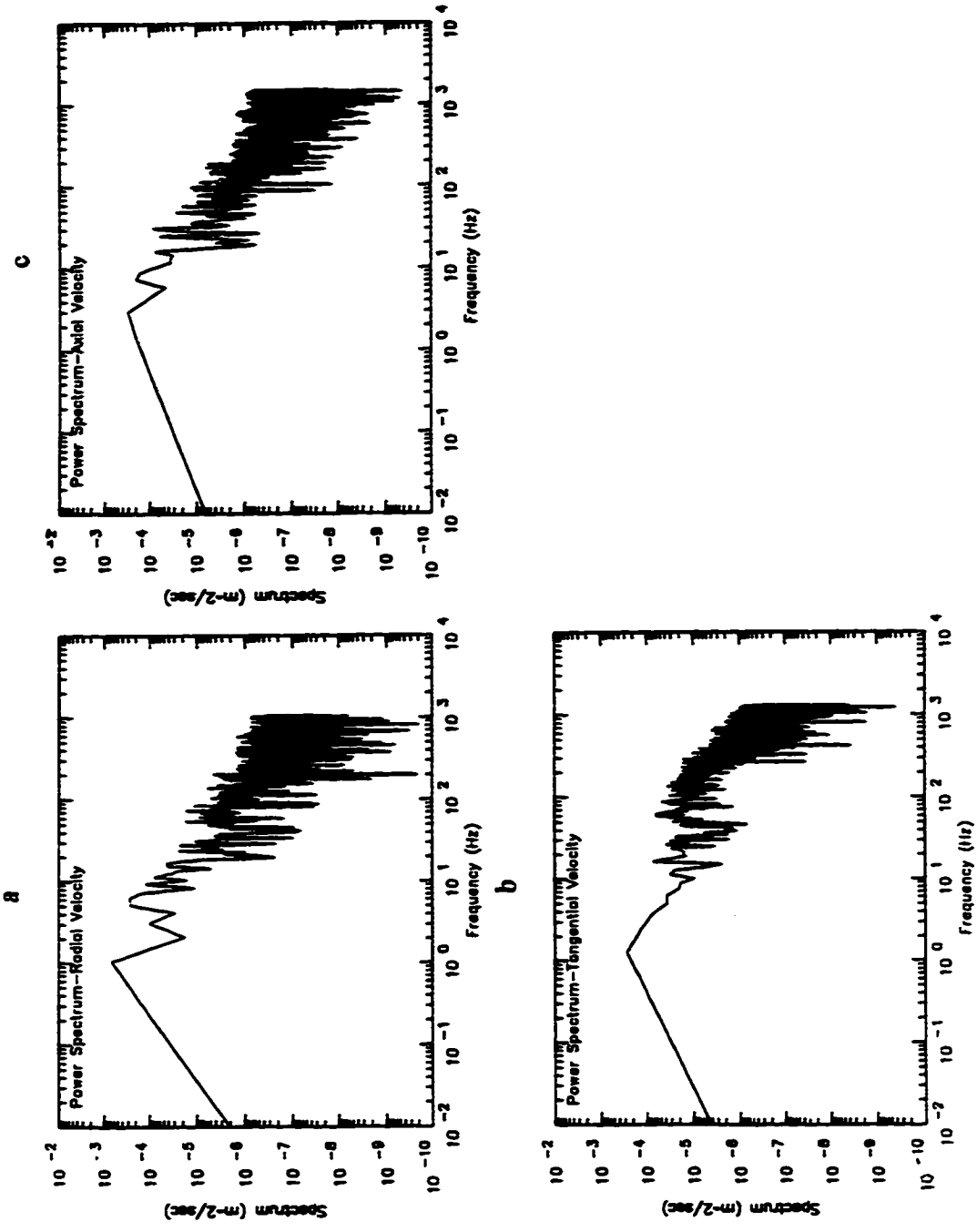

Figure 5.1.10: Power Spectra of the Turbulent Velocity Fluctuation without Periodic Component a) Radial Velocity Fluctuation, b) Tangential Velocity Fluctuation, c) Axial Velocity Fluctuation

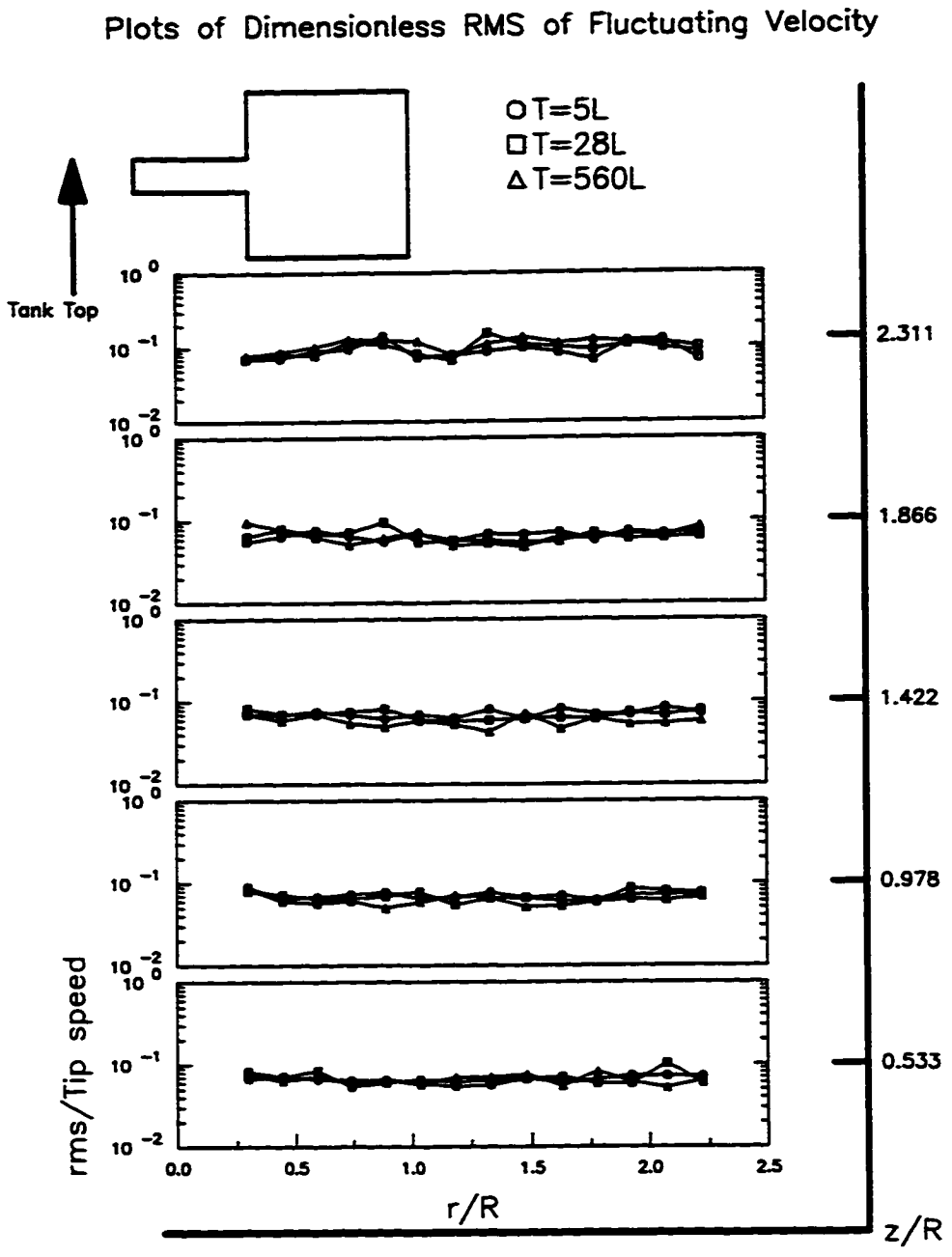

Figure 5.1.11: Resultant RMS Turbulent Fluctuating Velocity in the Direction of the Mean Flow For the Rushton Turbine below the Impeller Centerline

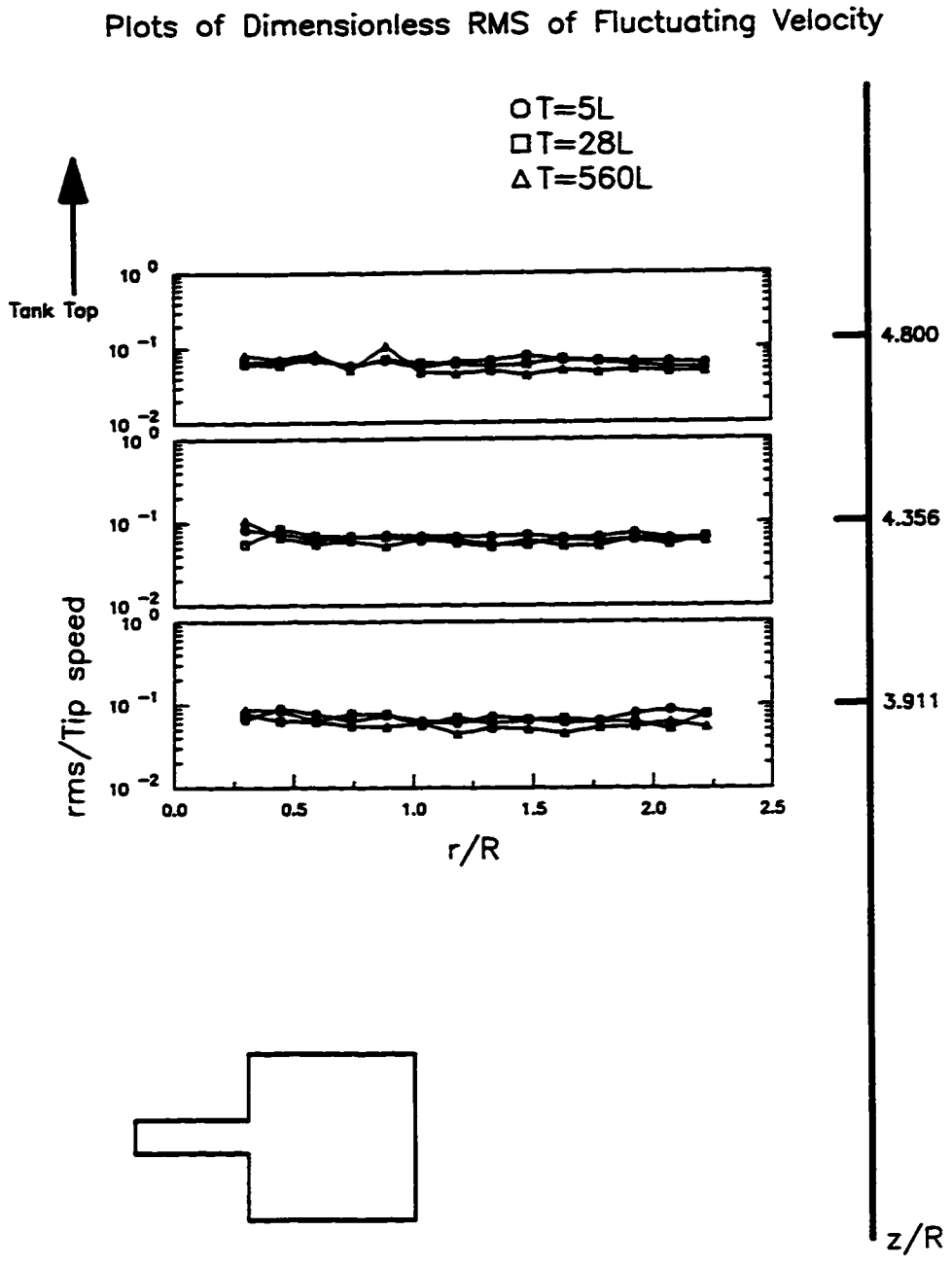

Figure 5.1.12: Resultant RMS Turbulent Fluctuating Velocity in the Direction of the Mean Flow For the Rushton Turbine above the Impeller Centerline

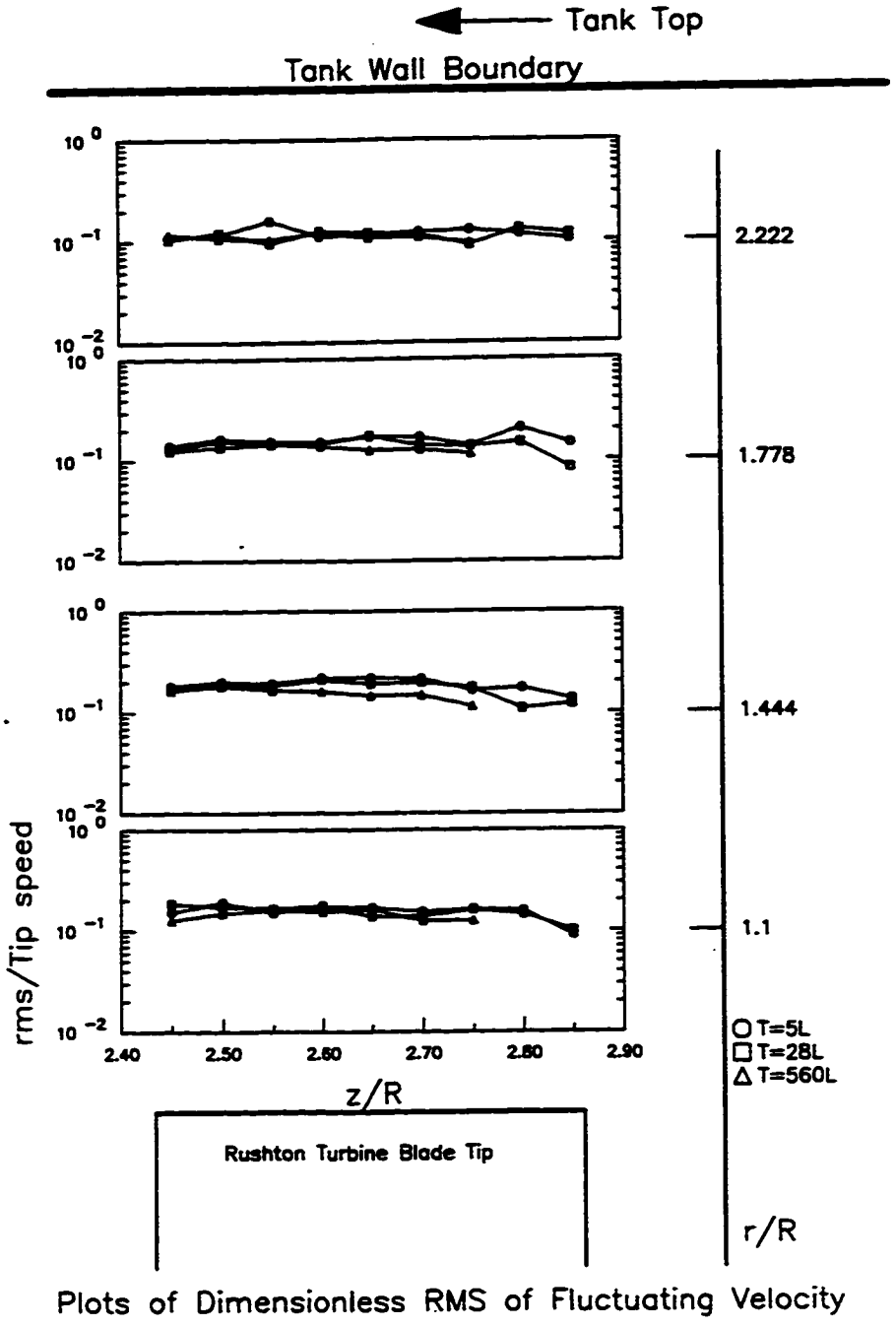

Figure 5.1.13: **Resultant RMS Turbulent Fluctuating Velocity in the Direction of the Mean Flow for the Rushton Turbine in the Impeller Discharge Region**

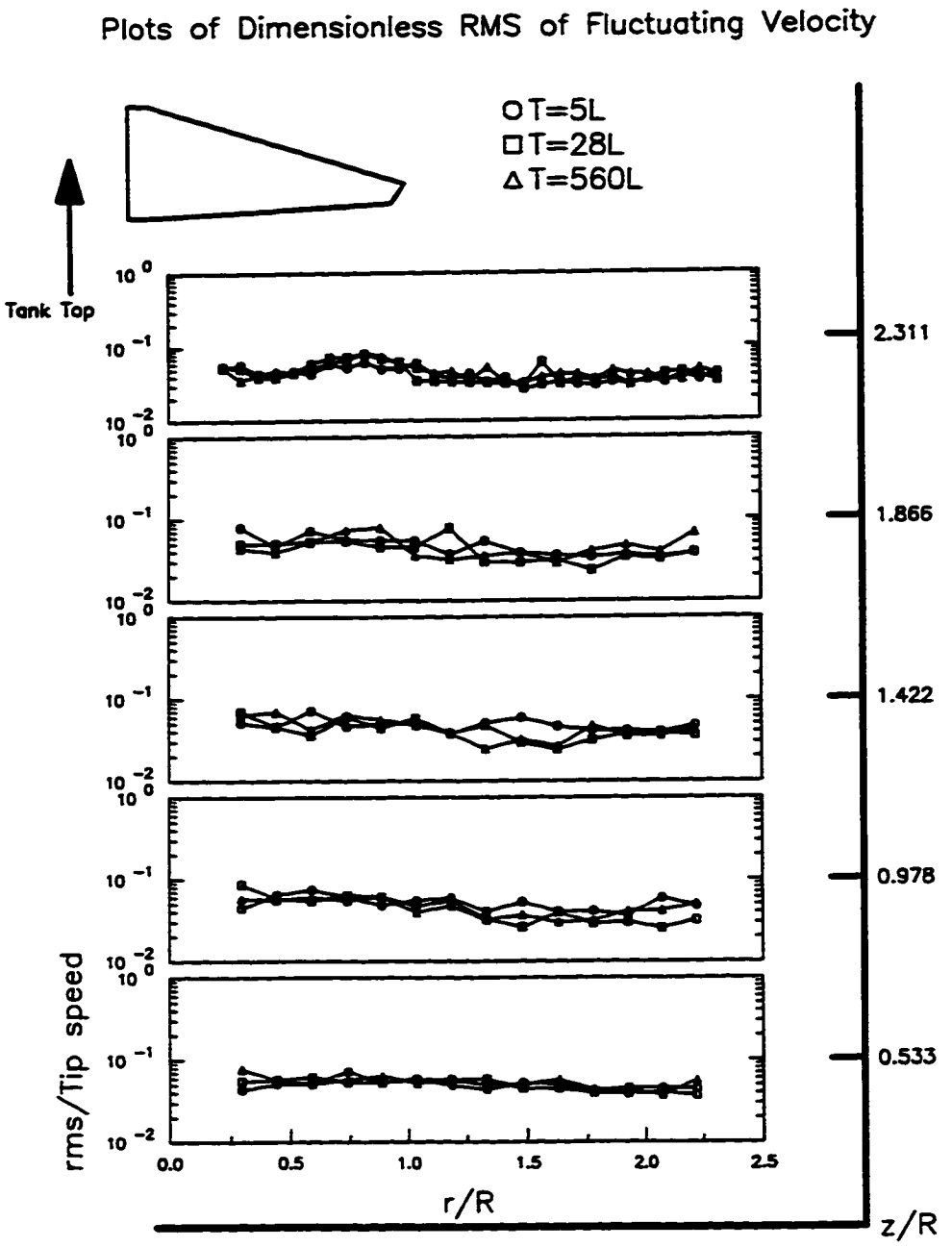

Figure 5.1.14: Resultant RMS Turbulent Fluctuating Velocity in the Direction of the Mean Flow for the A310 Foil Impeller Below the Impeller Centerline

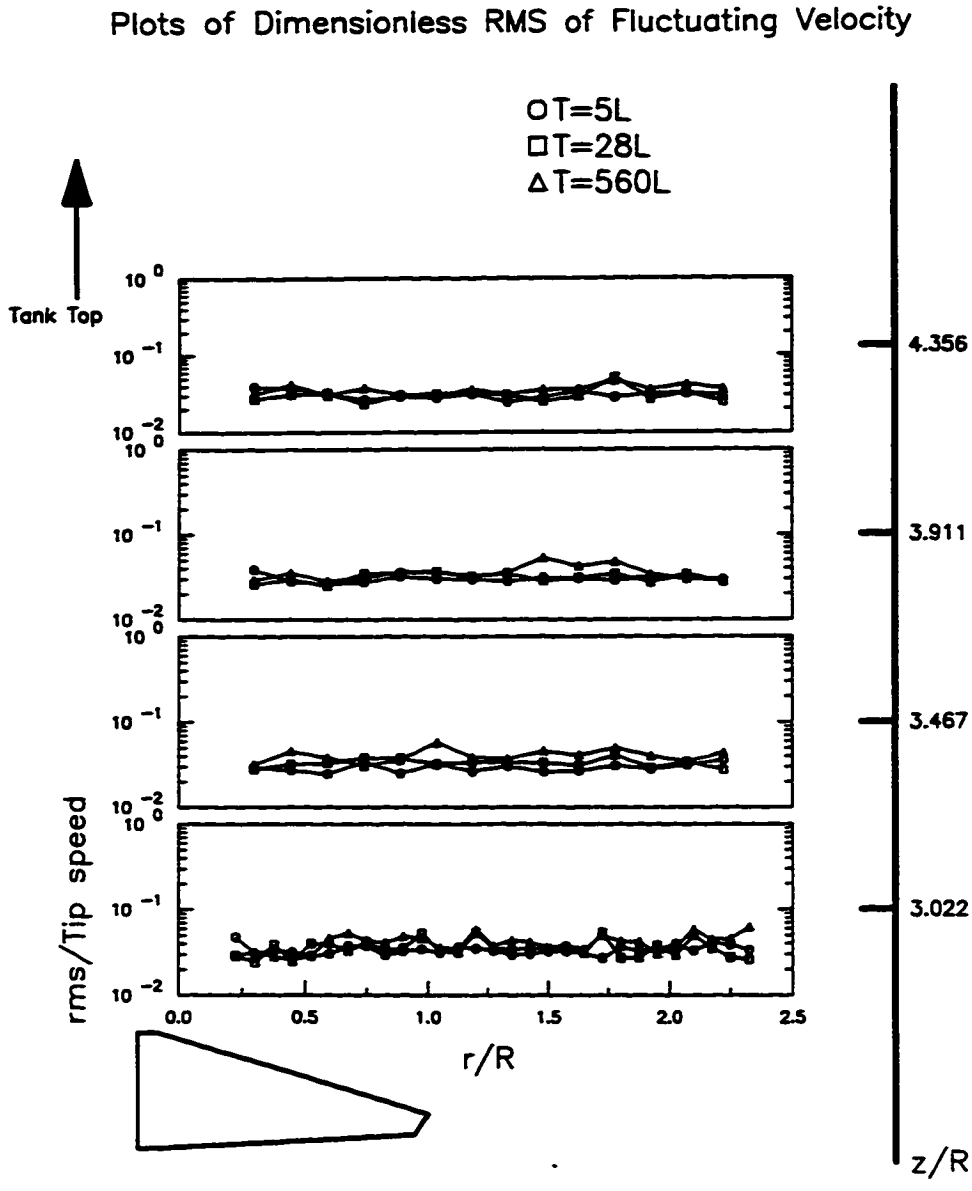

Figure 5.1.15: Resultant RMS Turbulent Fluctuating Velocity in the direction of the mean flow For the A310 Foil Impeller above the Impeller Centerline

The results for the rms fluctuating velocity indicate that there is a definite difference between the Rushton turbine and the A310 foil impeller. Figures 5.1.16 and 5.1.17 compare the dimensionless rms fluctuating velocity between the Rushton turbine and A310 foil impeller at T=5L and T=560L, respectively. Clearly, Figures 5.1.16 and 5.1.17 suggest that for the same average energy dissipation rate in the tank, the intensity of turbulence for the Rushton turbine is higher than for the A310 foil impeller. The difference in the turbulence intensity between the Rushton turbine and A310 foil impeller is even greater when one compares the impeller discharge region of both impellers (Figure 5.1.13, 5.1.14).

In Section 4.2.2, this author proposed that the rms turbulent fluctuating velocity is proportional to the product of the tip speed and N_p^x. Using the rms fluctuating velocity data in the impeller discharge region of both the Rushton turbine and the A310 foil impeller, x was found to equal 0.49. Table 5.1.3 displays some of the RMS fluctuating velocity data normalized by N_p^x and the tip speed for both impeller types. As can be seen from Table 5.1.3, the values are similar for both impeller types in the impeller discharge region. Based on Table 5.1.3, the average rms turbulent fluctuating velocity in the impeller discharge zone is about 10 percent of $N_p^{0.5}ND$ regardless of impeller type or tank size.

Table 5.1.3: Evaluation of Power x in the Relationship rms$\propto N_p^x ND$

Rushton Turbine				A310 Foil Impeller			
z/R	r/R	rms/Tip Speed	rms/$N_p^{0.49}$ Tip Speed	z/R	r/R	rms/Tip Speed	rms/ $N_p^{0.49}$ Tip Speed
2.45	1.1	0.1514	0.0914	2.31	0.75	0.0525	0.0917
2.5	1.44	0.1998	0.1206	1.87	0.6	0.0718	0.1255
2.45	1.78	0.1382	0.0834	1.42	0.75	0.0462	0.0807
2.55	2.22	0.1592	0.0961	.533	0.88	0.0526	0.0920
		Avg.=	0.10			Avg.=	0.10

The turbulent kinetic energy per unit mass was computed at each point using Equation 3.9. Figures 5.1.18, 5.1.19, and 5.1.20 display the results of the kinetic energy for the Rushton

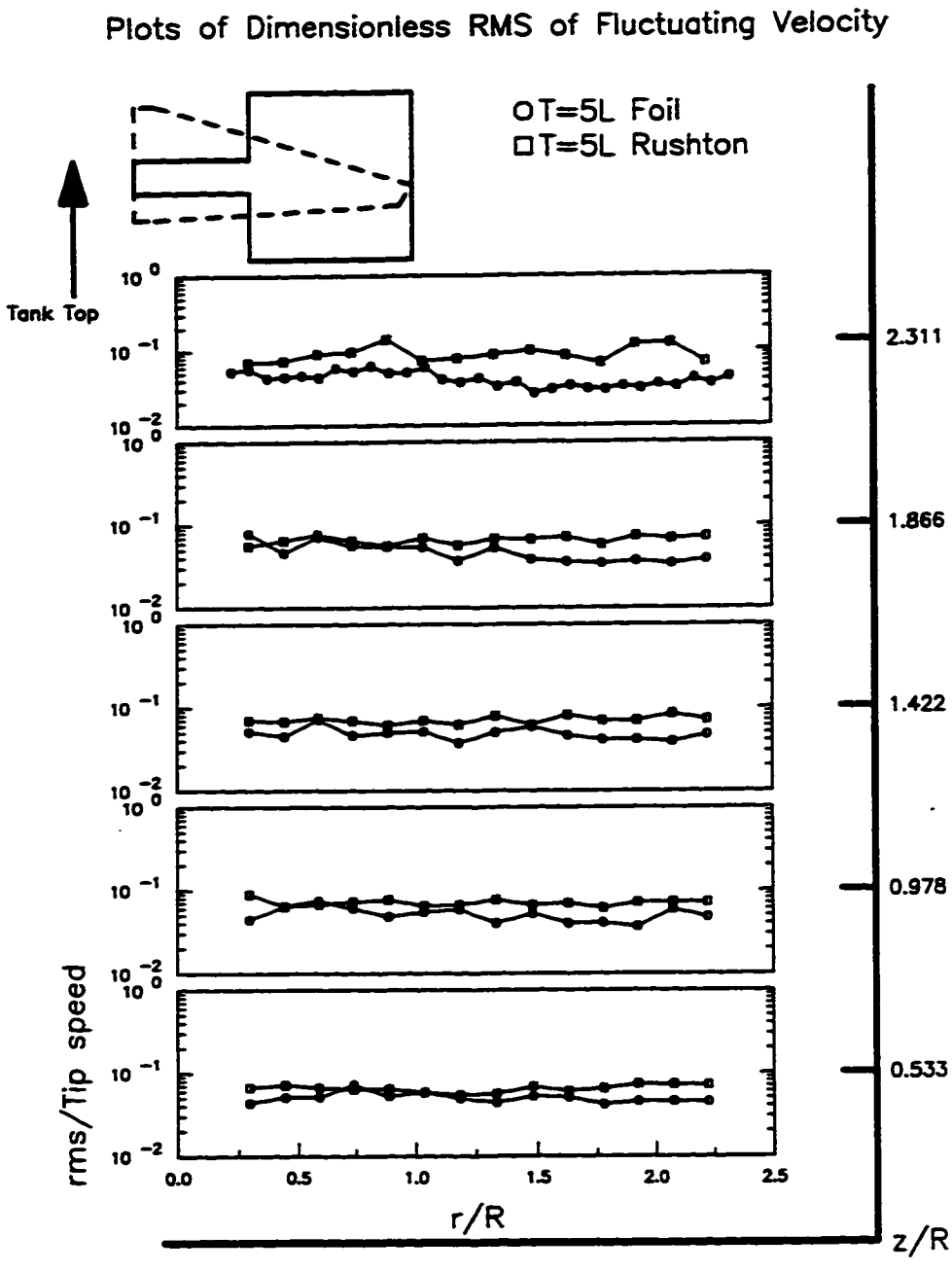

Figure 5.1.16: Comparison of the Resultant RMS Turbulent Fluctuating Velocity in the direction of the Mean Flow between A310 Foil Impeller and Rushton turbine at T=5L

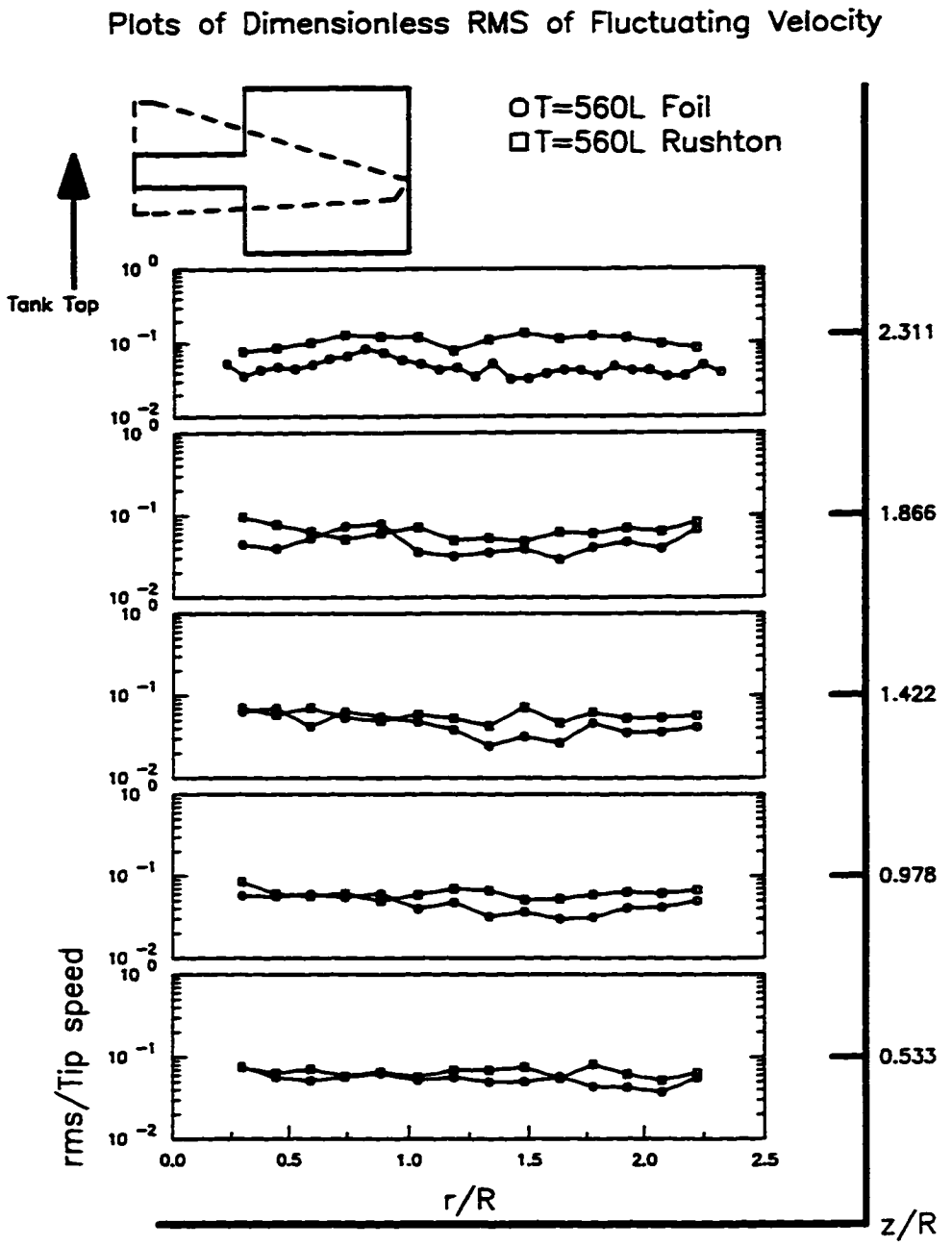

Figure 5.1.17: Comparison of the Resultant RMS Turbulent Fluctuating Velocity in the Direction of the Mean Flow between A310 Foil Impeller and Rushton Turbine at T=560L

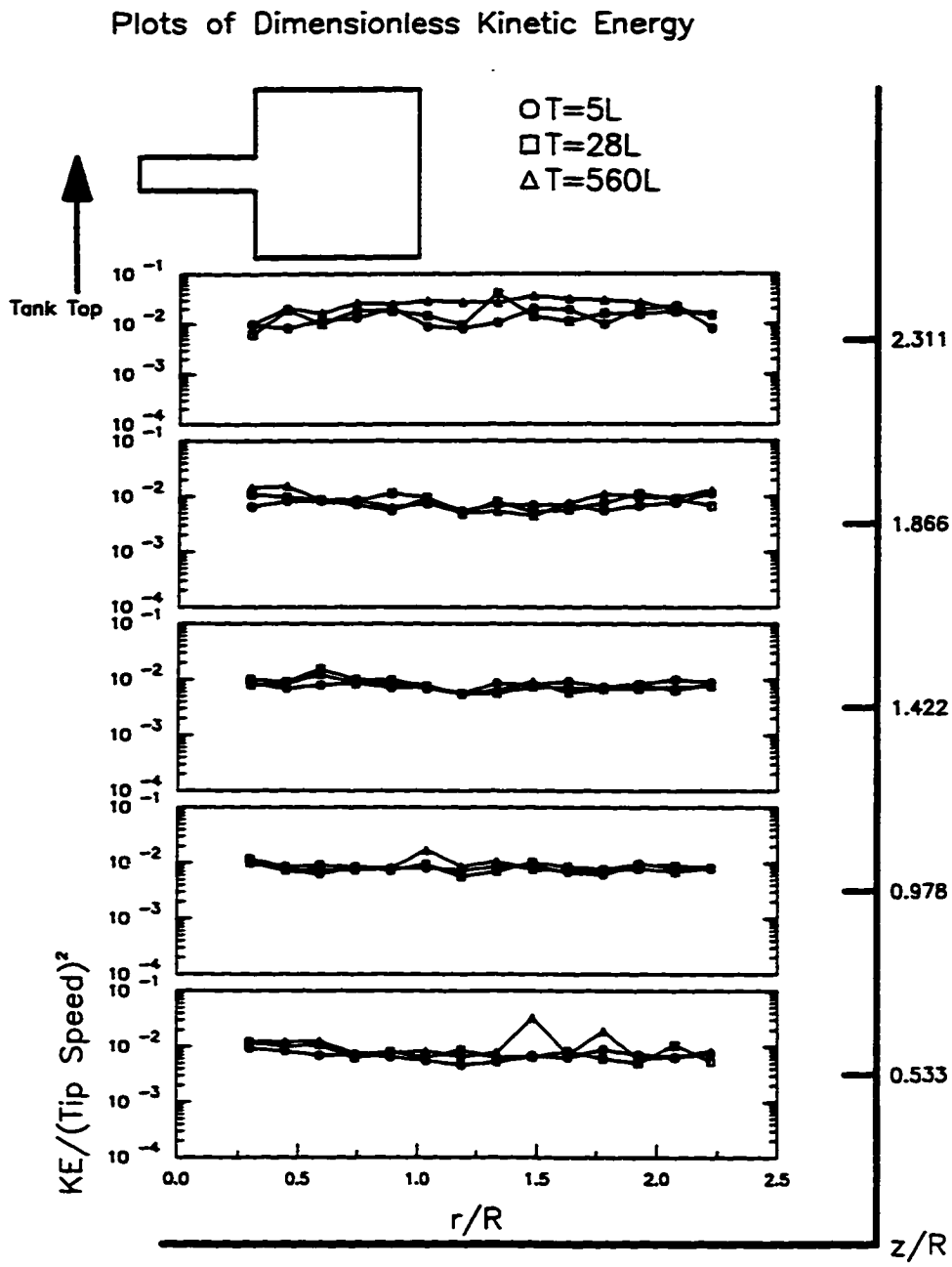

Figure 5.1.18: Turbulent Kinetic Energy for the Rushton Turbine below the Impeller Centerline

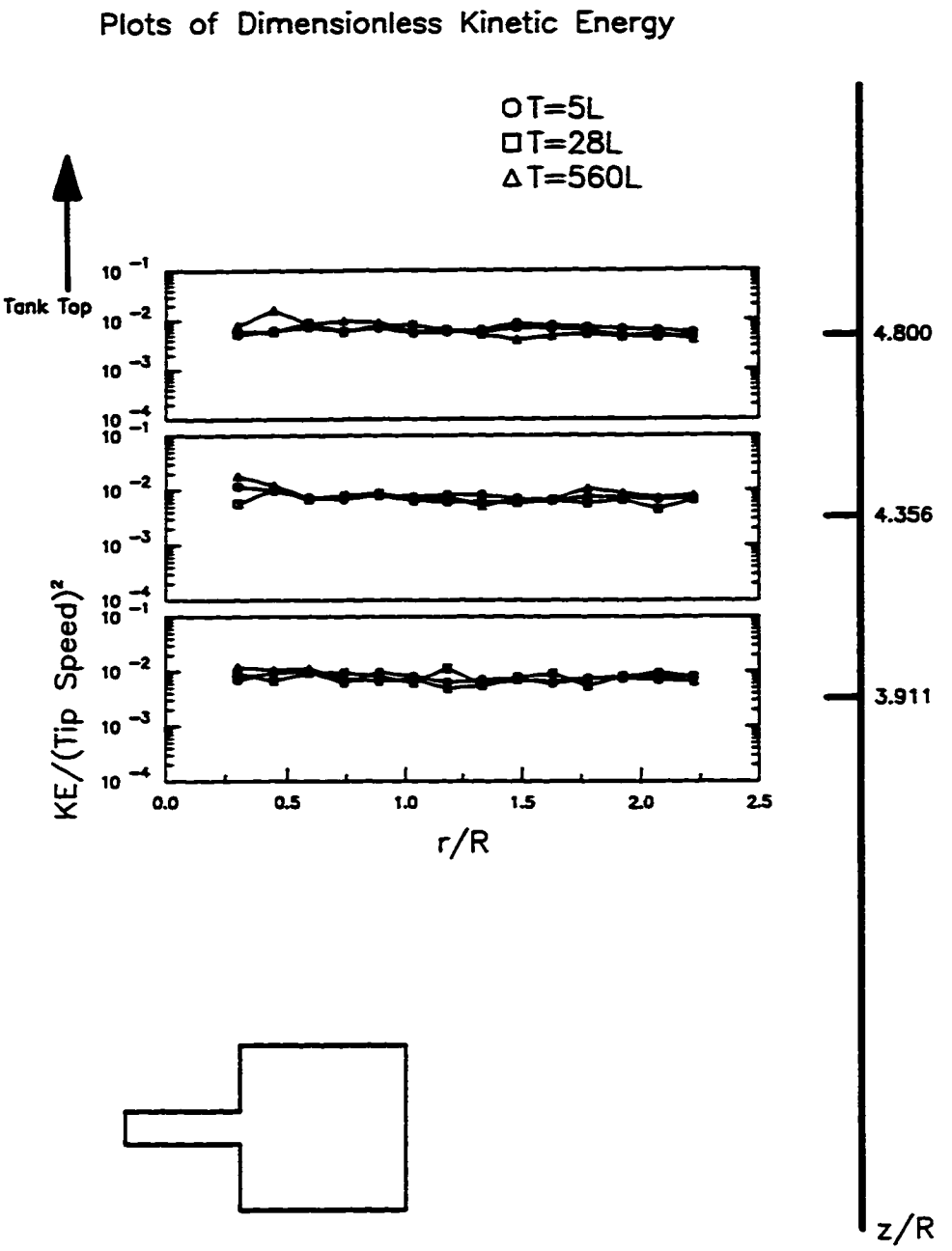

Figure 5.1.19: Turbulent Kinetic Energy for the Rushton Turbine above the Impeller Centerline

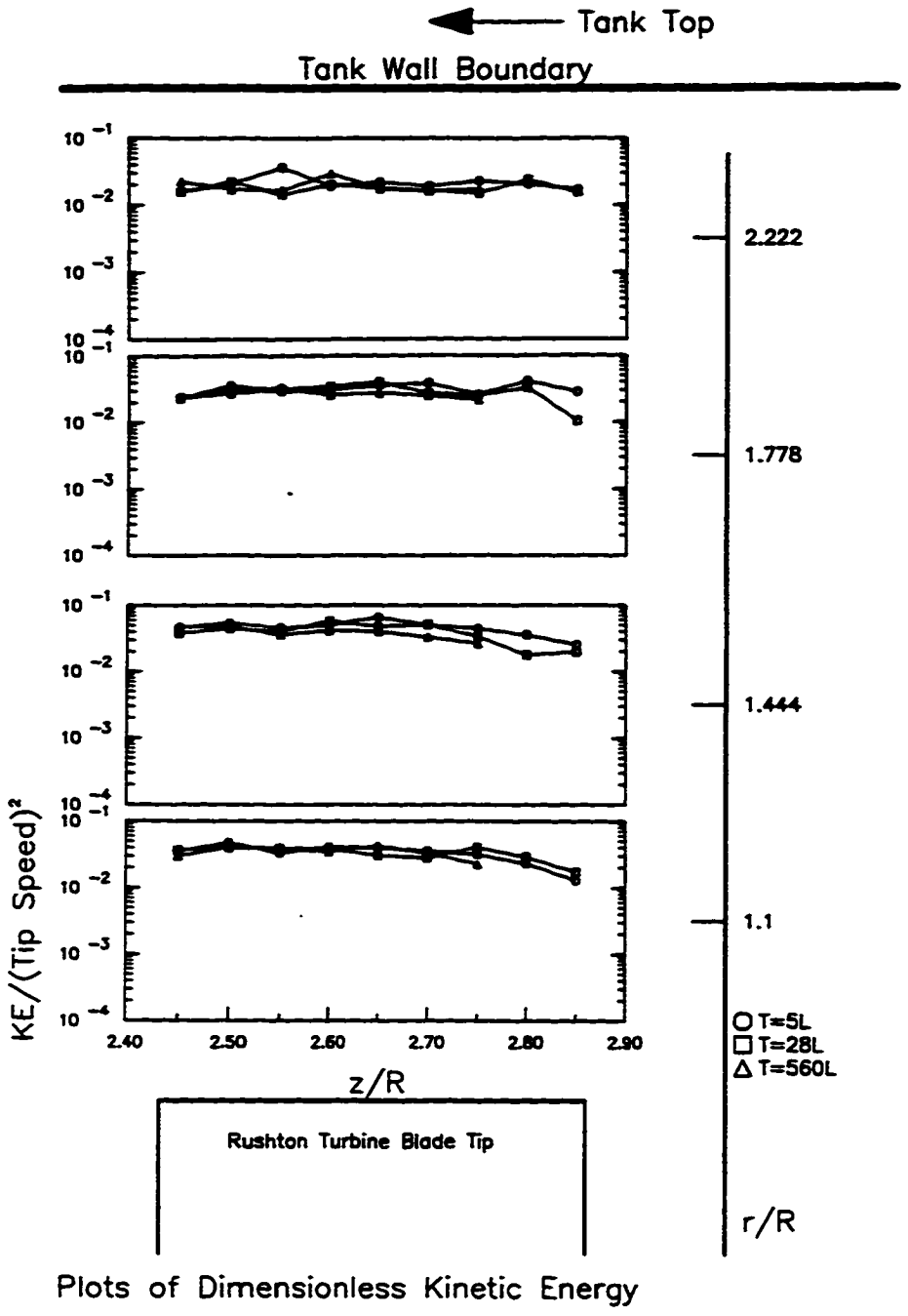

Figure 5.1.20: Turbulent Kinetic Energy for the Rushton Turbine in the Impeller Discharge Region

turbine in a square tank. Figures 5.1.18, 5.1.19, and 5.1.20 show that when the kinetic energy is normalized by the square of the impeller tip speed, it also does not depend on tank size. It only depends on the location of measurement within the tank. Figures 5.1.21 and 5.1.22 show that the dimensionless kinetic energy for the A310 foil impeller also does not depend on tank size. The turbulent kinetic energy results demonstrate that there is a distinct difference between the Rushton turbine and the A310 foil impeller. In Figures 5.1.23 and 5.1.24, the dimensionless kinetic energy for the Rushton turbine is higher than the dimensionless kinetic energy for the A310 foil impeller regardless of the tank size.

5.1.4 Turbulent Energy Dissipation Rate

The turbulent energy dissipation rate per unit mass was computed using Equation 3.8. Figures 5.1.25, 5.1.26 and 5.1.27 display the results of the energy dissipation rate for the Rushton turbine at T=5L, T=28L, and T=560L. In these figures, the local energy dissipation rate is normalized by the average energy dissipation rate in the tank. Figures 5.1.25, 5.1.26, and 5.1.27 show that at the locations measured, the local energy dissipation rate decreases with increasing tank size. The volume-weighted average local energy dissipation rate in the bulk region of the tank is about 81%, 54% and 35% of the tank average energy dissipation rate for T=5L, T=28L, and T=560L, respectively. In the impeller region, the volume-weighted average local energy dissipation rate is about 12.5 times, 7.6 times, and 3.5 times the tank average energy dissipation rate.

Figures 5.1.28 and 5.1.29 display the local energy dissipation rate for the A310 foil impeller at T=5L, T=28L, and T=560L. The results for the local energy dissipation rate for the foil impeller do not show a clear distinct difference between the tank sizes like the Rushton turbine results. In the impeller region, the volume-weighted average local energy dissipation rate is about 1.55 times, 1.43 times, and 1.66 times the tank average energy dissipation rate for T=5L, T=28L, and T=560L, respectively. In the bulk region, these values are 75%, 66% and 68%.

These results seem to indicate that for the A310 foil impeller, the local energy dissipation is not very sensitive to tank size. However, for the Rushton turbine, the local energy dissipation

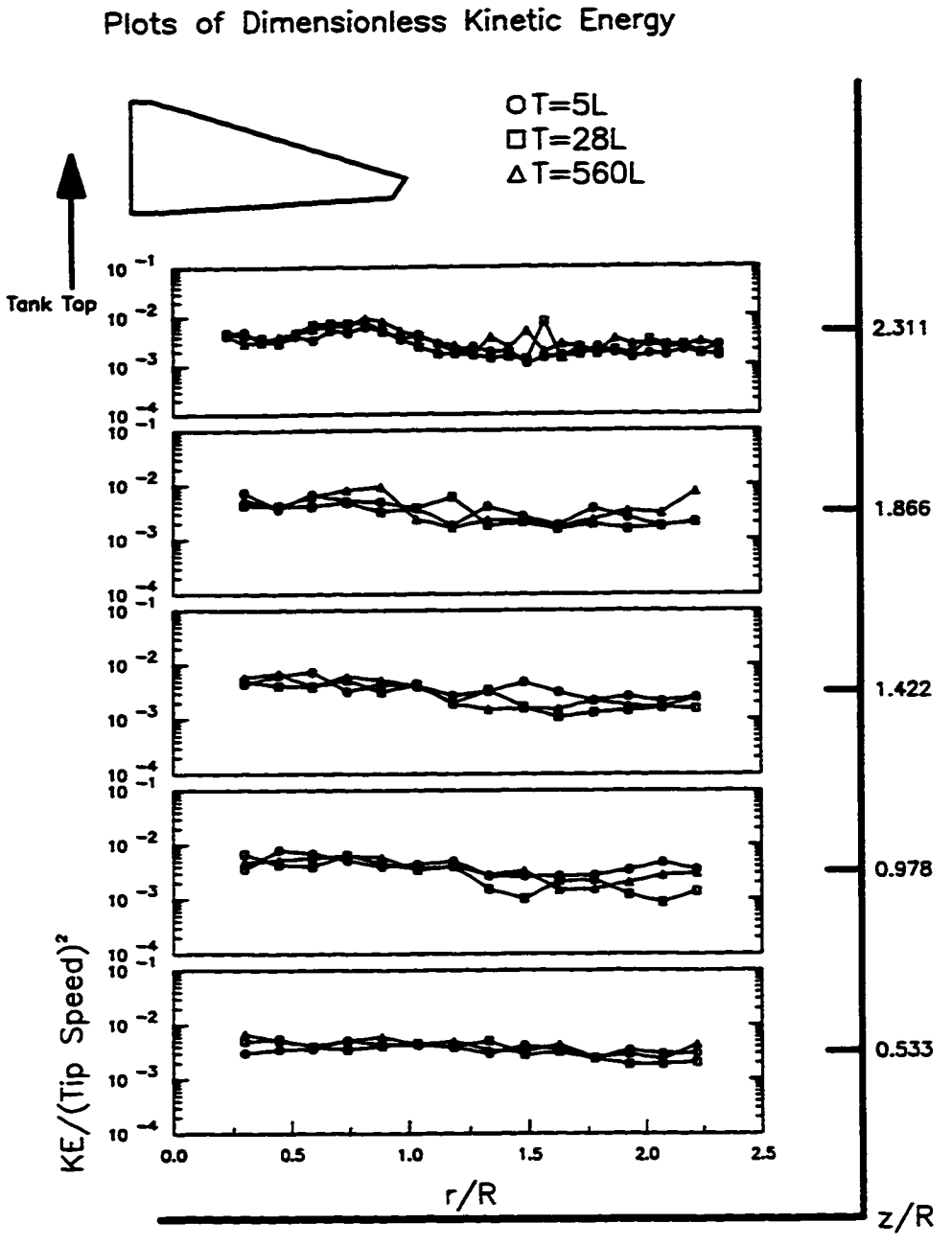

Figure 5.1.21: Turbulent Kinetic Energy for the A310 Foil Impeller below the Impeller Centerline

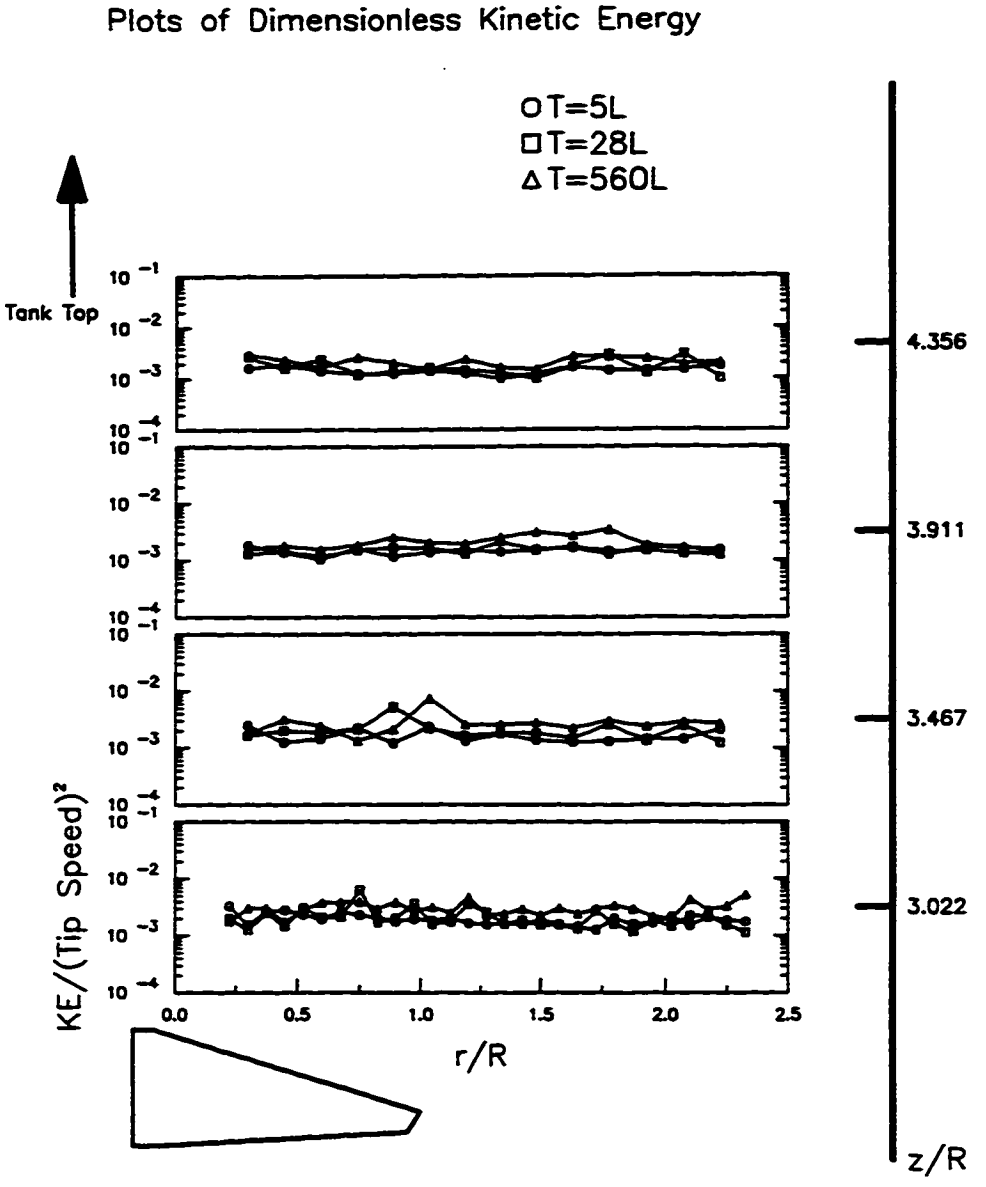

Figure 5.1.22: Turbulent Kinetic Energy for the A310 Foil Impeller above the Impeller Centerline

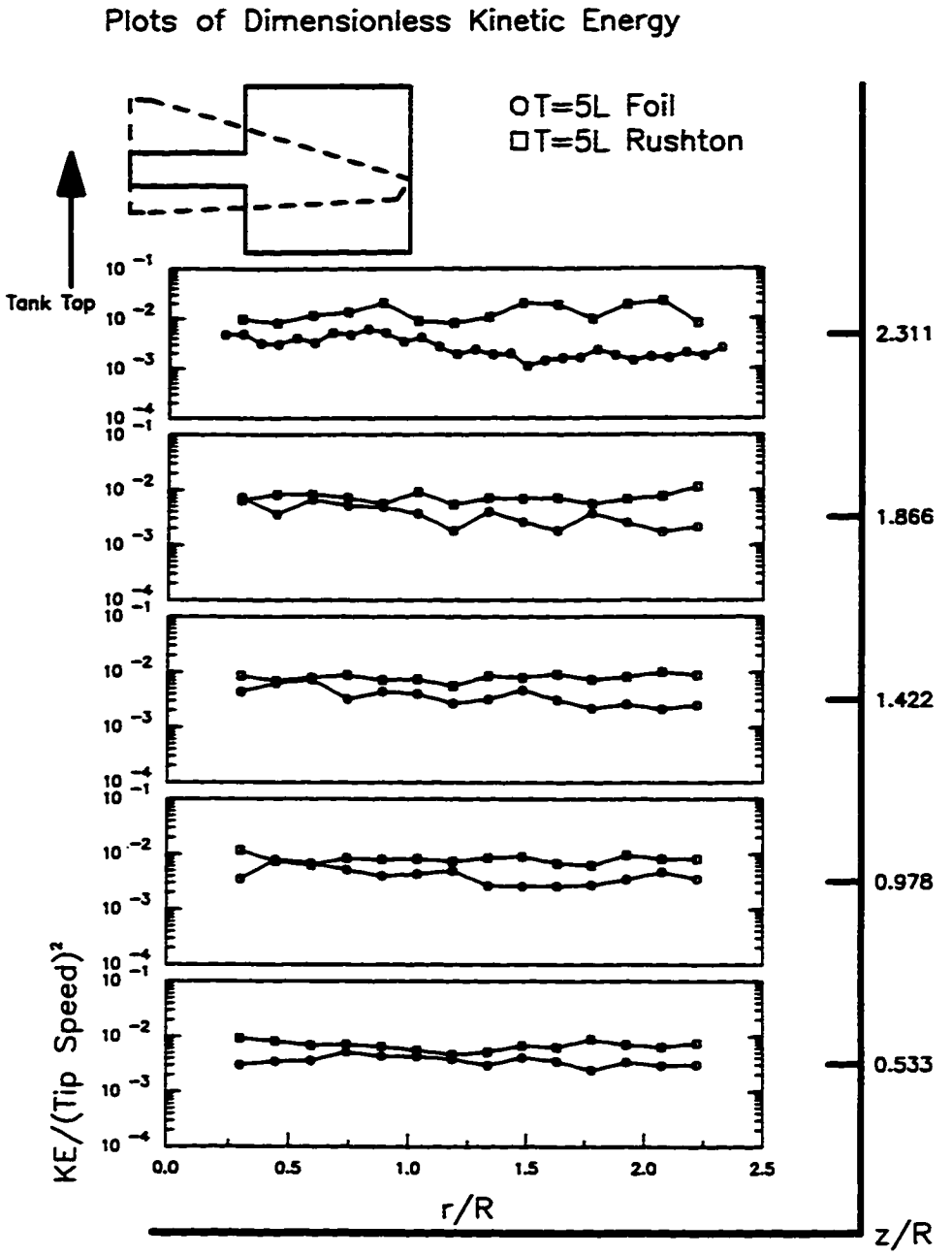

Figure 5.1.23: Comparison of the Turbulent Kinetic Energy between the Rushton Turbine and A310 Foil Impeller at T=5L

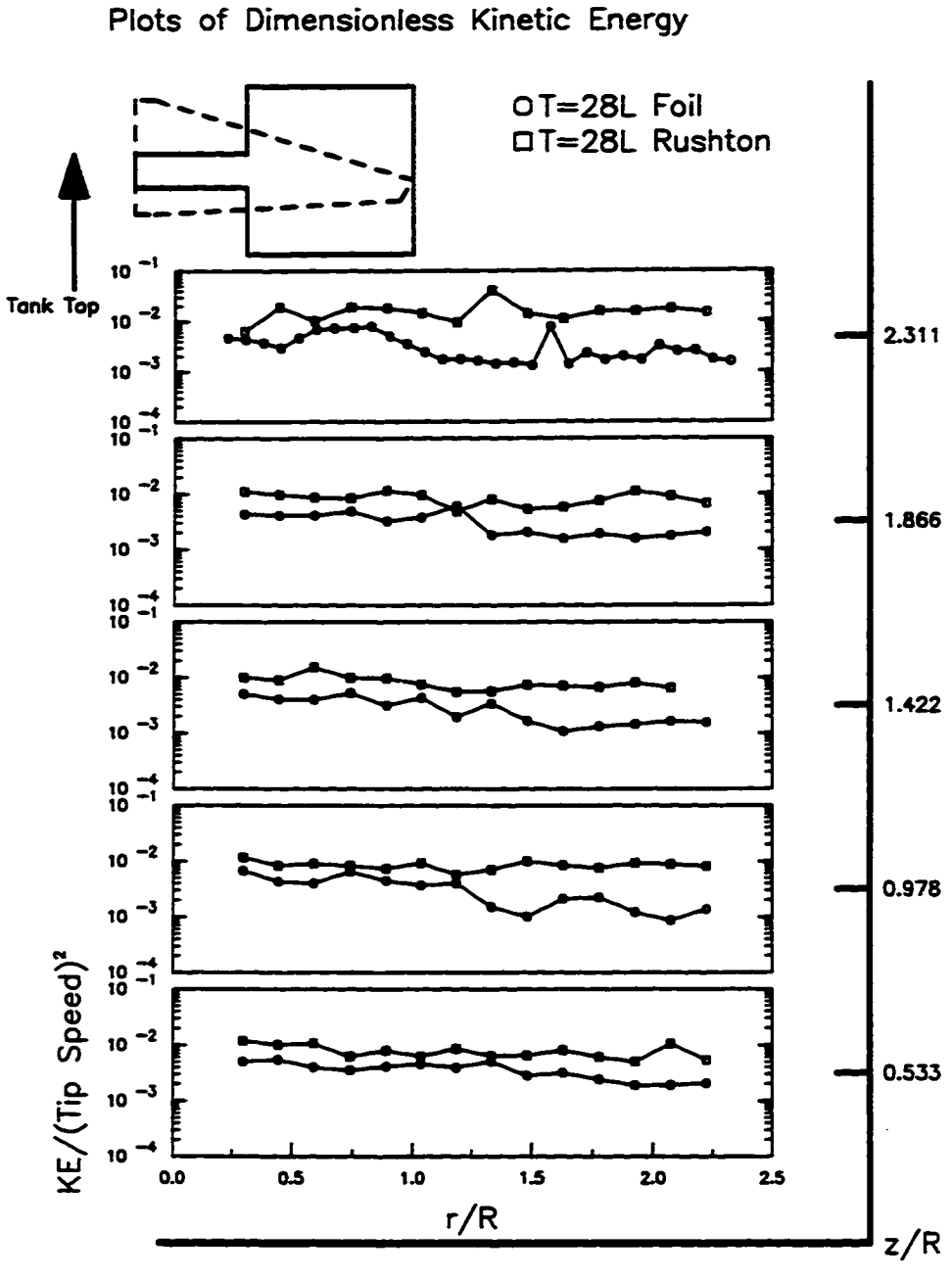

Figure 5.1.24: Comparison of the Turbulent Kinetic Energy between the Rushton Turbine and A310 Foil Impeller at T=28L

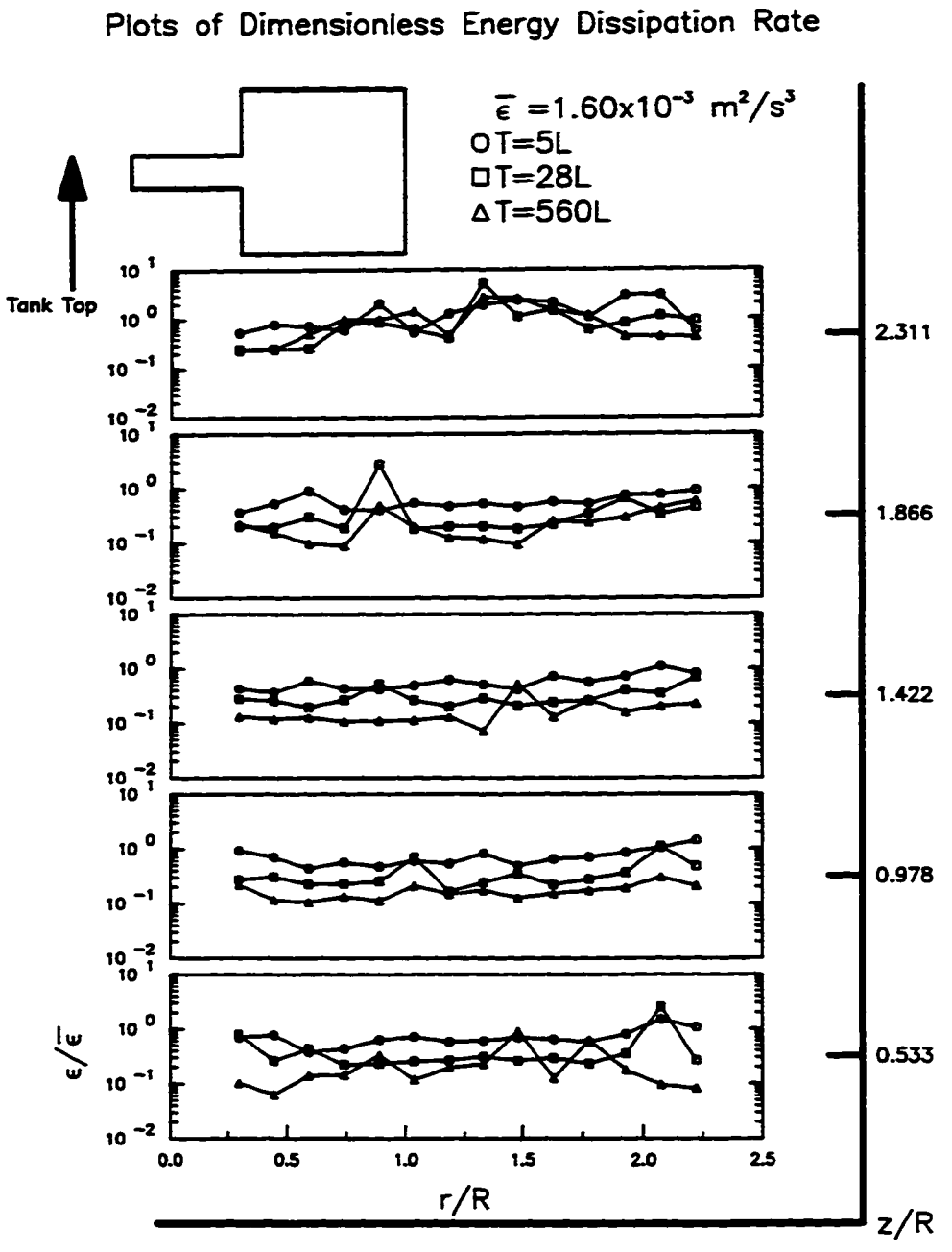

Figure 5.1.25: Turbulent Energy Dissipation Rate for the Rushton Turbine below the Impeller Centerline

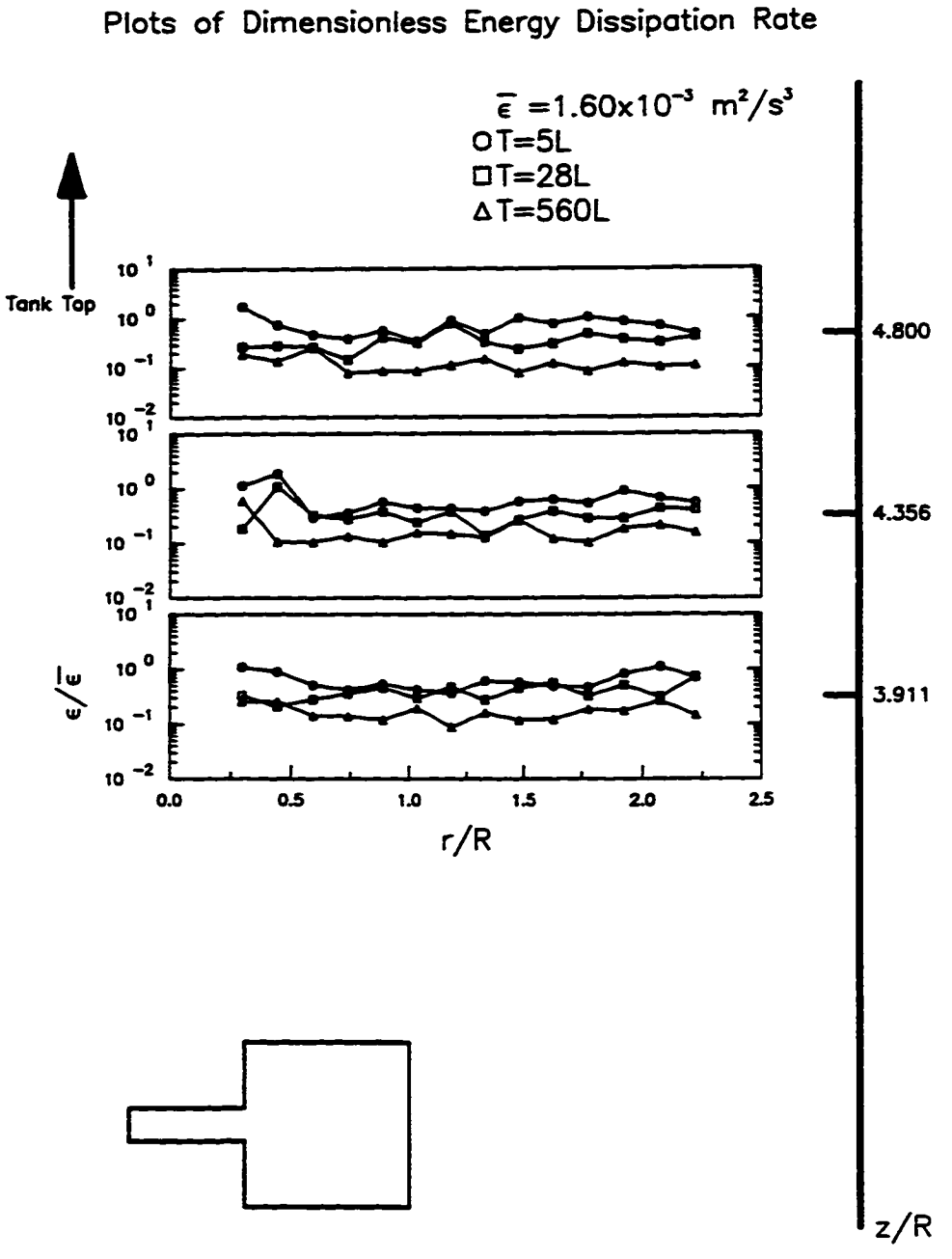

Figure 5.1.26: Turbulent Energy Dissipation Rate for the Rushton Turbine above the Impeller Centerline

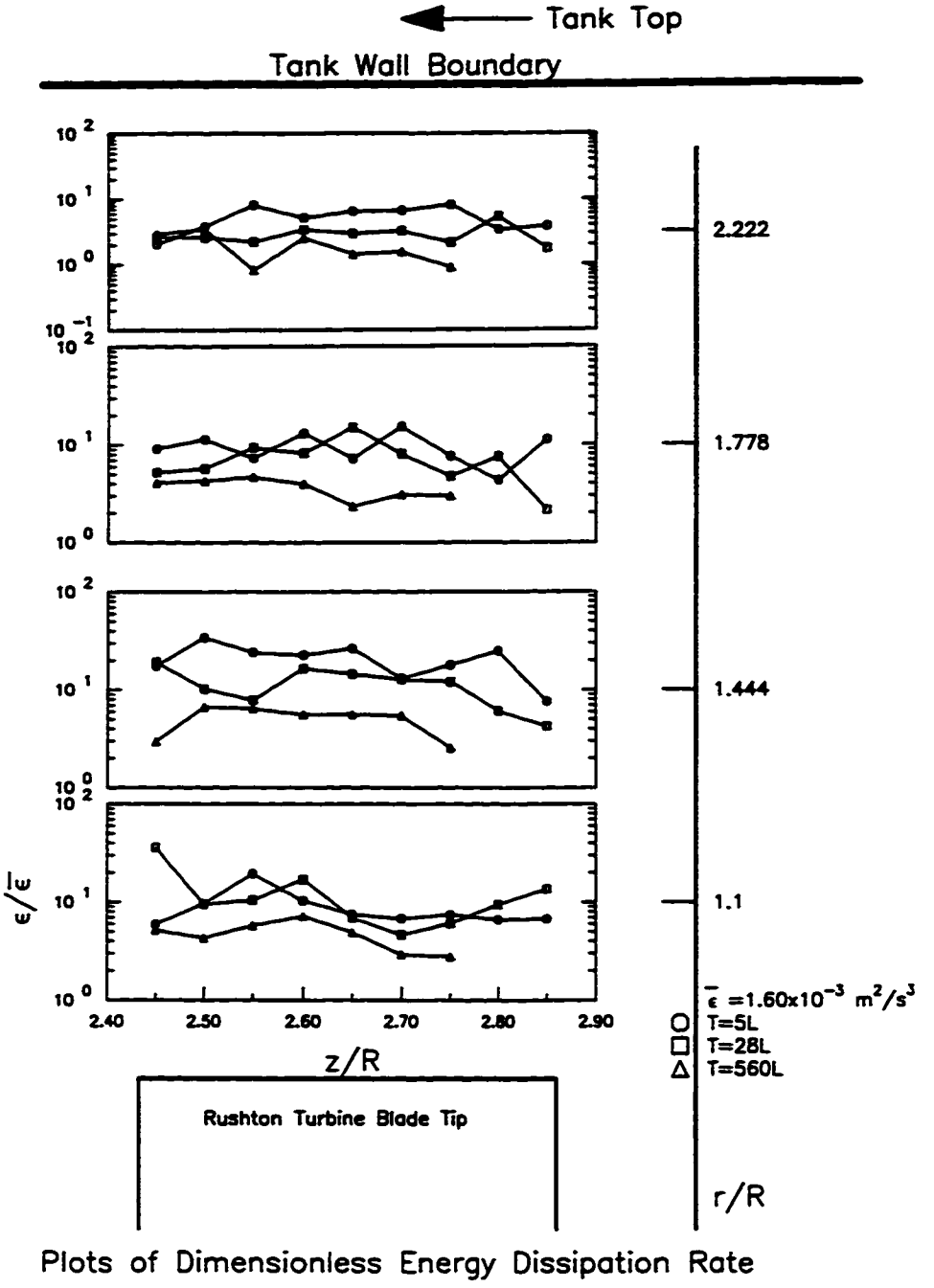

Figure 5.1.27: Turbulent Energy Dissipation rate for the Rushton Turbine in the Impeller Discharge zone

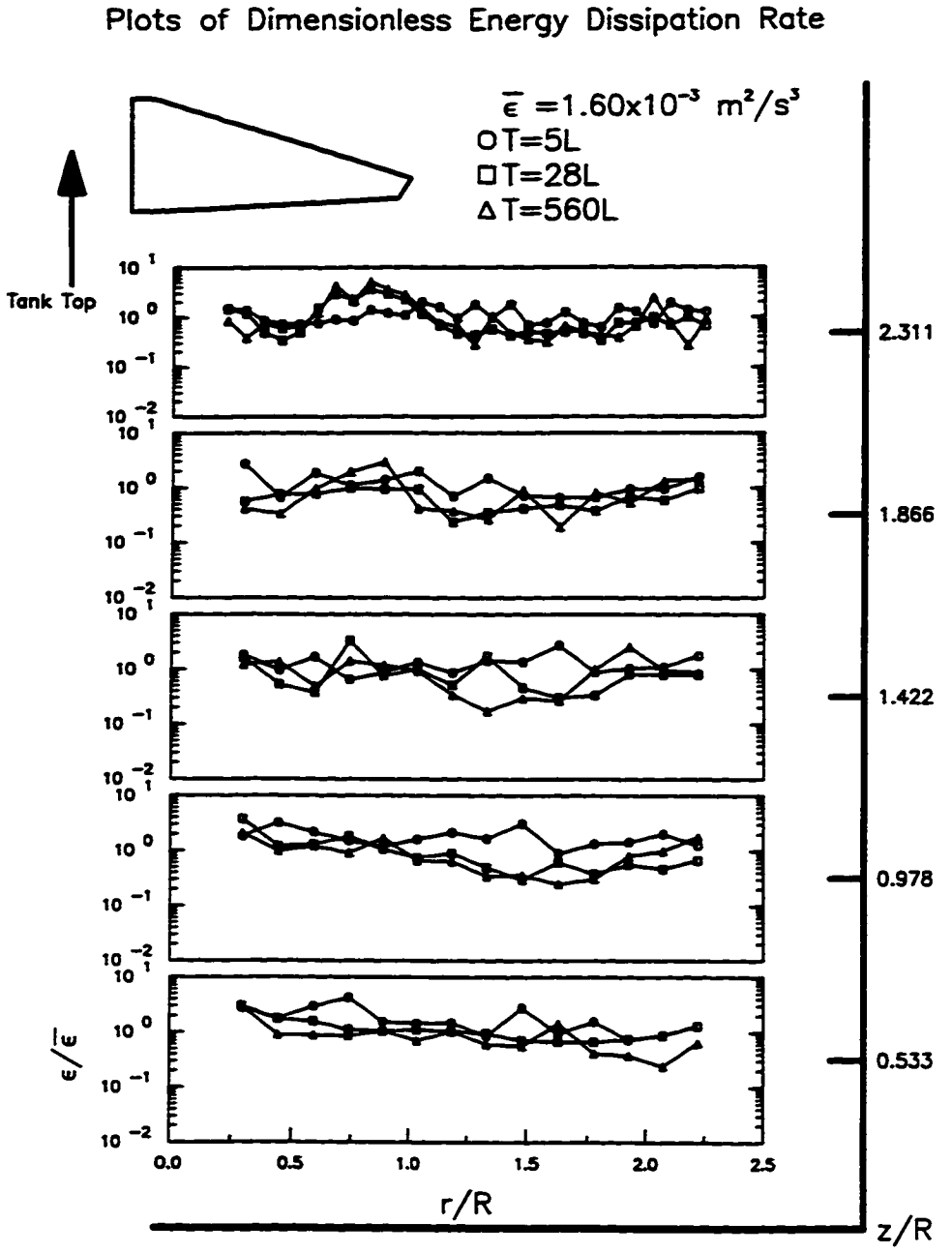

Figure 5.1.28: Turbulent Energy Dissipation Rate for the A310 Foil Impeller below the Impeller Centerline

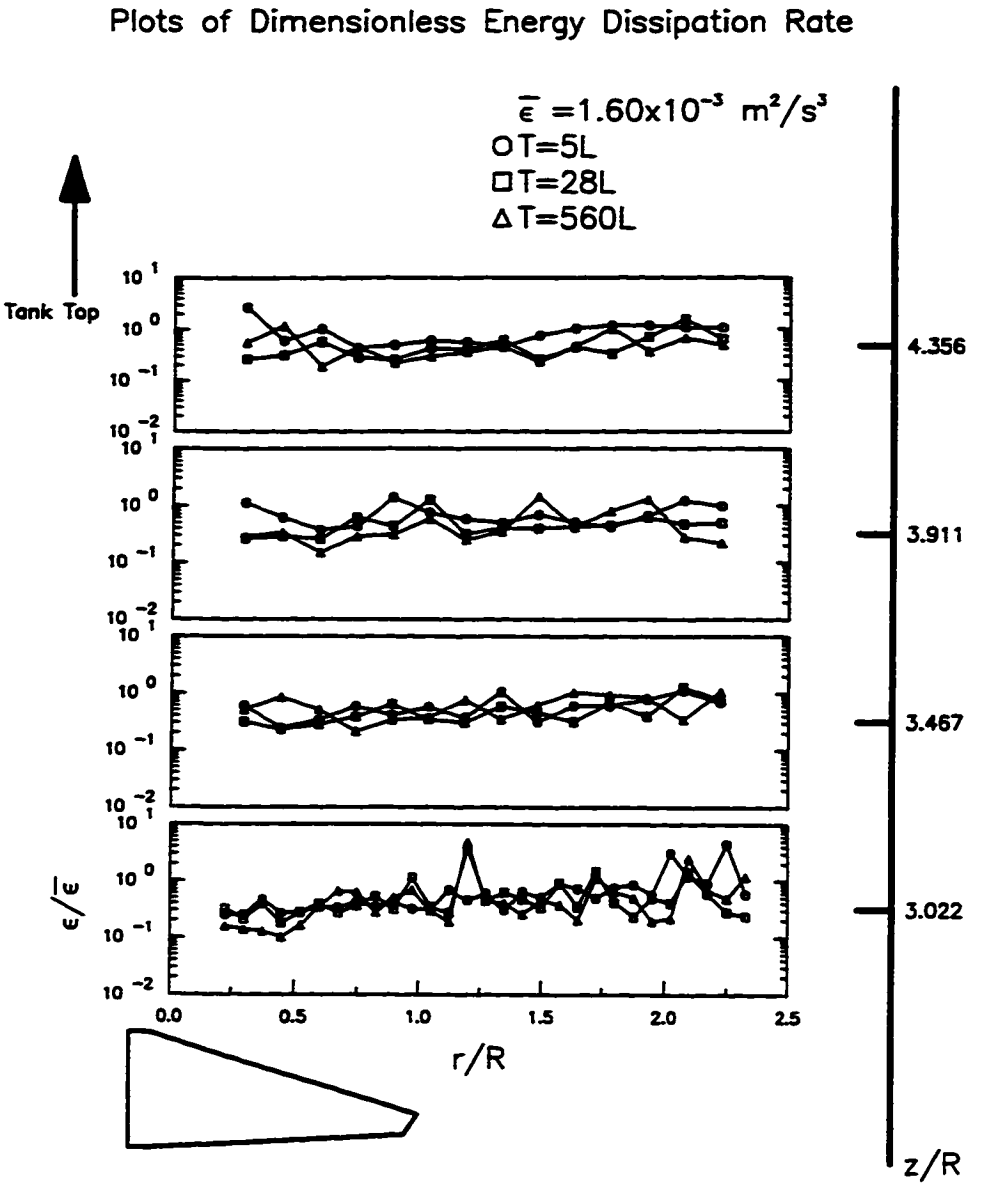

Figure 5.1.29: Turbulent Energy Dissipation Rate for the A310 Foil Impeller above the Impeller Centerline

rate is sensitive to tank size as seen by the results in Figures 5.1.25, 5.1.26, and 5.1.27. Clearly, these results show that for the same tank average energy dissipation rate, the local energy dissipation rate produced by the Rushton turbine is much higher in the impeller discharge region than the local energy dissipation rate produced in the impeller discharge zone of the A310 foil impeller.

5.1.5 Discussion

The results from the LDV experiments indicate that maintaining constant average energy dissipation rate (or G_m=constant) between different tank sizes or different impeller types does not translate to constant spatial distribution of the local turbulent flow properties. When G_m was kept constant, the rms fluctuating velocity was found not to depend on tank size when it was normalized by impeller tip speed. However, by maintaining G_m=constant, dimensional analysis predicts that the impeller tip speed increases with tank size as:

$$\frac{TS_l}{TS_s} \propto \left(\frac{T_l}{T_s}\right)^{1/3} \tag{5.1}$$

where

TS = tip speed
T = tank side dimension
subscript l = large tank
subscript s = small tank

In Section 5.1.3.2, the LDV experimental results (Figures 5.1.11 - 5.1.15) showed that the rms fluctuating velocity was proportional to the tip speed:

$$\frac{rms_l}{rms_s} \propto \left(\frac{TS_l}{TS_s}\right) \tag{5.2}$$

Substituting Equation 5.1 into 5.2, the rms value is related to the tank dimension as

$$\frac{rms_l}{rms_s} \propto \left(\frac{T_l}{T_s}\right)^{1/3} \tag{5.3}$$

Therefore, maintaining G_m=constant caused the rms fluctuating velocity to increase with tank size. Also, the spatial distribution of the dimensionless rms fluctuating velocity was much different between the Rushton turbine and the A310 foil impeller. For G_m=constant, the dimensionless rms fluctuating velocities or turbulence intensities were lower for the A310 foil impeller than for the Rushton turbine (Figures 5.1.16 & 5.1.17). The differences in the rms fluctuating velocity between the Rushton turbine and the A310 foil impeller are consistent with the turbulence results for these impellers reported by Weetman and Oldshue (1988).

Part of Weetman and Oldshue's (1988) report showed a velocity time trace at the impeller outlet for the Rushton turbine and A310 impeller. Their velocity time trace results showed that the Rushton turbine produces a higher peak to peak fluctuating velocity component than the A310 impeller. This indicates that the turbulence generated by the Rushton is greater than the turbulence produced by the A310.

The spatial distribution of the turbulent kinetic energy per unit mass was also found to increase with tank size when G_m =constant. In Section 5.1.3.2, the turbulent kinetic energy was found to be proportional to the square of the impeller tip speed (Figures 5.1.18 - 5.1.22):

$$\frac{KE_l}{KE_s} \propto \left(\frac{TS_l}{TS_s}\right)^2 \tag{5.4}$$

This relationship in Equation 5.4 was expected since the rms turbulent fluctuating velocity was found to be proportional to the impeller tip speed. By maintaining G_m=constant, dimensional analysis predicts the tip speed to increase with tank size as shown in Equation 5.1. Therefore, by substituting Equation 5.1 into 5.4, the kinetic energy increases with tank size as

$$\frac{KE_l}{KE_s} \propto \left(\frac{T_l}{T_s}\right)^{2/3} \tag{5.5}$$

Also, the dimensionless kinetic energy was found to be lower with the A310 foil impeller than with the Rushton turbine when G_m=constant (Figures 5.1.23 & 5.1.24).

Although the turbulent fluctuating velocities and kinetic energy were found to increase with increasing tank size, the local turbulent energy dissipation rate behaved quite differently. At the beginning of this research, this author expected the local energy dissipation rate to remain constant with increasing tank size since the power per unit volume was kept constant with increasing tank size (i.e. G_m = constant or $\bar{\varepsilon}$ = constant). Given constant power per unit volume for all three vessels, the spectral energy transfer from the large scale eddies to the small scale eddies should remain constant. Therefore, the energy dissipated at the small scale eddies to heat should be the same regardless of tank size when G_m = constant.

For the Rushton turbine, however, the local energy dissipation rate was found to decrease with increasing tank size as

$$\frac{\varepsilon_{loc,\,l}}{\varepsilon_{loc,\,s}} \propto \left(\frac{T_l}{T_s}\right)^x \tag{5.6}$$

where

x = -.70 between 5L tank & 28L tank bulk region

x = -.44 between 28L tank & 560L tank bulk region

x = -.85 between 5L tank & 28L tank impeller region

x = -.78 between 28L tank & 560L tank impeller region

This decreasing trend of the local energy dissipation rate with increasing tank size does not seem consistent with maintaining constant power per unit volume with tank size. On the contrary, for the A310 foil impeller, the local energy dissipation rate did not show any clear sensitivity to tank size. This constant energy dissipation rate with increasing tank size is expected since the impeller power per unit volume has been kept constant. One possible reason for a decreasing local energy dissipation rate with increasing tank size for the Rushton turbine might be due to the influence of the trailing vortices on the small scale eddies.

Van't Riet & Smith (1975) have shown that a significant portion of the turbulent kinetic energy produced by the Rushton turbine is in the form of trailing vortices. This author speculates that as the tank size increases with G_m=constant, the contribution of the energy transferred from the trailing vortices to the small scale eddies decreases with increasing tank size. This reduction in energy transfer from the trailing vortices to the small scale eddies with tank size might be due to either a change in the location of the vortex axis or due to a decrease in the rate of vortex production.

Yianneskis et al. (1987) showed that for the same Re number region studied by Van't Riet and Smith (1975) (i.e., $5 \times 10^3 < Re < 9 \times 10^4$), the location of the trailing vortex axis was found to be closer to the Rushton turbine blade tip for a larger impeller diameter. Results of Yianneskis et al. (1987) suggest that if the vortex axis is closer to the impeller, there would be less interaction between the trailing vortices and the flow regime in the impeller discharge region and the bulk region with increasing tank size. Consequently, the energy transferred from these vortices down to the small scale eddies would decrease in these regions.

It is also possible that the increase or decrease in the interaction between the trailing

vortices and the flow regime might be due to the number of vortices produced per unit time. If we assume that a trailing vortex is produced each time a blade passes a specific point. Then we can conclude that the frequency of vortex production is equal to the blade passage frequency. Since the blade passage frequency decreases with increasing tank size when G_m=constant, we can expect the frequency of vortex production to also decrease with increasing tank size. Therefore, the energy transferred from these vortices down to the small scale eddies would also decrease with tank size.

The experimental results also indicate that the energy dissipation rate does not decrease at the same rate with increasing tank size. This suggests the existence of some large tank size, beyond which, the local energy dissipation rate will not change with increasing tank size. Evidence of this trend can be seen by tracking the exponent in Equation 5.6. The magnitude of the negative exponent in Equation 5.6 was found to decrease between the different tank sizes. This result might suggest that beyond some tank size, the trailing vortices do not play a considerable role in determining how much energy will be dissipated at the small scale eddies when G_m = constant. Since there are no significant trailing vortices found for the A310 foil impeller due to its hydrodynamic shape and smooth leading edge, the energy dissipated at the small scale eddy size was not a function of tank size.

The LDV experimental results seem to suggest that if there is an increase in floc breakup with increasing tank size, then the explanation may lie with how the turbulent fluctuating velocity influences floc breakup. The LDV results also suggest that breakup does not depend on the turbulent energy dissipation rate. The LDV experimental results have shown a clear increase in turbulent fluctuating velocity with tank size whereas the LDV results also showed either a decrease in the local energy dissipation rate with increasing tank size for the Rushton turbine or no change in local energy dissipation rate with tank size for the foil impeller when G_m = constant. This decrease or constant trend in the local energy dissipation rate cannot explain the poorer flocculation performance with increasing tank size found by other investigators (Oldshue & Mady, 1978; Clark & Fiessinger, 1991; Clark et al., 1994).

The LDV results seem to support Oldshue and Mady's (1978) suggestion of constant tip speed as a possible scaleup rule, and dispute Trussell et al.'s (1992) suggestion of constant

Froude as a scaleup rule. If the tip speed is maintained constant with tank size, then the magnitude of the rms turbulent fluctuating velocity would also remain constant with tank size (Equations 5.2 & 5.3). However, flocculation experiments would need to be done using constant tip speed as a scaleup law to confirm this suggestion by Oldshue and Mady (1978). If the Froude number is maintained constant, then from dimensional analysis, the impeller tip speed would increase with tank size as:

$$\frac{TS_l}{TS_s} = \left(\frac{T_l}{T_s}\right)^{1/2}$$

With constant Froude number, the magnitude of the rms fluctuating velocity would also increase with tank size but at a higher rate than with constant G_m.

Therefore, maintaining constant Froude number with tank size might produce even more floc breakup with increasing tank size than with constant G_m. Again, flocculation experiments using constant Froude number as a scaleup law would need to be accomplished in order to verify this poorer flocculation performance with increasing tank size. The LDV results do imply that to model the breakup of aggregates in the flocculation process, researchers may need to include information about the turbulent fluctuating velocity in the breakup part of their population balance rate equation. This is the basic hypothesis of the model presented in this thesis (Section 4.2).

5.2 Numerical Modeling of a Square Stirred Tank Reactor

The three-dimensional nature of the turbulent flow produced by a Rushton turbine and an A310 foil impeller in a 5 L and a 28 L square stirred tank reactor has been modeled using FIDAP. The computational meshes are shown in Figures 5.2.1 - 5.2.4 for the Rushton turbine and the A310 foil impeller, at the two different tank sizes. The mesh was designed using the criteria in Section 4.1.3.2. The models were run using the procedure outlined in Section 4.1. Model A boundary conditions from Table 5.2.1 (Section 5.2.5) were used in all the following numerical simulations in Section 5.2.1 - 5.2.4.

Figure 5.2.1: FIDAP Mesh Design for the Rushton Turbine in a Square Tank T = 5L

Figure 5.2.2: FIDAP Mesh Design for the A310 Foil Impeller in a Square Tank T = 5L

Figure 5.2.3: FIDAP Mesh Design for the Rushton Turbine in a Square Tank T = 28L

Figure 5.2.4: FIDAP Mesh Design for the A310 Foil Impeller in a Square Tank T = 28L

5.2.1 Mean Velocity Flow Pattern

Figures 5.2.5 and 5.2.6 display the mean velocity flow pattern for the Rushton turbine in T = 5L and T = 28L respectively. As can be seen from Figures 5.2.5 and 5.2.6, FIDAP predicted the four quadrant circulation pattern indicative of a Rushton turbine. FIDAP seems to predict the location of the center of the circulation pattern in the bottom right quadrant at r/R = 2.0 and z/R = 1.8. In the radial direction, the location of the circulation center is in good agreement with the LDV experimental results. Figure 5.2.7 and 5.2.8 display the mean velocity profile in the plane bisecting the corners of the square tank for T = 5L and T = 28L respectively. Figures 5.2.7 and 5.2.8 show that the location of the circulation center has not changed. From Figures 5.2.5 - 5.2.8, the FIDAP results suggest that the location of the circulation center does not vary in the tangential direction. Figures 5.2.9 and 5.2.10 display the mean velocity flow pattern in the plane that bisects the centerline of the Rushton turbine for T = 5L and T = 28L respectively. Figures 5.2.9 and 5.2.10 show that the flow produced by a Rushton turbine in the square tank has a strong swirl component.

Figures 5.2.11 and 5.2.12 display the mean velocity flow pattern for the A310 fluid impeller in the 5L and 28L tanks respectively. The flow pattern displayed in Figures 5.2.11 and 5.2.12 are not typical of an axial flow impeller found by other investigators (Section 2.1.2). However, no previous work has been done in documenting an axial flow impeller in a square tank. In the plane perpendicular to the tank wall, the mean velocity flow pattern seems to display circulation patterns only in the bottom half of the tank. A similar result was also found in the LDV experimental results (Figure 5.1.6).

Figures 5.2.13 and 5.2.14 display the mean velocity flow pattern in the plane that bisects the tank corners for T = 5L and T = 28L respectively. As can be seen from Figures 5.2.13 and 5.2.14, the fluid flow does circulate in the tank corners and feeds the upper part of the square tank. Also note that there is less variation in the flow pattern produced by the Rushton turbine in the tangential direction than by the A310 foil impeller. It was speculated in Section 5.1 that in order to satisfy the continuity equation, the fluid flow feeding the top of the tank may be coming from the tank corners. The results from FIDAP seem to justify this speculation. The

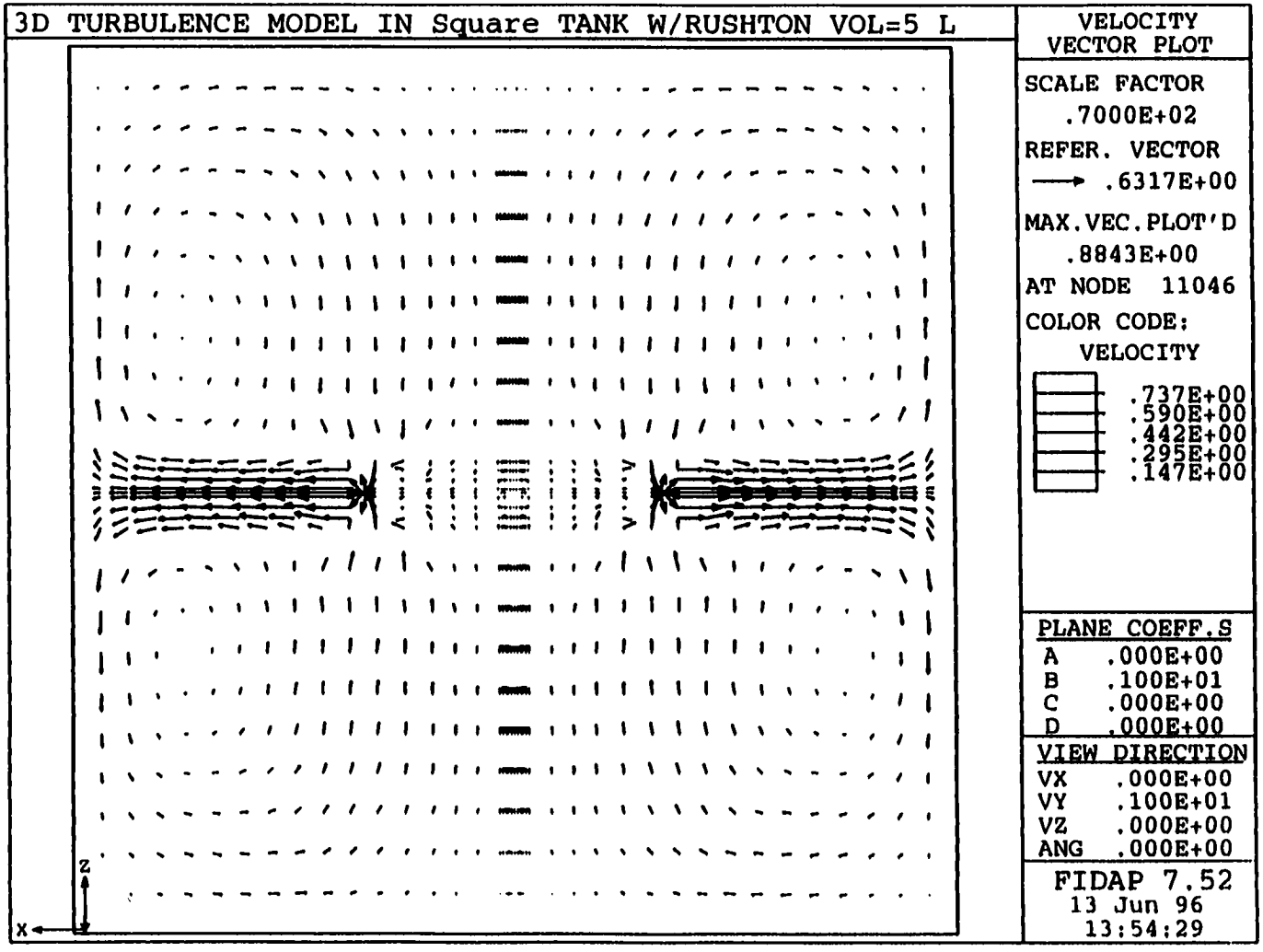

Figure 5.2.5: FIDAP Mean Velocity Flow Pattern for the Rushton Turbine in the Plane Perpendicular to the Tank Wall T = 5L (vectors non-dimensionalized with tip speed; tip speed=27.93 cm/s)

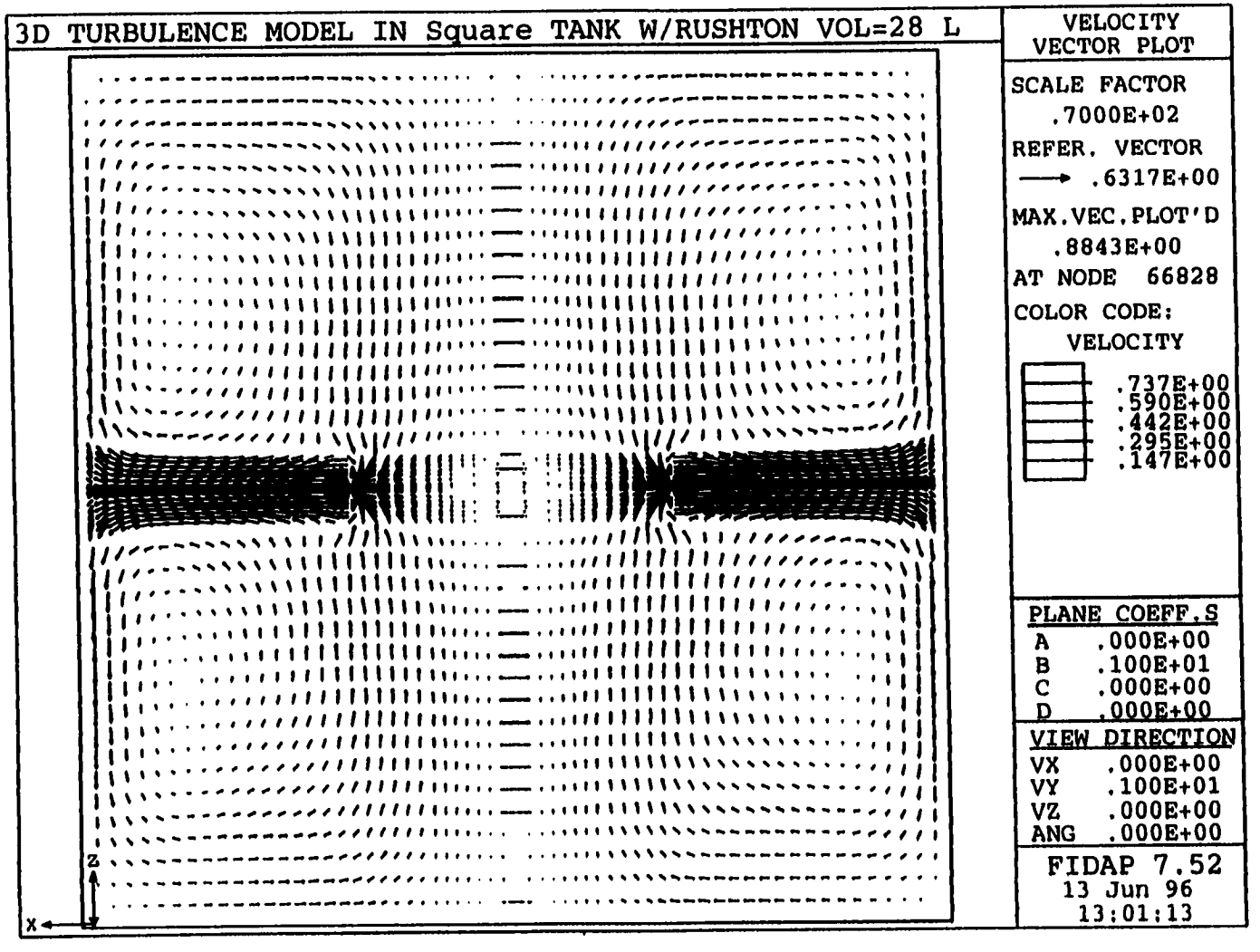

Figure 5.2.6: FIDAP Mean Velocity Flow Pattern for the Rushton Turbine in the Plane Perpendicular to the Tank Wall T = 28L (vectors non-dimensionalized with tip speed; tip speed=33.51 cm/s)

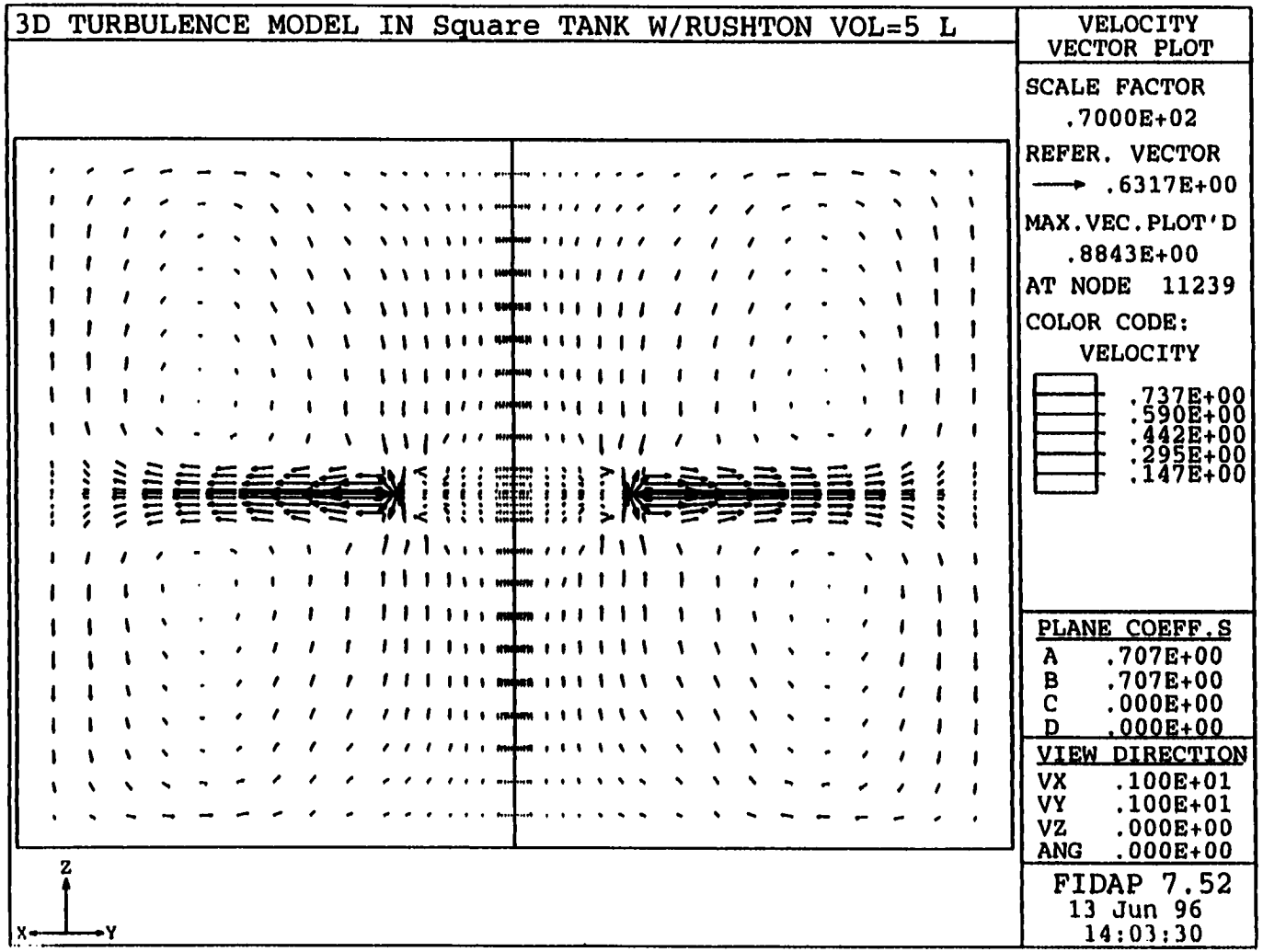

Figure 5.2.7: FIDAP Mean Velocity Flow Pattern for the Rushton Turbine In the Plane, Bisecting the Tank Corners T = 5L (vectors non-dimensionalized with tip speed; tip speed=27.93 cm/s)

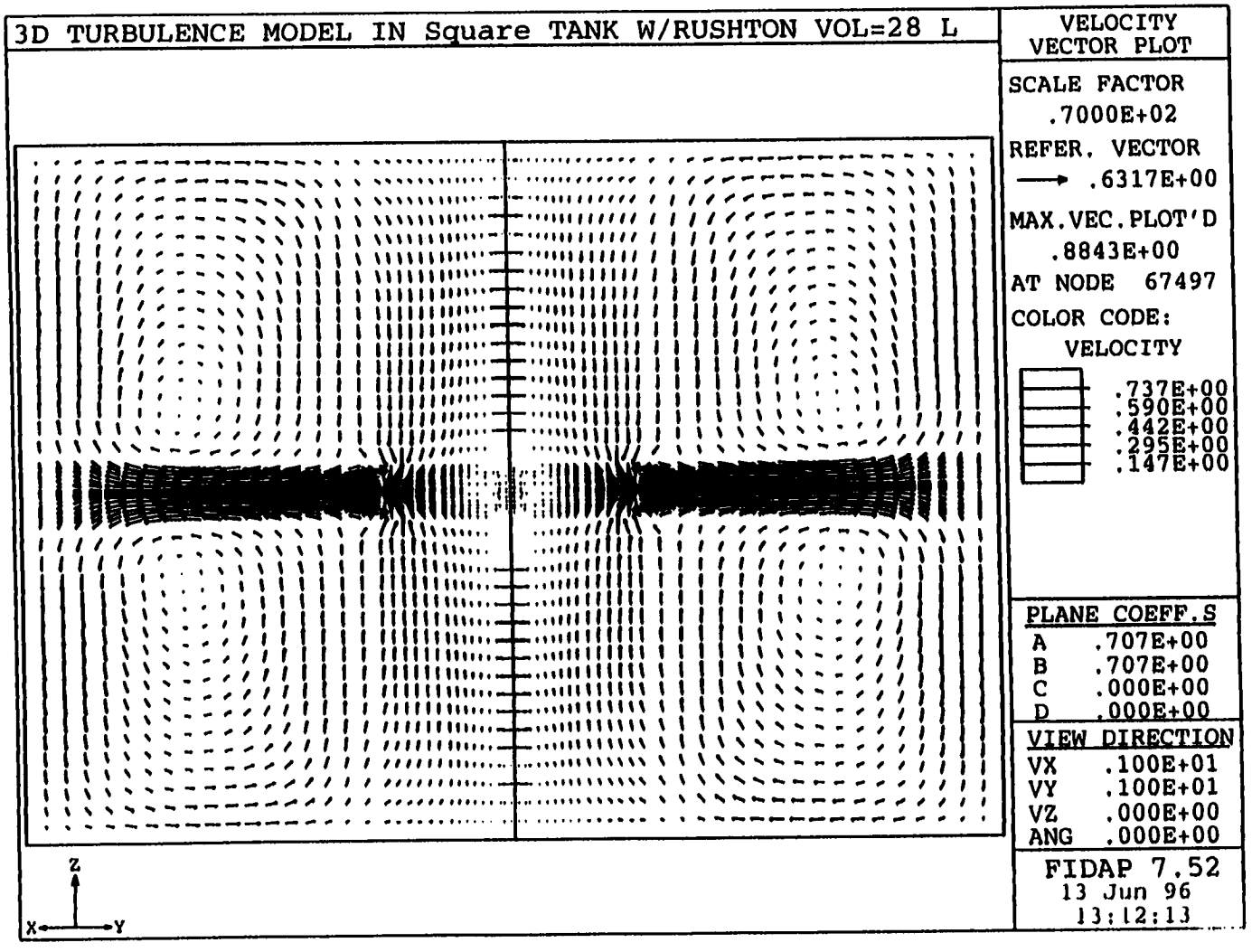

Figure 5.2.8: FIDAP Mean Velocity Flow Pattern for the Rushton Turbine In the Plane Bisecting the Tank Corners T = 28L (vectors non-dimensionalized with tip speed; tip speed=33.51 cm/s)

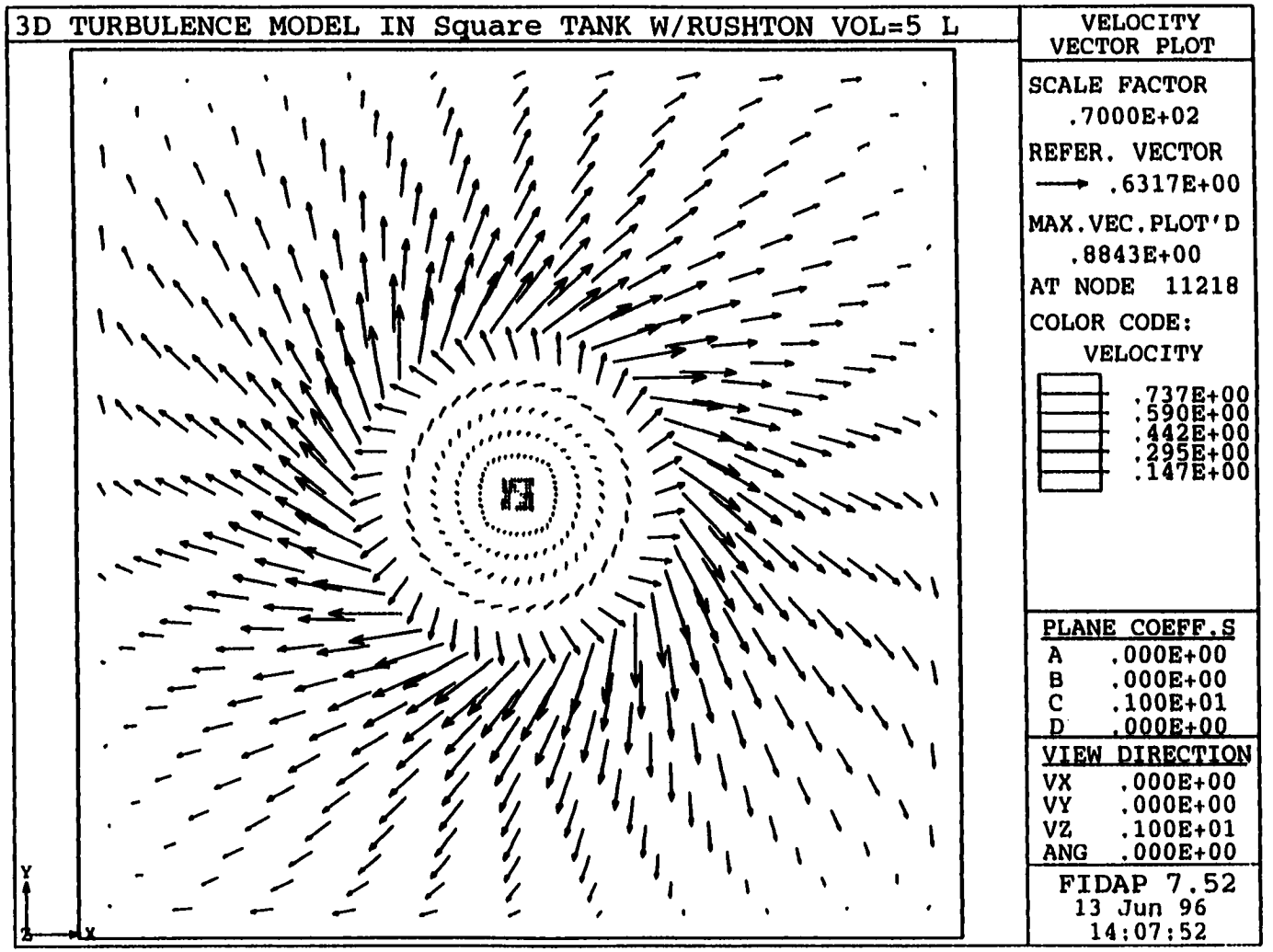

Figure 5.2.9: Mean Velocity Flow Pattern in the Plane that Bisects the Rushton Turbine Centerline T = 5L (impeller rotation is clockwise; vectors non-dimensionalized with tip speed; tip speed=27.93 cm/s)

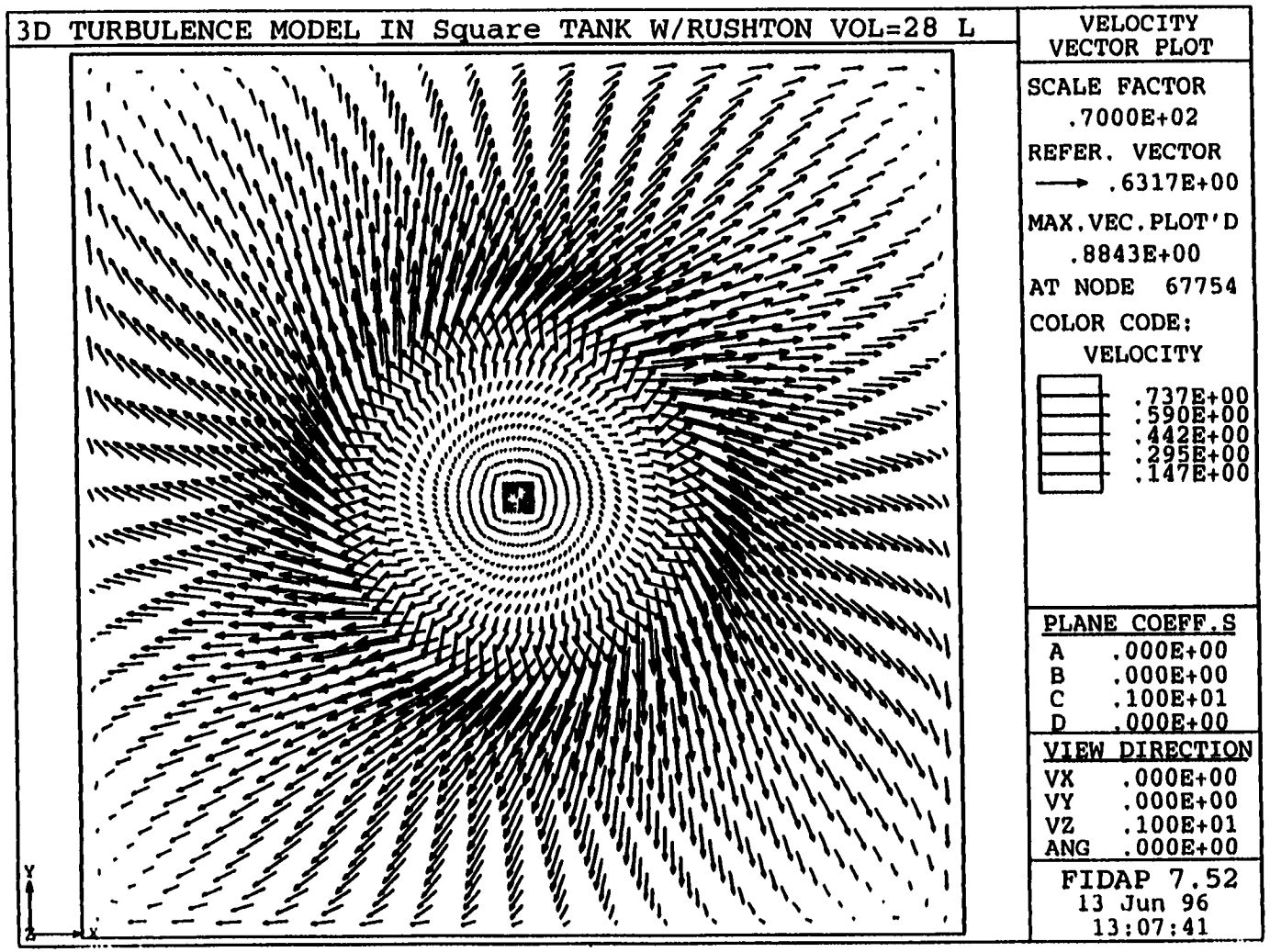

Figure 5.2.10: Mean Velocity Flow Pattern in the Plane that Bisects the Rushton Turbine Centerline T = 28L (impeller rotation is clockwise; vectors non-dimensionalized with tip speed; tip speed=33.51 cm/s)

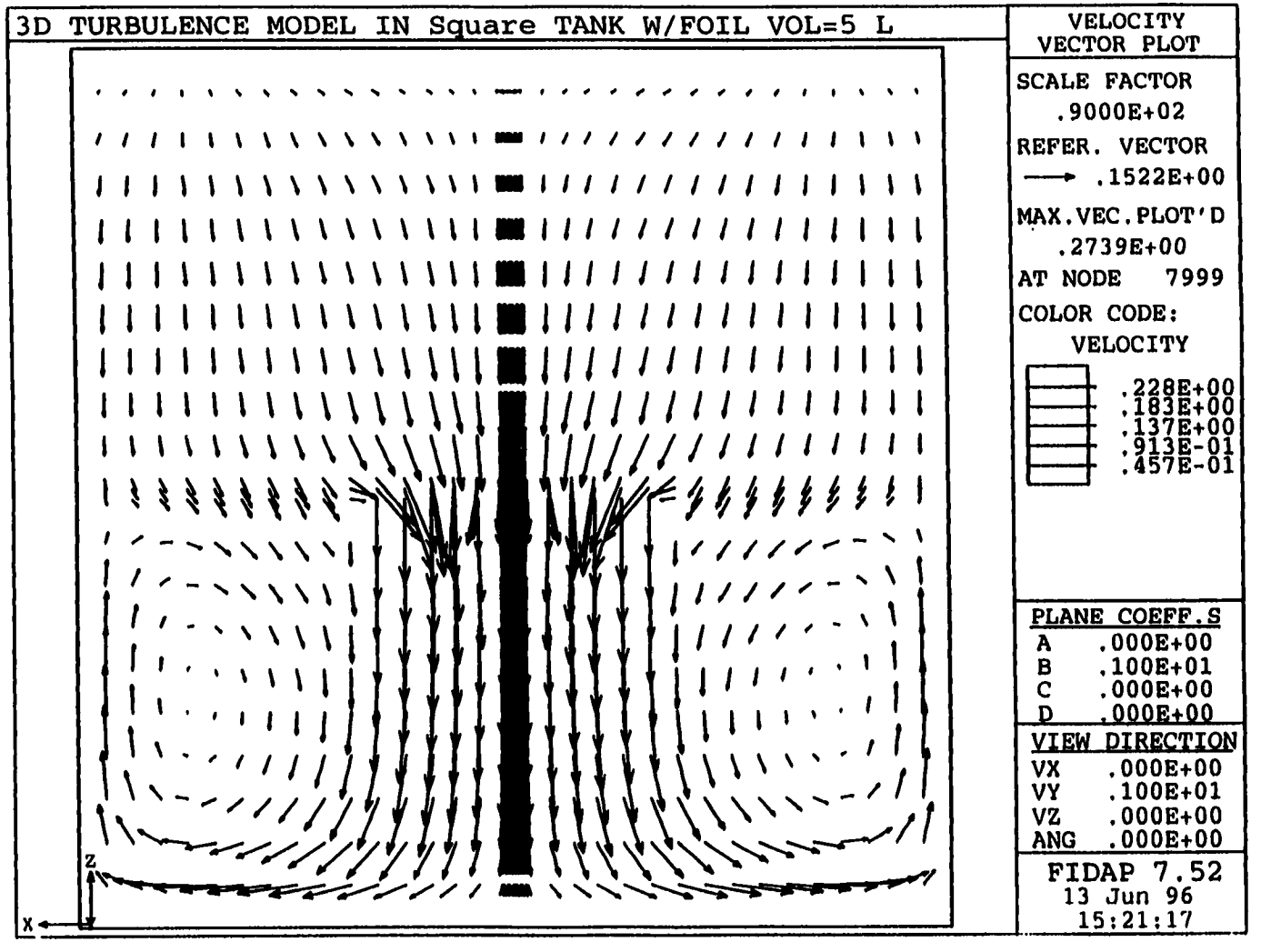

Figure 5.2.11: FIDAP Mean Velocity Flow Pattern for the A310 Foil Impeller in the Plane Perpendicular to Tank Wall T = 5L (vectors non-dimensionalized with tip speed; tip speed=57.85 cm/s)

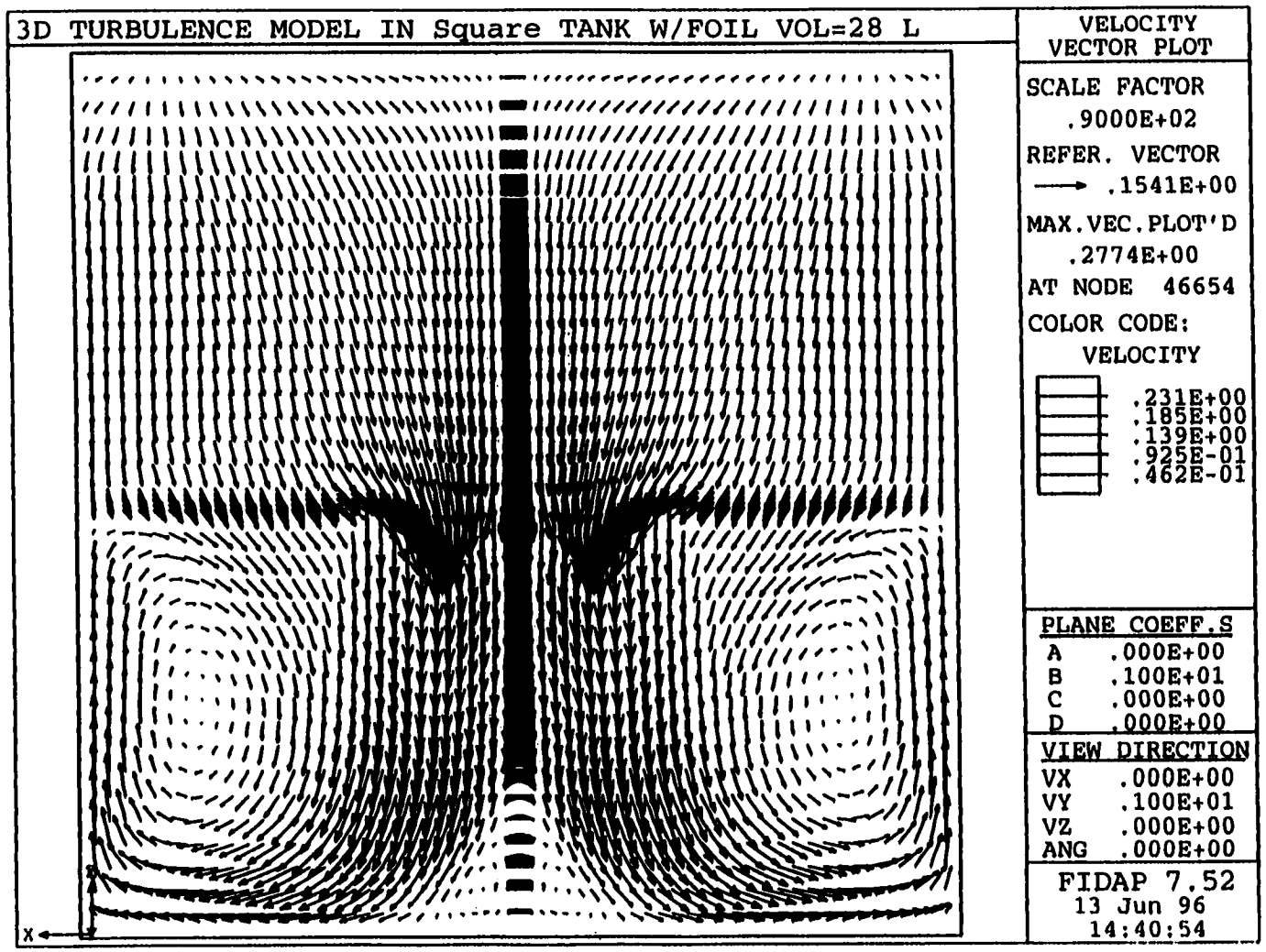

Figure 5.2.12: FIDAP Mean Velocity Flow Pattern for the A310 Foil Impeller in the Plane Perpendicular to Tank Wall T = 28L (vectors non-dimensionalized with tip speed; tip speed=69.42 cm/s)

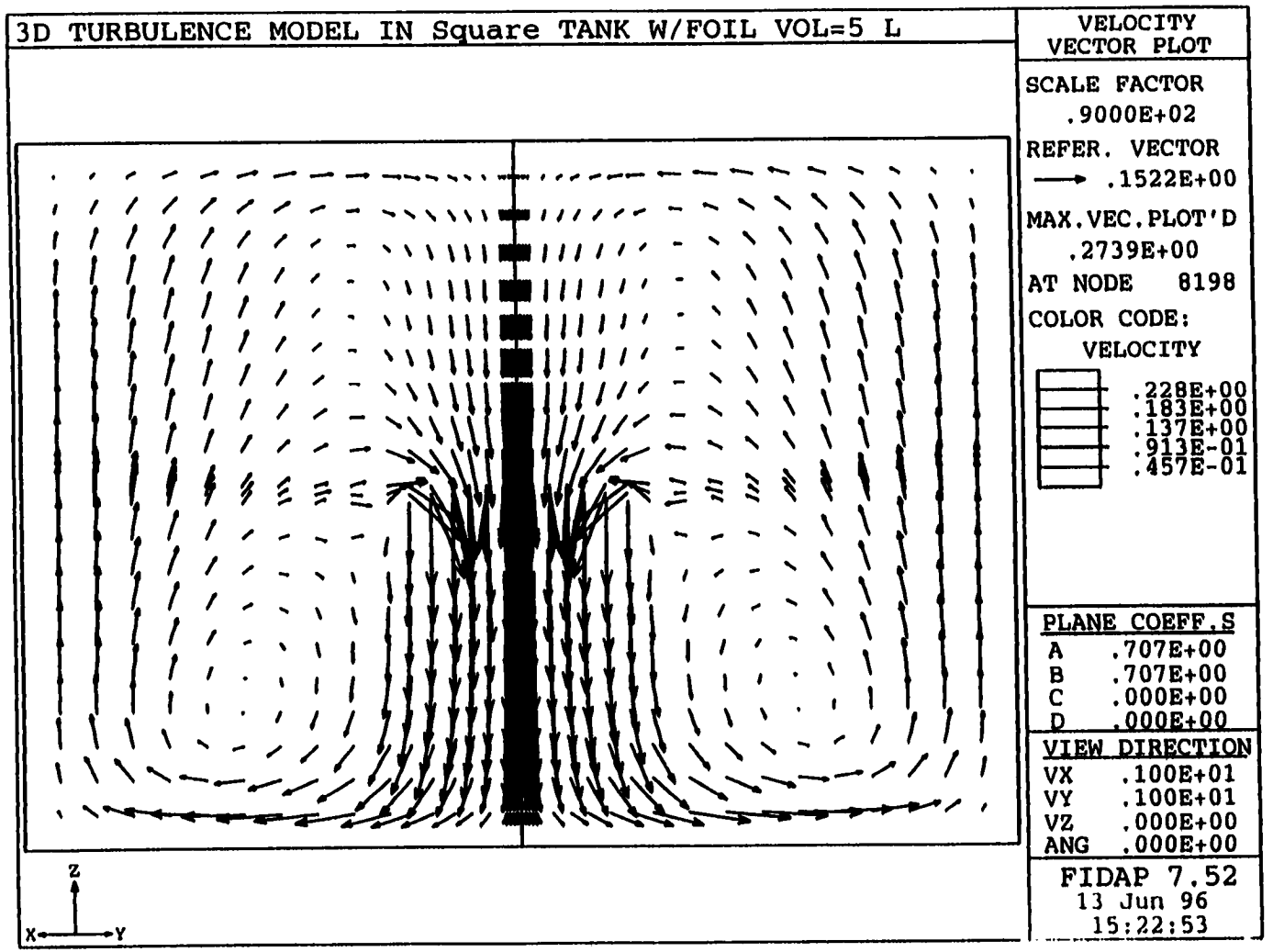

Figure 5.2.13: FIDAP Mean Velocity Flow Pattern for the A310 Foil Impeller in the Plane Bisecting the Tank Corners T = 5L (vectors non-dimensionalized with tip speed; tip speed=57.85 cm/s)

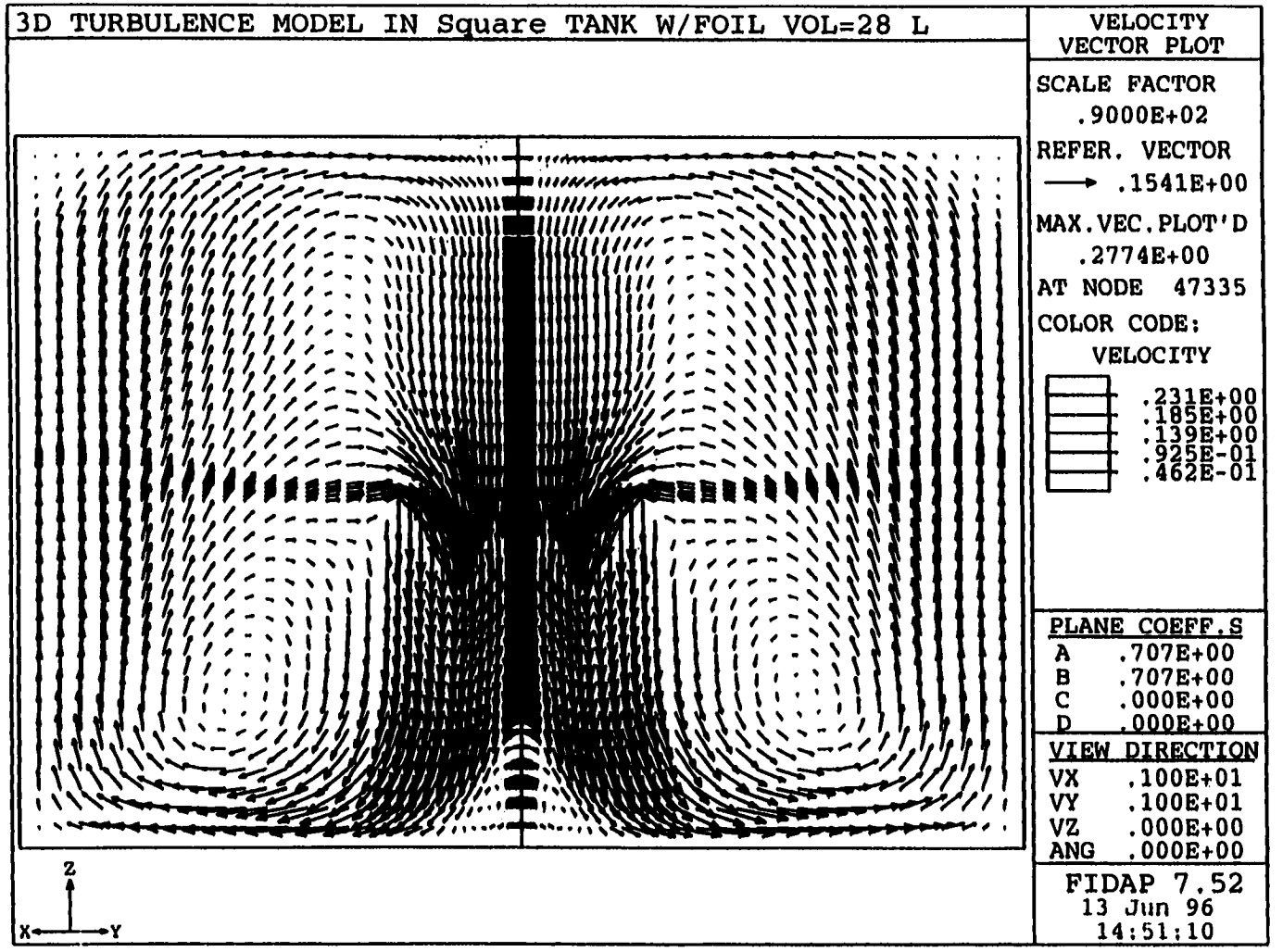

Figure 5.2.14: FIDAP Mean Velocity Flow Pattern for the A310 Foil Impeller in the Plane Bisecting the Tank Corners T = 28L (vectors non-dimensionalized with tip speed; tip speed=69.42 cm/s)

results from FIDAP also show that tank size does not affect the flow pattern and that the mean velocity is proportional to the tip speed.

5.2.2 Turbulent Kinetic Energy

Figures 5.2.15 - 5.2.17 compare the results of the turbulent kinetic energy generated by FIDAP with the experimental measurements for the 5 L square tank with a Rushton turbine. Figures 5.2.18 - 5.2.20 also compare the FIDAP turbulent kinetic energy results with the LDV turbulent kinetic energy results for the 28L tank size with a Rushton turbine. Based on the results in Figures 5.2.15 - 5.2.20, the FIDAP model seems to match the measured experimental results fairly well. Only the measured values closest to the impeller blade tip in the impeller discharge zone (Figure 5.2.17, 5.2.20) seem to be much lower than the model predictions.

Figures 5.2.21 and 5.2.22 compare FIDAP's kinetic energy results with the experimental results for the A310 foil impeller in the 5 L square tank. Figures 5.2.23 and 5.2.24 compare FIDAP's kinetic energy results with the experimental results for the A310 impeller in the 28L tank. In Figures 5.2.21 and 5.2.23, the model seems to predict the experimental results fairly well for most of the points below the impeller centerline. In Figures 5.2.22 and 5.2.24, the model under predicted the experimental kinetic energy in the regions closest to the fluid surface. These differences between the model and the LDV experimental results are probably due to the limitations of the k-ε model used in FIDAP.

However, from Figures 5.2.15 - 5.2.24, FIDAP also shows that the turbulent kinetic energy is proportional to the square of the tip speed regardless of tank size. In Section 5.1.4, the tip speed was shown to increase with increasing tank size from dimensional analysis when the power per unit volume was kept constant. Like the LDV experimental results, the FIDAP results confirm the increasing value of the local turbulent kinetic energy with increasing tank size when G_m = constant.

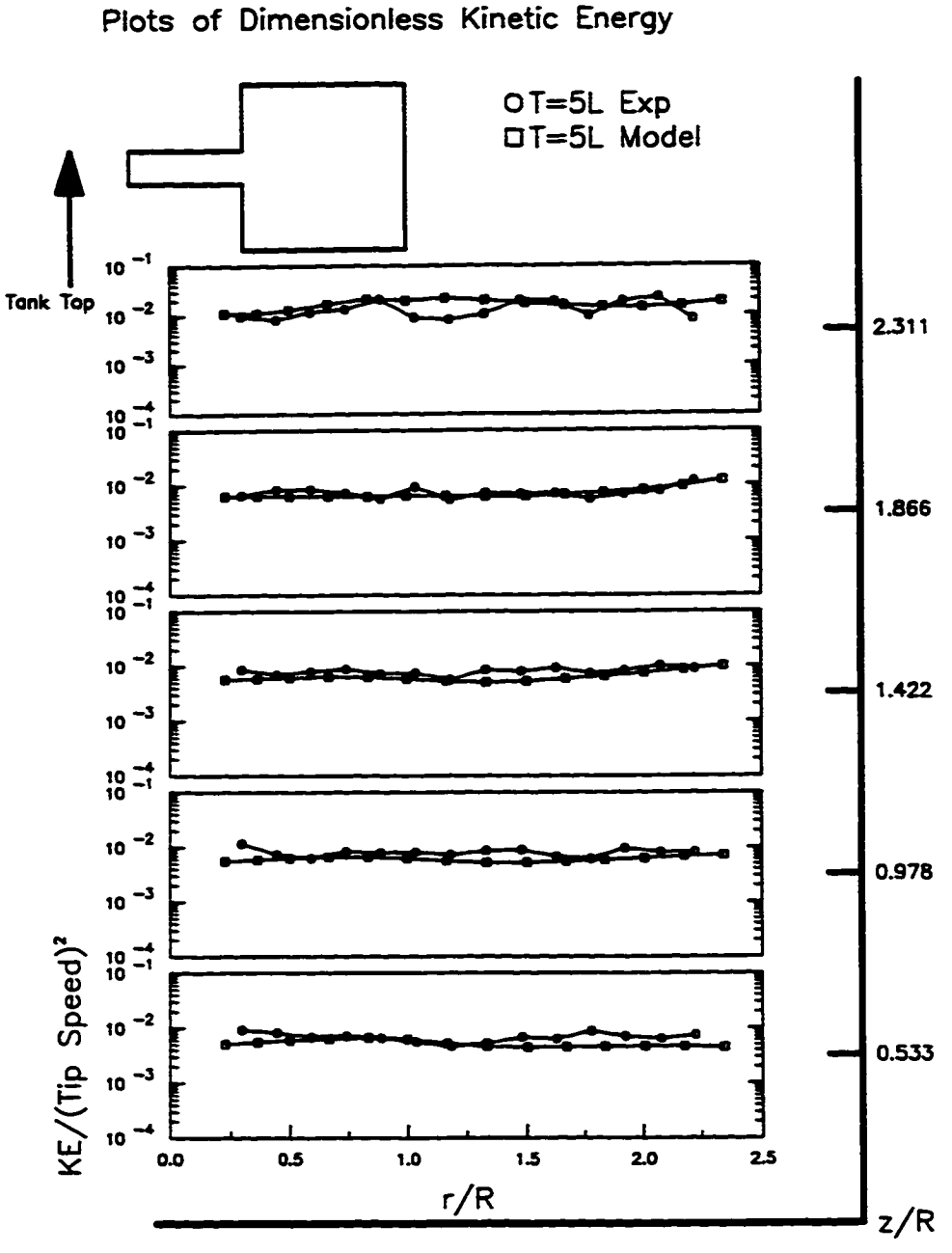

Figure 5.2.15: Turbulent Kinetic Energy for the Rushton Turbine: Comparison between FIDAP Model and Experimental Results below Impeller Centerline T = 5L

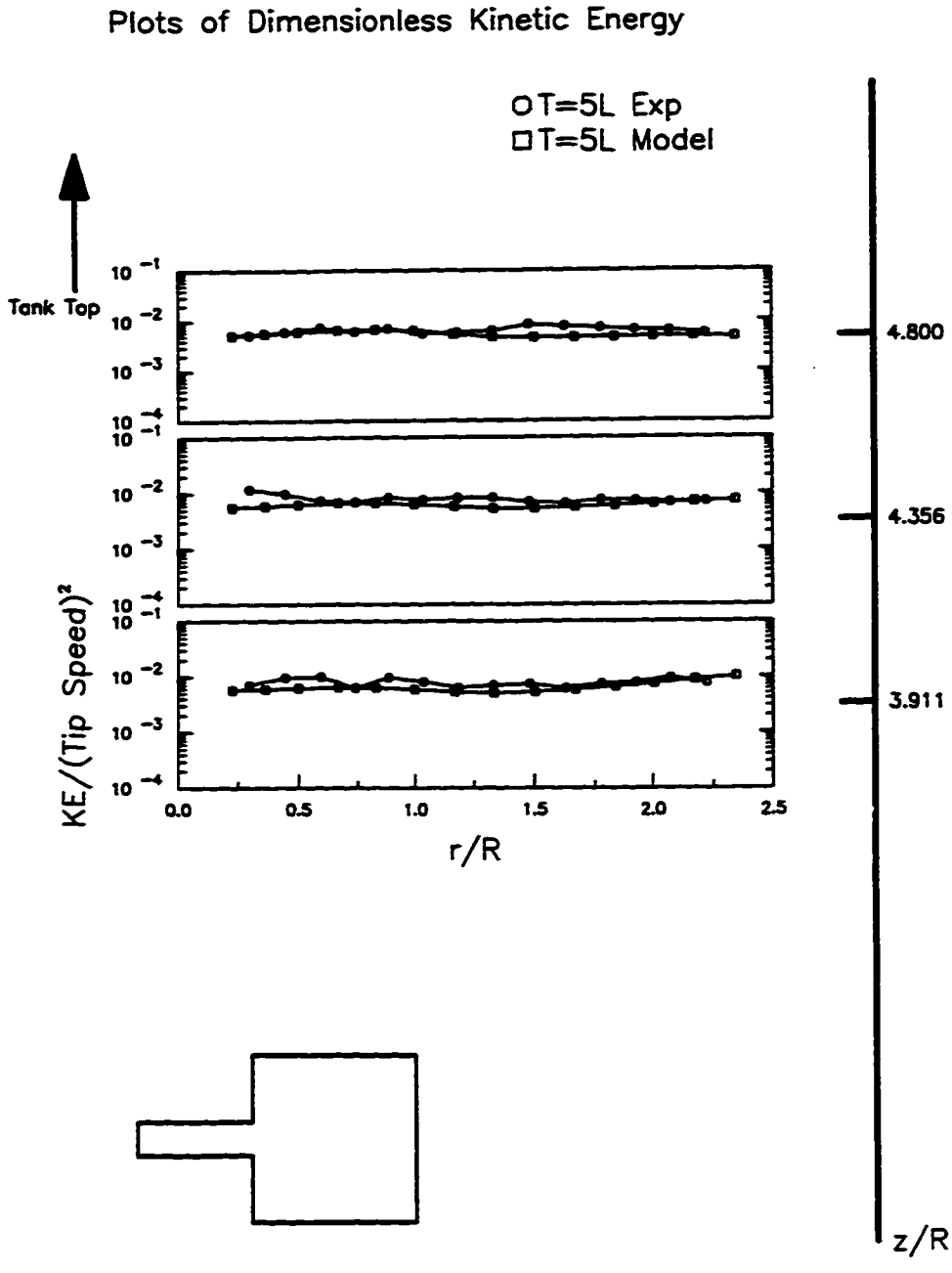

Figure 5.2.16: Turbulent Kinetic Energy For the Rushton Turbine: Comparison between FIDAP Model and Experimental Results above Impeller Centerline T = 5L

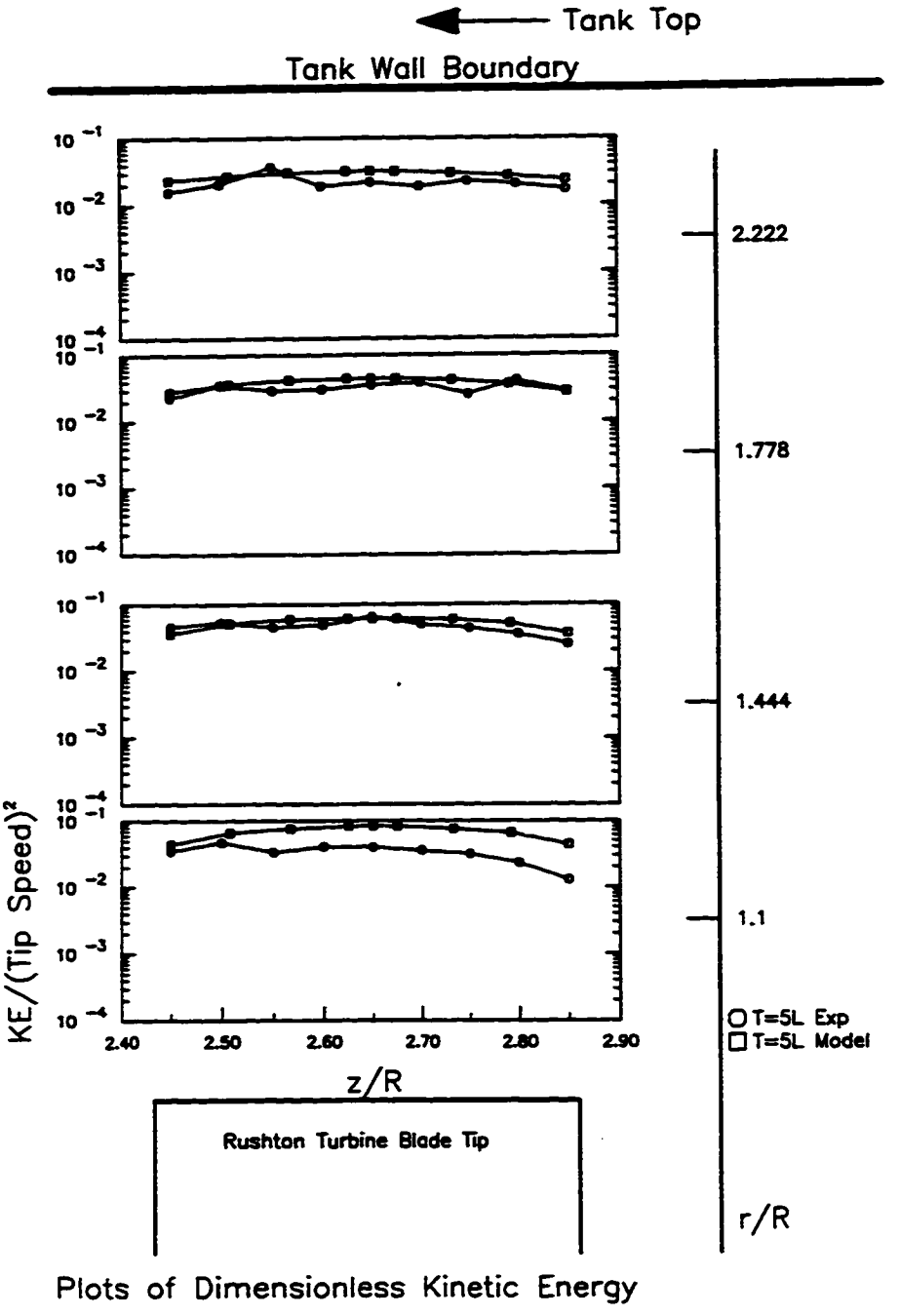

Figure 5.2.17: Turbulent Kinetic Energy for the Rushton Turbine: Comparison between FIDAP Model and Experimental Results in the Impeller Discharge Zone T = 5L

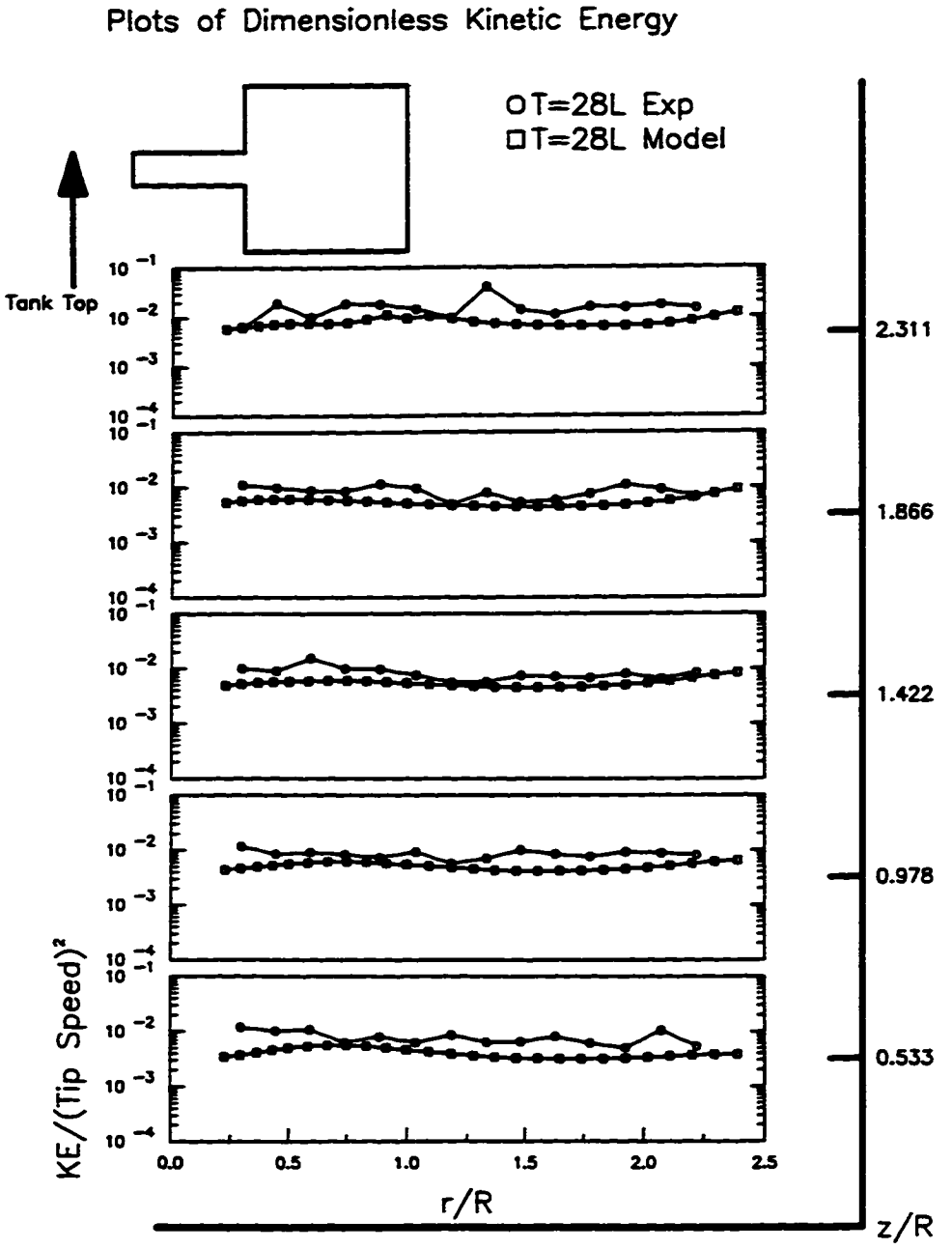

Figure 5.2.18: Turbulent Kinetic Energy for the Rushton Turbine: Comparison between FIDAP Model and Experimental Results below Impeller Centerline T = 28L

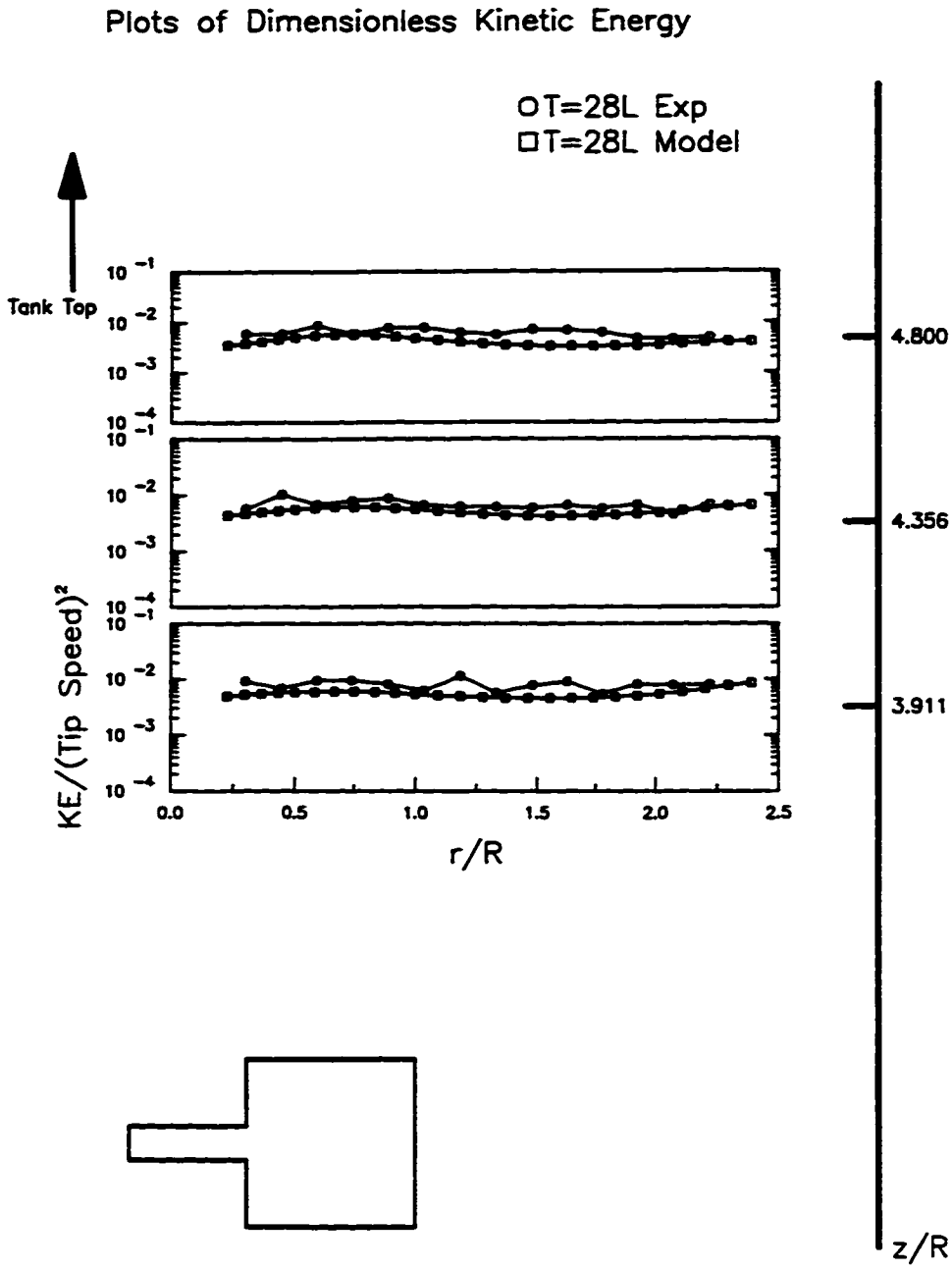

Figure 5.2.19: Turbulent Kinetic Energy For the Rushton Turbine: Comparison between FIDAP Model and Experimental Results above Impeller Centerline T = 28L

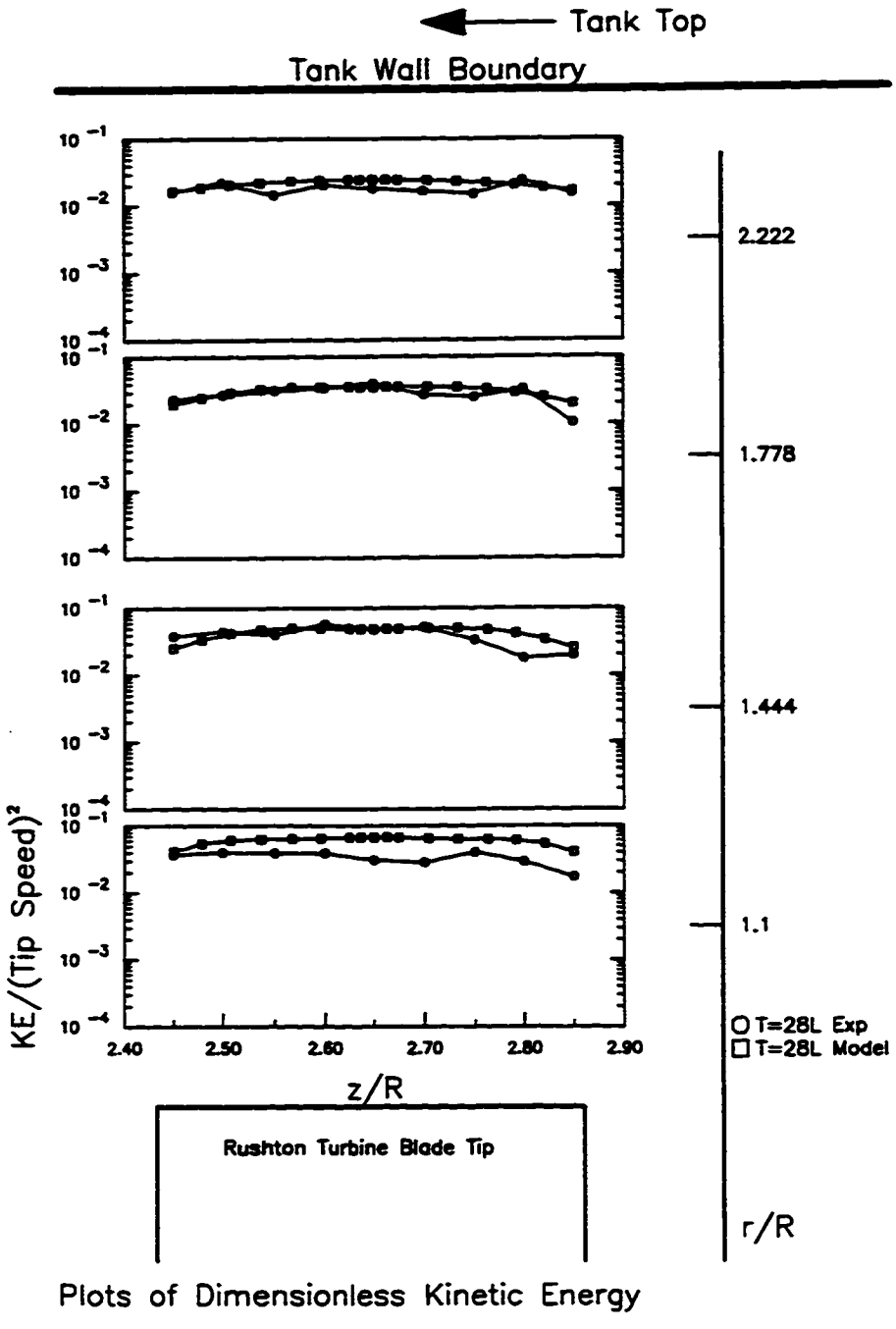

Figure 5.2.20: Turbulent Kinetic Energy for the Rushton Turbine: Comparison between FIDAP Model and Experimental Results in the Impeller Discharge Zone T = 28L

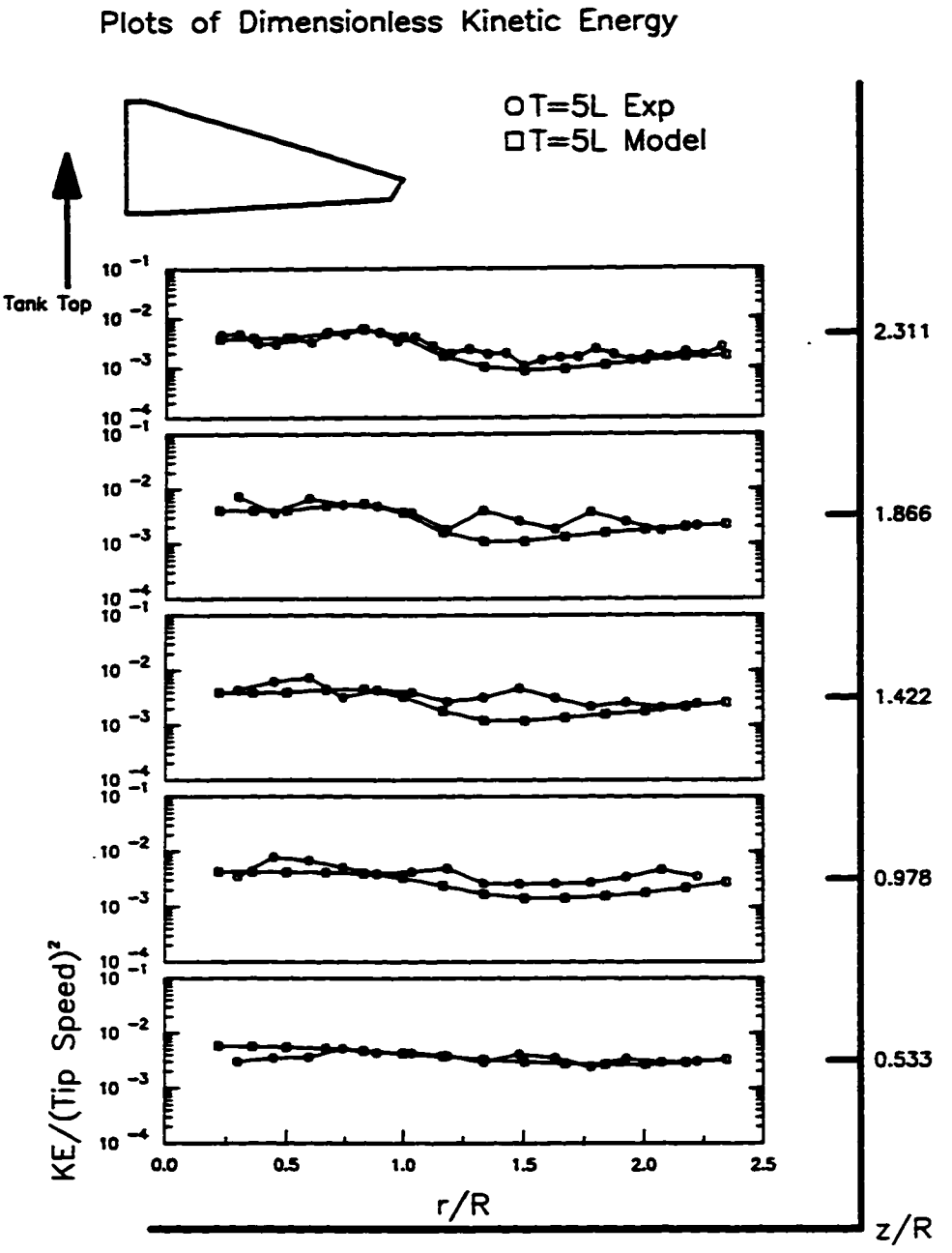

Figure 5.2.21: Turbulent Kinetic Energy for the A310 Foil Impeller: Comparison between FIDAP Model and Experimental Results below the Impeller Centerline T = 5L

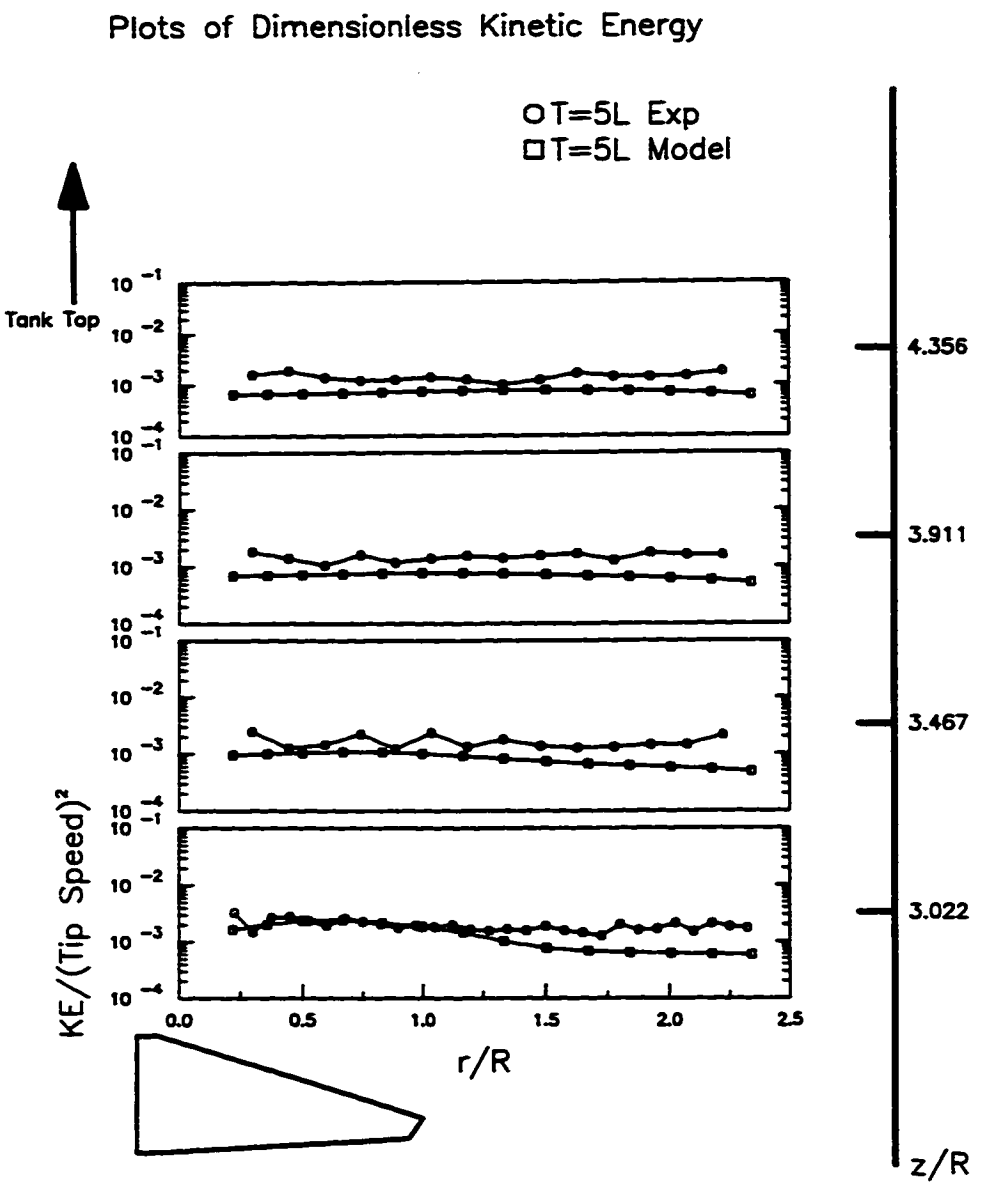

Figure 5.2.22: Turbulent Kinetic Energy for the A310 Foil Impeller: Comparison between FIDAP Model and Experimental Results Above the Impeller Centerline T = 5L

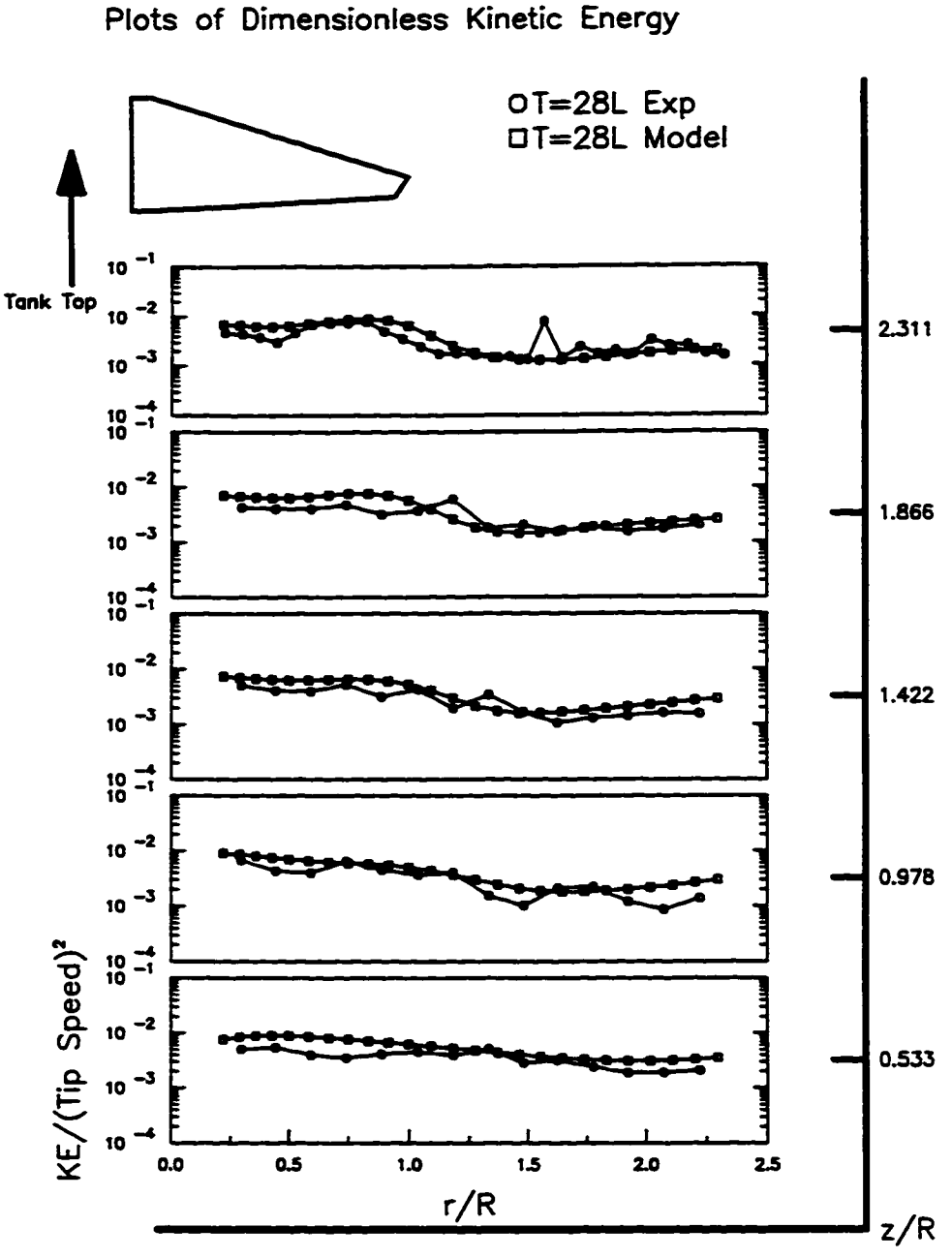

Figure 5.2.23: Turbulent Kinetic Energy for the A310 Foil Impeller: Comparison between FIDAP Model and Experimental Results below the Impeller Centerline T = 28L

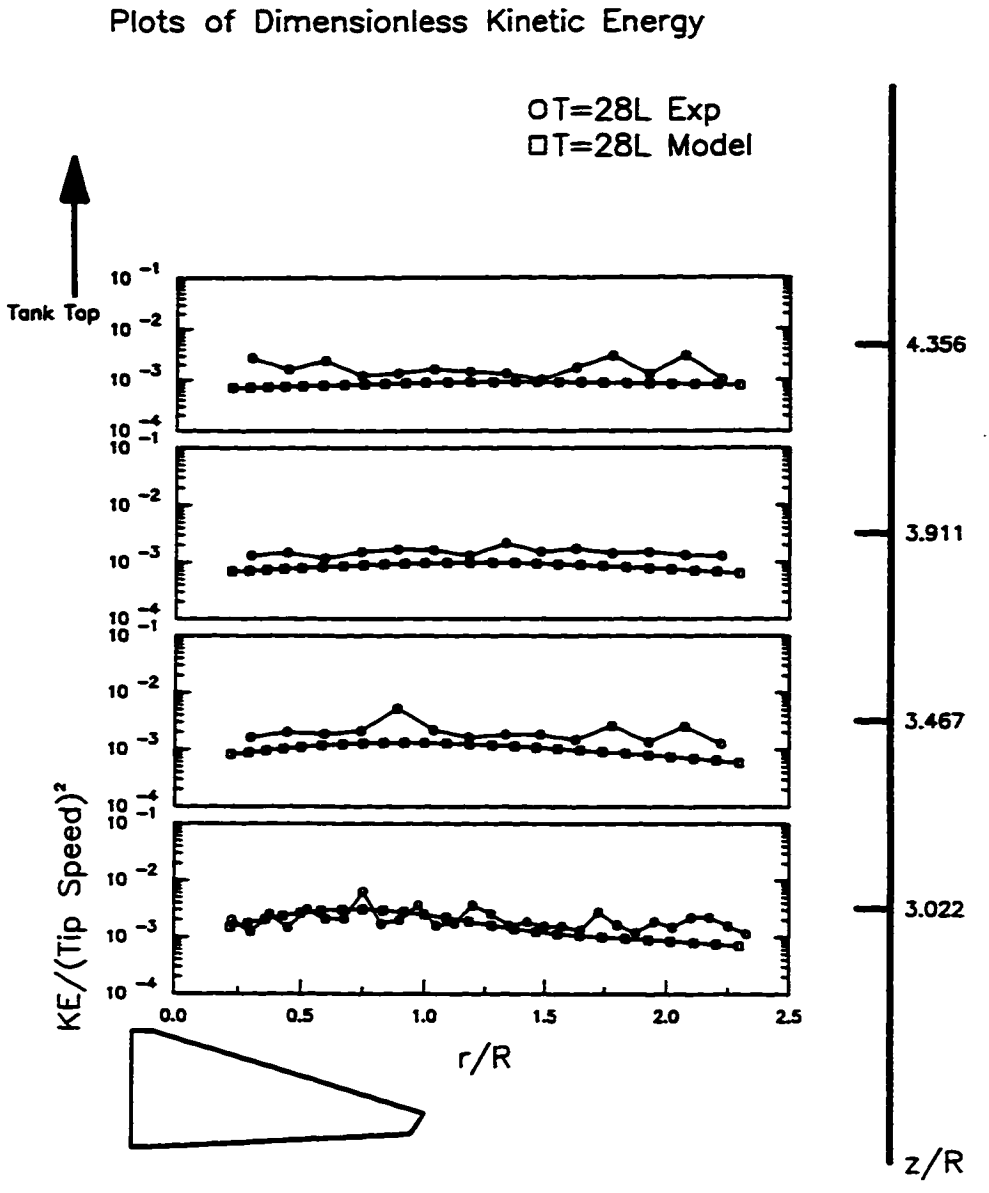

Figure 5.2.24: Turbulent Kinetic Energy for the A310 Foil Impeller: Comparison between FIDAP Model and Experimental Results Above the Impeller Centerline T = 28L

5.2.3 Turbulent Energy Dissipation Rate

Figures 5.2.25 - 5.2.27 compare the local energy dissipation rate results between the model and the experimental values for the Rushton turbine in a 5 L square tank. Likewise, Figures 5.2.28 - 5.2.30 compare the local energy dissipation rate between the FIDAP model and the LDV experimental results for the 28L tank. The model results appear to significantly under predict the measured local energy dissipation rate values in the bulk regions of the 5L tank above and below the impeller centerline (Figures 5.2.25, 5.2.26). Although the model under predicts the measured local energy dissipation rate in the bulk region of the 28L tank, the difference between the model and experimental results is less than in the 5L tank. (Figures 5.2.28, 5.2.29). In the impeller discharge region (Figure 5.2.27), the model over predicted the local energy dissipation rate values at points closest to the Rushton blade tip and slightly under predicted these values at points further away from the impeller blade tip. In the 28L tank, the model also over predicted the local energy dissipation rate in the region closest to the blade tip (Figure 5.2.30). However, the model was able to predict the local energy dissipation rate in the rest of the impeller discharge region of the 28L tank.

The inability of the FIDAP model to predict the local energy dissipation produced by the Rushton turbine might be due to either the trailing vortices or the impeller boundary conditions. The effects of varying the impeller boundary conditions on the turbulent quantities will be explored in Section 5.2.5. It is a well known fact that trailing vortices are produced behind the Rushton turbine blade. In Section 5.1.4, this author speculated that a portion of the energy transferred to the small scale eddies was coming from the energy contained in trailing vortices. If this hypothesis is true , then it is reasonable to expect the FIDAP model to under predict the local energy dissipation rate since it is difficult to include the dynamics of the trailing vortices in the flow domain with the present modeling approach. In Section 5.1.4, this author also speculated that the influence of the trailing vortices on the small scale eddies decreased with increasing tank size. This was demonstrated by the decreasing exponent in Equation 5.6. The results from FIDAP seems to confirm this experimental trend. The difference between the experimental results and the model for the local energy dissipation rate in the 28L tank is less than

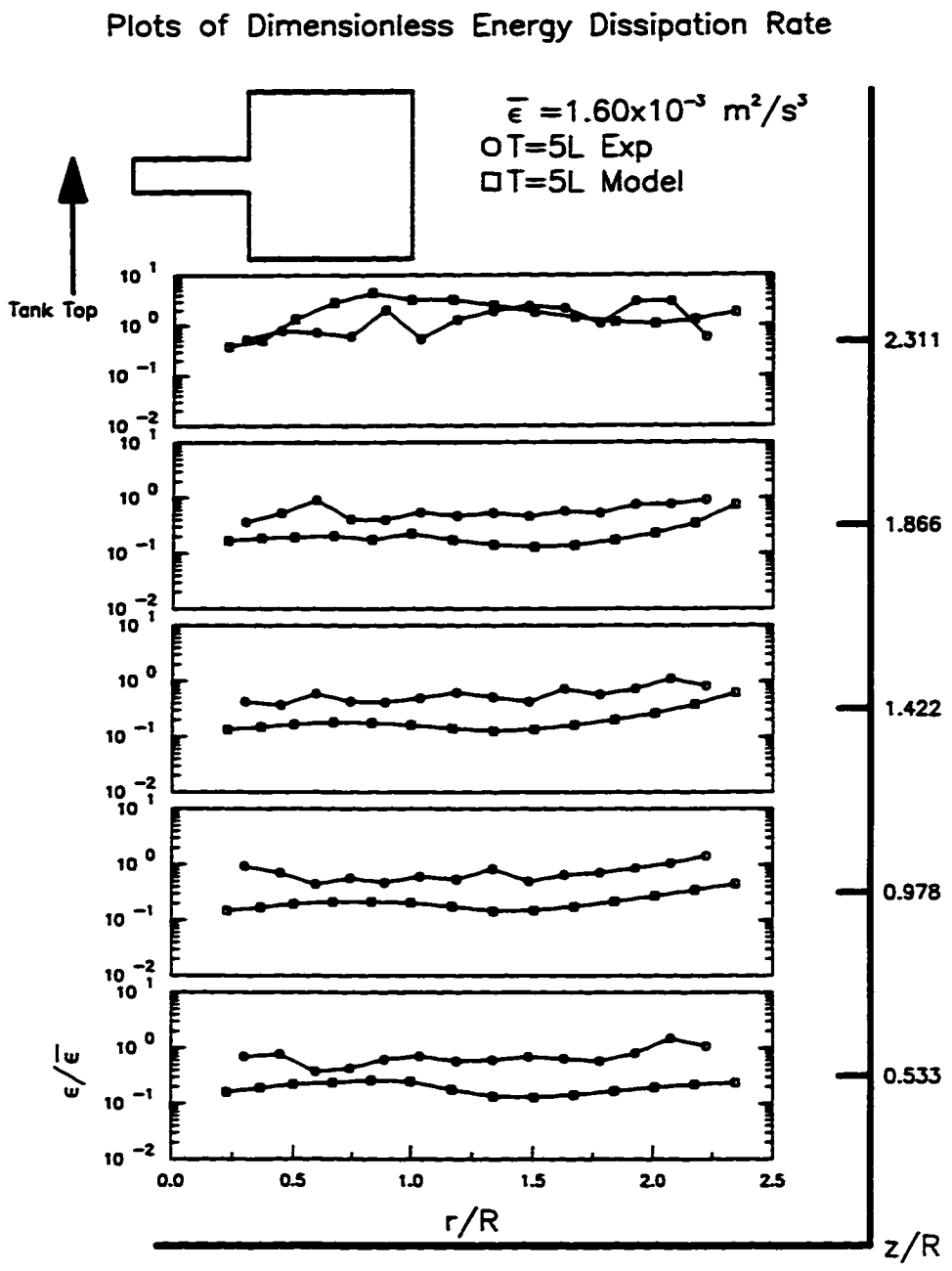

Figure 5.2.25: Turbulent Energy Dissipation Rate for the Rushton Turbine: Comparison between FIDAP Model and Experimental Results below Impeller Centerline T = 5L

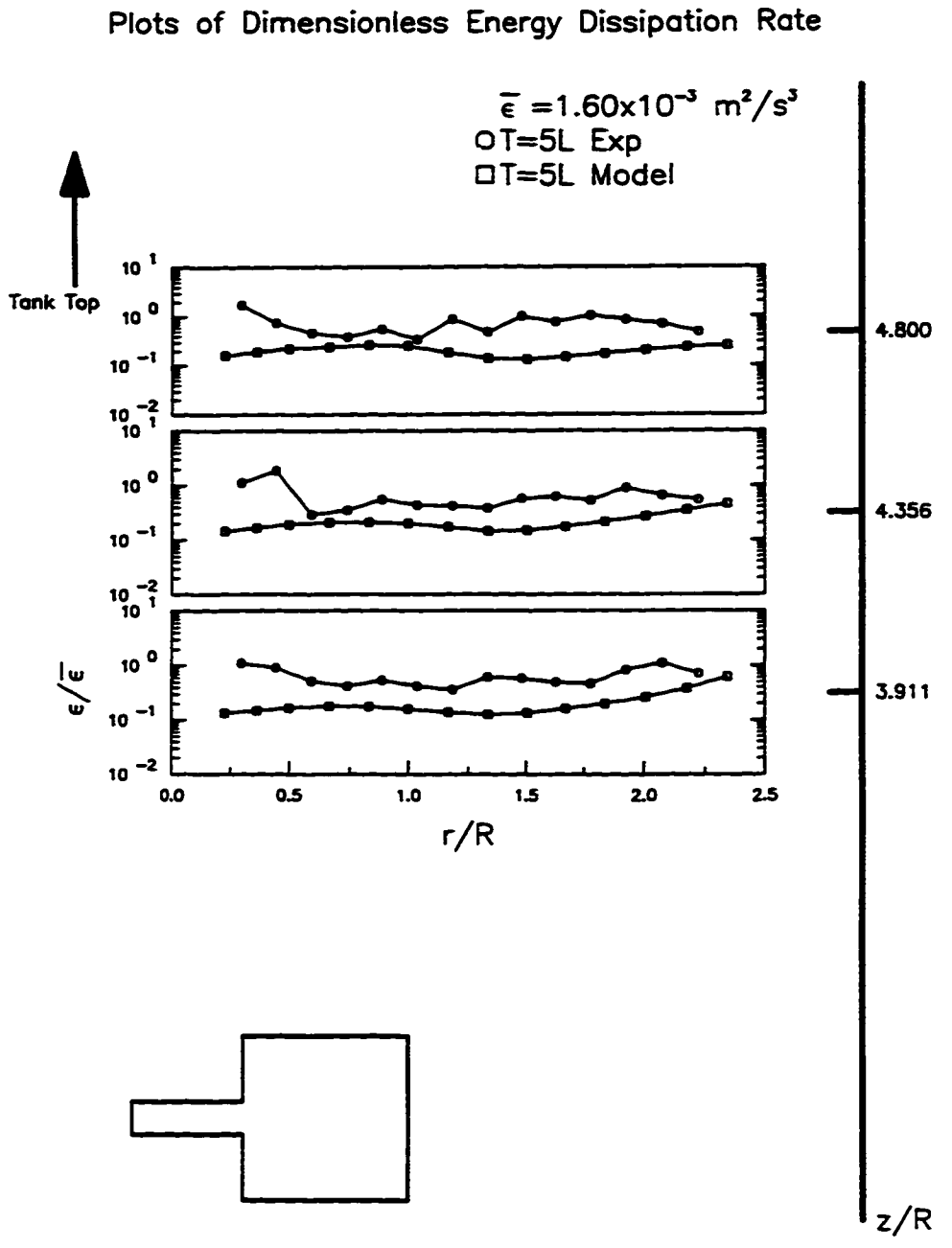

Figure 5.2.26: Turbulent Energy Dissipation Rate for the Rushton Turbine: Comparison between FIDAP Model and Experimental Results above Impeller Centerline T = 5L

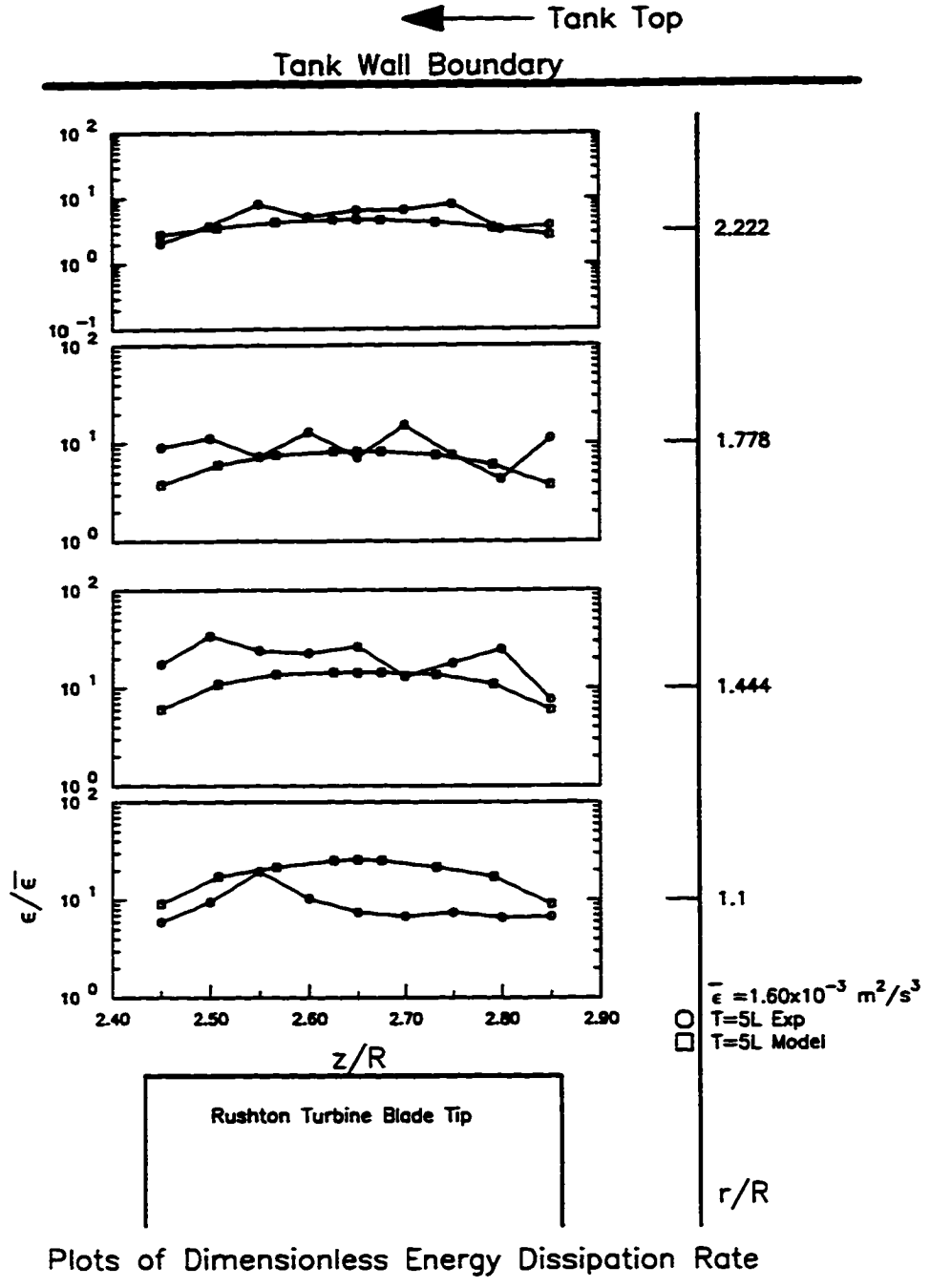

Figure 5.2.27: Turbulent Energy Dissipation Rate for the Rushton Turbine: Comparison between FIDAP Model and Experimental Results in the Impeller Discharge Zone T = 5L

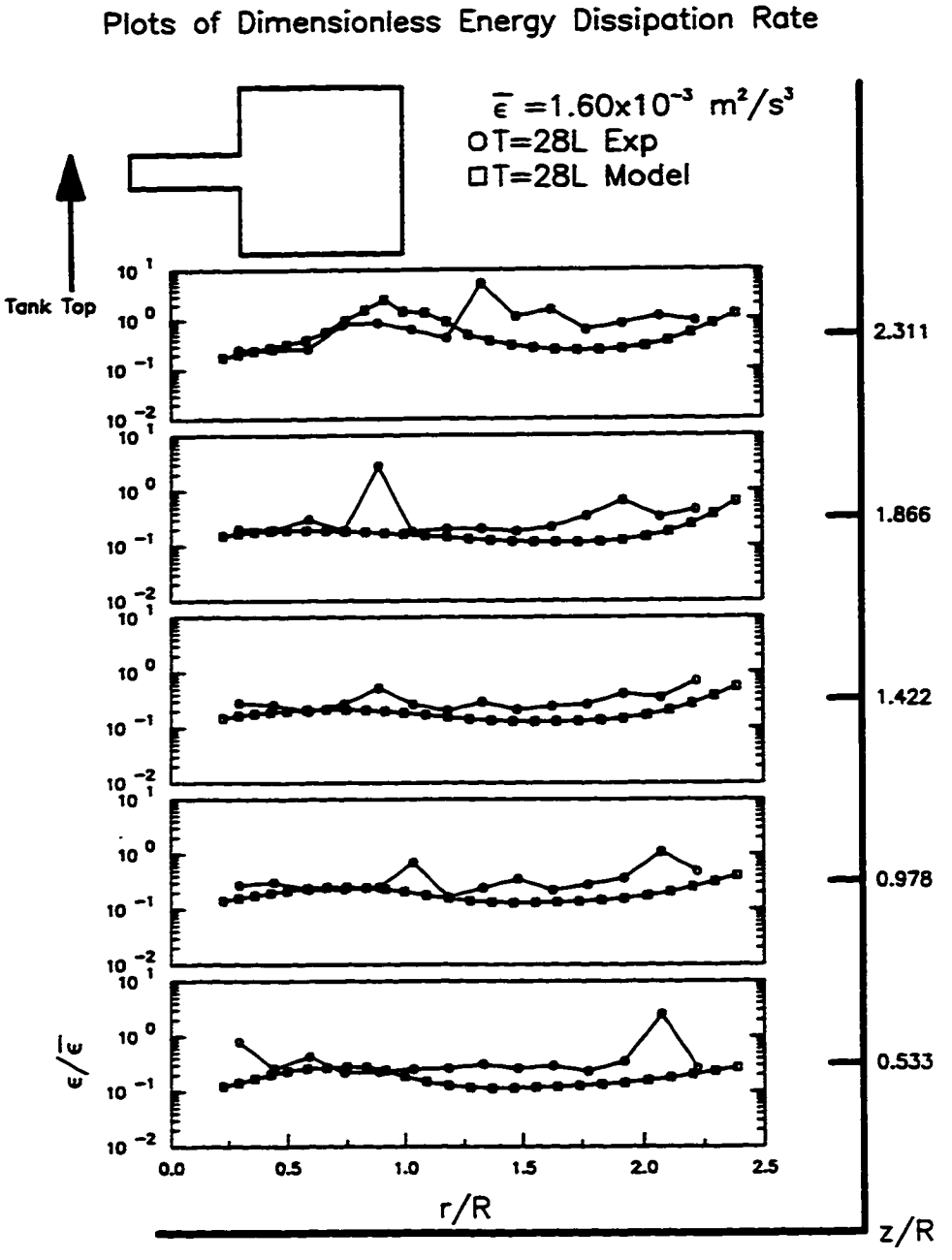

Figure 5.2.28: Turbulent Energy Dissipation Rate for the Rushton Turbine: Comparison between FIDAP Model and Experimental Results below Impeller Centerline T = 28L

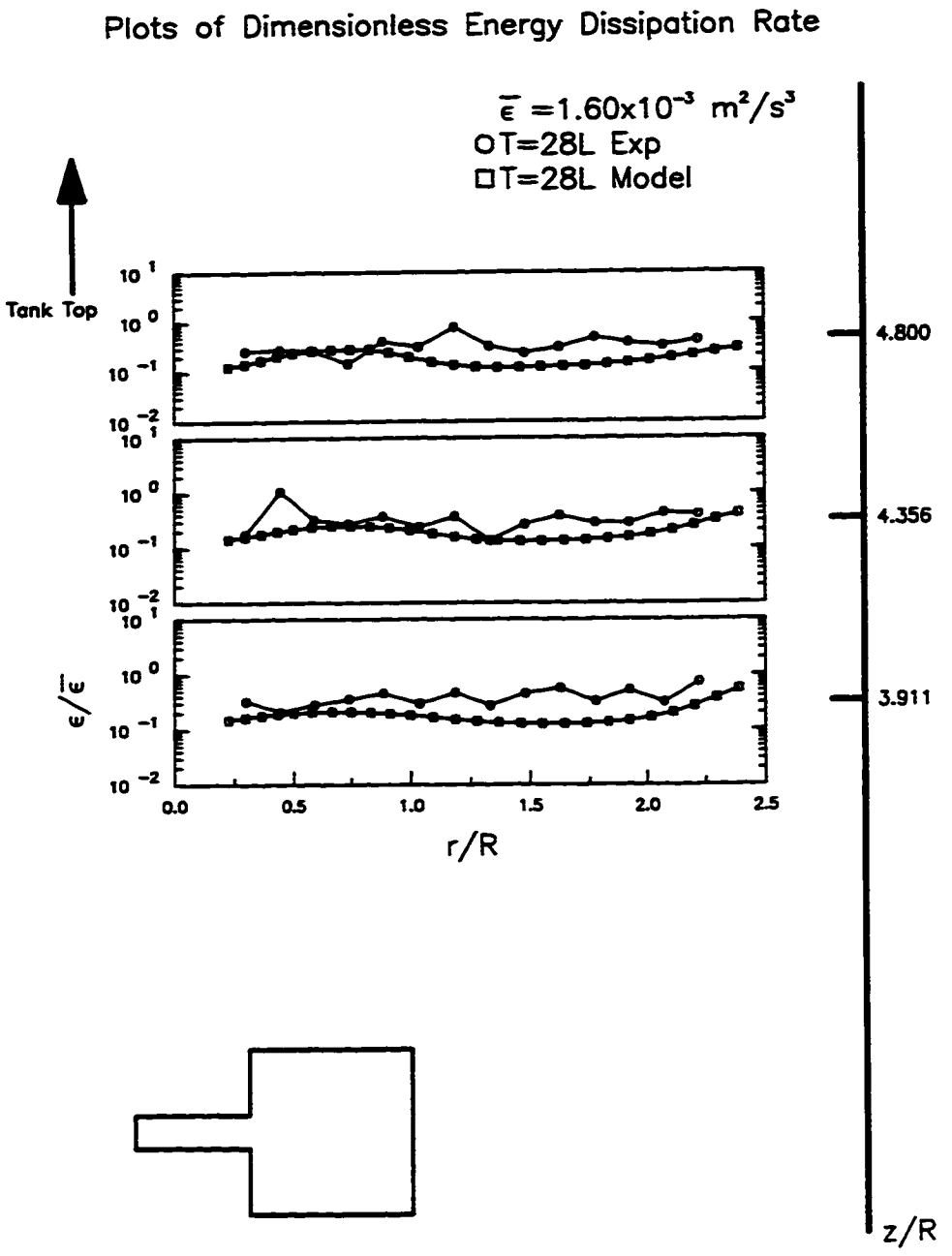

Figure 5.2.29: Turbulent Energy Dissipation Rate for the Rushton Turbine: Comparison between FIDAP Model and Experimental Results above Impeller Centerline T = 28L

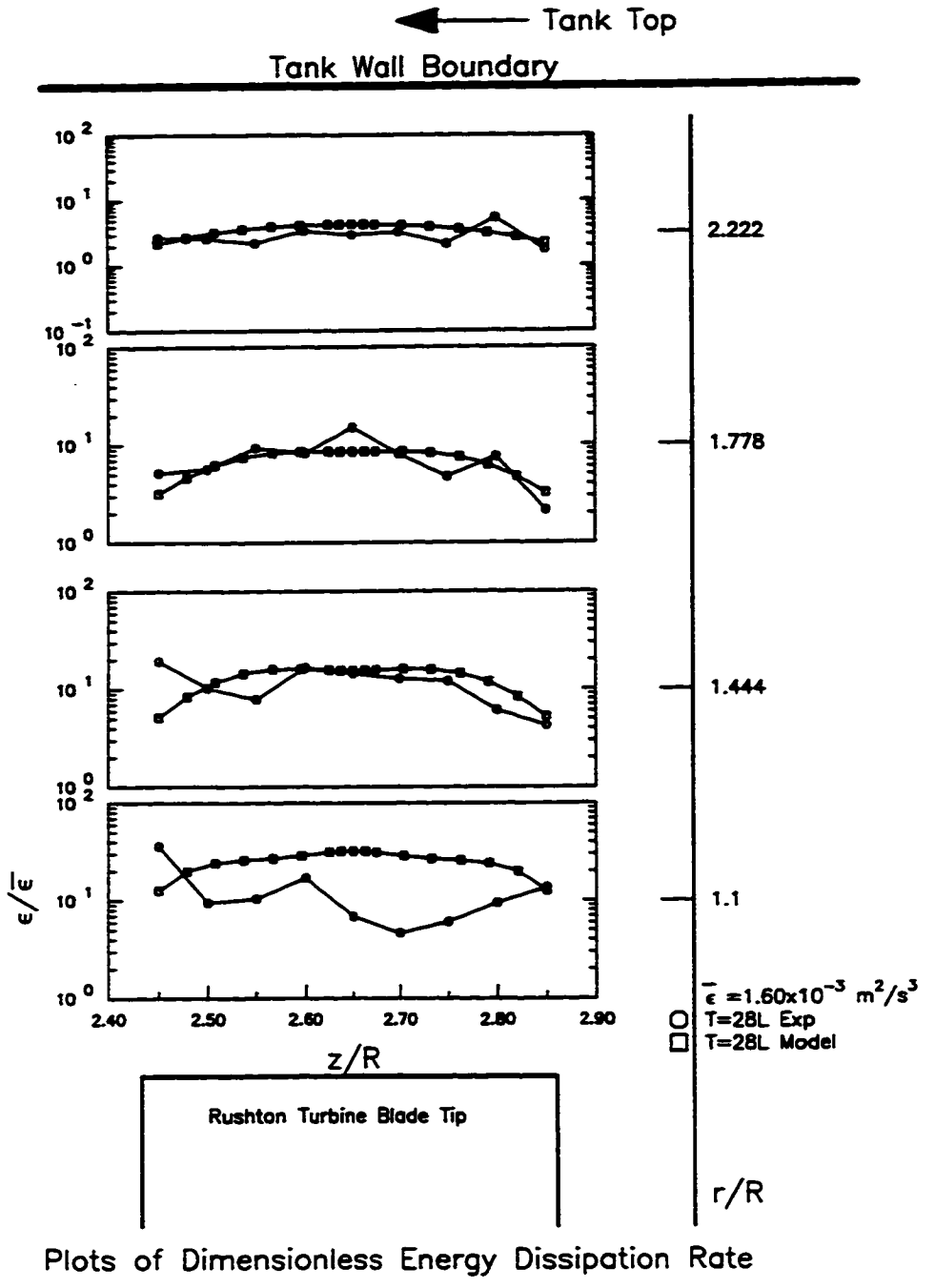

Figure 5.2.30: Turbulent Energy Dissipation Rate for the Rushton Turbine: Comparison between FIDAP Model and Experimental Results in the Impeller Discharge Zone T = 28L

the difference between the experimental and modeling results in the 5L tank. With constant power per unit volume, FIDAP predicts that the local energy dissipation rate does not vary with tank size (Figure 5.2.31, 5.2.32). Therefore, this smaller difference between the experimental and modeling results with the 28L tank size may indicate that the energy transfer from the trailing vortices to the small eddies, decreases with increasing tank size when G_m = constant.

Figures 5.2.33 and 5.2.34 compare the local energy dissipation rate results between the model and the experimental values for the A310 foil impeller in the 5L tank size. Figures 5.2.35 and 5.2.36 compare the local energy dissipation results between the model and the experimental values for the A310 foil impeller in the 28L tank. From the modeling results in Figures 5.2.33 - 5.2.36, FIDAP seems to predict the local energy dissipation rate fairly well between z/R = 0.533 and z/R = 3.467. In the lower part of the tank, the model over predicts the experimental values of the local energy dissipation rate in the impeller discharge region (r/R = 0.2 ~ 1.0) (Figures 5.2.33, 5.2.35). Figures 5.2.33 and 5.2.35 also show that the model tends to under predict the local energy dissipation rate between r/R - 1.25 - 2.25. In the upper part of the tank, the model appears to under predict the experimental values for the energy dissipation rate. The inability of the model to exactly match the measured energy dissipation rate might be due to experimental inaccuracies from leaving out the Reynolds shear stresses, or due to limitations of the k-ε turbulence model. The impeller boundary conditions may also be a source of model inaccuracies. The effect of varying the boundary conditions on the turbulent quantities will be explored in Section 5.2.5.

5.2.4 Effect of Mesh Density on Turbulent Quantities

The stability of the results produced by FIDAP is influenced by the grid size used to discretized the flow domain. In general, a finer grid mesh tends to improve the numerical stability of the model. In some cases, a finer mesh may also improve the accuracy of the model to fit the experimental results. In this study, the mesh density was increased by 6 times in the 5L tank to understand the influence of the grid size on the turbulent kinetic energy and energy dissipation

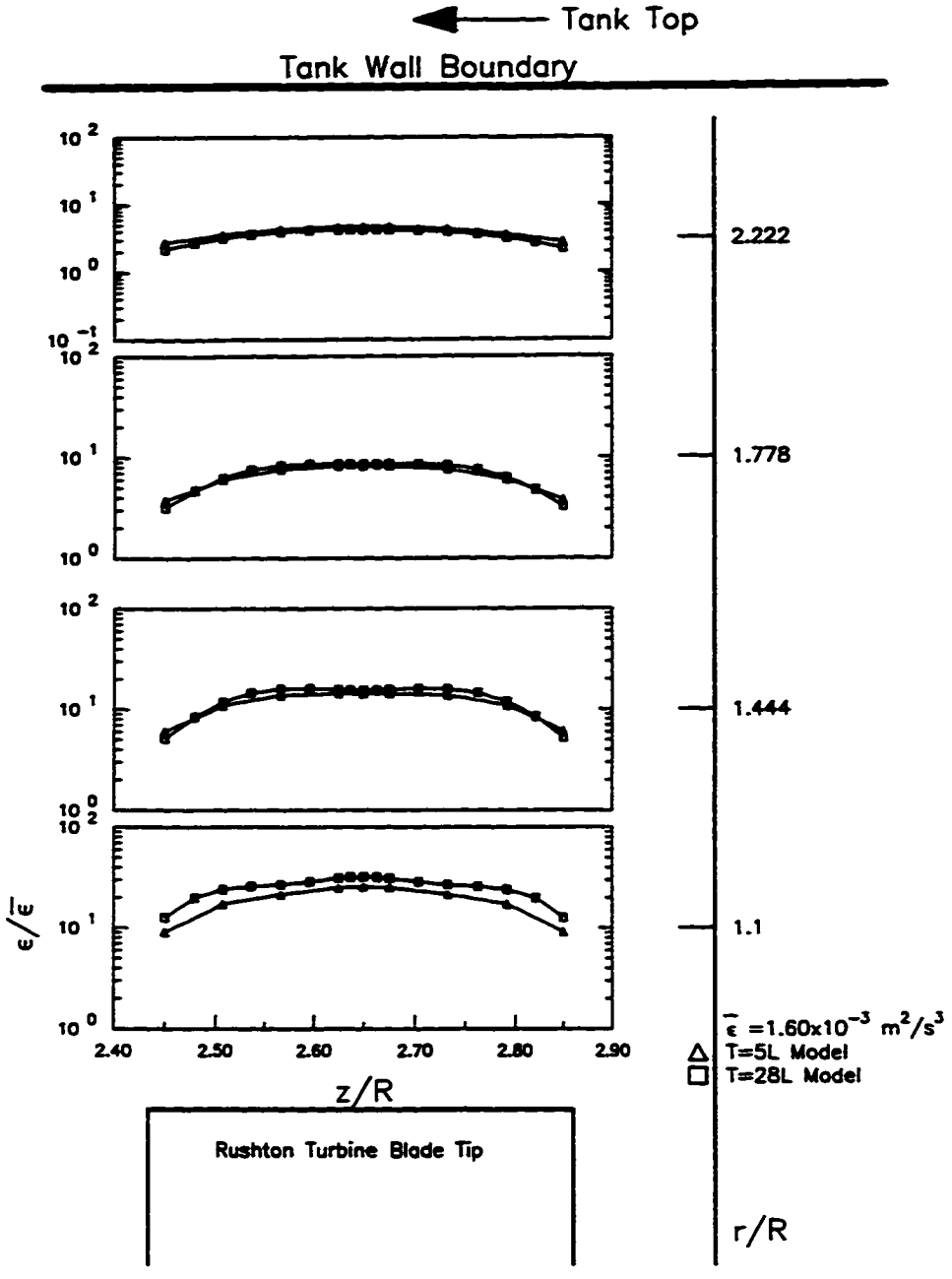

Figure 5.2.31: Turbulent Energy Dissipation Rate for the Rushton Turbine: Comparison between FIDAP model T = 5L & T = 28L in the Impeller Discharge Zone

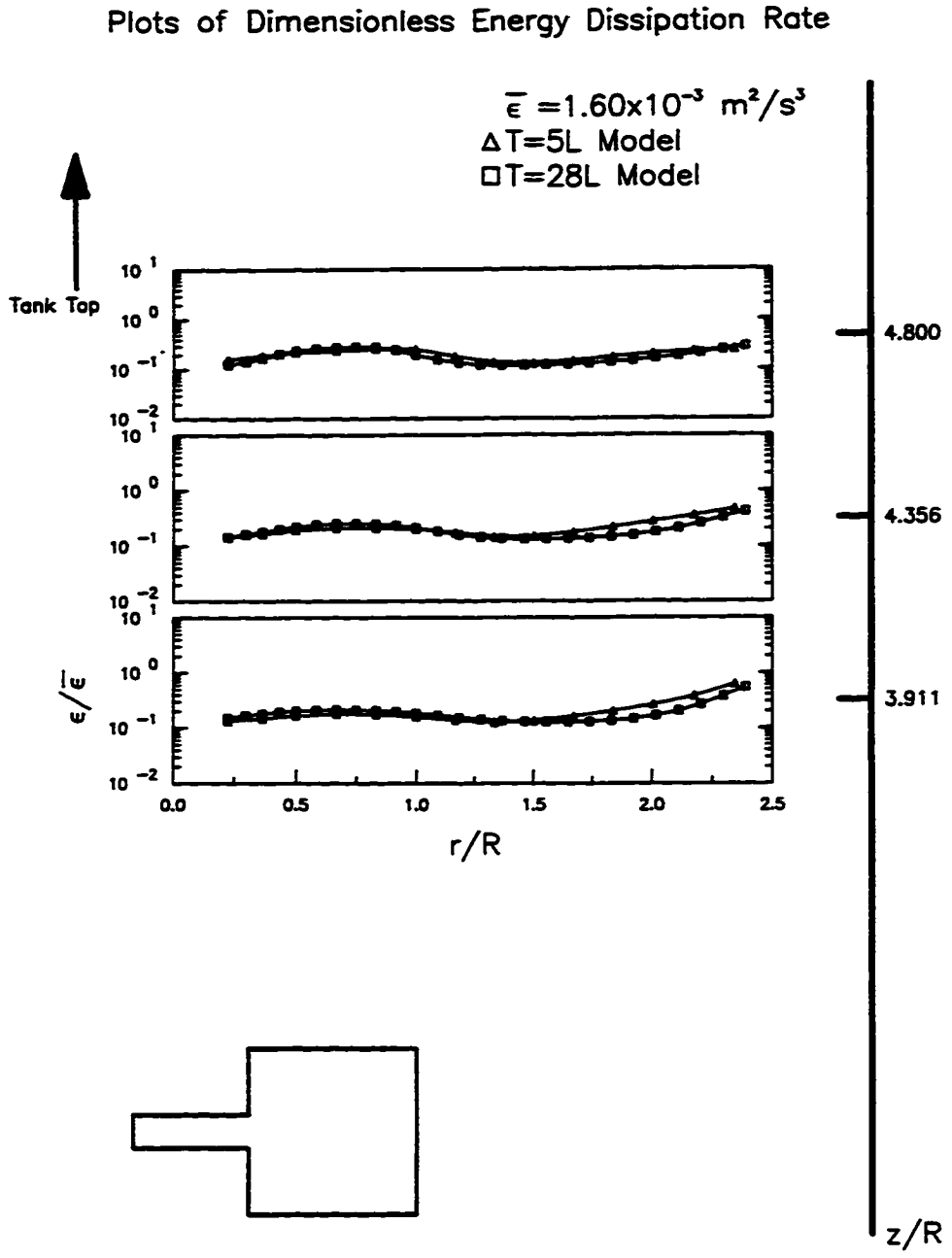

Figure 5.2.32: Turbulent Energy Dissipation Rate for the Rushton Turbine: Comparison between FIDAP model T = 5L & T = 28L above impeller Centerline

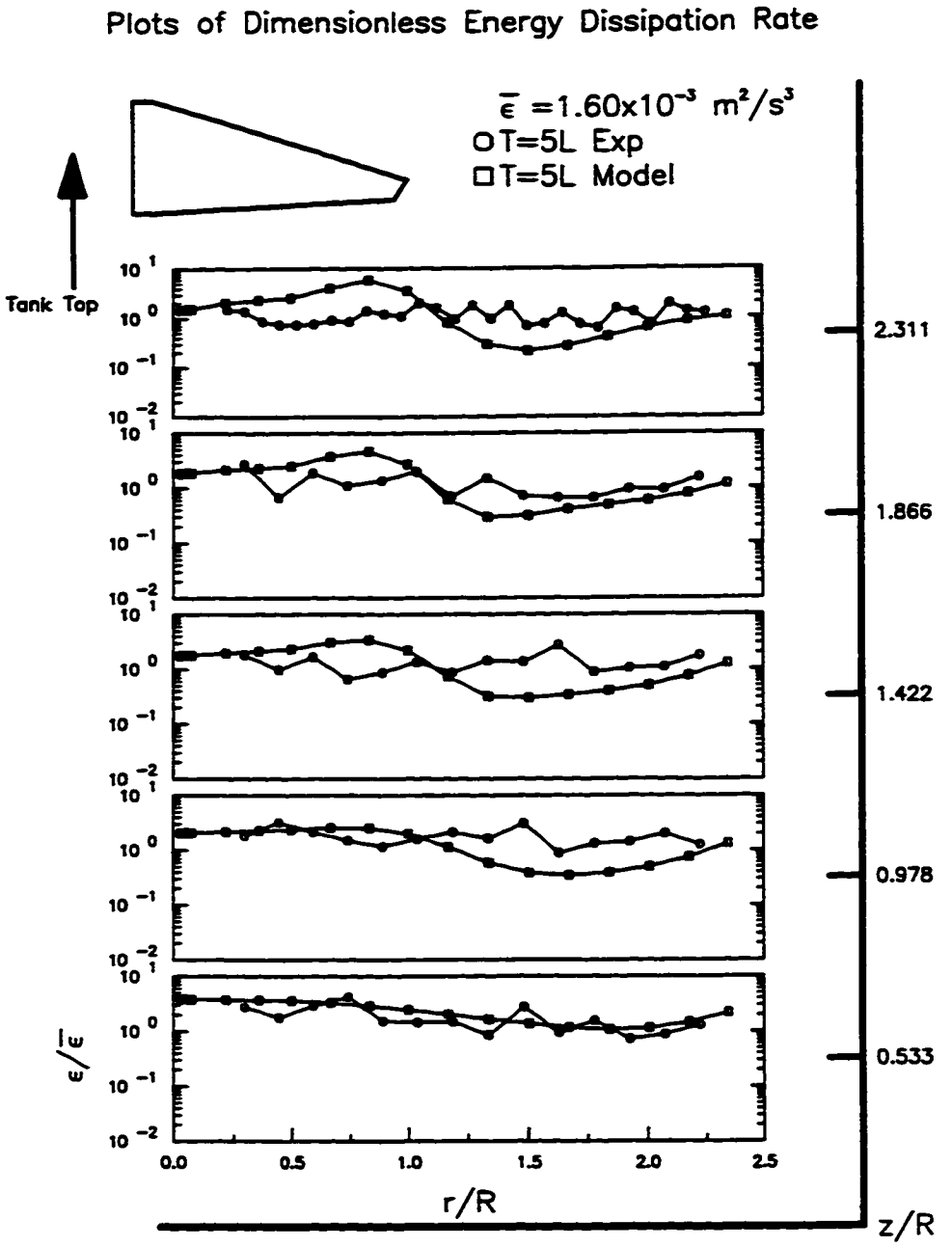

Figure 5.2.33: Turbulent Energy Dissipation Rate for the A310 Foil Impeller: Comparison between FIDAP Model and Experimental Results below the Impeller Centerline T = 5L

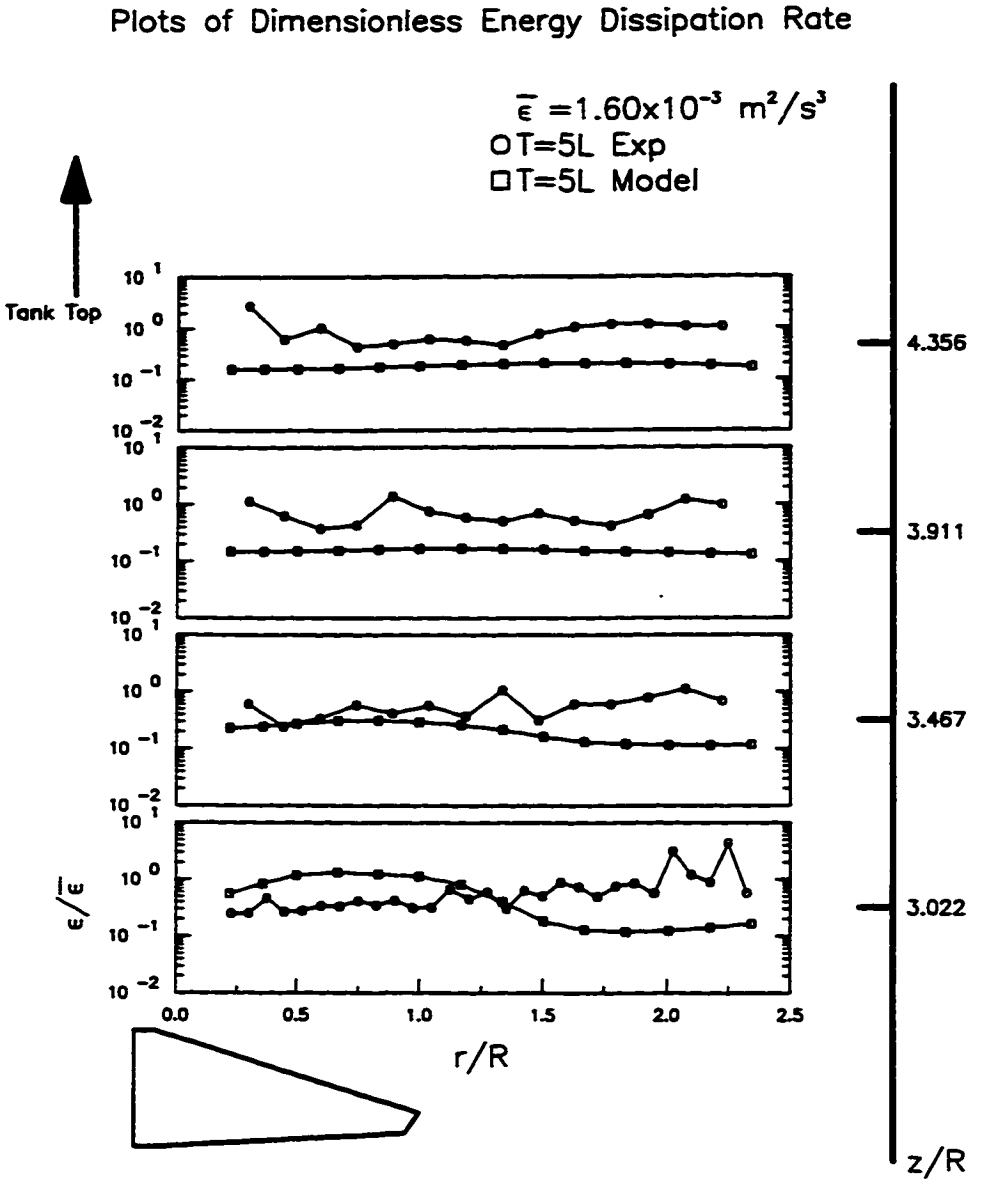

Figure 5.2.34: Turbulent Energy Dissipation Rate for the A310 Foil Impeller: Comparison between FIDAP Model and Experimental Results Above the Impeller Centerline T = 5L

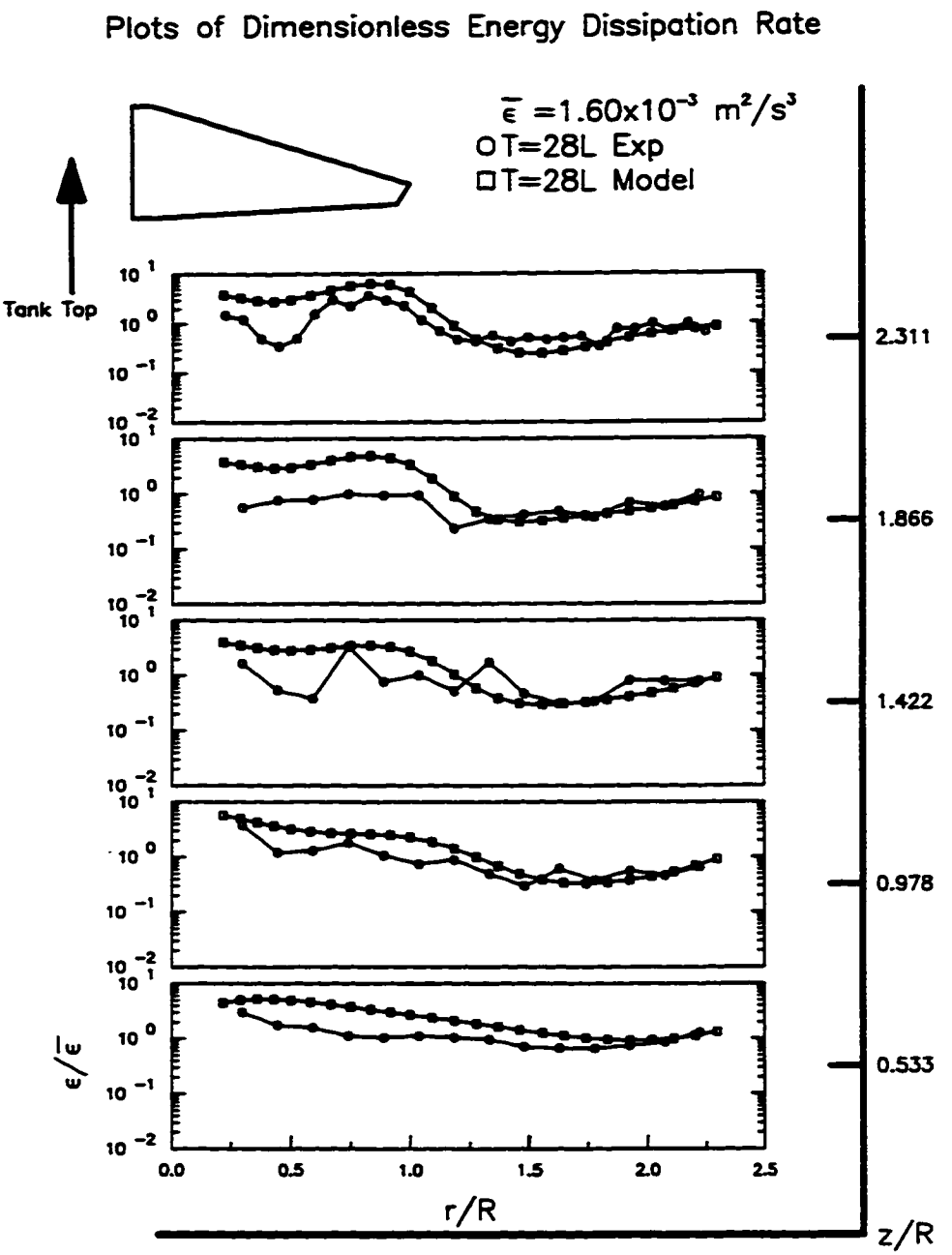

Figure 5.2.35: Turbulent Energy Dissipation Rate for the A310 Foil Impeller: Comparison between FIDAP Model and Experimental Results below the Impeller Centerline T = 28L

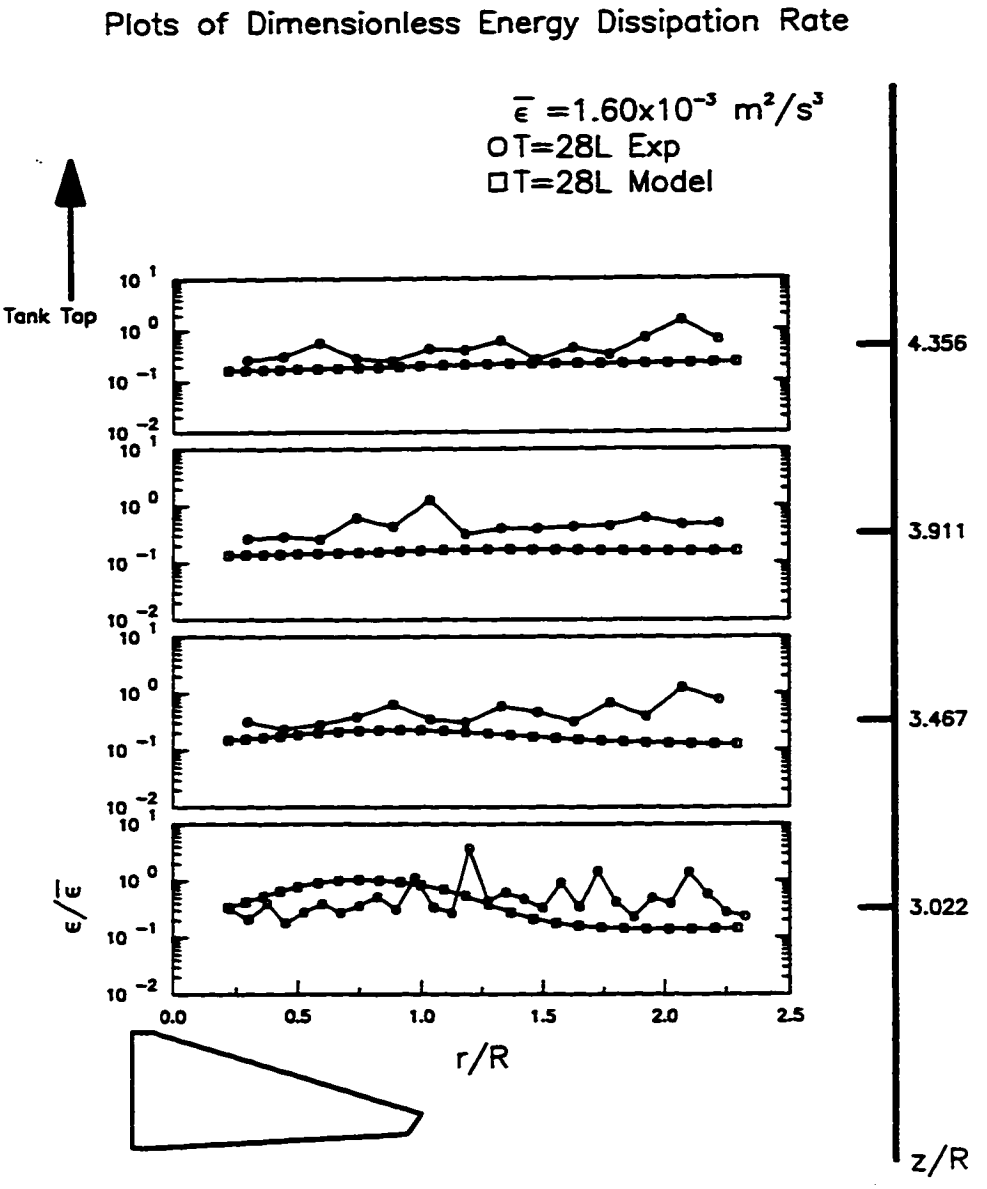

Figure 5.2.36: Turbulent Energy Dissipation Rate for the A310 Foil Impeller: Comparison between FIDAP Model and Experimental Results Above the Impeller Centerline T = 28L

rate. Figures 5.2.37 through 5.2.42 display the results of the coarse grid and fine grid FIDAP model for the 5L tank with a Rushton turbine.

The effects of the mesh density on the turbulent kinetic energy are displayed in Figures 5.2.37 - 5.2.39. As can be seen in Figures 5.2.37 - 5.2.39, the value of the local turbulent kinetic energy decreases by increasing the mesh density. However, the difference between the coarse grid and the fine grid kinetic energy results is negligible in most locations.

Figures 5.2.40 - 5.2.42 display the effects of the mesh density on the local turbulent energy dissipation rate. As can be seen in Figures 5.2.40 - 5.2.42, the value of the local energy dissipation rate is not affected by the increased mesh density in most regions of tank. In the region closest to the impeller blade tip (z/R = 2.311: Figure 5.2.40 and r/R = 1.1: Figure 5.2.42), the increased mesh density appears to decrease the local energy dissipation rate slightly.

Figures 5.2.43 through 5.2.46 display the results of the coarse grid and fine grid FIDAP model for the 5L tank with an A310 foil impeller. The effects of the mesh density on the turbulent kinetic energy are shown in Figures 5.2.43 and 5.2.44. From Figures 5.2.43 and 5.2.44, the turbulent kinetic energy does not appear to be influenced by the increased mesh density in the bulk region (r/R = 1.5 ~ 2.5) below the impeller centerline and in the entire region above the impeller centerline. In the impeller discharge region, the turbulent kinetic energy increased slightly with the higher mesh density. Figures 5.2.45 and 5.2.46 display the influence of the mesh density on the local turbulent energy dissipation rate. As can be seen from Figures 5.2.45 and 5.2.46, the local turbulent energy dissipation rate was not significantly affected by the increased mesh density.

5.2.5 Effect of Varying Boundary Conditions on Turbulent Quantities

In this section, the boundary conditions used in Section 5.2.1 - 5.2.4 and three other boundary conditions based on experimental measurements were evaluated. Table 5.2.1 displays the boundary and initial conditions from Section 4.1.3.1 and the three new boundary and initial

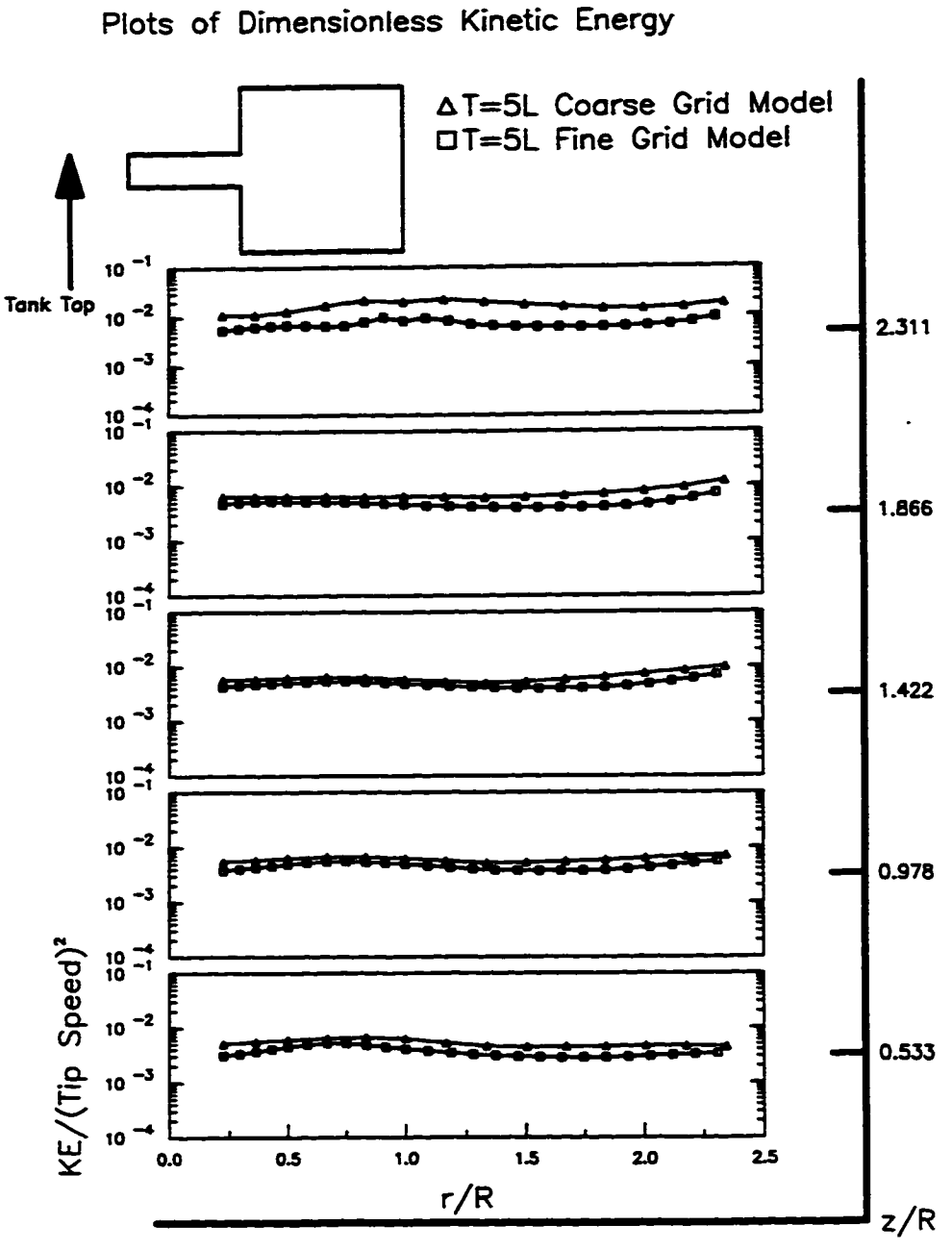

Figure 5.2.37: Effect of Mesh Density on the Turbulent Kinetic Energy in the Bulk Region of the Rushton Turbine below the Impeller Centerline T = 5L

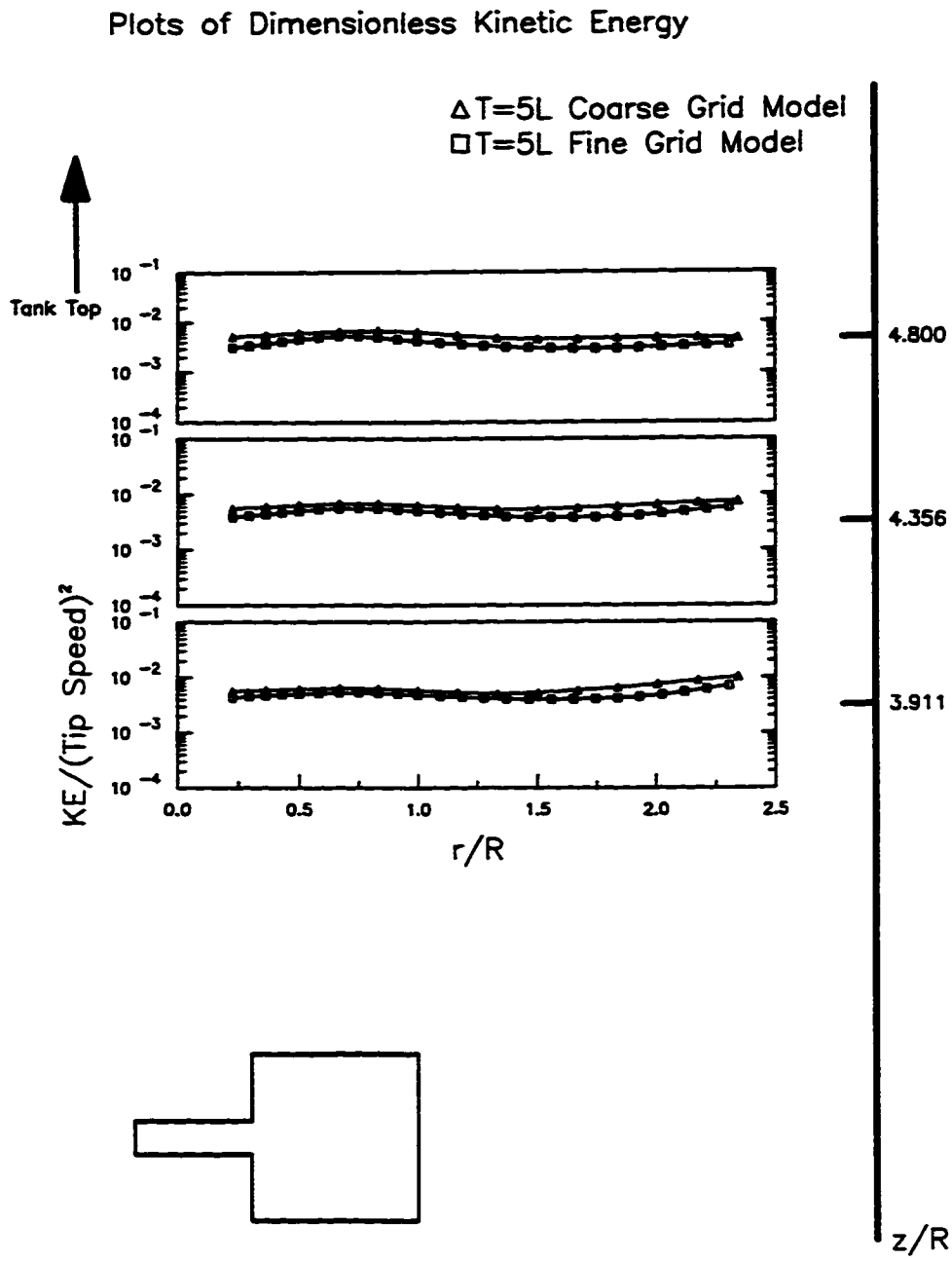

Figure 5.2.38: Effect of Mesh Density on the Turbulent Kinetic Energy in the Bulk Region of the Rushton Turbine above the Impeller Centerline T = 5L

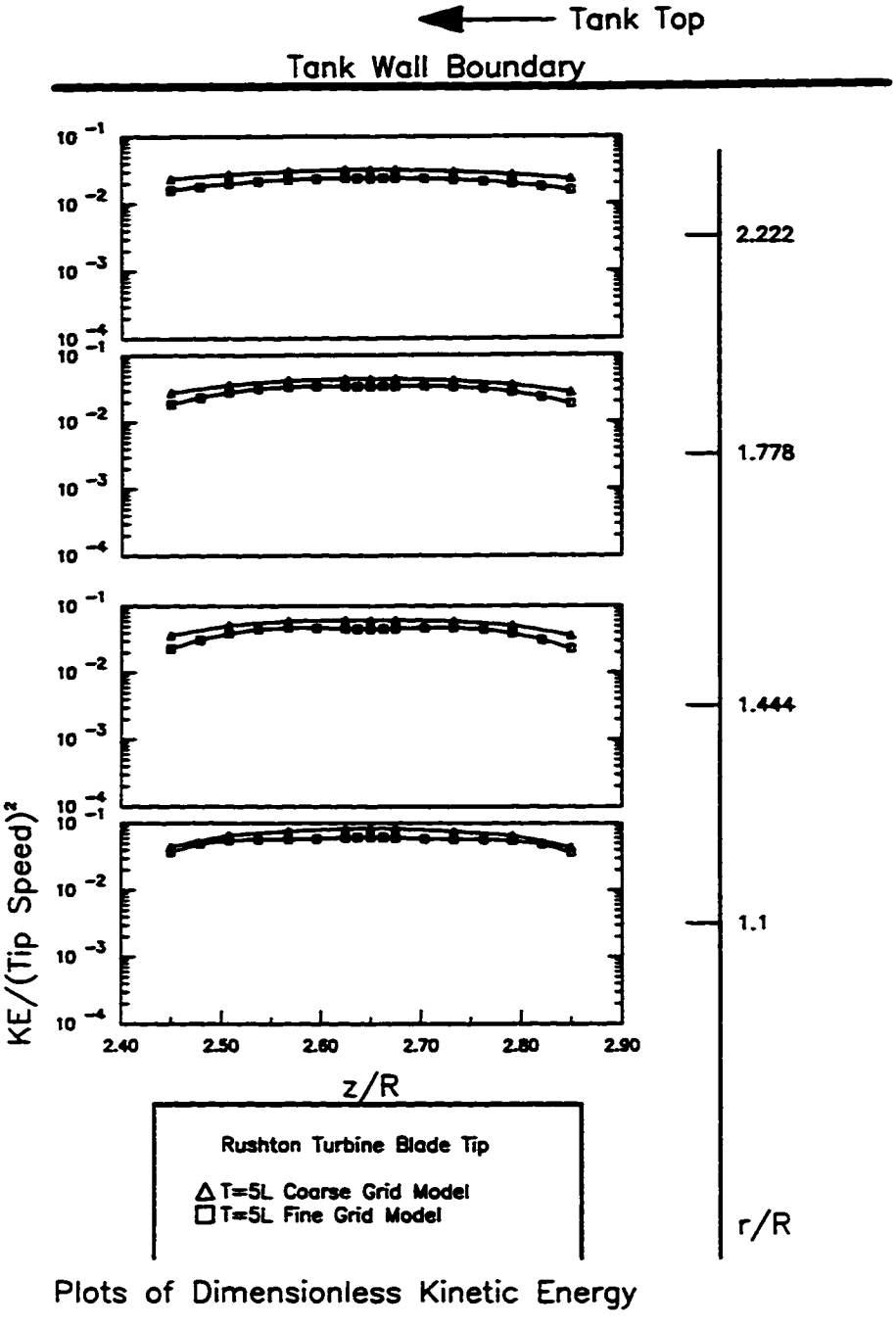

Figure 5.2.39: Effect of Mesh Density on the turbulent Kinetic Energy in the Impeller Discharge Region of the Rushton turbine T = 5L

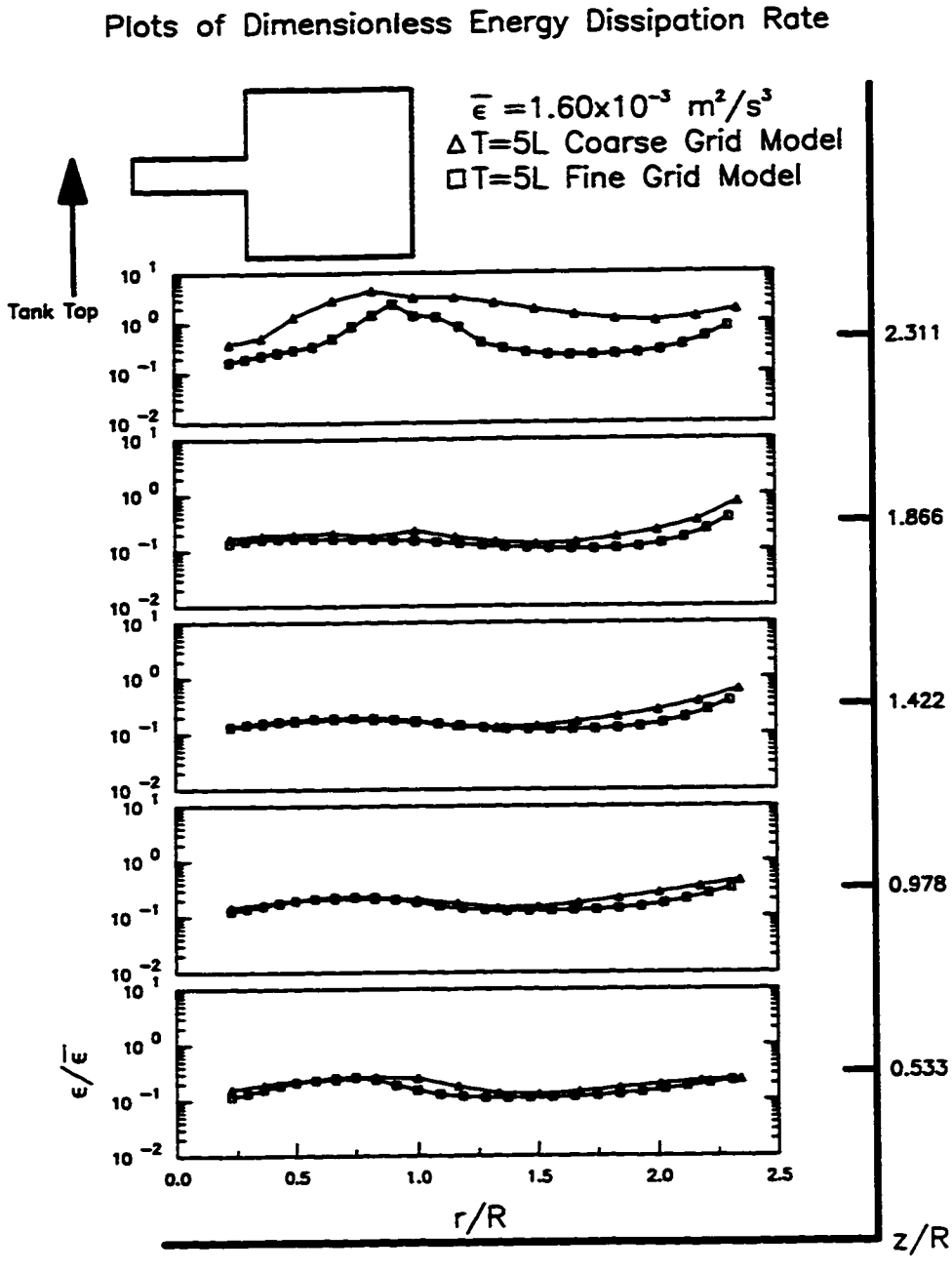

Figure 5.2.40: Effect of Mesh Density on the Turbulent Energy Dissipation Rate in the Bulk Region of the Rushton Turbine below the Impeller Centerline T = 5L

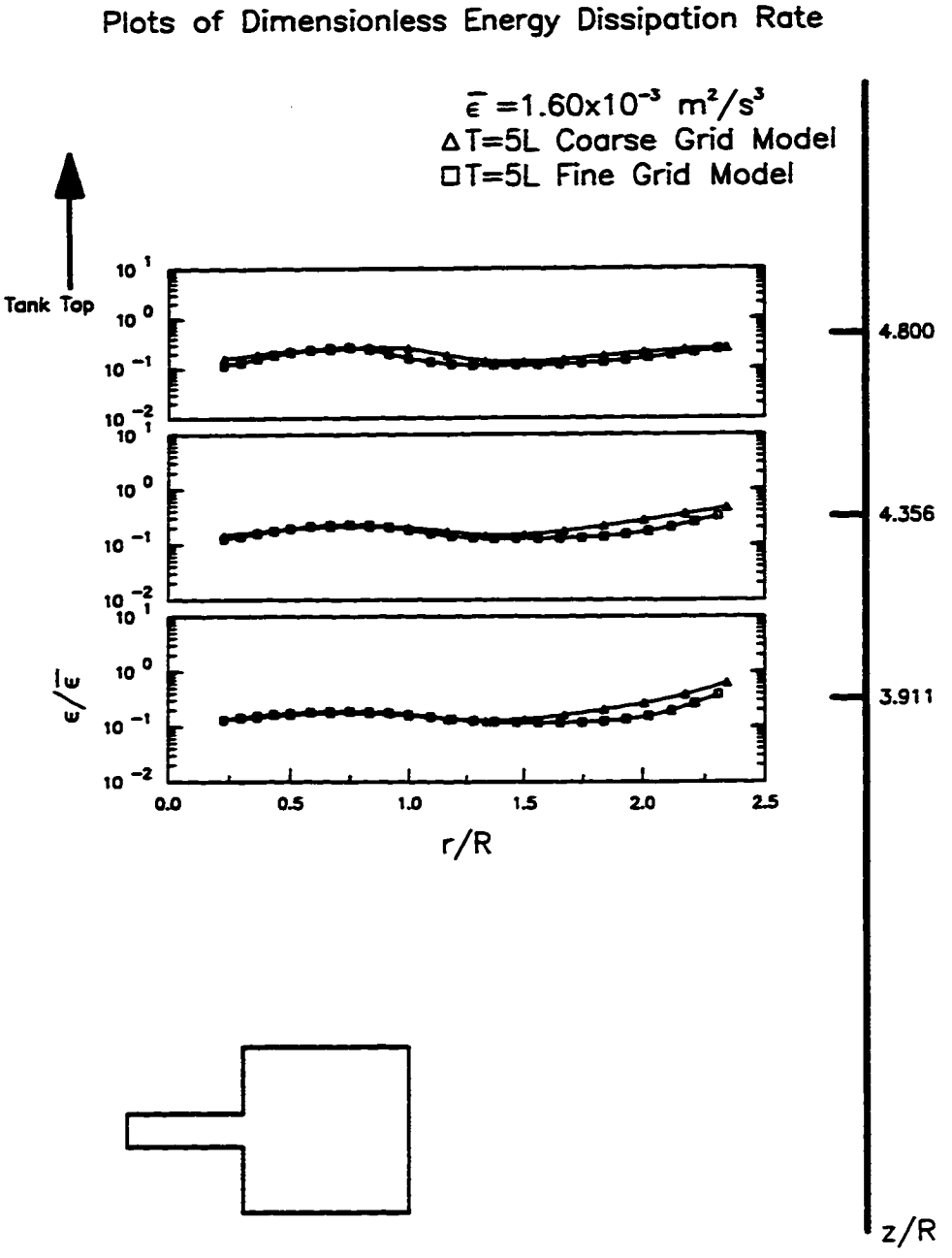

Figure 5.2.41: Effect of Mesh Density on the Turbulent Energy Dissipation Rate in the Bulk Region of the Rushton Turbine above the Impeller Centerline T = 5L

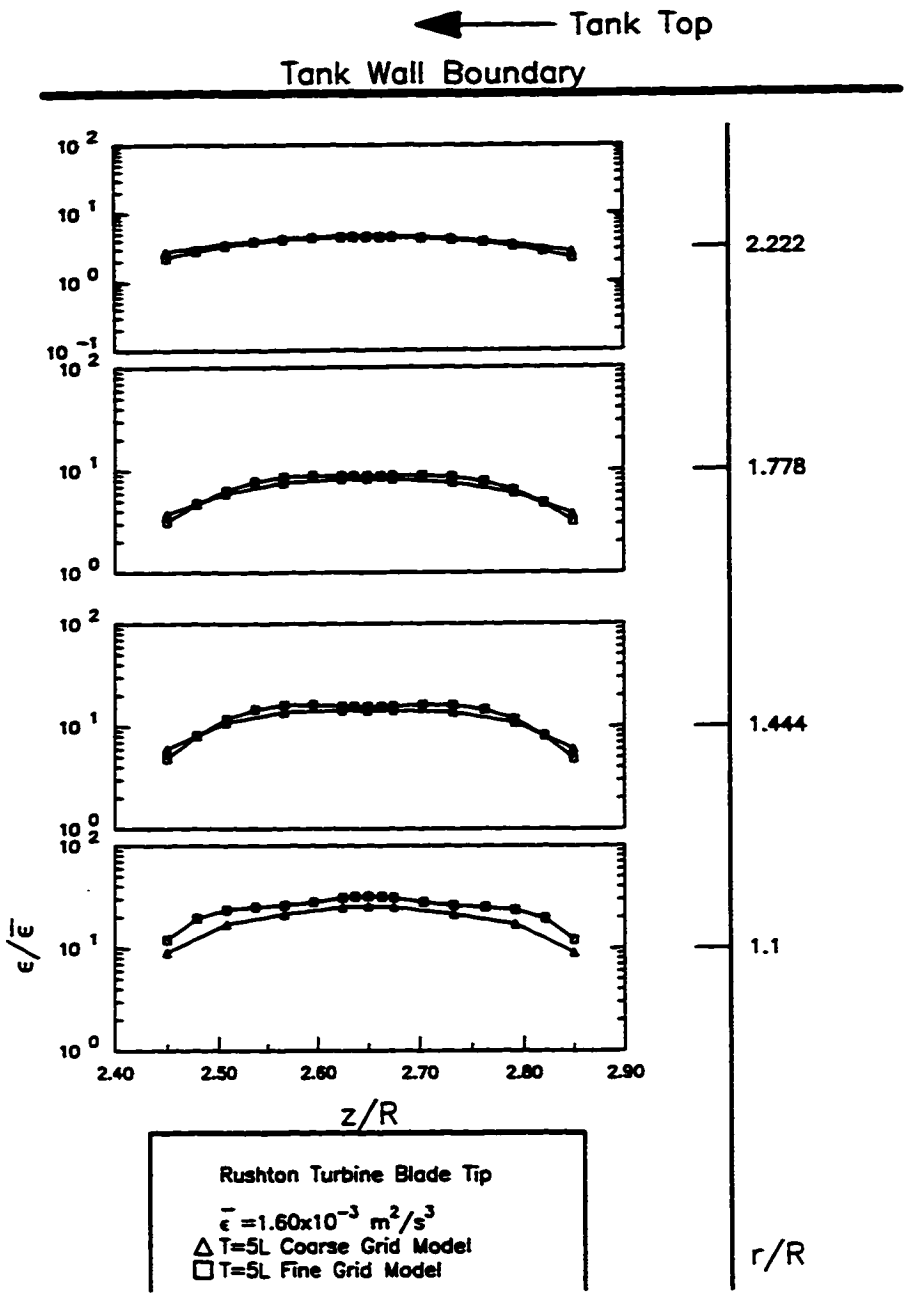

Figure 5.2.42: Effect of Mesh Density on the Turbulent Energy Dissipation Rate in the Impeller Discharge Region of the Rushton Turbine T = 5L

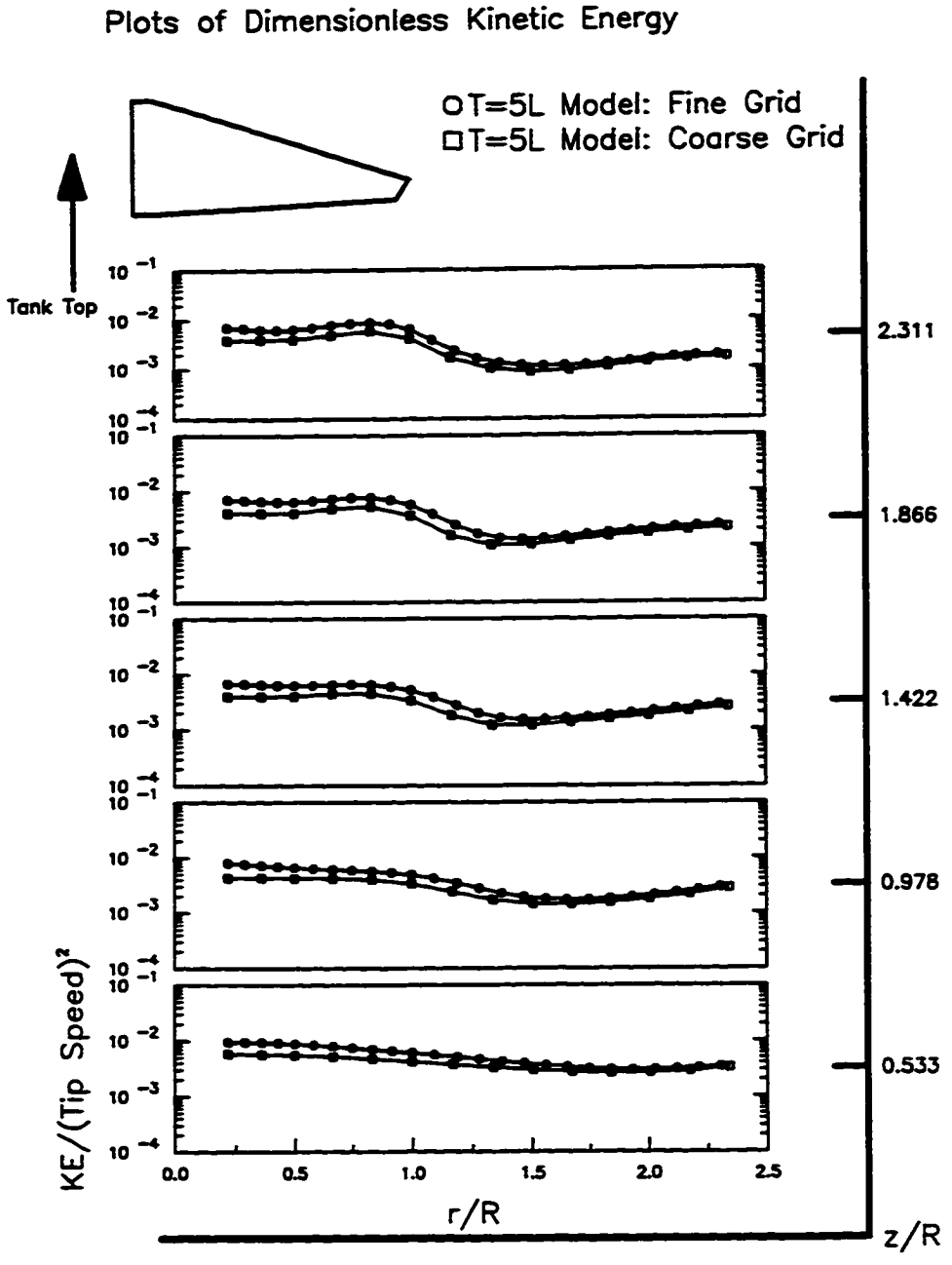

Figure 5.2.43: Effect of Mesh Density on the Turbulent Kinetic Energy for the A310 foil Impeller below the Impeller Centerline T = 5L

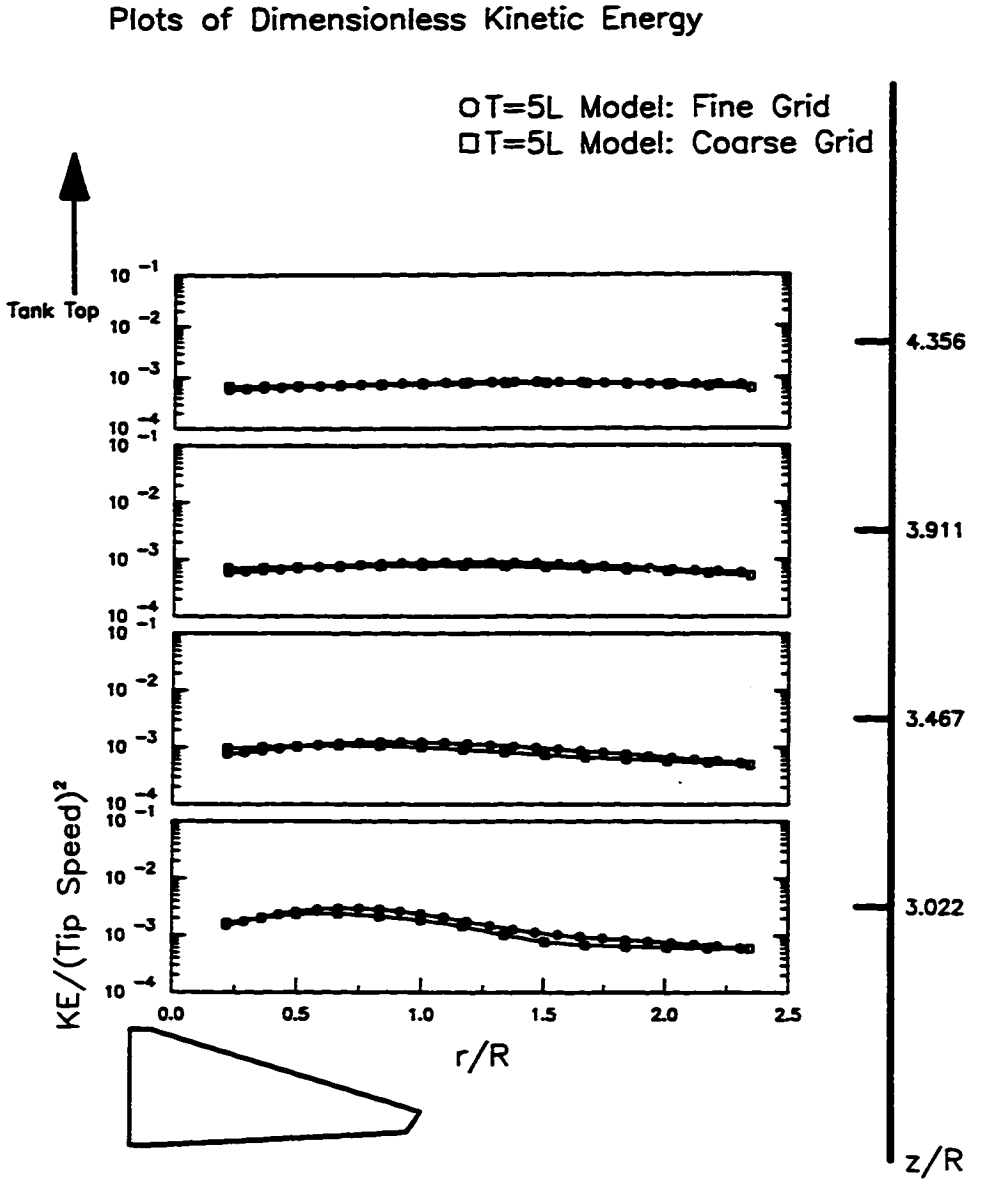

Figure 5.2.44: Effect of Mesh Density on the Turbulent Kinetic Energy for the A310 Foil Impeller above the Impeller Centerline T = 5L

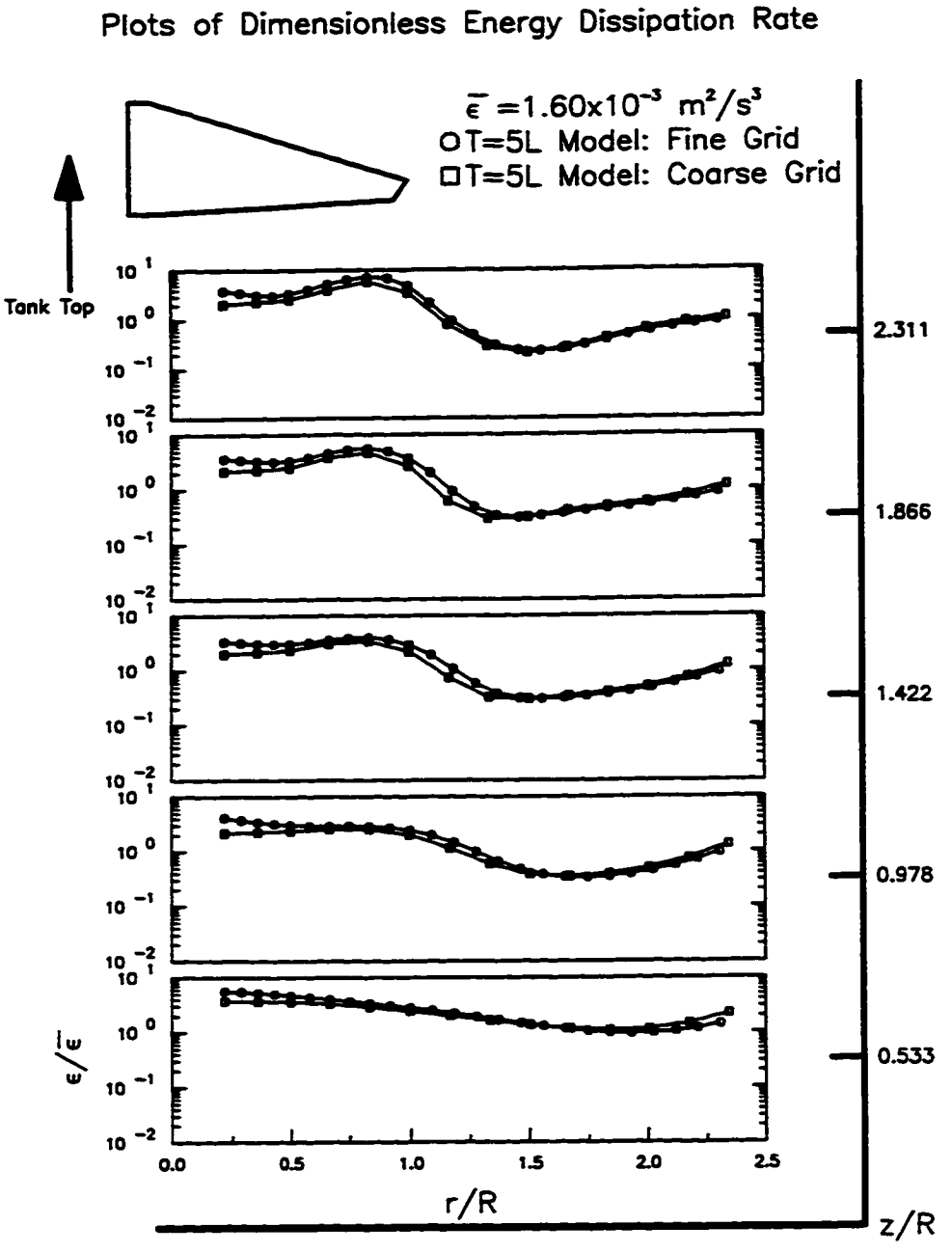

Figure 5.2.45: Effect of Mesh Density on the Turbulent Energy Dissipation Rate for the A310 Foil Impeller below the Impeller Centerline T = 5L

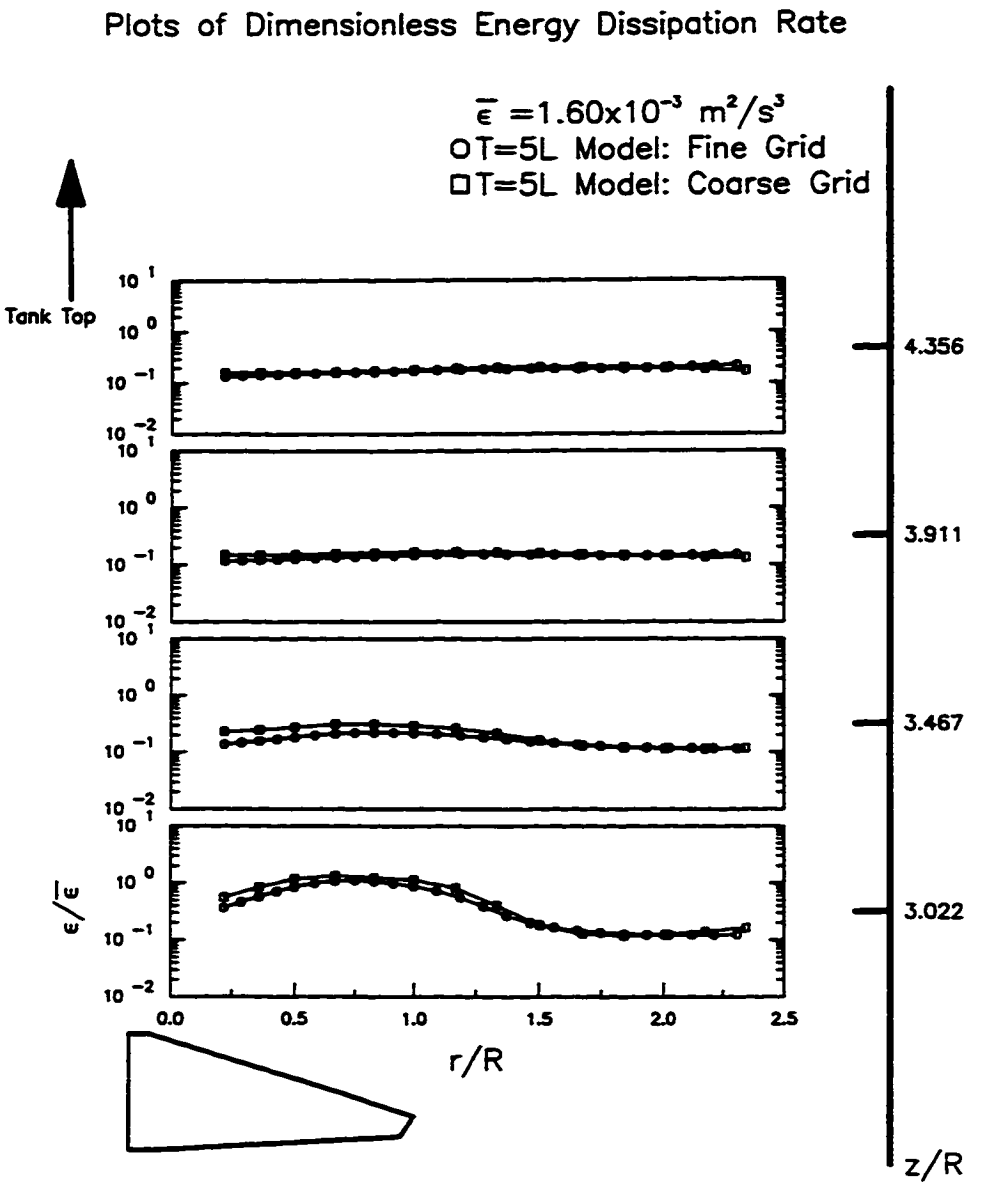

Figure 5.2.46: Effect of Mesh Density on the Turbulent Energy Dissipation Rate for the A310 Foil Impeller above the Impeller Centerline T = 5L

Table 5.2.1: FIDAP Model Boundary and Initial Conditions (The LDV Velocity data, k data, and ε data were fitted with a least squares polynomial and used as FIDAP boundary conditions. These polynomial equations are shown in Appendix C.)

Model	Impeller Boundary	Wall Boundary	Initial Conditions for FIDAP Simulations
A	LDV Velocity Data (See Appendix C)	Velocity = 0	k(Imp. Boundary) = 1000 cm^2/s^2 ε(Imp. Boundary) = 10,000 cm^2/s^3 k(Bulk Region) = 100 cm^2/s^2 ε(Bulk Region) = 1000 cm^2/s^3
B	LDV Velocity Data (See Appendix C)	Velocity = 0	k(Imp. Boundary) = 50 cm^2/s^2 ε(Imp. Boundary) = 100 cm^2/s^3 k(Bulk Region) = 10 cm^2/s^2 ε(Bulk Region) = 50 cm^2/s^3
C	LDV Velocity Data (See Appendix C) k = I * (Velocity)^2 ε = $k^{1.5}$/(D * F) I = Turbulence Intensity = 0.08 A310 = 0.2 Rushton D = Impeller Diameter F = Length Scale Fraction = 0.5 A310 = 0.15 Rushton	Velocity = 0	k(Bulk Region) = 10 cm^2/s^2 ε(Bulk Region) = 50 cm^2/s^3
D	LDV Velocity Data LDV k Data LDV ε Data (See Appendix C)	Velocity = 0	k(Bulk Region) = 10 cm^2/s^2 ε(Bulk Region) = 50 cm^2/s^3

conditions. The effect of these conditions on the turbulent kinetic energy and the energy dissipation rate in the 5L tank are investigated in this section.

Figures 5.2.47 - 5.2.50 show the influence of the different boundary conditions on the turbulent kinetic energy for both the Rushton turbine and A310 foil impeller. For the Rushton turbine, the different boundary conditions do not significantly affect the kinetic energy in the bulk region ($z/R < 1.866$). However in Figure 5.2.47, model C does seem to produce the largest deviation from the experimental kinetic energy results as you approach the Rushton turbine in the bulk region ($z/R \geq 1.866$). In the impeller discharge zone of the Rushton turbine (Figure 5.2.48), the different boundary conditions do produce different kinetic energy results as one approaches the blade tip. Model D produces the best results near the blade tip. This is not surprising since model D incorporates all the turbulence data from the LDV experiments in the boundary conditions. However, all the models seem to perform equally well in the regions closest to the wall.

In Figures 5.2.49 and 5.2.50, models A, B, and D tend to produce similar kinetic energy results above and below the A310 foil impeller centerline. Again, only model C appears to produce the largest deviation from the kinetic energy experimental results in the impeller discharge zone and parts of the bulk region. From the standpoint of the kinetic energy results, model A, B, and D perform equally well for both the Rushton turbine and A310 foil impeller.

Figures 5.2.51 - 5.2.54 show the influence of the different boundary conditions on the turbulent energy dissipation rate for both the Rushton turbine and A310 foil impeller. As can be seen in Figure 5.2.51, models A - D appear to produce similar turbulent energy dissipation rates in the bulk region of the Rushton turbine. However, all four models are unable to predict accurately the experimental energy dissipation rate in this bulk region. The inability of models A- D to predict the experimental energy dissipation rate is probably due to lack of information about the energy contained in the trailing vortices and the inclusion of this energy in the boundary conditions.

In Figure 5.2.52, the energy dissipation rate in the impeller discharge zone, near the blade tip, is very sensitive to the impeller boundary condition imposed. Clearly, model D produces the best result in the region closest to the blade tip. But model D also performs poorly at other

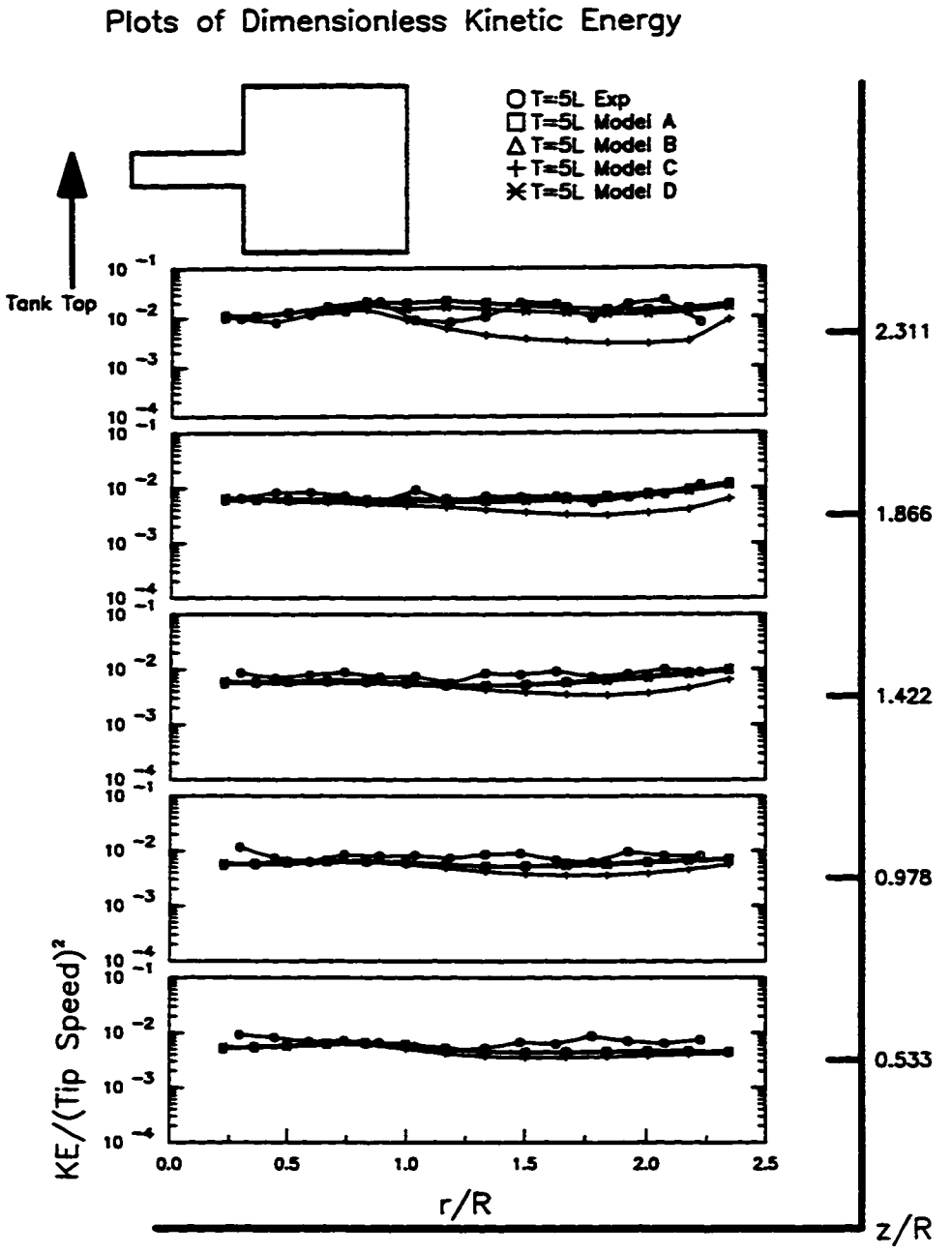

Figure 5.2.47: Influence of Boundary Conditions on the Turbulent Kinetic Energy for the Rushton Turbine below the Impeller Centerline

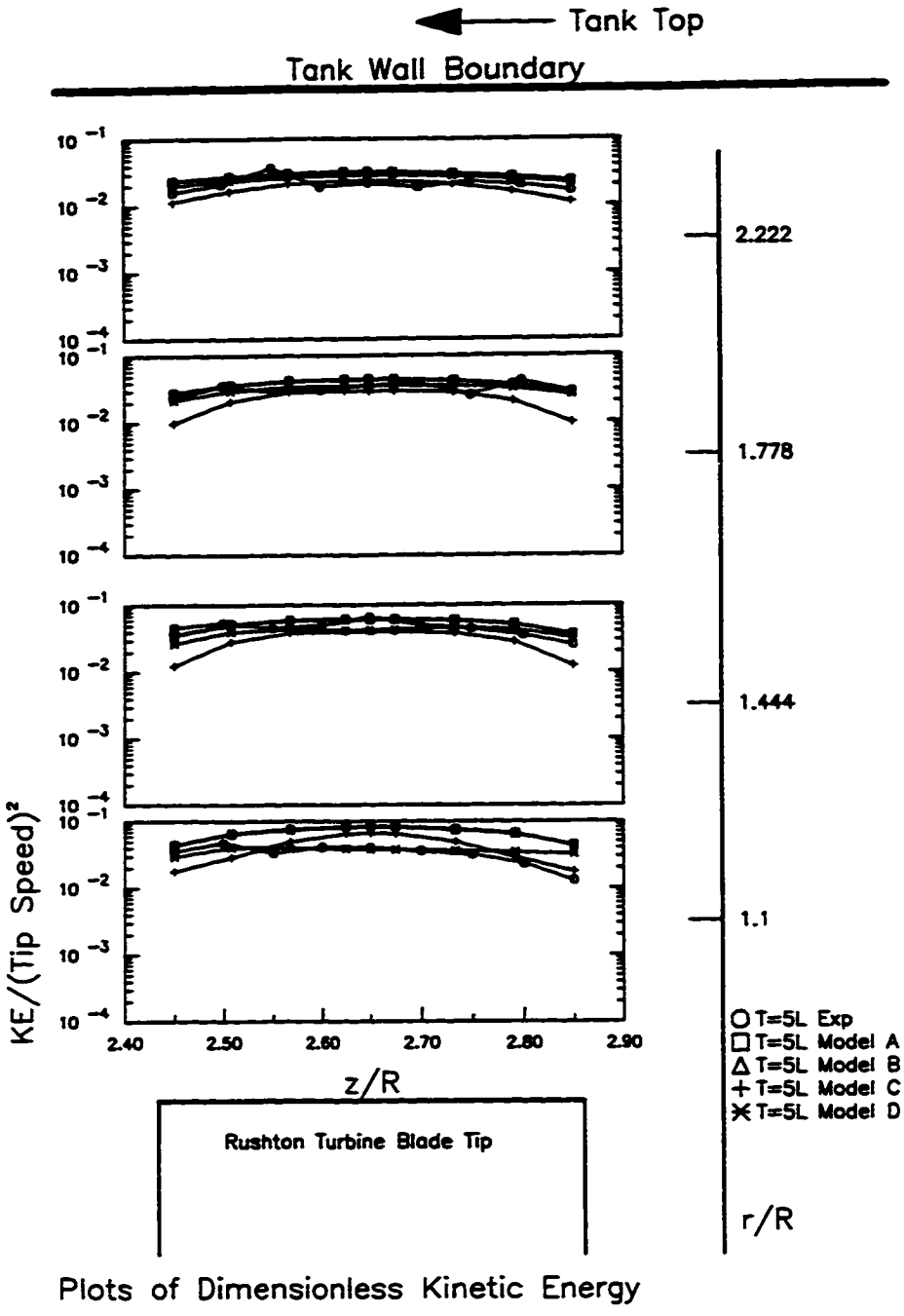

Figure 5.2.48: Influence of Boundary Conditions on the Turbulent Kinetic Energy for the Rushton Turbine in the Impeller Discharge Region

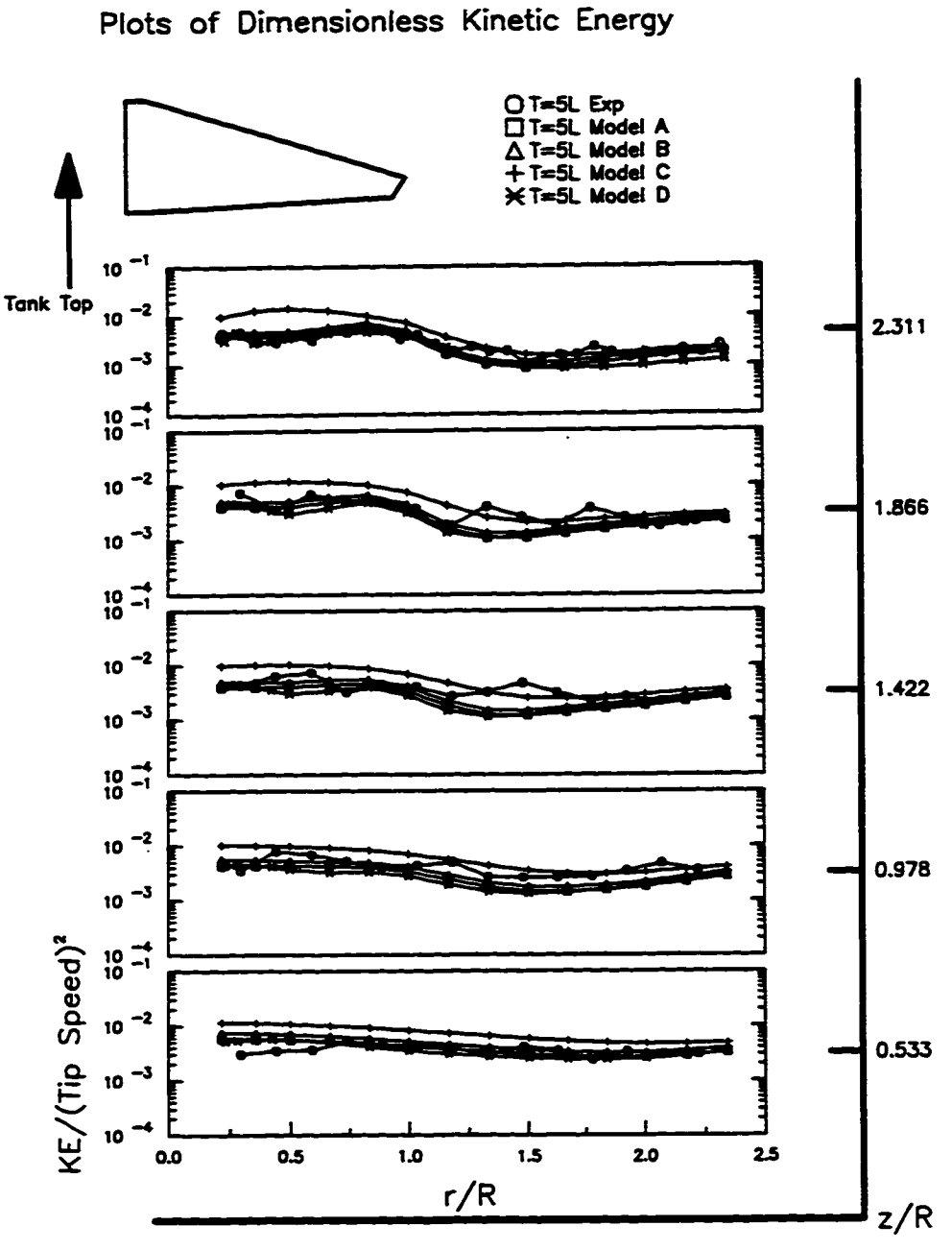

Figure 5.2.49: Influence of Boundary Conditions on the Turbulent Kinetic Energy for the A310 Foil Impeller below the Impeller Centerline

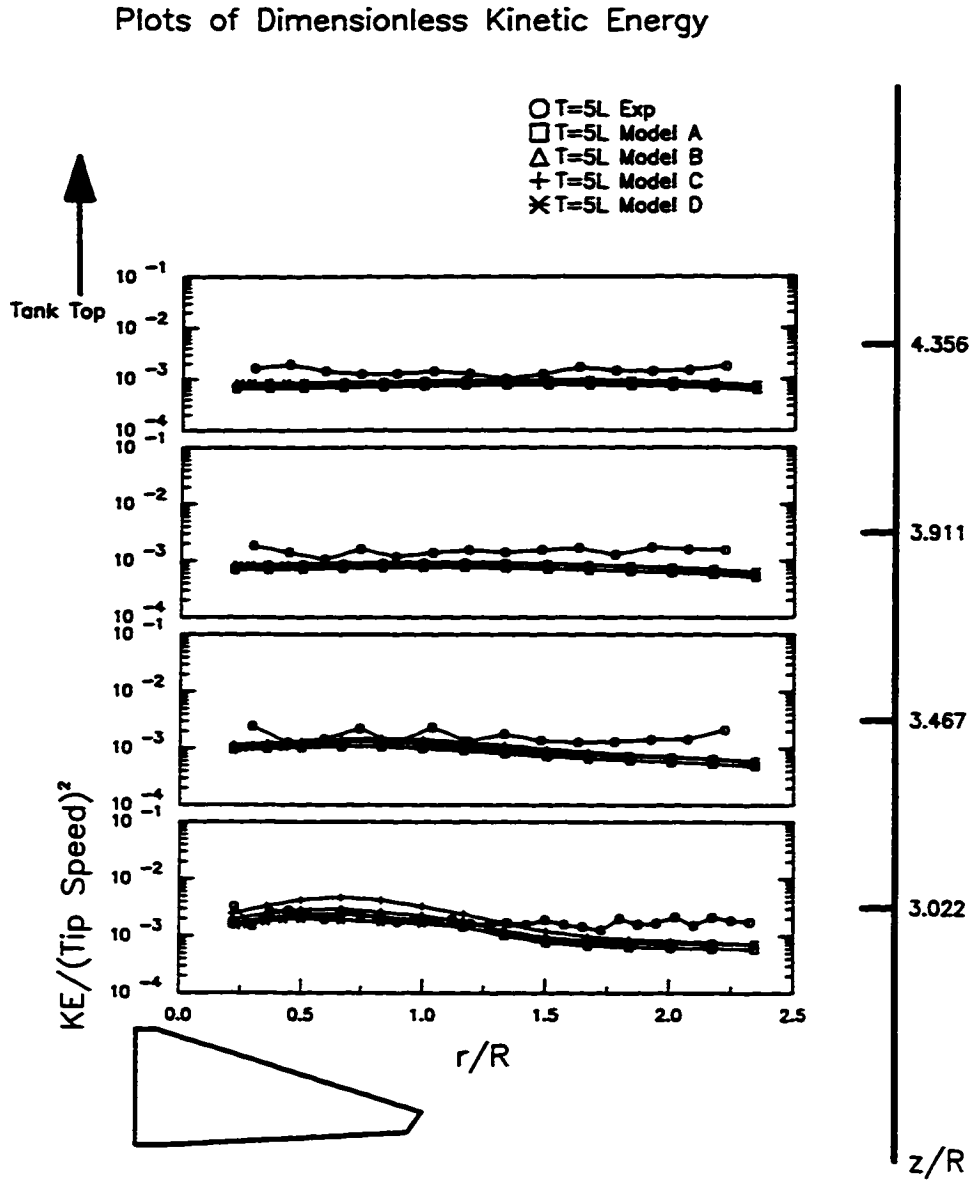

Figure 5.2.50: Influence of Boundary Conditions on the Turbulent Kinetic Energy for the A310 Foil Impeller above the Impeller Centerline

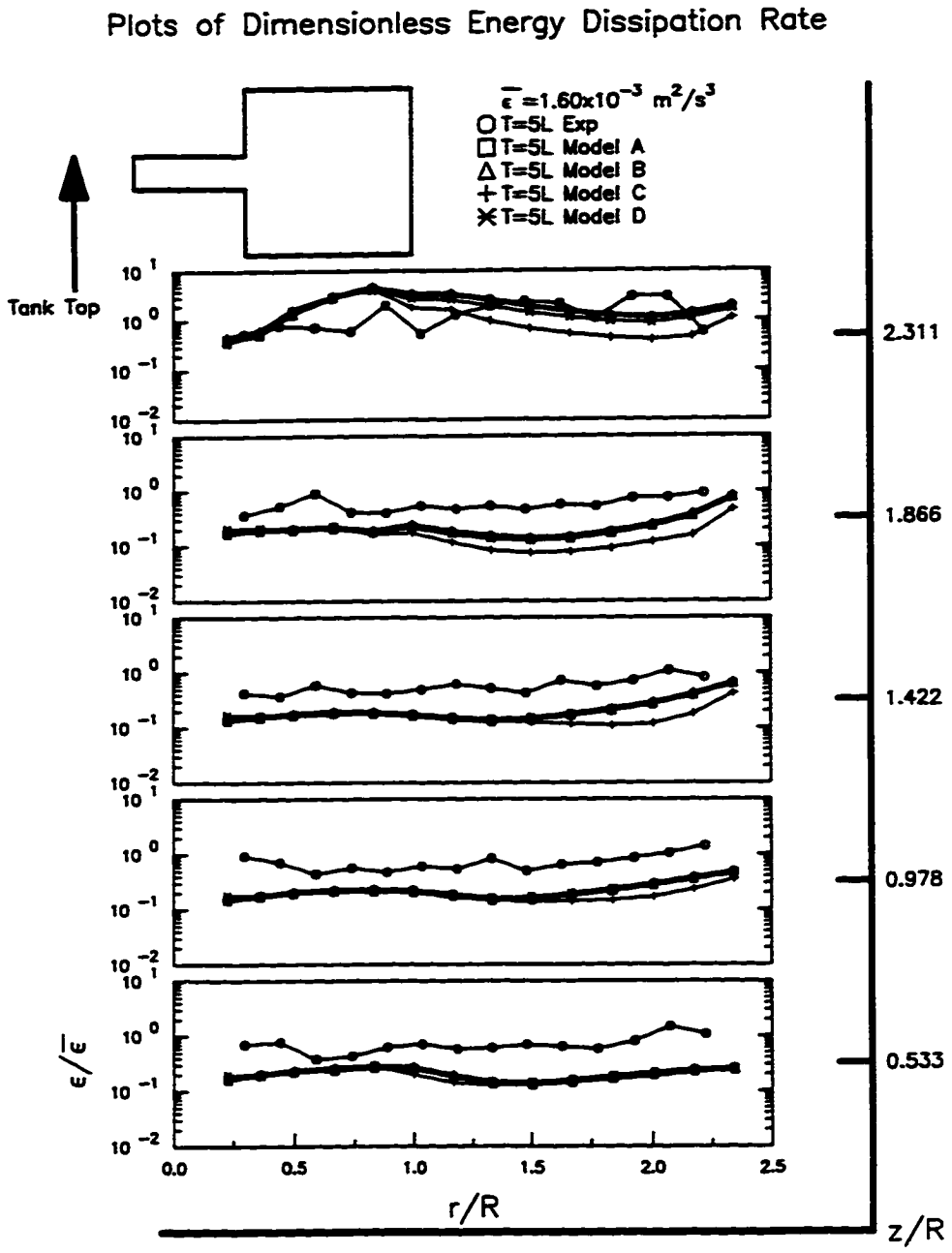

Figure 5.2.51: Influence of Boundary Conditions on the Turbulent Energy Dissipation Rate for the Rushton Turbine below the Impeller Centerline

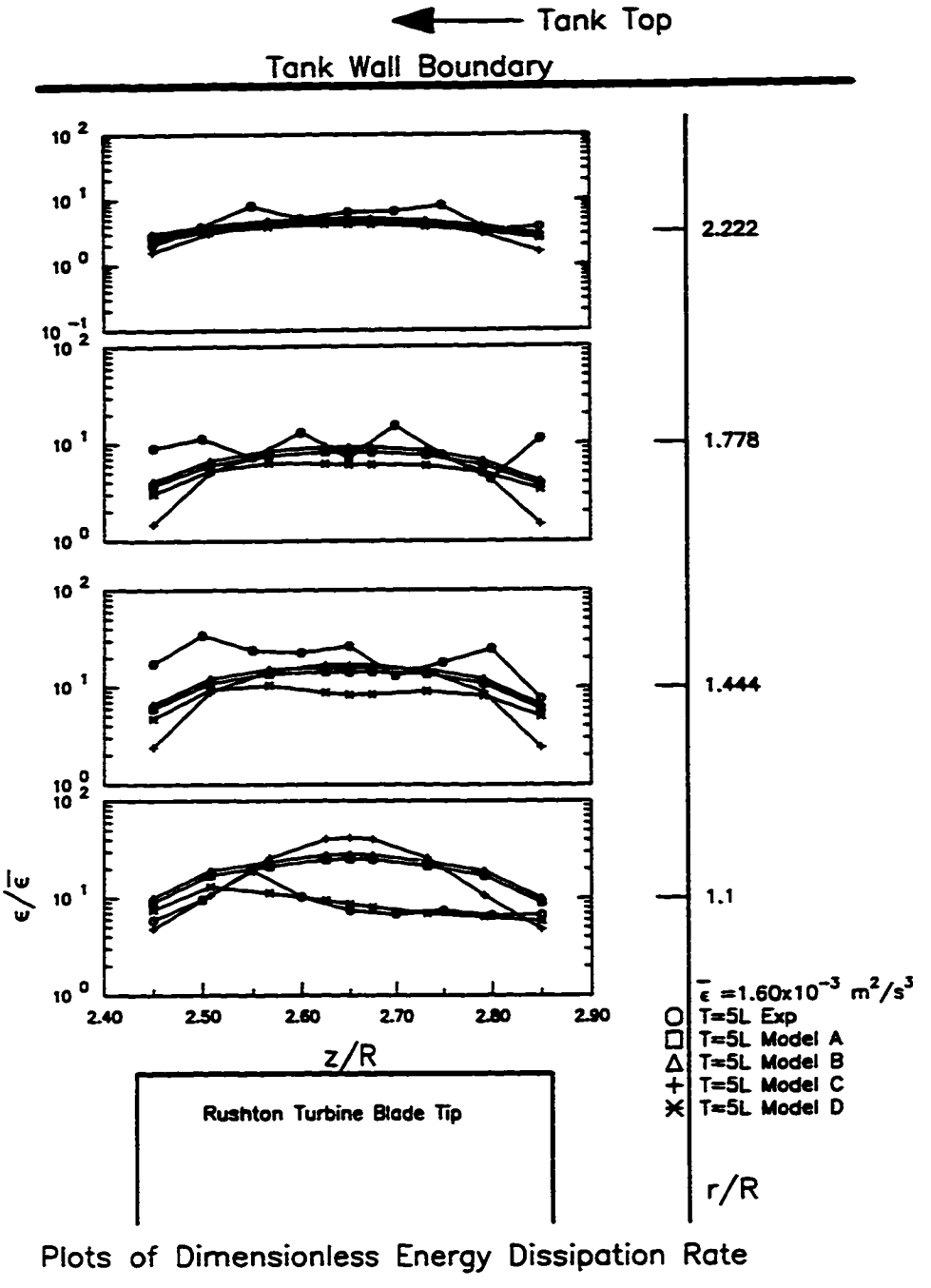

Figure 5.2.52: Influence of Boundary Conditions on the Turbulent Energy Dissipation Rate for the Rushton Turbine in the Impeller Discharge Region

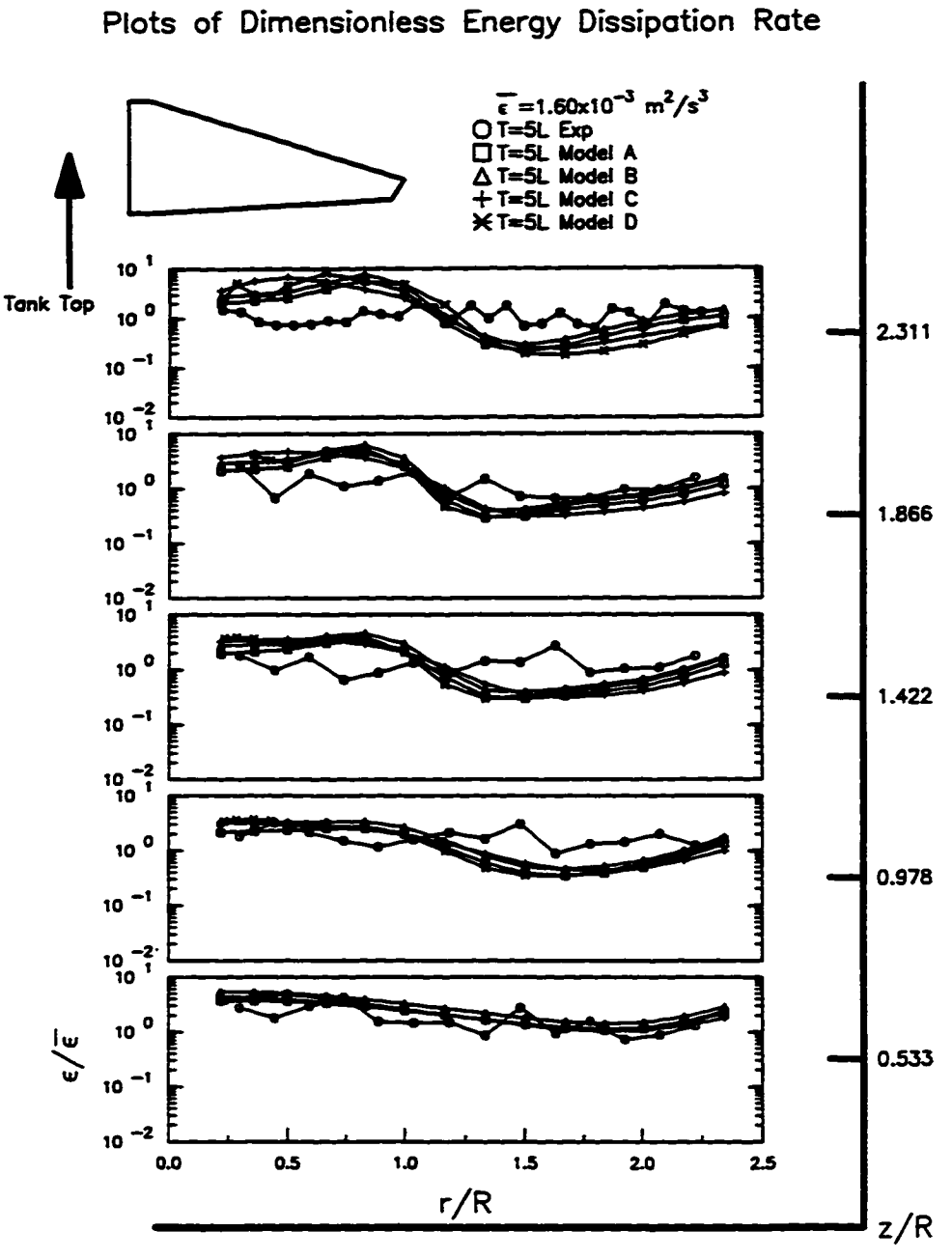

Figure 5.2.53: Influence of Boundary Conditions on the Turbulent Energy Dissipation Rate for the A310 Foil Impeller below the Impeller Centerline

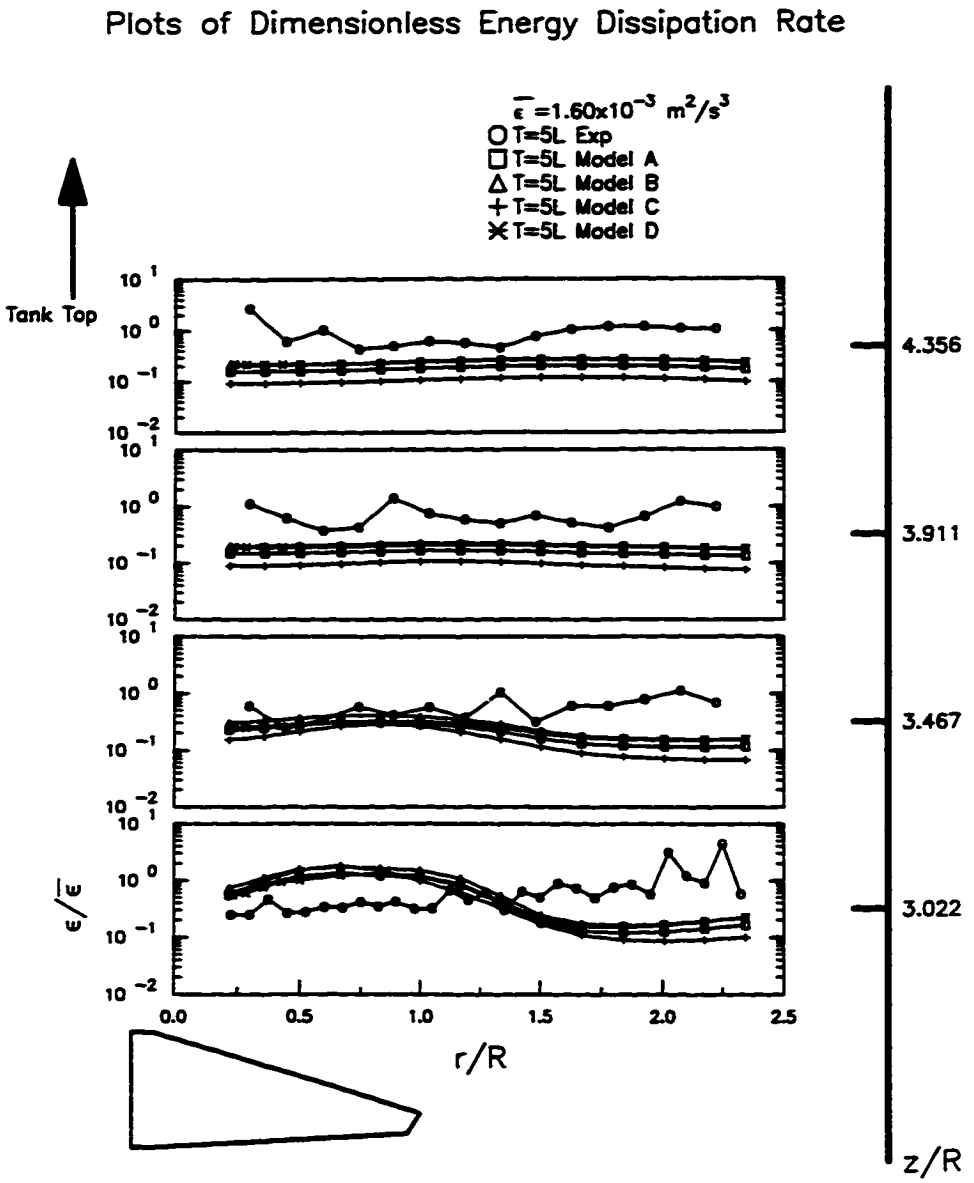

Figure 5.2.54: Influence of Boundary Conditions on the Turbulent Energy Dissipation Rate for the A310 foil Impeller above the Impeller Centerline

locations in the impeller discharge zone. The poor performance of model D in the impeller discharge zone ($1.1 < r/R \leq 1.777$) is probably due to using experimentally measured ε values as part of the boundary conditions. Recall that the experimental ε values were computed without the Reynolds shear stresses. Recall also that the error in calculating the energy dissipation rate without the Reynolds shear stresses is greatest near the impeller blade tip. Because of this error, model D would tend to severely under predict the experimental ε values at other locations in the impeller discharge zone.

In Figure 5.2.52, models A, B, and C appear to over predict the experimental ε values in the region closest to the impeller blade tip and slightly under predict the ε values at the rest of the impeller discharge region. The failure of models A - C to accurately predict the experimental ε values near the blade tip is probably due to the lack of the Reynolds shear stresses in the experimental ε calculation. The inaccuracies of models A - C in the rest of the discharge zone may be due to not including the energy contained in the trailing vortices as part of the boundary conditions.

In Figures 5.2.53 and 5.2.54, models A - D appear to predict the local energy dissipation rate in a similar manner. Typically, all the models seem to over predict the experimental ε values in the impeller discharge zone of the A310 and under predict the ε values in the bulk region and above the impeller centerline. Of the 4 models, model C seems to predict the worst ε values, particularly above the impeller centerline.

5.2.6 Discussion

The FIDAP simulation for the Rushton turbine and A310 foil impeller in a square tank seems to predict the unique spatial distribution of the turbulence fairly well. Clearly, FIDAP was able to show the high energy dissipation rate and kinetic energy in the Rushton turbine discharge zone and the low turbulence values in the bulk region as seen in the LDV experimental results.

In modeling the Rushton turbine in a 5 L and 28 L square tank, FIDAP was able to match the experimental turbulent kinetic energy very well. The model deviated from the experimental

data only at the points located closest to the blade tip. This difference might be due to errors in experimental measurements at those points. However, the FIDAP results for the turbulent energy dissipation rate did not match the experimental results with the Rushton turbine as well as the kinetic energy results. In the impeller discharge region, the model over predicted the results at r/R = 1.1 and slightly under predicted the results at r/R = 1.444, 1.778, and 2.222. In the bulk region, FIDAP under predicted the experimental data at all locations except for z/R = 2.311 where FIDAP slightly over predicted the experimental results. There are four possible reasons why FIDAP did not match the experimental local energy dissipation rate values:

1) As postulated in Section 5.1, the local energy dissipation rates are influenced by the energy contained in the trailing vortices. Since it is presently very difficult to model the trailing vortices with FIDAP, the model would tend to under predict the experimental energy dissipation rate values.

2) The accuracy of the results produced by FIDAP is influenced by the size of grid used to discretize the flow domain. Finer grid mesh may improve the accuracy of model to fit the experimental results in certain regions of the flow domain.

3) The method used to calculate ε experimentally is not accurate at the turbulence intensities typically found in stirred tanks.

4) Leaving out the Reynolds shear stresses in the computation of ε near the Rushton blade tip induces errors in the accuracy of the measured ε.

Reason # 1 states that the FIDAP model will under predict the LDV experimental results in the 5 L and 28 L tanks because the model does not incorporate the transfer of energy from the trailing vortices to the small scale eddies. In Section 5.1, this author speculated that the reduction in the local energy dissipation rate values with increasing tank size is due to a decreasing influence of the energy contribution from the trailing vortices to the small scale eddies with tank size. If

there were no trailing vortices in the flow domain, then the local energy dissipation rate would not be a function of tank size since the power per unit volume is constant with tank size. Therefore, if we compare the FIDAP results of the local energy dissipation rates between the 5 L and the 28 L tanks and observe no difference between the two simulations, then the assumption that the trailing vortices influence the rate of energy dissipation at the small scale eddies is plausible. As can be seen in Figures 5.2.31 and 5.2.32, the FIDAP model predicts no significant change in the local energy dissipation rate with tank size. Figures 5.2.31 and 5.2.32 seem to confirm the assumption that the trailing vortices influence the rate of energy dissipation at the small scale eddies.

In Section 5.2.4, the influence of the mesh density on the turbulent kinetic energy and the energy dissipation rate was explored. The result of increasing the mesh density six times showed only a slight improvement in the model performance. Improvements were made in both the prediction of the kinetic energy and the energy dissipation rate in the impeller discharge region and in the bulk region near the impeller. However, the penalty for reducing the grid size comes in increasing the time it takes to obtain a converged solution. By increasing the mesh density six times, the time to reach a converged solution increased from 7 hours to 10 days on an HP 715/75 workstation. The resulting increase in computation time does not justify the improved performance since the improvements in the prediction of the turbulent quantities were not that significant.

Reason # 3 suggests that since there are only indirect methods in determining the turbulent energy dissipation rate, these methods might be in error under certain circumstances. One possible error has to do with whether Taylor's frozen field hypothesis is valid when the turbulence intensity is greater than 5 percent. Taylor's frozen field hypothesis has to do with defining spatial variations in turbulence with temporal variations. Taylor's hypothesis states that the fluctuations at a fixed point of a homogeneous turbulent flow with a constant mean velocity in one direction may behave as if the whole turbulent flow field passes that point with a constant mean velocity. This assumes that the mean velocity is much greater than the turbulent fluctuating velocity at that point.

Using this hypothesis, experimental estimates of the turbulent eddy size can be made with

time variations of the turbulent flow instead of spatial variations. However, Taylor (1938) proposed this hypothesis for a case in which the magnitude of the turbulent fluctuating velocity was 5 percent of the mean velocity. In mixing tanks, the fluctuating velocity can be as much as 50 percent of the mean velocity. Technically under these conditions, Taylor's hypothesis is not valid. Consequently, the integral length scales in Equation 3.8 (energy dissipation rate equation) would be in error. Unfortunately, Taylor's hypothesis must be used because it is considerably easier to measure time variations with a single probe than spatial variations with several probes.

And finally, reason # 4 was described in detail in Section 5.1.1. The FIDAP model will tend to over predict the energy dissipation results near the impeller discharge outlet since the experimental measurements of ε are missing the Reynolds shear stresses. Ito et al (1974, 1975) found the magnitude of the Reynolds shear stress the highest near the impeller discharge outlet. Consequently, the local ε values in this region would deviate greatly from the true value.

The turbulent kinetic energy and energy dissipation rate generated by FIDAP for the A310 foil impeller in the 5L and 28L square tank seem to match the experimental results fairly well. At most locations, the simulation was able to predict on average the local energy dissipation rate values. As can be seen in Figure 5.2.33 and 5.2.35, part of the modeled results would be above the experimental measurements and part would be below the experimental values. However, for both the kinetic energy and energy dissipation rate, FIDAP under predicted the experimental values near the tank surface. (Figures 5.2.34 and 5.2.36). One possible reason for this under prediction might be due to some limitations of the k-ε model. Another possible reason could be that not enough boundary conditions were specified at the walls which surround the bulk region. And finally, the measured turbulence may not have been calculated accurately since it is based on Taylor's frozen field hypothesis.

In simulating both the Rushton turbine and the A310 foil impeller at T = 5L and T = 28L, a free surface was not included. Since the LDV measurements were done in tanks where a free surface exists, one might expect the omission of a free surface would introduce some errors to the FIDAP simulations. These errors would include higher local kinetic energy and energy dissipation rate values above the impeller centerline and a deviation in the trajectory of the velocity vectors. However, the trajectory of the velocity vectors from the FIDAP simulation

seems to match the experimental results well (Figures 5.1.5, 5.1.6, 5.2.5, 5.2.11). More importantly, FIDAP simulation of the local kinetic energy above the impeller centerline matched the LDV experimental results very well (Figures 5.2.16, 5.2.19, 5.2.22, 5.2.24).

The FIDAP simulation of the local energy dissipation, however, under predicts the LDV experimental results above the impeller centerline (Figures 5.2.26, 5.2.29, 5.2.34, 5.2.36). This result in the numerically computed local energy dissipation rate contradicts the expected higher values in the energy dissipation rate due to the presence of wall. The difference between the experimentally measured and the numerically simulated energy dissipation rate above the impeller centerline are not due to the absence of a free surface form the FIDAP simulation. It is likely that the errors are due to the problems outlined in points 1-4. Overall, the omission of the free surface from the FIDAP simulation did not impact the simulation performance.

5.3 Summary

The study of the fluid mechanics generated in a square tank with a Rushton turbine or an A310 foil impeller for G_m = constant has demonstrated the following:

- The impeller power number, N_P, and flow number, N_Q, were found to be a function of impeller type and not a function of tank size. This is consistent with dimensional arguments.

- The mean velocities and rms turbulent fluctuating velocities are proportional to the impeller tip speed. The turbulent kinetic energy per unit mass is proportional to the square of the impeller tip speed.

- The dimensionless rms turbulent fluctuating velocity and the dimensionless turbulent kinetic energy are lower for the A310 fluid foil impeller than for the Rushton turbine.

- The rms turbulent fluctuating velocity has been shown to increase with tank size as $D^{1/3}$. As expected, the kinetic energy also increased with tank size as $D^{2/3}$. This was true regardless of impeller type.

- The local energy dissipation rate for the Rushton turbine was found to decrease with increasing tank size as D^{-x}

  where x = .70 in bulk region between T = 5L and T = 28L
  x = .44 in bulk region between T = 28L and T = 560L
  x = .85 in impeller region between T = 5L and T = 28L
  x = .78 in impeller region between T = 28L and T = 560L

- The local energy dissipation rate for the A310 fluid foil impeller did not vary with tank size.

- The local energy dissipation rate in the impeller discharge zone of the A310 foil impeller was found to be much lower than the local energy dissipation rate produced in the impeller discharge zone of the Rushton turbine.

- The root mean square turbulent fluctuating velocity in the impeller discharge zone did not vary with impeller type or tank size when it was normalized by $N_p^{0.5}ND$.

- FIDAP accurately predicted the mean velocity flow patterns for both the Rushton turbine and the A310 foil impeller in the 5L and 28L square tanks.

- FIDAP also accurately predicted the turbulent kinetic energy for both impeller types in the 5L and 28L square tanks.

- FIDAP was unable to match the experimental results of the local energy

dissipation rate for the Rushton turbine. However, FIDAP was able to show the spatial variations of the local turbulent energy dissipation rate (i.e. high regions in the impeller discharge zone and low regions in the bulk zone) in the 5L and 28L square tanks.

- FIDAP was able to match on average the experimental results of the local energy dissipation rate for the A310 foil impeller in the 5L and 28L square tanks (i.e. some of the model predictions were higher than the experimental results and some were below the experimental results).

- FIDAP clearly predicted the difference in the turbulence produced by the Rushton turbine and the A310 foil impeller.

- Some improvement in the FIDAP model performance was accomplished by increasing the mesh density 6 times. However, the marginal improvement in the accuracy of the model was more than offset by the increase in computational resources.

- FIDAP clearly confirmed that with constant power per unit volume, the local turbulent kinetic energy is proportional to the impeller tip speed squared and increases with increasing tank size regardless of impeller type.

- FIDAP also showed that with constant power per unit volume, the local turbulent energy dissipation rate is constant with increasing tank size regardless of impeller type.

5.4 Implication of Fluid Mechanics Results on Flocculation Performance

Several experiments have been done by previous investigators which showed that an inverse relationship exists between the maximum stable floc size developed during the flocculation process and Camp & Stein's (1943) mean velocity gradient (G_m) (Thomas, 1964; Parker et al., 1972; Francois, 1987; Sonntag & Russel, 1987; Tambo & Francois, 1991; Kusters, 1991). However, experiments done by Oldshue & Mady (1978), Clark & Fiessinger (1991), and Clark et al. (1994) have shown that maintaining G_m = constant with increasing tank size does not produce similar flocculation performance. In fact, all three reports indicate a tendency for the flocculation performance to decrease with increasing tank size. Other investigators have also found that with constant G_m, the flocculation performance varies with impeller type (Drobny, 1963; Patwardhan & Mirajgaonkar, 1970; Hanson & Cleasby, 1990; Clark et al., 1994; Sajjad & Cleasby, 1995).

This decrease in flocculation performance may be due to an increase in the breakup of floc particles with increasing tank size rather than a decrease in the agglomeration of floc particles. Researchers know that the breakup of floc particles ultimately determines the performance of the flocculation process since there is experimental evidence of a maximum stable floc size. The maximum stable floc size occurs when the agglomeration rate is balanced by the breakup rate of the floc particle. Typically, this balance occurs at time scales smaller than the time given for flocculation in the water treatment process. Therefore, something must have changed in the fluid mechanics to cause a change in the breakup rate of the floc particles.

The results of both the LDV experiments and the FIDAP simulations suggest that by maintaining G_m=constant, the rms turbulent fluctuating velocity and turbulent kinetic energy increased with increasing tank size regardless of impeller type. Those same LDV experiments also indicate that for the Rushton turbine, the local energy dissipation rate decreases with increasing tank size, and for the A310 foil impeller, the dissipation rate remains the same. FIDAP showed that by maintaining G_m constant, the local energy dissipation rate does not vary with tank size regardless of impeller type. These results seem to indicate that if floc breakage is increasing with tank size, it could be due to the difference between the turbulent fluctuating velocities across

the aggregate diameter and not the local energy dissipation rate.

Some researchers may argue that the difference between the turbulent fluctuating velocities across the aggregate diameter and the local energy dissipation rate are related to each other if local isotropic conditions exists (Delichatsios & Probstein, 1975; Tambo & Watanabe, 1979; Kusters, 1991). Batchelor (1953), Tennekes and Lumley (1972), and Hinze (1973) mentioned that when the Reynolds number is large, the small scale structure of turbulence tends to be independent of any orientation effects introduced by the large scale motion. Therefore, local isotropy at the small scale can be assumed. This range of scales of turbulence where local isotropy exist is called the Kolmogoroff universal equilibrium range. At these small scales of motion, the length scales and velocity scales can be uniquely defined by the energy dissipation rate in the inertial sub-range and by both the kinematic viscosity and the energy dissipation rate below the Kolmogoroff microscale.

In developing the relationship between maximum floc size and G_m, researchers assumed that the dynamics of agglomeration and breakup of particles occur at scales of motion in the universal equilibrium range. Saffman and Turner (1956) showed that G_m is related to the energy dissipation rate at the small scale eddy size when the turbulence is isotropic. If agglomeration and breakup of particles occurred at these scales, then the resulting particle size distribution should not be a function of the flocculator geometry. The effects of flocculator geometry such as tank size, impeller type, and tank shape only influence the large scales of motion. However, if breakup occurred at scales where the flow regime is anisotropic or at scales outside the universal equilibrium range, then the maximum floc size cannot be uniquely described by G_m and can be influenced by flocculator geometry.

During emulsification, Konno et al. (1983) and Chang et al. (1981) displayed photographic evidence that a large portion of the oil droplets was broken behind the Rushton turbine blade. The breaking drops appeared to follow the outward flow along the impeller blade. Hsu and Glasgow (1983) also displayed photographic evidence that particle breakup occurred in the impeller discharge zone of the Rushton turbine. The breakage event occurred in the immediate vicinity of the impeller blade tip. In the Hsu and Glasgow (1983) study, the fragmented particles seem to break in the direction of the mean velocity. This regularity in the

direction of drop elongation or particle fragmentation would indicate that breakup occurred in the anisotropic turbulent region. Experimental and modeling results presented by Konno et al. (1983) and Chang et al. (1981) and Hsu and Glasgow (1983) might suggest that the rms turbulent fluctuating velocities in regions where the flow regime is anisotropic could be important in the breakup of floc particles. Therefore, an increase in the rms fluctuating velocity with increasing tank size, as shown in this study, could explain why investigators have seen a degradation in flocculation performance with increasing tank size.

If the rms turbulent fluctuating velocity in the regions of the tank where the turbulent flow is anisotropic (i.e. the impeller discharge zone) is important in the breakup of floc particles, then the population balance model (Equation 4.17) should describe the dynamics of particle breakup. In Equation 4.17, the particle breakup frequency, k_b (Equation 4.15), is a function of the particle circulation frequency into the impeller discharge zone, impeller power number, tip speed, floc diameter, fluid properties, and vessel geometry. It is not a function of the energy dissipation rate at the small scales of fluid motion. If the population balance model is going to show the correct response to tank size or impeller type, then k_b must behave in the following manner:

Increase tank size $\rightarrow$increase k_b

Change impeller type from A310 foil to Rushton turbine $\rightarrow$increase k_b

The agglomeration part of the population balance model (Equation 4.7) is assumed not to change with tank size. Since the primary particles are typically much smaller than the Kolmogorov microscale, the relative particle velocity can be described by the energy dissipation rate. Because the power per unit volume is kept constant with increasing tank size, the energy dissipation rate should not change with tank size. Therefore, the rate of particle agglomeration should also not vary with tank size.

However, with regard to the breakup frequency, recall Equation 4.15:

$$k_b(d) = C_1 N_Q N \, erfc[\, C_3/(N_P^{0.5} N D \rho^{1/2} d^{1/2}) \,]$$

Substituting the experimental operating conditions for the flocculation experiments (Table 3.3.1) for a given floc diameter, the breakup frequency was determined for each tank size and impeller type. In Equation 4.15, C_1, C_3, and the fluid density were set to 1. This is shown in Figure 5.4.1. As can be seen in Figure 5.4.1, k_b increases as the tank size increases. Figure 5.4.1 also shows that k_b is higher for the Rushton turbine than for the A310 foil impeller. These two trends occurred regardless of particle size. Based on the behavior of k_b with tank size and impeller type, the population balance model should display sensitivity to tank size and impeller type. Moreover, the population balance model may confirm that floc breakup has more to do with the turbulent fluctuating velocity across the particle diameter in the regions of the tank where the turbulence is anisotropic. The behavior of the resulting steady state particle size distribution and the population balance model performance will be discussed in chapter 6.

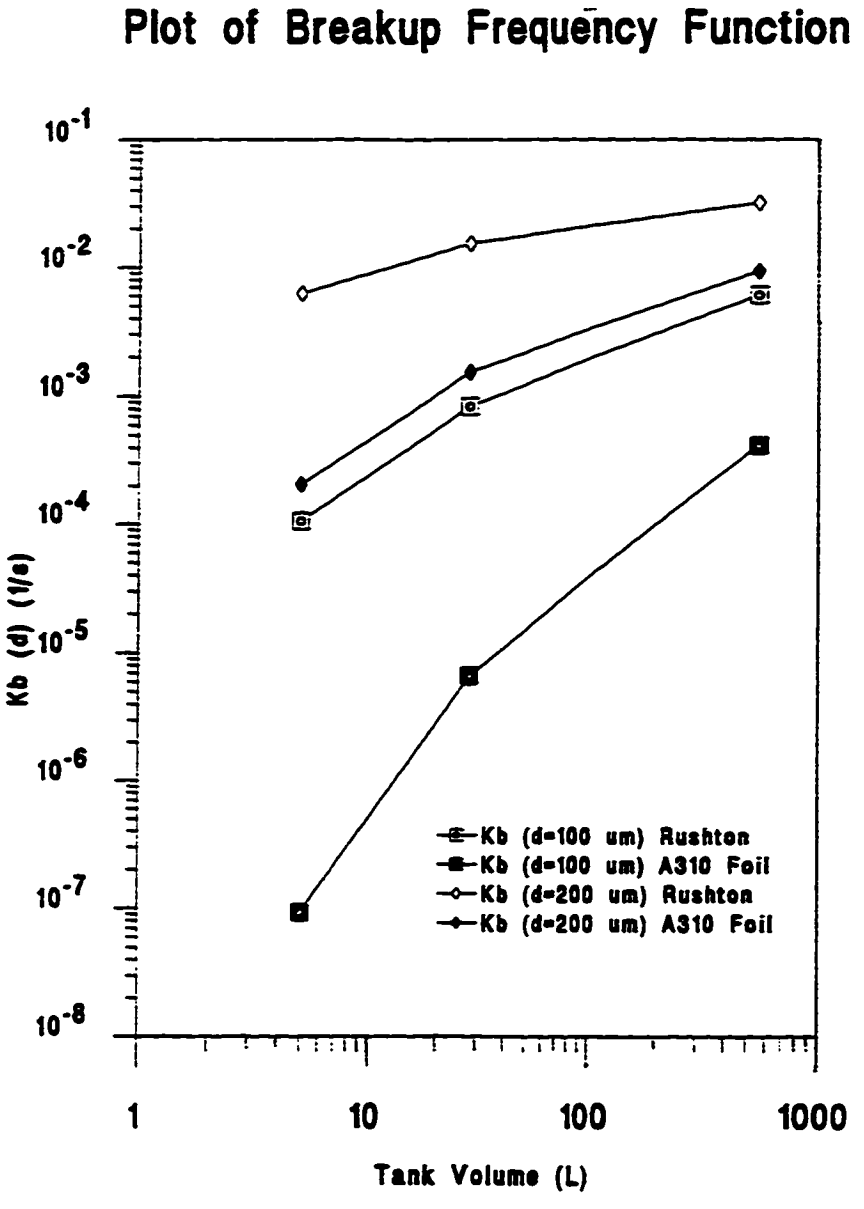

Figure 5.4.1: Plot of Floc Breakup Frequency Function, d = floc diameter

6.0 FLOCCULATION IN STIRRED SQUARE VESSELS

6.1 Flocculation Experimental Results

6.1.1 Initial Particle Size Distribution

The initial particle size distribution was determined using the microscopic photographic technique discussed in Section 3.5. Figure 6.1.1 displays the initial cumulative particle size distribution measured in the rapid mixer/560L tank immediately after the rapid mix stage. As can be seen in Figure 6.1.1, the initial particle size ranges from .5μm to 5μm. The volume mean diameter and standard deviation were found to be 3.13μm and 1.09μm respectively. These values are the averaged quantities of six experimental runs (Figure 6.1.2). As shown in Figure 6.1.2, the initial particle size distribution was fairly consistent from one experiment to another.

6.1.2 Influence of Tank Size on Particle Size Distribution

Figures 6.1.3 and 6.1.4 display the particle size distribution and the cumulative particle size distribution respectively for the Rushton turbine in the 5L, 28L, and 560L tank size after 30 minutes of flocculation. In Figure 6.1.3, the particle size distribution curve is the derivative of the cumulative particle size distribution shown in Figure 6.1.4. Phi is the cumulative particle volume frequency and d_p is the particle diameter. The values for the cumulative particle volume frequency are derived assuming spherical particles. In Figure 6.1.3, the area under the curves between two particle size bins represents the volume of particles within that bin size.

As can be seen in Figure 6.1.4, the cumulative particle size distribution appears to shift to the left with increasing tank size. This shift suggests that floc particles are being fragmented to smaller particles with increasing tank size. The shift to smaller particles occurred even though G_m was constant for the three tank sizes.

In Figure 6.1.3, the particle size distribution curve clearly shows the increase in frequency of the smaller particles with increasing tank size. This shift to smaller particle sizes with increasing tank size was true regardless of the impeller type used. Figures 6.1.5 and 6.1.6 display the particle size distribution and the cumulative particle size distribution respectively for the A310

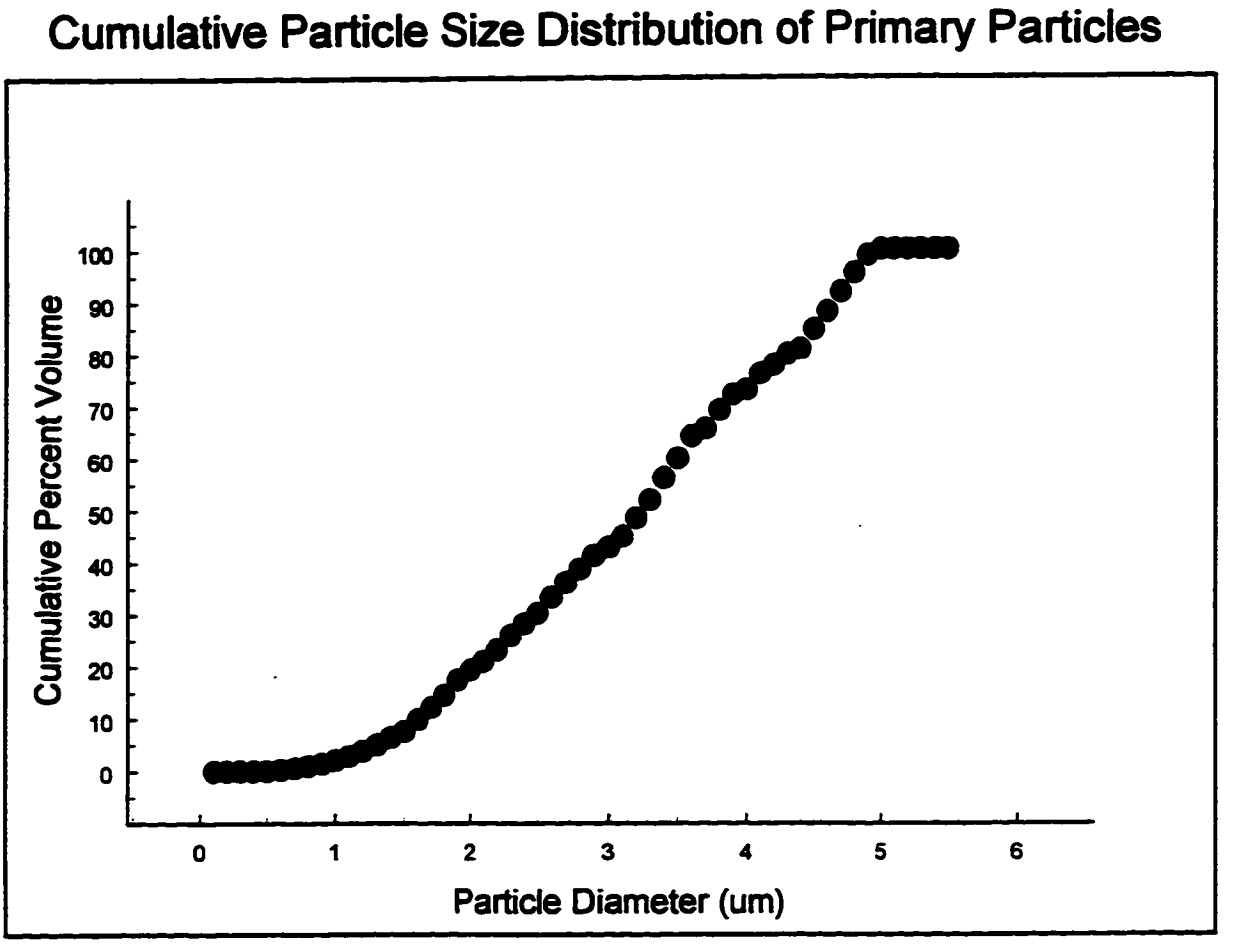

Figure 6.1.1: Initial Cumulative Particle Size Distribution

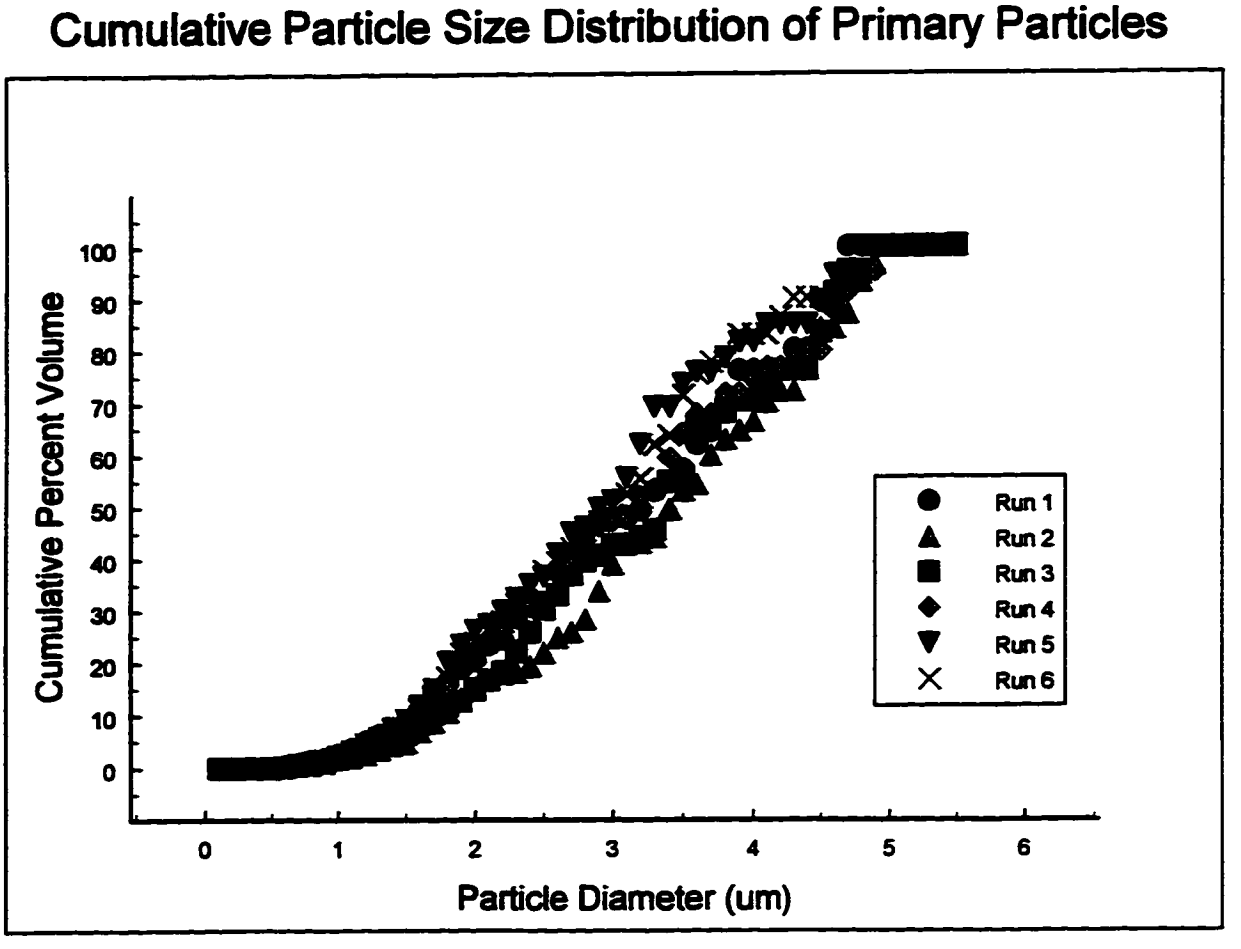

Figure 6.1.2: Reproducibility of Initial Cumulative Particle Size Distribution

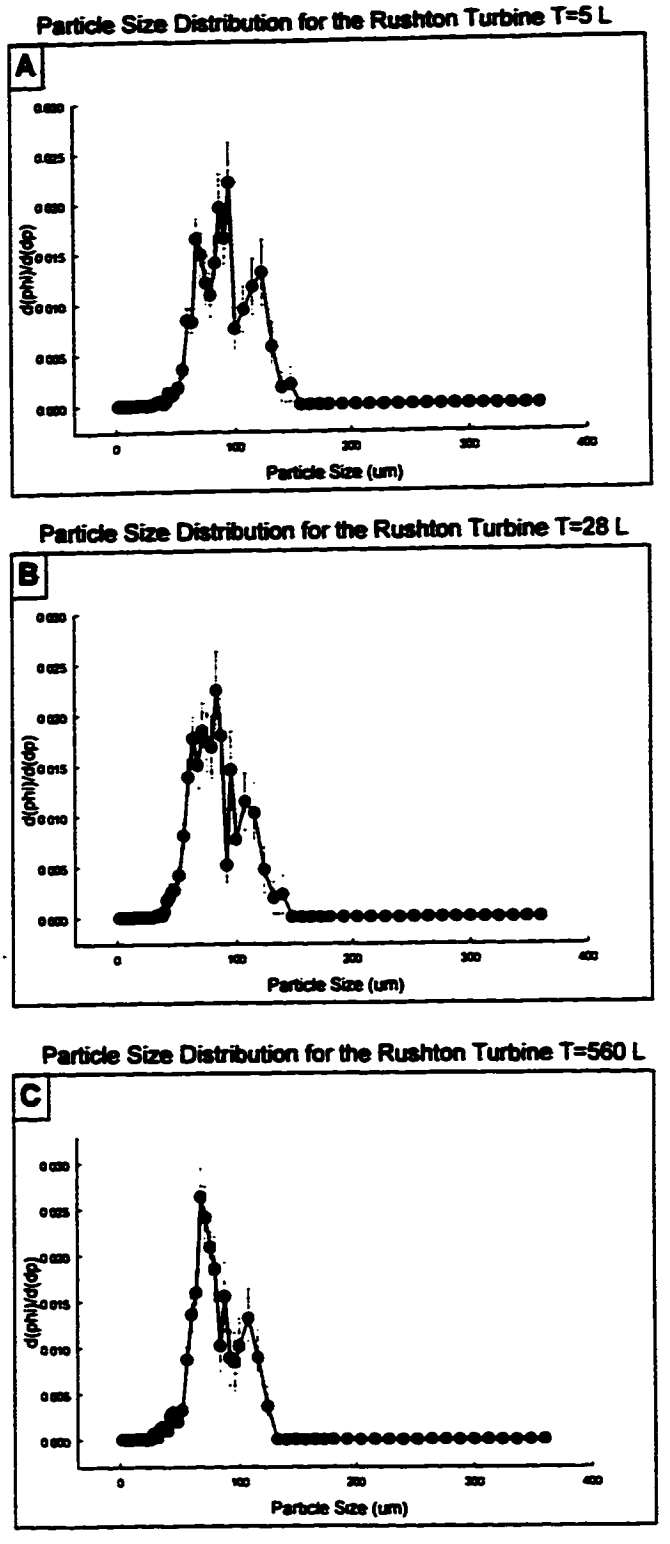

Figure 6.1.3: Particle Size Distribution with the Rushton Turbine after 30 Minutes of Flocculation: Effect of Tank Size A) T = 5L B) T = 28L C) T = 560L

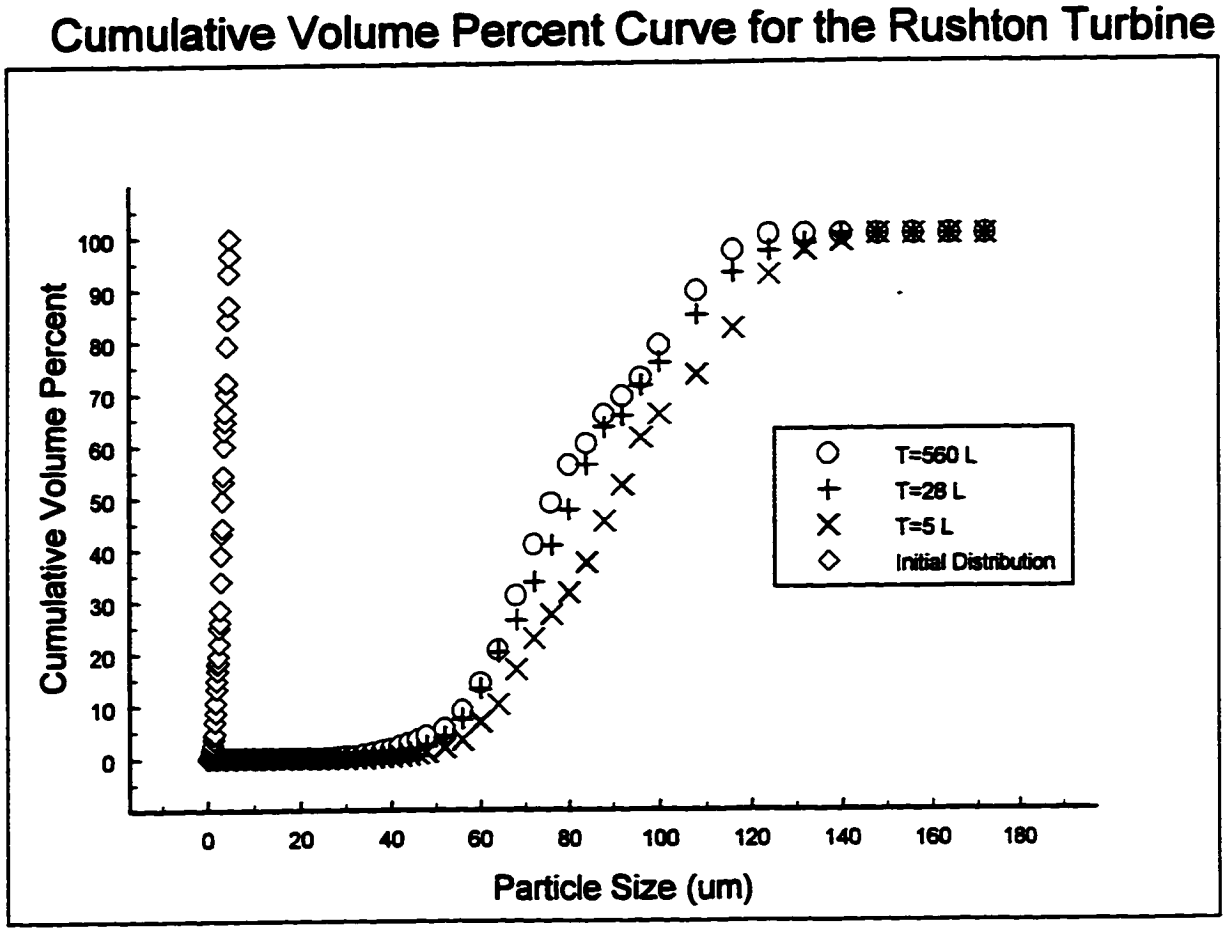

Figure 6.1.4: Cumulative Particle Size Distribution with the Rushton Turbine after 30 Minutes of Flocculation: Effect of Tank Size

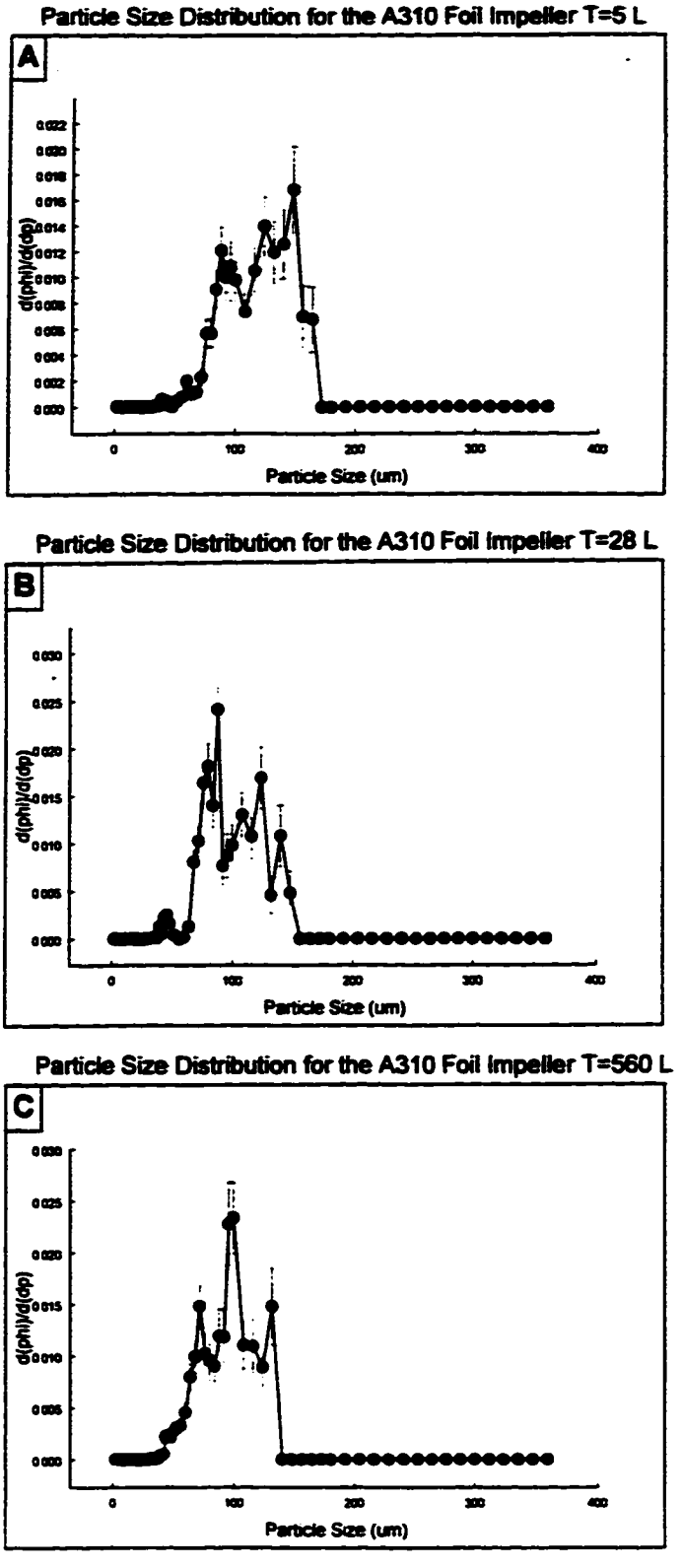

Figure 6.1.5: Particle Size Distribution with the A310 Foil Impeller after 30 Minutes of Flocculation: Effect of Tank Size A) T = 5L B) T = 28L C) T = 560L

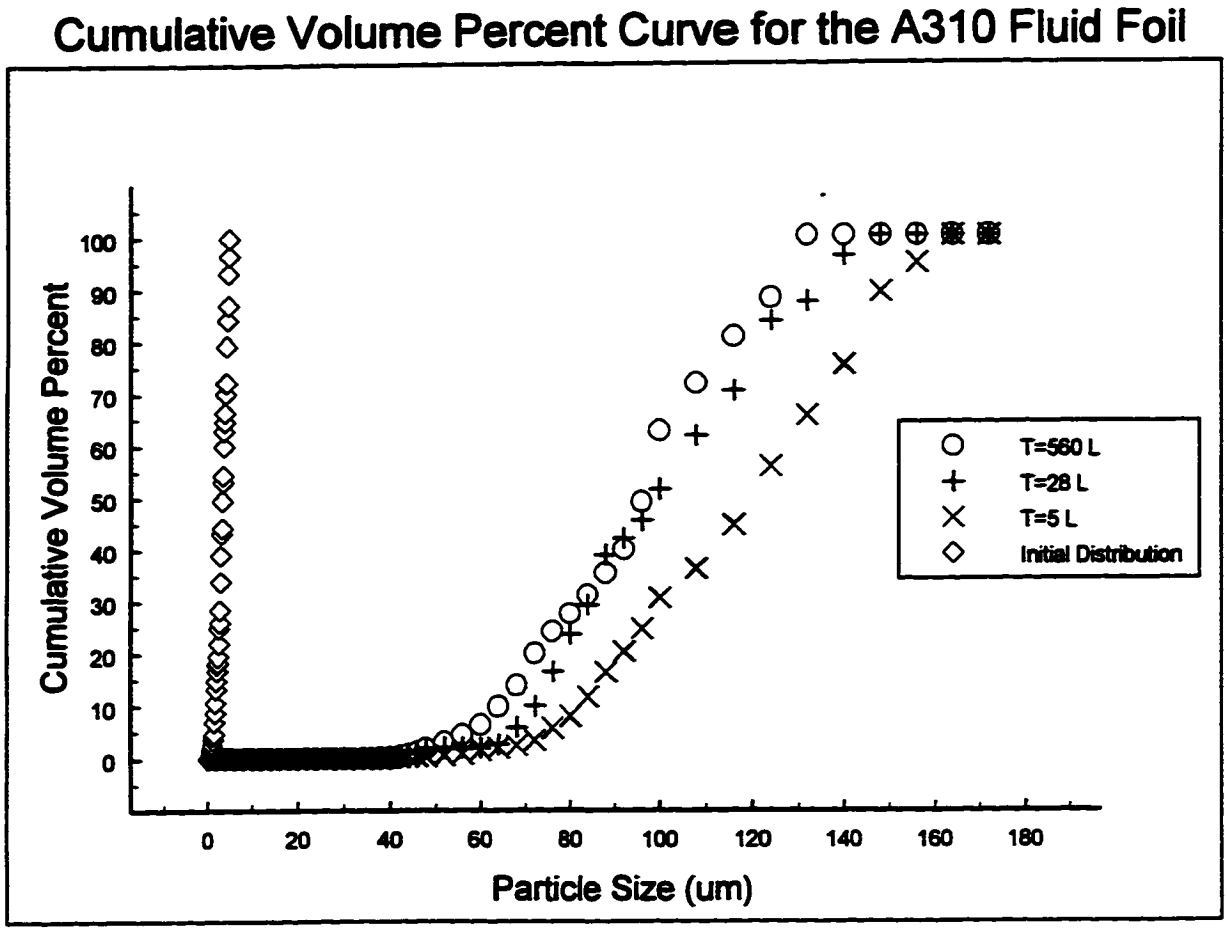

Figure 6.1.6: Cumulative Particle Size Distribution with the A310 Foil Impeller after 30 Minutes of Flocculation: Effect of Tank Size

foil impeller at T = 5L, T = 28L and T = 560L. Figures 6.1.5 and 6.1.6 display a similar shift in both distribution curves to the smaller particle size range for the A310 foil impeller. Figures 6.1.7 - 6.1.12 display the cumulative particle size distribution of three experimental runs for each of the tank sizes and impeller types. As shown in Figures 6.1.7 - 6.1.12, the cumulative particle size distribution results were found to be consistent between the three experimental runs.

The volume mean particle size, the standard deviation, and the maximum particle size were computed for each tank size. The volume mean particle size and standard deviation were computed using the following equations:

$$\overline{d_p} = \frac{\int Vol(d_p) d_p d(d_p)}{\int Vol(d_p) d(d_p)} \qquad (6.1)$$

$$\sigma_{dp} = \left[\frac{\int Vol(d_p) d_p^2 d(d_p)}{\int Vol(d_p) d(d_p)} - \overline{d_p}^2 \right]^{1/2} \qquad (6.2)$$

where

d_p = particle size bin

$Vol(d_p)$ = total volume within d_p bin size

Table 6.1.1 displays the volume mean particle size, standard deviation and the maximum particle size for each tank size with both impeller types. As expected, the data in Table 6.1.1 shows a decreasing trend in the volume mean particle size and maximum particle size with increasing tank size regardless of impeller type. What the author did not anticipate was that the standard deviation also decreased with increasing tank size. This decrease in the standard deviation also

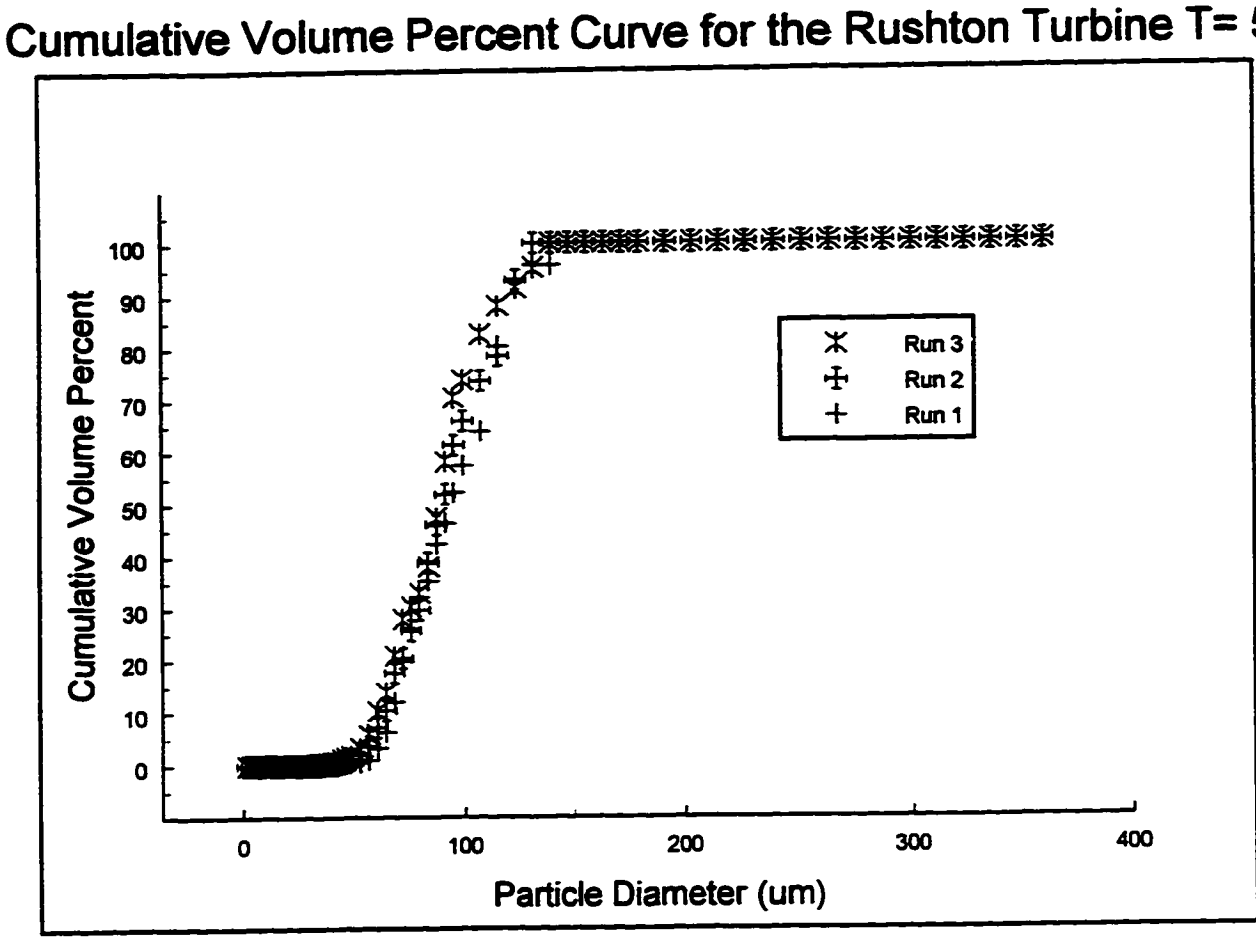

Figure 6.1.7: Reproducibility of Three Experimental Runs for the Cumulative Particle Size Distribution with Rushton Turbine T = 5L after 30 Minutes of Flocculation

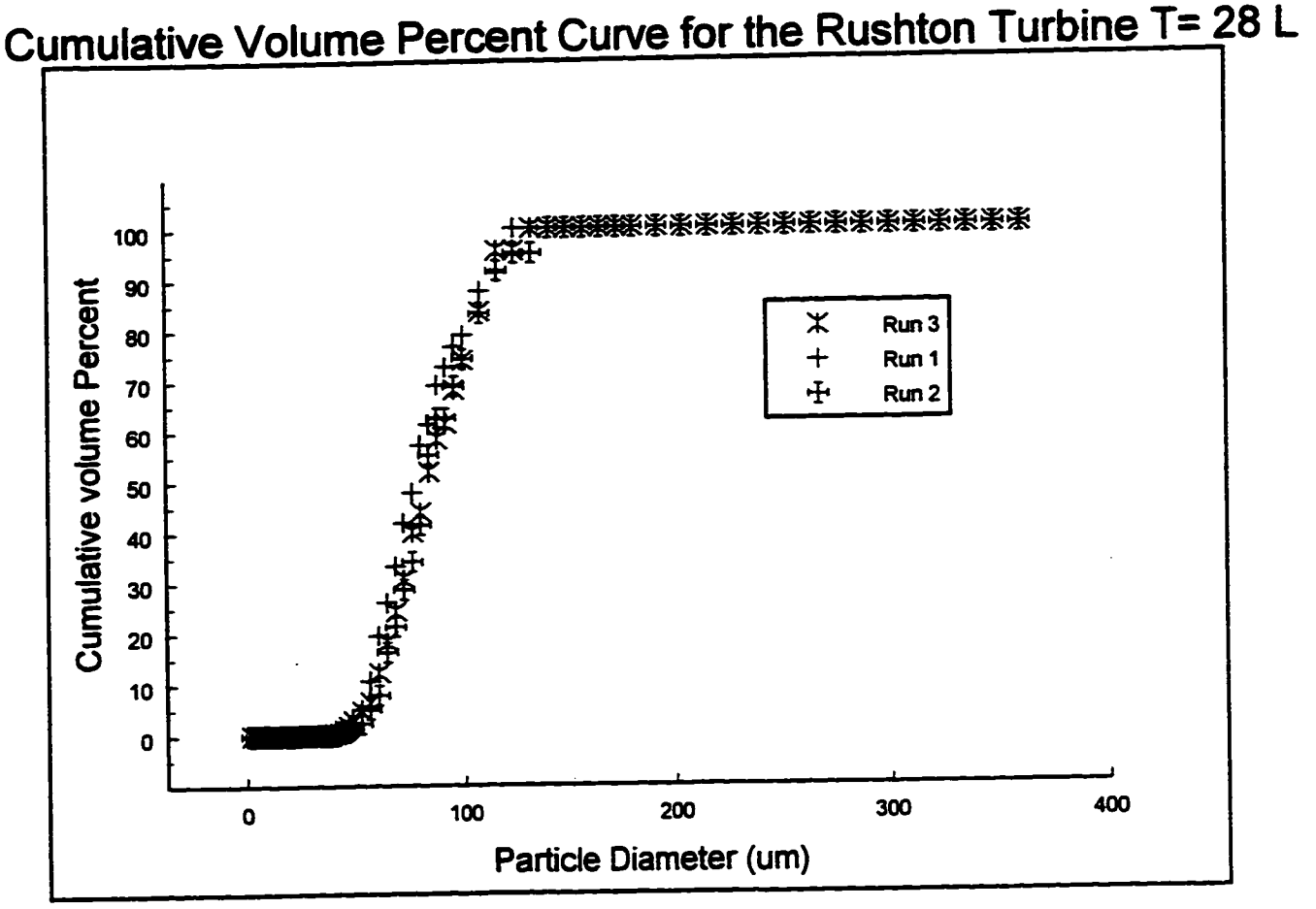

Figure 6.1.8: Reproducibility of Three Experimental Runs for the Cumulative Particle Size Distribution with Rushton Turbine T = 28L after 30 Minutes of Flocculation

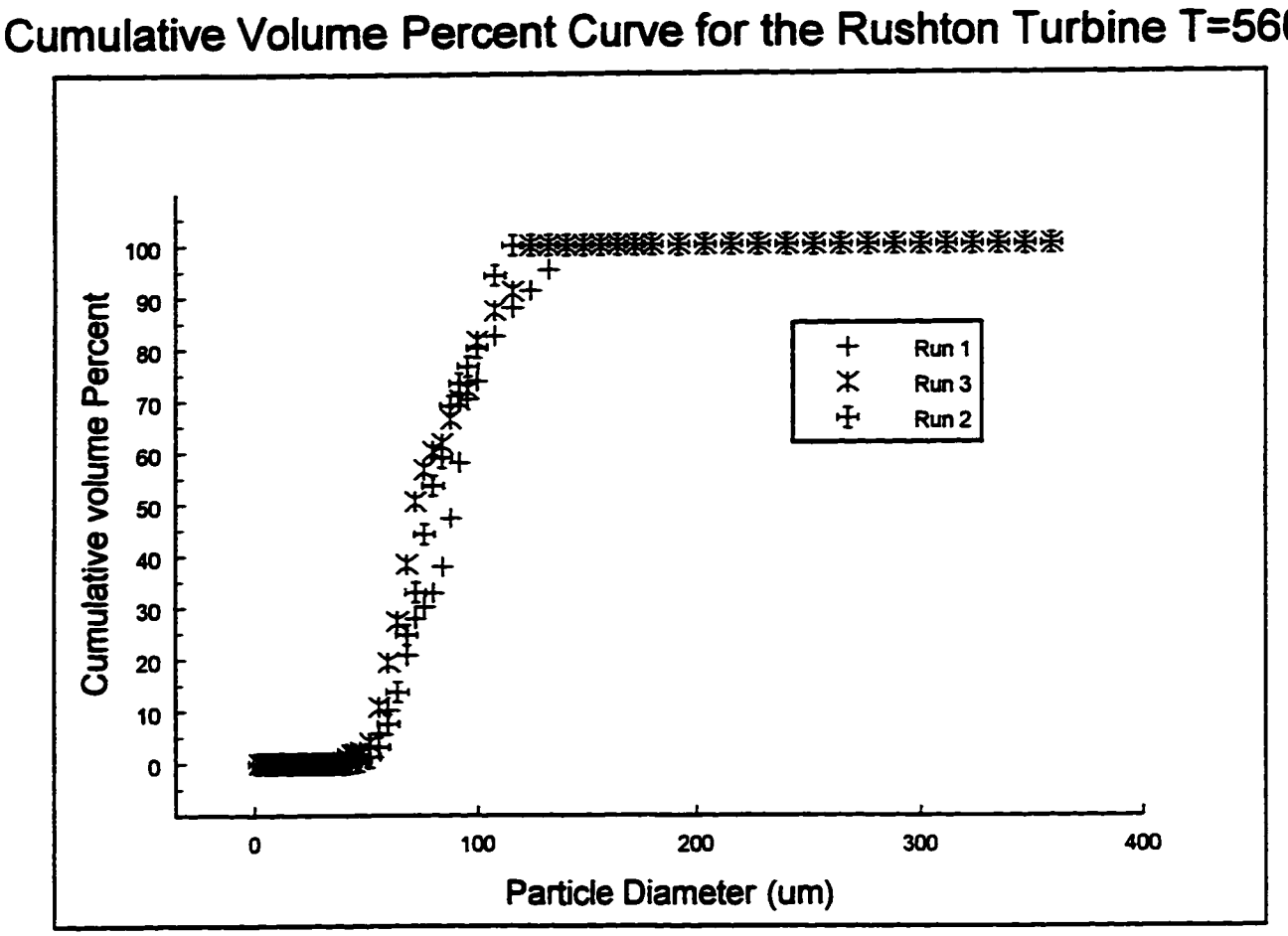

Figure 6.1.9: Reproducibility of Three Experimental Runs for the Cumulative Particle Size Distribution with Rushton Turbine T = 560L after 30 Minutes of Flocculation

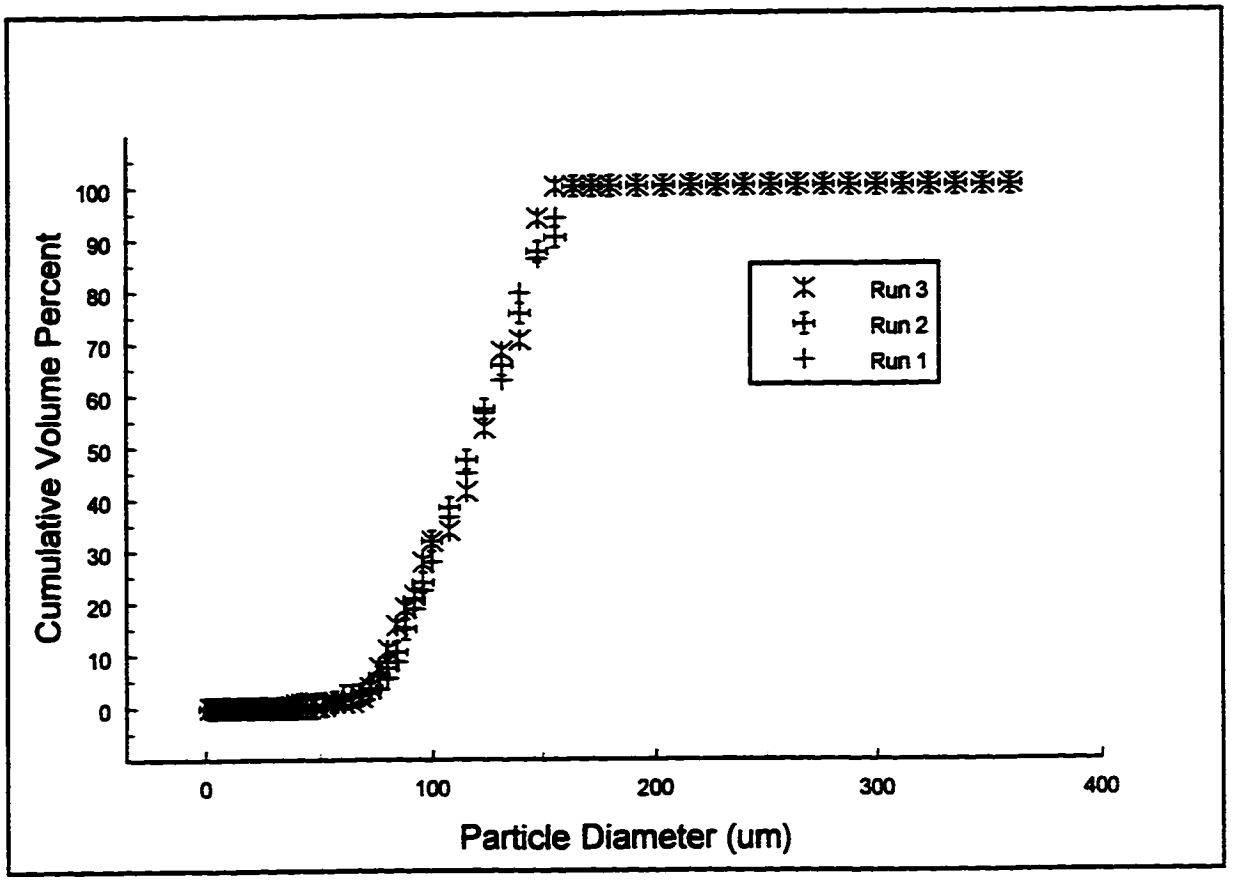

Figure 6.1.10: Reproducibility of Three Experimental Runs for the Cumulative Particle Size Distribution with A310 Foil Impeller T = 5L after 30 Minutes of Flocculation

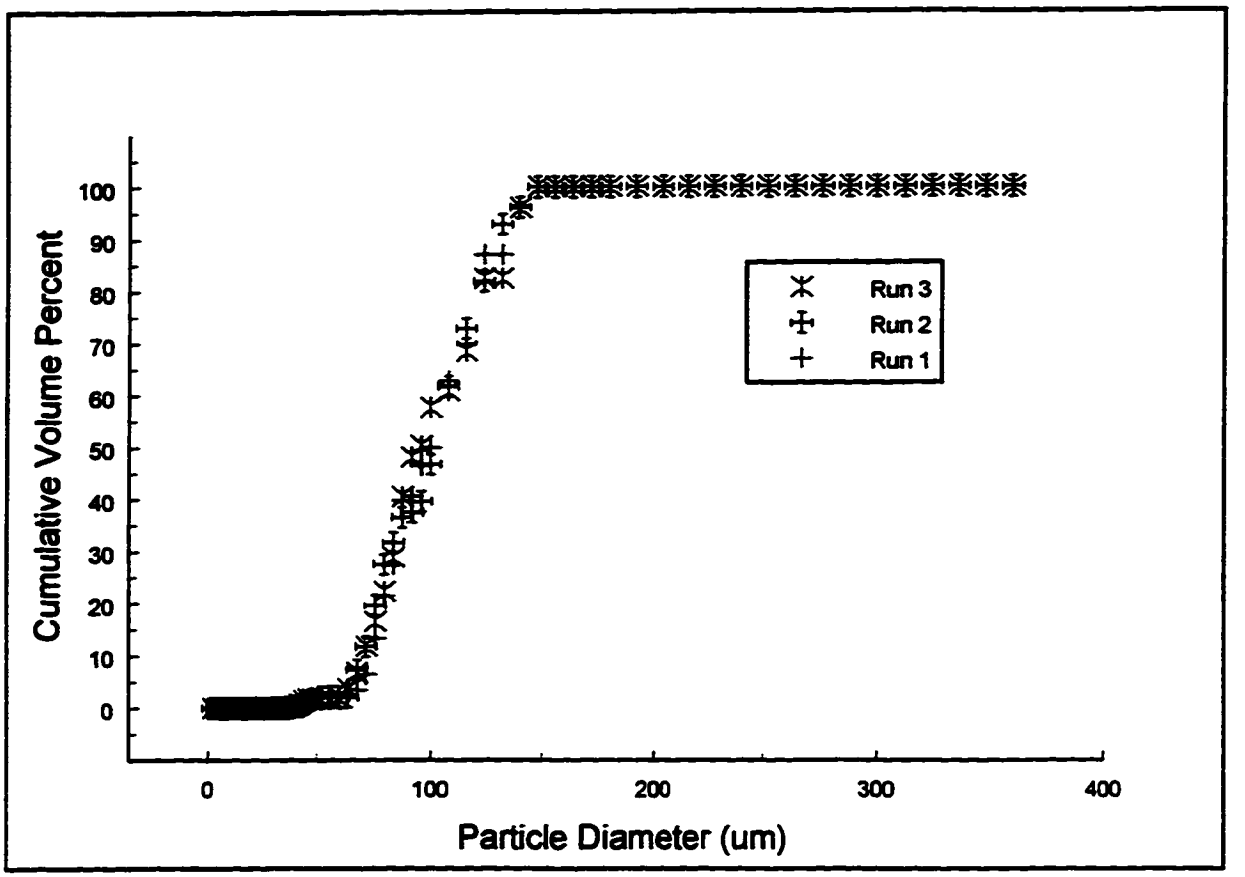

Figure 6.1.11: Reproducibility of Three Experimental Runs for the Cumulative Particle Size Distribution with A310 Foil Impeller T = 28L after 30 Minutes of Flocculation

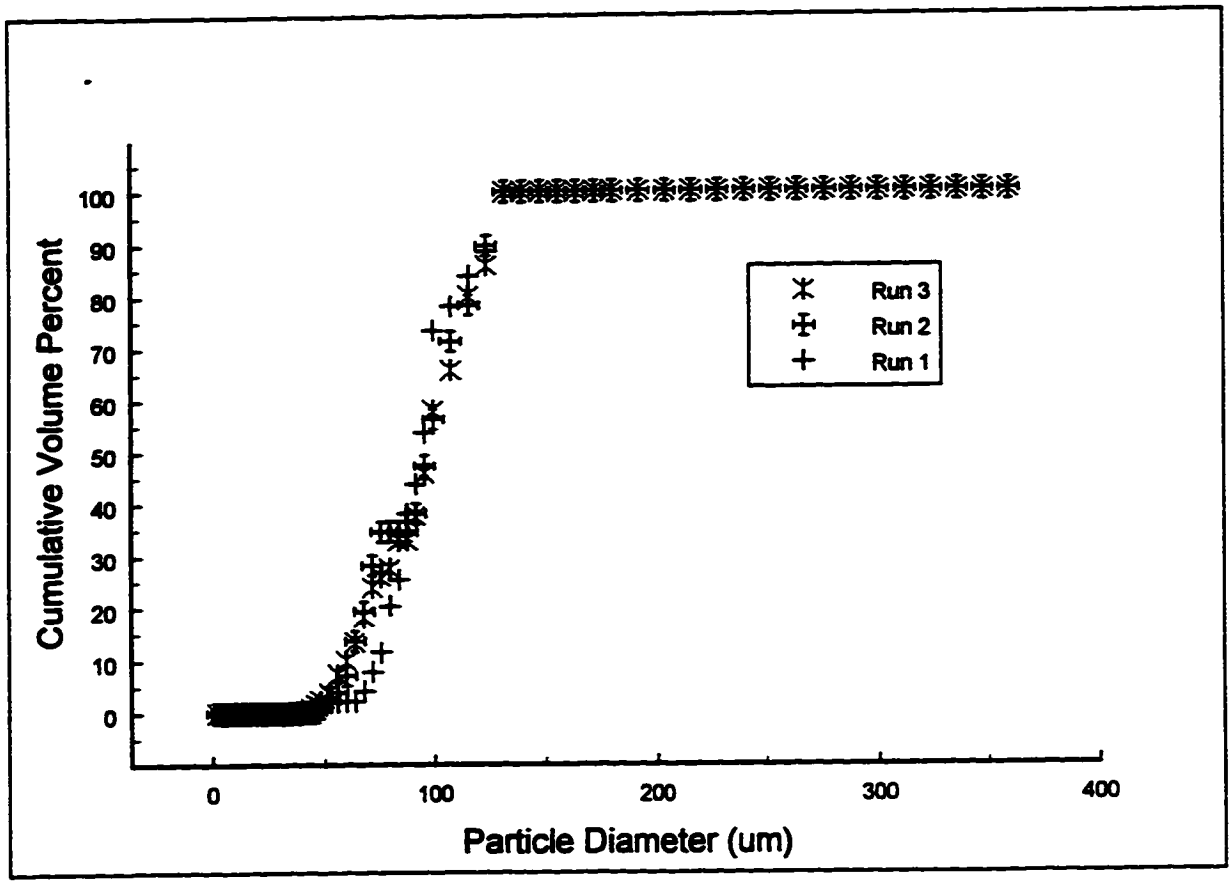

Figure 6.1.12: Reproducibility of Three Experimental Runs for the Cumulative Particle Size Distribution with A310 Foil Impeller T = 560L after 30 Minutes of Flocculation

Table 6.1.1: Particle Size Result for Different Tank Sizes and Impeller Types

Impeller	Tank Size	Mean Diameter	Standard Deviation	Maximum Size
Rushton	T = 5L	94.43	22.93	135.51
Rushton	T = 28 L	85.91	21.68	127.82
Rushton	T = 560L	82.56	20.54	116.83
A310 Foil	T = 5L	120.63	26.86	158.06
A310 Foil	T = 28L	102.90	24.38	140.25
A310 Foil	T = 560L	97.00	22.58	126.96

occurred regardless of impeller type. This trend in the standard deviation suggests that as more floc particles breakup, the spread in the particle size range tends to be more narrow. More than likely, as the intensity of turbulence increases and causes an increase in the breakup rate of the floc particles, the spread of the particle size distribution continues to reduce until the initial standard deviation is reached. The initial standard deviation was 1.09 μm (Section 6.1.1).

It is clear from these results that constant G_m does not result in the same particle size distribution with different tank sizes. As suggested in Section 5.4, the particle size distribution might be dependent on the large scale turbulent motion produced in the impeller discharge zone. Recall that the large scale turbulent fluctuating velocity was found to increase with increasing tank size. It is possible that the increase in the turbulence intensity with tank size might be the cause of the increase in floc breakup with tank size. The relationship between the steady state particle size distribution and the large scale turbulent motion will be discussed in Section 6.1.4.

6.1.3 Influence of Impeller Type on Particle Size Distribution

Figures 6.1.13 - 6.1.15 compares the cumulative particle size distribution produced by the Rushton turbine and the A310 fluid foil impeller in the 5L, 28L, and 560L tanks respectively. As can be seen from Figures 6.1.13 - 6.1.15, the Rushton turbine produces a cumulative particle size

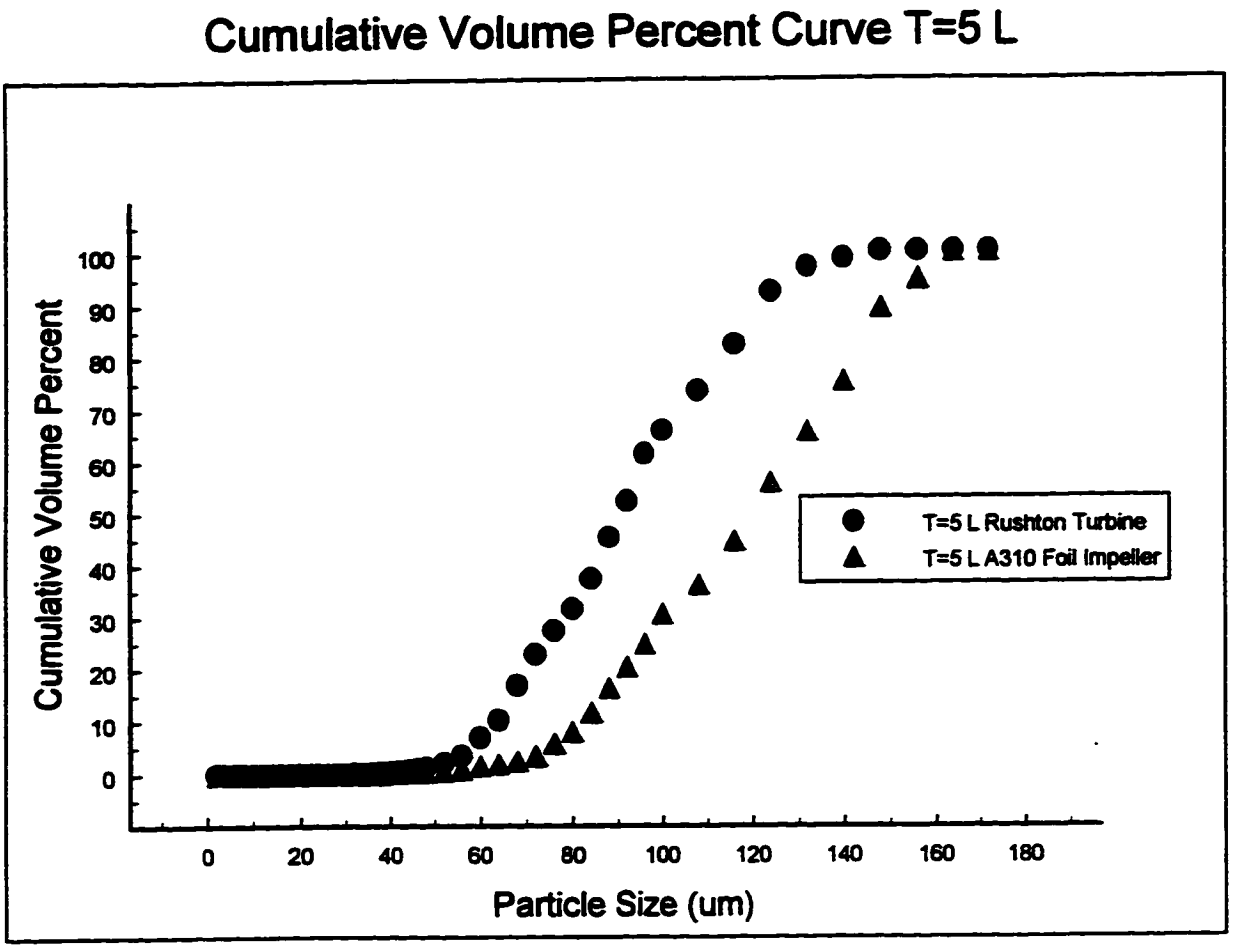

Figure 6.1.13: Cumulative Particle Size Distribution after 30 Minutes of Flocculation: Comparison Between the Rushton Turbine and A310 Foil Impeller at T = 5L

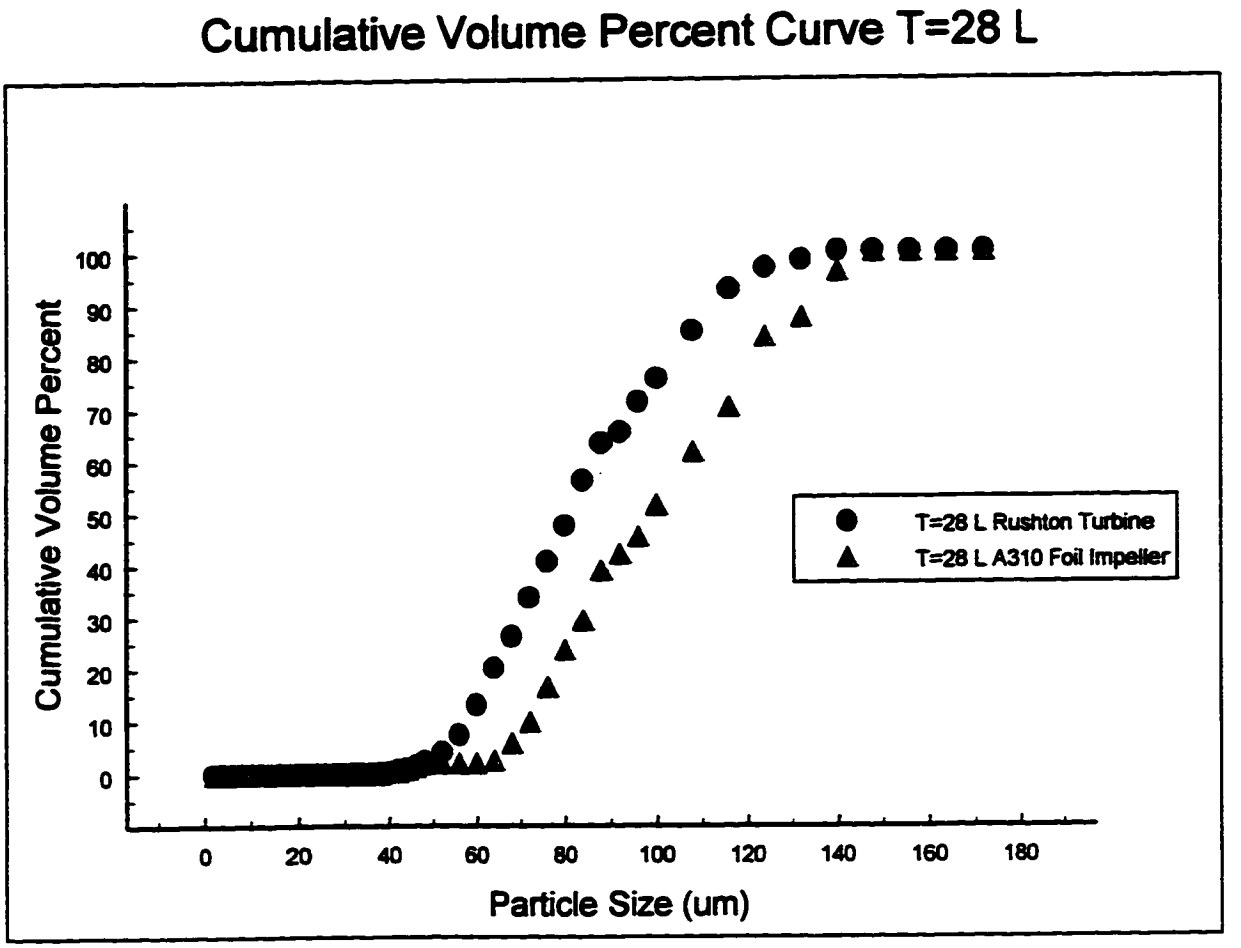

Figure 6.1.14: Cumulative Particle Size Distribution after 30 Minutes of Flocculation: Comparison Between the Rushton Turbine and A310 Foil Impeller at T = 28L

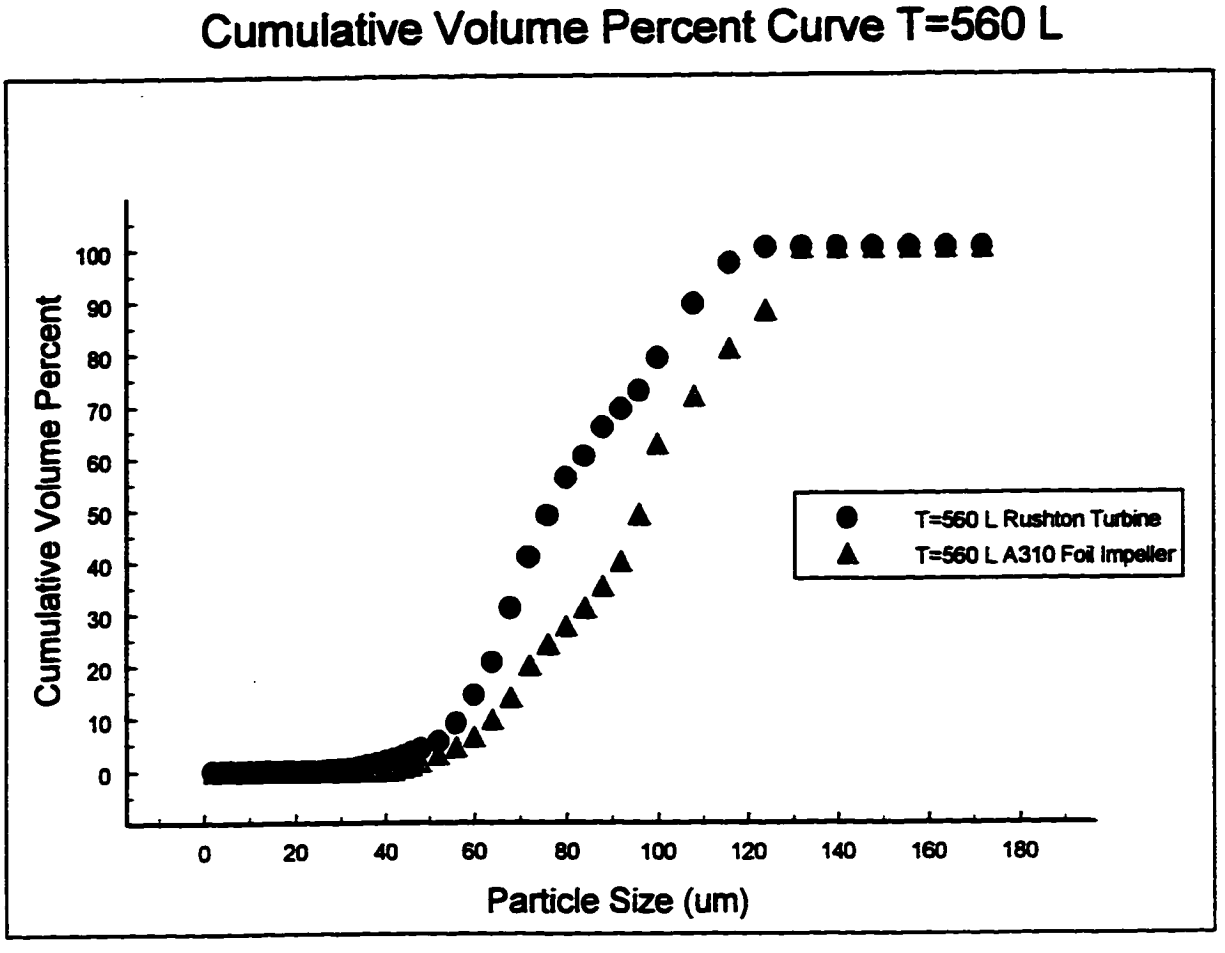

Figure 6.1.15: Cumulative Particle Size Distribution after 30 Minutes of Flocculation: Comparison Between the Rushton Turbine and A310 Foil Impeller at T = 560L

distribution that is always to the left of the distribution produced by the A310 foil impeller. This trend occurred regardless of tank size and with G_m = constant. In Table 6.1.1, the volume mean particle size, standard deviation, and maximum particle size were lower for the Rushton turbine than for the A310 foil impeller at all three tank sizes. These results are consistent with the shift in the cumulative particle size distribution curve to the smaller particle size range from the A310 foil impeller to the Rushton turbine.

The results shown in Figures 6.1.13 - 6.1.15 confirm one hypothesis of this work that the same steady state particle size distribution cannot in general be produced with two different impellers at constant G_m. In Section 5.3, the turbulence intensity in the impeller discharge zone of the Rushton turbine was higher than the turbulence intensity in the impeller discharge zone of the A310 foil impeller at constant G_m. A higher turbulence intensity may be the reason for the increase in the floc breakup from the A310 foil impeller to the Rushton turbine. This relationship between the turbulence generated in the impeller discharge zone and the steady-state particle size distribution are discussed in the following section.

6.1.4 Relationship Between the Steady State Particle Size Distribution and $N_p^{0.5}ND$

In Section 5.3, the results of the LDV measurements in the 5L, 28L, and 560L tank sizes showed that with G_m = constant, the intensity of the large scale turbulent fluctuating velocity increased with increasing tank size and was proportional to the impeller tip speed. This trend occurred regardless of the impeller type being used in the reactor. It was speculated in Section 5.4 that this increase in the turbulence level may explain the degradation in the flocculation performance with tank size. If this speculation is true, then a relationship should exist between the steady state particle size distribution and the tip speed.

Figures 6.1.16 - 6.1.18 display plots of the volume mean particle size, standard deviation, and the maximum particle size respectively as a function of the tip speed. The results of both the Rushton turbine and the A310 foil impeller at the three different tank sizes are shown in Figures 6.1.16 - 6.1.18. As can be seen in figures 6.1.16 - 6.1.18, the volume mean particle size, standard deviation, and maximum particle size all display a power law dependence to the tip speed.

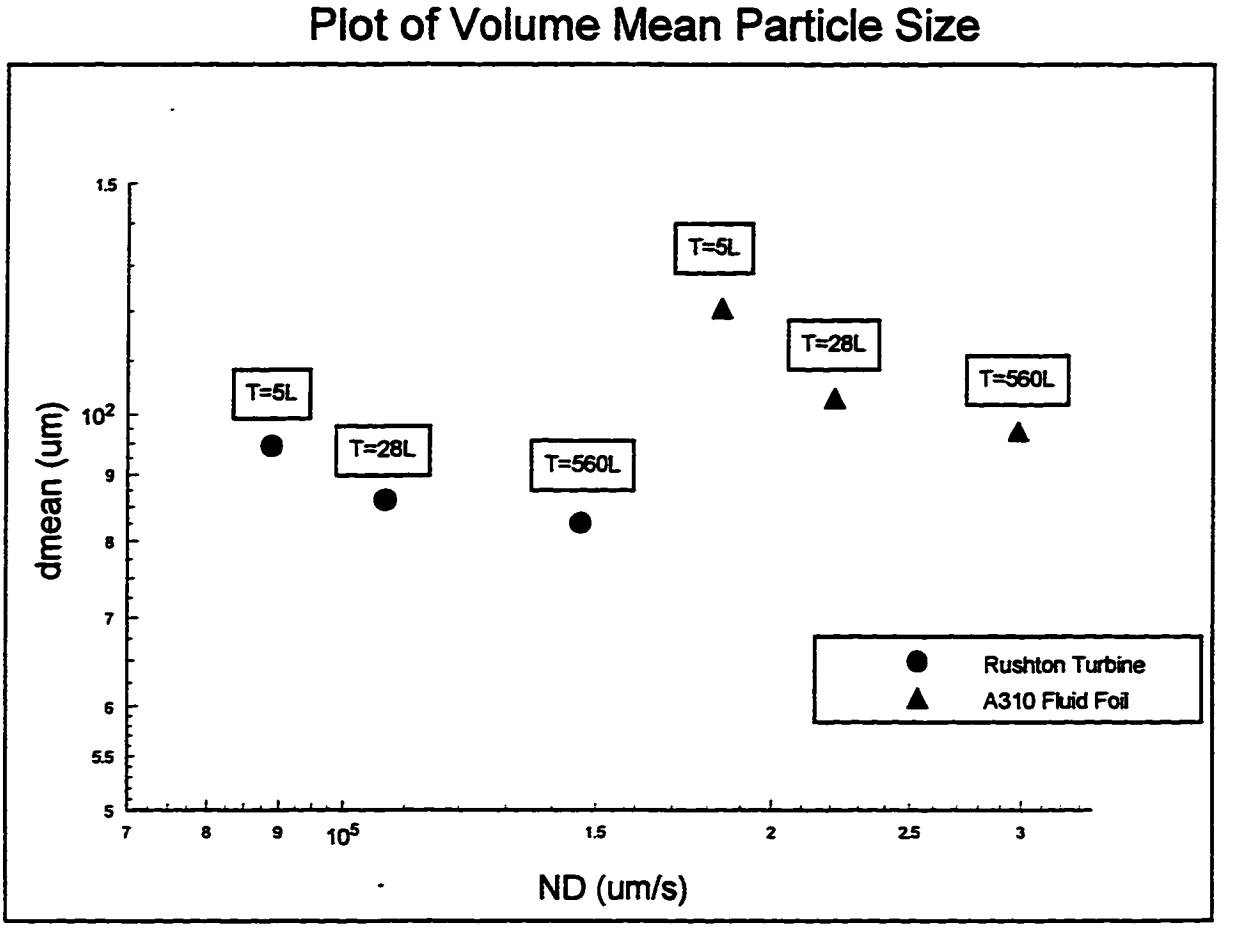

Figure 6.1.16: Plot of the Volume Mean Particle Size as a Function of the Impeller Tip Speed

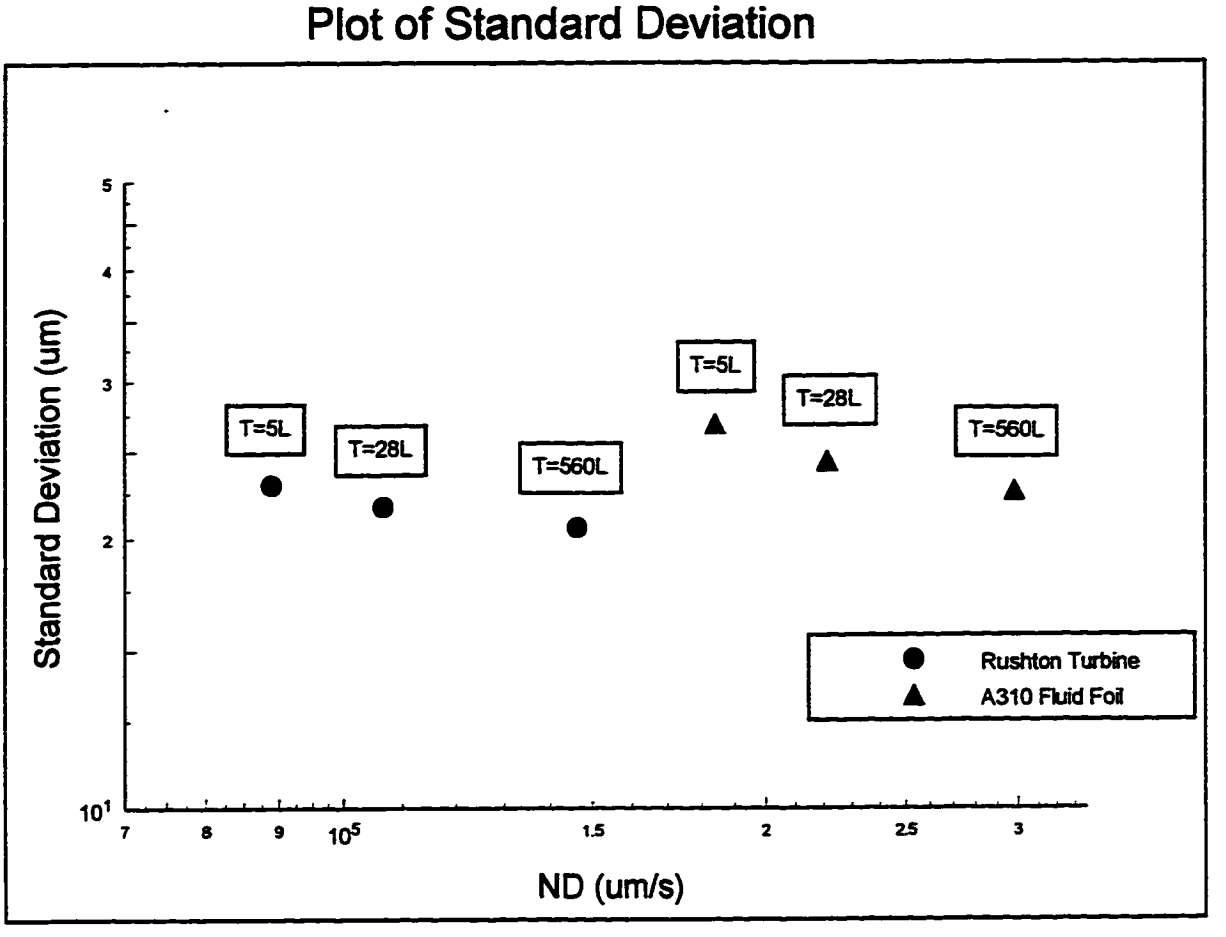

Figure 6.1.17: Plot of the Standard Deviation as a Function of the Impeller Tip Speed

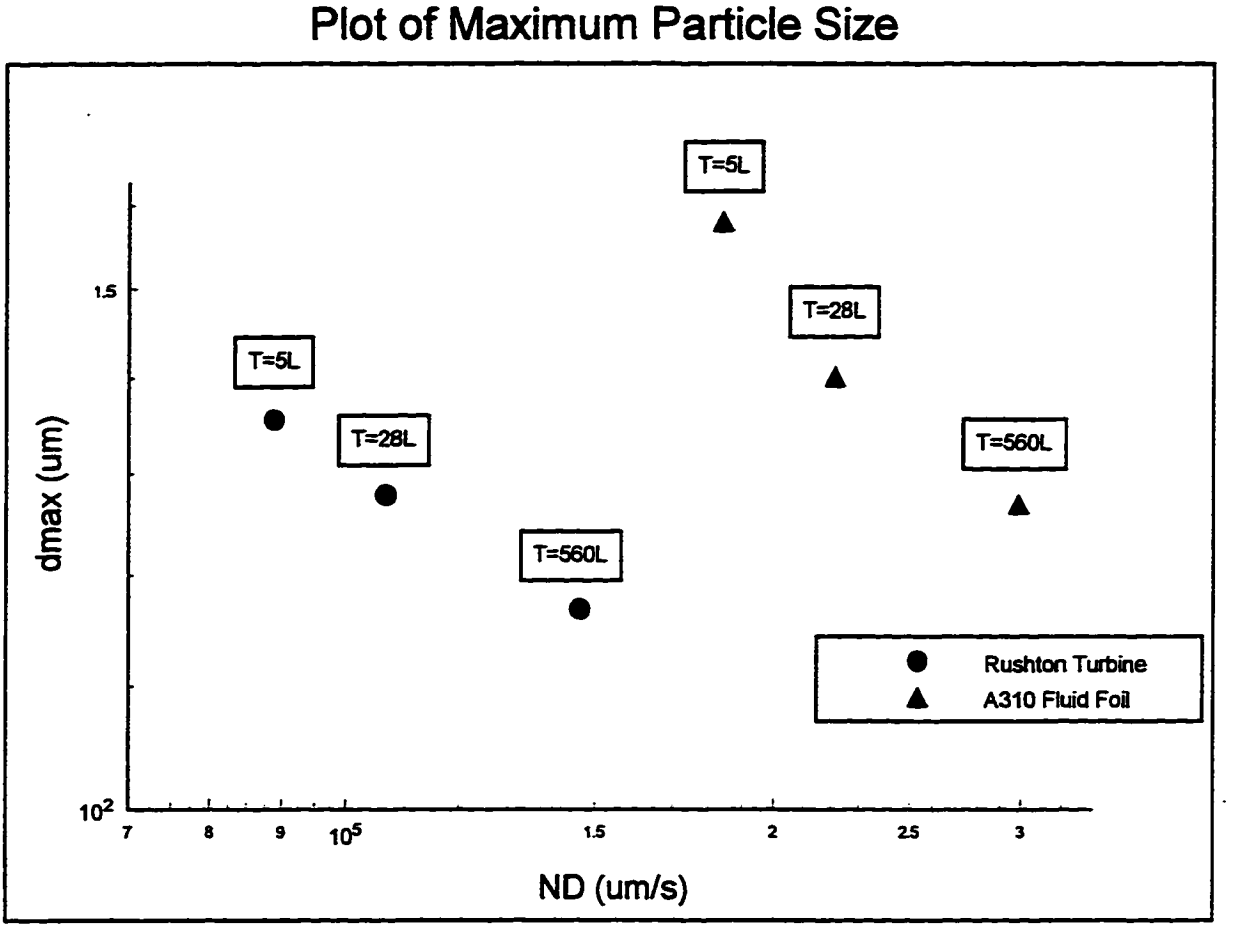

Figure 6.1.18: Plot of the Maximum Particle Size as a Function of the Inpeller Tip Speed

Figures 6.1.16 - 6.1.18 clearly show that the relationship is different between the Rushton turbine and the A310 foil impeller. However, in Table 5.1.3, the rms turbulent fluctuating velocity in the impeller discharge zone for the Rushton turbine and A310 foil impeller were found to collapse to the same value when the rms was normalized by $N_p^{0.5}ND$. Based on Table 5.1.3, the results in Figures 6.1.16 - 6.1.18 might not show any variation with impeller type if re-plotted with $N_p^{0.5}ND$.

Figures 6.1.19 - 6.1.21 display plots of the volume mean particle size, standard deviation, and the maximum particle size respectively as a function of $N_p^{0.5}ND$. As can be seen from figures 6.1.19 - 6.1.21, the mean particle size, standard deviation, and maximum particle size of both the Rushton turbine and A310 foil impeller appear to collapse to one curve. From Figures 6.1.19 - 6.1.21, a relationship does exist between the steady state particle size distribution and the intensity of the turbulence in the impeller discharge region.

In Figures 6.1.19 - 6.1.21, the volume mean particle size standard deviation, and the maximum particle size data were fitted with the following function:

$$d_i = \frac{constant}{(N_p^{0.5}ND)^y} \tag{6.3}$$

where

d_i = dependant parameter (i.e. volume mean particle size, standard deviation, maximum particle size)

constant, y = fitting parameters determined by a nonlinear least squares algorithm.

Figures 6.1.22 - 6.1.24 display the results of fitting Equations 6.3 to the volume mean particle size, standard deviation, and maximum particle size data. Table 6.1.2 displays the values of the fitting parameters in Equation 6.3. From Table 6.1.2, the volume mean particle size appears to have a slightly stronger dependence on $N_p^{0.5}ND$ than the standard deviation or the maximum particle size. The stronger dependence of the volume mean particle size on $N_p^{0.5}ND$ suggests that increasing the turbulence intensity in the impeller discharge zone has a slightly stronger effect on

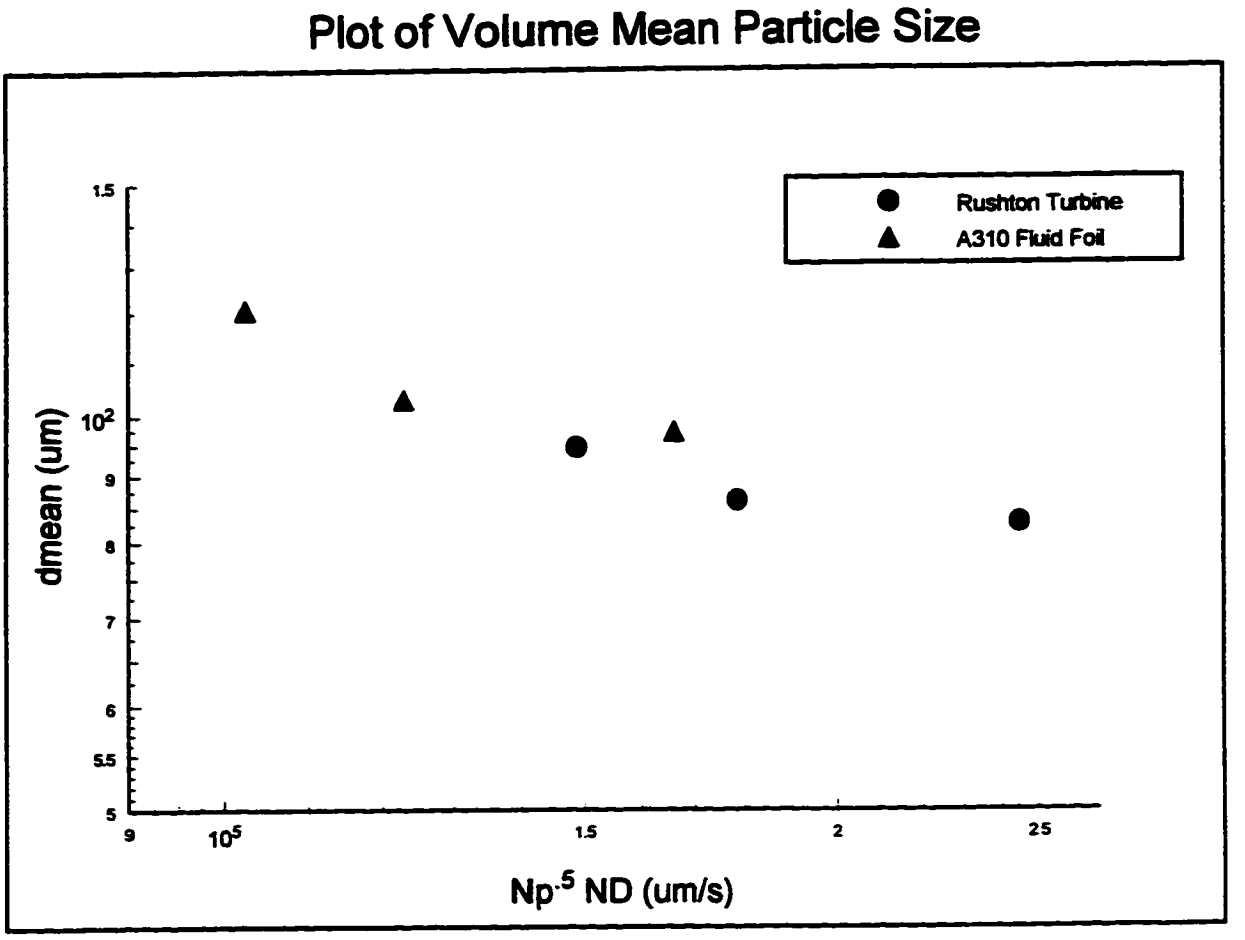

Figure 6.1.19: Plot of the Volume Mean Particle Size as a Function of $N_p^{0.5}ND$

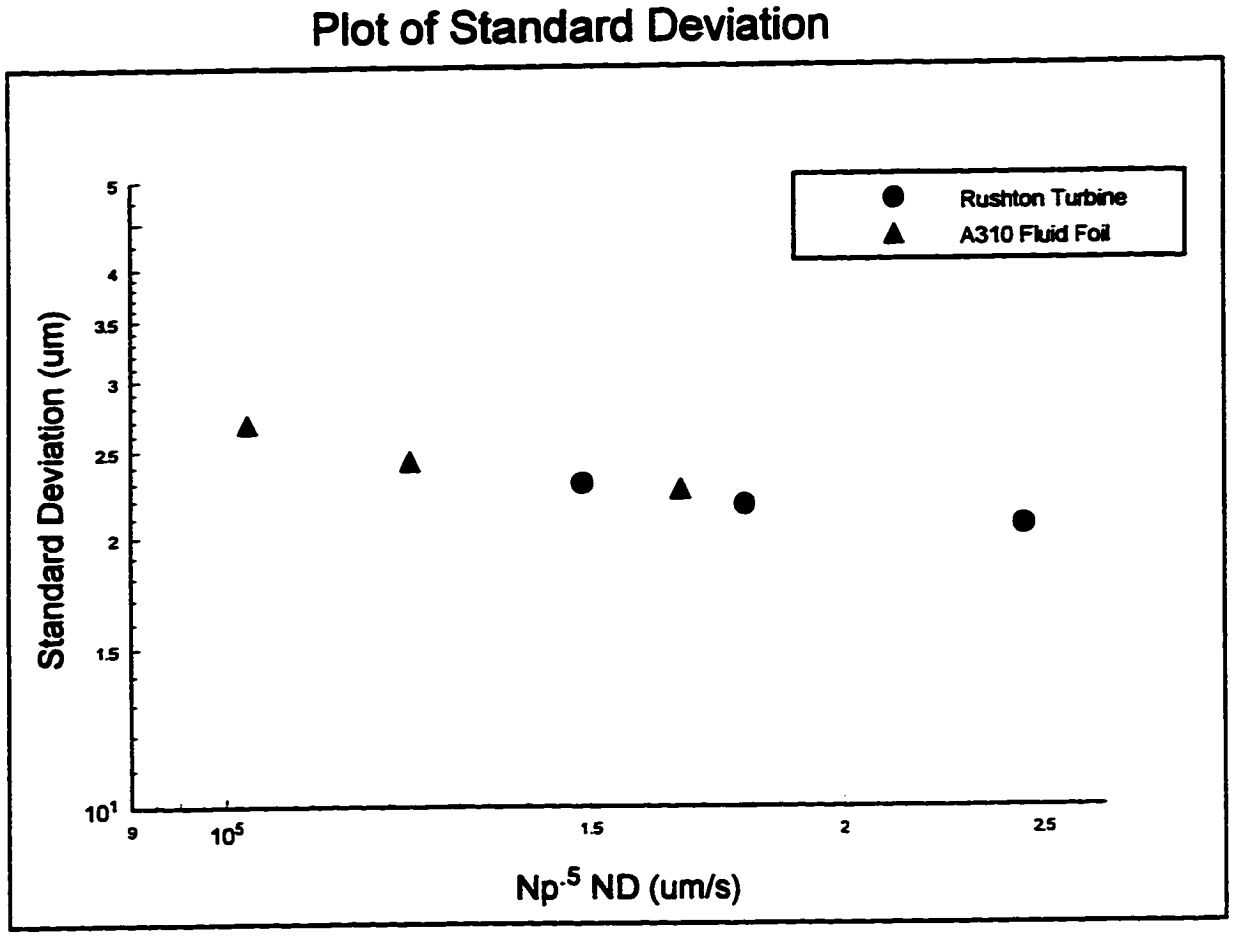

Figure 6.1.20: Plot of the Standard Deviation as a Function of $N_p^{0.5}ND$

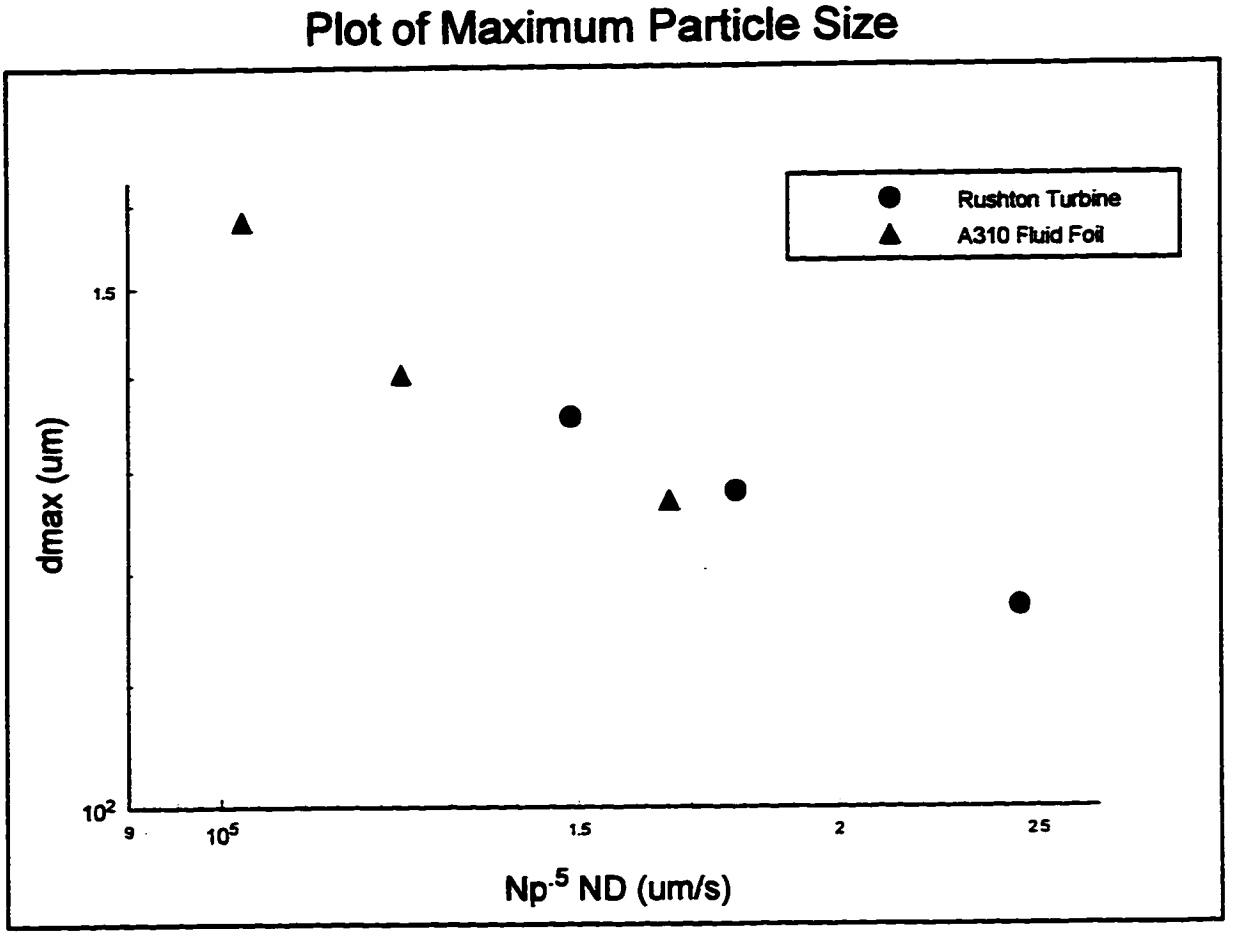

Figure 6.1.21: Plot of the Maximum Particle Size as a Function of $N_p^{0.5}ND$

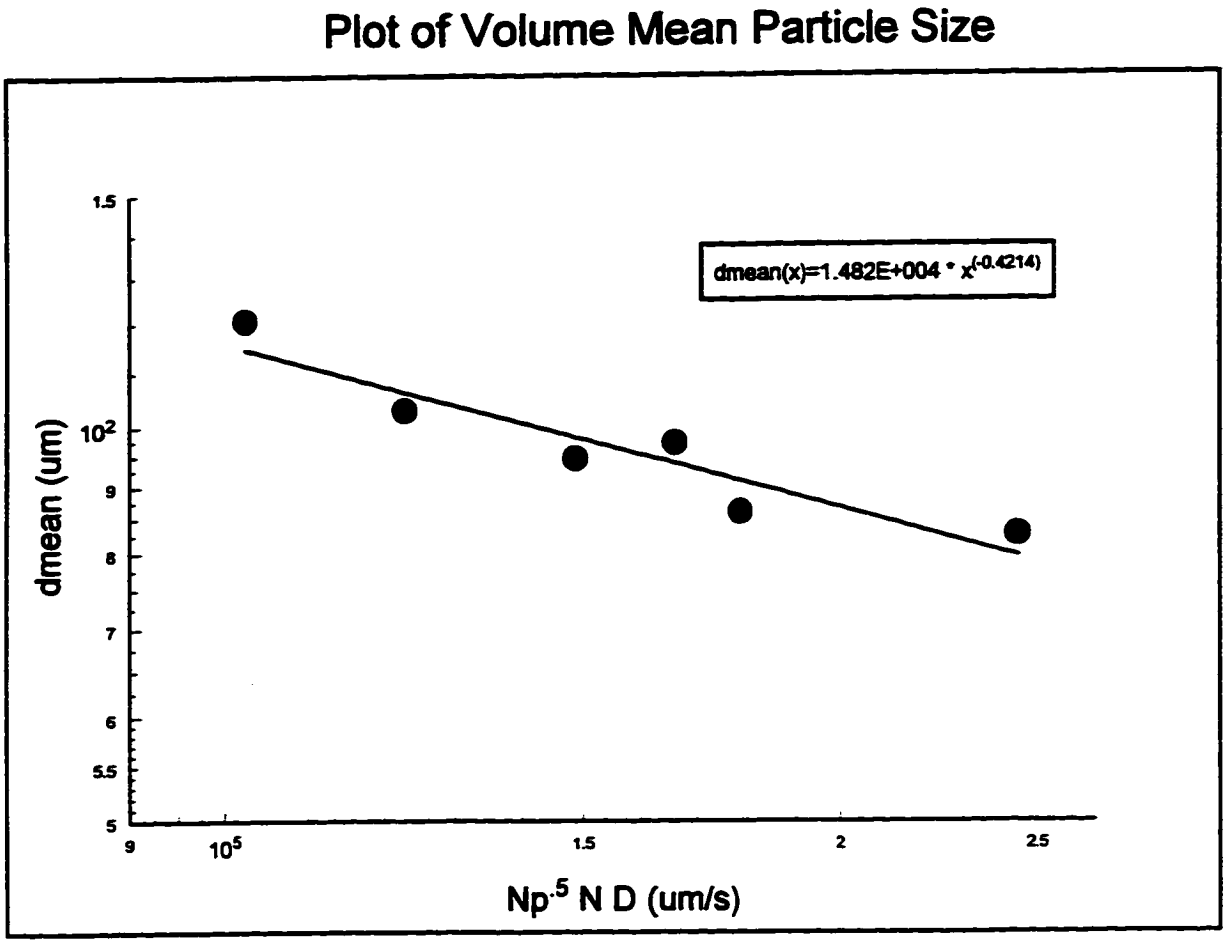

Figure 6.1.22: Curve Fit of d_i = constant/$(N_p^{0.5}ND)^y$ to the Volume Mean Particle Size Data

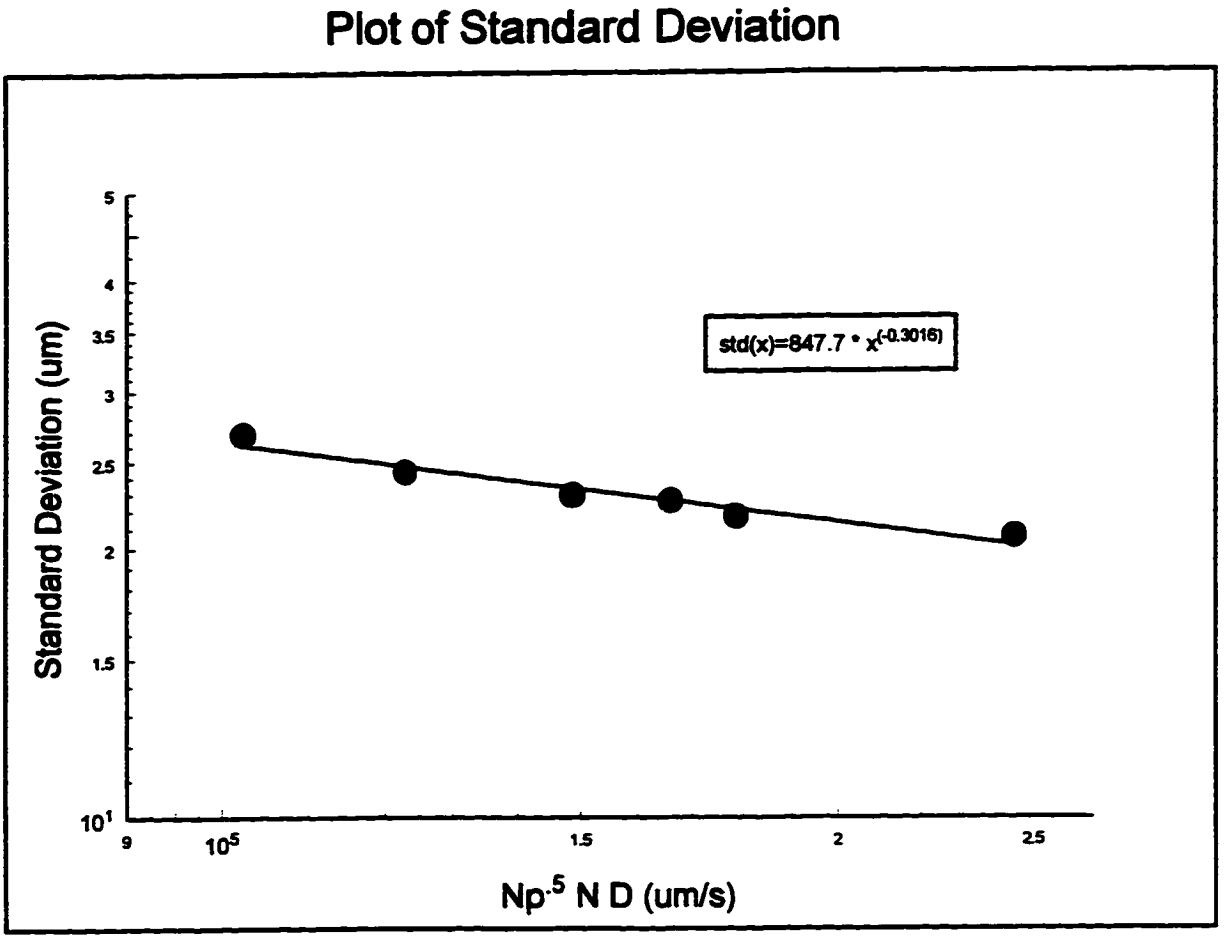

Figure 6.1.23: Curve Fit of d_i = constant/$(N_p^{0.5}ND)^y$ to the Standard Deviation Data

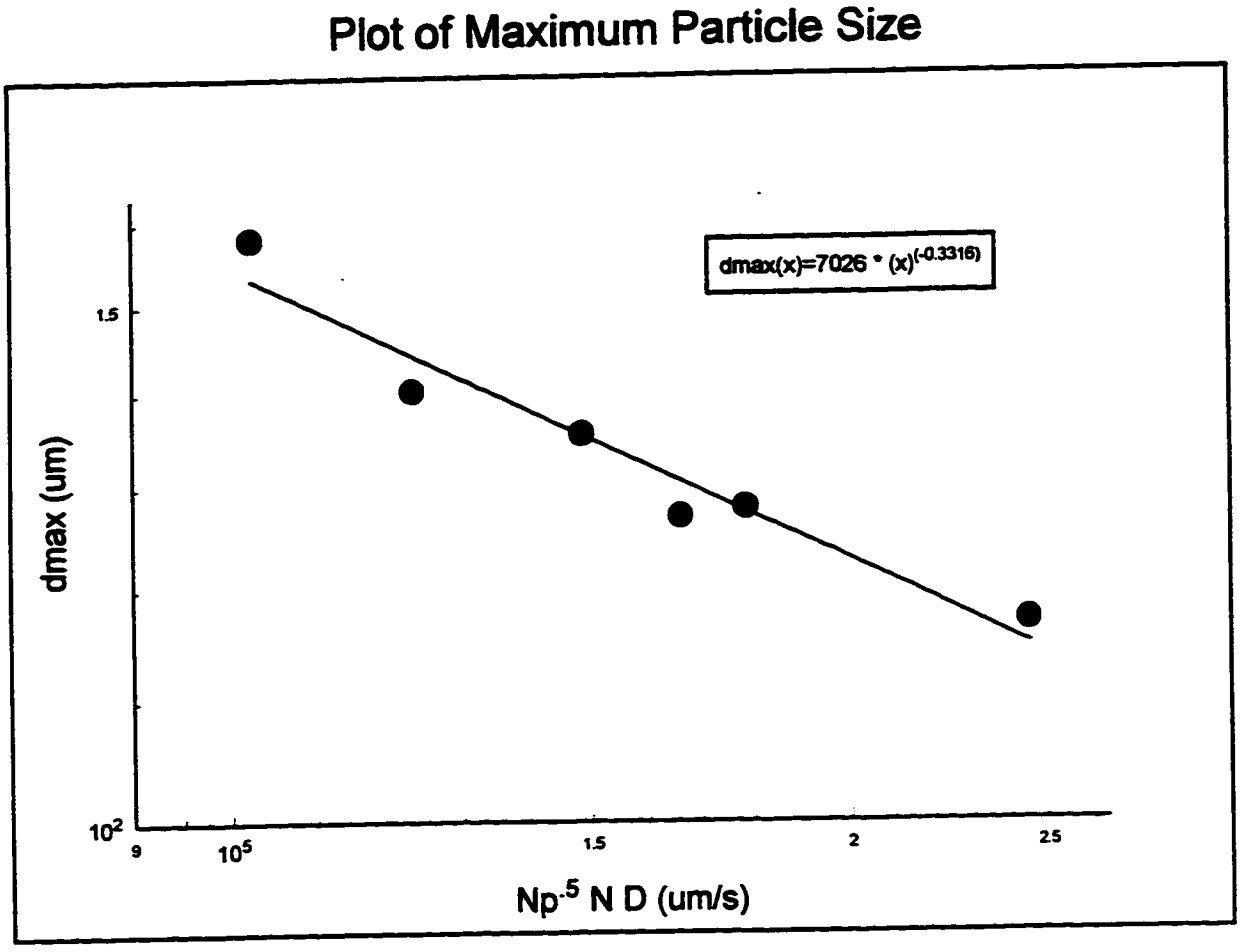

Figure 6.1.24: Curve Fit of d_i = constant/$(N_p^{0.5}ND)^y$ to the Maximum Particle Size Data

Table 6.1.2: Fitting Parameters in Equation 6.3

d_i	Constant	y
Volume Mean Particle Size	14820 (s)	0.42
Standard Deviation	847.7 (s)	0.30
Maximum Particle Size	7026 (s)	0.33

increasing the population of smaller size class particles. The increased population of smaller size class particles would shift the mean particle size to a smaller value. The lower dependence of the standard deviation and the maximum particle size on $N_p^{0.5}ND$ suggests that increasing the turbulence intensity in the impeller discharge zone does not have as strong effect on decreasing the spread of the particle size distribution or the maximum stable floc size. It is clear, however, that the turbulence intensity in the impeller discharge zone plays a significant role in determining the outcome of the steady state particle size distribution.

6.1.5 Discussion

The flocculation experimental results demonstrate that the steady state particle size distribution changes with different tank sizes and impeller types when G_m = constant. In Section 6.1.2, the experimental data showed that the cumulative particle size distribution curve shifts to a smaller particle size range with increasing tank size (Figure 6.1.4 & 6.1.6). This shift to the smaller particle size range is due to the growing population of smaller particles with increasing tank size (Figures 6.1.3 & 6.1.5). Although G_m = constant with increasing tank size should imply the same production of the steady state particle size distribution with tank size, the results in Figures 6.1.3 - 6.1.6 do not support this relationship. In fact, these results confirm work done by previous investigators that the flocculation performance degrades with increasing tank size (Section 2.2).

In Section 6.1.3, the experimental data also showed that for constant G_m, the cumulative particle size distribution curve for the Rushton turbine is consistently to the left of the cumulative particle size distribution for the A310 foil impeller regardless of tank size. These results

demonstrate that more particles are being fragmented by the Rushton turbine than by the A310 foil impeller even with G_m = constant. Again, these results confirm other investigators' work showing that the A310 foil impeller yielded better flocculation results than the Rushton turbine (Section 2.2).

The flocculation experimental results seem to imply that the steady state particle size distribution is sensitive to the turbulence level that is unique to the tank size and the impeller type being used. Clearly, G_m cannot describe this turbulence level as demonstrated by these experimental results. However, the flocculation experimental results do suggest that the parameter, $N_p^{0.5}ND$, uniquely describes the turbulence level and correlates several statistics of the particle size distribution, regardless of the tank size and impeller geometry.

$N_p^{0.5}ND$ represents the turbulence level of the large scale eddies in the impeller discharge zone. In Section 5.1, the LDV experimental results showed that with G_m = constant, the turbulence level of the large scale eddies increased with increasing tank size and was proportional to the tip speed (ND). Clearly, $N_p^{0.5}ND$ would be sensitive to the increasing turbulence levels with tank size since it incorporates the tip speed. The LDV experimental results also showed a higher turbulence level in the impeller discharge zone of the Rushton turbine than for the A310 foil impeller. Again, $N_p^{0.5}ND$ would also describe this increase in the turbulence level from the A310 foil to the Rushton because it contains N_p, the impeller power number. N_p is higher for the Rushton turbine than for the A310 foil impeller.

Using $N_p^{0.5}ND$, the volume mean particle size, standard deviation, and the maximum particle size seem to collapse to one curve in Figures 6.1.22 - 6.1.24 respectively. In each of the Figures 6.1.22 - 6.1.24, the experimental data were fitted with a least square approximated power law curve. The results show that a simple relationship does exist between turbulence produced in the impeller discharge zone and the volume mean particle size, standard deviation, and the maximum particle size. Based on the results in Figures 6.1.22 - 6.1.24, it might be possible to predict the steady state floc size distribution of a vertical shaft mechanical mixer knowing just the impeller power number and the impeller tip speed. These results also imply that the frequency of particle circulation into the impeller discharge zone are not as important as the turbulence intensity in that region for determining the steady state particle size distribution. However, more

experiments would be needed with more impeller types, tank shapes, impeller locations, and water chemistry to determine whether these equations in Figures 6.1.22 - 6.1.24 are universal.

6.2 Numerical Modeling of Flocculation Process

6.2.1 Model Sensitivity to Empirical Constants

The empirical constants (α, c_1, c_3) in Equation 4.15 and 4.17 were varied in order to determine the population balance model's sensitivity to each constant. The range of values chosen for α, c_1, and c_3 are in close proximity to the location of the optimal values determined in Section 6.2.2. Figures 6.2.1 - 6.2.3 display the effects of changing the value of α, c_1, and c_3 respectively on the population balance model. In Figure 6.2.1, the value of α is increased from 0.03 to .3.

As can be seen in Figure 6.2.1, increasing the value of α causes a shift in the cumulative particle size distribution curve to a larger particle size range. The shift in the cumulative particle size distribution to the larger particle size range is logical since α represents the collision efficiency. A higher collision efficiency suggests that a higher percentage of particles will stick together upon collision.

In Figure 6.2.2, the value of c_1 is increased from 0.01 to 0.1. From Figure 6.2.2, increasing the value of c_1 causes a shift in the cumulative particle size distribution curve to a smaller particle size range. The shift in the cumulative particle size distribution to the smaller particle size range is logical since c_1 represents a constant within the breakup frequency function k_b (Eqn. 4.15). A higher c_1 value will increase the particle breakup frequency and increase the population of small particles.

In Figure 6.2.3, the value of c_3 is increased from 0.01 to 0.1. From Figure 6.2.3, increasing the value of c_3 also causes a shift in the cumulative particle size distribution curve to a larger particle size range. This shift in the cumulative particle size range is logical since c_3 represents the strength of the particle's binding energy per unit area. A higher c_3 value means that the floc particle is more resilient to the fluid forces which cause breakup. From Equation 4.17,

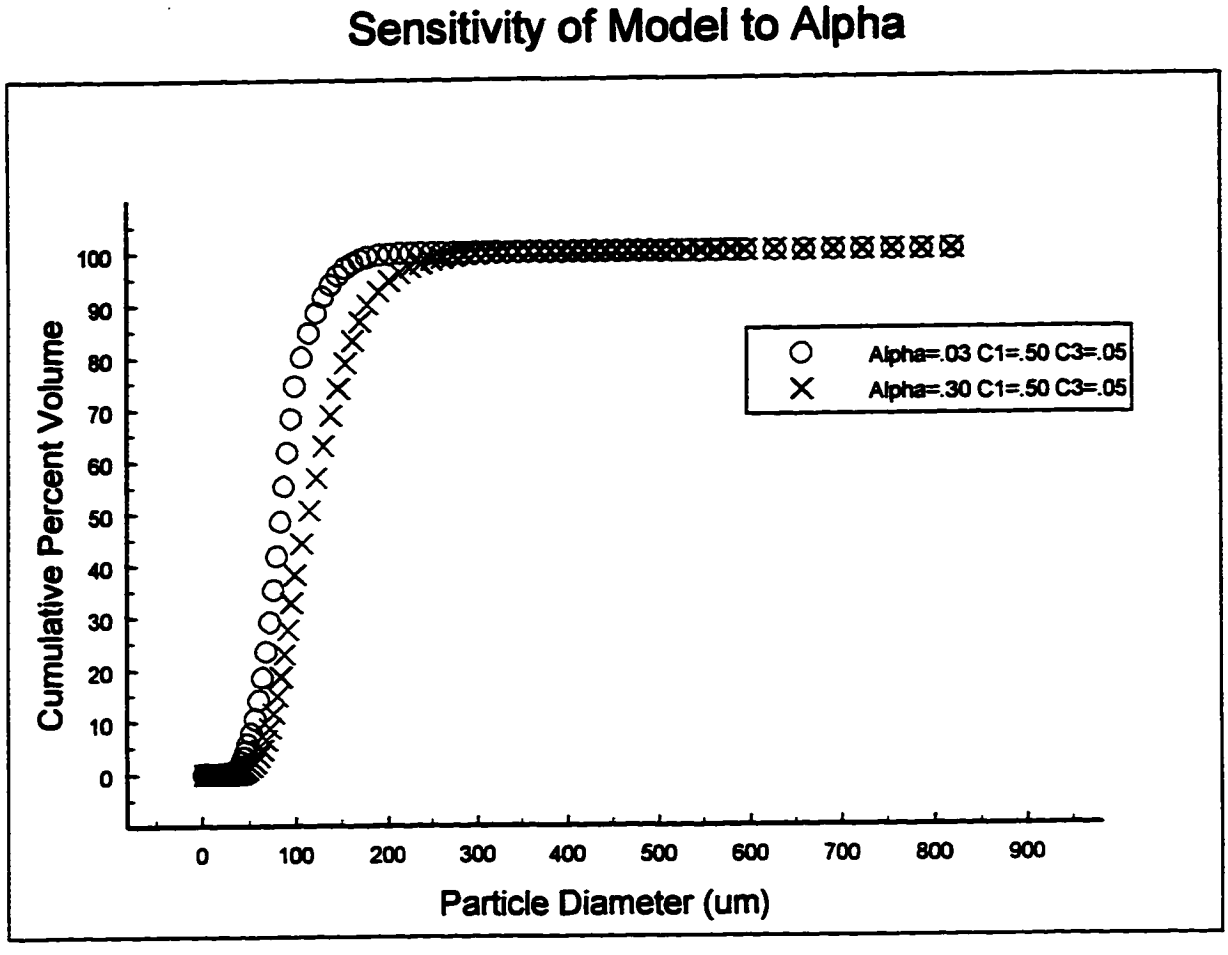

Figure 6.2.1: Effect of α on the Population Balance Model

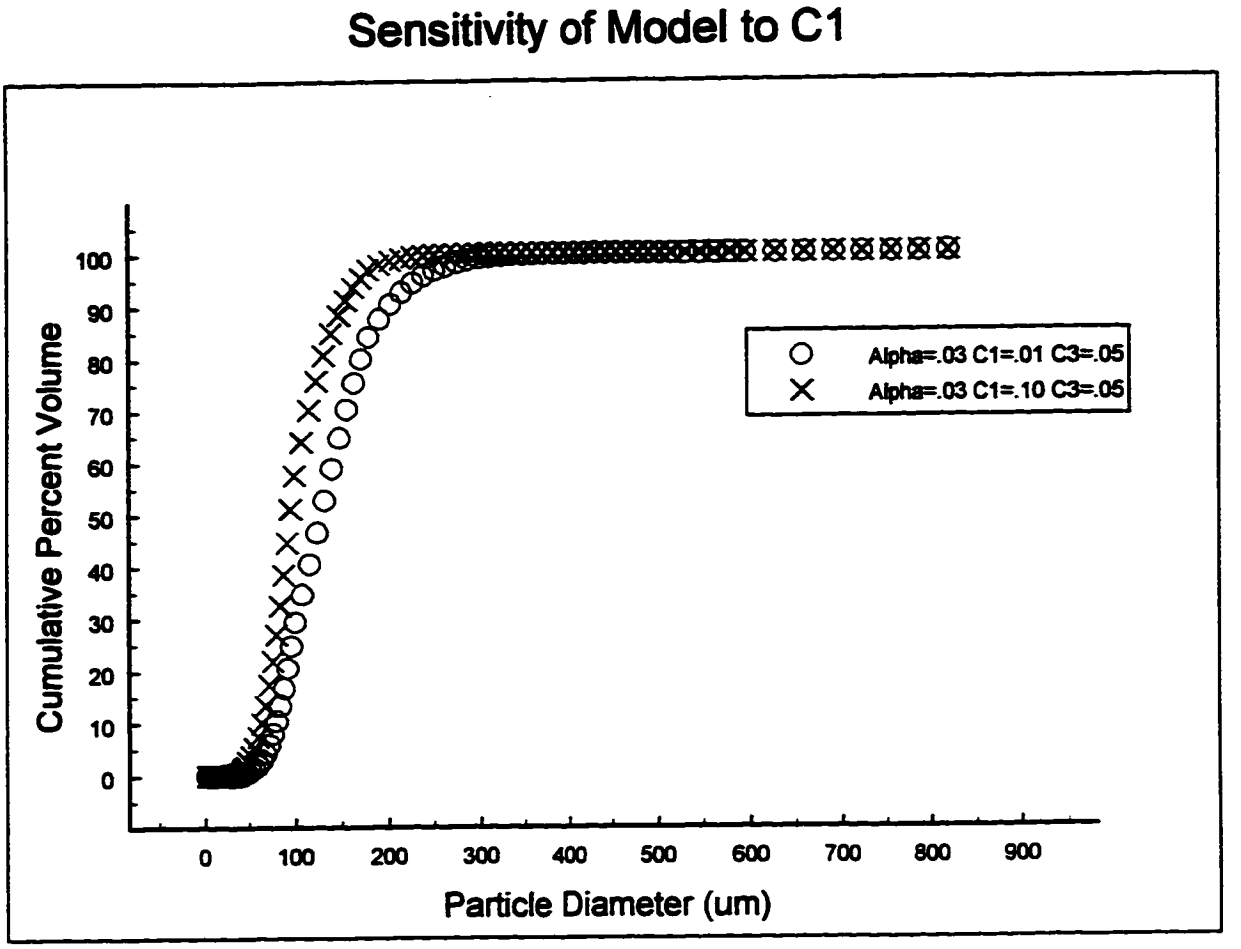

Figure 6.2.2: Effect of c_1 on the Population Balance Model

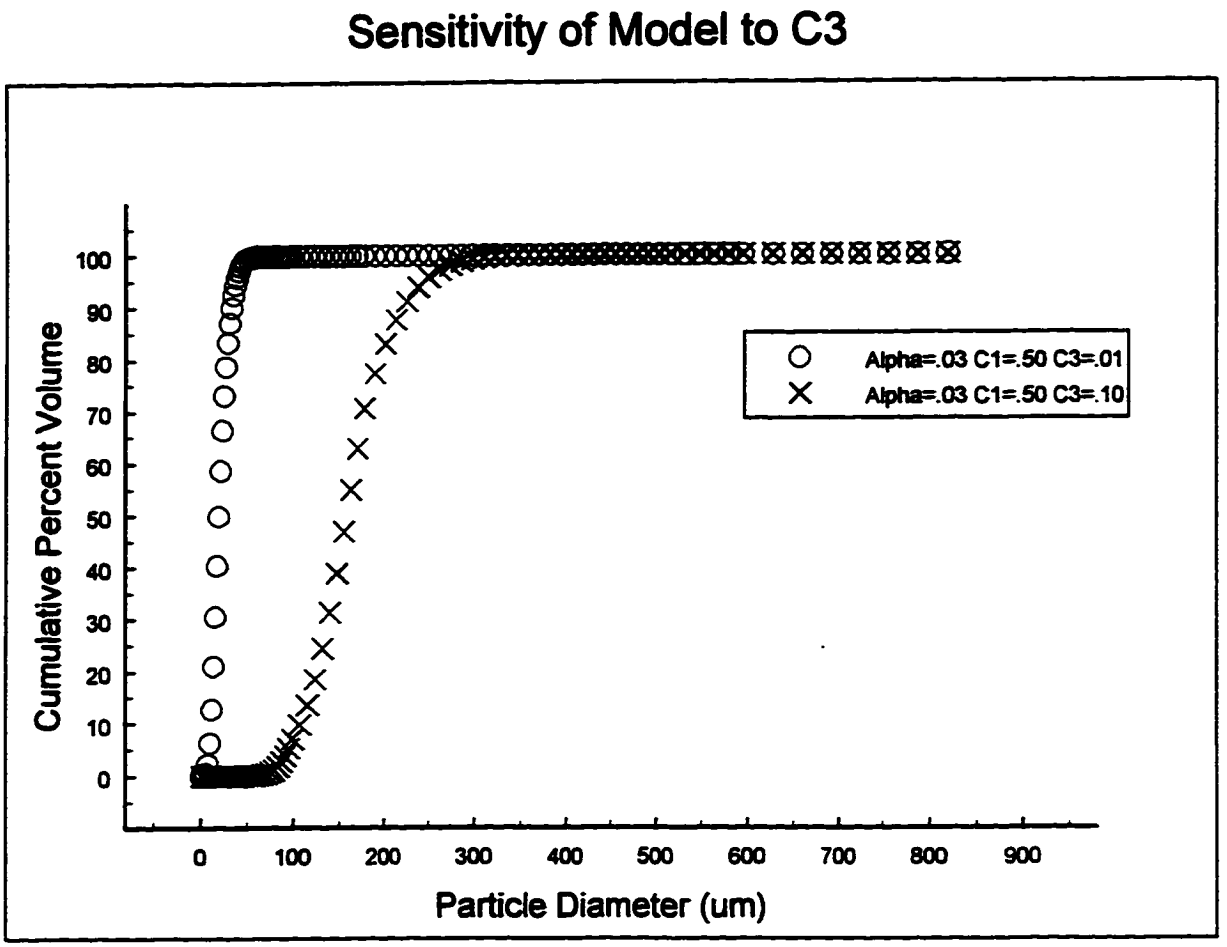

Figure 6.2.3: Effect of c_3 on the Population Balance Model

Table 6.2.1:Sensitivity Analysis of Population Balance Model

α	c_1	c_3	Mean Particle Size	Standard Deviation
0.03	0.50	0.05	90.84	29.91
0.30	0.50	0.05	126.47	46.75
0.03	0.01	0.05	139.02	52.53
0.03	0.10	0.05	105.68	36.91
0.03	0.50	0.01	22.51	9.13
0.03	0.50	0.10	167.68	46.52

increasing c_3 will reduce the value of k_b.

Based on the results in Figures 6.2.1 - 6.2.3, the population balance model appears to be very sensitive to the value of c_3. Table 6.2.1 displays the values of the volume mean particle size and the standard deviation produced by Equation 4.17. As can be seen in Table 6.2.1, increasing the value of c_3 by one order of magnitude has a significant effect on the mean particle size and the standard deviation. Whereas increasing the value of α and c_1 by one order of magnitude only changes the volume mean particle size and the standard deviation by a relatively small amount.

6.2.2 Determination of Optimal Empirical Constants

The determination of the optimal values for α, c_1, and c_3 was done by finding the minimum sum of the squares of residuals (SSR) value between the experimental and simulated cumulative particle size distributions (Eqn 4.19: SSR(α, c_1, c_3)) from the 5L Rushton turbine results. The minimum SSR value was found by developing a sum of squares surface showing the behavior of Equation 4.19 as a function of α, c_1, and c_3. The range of values tested for α, c_1 and c_3 are shown in Table 6.2.2. The range of α values used in this study is based on experimentally observed α values by previous investigators (Curtis and Hocking, 1969; Higashitani et al., 1983; Logtenberg and Stein, 1985; DeBoer et al., 1989; Kusters, 1991; Jiang and Logan, 1996). The

Table 6.2.2: Range of Empirical Constants Tested in the Population Balance Model

α	c_1	c_3
0.001 - 0.3	0.01 - 2.45	0.01 - 0.1

range of c_3 was determined based on the extreme sensitivity of the population balance model to c_3 (Section 5.2.1). Contours of the SSR values are displayed in Figures 6.2.4 - 6.2.11. Each figure represents a different α value. As can be seen in Figures 6.2.4 - 6.2.11, there is a wide range of SSR values. The high SSR values seem to occupy the high and low values of c_3 ($0.01 \leq c_3 \leq 0.03$ & $0.07 \leq c_3 \leq .1$). The low values of the SSR occupies the mid range values of c_3 ($0.04 \leq c_3 \leq 0.06$).

From Figures 6.2.4 - 6.2.11, it is evident that the SSR values are decreasing as α decreases until $\alpha = 0.005$. At an $\alpha = 0.001$, the SSR value is a constant high value equal to 41,488 regardless of c_1 and c_3. An SSR contour plot was not possible with $\alpha = 0.001$ since a constant value was produced at all c_1 and c_3 values. With an α value of 0.001, no growth was found to occur with the population balance model. This explains the constant high SSR value at all c_1 and c_3 locations. However, the relationship between the SSR value and c_1 is not that clear. From Figures 6.2.4 - 6.2.11, there appears to be a slight increase in the SSR value with increasing c1 value. But the change in SSR value with c_1 is very small. This is evident by the contours of the SSR values being almost parallel to the c_1 axis.

Figure 6.2.12 displays the local minimum SSR found for each α value. As can be seen in Figure 6.2.12, the global minimum SSR value appears to reside between an alpha of 0.005 and 0.03. With further refinement, the global minimum SSR value occurred at $\alpha = 0.006$, $c_1 = 0.4$, and $c_3 = 0.06$. The value of SSR_{min} was 76.67.

Based on SSR_{min}, a 95% confidence region of where the global minimum SSR could reside was determined for α, c_1, and c_3 (Box, Hunter, Hunter, 1978). A $(1 - \alpha_c)$ joint confidence region for α, c_1, and c_3, is bounded by a sum of squares contour SSR_c such that

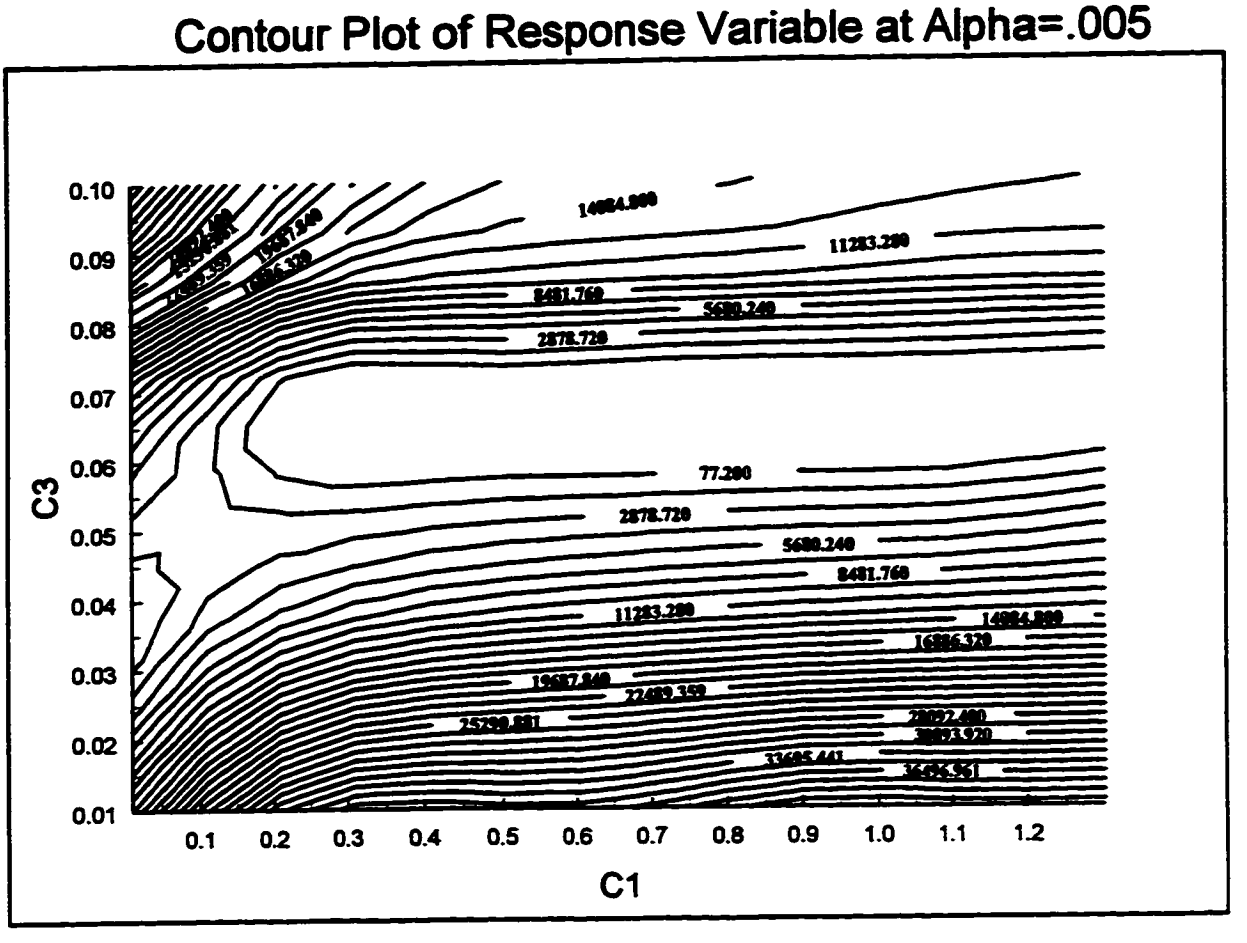

Figure 6.2.4: Contours of SSR(α, c_1, c_3) with $\alpha = 0.005$

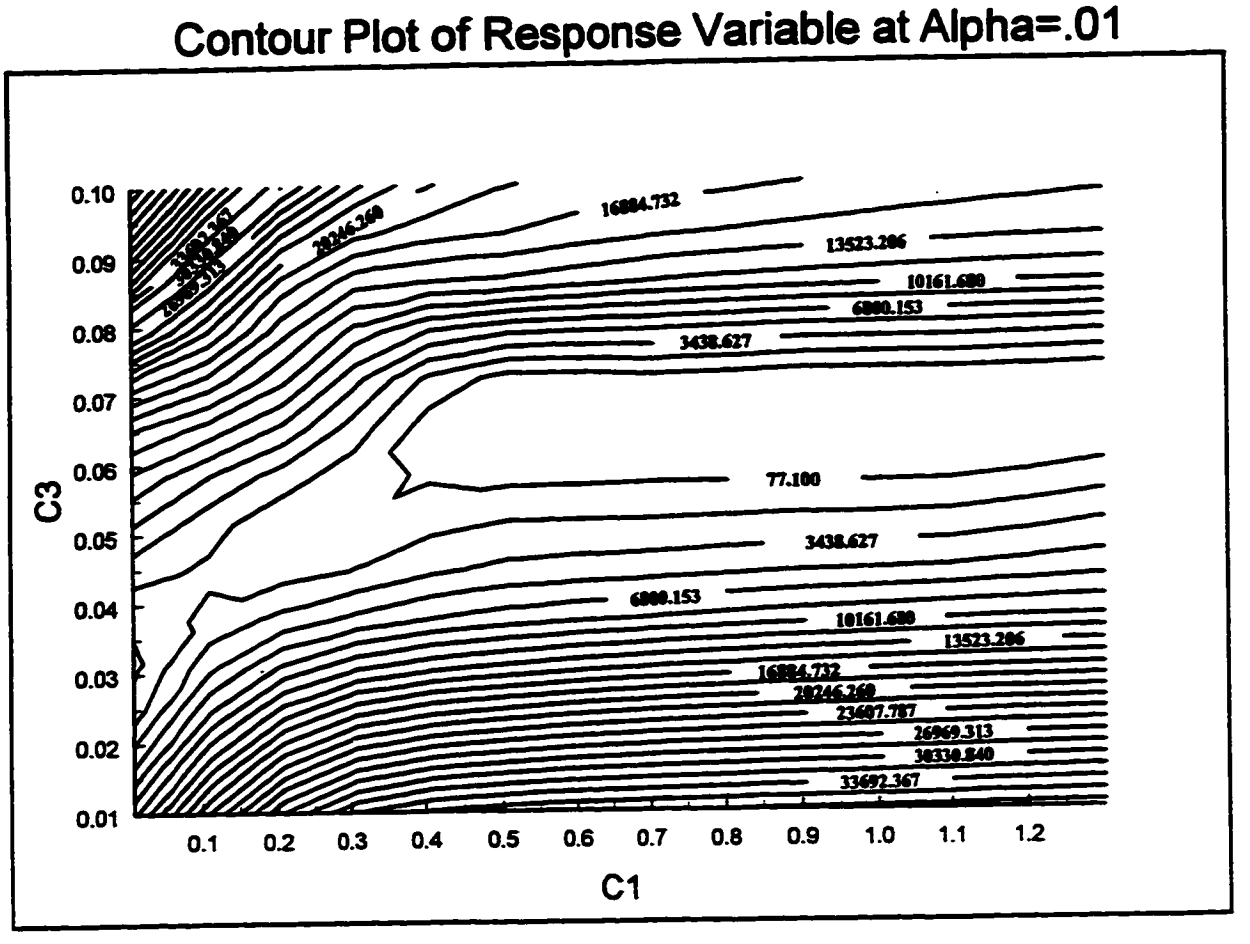

Figure 6.2.5: Contours of SSR(α, c_1, c_3) with $\alpha = 0.01$

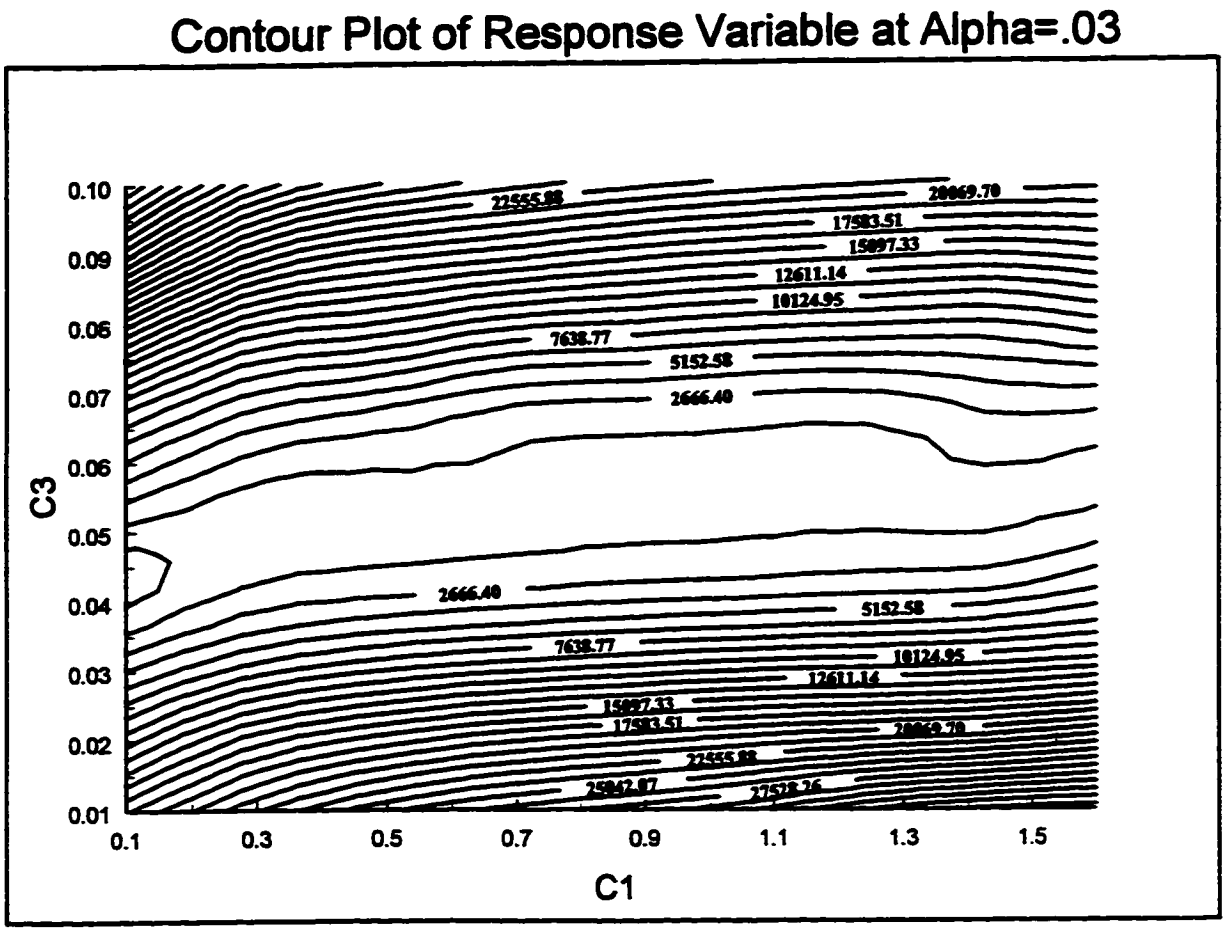

Figure 6.2.6: Contours of SSR(α, c_1, c_3) with $\alpha = 0.03$

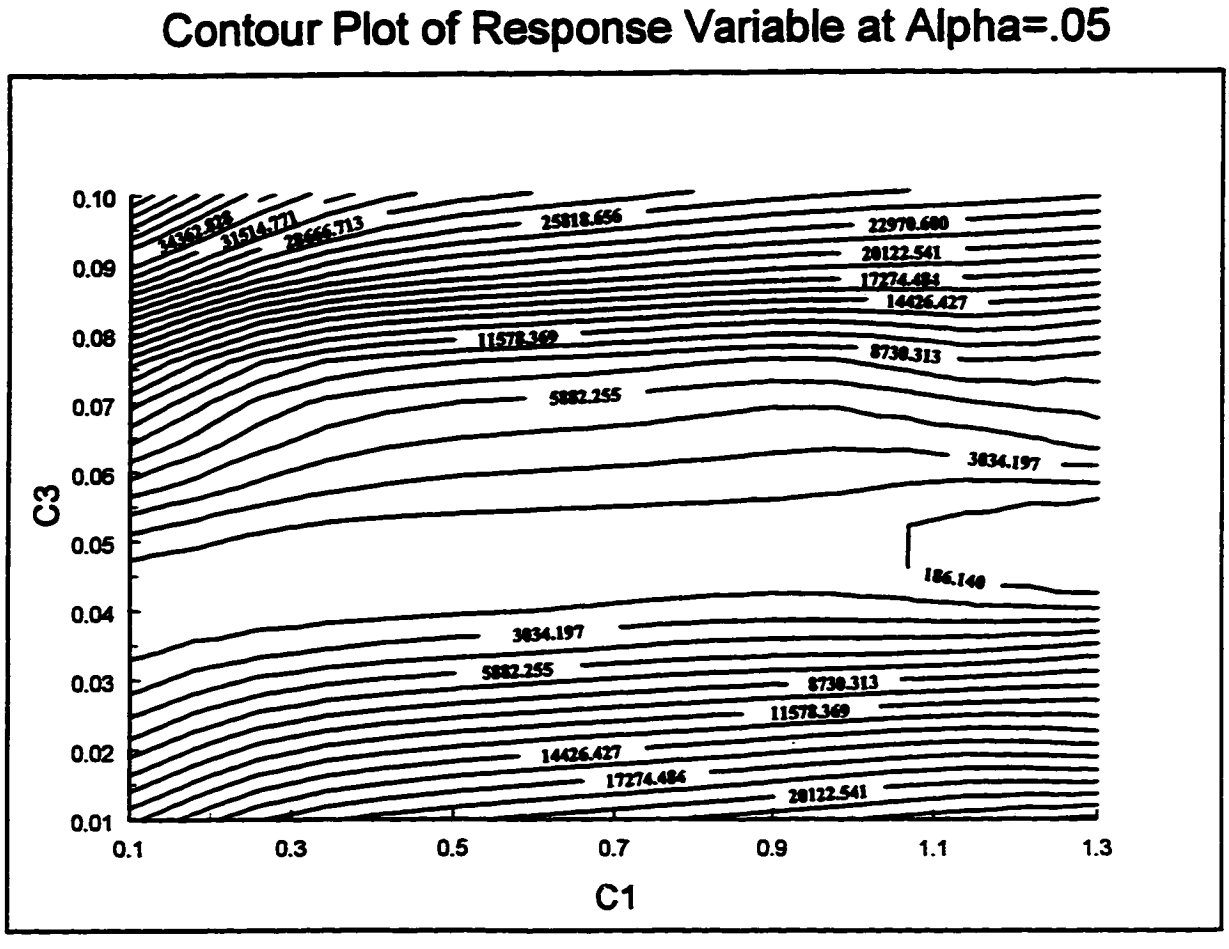

Figure 6.2.7: Contours of SSR(α, c_1, c_3) with $\alpha = 0.05$

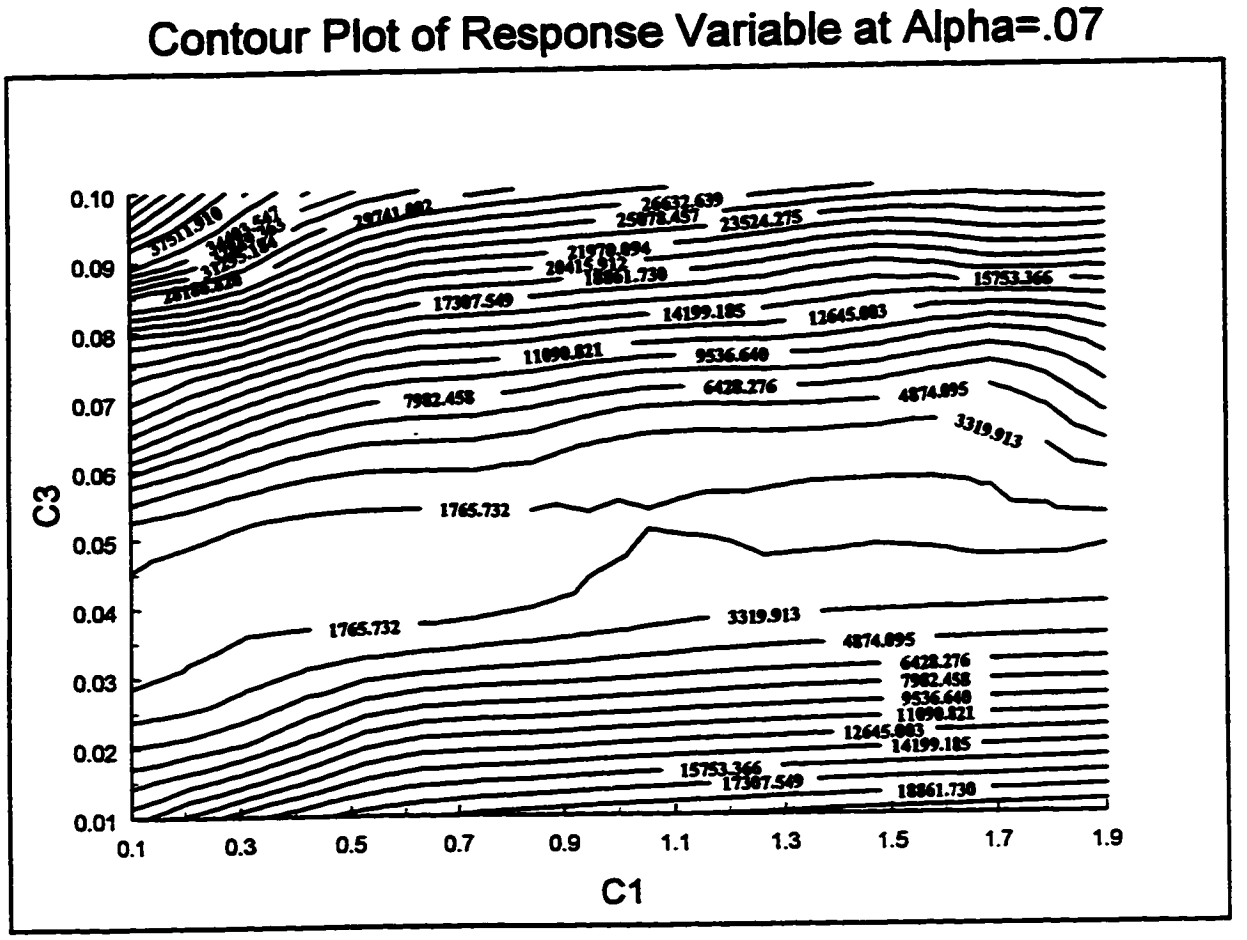

Figure 6.2.8: Contours of SSR(α, c_1, c_3) with $\alpha = 0.07$

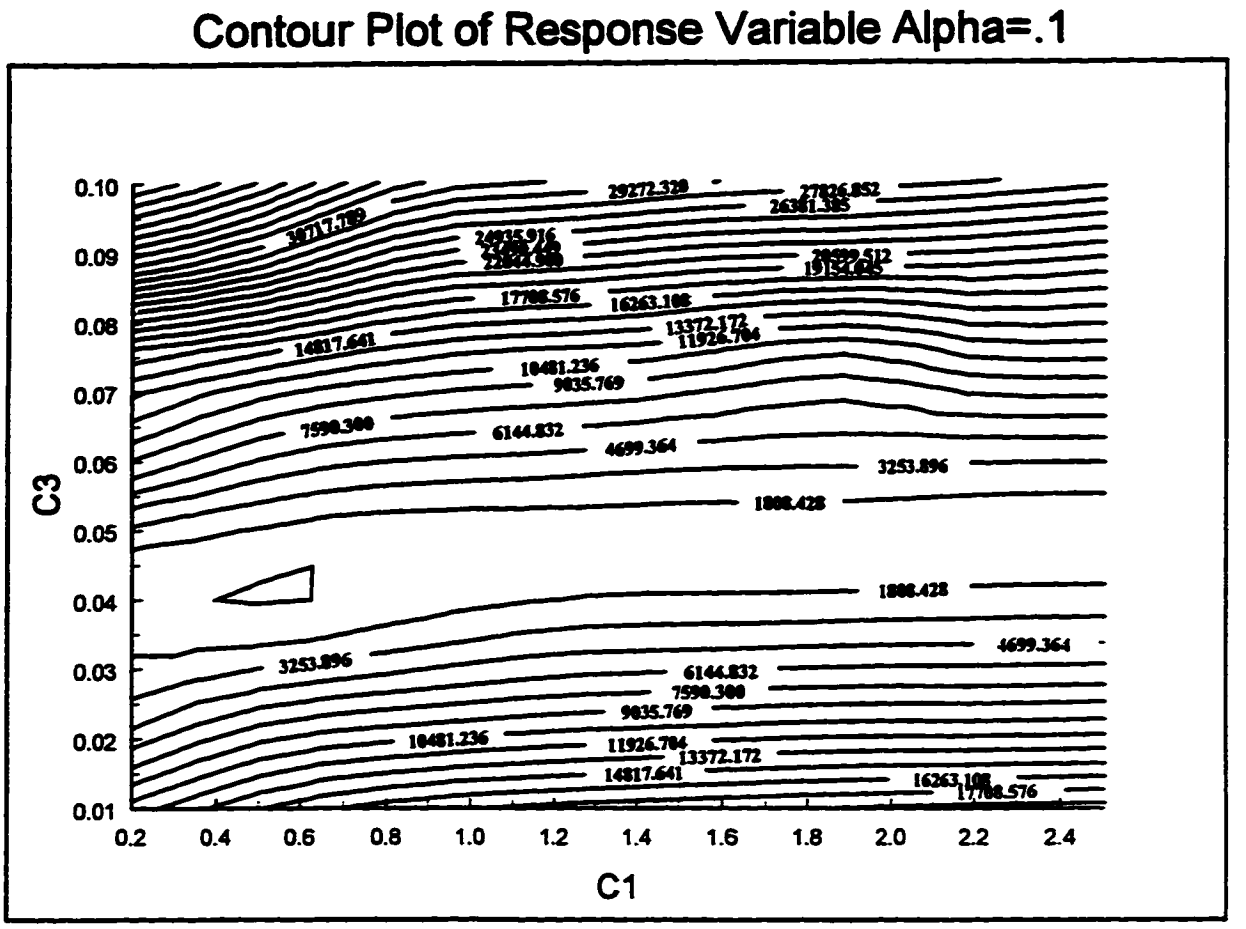

Figure 6.2.9: Contours of SSR(α, c_1, c_3) with $\alpha = 0.1$

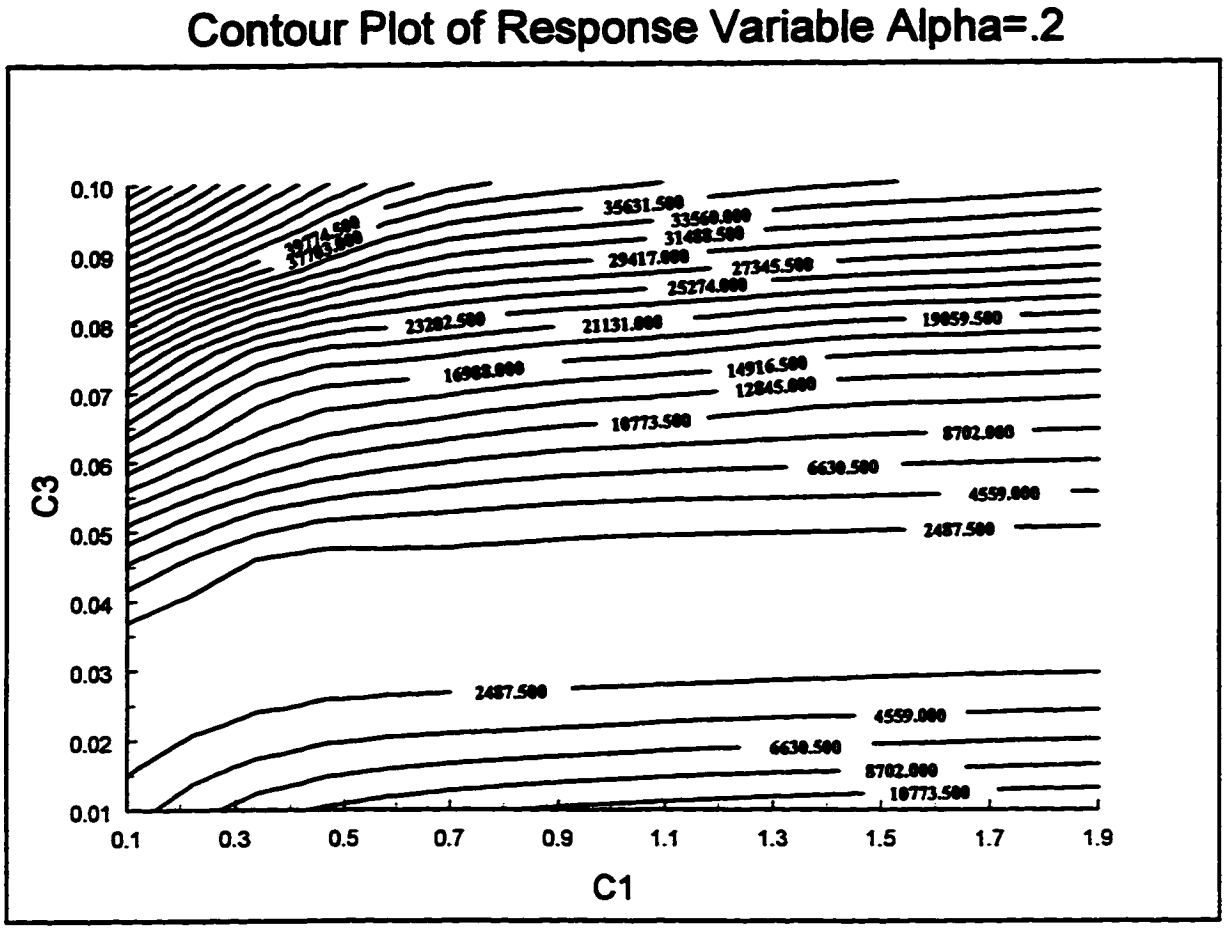

Figure 6.2.10: Contours of SSR(α, c_1, c_3) with $\alpha = 0.2$

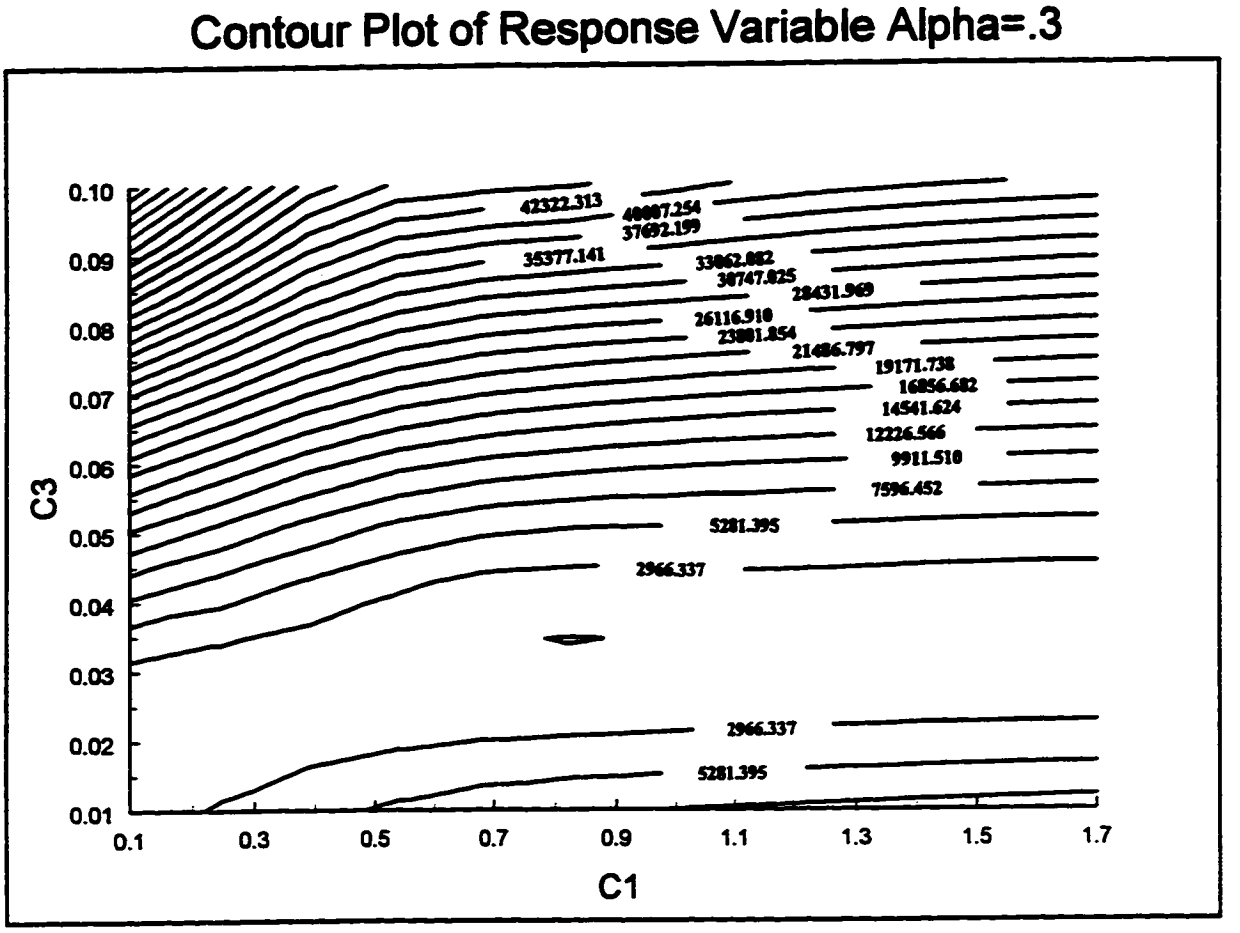

Figure 6.2.11: Contours of SSR(α, c_1, c_3) with $\alpha = 0.3$

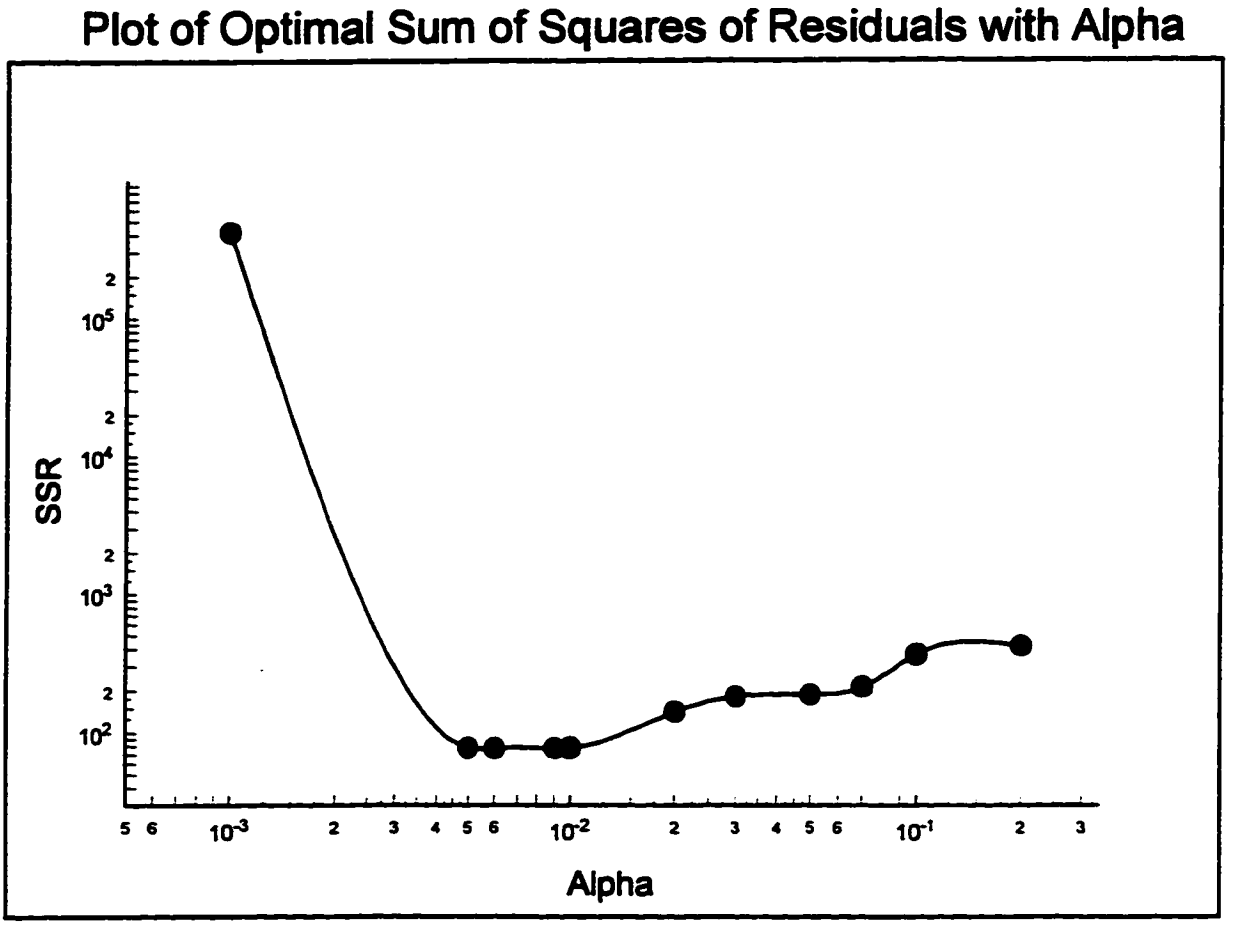

Figure 6.2.12: Plot of Local Minimum SSR(α, c_1, c_3)

$$SSR_c(\alpha, c_1, c_3) = SSR_{min}\left[1 + \frac{p}{n-p}F_{\alpha c}(p, n-p)\right] \quad (6.4)$$

where

p = number of fitting parameters

n = number of parameters in the sum of squares of residual

$F_{\alpha c}(p,n-p)$ = the significance point of the F distribution

In this study, p = 3, n = 5, and $F_{.05}(3,2) = 19.16$. Substituting those values and $SSR_{min} = 76.67$ into Equation 6.4, SSR_c was found to be 2280. Hence, there is a 95% probability that the optimal value for α, c_1, and c_3 resides in the region bounded by $SSR_c = 2280$. Figures 6.2.13 and 6.2.14 display the SSR_c contour for each alpha value investigated in this study. As can be seen in Figures 6.2.13 and 6.2.14, SSR_c extends throughout the entire region of c_1 values, between 0.005 - 0.3 for α, and between 0.03 - 0.08 for c_3.

The results in Figures 6.2.13 and 6.2.14 suggest that the model may be improved by removing the c_1 term from Equation 4.15. By removing c_1, the 95% confidence region would be reduced. Using the optimal empirical constants in this section, the model will be used to predict the steady state particle size distribution in the 5L, 28L, and 560L tank size with the Rushton turbine and A310 foil impeller.

6.2.3 Influence of Tank Size on Particle Size Distribution

The model presented in Section 4.2 was used to predict the flocculation experimental results in Section 6.1.2. Figure 6.2.15 displays the cumulative particle size distribution of the model and the experimental results for the 5L, 28L, and 560 L tank sizes with a Rushton turbine. As can be seen in Figure 6.2.15, the model clearly shows the shift in the cumulative particle size distribution to the smaller particle size range with increasing tank size. However, the model does

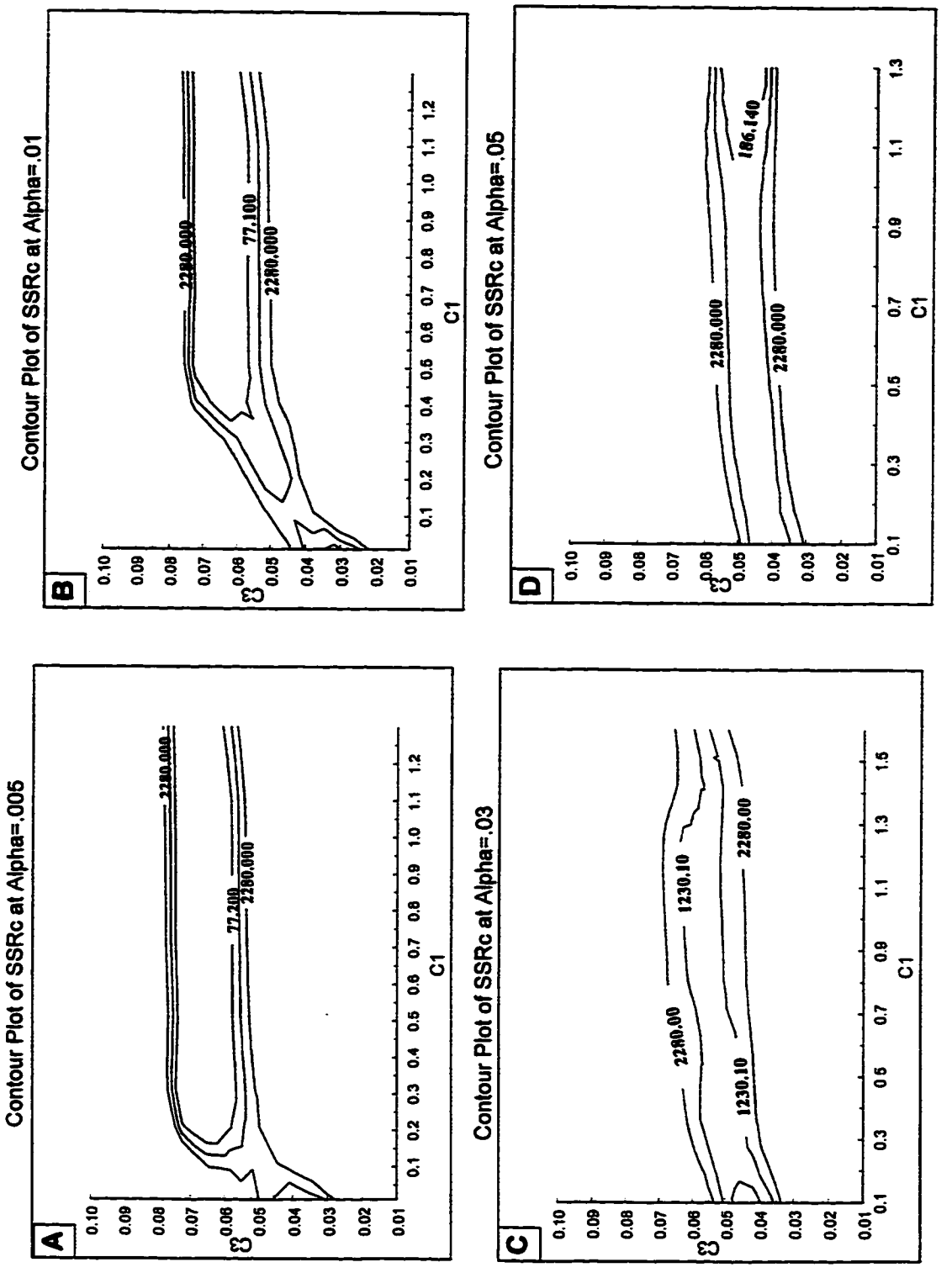

Figure 6.2.13: Plot of SSR_c for A) $\alpha = 0.005$, B) $\alpha = 0.01$, C) $\alpha = 0.03$, D) $\alpha = 0.05$

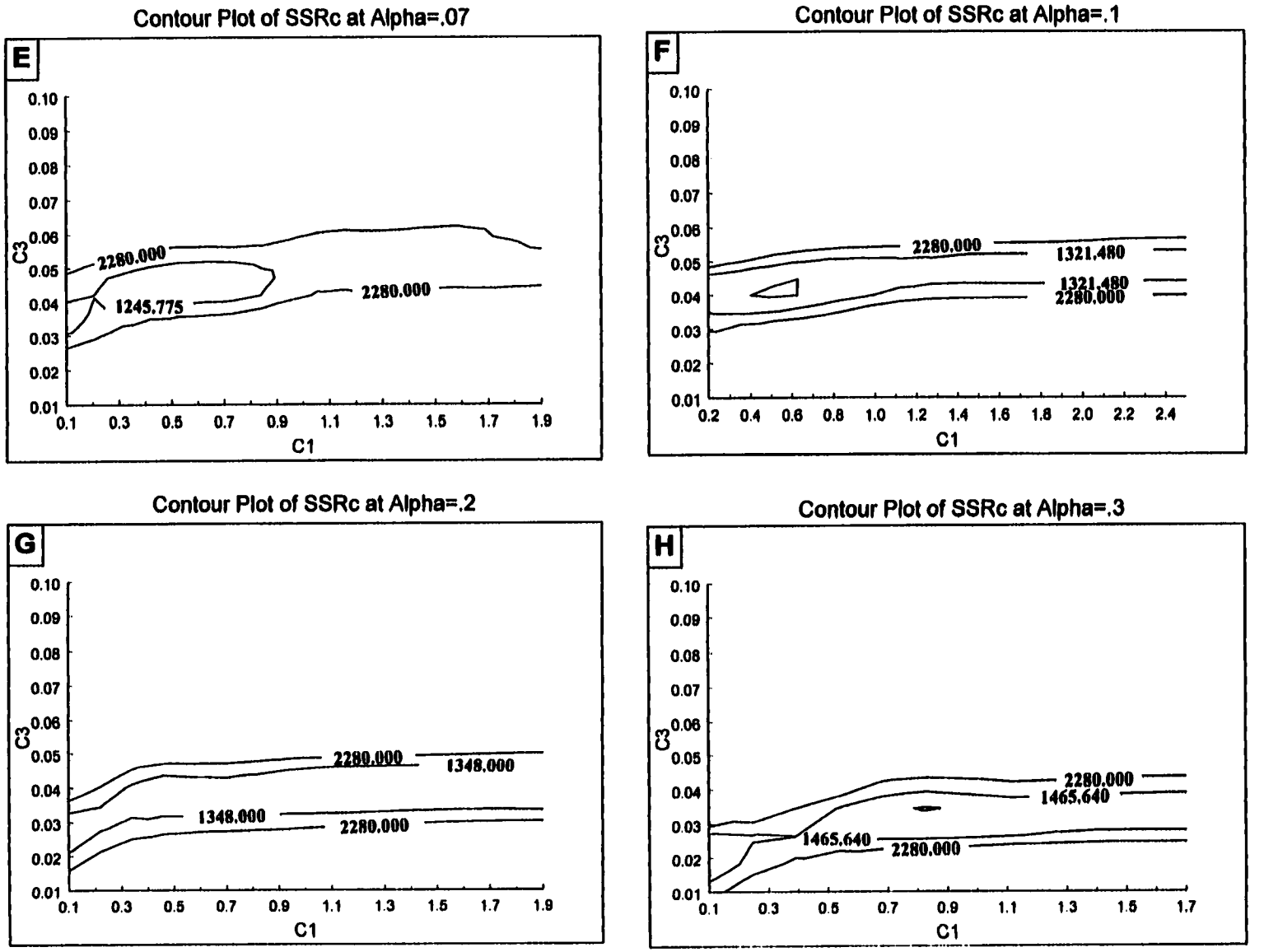

Figure 6.2.14: Plot of SSR_c for E) $\alpha = 0.07$, F) $\alpha = 0.1$, G) $\alpha = 0.2$, H) $\alpha = 0.3$

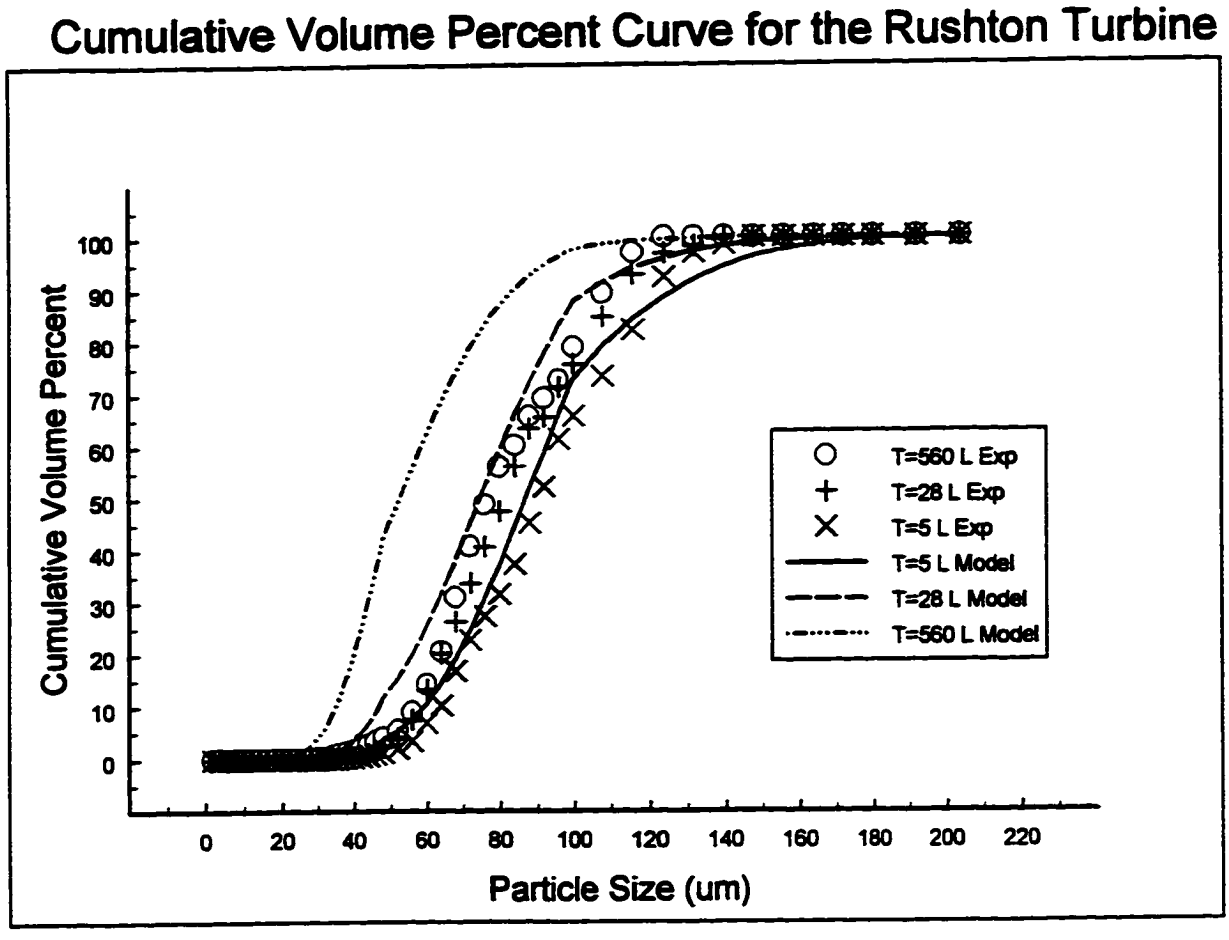

Figure 6.2.15: Cumulative Particle Size Distribution for the Rushton Turbine: Comparison between the Model and Experimental Results

seem to predict more particle breakup with increasing tank size than what was determined experimentally. As a result of this higher breakup rate, the model predicts a much lower particle size range in the 560L tank size than what was found experimentally.

Figure 6.2.16 displays the cumulative particle size distribution of the model and experimental results for the three tank sizes with an A310 foil impeller. From Figure 6.2.16, the model also predicts the shift in the distribution to the smaller particle size range with increasing tank size. But again, the model predicts more particle breakup with increasing tank size. As with the Rushton turbine prediction, the model produces a much lower particle size range in the 560L tank size than the experimental results.

Table 6.2.3 presents a comparison between the model and experimental results of the volume mean particle size and the standard deviation at different tank sizes. The volume mean particle size and standard deviation for the population balance model were calculated using Equations 6.1 and 6.2 respectively. From Table 6.2.3, the model predicts the decreasing value of the mean particle size and the standard deviation that was found experimentally. Table 6.2.3 clearly shows a significant difference between the predicted and experimental mean particle size at the 560 L tank size. Again this discrepancy between the model and experimental mean particle size at T=560L is due to the model's over prediction of the particle breakup at that tank size.

Table 6.2.4 presents a comparison between the model and the experimental maximum particle size. In Table 6.2.4, four particle sizes (d_{90}, d_{95}, d_{99}, $d_{99.9}$) were chosen to represent the range of particle sizes predicted by the model where the true maximum particle size may exist. The model results for the maximum particle size were displayed with these four diameter sizes because it is difficult to know with extreme accuracy that the experimentally measured maximum particle size is the true maximum particle size. It might be possible to obtain larger maximum particle sizes by increasing the number of floc particles that are analyzed for each tank size (Clark, 1985). Therefore, d_{90}-$d_{99.9}$ represents the model's prediction of a possible range of particle sizes where the true maximum particle may reside.

As can be seen in Table 6.2.4, the value of the experimental maximum particle size lies between the predicted d_{90} and $d_{99.9}$ of the model for the Rushton turbine at all three tank sizes and for the A310 foil impeller at the 560L tank size. The population balance model, however, predicts

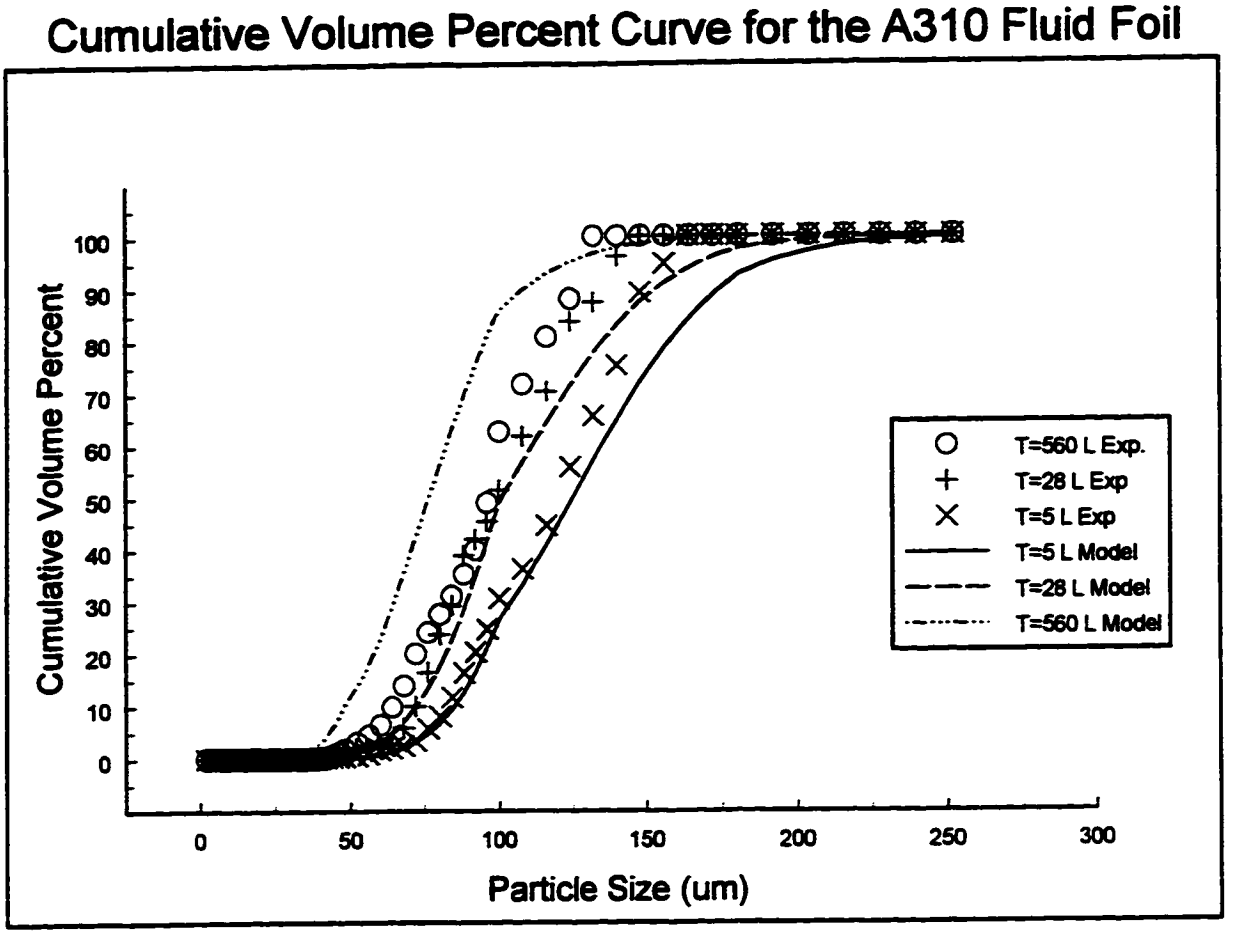

Figure 6.2.16: Cumulative Particle Size Distribution for the A310 Foil Impeller: Comparison between the Model and Experimental Results

Table 6.2.3: Influence of Tank Size and Impeller Type on Particle Size Distribution: Comparison Between Model & Experiments

Tank Size	Impeller Type	Volume Mean Particle Size		Standard Deviation	
		EXP	MODEL	EXP	MODEL
5L	Rushton	94.43	92.86	22.93	28.12
28L	Rushton	85.91	78.36	21.68	24.54
560L	Rushton	82.56	58.10	20.54	20.21
5L	A310 Foil	120.63	131.44	26.86	37.51
28L	A310 Foil	102.90	111.47	24.38	33.54
560L	A310 Foil	97.00	80.45	22.58	25.31

Table 6.2.4: Influence of Tank Size and Impeller Type on the Maximum Particle Size: Comparison between Model and Experimental Results

Tank Size	Impeller Type	Maximum Particle Size				
		EXP	Model d_{90}	Model d_{95}	Model d_{99}	Model $d_{99.9}$
5L	Rushton	135.51	127.49	142.91	171,65	212.83
28L	Rushton	127.82	104.79	119.54	149.03	182.12
560L	Rushton	116.83	83.77	92.49	112.95	146.95
5L	A310 Foil	158.06	174.57	191.14	231.06	281.60
28L	A310 Foil	140.25	153.58	168.47	201.44	250.05
560L	A310 Foil	126.96	108.33	123.45	153.9	188.98

a higher maximum particle size range for the A310 foil impeller at the 5L and 28L tank size. This higher maximum particle size range for the A310 foil impeller at the 5L and 28L tank size suggests that the experimentally measured maximum particle size may be in error at these tank sizes. However, more experiments would need to be done at the 5L and 28L tank sizes with the A310 impeller in order to verify the value of the maximum particle size. The model results in Table 6.2.4 do predict the same decreasing trend in the maximum particle size with increasing tank size that was found experimentally.

6.2.4 Influence of Impeller Type on Particle Size Distribution

The model in Section 4.2 was also used to predict the flocculation performance with the Rushton turbine and the A310 foil impeller. To the authors knowledge, no previous population balance model has demonstrated this capability. Figures 6.2.17 - 6.2.19 compare the cumulative particle size distribution between the Rushton turbine and the A310 foil impeller in the 5L, 28L and 560L tank size respectively.

As shown in the flocculation experimental results, the model predicts the degradation in flocculation performance moving from the A310 foil impeller to the Rushton turbine. This degradation in flocculation performance is evident by the shift in the cumulative particle size distribution in Figures 6.2.17- 6.2.19 to the smaller particle size range from the A310 foil to the Rushton impeller. Although the model does predict the difference in the flocculation performance between the Rushton turbine and A310 foil impeller in the 560L tank, the model produced a cumulative particle size distribution that is far to the left of the experimental distribution. Again, this is probably due to the model's incorrect prediction of the amount of particle breakup in the 560L tank size.

In Table 6.2.3, the volume mean particle size and the standard deviation are shown for the Rushton turbine and A310 foil impeller. As can be seen in Table 6.2.3, the model correctly predicts the shift to a higher mean particle size and standard deviation from the Rushton turbine to the A310 foil impeller. However, the shift to these higher values was more dramatic for the model than for the experimental results. The discrepancy between the model and experimental

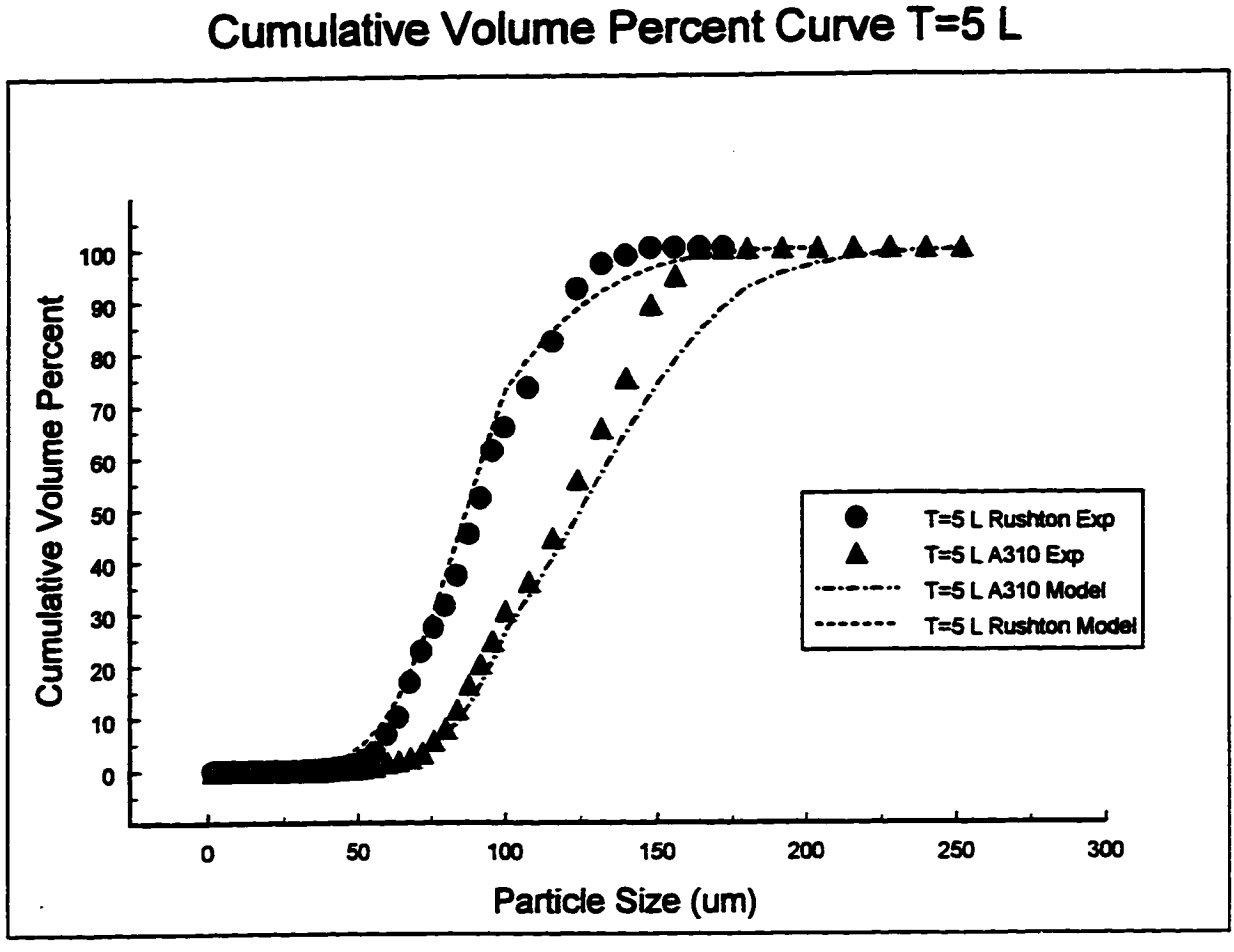

Figure 6.2.17: Cumulative Particle Size Distribution Between Rushton Turbine and A310 Foil Impeller after 30 Minutes of Flocculation: Comparison Between Model and Experimental Results T = 5L

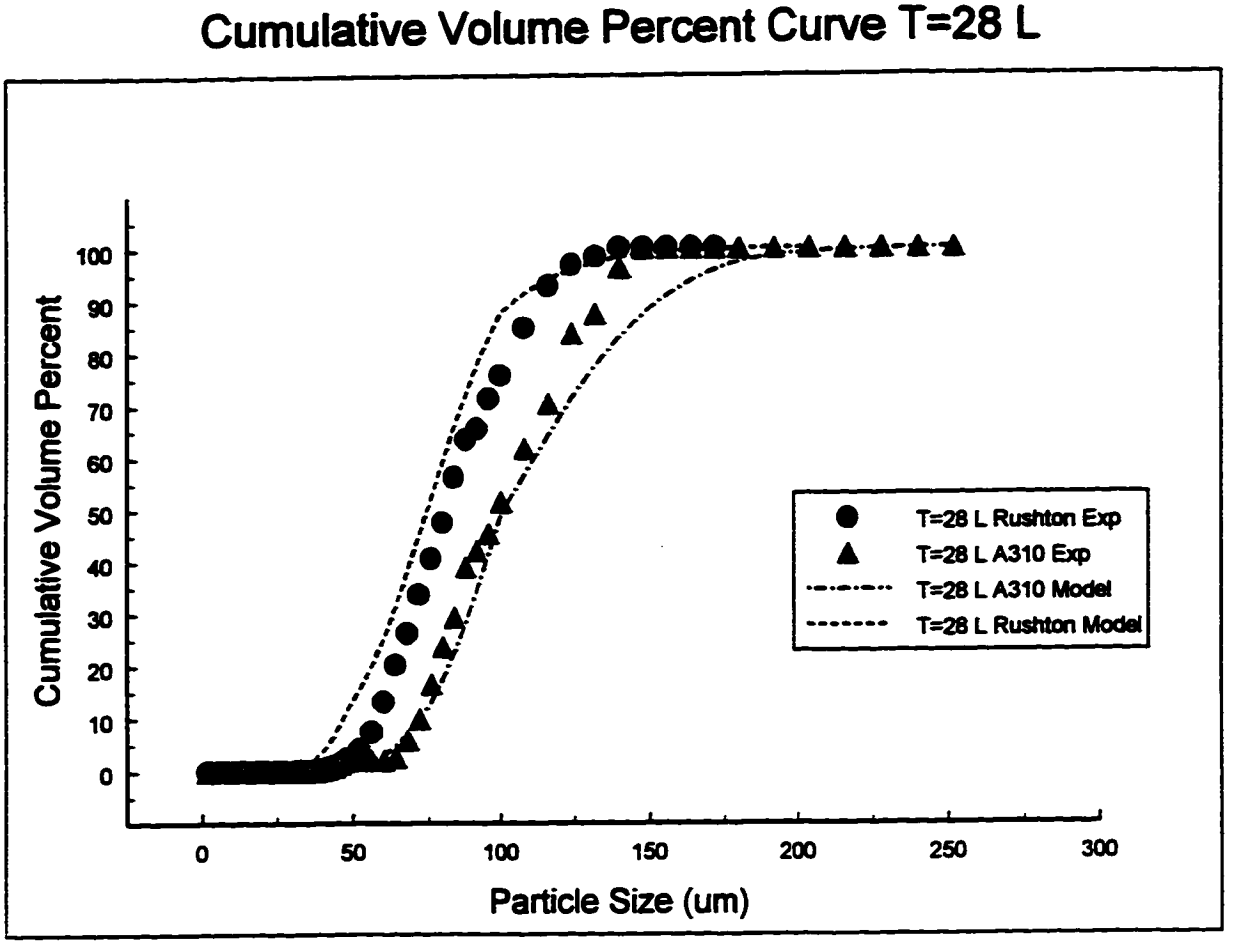

Figure 6.2.18: Cumulative Particle Size Distribution Between Rushton Turbine and A310 Foil Impeller after 30 Minutes of Flocculation: Comparison Between Model and Experimental Results T = 28L

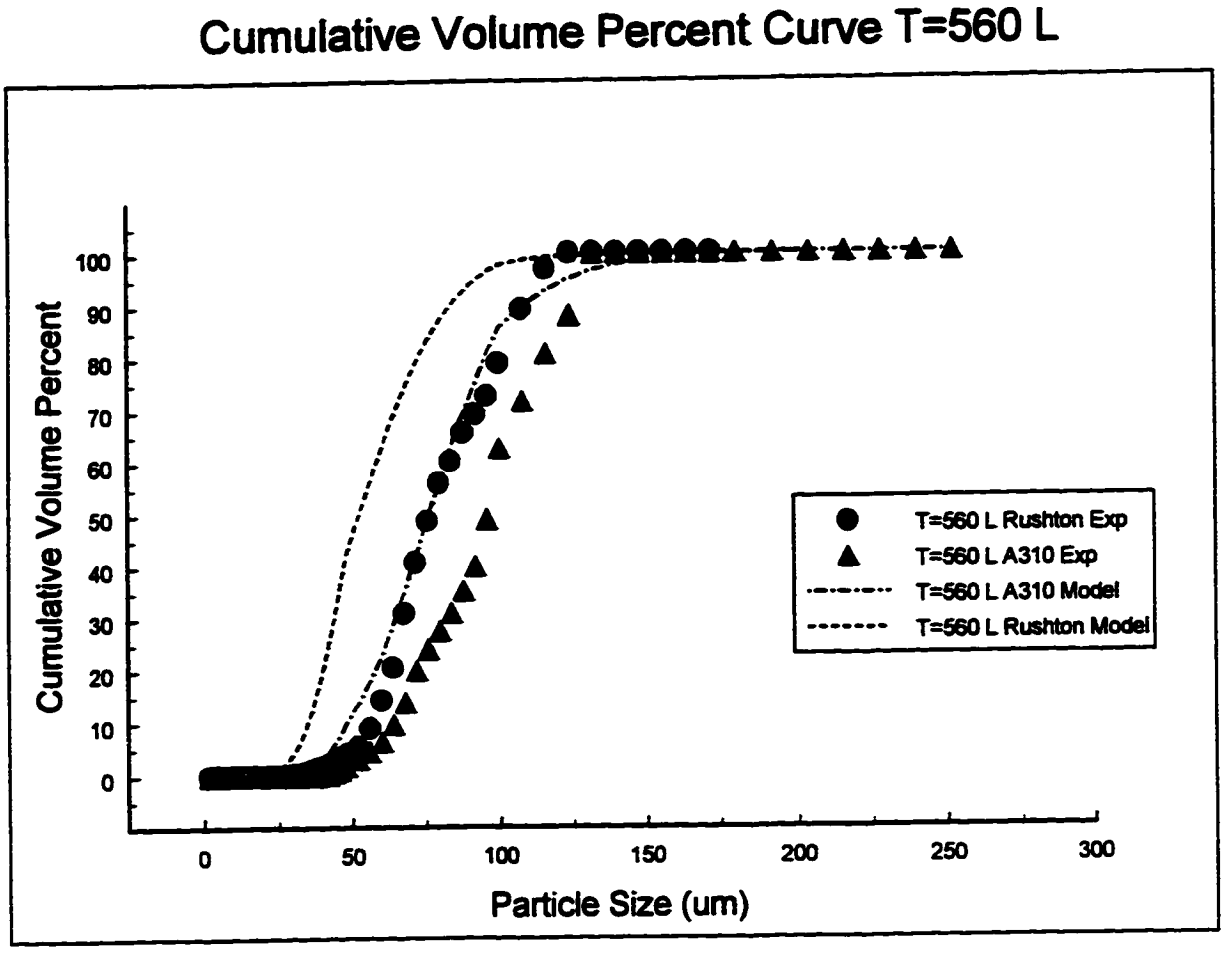

Figure 6.2.19: Cumulative Particle Size Distribution Between Rushton Turbine and A310 Foil Impeller after 30 Minutes of Flocculation: Comparison Between Model and Experimental Results T = 560L

results in Table 6.2.3 is probably due to the model's over prediction of the particle breakup frequency between the Rushton turbine and the A310 foil impeller.

6.2.5 Discussion

The model presented in Section 4.2 was evaluated to determine its effectiveness in predicting the influence of tank size and impeller type on the steady state floc size distribution. Until now, no simple population balance model was capable of predicting the shift in the particle size distribution to a smaller particle size range with increasing tank size when G_m = constant. Furthermore, no model was capable of predicting the shift in the particle size distribution to the smaller particle size range going from the A310 foil impeller to the Rushton turbine when G_m = constant. What makes this model even more superior than its predecessors is that the three empirical constants were optimally determined using only the Rushton turbine experimental data at T = 5L. This method of determining the empirical constants suggests that by obtaining the experimental data from one tank size and impeller type, researchers or engineers might be able to predict the flocculation results in another tank size and with a different impeller.

By achieving these two conditions, this model demonstrates that in order for a simple population balance model to predict the effects of tank size and impeller type on the flocculation performance, the population balance model must include the intensity of the large scale eddies in the impeller discharge zone in the particle breakup frequency. From Figures 6.2.15 and 6.2.16, the model clearly demonstrated its ability to track the degradation in the flocculation performance with increasing tank size regardless of the impeller type. In Figures 6.2.17 - 6.2.19, the model also demonstrated its ability to predict the degradation in flocculation performance moving from the A310 foil impeller to the Rushton turbine. Although the model was capable of accurately predicting the trend in flocculation performance with increasing tank size, the model seems to over predict the amount of particle breakup with increasing tank size.

In Figure 6.2.19, the model predicts a much lower particle size range in the 560L tank than what was found experimentally. The higher breakup rate in the 560L tank size is due to the influence of the turbulence intensity in the impeller discharge zone on $k_b(d)$. Recall that the

turbulence intensity in the impeller discharge zone is approximated by $N_p^{0.5}ND$. At constant G_m, $N_p^{0.5}ND$ increases with increasing tank size. This causes $k_b(d)$,

$$k_b(d) = C_1 N_Q N erfc[C_3 / N_p^{0.5} ND \rho^{1/2} d^{1/2}]$$

to increase with increasing tank size (Figure 6.2.20). However, the breakup frequency curve for the 560L tank size in Figure 6.2.20 is higher than what the experimental results suggest. A higher breakup frequency curve for the 560L tank size model will cause the particle size distribution to reside in a smaller particle size range than the experimental results.

One way to observe the difference in dependence on $N_p^{0.5}ND$ between the model and experimental results is to compare the relationship between the volume mean particle size, standard deviation and $N_p^{0.5}ND$. Figures 6.2.21 - 6.2.22 present a comparison between the model and experimental mean particle size and standard deviation as a function of $N_p^{0.5}ND$. As can be seen in Figures 6.2.21 - 6.2.22, the slope of the model data is higher than the experimental data for all three parameters. This higher slope for the model results confirm the higher sensitivity of the model predictions to $N_p^{0.5}ND$. The slope of the model in Figures 6.2.21 - 6.2.22 were quantified by fitting the power law equation in Section 6.1.4 (Eqn. 6.3).

Figures 6.2.23 - 6.2.24 display the curve fit equation for both the experimental and model results. A summary of the constant and the value of the exponent in Equation 6.3 are displayed in Table 6.2.5. As can be seen in Table 6.2.5, the value of the exponents are higher for the model predictions than for the experimental data. The results in Figures 6.2.23 - 6.2.24 and Table 6.2.5 suggest that further model improvements will come from reducing the sensitivity of $N_p^{0.5}ND$ on the breakup frequency.

Overall, the model demonstrates that the steady state particle size distribution does not simply depend on G_m. The steady state particle size distribution depends in part on the turbulence intensity produced in the impeller discharge zone. By including this information into the population balance model the steady state particle size distribution can be correctly predicted for different tank sizes and impeller types.

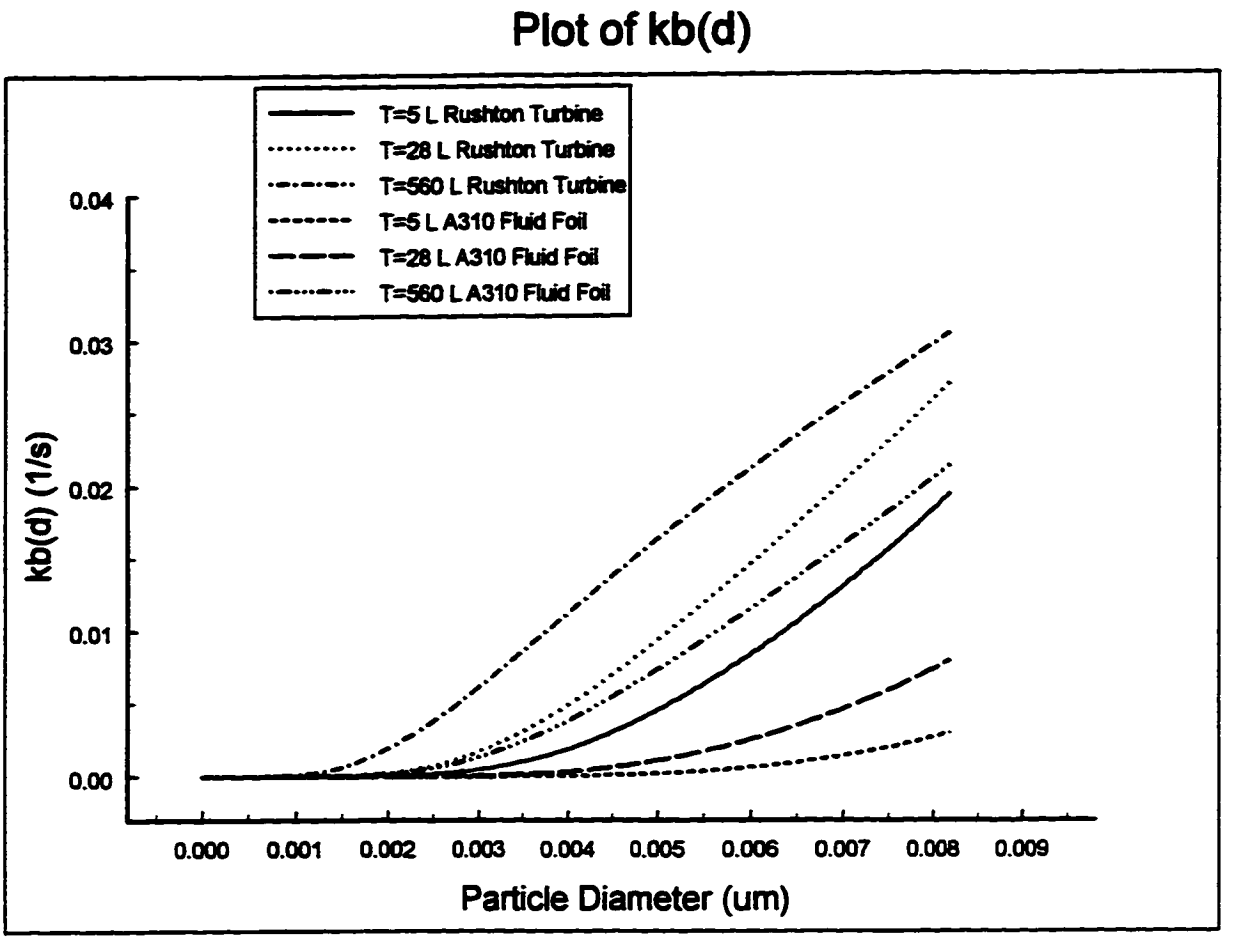

Figure 6.2.20: Plot of $k_b(d)$: Effect of Tank Size and Impeller Type

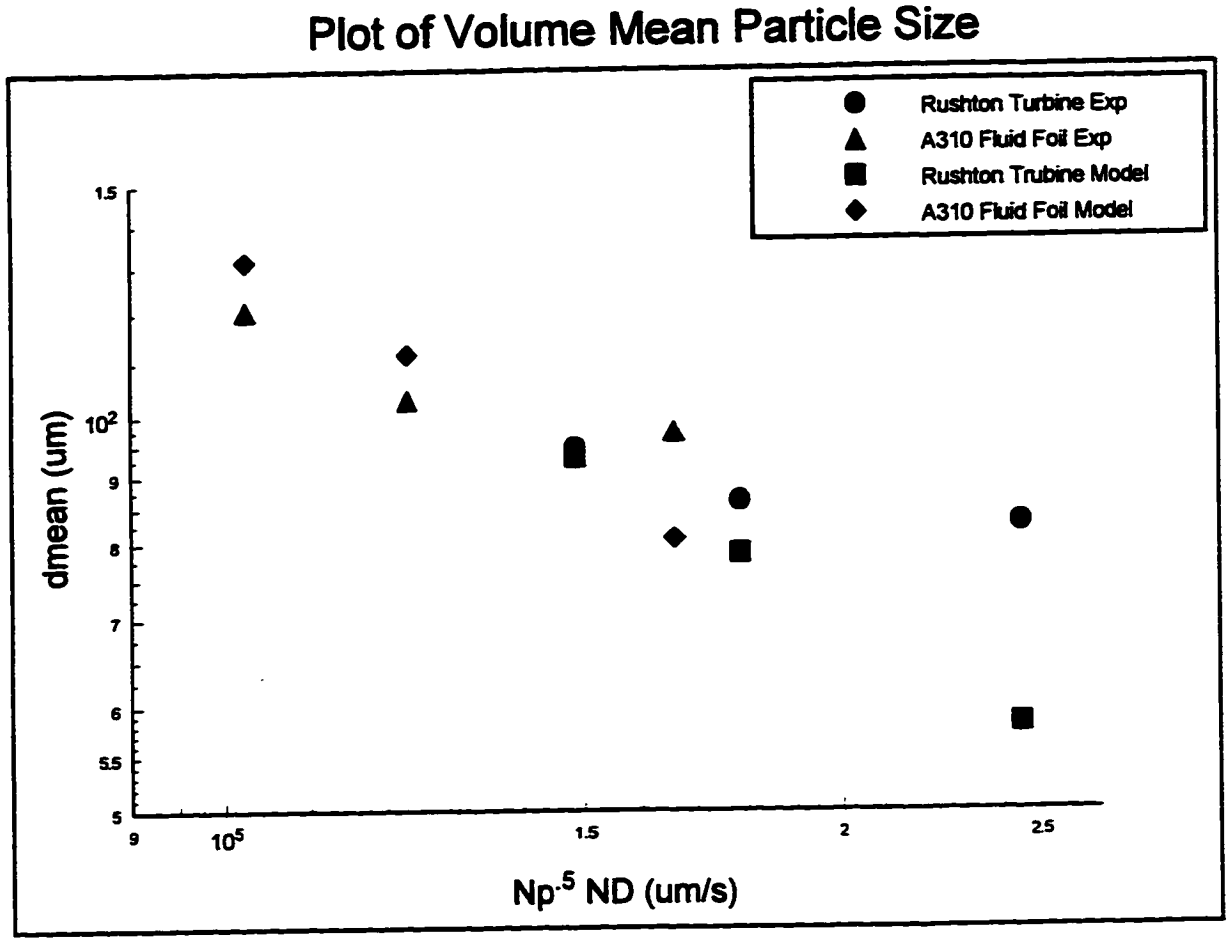

Figure 6.2.21: Volume Mean Particle Size as a Function of $N_p^{0.5}ND$: Comparison Between Model and Experimental Results

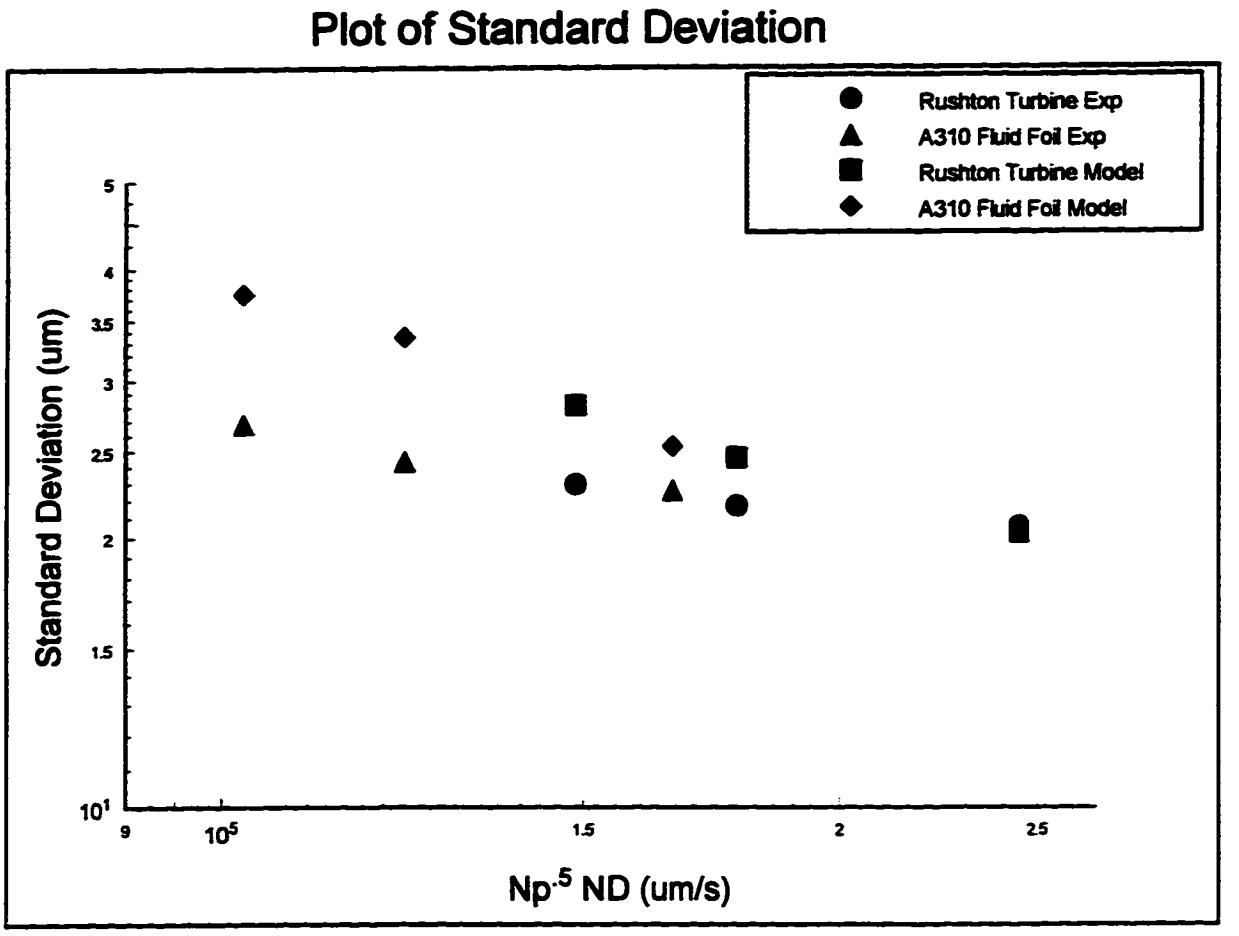

Figure 6.2.22: Standard Deviation as a Function of $N_p^{0.5}ND$: Comparison Between Model and Experimental Results

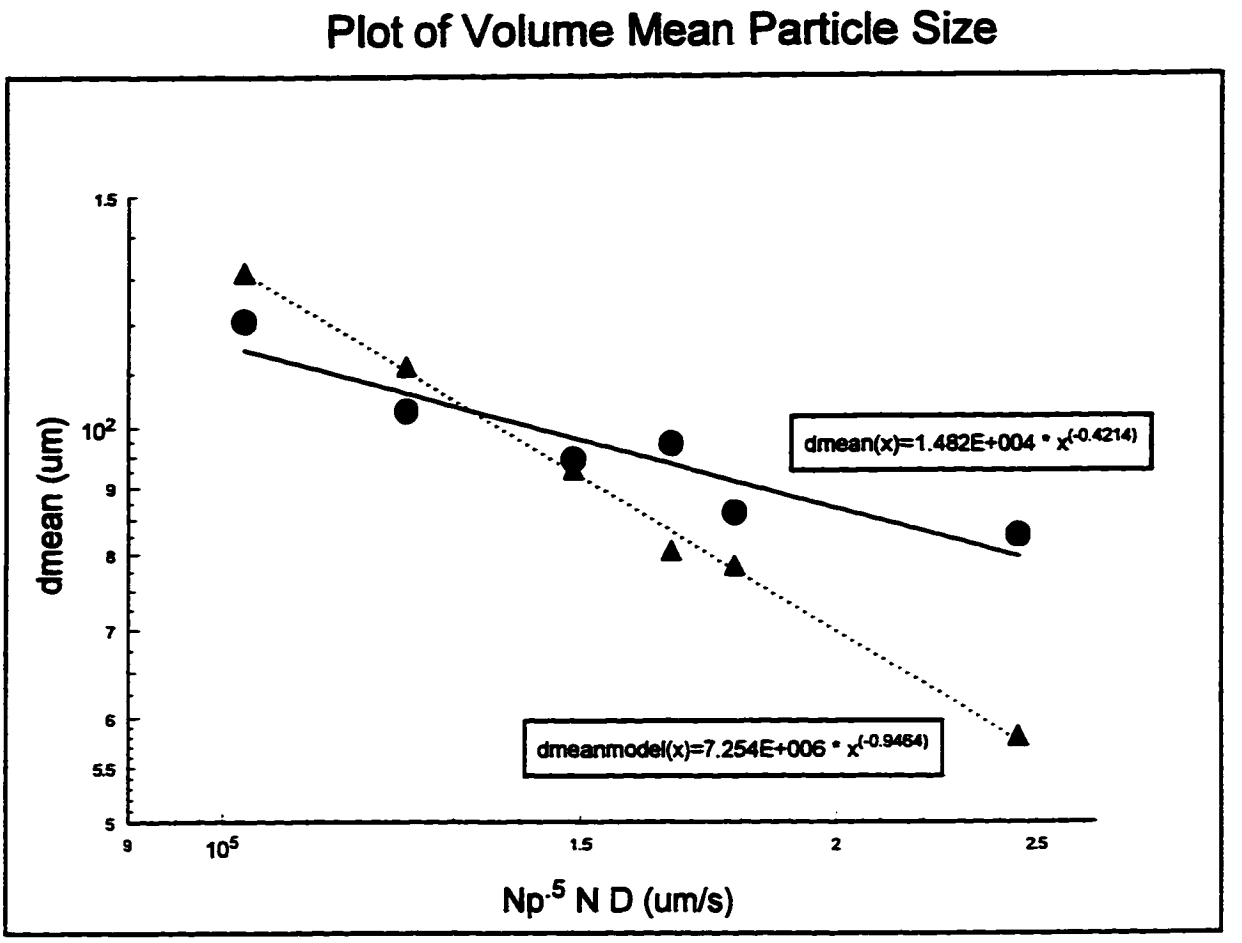

Figure 6.2.23: Curve Fit of Equation $d_i = \text{Constant}/(N_p^{0.5}ND)^y$ to the Volume Mean Particle Size Data: Comparison Between Model and Experimental Results

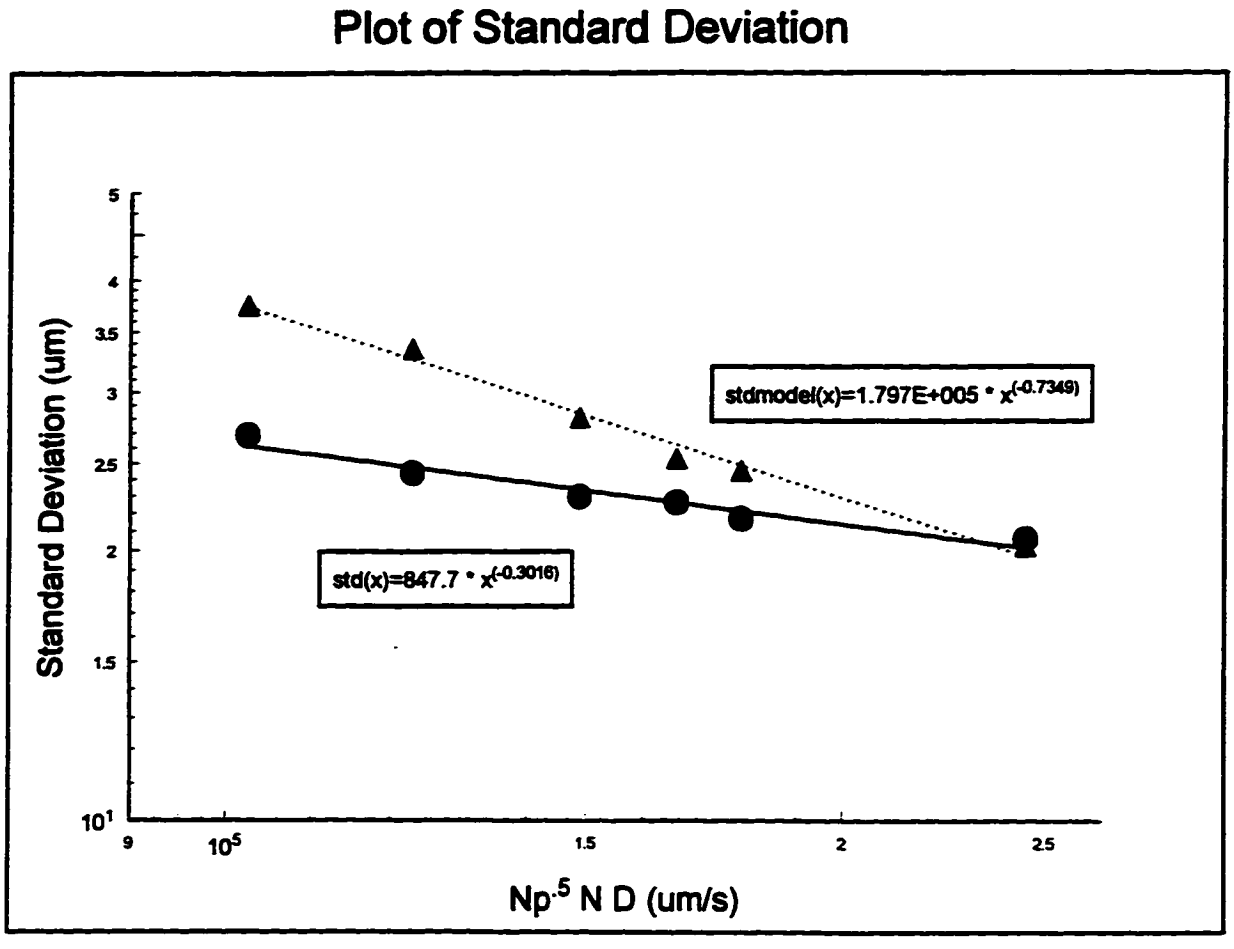

Figure 6.2.24: Curve Fit of Equation d_i = Constant/$(N_p^{0.5}ND)^y$ to the Standard Deviation Data: Comparison Between Model and Experimental Results

Table 6.2.5: Comparison Between Model Predictions and Experimental Results with d_i = constant/$(N_p^{0.5}ND)^y$

d_i	Constant		Y	
	EXP	MODEL	EXP	MODEL
Volume Mean Particle Size	14820(s)	7254000(s)	0.42	0.95
Standard Deviation	848(s)	179700(s)	0.30	0.74

6.3 Summary

The results of the flocculation experiments and population balance model at G_m = constant have demonstrated the following:

- The experimental cumulative particle size distribution shifts to a smaller particle size range with increasing tank size regardless of impeller type.

- The experimental cumulative particle size distribution shifts to a smaller particle size range moving from the A310 fluid foil impeller to the Rushton turbine regardless of tank size.

- The experimental volume mean particle size is proportional to $(N_p^{0.5}ND)^{-0.42}$ regardless of tank size or impeller type.

- The experimental particle standard deviation is proportional to $(N_p^{0.5}ND)^{-0.30}$ regardless of tank size or impeller type.

- The experimental maximum particle size is proportional to $(N_p^{0.5}ND)^{-0.33}$ regardless of tank size or impeller type.

- It might be possible to predict the volume mean particle size, standard deviation, and maximum particle size at steady state for the flocculation process given $N_p^{0.5}ND$. However, more experiments with different tank geometries, impeller types and location, and water chemistry are needed to confirm the robustness of this relationship.

- The flocculation performance is limited by the intensity of the turbulence in the impeller discharge zone.

- The population balance model predicts the shift in the cumulative particle size distribution to a smaller particle size range with increasing tank size regardless of impeller type.

- The model also predicts the shift in the cumulative particle size distribution to a smaller size range moving from the A310 fluid foil impeller to the Rushton turbine regardless of tank size.

- The model predicts that the volume mean particle size is proportional to $(N_p^{0.5}ND)^{-0.95}$ regardless of tank size or impeller type.

- The model also predicts that the standard deviation is proportional to $(N_p^{0.5}ND)^{-0.74}$. This relationship is independent of tank size or impeller type.

- It might be possible to predict the cumulative particle size distribution at a larger tank size or with different impellers given experimental data from one impeller type and one tank size. This assumes a constant geometric configuration (i.e. D/T

= constant, H/T = constant, etc.). However, more simulations with different tank sizes, impeller types, and water chemistry are necessary to confirm this model.

- The sensitivity of the breakup frequency, k_b, to $N_p^{0.5}ND$ needs to be reduced in order to accurately predict the cumulative particle size distribution in the 560L tank size.

- The population balance model clearly demonstrates that by incorporating the level of the turbulence intensity in the impeller discharge zone, the model can qualitatively predict the flocculation performance at different tank sizes and with different impeller types.

6.4 Implication of Flocculation Results on Design Standards for Vertical Mixers

In general, the design of the flocculation process depends on evaluation of the raw water quality to be treated and the downstream treatment processes that follow. In designing the flocculation facility, the inlet and outlet configuration, basin shape, number of baffles, mixer intensity (G_m), mixer tip speed, and detention time are the most important parameters that influence the flocculation performance.

In this study, the only parameters which played a role in determining the flocculation performance include the mixer intensity, mixer tip speed, and detention time. No inlet and outlet design considerations were necessary since the flocculation process was done in batch mode. A constant square shape basin was used for each tank size and no baffles were employed.

If we assume that the sedimentation basin follows the flocculation basin, then the basic design standards recommend a range of 30 - 80 s^{-1} for G_m and a detention time between 15 - 45 minutes. The design standards also recommend a maximum allowable mixer tip speed of 2 m/s. The actual value of G_m and detention time used would depend on the raw water quality, type of coagulant, and water temperature. Once G_m and detention time have been chosen and the maximum tip speed has not been violated, theory dictates that the flocculation performance

should be the same regardless of tank size or shape of the mechanical mixer.

However, the flocculation results in this study suggest that the flocculation performance is a function of the tank size being used and the impeller type causing the agitation even with constant G_m and detention time. These results further imply that G_m and detention time for this simple batch flocculation setup are not enough to reliably predict the flocculation performance from a bench top flocculation to a full scale system. Also, G_m and detention time cannot be used to compare two different kinds of impellers. Clearly, the fluid motion generated in these different tank sizes and impeller types are more complex than what G_m indicates. This complex fluid motion was demonstrated with the LDV experimental results in Section 5.0.

The flocculation results showed that the steady state cumulative particle size distribution shifts to the smaller particle size range with increasing tank size when G_m = constant. These results also demonstrated that the steady state cumulative particle size distribution shifts to the smaller particle size range moving from the A310 fluid foil impeller to the Rushton turbine when G_m = constant. These results suggest that maintaining G constant will cause more particle breakup with increasing tank size. Furthermore, maintaining constant G_m will also cause more particle breakup moving from the A310 foil impeller to the Rushton turbine. The question then seems to be what in the turbulent motion produced by a mechanical mixer is controlling the steady state cumulative particle size distribution.

Based on the flocculation experimental results and the population balance model, the steady state cumulative particle size distribution is controlled by the turbulence intensity in the impeller discharge zone. Both the flocculation experimental results and the population balance model demonstrated that the volume mean particle size and the particle standard deviation are a function of $N_p^{0.5}ND$ regardless of tank size or impeller type. In Section 5.0 the LDV experimental results showed that the turbulence intensity in the impeller discharge zone is proportional to $N_p^{0.5}ND$. The flocculation results show that the volume mean particle size, standard deviation, and maximum particle size decreases with increasing $N_p^{0.5}ND$ even though G_m was constant.

These flocculation results indicate that it might be better to control $N_p^{0.5}ND$ instead of G_m in order to accurately predict the steady state particle size distribution. With $N_p^{0.5}ND$, the turbulence controlling the flocculation performance is properly represented. Using $N_p^{0.5}ND$,

water treatment engineers might be able to determine the best flocculation results that can be achieved for a given vertical shaft mechanical mixer at any tank size. However, the relationship between the floc size distribution and $N_p^{0.5}ND$ has only been proven for a limited number of tank sizes, two impeller types, one H/T and D/T ratio, and one water chemistry condition. More extensive flocculation experiments will be necessary to confirm this relationship between the floc size distribution and $N_p^{0.5}ND$ before it can be used as a universal flocculation design parameter.

7.0 CONCLUSIONS

This study demonstrated the effects of tank size and impeller type on the flocculation process in a turbulent mixing vessel at constant power per unit volume, G_m. The study was conducted with three square tank sizes of 5L, 28L, and 560L volume and with a Rushton turbine and an A310 fluid foil impeller. The study comprised of four major parts. Part 1 included measuring the local turbulence intensity in different regions of the mixing vessel using laser Doppler velocimetry (LDV). Part 2 included modeling the local turbulence intensity in different regions of the mixing vessel using a general computational fluid dynamics software called FIDAP. Part 3 included measuring the steady state particle size distribution in situ using a photographic technique. And Part 4 included modeling the agglomeration and breakup mechanism during the flocculation process with a population balance rate equation.

The results of the fluid mechanics measurements showed that the local turbulence produced by a Rushton turbine or A310 fluid foil impeller in the 5L, 28L, and 560L tank size is much too complex to be described by G_m. The turbulence measurements demonstrated that when G_m = constant, the intensity of the large scale turbulent motion increased with increasing tank size. The LDV results also showed that the intensity of the large scale turbulent motion was higher for the Rushton turbine than for the A310 foil impeller in the impeller discharge zone. These experimental results were confirmed by computer simulations with FIDAP. Furthermore, FIDAP confirmed the unique flow pattern produced by the A310 foil impeller in a square tank reactor.

FIDAP demonstrated that the flow produced by the A310 foil impeller circulates from the bottom to the top of the tank in the tank corners. FIDAP was capable of predicting the magnitude of the turbulent kinetic energy throughout the square tank reactor and at both the 5L and 28L tank sizes. The FIDAP results verified that the turbulent kinetic energy increases with increasing tank size. This increase in kinetic energy suggests that the large scale turbulent motion increases with increasing tank size. FIDAP also demonstrated that the turbulent kinetic energy was higher for the Rushton turbine than for the A310 foil impeller particularly in the impeller discharge zone. Based on these fluid mechanics results, the intensity of the large scale turbulent

motion in the impeller discharge zone can be described by the parameter $N_p^{0.5}ND$.

The flocculation experimental results have shown that the steady state particle size distribution does not remain constant when G_m = constant for the three tank sizes and two impeller types used in this study. These results confirm work done by previous investigators that the flocculation performance degrades with increasing tank size. The flocculation results also show a degradation in flocculation performance moving from the A310 foil impeller to the Rushton turbine.

Based on the flocculation experimental results, the intensity of the large scale turbulent motion in the impeller discharge region directly influences the steady state floc size distribution. The volume mean particle size, standard deviation, and maximum particle size were all found to be a function of $N_p^{0.5}ND$ regardless of tank size and impeller type. Increasing the value of $N_p^{0.5}ND$ caused a decrease in the mean particle size, standard deviation, and maximum particle size. These experimental results suggest that particle breakup is controlled by the intensity of the turbulence in the impeller discharge zone. Confirmation of this relationship between $N_p^{0.5}ND$ and the particle breakup rate was done using the population balance model.

The results of the population balance model showed that by including the turbulence intensity in the impeller discharge zone into the breakup frequency, the model displayed sensitivity to tank size and impeller type as the experimental results demonstrated. The model predicts the shift in the cumulative particle size distribution to the smaller particle size range with increasing tank size. The model also predicts the shift in the particle size distribution to a smaller particle size range moving from the A310 foil impeller to the Rushton turbine. And finally, the model demonstrates the volume mean particle size, standard deviation, and maximum particle size range decreases with increasing $N_p^{0.5}ND$ regardless of tank size or impeller type.

The overall conclusion of this study suggests that the steady state particle size distribution is not determined by Camp & Stein's G_m. It is, however, determined by the level of turbulence produced in the impeller discharge zone. This assumes that the mechanical mixer is mounted on a vertical shaft and that most of the energy is dissipated in the impeller discharge zone. In designing a flocculator system with a vertical shaft mechanical mixer, engineers should include $N_p^{0.5}ND$ as part of evaluating the flocculation performance. With $N_p^{0.5}ND$, engineers can compare

the level of turbulence in the impeller discharge zone at different tank sizes or impeller types to determine whether the flocculation performance will improve or degrade in the new setup. If more information about the flocculation performance is desired, then engineers might be able to reproduce the particle size distribution using the population balance model developed in this study. This assumes that the engineer has calibrated the model's empirical constant using experimental data for an impeller in a geometrically similar tank. With the recommendations for model improvement in Section 8.0, the population balance model should be able to predict the floc size distribution curve for a vertical shaft mechanical mixer in any tank size.

8.0 FUTURE RESEARCH RECOMMENDATIONS

1) In measuring the fluid mechanics in the flocculation tank the Reynolds shear stresses were not included. The error in leaving out the Reynolds shear stresses is largest near the blade tip. The incorporation of the Reynolds shear stresses will improve the accuracy of the turbulence measurements around the impeller blade tip and in the impeller discharge zone.

2) The fluid mechanics measurements showed that a significant portion of the energy produced by the Rushton turbine comes in the form of trailing vortices. The energy contained in these vortices cannot be measured properly with the method used in this study. The method of 1° phase average is the proper technique to quantify the turbulence contained in the vortices (Yianneskis & Whitelaw, 1993). Including the energy contained in these vortices will also improve the accuracy of the turbulence measurements in a stirred vessel with a Rushton turbine.

3) The turbulence measurements were only made in the plane perpendicular to the tank wall. Results from the computational fluid mechanics simulation showed that the turbulence varies not only in the axial and radial direction, but also in the tangential direction. Turbulence measurements at other locations in the stirred tank can help completely describe the fluid motion throughout the stirred vessel.

4) FIDAP has the potential to accurately model the turbulence produced by a mechanical mixer in a stirred vessel. This high accuracy requires that proper boundary conditions be imposed. In modeling the Rushton turbine, FIDAP was not able to predict the energy dissipation in the bulk region. The inability of FIDAP to model the energy dissipation rate in this region is due to not including the energy contained in the trailing vortices as part of the boundary conditions. Once the energy contained in the trailing vortices has been determined, it should

be incorporated into the boundary conditions in order to improve the model's prediction of the experimental data.

5) In the turbulence simulations conducted with FIDAP, the standard k-ε model was the only turbulence model used. Other turbulence models such as the extended k-ε model, Wilcox's k-ε model, anisotropic k-ε model, and the RNG k-ε model can be invoked in the FIDAP software. A description of all these models are given in the FIDAP manuals (Fluid Dynamics International, 1993). The use of these other models with the flow conditions in a flocculation basin may improve the accuracy of the simulation.

6) The flocculation experimental results showed that the steady state particle size distribution is a function of the turbulence intensity produced in the impeller discharge zone. However, only three tank sizes, two impeller types, and one H/T and D/T ratio were used in this study. A wider range of tank sizes, more impeller types, and different H/T and D/T ratios should be studied to confirm the relationship between the particle size distribution and the turbulence produced in the impeller discharge zone. For example, other impeller types which fall under the same category as the impellers used in this study include a pitch blade turbine, marine propeller, and a two blade paddle.

7) The types of impellers studied in this thesis are considered to be locally turbulent impellers where most of the energy is dissipated in a small region. These impellers usually sweep out a small percentage of the total volume in a stirred vessel. Other impellers such as the rake sweep out a larger portion of the tank volume and have a narrow spatial distribution of the energy dissipation. Flocculation experiments should be done with these types of impellers in order to determine whether a relationship exists between the particle size distribution and the turbulence intensity of the large scale fluid motion.

8) A relationship between $N_p^{0.5}ND$ and the particle size distribution was found in this study. However, this relationship was developed using the experimental results from three different tank sizes and two impeller types. This relationship should be tested at one tank size with increasing values of $N_p^{0.5}ND$. This will also help determine if the relationship between $N_p^{0.5}ND$ and the particle size distribution holds for one tank size.

9) The relationship between $N_p^{0.5}ND$ and the particle size distribution has only been studied with one coagulant type and one method of particle destabilization. Other coagulants such as $FeCl_3$ and different particle destabilization methods such as charge neutralization should be investigated to determine the robustness of this relationship.

10) The population balance model developed in this thesis is the first model to demonstrate a shift in the particle size distribution to a smaller particle size range with increasing tank size or moving from the A310 foil impeller to the Rushton turbine. However, the model predicts more particle breakup with increasing tank size than what the experimental data suggests. The breakup frequency, k_b, needs to be refined in order to reduce the breakup rate with tank size.

REFERENCES

ABBOT, I. H., and VON DOENHOFF, A. E., 1959, Theory of Wing Sections, Dover Publications, Inc. N.Y., pg. 111.

ADLER, P. M., and MILLS, L. B. H. P., 1979, Motion and Rupture of a Porous Sphere in a Linear Flow Field, Soc. Rheology, vol. 23, 25.

AMIRTHARAJAH, A., MILLS, K.M., 1982, Rapid Mix Design Mechanisms of Alum Coagulation, J. AWWA Vol. 74 No. 5, 232

ANDREAU-VILLEGAS, R., LETTERMAN, 1976, Optimizing Flocculator Power Input, Journal EED, ASCE, April, Vol. 102, pp. 251-265.

ADRIAN, R. J. and YAO, C. S., 1987, Power Spectra of Fluid Velocities Measured by Laser Doppler Velocimetry, EXP. In Fluids 5, 17-28.

ADRIAN, R.J., 1993, Experimental Methods of Fluid Mechanics Class Notes, University of Illinois Urbana-Champaign

ARGAMAN, Y., and KAUFMAN, W. J., 1970, Turbulence and Flocculation, J. Sanitary Engineering Div. A.S.C.E., vol. SA 2, 223.

ARMSTRONG, S. G. and RUSZKOWSKI, S., 1988, The Rushton Turbine Discharge Flow: The Effects of Impeller Geometry and Tank Geometry on Mean and Fluctuating Velocities, 6th Europ Conf on Mixing, Pavia, (BHRA-Cranfield), p. 1.

BATCHELOR, G. K., 1953, The Theory of Homogeneous Turbulence, Cambridge Press, Cambridge, London.

BATTERHAM, R. J., HALL, J. S., BARTON, G., 1981, Pelletizing Kinetics and Simulation of Full Scale Balling Circuits, Proc. 3rd Int. Symp. on Agglomeration, Nermberg F. R. G.

BEAN, E. L., 1953, Study of Physical Factors Affecting Flocculation, Water Works Engineering, pg. 33.

BEAUCHAMP, K. and YUEN, C., 1979, Digital Methods for Signal Analysis, George Allen & Unovin LTD, London.

BENAYAD, S., DAVID, R., COGNET, G., 1985, Measurement of Coupled Velocity and Concentration Fluctuations in a Discharge Flow of a Rushton Turbine in a Stirred Tank, Chem. Eng. Process 19, 157-165.

BERTRAND, J., COUDERC, J. P. and ANGELINO, H., 1980, Power Consumption, Pumping Capacity and Turbulence Intensity in Baffled Stirred Tanks: Comparison Between Several Impellers, Chem Eng Sci, 35: 2157.

BORTS, M. A., and GUPALO, Y. P., 1971, Mechanism of the Breakdown of Floccules in Turbulent Flows inside the Rotor of a Centrifuge, Theor. Found. Chem. Engr. vol. 5, 383.

BOX, G. E. P., HUNTER, W. G., HUNTER, J. S., 1978, Statistics for Experimenters: An Introduction to Design, Data Analysis and Model Building, John Wiley & Sons, Inc. New York.

CALABRESE, R. V. and STOOTS, C. M., 1989, Flow in the Impeller Region of a Stirred Tank, Chem. Eng. Prog, 85(5), 43.

CAMP, T. R. and STEIN, P.C., 1943, Velocity Gradients and Internal Work in Fluid Motion, J. Boston Soc. Civ. Eng. 30, 219-237.

CELIA, M. A. and GRAY, W. G., 1992, Numerical Methods for Differential Equations: Fundamental Concepts for Scientific and Engineering Applications, Prentice Hall, Englewood Cliffs N. J.

CHANG, T.P.K., SHEU, Y.H.E., TATTERSON, G.B., DICKEY, D.S., 1981, Liquid Dispersion Mechanisms in Agitated Tanks: Part II Straight Blade and Disc Style Turbines, Chem. Eng. Commun. 10, 215.

CHEN, W., FISHER, R. R., BERG, J. C., 1990, Simulation of Particle Size Distribution in an Agglomeration-Breakup Process, Chem. Eng. Sci. Vol 45 No. 9 pp. 3003-3006.

CLARK, M.M., 1985, Drop Breakup in a Turbulent Flow, Ph.D dissertation, The John Hopkins University, Baltimore, Md.

CLARK, M.M., 1988, Drop Breakup in a Turbulent Flow: II. Experiments in a Small Mixing Vessel, Chemical Engineering Science, 43, pp. 681-692.

CLARK, M.M. and FIESSINGER, F., 1991, Mixing and Scaleup. in Mixing in Coagulation and Flocculation, AWWARF Denver, CO. pp. 282-306.

CLARK, M.M., SRIVASTAVA, R.M., LANG, J.S., TRUSSELL, R.R., McCOLLUM, L.J., BAILEY, D., CHRISTIE, J.D., STOLARIK, G., 1994, Selection and Design of Mixing Processes for Coagulation, AWWARF Report Denver CO.

CLARK, M. M., 1985, Critique of Camp and Stein, RMS Velocity Gradient, J. Env. Eng. Vol 111, No. 6 ASCE.

CLARK, M.M., 1996, Transport Modeling for Environmental Engineers and Scientists, J. Wiley Interscience, New York.

CLEASBY, J. L., 1984, Is Velocity Gradient a Valid Turbulent Flocculation Parameter, J. Env. Eng. 110, No. 5 ASCE.

CHEN, K. Y., HAJDUK, J. C. and JOHNSON, J. W., 1988, Laser Doppler Anemometry in a Baffled Mixing Tank, Chem Eng Commun, 72: 141.

COOPER, R. G. and WOLF, D., 1968, Velocity Profile and Pumping Capacities for Turbine Type Impellers, Can J Chem Eng, 46: 34.

CORNELL, J.A., 1990, How to Apply Response Surface Methodology, American Society for Quality Control.

COSTES, J. and COUDERC, J. P., 1988a, Study by Laser Doppler Anemometry of the Turbulent Flow Induced by a Rushton Turbine in a Stirred Tank: Influence of the Size of the Units I Mean Flow and Turbulence, Chem Eng Sci, 43: 2751.

COSTES, J. and COUDERC, J. P., 1988b, Study by Laser Doppler Anemometry of the Turbulent Flow Induced by a Rushton Turbine in a Stirred Tank: Influence of the Size of the Units II Spectral Analysis and Scales of Turbulence, Chem Eng Sci, 43: 2765.

CURTIS, A.S.G. and HOCKING, L.M. 1969, Collision Efficiency of Equal Spherical Particles in a Shear Flow, Transactions of the Faraday Soc., Vol. 66, No 570, pg. 1381.

CUTTER, L. A., 1967, Flow and Turbulence in a Stirred Tank, AIChEJ, 4: 485.

DEBOER, G. B. J., HOEDEMAKERS, G. F. M., THOENES, D.,1989, Coagulation in Turbulent Flow: Part I, Chem. Eng. Res. Des. Vol. 67, pg. 301.

DESOUZA, A. and PIKE, R. W.,1972, Fluid Dynamics and Flow Patterns in Stirred Tanks with

a Turbine Impeller, Can. J. Chem. Eng. 50, 15-23.

DELICHATSIOS, M.A. AND PROBSTEIN, R.F., 1975, Coagulation in Turbulent Flow: Theory and Experiment, J. Colloid and Interface Science Vol 51, No. 3.

DRBOHLAV, J., FORT, I., MACA, K. and PLACEK, J., 1978, Turbulent characteristics of Discharge Flow from Turbine Impeller, Coll Czech Chem Commun, 43: 3148.

DROBNY, N. L., 1963, Effect of Paddle Design on Flocculation, J. Sanitary Engineering Div. ASCE, SA2 pg. 17.

ENVIRONMENTAL PROTECTION AGENCY, 1985, Technologies for Upgrading Existing or Designing New Drinking Water Treatment Facilities, Technomic Publishing, Lancaster, P.A.

FLUID DYNAMICS INTERNATIONAL,1995, FIDAP 7.0 Theory Manual, Evanston, IL.

FORT, I. and MALA, J., 1982, Hydraulic Characteristics of Turbine Impeller, Coll Czech Chem Commun, 47: 421.

FRANCOIS, R. J., 1987, Strength of Aluminum Hydroxide Flocs, Water Resources Vol. 21, No. 9., 1023.

FROST, W. and MOULDEN, T.H., 1977, Handbook of Turbulence Volume I: Fundamentals and Applications, Plenum Press, New York.

GEISLER, R., KREBS, R., FORCHNER, P., 1994, Local Turbulent Shear Stress In Stirred Vessels and its Significance for Different Mixing Tasks, ICHEME Symposium Series, 136.

GOLDSTEIN, R. J., 1983, Fluid Mechanics Measurement, (Hemisphere, New York).

GUNKEL, A. A. and WEBER, M. E., 1975, Flow Phenomena in Stirred Tanks Part I: The Impeller Stream, AIChEJ, 21: 931.

HANSON, A. T., 1989, The Effect of Water Temperature and Reactor Geometry on Turbulent Flocculation , Ph.D Thesis Iowa State University.

HANSON, A. T. and CLEASBY, J.L., 1990, Effect of Temperature on Turbulent Flocculation: Fluid Dynamics and Chemistry, J. AWWA, 82, 11:56.

HOUNSLOW, M. J., 1990, A Discretized Population Balance for Continuous Systems at Steady State, J. AIChE Vol. 36, No. 1, pg. 106.

HOUNSLOW, M. J., RYALL, R. L., MARSHALL, V. R., 1988, A Discretized Population Balance for Nucleation, Growth and Aggregation, J. AIChE., Vol. 34 No. 11, pg. 1821.

HEALTH EDUCATION SERVICES, 1976, Recommended Standards for Water Works, Great Lakes - Upper Mississippi River Board of State Sanitary Engineers, Albany, N.Y.

HIGASHITANI, K., YAMAUCHI, K., MATSUNO, Y., HOSOKAWA, G., 1983, Turbulent Coagulation of Particles Dispensed in a Viscous Fluid, J. Chem. Eng. Japan Vol. 16, No. 4 pg 299.

HILL, P. J. and NG, K. M., 1995, New Discretization Procedure for the Breakage Equation, J. AIChE Vol. 41, No. 5, pg. 1204.

HILL, P. J. and NG, K. M., 1996, New Discretization Procedure for the Agglomeration Equation, J. AIChE Vol. 42, No. 3, pg. 727.

HINZE, J.O., 1975, Turbulence, McGraw-Hill, New York.

HOLLAND, F. A. and CHAPMAN F. S., 1966, Liquid Mixing and Processing in Stirred Tanks, Reinhold, New York.

HONG-XIAO and STUMM, W., 1987, The Coagulating Behaviors of Fe(III) Polymer Species I: Preformed Polymers by Base Addition, Water Research, January, Vol. 21, pp. 115-123.

HSU, J. P. and GLASGOW, J. B., 1983, Floc Size Reduction in the Turbulent Environment, Particulate Science and Technology 1: 205.

HUDSON, J.D., 1993, The Effect of a Wavy Boundary on Turbulent Flow, Ph.D. Thesis University Of Illinois Urbana-Champaign

HUTCHINGS, B.J., WEETMAN, R.J., BHARATA, R.P., 1989, Computation of Flow Fields in Mixing Tanks with Experimental Verification, Paper presented at the ASME Winter Annual Meeting, San Francisco, CA.

ITO, S., URUSHIYAMA, S., OGAWA, K., 1974, Measurement of Three-Dimensional Fluctuating Liquid Velocities, J. Chem. Eng. Japan Vol. 7 No. 6, 462.

ITO, S., OGAWA, K., YOSHIDA, N., 1975, Turbulence in Impeller Stream in a Stirred Vessel, J. Chem. Eng. Japan, Vol. 8 No. 3, 206.

JACOBSON, R. E., 1978, The Manual of Photography, Butterworth and Co., London, England.

JAMES M. MONTGOMERY ENGINEERS, 1985, Water Treatment Principles & Design, John Wiley-Interscience, N.Y., N.Y.

JIANG, Q. And LOGAN, B. E., 1996, Fractal Dimensions of Aggregates from Shear Devices, J. American Water Works Assoc. Vol. 88, No. 2, pg. 100.

KAO, S. V., and MASON, S. G., 1975, Dispersion of Particles by Shear, Nature, vol. 253, 619.

KOH, P. T. L., ANDREWS, J. R. G., and UHLHERR, P. H. T., 1984, Modeling Shear Flocculation by Population Balances, Chem. Engr. Sci., vol. 39, no. 6, 975.

KONNO, M., AOKI, M., and SAITO, S., 1983, Scale Effects on Breakup Processes in Liquid-Liquid Agitated Tanks, Journal Chem. Engrg. Jpn. 16:4:312.

KRAMER, T. A. and CLARK, M. M., 1996a, The Influence of Strain - Rate on Coagulation Kinetics, Accepted for Publication in JEED, ASCE.

KRAMER, T. A. and CLARK, M. M., 1996b, The Measurement of Particles Suspended in a Stirred Vessel, Particle and Particle System Characterization Vol. 13, pgs. 3-9.

KRESTA, S. M. and WOOD, P. E., 1991, Prediction of the Three Dimensional Turbulent Flow in Stirred Tanks, J. AICHE Vol 37 No. 3.

KUSTERS, K.A., 1991, The Influence of Turbulence on Aggregation of Small Particles in Agitated Vessels, Ph.D dissertation, University of Eindohen, Germany.

LAUFHUTTE, H. D. and MERSMANN, A. B., 1985, Dissipation of Power in Stirred Vessels, Chem Ing Tech, 57: 1104.

LITSTER, J. D., SMIT, D. J., HOUNSLOW, M. J., 1995, Adjustable Discretized Population Balance for Growth and Aggregation, J. AIChE, Vol. 41, No. 3, pg. 591.

LOGTENBERG, E. H. P. And STEIN, H. N., 1985, Coagulation in a Shear Field Generated by Stirring in a Cylindrical Vessel, J. Colloid & Interface Sci. Vol. 104, No. 1, pg 258.

LU, C. F., and SPIELMAN, L. A., 1985, Kinetics of Floc Breakage and Aggregation in Agitated Liquid Suspensions, J. Colloid Interface Sci., vol. 103, 95.

MAGNI, F., COSTES, J., BERTRAND, J. and COUDERC, J.P., 1988, 6th Europ Conf on Mixing, Pavia (BHRA-Cranfield), p. 7.

McCONNACHIE, G. L., 1991, Turbulence Intensity of Mixing in Relation to Flocculation, J. Env. Eng. Div., ASCE, 117 6: 731.

MERSMANN, A. B., GEISLER, R. K., 1991, Determination of the Local Turbulent Energy Dissipation Rates in Stirred Vessels and its Significance for Different Mixing Tasks, 4th World Congress on Chemical Engineering, Karlsruke (FRG).

MORTON, R.A., 1984, Photography for the Scientist, Academic Press, London.

MUJUMDAR, A.R., HUANG, B., WOLF, D., WEBER, M.E., and DOUGLAS, W. J. M., 1970, Turbulence Parameters in a Stirred Tank, Can. J. Chrm. Eng. 48, 475-483.

MULLER, H.W., 1982, Untersuchungen zun Transportprozess bei der Flockung in Turbulenten Strmungen, Chem. Tech., 34:10:517.

OKAMOTO, Y., NISHIKAWA, M. and HASHIMOTO, K., 1981, Energy Dissipation Rate Distribution in Mixing Vessels and its Effects on Liquid-Liquid Dispersion and Solid-Liquid Mass Transfer, Int Chem Eng, 21: 88.

OLDSHUE, J.Y. and MADY, O.B., 1978, Flocculation Performance of Mixing Impellers,

Chemical Engineering Progress, 74:103.

OLDSHUE, J.Y., 1983, Fluid Mixing Technology, McGraw Hill, N.Y., pp. 185-189.

OLDSHUE, J.Y., HERBST, N.R., 1992, A Guide to Fluid Mixing, LIGHTNIN, Rochester, N.Y.

PARKER, D.S., KAUFMAN, W.J., and JENKINS, D., 1972, Floc Breakup in Turbulent Flocculation Processes, J. Sanitary Div. A.S.C.E., vol. SA 1, 79.

PATWARDHAN, S. V. and MIRAJGAONKAR A.J., 1970, Hydraulics of Flocculation and Paddle Characteristics, J. Institution of Engineers (India) Public Health, 50: 60.

PENG, S. J. and WILLIAMS, R. A., 1994, Direct Measurement of Floc Breakage in Flowing Suspensions, J. Colloid & Interface Sci., 166; 321.

PLACEK, J. and TAVLARIDES, L. L., 1985, Turbulent Flow in Stirred Tanks Part I: Turbulent Flow in the Turbine Impeller Region, AIChEJ, 31: 1113.

PRESS, W.H., TEUKOLSKY, S.A., VETTERLING, and W.T., FLANNERY, B.P., 1992, Numerical Recipes in Fortran: The Art of Scientific Computing, Cambridge Press, New York.

RANADE, V. V., JOSHI, J.B., 1990, Flow Generated by a Disk Turbine: Experimental, Trans ICHEME Vol. 68, Part A., Part I, 19-33.

RANADE, V. V., JOSHI, J.B., 1990, Flow Generated by a Disk Turbine: Mathematical Modeling and Comparison with Experimental Data, Trans ICHEME Vol. 68, Part A., Part II.

RANADE, V. V., JOSHI, J. B., MARATHE, A. G., 1989, Flow Generated by Pitched Blade Turbine II: Simulation Using k-ε Model, Chem. Eng. Comm. Vol 81, 225-248.

RANADE, V. V., MESHRA, V. P. SARAPH, V. S., DESHPANDE, G. B., JOSHI, J. B., 1992, Comparison of Axial Flow Impellers Using a Laser Doppler Anemometer, IND. Eng. Chem. Res. Vol. 31 No. 10, p. 2370.

RAY, D. T. and HOGG, R., 1986, Agglomerate Breakage in Polymer - Flocculated Suspensions, J. Colloid & Interface Sci., 116: 256.

RODI, W., 1984, Turbulence Models and Their Applications in Hydraulics, International Association for Hydraulic Research, Rotterdamseweg, Netherlands

RUTHERFORD, K., LEE, K. C., MAHMOUDI, M. S., YIANNESKIS, M., 1996, Hydrodynamic Characteristics of Dual Rushton Impeller Stirred Vessels, J. AIChE Vol. 42 No. 2.

SAFFMAN, P. G., TURNER, J. S., 1956, On the Collision of Drops in Turbulent Clouds, J. Fluid Mech. 1, 16-30.

SAHU, A. K. and JOSHI, J. B., 1995, Simulation of Flow in Stirred Vessels with Axial Flow Impellers: Effects of Various Numerical Schemes and Turbulence Model Parameters, Ind. Eng. Chem. Res. 34, 626.

SAJJAD M. W. and CLEASBY, J. L., 1995, Effect of Impeller Geometry and Various Mixing Pattern on Flocculation Kinetics of Kaolin Clay Using Ferric Salt, Proceedings of AWWA National Conference, Anaheim, CA.

SASTRY, K. V. S. and GASCHLGNARD, P., 1981, Discretization Procedure for the

Coalescence Equation of Particle Processes, J. IND Eng. Chem. Fundam., 20: 355.

SMOLUCHOWSKI, M., 1918, Versuch einer Mathematischen Theorie der Koagulationshinetik Kolloider Lasungen, Z. Phys. Chem. 92, 156.

SONNTAG, R. C., and RUSSEL, W.B., 1986, Structure and Breakup of Flocs Subjected to Fluid Stresses I: Shear Experiments, J. Colloid Interface Sci., Vol. 113, 399.

SONNTAG, R. C., and RUSSEL, W. B., 1987, Structure and Breakup of Flocs Subjected to Fluid Stresses II: Theory, J. Colloid Interface Sci., Vol. 115, pg. 378.

STOOTS, C. M. and CALABRESE, R.V., 1995, Mean Velocity Field Relative to a Rushton Turbine Blade, J. AIChE Vol. 41 No. 1.

TAMBO, N. and FRANCOIS, R. J., 1991, Mixing, Breakup, and Floc Characteristics in Mixing in Coagulation and Flocculation, A. Amirtharajah and M. Clark, eds., American Water Works Research Foundation, Denver, CO.

TAMBO, N. and WATANABE, Y., 1979, Physical Aspect of Flocculation Process I: Fundamental Treatise, Water Research, vol. 13, 409.

TAYLOR, G. I., 1938, The Spectrum of Turbulence, Proc. Royal Society A164, 476-490.

TEKIPPE, R.J., HAM, R.K., 1971, Velocity Gradient Paths in Coagulation, Journal AWWA, July, Vol. 63, pp. 439-449.

TENNEKES, H. and LUMLEY, J.L., 1972, A First Course in Turbulence, MIT press, Cambridge.

THOMAS, D. G., 1964, Turbulent Disruption of Flocs in Small Particle Size Suspensions, AICHE J. 10, 517-523.

TRUSSELL, R.R., LANG, J.S., McCOLLUM, L., ZFIRA, G., BAILEY, D., CLARK, M.M., 1992, Testing the Performance of Vertical Flocculation Impellers, Paper presented at AWWA Annual Conference, Vancouver Canada.

VAN DER MOLEN, K. and VAN MAANEN, H. R. E., 1978, Laser Doppler Measurements of Turbulent Flow in Stirred Vessels to Establish Scaling Rules, Chem Eng Sci, 33: 1161.

VAN'T RIET, K. and SMITH, J. M., 1975, The Trailing Vortex System Produced by Rushton Turbine Agitators, Chem Eng Sci, 30: 1093.

VRALE, L., JORDEN, R.M., 1971, Rapid Mixing in Water Treatment, Journal AWWA, January, Vol. 63, pp. 52-59.

WEETMAN, R.J., OLDSHUE, J. Y., 1988, Power, Flow and Shear Characteristics of Mixing Impellers, 6th European Conference On Mixing, Pavia Italy.

WU, H., PATTERSON, G.K., VAN DOORN, M., 1989, Distribution of Turbulence Energy Dissipation Rates in a Rushton Turbine Stirred Mixer, Exp. In Fluids 8, 153-160.

YIANNESKIS, M., POPIOLEK, Z. and WHITELAW, J. H., 1987, An Experimental Study of the Steady and Unsteady Flow Characteristics of Stirred Reactors, J Fluid Mech, 175: 537.

YIANNESKIS, M. and WHITELAW, J. H., 1993, On the Structure of the Trailing Vortices Around Rushton Turbine Blades, Trans. I ChemE Vol. 71 Part A.

ZIPP, R.P., WU, H., PATTERSON, G.K., SCHNEIDER, K.W., VERGUNST, R.D., 1987, Turbulence Data for the Rushton and Prochem Max Flo Impeller with Comparisons Made to a Three Dimensional Turbulence Model Using k-e Closure, Presentation at Engineering Foundations of Mixing.

APPENDIX A

Table A.1 Experimental Data for Rushton Turbine in Fully Baffled Cylindrical Vessel.

Reference	Geometrical Operating Parameters	Measurement Technique	Scope of Measurements	Brief Results and Comments
Cutter (1967)	T = 0.29m H/T = 1, D/T = 1/3 H/T = 1/3 WF:water N:200-700	Streak photography	"Mean radial and tangential velocities at impeller center plane, turbulent radial and tangential length scales in impeller stream, energy dissipated in the impeller region and radial profile of local energy dissipation rates at impeller center plane." (Ranade & Joshi, 1990)	"Mean velocities are found to be proportional to tip speed. Tangential velocity decreases faster than the radial velocity with increase in r. Maximum radial velocity exists near impeller tip and is equal to 0.6-0.7 time tip speed. His calculations predicted 20% of input energy dissipates in impeller region and next 50% dissipates in the impeller stream." (Ranade & Joshi, 1990)
Cooper and Wolf (1968)	T = 0.38 m H/T = 1, D/T = 0.2-0.6 H_s/T = 1/3 WF:water N:200-300	Hot wire anemometer with two and three dimensional Pitot tubes	"Mean velocity (radial, tangential) profiles in impeller stream. Radial profile of pumping capacity." (Ranade & Joshi, 1990)	"The axial profile of radial velocity is parabolic in shape while the tangential velocity profile is flatter. Maximum radial velocity is around 0.83 times tip speed. The pumping numbers are in the range of 0.73-0.9. The maximum entrained radial flow was found to be 0.8 times the actual discharge flow." (Ranade & Joshi, 1990)

Gunkel and Weber (1975)	T=0.457 m H/T = 1, D/T = 1/2 H_s/T = 1/2 W/F:air N:200-600	Shielded hot wire anemometer	"Mean velocity (radial and tangential) and resultant turbulent intensities at impeller center plane, mean velocity profiles between the impeller blades, axial velocity profiles on horizontal surface of impeller swept volume, radial profile of pumping capacity, energy dissipated in the impeller region, axial velocity (mean and rms) profile at one axial location lying in the bulk region of the tank, energy spectra (one edimensional) and turbulent length scales in the impellor stream." (Ranade & Joshi, 1990)	"Velocity profiles in between the blades suggest existence of the pair of vortices generated behind blades. Maximum radial (and tangential) velocity exists at some distance from the impeller tip and the maximum value almost equals the tip speed. Their data show that turbulence near impeller tip has large periodic component. Maximum entrained radial flow was found to be equal to 1.8 times the actual discharge flow. Their calculations of energy balance predict little of the input energy is dissipated within impeller region or in the impeller stream. The turbulence in the bulk of the tank was found to be approximately homogeneous (and nearly isotropic) having a variation about the space average value on the order of 14%. The integral length scale also was not found to change significantly over the range of conditions studied." (Ranade & Joshi, 1990)

Van der Molen and Van Maanen (1978)	T = 0.12, 0.29, 0.9m H/T = 1, D/T= 1/3 H_c/T = 1/2 WF:water N:125-300	One dimensional laser Doppler anemometer (reference beam mode)	"Mean radial velocity profile (with periodic component) at impeller center plane, one dimensional energy spectra at same relative positions in three vessels have been reported. They have calculated intensity of random turbulence from the integration of energy spectra." (Ranade & Joshi, 1990)	"Mean radial velocity at impeller center plane decreases monotonically with $r(\alpha\ r^{7/6})$ and maximum radial velocity is around 0.75 times tip speed, the intensity of random turbulence was found to increase with scale-up, approximately $D^{1/6}$. Energy of the smaller eddies decreases with scale at $D^{1/2}$." (Ranade & Joshi, 1990)
Drbohlav et al. (1978)	T=1.0m H/T=1, D/T=1/3,1/4 H_c/T=1/3 WF:water N:90,140	Hot film anemometer and five hole directional pilot tube	"They have reported axial profiles of mean and rms velocities for all the three components in the impeller stream. Some data of Reynolds stress measurements (u'w' only) have also been reported." (Ranade & Joshi, 1990)	"Tangential and radial components of velocities were found to be monotonically decreasing with increase in r, with rate of decrease of tangential component being more than that of radial. Their data of rms values can be used to generate turbulent kinetic energy profiles. However, they have not reported data close to impeller tip. Therefore, it can not be used to generate boundary condition for k at impeller." (Ranade & Joshi, 1990)
Bertrand et al. (1980)	T=0.4 H/T=1, D/T=1/3 H_c/T=1/2,1/3 WF:water N:50-220	Hot film anemometer	"Profiles of mean velocity (radial and tangential) and three components of turbulence intensities on the vertical surface of impeller swept volume have been presented along with the pumping numbers, for two impeller locations." (Ranade & Joshi, 1990)	"The maximum radial and tangential velocities were found to be more than or equal to tip speed. Change of impeller location from T/2 to T/3 significantly increases N_Q from 1.19 to 1.61." (Ranade & Joshi, 1990)

Fort and Mala (1982)	T=0.29, 1.0m H/T=1, D/T=1/3,1/4 H_c/T=1/3 WF:water N:100-750	Hot film anemometer and 3.5 hole Pitot tube	"Axial profile of mean radial velocity on vertical surface of swept volume, radial profile of axial velocity on horizontal surface of impeller swept volume. They have presented results of the energy balance calculations around the impeller region." (Ranade & Joshi, 1990)	"Maximum radial velocity is around 0.7 times tip speed. They have found that on an average, 40% of the input energy dissipates in the impeller region." (Ranade & Joshi, 1990)
Wu and Patterson (1986)	T=0.27m H/T=1, D/T=1/3 H_c/T=1/3 WF:water N:100,200,300	One dimensional laser Doppler anemometer (Dual beam, back scatter mode)	"Profiles of mean and rms values of all the three components of velocities on vertical surface of impeller swept volume with data for impeller center line. Radial profiles of pumping capacity in impeller stream have been presented. Detailed data of correlation coefficient and turbulent length scale have been reported for impeller stream. Energy balance around the impeller region and profiles of local energy dissipation rates (calculated indirectly form intensity and length scales) have been presented." (Ranade & Joshi, 1990)	"The maximum radial velocity exists near impeller tip and is around 0.75 times tip speed. The tangential velocity decreases more steeply than that of radial velocity with increase in r. The pumping capacity increases with radius, and maximum is around 2.5 times the discharge pumping capacity. In the impeller stream, turbulent length scales are slightly smaller than the half width of impeller blades. Outside the impeller stream, these scales were much larger. Their energy balance calculations predict. 30% of input energy dissipated in impeller region, about the same dissipated in the impeller stream." (Ranade & Joshi, 1990)

Yianneskis et al. (1987)	T=0.294m H/T=1, D/T=1/3 H_c/T=1/4, 1/3, 1/2 WF:water N:300	Laser Doppler anemometer (Dual beam, forward scatter mode)	"Detailed flow data for the trailing vortices and flow between two blades of impeller (mean as well as turbulence). Some data for the bulk region of the tank have also been reported." (Ranade & Joshi, 1990)	"Data presented in various r-z and r-t planes near impeller were used to characterize the trailing vortices behind the blades. Velocities in the vortices were of the order of 0.25 U_{tip}. The plane of maximum radial velocity bends upward form impeller centre plane and this angle depends on impeller clearance. They also report: maximum radial velocity =0.7 Utip primary pumping number =0.785." (Ranade & Joshi, 1990)
Chen et al. (1988)	T=0.089m H/T=1, D/T 1/3 H_c/T=1/2, 1/3 WF:water N:100,200,400	Laser Doppler anemometer (Dual beam, forward scatter mode)	"Mean and turbulence intensity data in the impeller stream." (Ranade & Joshi, 1990)	"They have reported maximum radial velocity of 0.6Utip." (Ranade & Joshi, 1990)

Costes and Coudere (1988a, 1988b)	T=0.44, 0.63m H/T=1,D/T=1/3 H_c/T=1/2 WF:water N:75,165,115	Laser Doppler anemometer (Dual beam forward scatter mode)	"Mean and rms velocity data for all the three components in the bulk region of the tank. (Data of tangential velocity is for the lower half of vessel.) Some data of energy spectra, correlation coefficients, integral scales and energy dissipation rate have also been presented." (Ranade & Joshi, 1990)	"Non-dimensional velocity profiles are independent of the system size and impeller speed. They report the existence of region where tangential velocity is in the opposite direction of impeller rotation. Primary pumping capacity is reported as 0.73. The three components of turbulence intensity are found to be of the same order in the bulk region of the tank, and therefore, turbulence may be considered as isotropic. Spectral measurements at corresponding locations in two vessels were practically identical. In impeller stream, integral length scale was found to be of the order of 0.25 blade width. In the bulk region the average length was found to be D/4.4." (Ranade & Joshi, 1990)

Armstrong and Ruszkowski (1988)	T=0.305m H/T=1,D/t=1/3 H_c/T=1/3 WF:water N:200,300	Two component laser Doppler anemometer (in back scatter mode)	"They have studied the effect of hub size (25x6.35x25mm) on flow in impeller stream region. Radial and axial velocity data in the plane of two baffles and 1mm away from blade tip are presented." (Ranade & Joshi, 1990)	"Flow near impeller is strongly influenced by hub size. The maximum radial velocity for the small hub impeller is 0.72 U_{tip} whereas for large hub impeller it was 0.6 U_{tip}. Primary pumping number for small hub impeller is 0.73. Periodic component of fluctuating velocity was significantly smaller for the large hub impeller, though total rms velocity was only slightly smaller." (Ranade & Joshi, 1990)
Magni et al. (1988)	T=0.4, 0.44, 0.63m H/T=1/2,1/3 D/T=1/3,0.45 H_c/T=1/2,1/3 WF:water N:65,75,115,165 Shape of bottom-flat and curved	Laser Doppler anemometer (Dual beam forward scatter mode)	"Mean velocity data has been presented for the bulk region of the tank (in the form of vector plots)." (Ranade & Joshi, 1990)	"The characteristics of impeller discharge are not affected by the shape of the vessel bottom. They have reported the region of strong tangential motion near vessel bottom for the vessel with curved bottom. They have observed the decrease in primary pumping capacity with decrease in impeller clearance. Relative induced flow rate decreases with increase in D/T value." (Ranade & Joshi, 1990)

Mujumdar et al. (1970)	T=.38m H/T=.467, D/T=1/3 & .4 WF=AIR H/T=1 N=600-1100	Hot wire Anemometry	Mean radial velocities at impeller center plane, rms radial fluctuating velocities one dimensional frequency spectrum, one dimensional energy dissipation function, integral length scale, turbulence intensity were computed.	Mean radial velocity was .6 to .7 times tip speed and decreases radially. Turbulence intensity range from 30 to 60% of impeller tip speed. One dimensional frequency spectrum showed a sharp peak at blade passage frequency. No kolmogoroff -5/3 slope range seen in spectra, possible due to presence of non-random component. Integral length scale was .5 times the impeller blade width. Probability density function of radial velocity fluctuations was not gaussian near the impeller tip and was gaussian further from the impeller tip.
Mersmann and Geisler (1991)	T=.150m H_c/T=.33 D/T=.33 WF=Water H/T=1 Impeller Re#>10^4	One dimensional Laser Doppler Velocimetry	Local energy dissipation rate measured throughout tank.	The distribution & maximum values of the local turbulent energy dissipation rate depends on impeller type & vessel geometry (N_p & D/T). Maximum energy dissipation rate near impeller tip was 30 times average impeller energy dissipation rate.

Okamoto et al (1981)	T=15, 30, 60cm H/T=1, D/T=.5, H_c/T=1/2 WF=Water N=80	Hot film current meter	Local energy dissipation rate measured throughout tank.	The energy dissipation rate in the impeller region was 50 times larger than the energy dissipation rate in the bulk region. The maximum energy dissipation rate was 7-11 times the average energy dissipation rate in the tank. The energy dissipation rate also varied in the theta direction around the impeller.
Wu et al. (1989)	T=.27m H_c/T=1/3 D/T=1/3, H/T=1 WF=Water N=200	Laser Doppler Velocimetry	Mean & Fluctuating radial velocities around impeller region. One dimensional power spectra & energy dissipation rate are also reported.	Mean radial velocity was .6 times the impeller tip speed at impeller blade centerline. A periodic velocity was found near the impeller tip with a frequency of the blade passage. RMS of the fluctuating velocity was significantly less when periodic velocity was removed. Maximum energy dissipation rate was 13 times the average energy input by the impeller. A double peak in energy dissipation rate profile near the impeller tip was shown.
Desouza & Pike (1972)	T=.29m, .31m H/T=1 D/T=.26, .24 H_c/T=.5 WF=Water N=243-500	Three dimensional pilot tube	Velocity profiles were measured in the vicinity of impeller centerline & in the bulk of the tank.	It was shown that the flow in the vicinity of the impeller discharege stream can be described as a jet flow. The impeller flow number N_Q was found to be equal 1.0. In the bulk region a three dimensional velocity flow field exists and the center of circulation is not a true stagnation point. The flow at this point is in the theta direction.

Laufhutte & Mersmann (1985)	T=.12m H/T=1, D/T=1/3 H_c/T=1/3 WF=Water N=500	One dimensional laser Doppler anemometry	Radial & axial mean velocities and fluctuating velocities are reported in baffle plane. Measurements are done in both the impeller region & bulk region tank.	Mean radial velocity at impeller centerline near the impeller tip is .7 times the impeller tip speed. Radial & axial fluctuating velocities are .3 to .4 times the tip speed near the impeller & .1 to .2 times the tip speed in the bulk region. No energy disipation rates were computed.
Benayad et al. (1985)	T=.2m H/T=1, D/T=1/3 H_c/T=.5 WF=Water N=410	One dimensional laser Doppler velocimetry	Fluctuating velocites, integral length scales, Taylor microscales, and energy dissipation rate are reported from different parts of the tank.	The integral length scales were found to be .5 times the impeller blade width in the impeller discharge zone and 1.5 times the blade width in the bulk region. The Taylor microscales were .25-.3 times the blade width in the impeller discharge zone and equal to the blade width in the bulk region. The resultant fluctuating velocity was .16 times the impeller tip speed near the impeller. The local energy dissipation rate ranged from .01 to .4 times the impeller power input near the impeller discharge zone. The authors commented that these values needed to be checked in future experiments.

Ranade & Joshi (1990)	T=.3m, .5m H/T=1, D/T=1/3, H_c/T=1/2 WF=Water N=200-700	One dimensional laser Doppler velocimetry	Mean velocities and turbulence intensity profiles in all three directions were measured at different points in the bulk region of the tank. Some measurements were taken in the impeller stream in order to compute the amount of energy dissipated in the impeller region.	Energy balance calculations showed that around 40% of the input energy is dissipated in th impeller region. Tangential velocities located at 45° from the baffle were found to be negative to the sense of rotation near the tank bottom. Turbulent fluctuating velocities were around .1 times the tip speed. Velocity profiles near the baffle indicated that a strong vortex exists behind the baffle.
Kusters (1991)	T=.102m, .2m, .388m H/T=1, D/T=1/3, H_c/T=1/2 WF=Water N=200-450	One dimensional laser Doppler velocimetry	Mean & fluctuating velocities, integral length scales, and energy dissipation rate were measured in both the bulk and impeller discharge zones.	Maximum mean radial & tangential velocities at the impeller centerline near the impeller tip were .65 times impeller tip speed. A periodic velocity was measured near the blade tip equal to the blade passage frequency. The maximum fluctuating velocity was around .3 times the impeller tip speed near the impeller and .1 times the tip speed in the bulk. At constant impeller input power between different size tanks, rms of the fluctuating velocity increased with scale in the bulk region and decreased with scale in the impeller region. The maximum energy dissipation rate was also found to decrease in the impeller region. For T=.102 $\varepsilon/\varepsilon_{avg}$=45, T=.2 $\varepsilon/\varepsilon_{avg}$=37, T=.39 $\varepsilon/\varepsilon_{avg}$=28. In the bulk region, the energy dissipation rate increased with scale.

Calabrese & Stoots (1989)	A water channel to simulate environment of single turbine blade WF: Water N = 180 T = 25cm D/T = 0.5	1 Color Laser Doppler anemometer forward scatter mode	Flow measurements around a single Rushton turbine blade is discussed. The three components of the mean & rms turbulent velocity are used to obtain the magnitude & direction of the mean velocity, mean velocity gradients, turbulent kinetic energy and energy dissipation rate.	Flow visualization studies revealed that flow upstream from the impeller is quite streamlined & that two well defined trailing vortices are produced behind the blade. Mean velocity vectors show that vortices rotate in opposite direction. The velocity at center of vortex is zero. Vortices maintain identity to distance of r/R=1.4. The turbulent kinetic energy is relatively low near the blade tip & reaches a max around r/R=1.4. The maximum energy dissipation rate occurred in the vortex breakdown region (r/R=1.4).
Yianneskes & Whitelaw (1993)	T = 294mm D/T = 1/3, H/T = 1 H_c/T = 1/3 WF: water N = 300	Laser Doppler Anemometer Dual beam forward scatter mode	Flow measurements around a Rushton turbine is discussed. Detailed information about turbulence generated between two blades is reported. The measurements were sychronized with the rotation of the agitator.	The time trace of the instantaneous velocity in impeller discharge zone reveal the presence of 6 velocity fluctuation cycles per 2π intervals. The change in sign of the velocity indicates the presence of vortical motion. The results also indicate that the vortex appears only after the blade passage. The maximum kinetic energy occurs between 0 - 10 degrees behind the tip of blade. The flow is strongly anisotropic in this region. Due to the free surface and shaft movement, the vortex axis is subject to erratic motion.

Stoots & Calabrese (1995)	T = 299mm D/T = 1/3, H/T = 1 H_o/T = ½ WF: water N = 140, 180, 220	2 color Laser Doppler Velocimeter (Back-scatter mode)	Comprehensive flow measurements in the impeller discharge region of a Rushton turbine is reported. Mean velocity, deformation rates, and energy dissipation rates based on mean velocity gradients are discussed. Measurements were made in a frame of reference rotating with the impeller.	The results of the velocity measurements between two blades show a strong periodicity in the mean velocity data. The data shows evidence of an intense recirculation zone behind the impeller blade. It is speculated to be caused by a clinging vortex. For angular displacements of 20° or more behind the leading blade, the trailing vortex no longer exhibits a complete recirculation loop. The regions of high deformation rate include the location of the clinging vortex and the blade edge. The local energy dissipation rate based on the mean velocity gradients exceed the tank power draw per unit mass by as much as an order of magnitude near the blade edge.

Rutherford et al. (1996)	T = 100, 294 mm D/T = 1/3 H/T = 1 WF: water N = 100, 250	Laser Doppler Anenometer (Dual beam, forward scatter mode)	Detailed flow data between two blades, the impeller discharge region, and bulk region in a stirred vessel with a dual Rushton turbine is disoussed. Mean and turbulent velocity power consumption, and a comparison between 360° ensemble - averaged and 1° angle resolved LDV measurement technique are reported.	The flow visualization experiments showed that the clearance of the lower impeller from the base of the mixing vessel, the seperation between the two impellers, and the submergence of the upper impeller below the free surface strongly affects the overall flow structure. Three stable flow patterns were determined. Power numbers for these stable flow patterns was found to be 1.75 - 1.95 times the power number for one impeller. Mean and turbulent velocities are proportional to tip speed regardless of tank size. Turbulence in the impeller discharge zone show a clear presence of the trailing vortices. The flow in the impeller discharge region is mostly anisotropic.

APPENDIX B

This appendix is devoted to listing the past population balance models developed by Tambo & Watanabe (1979), Lu & Spielman (1985), Koh et al. (1986), Chen et al. (1990), and Kusters (1991). These models were chosen because of their ability to model both agglomeration and breakup in the flocculation process. The model equations and some of their assumptions are briefly outlined here. A review of these models' strengths and weaknesses are discussed in Section 2.4.

1) Tambo & Watanabe (1979)

Model description

$$\frac{dN_R}{dm} = \frac{1}{2}\sum_{i=1}^{R-1} \alpha_o \left(1-\frac{R}{S+1}\right)^6 \left[i^{1/(3-K_p)} + (R-i)^{1/(3-K_p)}\right]^3 N_i N_{R-i} - N_R \sum_{i=1}^{S-R} \alpha_b \left(1-\frac{R+i}{S+1}\right)^6 \left[i^{1/(3-K_p)} + R^{1/(3-K_p)}\right]^3 N_i$$

$$S = S_m^{1/(3-K_p)}$$

$$S_m = \left(\frac{d_{max}}{d_1}\right)^3$$

$$d_{max} = K\varepsilon_o^{-3/2(3+K_p)} \qquad d \le \lambda_o$$

$$d_{max} = K'\varepsilon_o^{-1/(1+K_p)} \qquad d > \lambda_o$$

Nomenclature

d_{max}	=	maximum floc diameter
ε_0	=	turbulent energy dissipation rate
λ_0	=	Kolmogorov microscale
K,K′	=	constants relating floc strength
S	=	number of primary particles contained in max floc size
R	=	number of primary particles contained in floc under consideration

N_R = concentration of R-fold particle

m = dimensionless floc time

Model Assumptions

1) Model takes into account that the floc density decreases with increasing size of agglomerate.

2) Floc particles can grow to size S-fold particles without any breakup.

3) Any combination of particles which produces a particle larger than S-fold will break into its original individual particles.

4) Below S-fold size particles not all collisions will result in an agglomeration.

5) Turbulence is homogeneous and isotropic.

2) Lu & Spielman (1985)

Model description

$$\frac{dn(v,t)}{dt} = \int_v^\infty c(v')g(v')n(v',t)P_s(v,v')dv' - g(v)n(v,t)$$
$$+ \int_v^\infty q_e(v')n(v',t)P_e''(v,v')dv' - \frac{d}{dv}\left[\left(\frac{dv}{dt}\right)_e n(v,t)\right]$$
$$+ \frac{1}{2}\int_0^v \alpha\beta(v',v-v')n(v',t)n(v-v',t)dv'$$
$$- \int_0^\infty \alpha\beta(v,v')n(v,t)n(v',t)dv'$$

$$g(v) = k_s v^m \qquad v>v_{ss}$$
$$= 0 \qquad 0<v\le v_{ss}$$

$$\left(\frac{dv}{dt}\right)_e = \frac{-k''\int_0^v v'P_e(v')dv'}{\int_0^v P_e(v')dv'}G \qquad v>v_{se}$$
$$= 0 \qquad 0<v\le v_{se}$$

$$q_e(v) = k''G \qquad v>v_{se}$$
$$= 0 \qquad 0<v\le v_{se}$$

$$P_e(v) = \frac{1}{v\sqrt{2\pi}\ln\sigma_{ge}} \exp\left[-\frac{(\ln v - \ln\overline{v_{ge}})^2}{2\ln^2\sigma_{ge}}\right]$$

$$P_s(v,v') = \frac{1}{\sqrt{2\pi}\sigma_s(v')} \exp\left[-\frac{(v-\overline{v}_s(v'))^2}{2\sigma_s^2(v')}\right]$$

$$\overline{v}_s(v') = v'/v(v')$$

$$\sigma_s(v') = k_3 v'^g \overline{v}_s(v')$$

$$vc(v') = 2 + k_2 v'^p$$

$$\beta(v,v') = .31\left(\frac{\varepsilon}{\nu}\right)^{1/2}(v^{1/3} + v'^{1/3})^3$$

Nomenclature

α	=	binary collision efficiency
$\beta(v,v')$	=	collision frequency
v	=	particle volume at t
$c(v')$	=	average daughter floc size formed by splitting of parent flocs of size v'
$g(v')$	=	frequency of splitting parent floc v'
$P_s(v,v')$	=	probability density function of producing a daughter fragment on the size interval v, v + dv from the split of v'
$P_e''(v,v')$	=	probability density function of producing a daughter particle on size interval v, v + dv from the erosion of v'
$\left(\frac{dv}{dt}\right)_e$	=	volume erosion rate of a parent floc of size v
$q_e(v')$	=	total rate of formation (by number) of erosion fines of all sizes per eroding floc size v'
$\overline{v_{ge}}$	=	geometric mean
σ_{ge}	=	geometric standard deviation
v_{ss}	=	maximum stable size for splitting
v_{se}	=	maximum stable size for erosion

K_s, m, K_2, P, K_3, q = fitting parameters

Model Assumptions

1) Model is based on the assumption that 2 modes of floc breakage occurs: a) surface erosion of fine particles b) splitting of flocs into smaller fragments
2) Size distribution of erosion fines is independent of massive parent agglomerate
3) Turbulence is homogeneous and isotropic
4) Constant floc density

3) Koh et al (1986)

Model description

$$\frac{dn(2^j)}{dt} = \frac{3}{8}\beta(2^{j-2},2^{j-1})n(2^{j-2})n(2^{j-1}) + \frac{3}{4}\beta(2^{j-1},2^j)n(2^{j-1})n(2^j) + \beta(2^{j-1},2^{j-1})[n(2^{j-1})]^2 + \sum_{m=0}^{j-2}\left(\frac{2^j+2^m}{2^j}\right)\beta(2^j,2^m)n(2^j)n(2^m) - \sum_{m=0}^{h-1}\beta(2^j,2^m)n(2^j)n(2^m)\cdot q$$

$$q = 1 \qquad m \neq j$$
$$q = 2 \qquad m = j$$
$$\beta(i,j) = \frac{4}{3}\alpha(i,j)(a_i+a_j)^3 G$$
$$\alpha(i,j) = \alpha_0\left(1 - \frac{a_i+a_j}{2a_{max}}\right)^{\gamma}$$

Nomenclature

$n(2^j)$ = number of particles of class size 2^j
$\beta(i,j)$ = collision frequency function
$\alpha(i,j)$ = collision efficiency function
a_i = radius of particle size I
a_{max} = radius of maximum particle

G = average root mean square velocity gradient

Model Assumptions

1) An empirical collision efficiency function provides a continuous decrease in efficiency factor to zero as aggregate size increases.

2) Homogeneous and isotropic turbulence exists.

4) Chen et al (1990)

Model description

$$\frac{dn(d,t)}{dt} = B_a(d,t) - D_a(d,t) + B_b(d,t) - D_b(d,t)$$

$$B_a(d,t) = \frac{1}{2}\int_0^d \alpha[l,(d^3-l^3)^{1/3}]K[l,(d^3-l^3)^{1/3}]n(l,t)n[(d^3-l^3)^{1/3},t]dl$$

$$D_a(d,t) = n(d,t)\int_0^\infty \alpha(l,d)K(l,d)n(l,t)dl$$

$$D_b(d,t) = k_b d^\beta n(d,t)$$

$$B_b(d,t) = 2D_b(1.26d,t) = 2k_b(1.26d)^\beta n(1.26d,t)$$

$$K(l,d) = .1616(l+d)^3\left(\frac{\varepsilon}{\nu}\right)^{1/2}$$

Nomenclature

$B_a(d,t)$ = Birth rate due to agglomeration of smaller particles to size class d

$B_b(d,t)$ = Birth rate due to breakup from larger particles to size class d

$D_a(d,t)$ = Death rate due to agglomeration to larger particles from size class d

$D_b(d,t)$ = Death rate due to breakup of size class d to smaller particles

$K(l,d)$ = Collision frequency function

$\alpha(l,d)$ = collision efficiency function

k_b, β = fitting parameters

Model Assumptions

1) Particles aggregate into spherical, non-porous agglomerates
2) Collision frequency is based on Saffman & Turner (1956)
3) The breakup of an aggregate is a splitting process resulting in two fragments of equal size
4) Rate of breakup has a power law dependence
5) Particles do not lose the ability to reaggregate after being broken

5) Kusters (1991)

Model Description

$$\frac{dN(2^j)}{dt} = \frac{3}{8}J^*(2^{j-2},2^{j-1}) + \frac{3}{4}J^*(2^{j-1},2^j) + J^*(2^{j-1},2^{j-1}) + \sum_{m=0}^{j-2}\left[\frac{2^j+2^m}{2^j}\right]J^*(2^j,2^m) - \sum_{m=0}^{max-1}J^*(2^j,2^m) - J^*(2^j,2^j) - S^*(S2^j) + \sum_{i=j}^{max}\sum_{m=0}^{j-2}\left[\frac{2^j+2^m}{2^j}\right]\beta(2^j+2^m,2^i)S^*(2^i) + \sum_{i=j}^{max}\beta(2^j,2^i)S^*(2^i) + \sum_{i=j}^{max}\frac{3}{8}\beta\left(\frac{3}{4}\cdot 2^j,2^i\right)S^*(2^i) + \sum_{i=j}^{max}\frac{3}{4}\beta\left(\frac{3}{2}\cdot 2^j,2^i\right)S^*(2^i)$$

$$J^*(2^i,2^m) = f_r(2^j)\alpha(2^i,2^m)\left[D(2^i) + D(2^m)\right]^3 N(2^i)N(2^m)\pi\overline{sS_T}/4$$

$$D(2^j) = (2^{j/D})2a_1$$

$$S^*(2^j) = f_b(2^j)N(2^j)$$

$$f_r(2^j) = 2.94(\varepsilon_{min}/\bar{\varepsilon})^{1/2}erf\left((\varepsilon_b(2^j)/\varepsilon_{min})^{1/2}\right)$$

$$f_b(2^j) = \left(\frac{2}{\pi}\right)^{1/2}\left(\frac{2\varepsilon_{min}}{15\nu}\right)^{1/2}\exp(-\varepsilon_b(2^j)/2\varepsilon_{min})$$

$$\overline{S_T} = .68(2\bar{\varepsilon}/15\pi\nu)$$

Nomenclature

$N(s^j)$ = number concentration of size class 2^j

$J^*(2^i,2^m)$	=	effective collision frequency function
$S^*(2^j)$	=	effective breakup rate of aggregates of size class 2^j
$f_r(2^j)$	=	coagulation rate reduction factor for size class 2^j
$f_b(2^j)$	=	breakup frequency of size class 2^j
$\varepsilon_b(2^j)$	=	critical breakup energy dissipation rate of size class 2^j
ε_{min}	=	minimum energy dissipation rate in the stirred tank
$\bar{S}_T$	=	residence time weighted strain rate
$\beta(2^i,2^j)$	=	number of fragments of aggregates consisting of 2^i primary particles arising from breakup of aggregates made of 2^j primary particles
$\alpha(2^i,2^j)$	=	efficiency of collisions between aggregates consisting of 2^i and 2^j primary particles respectively

Model Assumptions

1) Homogeneous & isotropic turbulence exists in the flow field
2) Flow field in a fully baffled cylindrical tank is mostly 2 dimensional and axis symmetric
3) Breakup rate is first order in concentration
4) Three daughter size fragments are generated upon destruction of parent floc
5) Flocs break instantaneously when exposed to a critical shear stress

APPENDIX C

The LDV velocity data, LDV kinetic energy data, and the LDV energy dissipation rate at the impeller flow boundary were fitted with a least squares polynomial. The polynomials were then used as boundary conditions in the FIDAP simulation for the Rushton turbine and A310 foil impeller. The velocity data, k data, and ε data polynomials are presented below.

Rushton Turbine

(origin of axis at impeller blade tip centerline; Figure C.1)

T = 5L

$$\frac{v_{Tangent}}{v_{Tip}} = 0.6217 - 1.5418z^2 \quad v_{tip} = 27.9288 \text{cm/s}$$

$$\frac{v_{Radial}}{v_{Tip}} = 0.6289 - 1.5597z^2 \quad v_{tip} = 27.9288 \text{ cm/s}$$

$$v_{Axial} = 0.0$$

$$KE = 29.5672 - 5.1294z - 2.1144z^2 - 1.4936z^3 - 2.6874z^4 \quad (\text{units: } cm^2/s^2)$$

$$\varepsilon = 139.3186 - 136.8604z + 98.6041z^2 + 92.0621z^3 - 78.8428z^4 \quad (\text{units: } cm^2/s^3)$$

T = 28L

$$\frac{v_{Tangent}}{v_{Tip}} = 0.6217 - 0.4759z^2 \quad (v_{tip} = 33.5145 \text{ cm/s})$$

$$\frac{v_{Radial}}{v_{Tip}} = 0.6289 - 0.4814z^2 \quad (v_{tip} = 33.5145 \text{ cm/s})$$

$$v_{Axial} = 0.0$$

A310 Foil Impeller

(origin of axis at impeller hub centerline; Figure C.1)

T = 5L

$$\frac{v_{Radial}}{v_{Tip}} = 0.1147 - 0.5187r + 0.2015r^2 - 0.0175r^3 \quad (v_{tip} = 57.8524 \text{ cm/s})$$

$v_{Radial} = v_{Tangent} = 0.0$

$KE = 41.8528 - 75.5246r + 60.5632r^2 - 18.8768r^3 + 2.0283r^4$ (units: cm^2/s^2)

$\varepsilon = 906.8073 - 1995.4401r + 1580.2989r^2 - 515.3715r^3 + 59.1332r^4$ (unit: cm^2/s^3)

T = 28L

$$\frac{v_{Axial}}{v_{Tip}} = 0.1147 - 0.2882r + 0.0622r^2 - 0.003r^3 \quad (v_{tip} = 69.4229 \text{ cm/s})$$

$v_{Radial} = v_{Tangent} = 0.0$

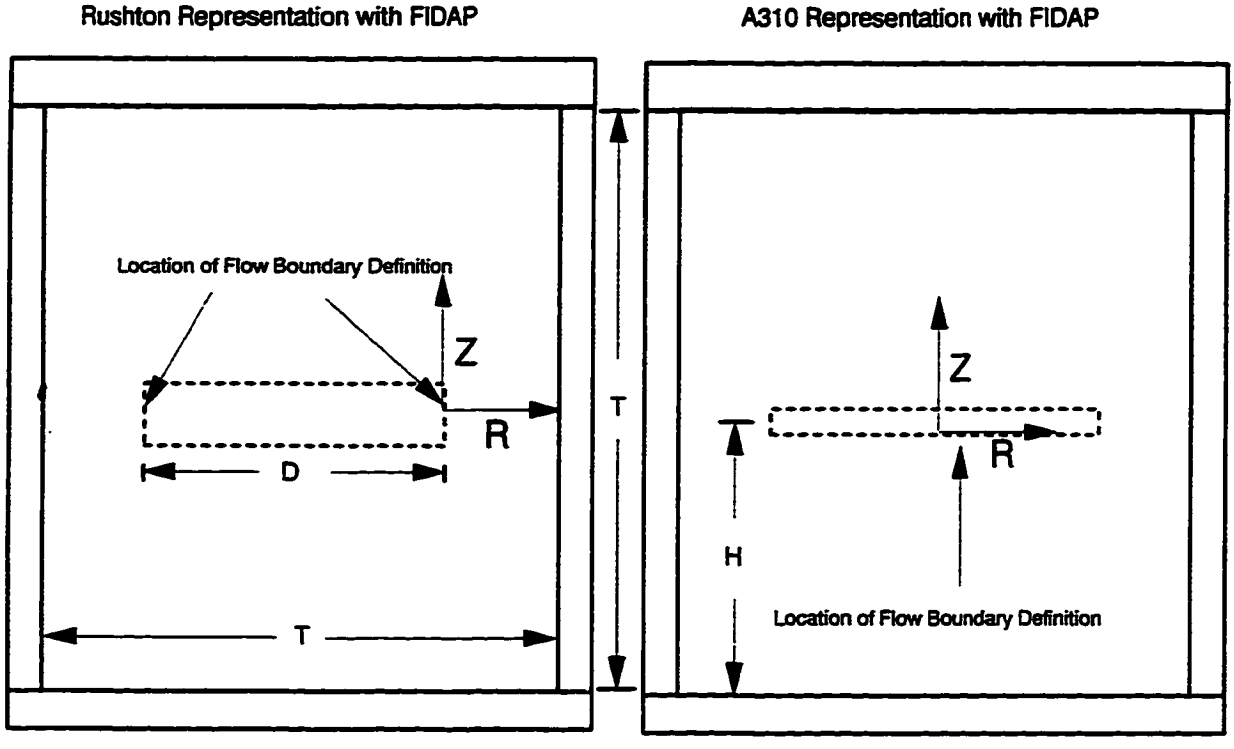

Figure C.1: Location of Origin for Boundary Conditions

VITA

Birth Date: August 14, 1966

Birth Place: Port Au Prince, Haiti

Education

University of Illinois	Champaign, IL
Doctor of Philosophy, Environmental Engineering	October 1996
Rensselaer Polytechnic Institute	Troy, NY
Master of Engineering, Mechanical Engineering	August 1989
Rensselaer Polytechnic Institute	Troy, NY
Bachelor of Science, Mechanical Engineering	May 1988

Research Experience

University of Illinois	*Urbana, IL*
Research Assistant	*9/91-9/96*

Conducted research in the area of particle agglomeration and breakup as it relates to the flocculation process in water and wastewater treatment.

- Developed a three dimensional finite element fluid mechanics model of the turbulence generated in a flocculation tank with a mixing impeller using a computational fluid dynamics software called FIDAP. Mean velocities, turbulent kinetic energy, and turbulent energy dissipation rates were computed by the model and compared with experimental results.
- Measured the turbulence generated in the flocculation tank using an experimental fluid mechanics technique called Laser Doppler Velocimetry.
- Designed a flocculation pilot plant to investigate the effects of tank size and impeller type on flocculation performance.
- Measured the particle size distribution in situ using an innovative photographic technique. Particles in the photograph were analyzed using an image analysis system.

- Developed a simple population balance model that simulates the change in flocculation performance due to changes in tank size and impeller type.

Developed a 2-D and 3-D finite element fluid mechanics model of a disinfection contact basin using FIDAP.

- Modeled the effects of tank geometry, baffles, and inlet & outlet locations on the residence time distribution of the disinfection contact basin.

Rensselaer Polytechnic Institute *Troy, NY*

Research Fellow *9/88-7/89*

Designed, built, and tested a compliant end-effector for a two arm IBM APAT assembly robot.

- Improved the range of the two arm robot to perform a successful peg in hole operation with an accuracy of 0.0001 inches by 0.25 inches.

Professional Experience

GE Aircraft Engine Business Group *Evendale, OH*

Maintenance Supervisor *1/91-8/91*

Managed the daily work assignment of eighteen trades persons involved in the maintenance of all machine tools in the Airfoils and Fabrications Parts Operation.

Sales Engineer *7/90-1/91*

Provided technical support and competitive analysis for sales campaigns to maximize GE's competitive advantage. This included developing a competitive risk analysis to highlight areas of strengths and weaknesses, creating performance comparisons to evaluate future competitive threats, and developing customer briefings/questionnaire responses.

- Designed and implemented an online computerized database of customer questionnaire answers which led to improved response time for customer questionnaires.

Construction Planner *1/90-7/90*

Planned and scheduled all rearrangements, machine tool installations, material handling jobs, and office construction work performed by in-plant personnel within the Evendale complex.

- Established a formal procedure for project "check-out" and "sign-off" to assure customer satisfaction.
- Coordinated the different trades required to complete a construction project.
- Provided support and training for a computerized project management software in order to improve construction planning efficiency.

Production Control Specialist *7/89-1/90*

Managed the planned input of tooling, organized the flow of hardware through the shop, and ensured shipment dates of material.

- Improved production control forms which streamlined the production control process.
- Managed the development plans to install a new parts tracking system.
- Developed a priority information system to increase the productivity of the production control specialist.

Mobil Chemical Company *Frankfort, IL*

Process Engineer *5/88-8/88*

- Designed and supervised construction of a unitized case sealing assembly which increased the box, pack, and ship process and reduced sealing errors by 35%.
- Analyzed and upgraded the performance of high speed thermoformers which reduced the changeover time by 20%.

Personal Information

Member, American Water Works Association

Member, National Society of Professional Engineers